



HAL
open science

Dynamic failure precursors in soft matter

Stefano Aime

► **To cite this version:**

Stefano Aime. Dynamic failure precursors in soft matter. Soft Condensed Matter [cond-mat.soft]. Université de Montpellier, 2017. English. NNT: . tel-01801958v1

HAL Id: tel-01801958

<https://theses.hal.science/tel-01801958v1>

Submitted on 28 May 2018 (v1), last revised 14 Sep 2018 (v2)

HAL is a multi-disciplinary open access archive for the deposit and dissemination of scientific research documents, whether they are published or not. The documents may come from teaching and research institutions in France or abroad, or from public or private research centers.

L'archive ouverte pluridisciplinaire **HAL**, est destinée au dépôt et à la diffusion de documents scientifiques de niveau recherche, publiés ou non, émanant des établissements d'enseignement et de recherche français ou étrangers, des laboratoires publics ou privés.



THÈSE

Pour obtenir le grade de
Docteur

Délivré par l'Université de Montpellier

Préparée au sein de l'école doctorale Information structure systèmes
Et de l'unité de recherche Laboratoire Charles Coulomb

Spécialité : **Physique**

Présentée par **Stefano AIME**

Dynamic failure precursors in soft matter

Soutenue le 14/09/2017 devant le jury composé de

M. Luca Cipelletti	Professeur, Université de Montpellier	Directeur de thèse
Mme Sylvie Cohen-Addad	Professeur, Université Pierre et Marie Curie	Président du jury
Mme Emanuela Del Gado	Professeur, Georgetown University	Rapporteuse
M. Thibaut Divoux	Chargé de recherche, CNRS	Examineur
Mme Laurence Ramos	Directrice de Recherche, CNRS	Co-directrice de thèse
M. Dimitris Vlassopoulos	Professeur, IESL-FORTH	Rapporteur



A Silvia e Giovanni

Acknowledgements

July 6th, 23h30, Montpellier, France. After 3 years, here we go: my PhD Manuscript is finally submitted. It's time to close my office, run back home and pack my bags, since the bus is leaving in two hours for Italy.

July 6th, 23h55, Monza, Italy. After 9 months (a bit less actually...), here we go: Giovanni, my first son, cries his first wail to the world and to his mother Silvia. A few minutes later, a WhatsApp message announces the event, reporting the unforgettable sound of his voice.

The last period has been so intense that it takes a while to realize the situation, but as I finally take my place in the bus, among the many confused thoughts that flood my mind, one clear feeling dominates: gratitude. That's why I am glad to open my manuscript with a huge thanks to all the people who accompanied me during this journey and who made it possible.

First and foremost, I would like to express my sincere gratitude to my supervisors, Luca and Laurence, who looked after me during these years with fatherly care, following with interest and commitment my progresses. Thank you, Luca and Laurence, because you gave me the opportunity to explore, follow my intuitions and find my own way like a child taking his first tentative steps, but you always assured me your support and suggestions every time I needed. Thank you, because under your enthusiastic and proactive supervision I had a great time, and never got bored. Thank you, because following, sometimes tentatively, your example, I grew up so much more than I had expected.

Second, I want to thank Thibaut Divoux and Dimitris Vlassopoulos for having followed my work step by step during these years, valorizing it and stimulating it with insightful discussions: many of the original ideas presented in this manuscript arose from their comments and suggestions. I also want to thank them, together with the other committee members, Emanuela Del Gado and Sylvie Cohen-Addad, for the enjoyable and instructive discussion that followed my PhD defense. Special thanks to Dimitris and Emanuela as well for accepting to read and evaluate this manuscript.

This thesis has been carried out in the framework of the EU Marie Curie Initial Training Network SUPOLEN (grant n. 607937), to which I am grateful not only for the funding and for the travel opportunities, but also for the high level multidisciplinary training I received all along my PhD. In particular, I am grateful to Daniel Read, Michael Rubinstein and Giuseppe Marrucci for their inspiring courses on polymer physics, to Wim Briels for his course on statistical physics, to Dimitris Vlassopoulos for his course on rheology, to Gareth McKinley for his course on fractional calculus, and to Evelyne van Ruymbeke for the coordination of the project. Moreover, I have to thank SUPOLEN for encouraging exchange programs with industrial partners, in which framework I had the opportunity to spend two months in the Research and Development department of DSM Ahead (Geleen, The Netherlands). It was a great experience, for which I want to thank

Carel Fitié and Luna Imperiali, as well as Tom Engels and Nancy Eisenmenger for their kind supervision.

I am also grateful to French ANR project FAPRES (grant n. ANR-14-CE32-0005-01) for funding and for promoting fruitful scientific exchange with the project partners, especially on the theoretic aspects of my work. In particular, I want to thank Kirsten Martens, Eric Bertin, Serge Mora and Christian Ligoure.

During my PhD, I had the opportunity to attend the Bombannes summer school on scattering. It was a unique learning experience, for which I want to thank the organizing committee and all the lecturers. In particular, I am truly grateful to Julian Oberdisse, for his course free of math and full of physical concepts, and to Otto Glatter, for his course on the inverse scattering problem, which taught me, to use his own words, that science is fun only if you are open for surprise.

Finally, I want to thank Ty Phou, Guillaume Prévot, Remi Jelinek and Jerome Barbat for technical support, Tina Rabeharivelo, Adoration Gabillard, Stéphanie Martegoutes, Béatrice Tomberli and Jean-Christophe Art for help with administrative tasks (not exactly my strong point), Justine Pincemaille and Dafne Musino for help with neutron scattering experiments, Adrian Philippe for sample preparation, Vishal Metri and Domenico Truzzolillo for stimulating discussions.

In the beginning of June 2013 my studies in physics at the University of Milan were about to finish, and I was looking for a master thesis, disoriented as a student who faces for the first time the vastness of the world. At that time, there was one person that, without asking for permission, came to me, gave me a few criteria to choose wisely among the myriad of opportunities, and finally suggested me to contact Luca Cipelletti. He is Roberto Cerbino, now associate professor at the University of Milan: we knew each other since I had spent a few months in his group for my bachelor thesis a couple of years before, and I probably will never thank him enough for his providential interference in that delicate moment of my life.

Together with Roberto, to whom I am also grateful because he introduced me to the fascinating world of light scattering and optical microscopy (I will never forget the first time I switched on a microscope after he explained me how the image was produced in my eyes), I would like to thank all the people who first instilled and then developed my passion for science. The list would be far too long to be mentioned here, but among all I would like to mention specially my father Fabio, and then my high school professors Alda Pellegrini, Raffaella Manara, and Paolo Bartesaghi who supervised my first scientific research on the geometric and mechanical properties of spider webs. Among my professors in University of Milan, I would like to mention Luciano Mandelli, Alberto Vailati, Antonio Giorgilli and Stefano Forte for their fantastic courses on classical, analytical and quantum mechanics, Luca Molinari for showing me the charm of theoretical physics, Luciano Reatto for teaching me, throughout his old-school course on statistical physics, that the whole is greater than the sum of its parts, and finally Giorgio Rossi and Marco Potenza for introducing me to experimental physics. I also owe much to Filippo Bertelli and Guido

dell'Orto from 4edu s.r.l., with whom I worked during my high school learning teamwork and computer programming.

Finally, I would like to thank all the people who contributed to my personal growth and liberal arts education, laying the foundation for a more balanced and open-minded approach to science. In particular, I would like to thank my first teachers Paola, Loredana, Serena and Cristina: the start of school has been a true shock for me, and your love was vital; don Giorgio, for welcoming me with a smile and a hug every morning for many years in the school hallway; Sergio, for teaching me how to play football and to play it in a team, and Fonta, for the basketball experience: results on the court were mediocre, but the human side of that experience was great; Paolo, Luca, Ivano and Massimo, as well as my grandmother Meris, for cultivating my passion for music; prof. Lapini, for teaching me technical drawing, which was so important during my PhD; prof. Olgiati, because I will never forget your first art history lesson: few people have shaped my mind so deeply in such a short time; prof. Giussani, because I learned to be serious about school thanks to you; prof. Cuccato, Bernabei and Fantolini, for taking me seriously in a delicate period of my life; prof. Macchi, for the passion for latin and Medieval literature and for Dante's verses that I still know by heart and still speak to me; prof. Bersanelli, because your way of doing science and talking about science bringing out its human side is fascinating and unique.

One classic question that was asked me after my PhD defense is: how do you feel now that you are a doctor? Caught off-guard by such question, I immediately realized that the answer was simple: just the same as before, perhaps with a bit more spare time to spend with my family. However, if on the one hand this hard-fought achievement left me unchanged, on the other hand it is clear as day that these years in Montpellier have deeply shaped my personality, and brought profound changes to my life. This happened mostly thanks to the company of so many old and new friends, to whom I address my deepest thanks.

Thanks to all friends from the L2C Soft Matter team: Elisa, for your welcome in Montpellier and your coaching during my first period in the lab; Luca, because you never allowed me to keep to myself and for the many Saturday afternoons in your place; Domenico, for hosting me, for your friendly and open-minded attitude, and for your continuous help, support and suggestions; Giuseppe, for your quiet but warm friendship; Clara and Adrian, for your conversations and your patient French courses-on-the-court; Rym, for leading our relay marathon team to victory; Cyrille, for the unforgettable bike tour on Mont Ventoux; Yassine, for all the fun time in Naples and eating tacos; Dario, for the summer spent eating toasts and working together before our respective marriages, and for the dinners in your place (thank you, Silvia, as well); Dafne, for remembering me from time to time that there were other people around me; Angelo, for teaching me patience and composure in front of the many obstacles faced in scientific research; Abir, for your enthusiasm and for the courage to always speak the truth, however inconvenient that truth may be; Anthony, for the best lab Christmas lunch of the last years; Myriam,

for sharing the office and bearing lots of italian chats without complaining; Alexey and Antonio, for our weekly basketball matches interrupted only by injuries; Martin, for the nontrivial talks during lunch; Guilhem, Salvatore and Ameer, for our SUPOLEN experience together; Vero and Savo, for bringing happiness and unpredictability to our lab; Smile, for your precious silent company during these years; Camillo, Fernando, Haifa, Laura, Alexandre, Benoit, Elise, Thibaut, Fanny; and of course thank you Srishti, my sister-in-science: thank you for your candor and your friendship all along our PhD.

When I first arrived in France I knew strictly nobody there, and my French vocabulary was restricted to very few words hardly memorized during the train trip, not even enough to ask for directions, as I realized at my own expense when I got off the train. I knew that learning a language and making new friends is also a matter of time, but I definitely couldn't expect the wealth of friendship that was waiting for me. Thanks therefore to all other friends from Montpellier (Titti, Filippo, Angelo, Anna, Ederson, Pamela, Giorgia, Virgilio, Clara, Sarah, Pierre, Greg, Claire, Diana, Elena, Valérie, Jean Baptiste, Véronique, and of course thank you René-Luc, for the fatherly company of these years) and from the rest of France (Davide, Mirco, Eloisa, Jeff, François, Cate, Olivier, Pierre and Sapi, Roberto, Sylvie, Hayat, Isabelle, Cami, Silvio, Piero and Martina, Philippe, Turo and Chiara, Richi and Marta, Canni, Scara, Robi, Pit, Ferra, and Gufi, because coming to your place in Paris has always been like coming back home). I would like to thank as well my old italian friends: I will always remember the dinner and the songs together the evening before my departure for Montpellier, with the gratitude mixed to the sense of bewilderment of who is afraid of losing something precious. Now I can say that the 700km that separated us during these years even refined our friendship, and I'm now closer (despite the distance) to many of you than I was before leaving.

Finally, my deepest gratitude goes to my family: to my parents, Chiara and Fabio, and to my brothers and sisters, Francesca, Maddalena, Giovanni and Marco. If I fully enjoyed my PhD, through all the ups and downs of scientific research, it was to a large extent thanks to their endless love and support, unaffected by geographical distance. Breathing the fresh air of our unique *normal family* has been essential to truly appreciate the moments of excitement and to go through the moments of dismay without being overwhelmed by them.

Last, but certainly not least, I want to thank who above all changed my life during the time span of my PhD. Silvia, three years ago you had the courage of leaving your job, your country, and your certainties, to follow me in this adventure. Was it insane? Perhaps it was, but time has shown that the seed planted back then was good enough to put down roots, stronger than the aridity of circumstances so often different from our plans. To conclude, thank you Giovanni, long-awaited son. Thank you, because you are a great and undeserved gift, and the happiness you brought to our family with your slow, imperceptible growth in Silvia's womb supported much of the efforts required by the last intense working period, one of the most beautiful periods of my life.

Contents

Ouverture	1
1 Motivation and State of Art	3
1.1 Objectives, originality and novelty	3
1.2 Historical excursus	11
1.3 State of the art	15
1.4 Outline of the thesis	46
2 Experimental Methods	49
2.1 Light Scattering	49
2.2 Rheology	59
I Light scattering under shear	69
3 A stress controlled shear cell for small-angle light scattering and microscopy	71
I Introduction	
II Setup	
III Setup characterization	
IV Tests with model samples	
V Dynamic light scattering under shear	
VI Conclusion	
4 Scattering signal from shear-induced nonaffine deformations	85
1 Introduction	
2 Materials and methods	
3 DLS for a sheared sample	
4 Conclusions	
II Colloidal gels	99
5 Structure, dynamics and viscoelastic properties	101
5.1 Introduction	101
5.2 Theoretical background	104
5.3 Material and methods	106
5.4 Results	108
5.5 Discussion	115

6	Microscopic dynamics and failure precursors of a gel under mechanical load	119
7	Irreversible dynamics under large amplitude oscillatory shear	129
7.1	Yielding transition in large amplitude oscillatory shear	129
7.2	Delayed yielding in LAOStress	135
7.3	Structural evolution under an oscillatory stress	137
7.4	Correlation echoes track plasticity across cycles	139
7.5	Discussion	143
III	Colloidal glasses	145
8	Dense microgel suspension: dynamics under shear	147
8.1	Introduction	147
8.2	Sample preparation	148
8.3	Structure and dynamics at rest	150
8.4	Rheology	153
8.5	Reversible and irreversible nonaffine dynamics	154
8.6	Conclusion	161
	General Conclusions and Perspectives	163
A	An efficient scheme for sampling fast dynamics at a low average data acquisition rate	175
1	Introduction	
2	Acquisition time scheme	
3	Materials and methods	
4	Results and discussion	
5	Conclusions	
B	A model for failure in thermoplastic elastomers based on Eyring kinetics and network connectivity	183
I	Introduction	
II	Materials and methods	
III	Experimental observations	
IV	Kinetic model	
V	Simulations	
VI	Conclusion	
	Bibliography	199

Overture

Most children learn early that things break, whether it is a stick excessively bent or a favorite toy dropped from sufficient height. Such events teach us that we have to protect our belongings from mechanical overload if we want to keep them safe. Nevertheless, it is with our greatest disappointment that from time to time we realize that our efforts were not enough: posters pinned to the wall fall down unexpectedly days after we accurately fixed them, and the cable of our laptop charger gets damaged after being bent several times. Yet, the poster appeared to be well fixed before, and the cable could safely withstand a few bending cycles without apparent damage.

Failure is the term conventionally used to indicate that something does not work anymore as it is supposed to do. Many little annoying examples demonstrate that failure is very often undesired, uncontrolled and unpredicted. This is all the more true for large scale catastrophic events, like the collapse of bridges or dams, but also geological events like snow avalanches, landslides or earthquakes. When such events happen, all of a sudden, the question that emerges is: *Why?* Which means: *For what reason?* but also: *Why then, not earlier nor later?* As a matter of fact, both questions are unanswered, and still challenge the mind of many scientists with widely different backgrounds, from geology and engineering to physics, chemistry and biology. Surprisingly, or maybe unsurprisingly, it turns out that what is so common in our daily experience is based on profound science that is not yet fully understood.

The complexity of failure mainly lies in its multiscale nature: a massive snow avalanche always arises from tiny cracks between snowflakes, and its origin cannot be fully understood without tracing back to them. Furthermore, accessing these microscopic events from which failure originates holds the promise of providing a means of predicting the collapse before its occurrence, which in most cases appears far too difficult, if not impossible, only looking at macroscopic observables. Any measurable feature anticipating failure, which is thus exploitable for its prediction, is called a precursor. Failure precursors do exist (for instance, animals behave differently before an earthquake, which indicates that they can feel it approaching), but detecting them and recognizing them in their role of precursors is extremely challenging, which explains the scarcity of successful works in this field so far. In fact, if it is now recognized that purely macroscopic approaches are doomed to fail, combining macroscopic and microscopic investigation is still far from trivial, for several reasons that will be discussed in chapter 1.

In this work we present one of the first successful attempts to measure microscopic failure precursors in model soft solids. Here, microscopic plasticity under shear is observed using a novel setup, presented in part I, coupling a custom-made stress controlled shear cell to small angle static and dynamic light scattering. The main results come from the study of a colloidal gel, and will be discussed in part II, whereas in part III the generality of those results is examined by comparing them with a colloidal glass.

Motivation and State of Art

Contents

1.1	Objectives, originality and novelty	3
1.1.1	Material failure in our everyday life	3
1.1.2	Failure in soft materials	5
1.1.3	Key questions	6
1.1.4	Challenges	9
1.2	Historical excursus	11
1.3	State of the art	15
1.3.1	Steady-rate experiments	15
1.3.2	Creep experiments	20
1.3.3	Dynamic fatigue test	32
1.3.4	Conclusion	45
1.4	Outline of the thesis	46

1.1 Objectives, originality and novelty

1.1.1 Material failure in our everyday life

Material failure is ubiquitous on length scales ranging from a few nanometers, as in fracture of atomic or molecular systems [Weibull 1939, Célarié 2003] up to geological scales, as in earthquakes [Myers 2001, Ben-Zion 2008]. While some attempts have been made to harness failure, e.g. in order to produce new materials with a well controlled patterning [Nam 2012], material failure remains in general an unwanted, uncontrolled and unpredictable process. Indeed, a better control of the conditions under which material failure may or may not occur and the detection of any precursors that may point to incipient failure are the Holy Grail in many disciplines, from material science [Amon 2013, Guarino 2002, Pradhan 2005, Vinogradov 2012, Koivisto 2016] and biology [Bell 1978, Erdmann 2004, Buehler 2009, Gobeaux 2010] to engineering [Bazant 1991] and geology [Jones 1979, Sommerfeld 1982, Swanson 1983, Sommerfeld 1983, Voight 1988,

McGuire 2005, Wu 2006, Ancy 2007, Duputel 2009, Van Herwijnen 2011a, Van Herwijnen 2011b, Kato 2012, Johnson 2013, Bouchon 2013, Kromer 2015, Agioutantis 2016]

Failure may occur almost instantaneously, as a consequence of an impulsive load [Field 2004]: in this case the main interest typically consists in evaluating the damage as a function of impact speed and energy [Richardson 1996, Camacho 1996, Ball 1999]. Often, however, it manifests itself in more elusive ways, as in the sudden, catastrophic breakage of a material submitted to a constant or cyclic load, where failure may be preceded by a long induction time with little if any precursor signs of weakening [Basquin 1910, Andrade 1910]. In the latter case, sometimes referred to as dynamic fatigue failure [Kahn 2004], one has the possibility to monitor the stroboscopic evolution of micro to mesoscopic damage developing before macroscopic failure [Ewart 1986, Patra 2016], whereas such a detection is much more delicate in the former case.

Delayed failure under a constant load has been reported in a wide spectrum of phenomena, from large scale systems such as earthquakes [Lockner 2002, Ōnaka 2013], rock sliding [Kromer 2015], snow avalanches, [Reiweger 2010] and structural materials [Bazant 1991, Maekawa 2016] to small scale ones such as biological materials [Bell 1978, Erdmann 2004, Gobeaux 2010] relevant to bioengineering [Anwar 2009]. Other examples include crystalline [Poirier 1985] solids like metals [Troiano 1959, Nakasato 1980, Golub 2003], ice [Ashby 1985, Sinha 1988] or colloidal polycrystals [Bauer 2006], as well as composite materials such as wood [Guarino 2002], paper [Koivisto 2016] or synthetic fibers [Nechad 2005b], and amorphous systems [Preston 1942, Gurney 1947, Aoki 1980], including viscoelastic soft materials [Gopalakrishnan 2007, Gibaud 2010, Divoux 2011, Siebenbürger 2012, Grenard 2014, Sentjabrskaja 2015], such as adhesives [Sancaktar 1985] and network-forming materials [Bonn 1998, Poon 1999, Skrzyszewska 2010, Sprakel 2011, Leocmach 2014].

The widespread occurrence of delayed failure represents a challenge for the durability of objects and structures, a well known problem in civil engineering [Bazant 1991]. In order to design durable applications, structural parameters have to be optimized, which requires control of the material lifetime under realistic conditions. Conversely, knowledge about the stress required to trigger failure and flow is relevant in other applications, from industrial processing to oil extraction and transportation, where engineers face the well known problem of pipe clogging [Zuriguel 2015, Van de Laar 2016, Koivisto 2016]. Thanks to the power of modern simulation schemes, nowadays such knowledge can often be considered satisfactory for applications, but it remains essentially empirical and system-specific: much still has to be done in order to achieve a unitary description of those phenomena.

At the same time, diagnosis of mechanical faults on existing structures is required in order to assure proper maintenance [Collacott 1977]. This is extremely important not only in civil engineering, where the catastrophic collapse of bridges, dams or buildings still represents a relevant origin of casualties, but also in the transportation industry, as in railway maintenance or in aircraft industry, where maintenance is delicate and expensive. As an example, more than 60% of the total ownership costs for US aviation

are represented by aircraft maintenance, due to inefficient Condition Based Maintenance (CBM) system [Bell 2008].

On a still larger scale, the detection of precursors of catastrophic events such as earthquakes, rockslides, landslides, snow avalanches or volcano eruptions is certainly of paramount importance for many self-evident social, economical and environmental reasons. It has been argued [Sommerfeld 1982, Voight 1988, Bouchon 2013, Kromer 2015] that this prediction might be achieved, and indeed in 1975 the Chinese Seismological Bureau successfully predicted a magnitude 7.3 earthquake [Jones 1979]. However, despite the optimistic wave generated by such successful prediction, to the best of our knowledge this remains the only documented example, although *a posteriori* analyses could in some cases identify detectable precursors [McGuire 2005, Duputel 2009, Van Herwijnen 2011b, Kato 2012].

1.1.2 Failure in soft materials

Because of the outstanding relevance for many applications and its interest from a fundamental point of view, material failure represents a very active field of research, which has the interesting feature of being multidisciplinary, arousing the curiosity of researchers with widely different backgrounds.

In particular, material failure is relevant to soft matter physics, where the typical energy scale governing interactions between particles is of the order of thermal energy: for this reason, soft materials are generally characterized by large mechanical susceptibilities, and they respond to small or moderate stresses with large deformations, often displaying yielding and failure under a suitable range of applied stresses. Typical examples include emulsions [Liu 1996, Mason 1996], foams [Kabla 2007, Cohen-Addad 2013, Dallet 2014], polymer gels [Bonn 1998, Baumberger 2006, Skrzyszewska 2010, Karobi 2016], and suspensions of colloidal particles, quenched out of equilibrium because of crowding [Siebenbürger 2012, Sentjabrskaja 2015] or of the presence of attractive interactions [Poon 1999, Gopalakrishnan 2007, Gibaud 2010, Sprakel 2011, Grenard 2014].

Because of its widespread occurrence, failure in soft materials has strong implications for many everyday life and industrially relevant problems, including the processing of food [Van Vliet 2013], such as gluten [Ng 2008], starch [Vliet 1995], dough [Moriera 2011], gelatine [McEvoy 1985, Groot 1996], thickeners [Ma 1996, Jaishankar 2014], yogurt [Leocmach 2014], and cheese [Faber 2017b], or biomaterials, such as living cells [Desprat 2005, Kollmannsberger 2011], tissues [Bell 1978], biopolymer networks [Wagner 2006, Janmey 2007, Gobeaux 2010] or protein assemblies [Liu 2007, Lieleg 2010, Brenner 2013].

Soft materials are excellent systems to investigate material failure, because their characteristic time and length scales are more readily accessible to experiments as compared to those of atomic systems: this opens the way to a detailed structural and dynamical characterization both before and after failure occurs. Moreover, a large variety of soft sys-

tems with a wide spectrum of interactions and structural and dynamical characteristics are available, thus allowing one to pinpoint the key parameters controlling the observed phenomena, possibly unveiling general behaviors. For these reasons, the emerging analogies between soft and hard materials [Schmoller 2013, Keshavarz 2017] make soft materials an ideal benchmark to investigate how a mechanical stress impacts condensed matter. Finally, the increasing relevance of soft materials in everyday life, as well as in industrial processes like for example in food industry [Stokes 2012, Spagnolie 2015, Faber 2017a] further alimnts the interest in a deeper understanding of their behavior under stress.

1.1.3 Key questions

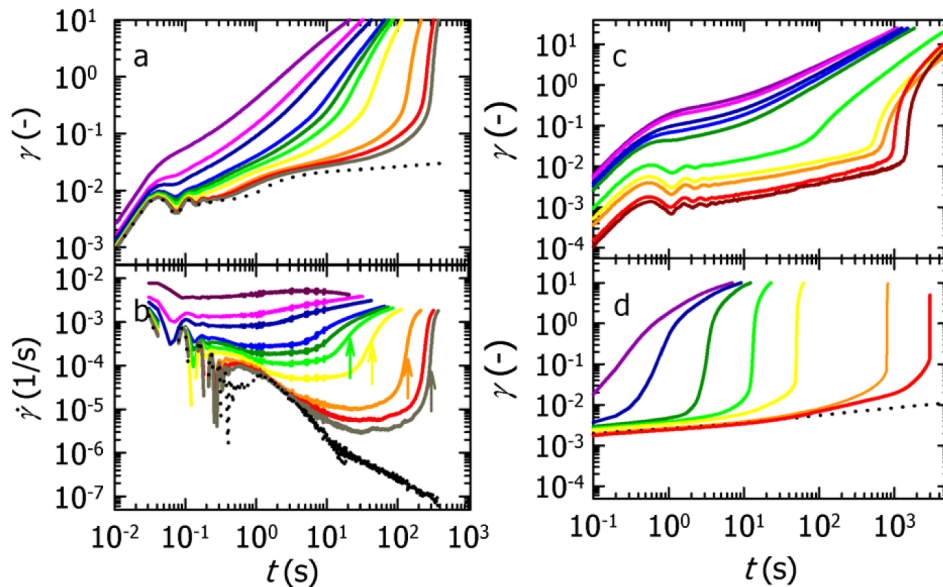


Figure 1.1: (a) Creep response of 8 wt% carbon black gel under a constant stress σ decreasing from left to right and (b) corresponding shear rate $\dot{\gamma}$. (c) Creep curves for a weak depletion gel of polystyrene particles and (d) for thermoreversible stearylated silica gels. Extracted from [Sprakel 2011].

Figure 1.1 illustrates an example of the delayed failure events that we address in this work. The sample is submitted to a constant mechanical shear stress that is applied at time $t = 0$, and it undergoes a very fast, solid-like deformation, followed by a so-called creep regime where the shear strain γ grows sublinearly, either logarithmically or as a power-law of time [Cottrell 1952]. Remarkably, this regime may last even hours, depending on the applied stress, until it is suddenly interrupted by a sharp increase in γ signaling material failure and the onset of flow.

The effects of failure are obvious at the macroscopic scale, and yet the dynamics that lead to such failure are governed entirely by the material's behavior at the smallest scales. Thus, to better understand the observed delayed onset of flow, we start investigating the

microscopic processes governing creep. Interestingly, although the ultimate fate of the material (formation of shear bands, ductile vs fragile fracture, permanent vs reversible damage) may differ according to the system, the macroscopic behavior before failure is quite general, as one can see by comparing the three samples investigated in Fig. 1.1.

Power-law creep is widespread in both crystalline and amorphous materials, however in the former case it is well understood and attributed to defect motion [Andrade 1910, Cottrell 1952, Poirier 1985, Miguel 2002], whereas in the latter case its microscopic origin remains controversial. Indeed it has been attributed in turn to the accumulation of irreversible, plastic rearrangements [Nechad 2005b, Caton 2008, Cousot 2006, Siebenbürger 2012, Sentjabrskaja 2015, Karobi 2016], to linear viscoelastic relaxation processes [Balland 2006, Gobeaux 2010, Leocmach 2014], or to a combination of both [Jagla 2011, Kun 2003], with different authors holding contrasting views on similar systems [Jagla 2011, Nechad 2005b].

For this reason, the first question that we want to answer with our work is the following: **What is the nature of the microscopic dynamics during the creep regime?**

More precisely, we want to understand if the power-law creep of amorphous systems is governed by the same irreversible microscopic processes evoked for crystalline solids, or if for those viscoelastic materials other deformation mechanisms are allowed, not necessarily implying structural damage, as it has been suggested for widely different systems, from biomaterials such as cells [Fabry 2001, Djordjevic 2003, Desprat 2005, Balland 2006, Kollmannsberger 2011, Hecht 2015], tissues [Kohandel 2005, Davis 2006, Freed 2006, Sinkus 2007, Klatt 2007, Shen 2013, Bentil 2014], or biopolymer networks [Amblard 1996, Gobeaux 2010, Patricio 2015] and pastes [Józwiak 2015], to food materials [Ma 1996, Zhou 1998, Goh 2003, Subramanian 2006, Caggioni 2007, Ng 2008, Korus 2009, Moreira 2011, Ronda 2013, Xu 2013, Jaishankar 2014, Leocmach 2014, Faber 2017a, Faber 2017b], colloidal gels [Grenard 2014] and polymer gels [Hung 2015, Lidon 2017], melts [Plazek 1960, Cherièrè 1997, Friedrich 1999, Hernández-Jiménez 2002, Metzler 2003], elastomers [Curro 1983] and composites [Metzler 1995].

Crucially, a detailed understanding of the creep regime holds the promise of unveiling the origin of the sudden failure of the material, potentially revealing any precursor signs of failure, which are difficult to detect by monitoring macroscopic quantities, such as the deformation rate [Koivisto 2016]. For this reason, the second question that we plan to answer with our work is the following: **How does the microscopic dynamics change as failure is approached? Could such evolution provide a means to detect an incipient failure?**

In order to properly address these questions, a different experimental protocol, represented in Fig. 1.2, can also be usefully employed, where yielding is not observed under constant stress, but under an oscillating stress (or strain, as in Fig. 1.2) with increasing amplitude. In such experiments, one typically observes a first linear regime, in the limit of small deformations, where the stress grows linearly with strain amplitude and the so-called viscoelastic moduli are independent of deformation. In this regime, linear rheology teaches us about the mechanical properties of the *unperturbed* sample, which in the case

of Fig. 1.2 is predominantly solid. However, when the sample is driven far enough from equilibrium (beyond γ_c in Fig. 1.2) it develops an amplitude-dependent response, with a growing loss modulus, which indicates that additional, nonlinear dissipative processes are triggered by the imposed deformation. Such processes become increasingly relevant at still higher amplitudes, and concomitantly the elastic modulus decreases, up to a point where the two moduli cross each other, so that in the large amplitude limit (beyond γ_f in Fig. 1.2) the mechanical response will be dominated by the loss modulus, showing that the initially solid-like material was fluidized by the applied deformation. Interestingly, this transition can be grasped as well by the stress vs. strain curve, which displays a clear crossover (around γ_y in Fig. 1.2) between the initial linear regime and the shear-thinning regime observed at larger amplitudes.

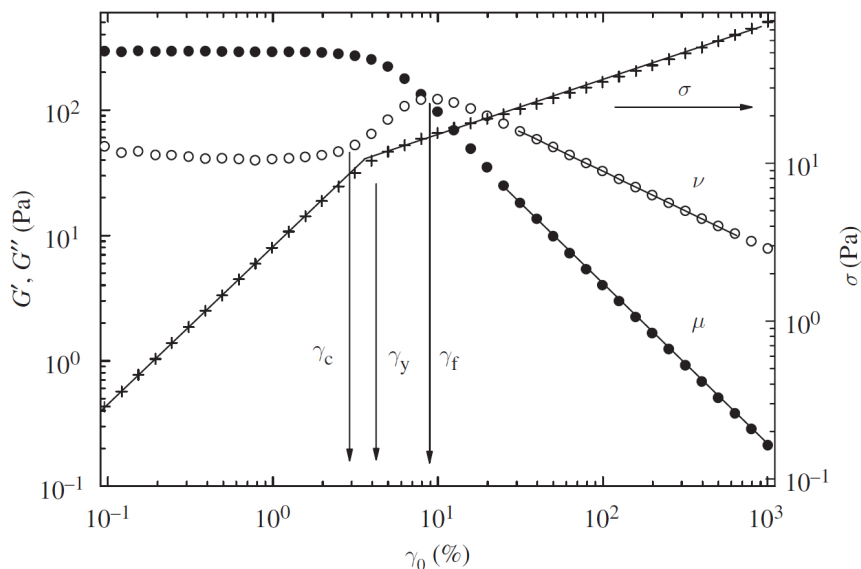


Figure 1.2: Circles, left axis: viscoelastic moduli G' (filled) and G'' (empty) for different values of the imposed strain amplitude γ_0 . Crosses, right axis: amplitude of the stress response as a function of strain. The vertical arrows indicate the end of the linear regime (strain γ_c), the onset of (viscoplastic) yielding (strain γ_y) and complete fluidization, that is, liquid-like response (strain γ_f). The sample is a star polymer solution. Extracted from [Christopoulou 2009].

The qualitative features observed in Fig. 1.2 seem to be quite general, being observed in a variety of soft systems like polymer solutions [Tirtaatmadja 1997], composites [Payne 1963], emulsions [Mason 1996, Bower 1999, Knowlton 2014], as well as colloidal gels [Raghavan 1995, Raghavan 1997, Yziquel 1999, Christopoulou 2009, Gibaud 2010, Kim 2014, Perge 2014, Moghimi 2017], glasses [Derec 2003, Petekidis 2003, Craciun 2003, Pham Trong 2008, Carrier 2009, Rogers 2011, Koumakis 2013, Hima Nagananasa 2014] and polycrystals [Louhichi 2015], whereas some other systems show a characteristic two-step yielding process, with a peculiar intermediate regime between

the onset of the nonlinear regime and the complete fluidization [Altmann 2004, Helgeson 2007, Pham Trong 2008, Koumakis 2011, Laurati 2014, Agrawal 2015, Brunel 2016].

Oscillatory yielding of soft solids has been rationalized by various models [Sollich 1998, Derec 2003, Miyazaki 2006, Carrier 2009, Radhakrishnan 2016], based on the idea that sample relaxation dynamics are essentially unperturbed by small amplitude shear, whereas the appearance of stress-induced plastic rearrangements determines the onset of the nonlinear regime at amplitudes beyond a given threshold. However, such threshold appears to be difficult to define unambiguously [Bonn 2017], as one can appreciate from the difference between γ_c , γ_y and γ_f in Fig. 1.2. In the attempt to investigate more deeply the nature of such yielding transition, recent experiments have addressed the microscopic reversibility of the imposed deformation, by detecting the onset of irreversible particle displacements either with direct imaging techniques [Pouliquen 2003, Marty 2005, Slotterback 2012, Keim 2014, Knowlton 2014, Hima Nagamanasa 2014], with scattering techniques, [Petekidis 2002a, Gibaud 2010, Amon 2013, Rogers 2014, Laurati 2014, Leheny 2015, Agrawal 2015], or in computer simulations [Regev 2015, Kawasaki 2015, Priezjev 2016, Priezjev 2017]. A transition from reversible to irreversible dynamics is indeed retrieved, although at a more detailed analysis the results appear rather controversial, and no consensus is found about the nature of this crossover, which has been described either as a smooth change [Keim 2013], a sharp crossover [Knowlton 2014, Kawasaki 2015] or a continuous nonequilibrium phase transition [Hima Nagamanasa 2014].

The possibility of bridging the gap between the (ir)reversible nature of microscopic dynamics and the macroscopic deformation makes oscillatory shear the ideal technique to precise and complete the first two questions. Therefore, in line with the recent work mentioned above, the third question that we plan to answer with our experiments is the following: **Which microscopic processes govern the reversible to irreversible transition observed upon yielding? How are they related to the change in rheological properties?**

1.1.4 Challenges

In order to address the above questions, several challenges have to be faced, essentially coming from the intrinsically multiscale nature of material failure [Ben-Zion 2008, Ritchie 2011], involving collective behaviors spanning characteristic energy, time and length scales from the constitutive elements to the system as a whole. Therefore, the essential challenge is to bridge over those scales. This is typically challenging in simulations, where computational performance sets severe limitations to the total number of unitary elements that can be simulated at once [Colombo 2014, Landrum 2016]. Incidentally, most numerical simulation schemes are currently implemented in a strain-controlled fashion, which is not adapted to capture the creep dynamics. In order to access realistic volumes, coarse grained models are available, like mesoscopic elastoplastic models

[Bocquet 2009, Martens 2011], the fuse model [De Arcangelis 1985, Sornette 1992], the fiber bundle model [Daniels 1945, Pradhan 2010] with its many modifications [Pradhan 2002, Pradhan 2003, Kun 2003, Kun 2008, Kovacs 2008, Baxevanis 2007, Jagla 2011], and finite element models [Fragiacomo 2004], even though most of them were developed to describe hard materials [Sornette 1992, Fragiaco 2004, Kun 2007] and do not contain thermal fluctuations, which might be relevant in softer materials like the ones we investigate. A different implementation of such elasto-plastic models is presented in appendix B as a way to describe thermoplastic elastomers [Aime 2017]. Another delicate point concerning coarse grained numerical simulations is that they rely on specific assumptions on the fundamental mechanisms governing the macroscopic deformation. As a consequence, even once the rheological behavior is correctly reproduced, the link between the information obtained at the mesoscopic scale and the physical mechanisms governing the real systems might not be straightforward. An example is again the debate on power-law creep, which is equally reproduced by numerical models built on fairly different assumptions [Pradhan 2002, Jagla 2011].

Bridging different length and timescales is also challenging for experiments, as it is well known by geologists struggling to predict earthquakes [McGuire 2005] and snow avalanches [Van Herwijnen 2011b], since the precursor of such macroscopic events is very likely to be represented by tiny, fast events occurring at the microscopic scale after a potentially long, unpredictable waiting time. In the present work we mainly address the above questions with experiments, by imposing a well-controlled load to the sample and by measuring simultaneously both its mechanical response and its microscopic dynamics. Such simultaneous measurements are quite rare [Chen 2010] and mostly restricted to rheo-microscopy (the coupling of a rheometer and a microscope) [Van der Linden 2003, Besseling 2009] or rheo-DWS (the coupling of a rheometer and a dynamic light scattering apparatus working in the multiple scattering regime) [Wagner 1998, Hébraud 1997]. Although both techniques represent an invaluable extension of standard rheology, they have different limitations that might make them unfit to our purposes. For example, real space measurements, like microscopy, suffer an intrinsic trade-off limiting the total volume that can be probed at a given rate and a given spatial resolution. On the other hand, diffusing wave spectroscopy (DWS) can effectively probe extremely small displacements (down to the nanometer scale) in macroscopic samples (several centimeters), but its main disadvantage is the lack of a direct connection between the observed signal and the nature of the probed displacements. To overcome these limitations, in our experiments we will mainly use time-resolved dynamic light scattering, a technique described in chapter 2, which will allow us to detect rearrangements involving motion on a very small scale - down to a fraction of μm -, while being able to probe a fairly large portion of the sample, up to some mm in (linear) size. On the other hand, investigating the microscopic dynamics of a sample under shear with dynamic light scattering is also challenging, since the physically interesting signal has to be decoupled from the trivial contribution coming from the so-called affine deformation of the sample. This requires a careful, nonstandard analysis of the light scattering signal (discussed in chapter 4), which proves in addition to

be very sensitive to the presence of eventual wall slip or shear banding, another positive side effect of dynamic light scattering.

A last nontrivial challenge is represented by imposing a well-controlled stress to the sample. From established works in literature (cf. e.g. Fig. 1.1) we know that delayed failure is highly stress dependent, so that we require that stress should be homogeneous in the sample. Among the deformation geometries commonly employed in mechanical testing, cone-plate rheology is the only one satisfying this requirement [Macosko 1994]. However, such a deformation geometry is particularly difficult to couple with light scattering, because of the optical quality of the conical surface. By contrast, rheo-optical setups are often based on plate-plate torsional rheometry, in which case the applied stress is far from being homogeneous. In order to meet both requirements of optical quality and stress uniformity we decided to work in a different shear geometry, with parallel sliding planes. To this aim, we realized a stress controlled shear cell, which will be described in chapter 3.

1.2 Historical excursus

"Dicebat Bernardus Carnotensis nos esse quasi nanos, gigantium humeris insidentes, ut possimus plura eis et remotiora videre, non utique proprii visus acumine, aut eminentia corporis, sed quia in altum subvenimur et extollimur magnitudine gigantea" (John of Salisbury, *Metalogicon*). The medieval image, reported by John of Salisbury, is particularly adapted to introduce a brief survey of the current knowledge around the topics that will be touched by this work. In English it would read: "Bernard of Chartres used to say that we [the Moderns] are like dwarves perched on the shoulders of giants [the Ancients], and thus we are able to see more and farther than the latter. And this is not at all because of the acuteness of our sight or the stature of our body, but because we are carried aloft and elevated by the magnitude of the giants" [Troyan 2004].

Although it is easy for us, modern scientists, to identify with this medieval image (Newton himself used it in a letter to Robert Hooke), we can linger on it, asking ourselves what exactly gives us our raised viewpoint. There is no doubt that the incredible amount of easily accessible information, which was unimaginable already 30 years ago, together with the improved data quality provided by modern scientific instruments and ever-increasing computational schemes and platforms, constitutes an absolutely favorable working condition for today's soft matter scientists. However, there is also another related aspect, which I would like to take as a starting point. To introduce it, another quotation will help, this time from C.S. Lewis, who writes that *"The universe rings true whenever you fairly test it"* [Lewis 1955]. This is specially true in science, being clear that to simply test is not enough: one has to do it fairly in order to obtain a true answer, and history has shown how long and curvy is the path through which we learn how to fairly test universe, and to ask relevant scientific questions in the proper way. If on the one hand this is necessarily the path of every young scientist wishing to become an adult scientist,

on the other hand this path is traced by the example of curious people that across the centuries have found out better ways to formulate scientific questions, and more proper ways to test them. The beginning of this work is dedicated to a short selection of those curious people, with particular focus on the research on material failure.

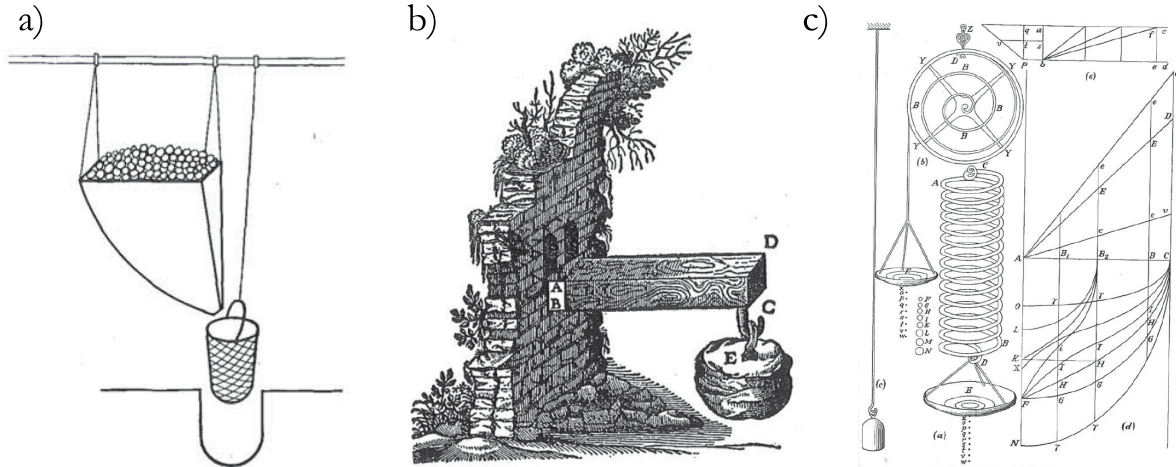


Figure 1.3: Schemes of the mechanical tests designed by (a) Leonardo da Vinci, (b) Galileo Galilei and (c) Robert Hooke. Extracted from [Timoshenko 1953].

Without any doubt, the dawn of this research dates back to ancient times: from the earliest times when people started to build, it was found necessary to have information regarding the strength of structural materials, so that rules for determining safe dimensions of building elements could be drawn up. Ancient civilizations as Egyptians, Greeks and Romans certainly had some empirical rules of this kind, since without them it would have been impossible to erect their great monuments, some of which still exist [Timoshenko 1953]. However, to the best of our knowledge, the first documented attempt to directly address the strength of structural materials with dedicated experiments is attributed to Leonardo da Vinci, in XV century [Parsons 1976]. In his note "Testing the Strength of Iron Wires of Various Lengths" he gives the sketch of the first tensile experiment of human history (Fig. 1.3a) and remarks: *"The object of this test is to find the load an iron wire can carry. Attach an iron wire [...] to something that will firmly support it, then attach a basket [...] to the wire and feed into the basket some fine sand through a small hole placed at the end of a hopper. A spring is fixed so that it will close the hole as soon as the wire breaks. [...] The weight of sand and the location of the fracture of the wire are to be recorded. The test is repeated several times to check the results. Then a wire of one-half the previous length is tested and the additional weight it carries is recorded; than a wire of one-fourth length is tested and so forth, noting each time the ultimate strength and the location of the fracture"* [Da Vinci 1972]. Besides the same idea of conceiving an *ad hoc* experiment to test the strength of a wire, independently from its application, which is certainly the most revolutionary aspect of Leonardo's approach, two interesting points have to be noted in his description of the experiments: first, one single

test is not enough, since its result has to be checked by several repetitions, suggesting that Leonardo had the intuition that statistics are particularly relevant for those phenomena. Five centuries afterwards, the work of Waloddi Weibull [Weibull 1939] will rationalize this concept in mathematical terms. Second, Leonardo understood that the length of the wire plays a role, longer wires carrying less load, which is indeed the starting point of Weibull model, namely that real wires are heterogeneous, so that longer wires are more likely to contain a critical defect [Lund 2001].

With a different accent, the question about the relationship between size and strength was also addressed by Galileo Galilei at the beginning of XVII century. In his book "Discorsi e dimostrazioni matematiche intorno a due nuove scienze", he investigates the strength of materials in simple tension, like in Leonardo's experiments, and he states that the strength of a bar is proportional to its cross-sectional area and independent of its length: this defines, for Galileo, the "absolute resistance to fracture". With respect to Leonardo's results, this remark suggests that Galileo worked with thicker and more homogeneous materials, whose strength did not display marked size dependence. Having the absolute resistance of a bar, Galileo then turns to a different experiment in which the resistance of the same bar is tested in bending geometry (Fig. 1.3b). By analyzing the deformation profile, he finds that geometrically similar bars are not equally strong, as the bending moment increases as the square of the length, whereas the resisting moment increases as the cube of the radius: thus, to keep the strength constant, the cross-sectional dimensions must be increased at a greater rate than the length. For this reason, he argues, *"you can plainly see the impossibility of increasing the size of structures to vast dimensions either in art or in nature; likewise the impossibility of building ships, palaces, or temples of enormous size [...]; nor can nature produce trees of extraordinary size because the branches would break down under their own weight. [...] Indeed, the smaller the body the greater its relative strength"* [Galilei 1638]. We see that the use of mathematics to rationalize his findings and the extrapolation, from the particular experiment, of a general result applicable to different systems characterizes Galileo's approach to material failure. For this reason, Galileo's work represents the beginning of the science of solid mechanics [Timoshenko 1953].

Later in XVII century, this new-born science evolved rapidly thanks to the contribution of Robert Hooke, who is rightfully considered the father of the theory of elastic bodies. In his manuscript "De potentia Restitutiva", Hooke explains the linear relationship between elastic force and spring deformation, which is also known as Hooke's law: *"Take a wire string [...] and fasten the upper part thereof to a nail, and to the other end fasten a scale to receive the weights: then with a pair of compasses take the distance of the bottom of the scale from the ground or floor underneath, and set down the said distance, then put in weights into the said scale and measure the several stretchings of the said string, and you will find that they will always bear the same proportions one to the other that the weights do that made them"*. By investigating other deformation geometries like torsion, bending and compression (Fig. 1.3c) he comes to the following general conclusion: *"It is very evident that the Rule or Law of Nature in every springing*

body is, that the force or power thereof to restore itself to its natural position is always proportionate to the distance or space it is removed therefrom" [Hooke 1678].

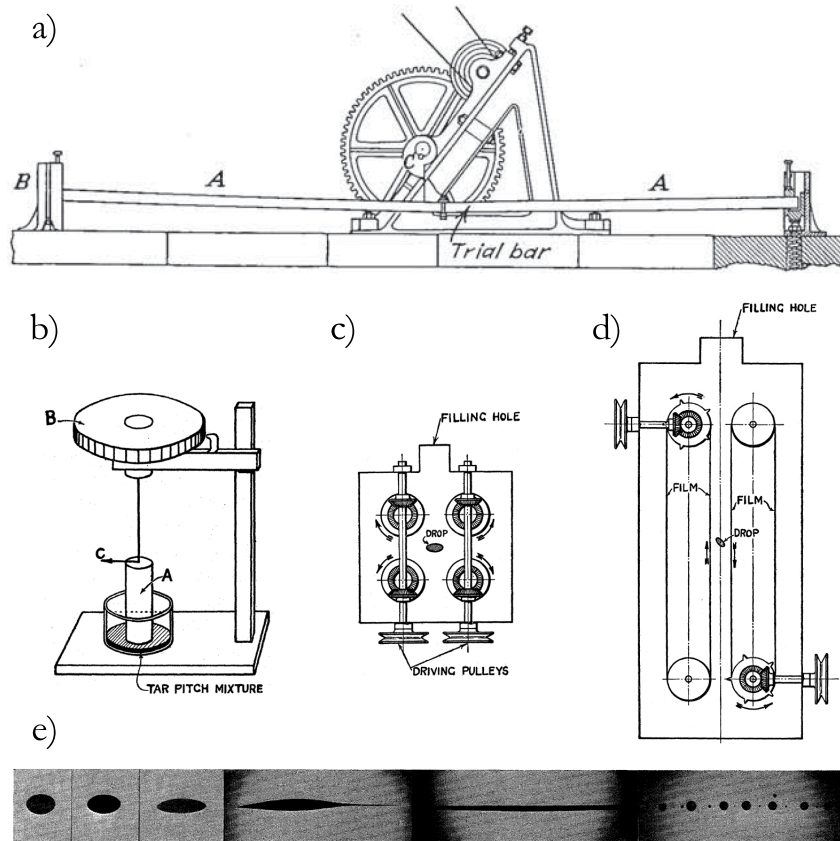


Figure 1.4: (a) James and Galton's fatigue-testing machine: a rotating eccentric is used to deflect and release the bar, with a frequency from 4 to 7 rpm [Timoshenko 1953]. (b) Torsional rheometer used by Taylor [Taylor 1934] to measure the viscosity of "highly viscous" (presumably viscoelastic) fluids. (c-d) Rheo-optical cells to visualize the deformation of a viscoelastic drop under biaxial deformation (c) and shear deformation (d). (e) Destabilization of a viscoelastic drop under biaxial deformation [Taylor 1934].

From seventeenth century to the modern era, contributions to this field, specially on the mathematical formulation of the theory of elasticity with the new instruments provided by infinitesimal calculus, are numerous. Mentioning most of them would largely go beyond the purpose of this section. However, it is fascinating to follow the close connection between the development of this science and the evolution of the practical problems posed by the increasingly demanding technological applications. As an example, the development of railroad transportation, combustion engines, and the introduction of steel as structural material brought many new problems dealing with strength of structures. Indeed, it was discovered that subjecting a metallic material to many cycles of stresses can produce fracture, by much smaller forces than would be required for static failure [Morin 1853]. This began the investigation of fatigue failure in iron, which initially aimed

at estimating how frequently locomotives had to be inspected and maintained in order to prevent fracture. To this aim, experiments applying a cyclic deformation to iron beams were performed (Fig. 1.4a), and the development of plasticity under finite strains was addressed, in connection with the onset of irreversibility of the macroscopic deformation [Fairbairn 1864]. At the same time, the microscopic origin of fatigue was investigated, but no consensus could be reached only based on macroscopic experiments. For this reason, in 1850 came the first suggestion of coupling fatigue test and microscopic investigation, from P.R. Hodge: *"To arrive at any true results as to the structure of iron it would be necessary to call in the aid of the microscope, to examine the fibrous and crystalline structure"* [Engineers 1851]. At the time such coupling was technologically out of reach, so that the change in iron microstructure had to be investigated separately. This limitation, coupled to the low sensitivity of existing imaging apparatuses, was such that no relevant observation could be made, yielding the conclusion that no real difference could be perceived between the sample before and after the fatigue treatment.

One has to wait almost one century before the first pioneering attempt, by G.I. Taylor [Taylor 1934], of coupling macroscopic deformation to a simultaneous measurement of microscopic structure and dynamics, with the aim of characterizing the destabilization and rupture of "highly viscous" drops under large deformations. To achieve this, a fixed stress was applied by controlling the deformation rate of the surrounding medium (Fig. 1.4c-d), while an imaging system provided magnified picture of the drop under increasing stress conditions, up to its failure (Fig. 1.4e). Interestingly, the mechanical properties of the bulk materials were also tested, using a home-made instrument which can be considered the ancestor of our stress-controlled rheometers (Fig. 1.4b).

1.3 State of the art

1.3.1 Steady-rate experiments

Many different protocols are used in literature to probe yielding and failure in soft materials. Probably the most straightforward of those protocols is represented by steady-rate experiments, where the material, initially at rest, is deformed at a constant deformation rate. Such an experiment can be performed in different deformation geometries, from well-defined ones like shear [Costanzo 2016, Keshavarz 2017], extension [Costanzo 2016] and compression [Antonaglia 2014], to more complex ones, like indentation or bending. In the following, we will focus on shear deformation, whereas appendix B will show simulations and experiments in uniaxial extension.

In steady-shear rate experiments, the stress σ is measured as a function of time, starting from the moment where the deformation rate is applied. An initial linear regime is observed at small deformations, where the stress growth is dictated by the linear viscoelastic properties of the sample. Beyond the linear regime, σ depends on the imposed shear rate $\dot{\gamma}$, in a way that can be rationalized in terms of the ratio between the largest

(terminal) relaxation time τ of the system and the experimental timescale $\tau_{exp} \sim \dot{\gamma}^{-1}$. When the product $Wi = \dot{\gamma}\tau$ (the so-called Weissenberg number)[Dealy 2010]) is small ($Wi \ll 1$), the deformation can be thought as quasistatic: the system relaxes faster than it is sheared, and can be considered at equilibrium at any time during the deformation. In this case, no deviations from linear rheology are expected. By contrast, in the opposite limit of $Wi \gtrsim 1$, the sample has no time to relax during deformation, and eventually is driven out of the linear regime. The linear to nonlinear transition can manifest in qualitatively different forms: brittle materials break abruptly, almost without any plastic deformation, whereas ductile ones exhibit substantial large plastic deformations after yielding. Because plasticity dissipates elastic energy, ductile yielding is generally associated to a downturn in the measured stress: eventually, after a first strain hardening regime [Groot 1996, Gardel 2004, Storm 2005, Pouzot 2006], the stress passes through a maximum (defining the failure stress and strain) and decreases afterwards [Mohraz 2005, Kabla 2007, Skrzyszewska 2010, Keshavarz 2017]. The detailed microscopic processes associated to departure from linear viscoelasticity and plastic yielding can be complex [Koumakis 2011, Costanzo 2016], so that in general their investigation is challenging and can usefully be supported by numerical works. To highlight the main open questions in this field, hereafter we review a few experimental studies, with particular focus on network forming systems and physical gels.

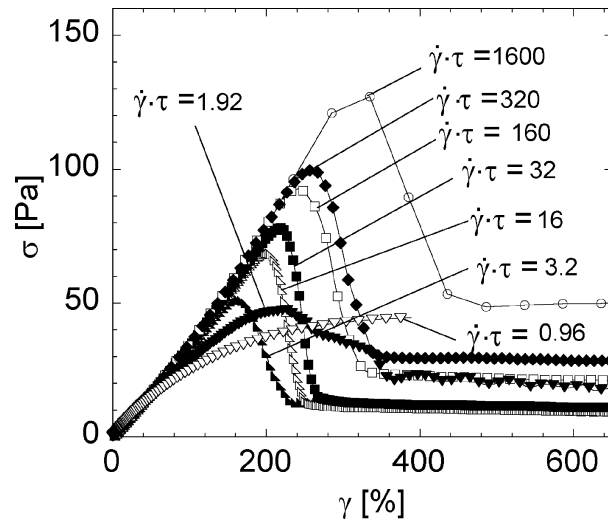


Figure 1.5: Protein physical gel. Time-resolved stress response as a function of strain ($\gamma = \dot{\gamma}t$) after start-up of steady shear. The reduced shear rates ($\dot{\gamma}\tau$) are indicated near the lines, with τ equal to 3200 s. Extracted from [Skrzyszewska 2010].

As a first example, working with a recombinant protein able to form supramolecular bonds with a well defined characteristic lifetime τ , Skrzyszewska *et al.* [Skrzyszewska 2010] show that a ductile to brittle transition is observed with increasing Weissenberg number beyond 1 (Fig. 1.5). The authors argue that at the lowest shear rates the stress deviates downwards because of the viscoelastic relaxation of the physical gel (associated to dis-

sociation and reformation of physical bonds), which leads to simple viscous flow in the steady state, whereas at larger shear rates this mechanism cannot happen anymore, and one observes instead a slight strain hardening, associated to the finite chain extensibility, followed by chain pull-out and brittle fracture.

In another work on a protein gel with no measurable terminal relaxation time, Keshavarz *et al.* observe brittle fracture for all values of $\dot{\gamma}$, since the condition $Wi \gg 1$ is always met [Keshavarz 2017]. Interestingly, the authors show that the whole stress-strain curve, up to the onset of mechanical instability, can be nicely predicted by a nonlinear viscoelastic model based on time-strain separation (Fig. 1.6). In this case, the departure from linearity can be accurately described in terms of a strain hardening and a strain softening term, and the deviation from the model is attributed to fracture. Indeed, thanks to direct visual inspection of the gel during deformation, the authors can detect the nucleation and growth of cracks, which appear at the yield point and are clearly associated to the subsequent stress drop. The authors argue that failure occurs as a consequence of stress-induced damage accumulation, which becomes critical beyond a given threshold. The rate of damage accumulation is assumed to be a function of stress alone, which provides an excellent prediction of failure stress and strain based on a failure criterion proposed by Bailey [Freeds 2002]. Therefore, one question that opens concerns the nature of the plastic rearrangements considered by Bailey's criterion. To elucidate this point, standard rheology might benefit from a microscopic investigation of the local structure and dynamics.

One example of such investigation can be found in the work of Mohraz and Solomon [Mohraz 2005], who study the structure of weak fractal colloidal gels subject to start-up of steady shear flow, by coupling shear rheology to time-resolved small angle light scattering. With increasing deformation, an anisotropic intensity pattern is detected in the light scattering signal, which signs a slight orientation in the gel structure [Vermant 2005]. The structural anisotropy initially increases as the gel is deformed, then reaches a maximum value at the yield strain (defined by the locus of the stress maximum) and afterwards decays to a plateau, in a qualitatively similar way to the macroscopic stress. Such similarity suggests that structural reorientation determines the nonlinear rheology of the gel. Moreover, by investigating the microscopic dynamics after flow cessation, the authors argue that minor connectivity loss should take place before the stress peak. It is interesting to compare this result to Bailey's criterion evoked by Keshavarz *et al.*, which rather suggests a more progressive weakening. The comparison is not trivial, and calls for a deeper understanding of the interplay between local plasticity and macroscopic rheology. On the other hand, both works agree in interpreting the stress drop as the macroscopic signature of gel rupture, which occurs abruptly at a large critical strain (around 100%), where the gel backbone should be fully extended. Accordingly, the rupture is associated to a maximum in structural anisotropy, and is followed by a partial relaxation of both stress and anisotropy, in a process read as the densification of fractal clusters.

More detailed insights on the microscopic processes occurring under shear are reported by Masschaele *et al.* [Masschaele 2009], who observe in real space the shear deformation

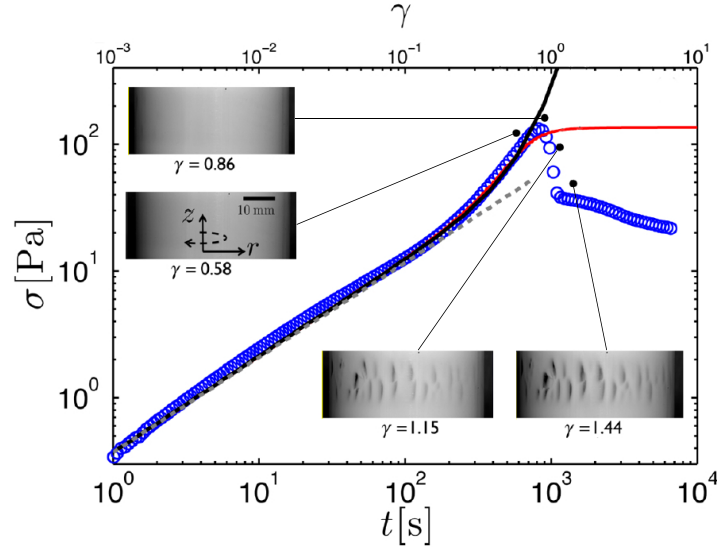


Figure 1.6: Protein gel. Stress response σ vs time t (lower axis) and vs strain $\gamma = \dot{\gamma}_0 t$ (upper axis) to a constant shear rate $\dot{\gamma}_0 = 10^{-3} \text{ s}^{-1}$ initiated at $t = 0$. The gray dashed line corresponds to the linear viscoelastic response (a power law of time). The black line corresponds to the nonlinear model (K-BKZ) constructed using only the strain-hardening part of the damping function, whereas the red line corresponds to the full K-BKZ equation, which includes both the hardening and the softening components of the damping function. Insets: images of the side view of Couette cell at different strains recorded simultaneously to the experiment reported in the main graph. Adapted from [Keshavarz 2017].

and rupture of 2D fractal gels at oil-water interface. Unfortunately, the shear stress could not be measured in their experiments, so that the linear to nonlinear transition and gel rupture are only investigated at the microscopic scale. The authors rely on the assumption that the rheology of interfacial gels would show the same qualitative features as the analogous three dimensional structures. In agreement with Mohraz and Solomon, Masschaele *et al.* find that at small strains the gel network remains intact, and percolation is only lost at higher strains, where rupture occurs abruptly, as a consequence of a cascade of break-up events, which are monitored throughout deformation. Interestingly, break-up events are found to be spatially localized and tend to cluster, which might suggest some interesting correlations, neglected by the simple additivity of Bailey's criterion. In the regime of increasingly nonlinear deformation, the authors address various microscopic structural indicators in order to quantify the increased heterogeneity of the structure during deformation. Essentially all indicators show minor evolution prior to rupture, whereas the heterogeneity increases after rupture, in line with the findings of Mohraz and Solomon. Finally, the authors show that the pertinent lengthscale for breaking and structural reorganization coincides with the lengthscale of structural heterogeneity, i.e. the cluster size. More precisely, Fig. 1.7 shows an example of the typical plastic rear-

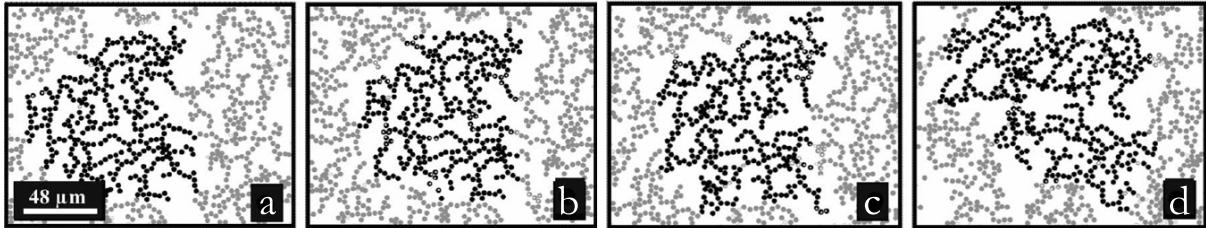


Figure 1.7: 2D colloidal gel: details of yielding of one particle cluster. The snapshots correspond to the network after a strain of, respectively, 0.25 (a), 0.5 (b), 0.75 (c), and 1.25 (d). Adapted from [Masschaele 2009].

rearrangement occurring at yielding: the bonds between clusters break, and as a consequence percolation is lost and groups of particles, which retain their integrity, are free to rotate collectively relative to the surroundings. This mechanism is in agreement with previous models for gel rupture, only based on rheological measurements [Shih 1990].

Many of the above results are corroborated and extended by numerical simulations, for which steady-rate experiments represent a particularly convenient framework. For example, the work of Park *et al.* [Park 2013, Park 2017] agrees on the observation of a structural anisotropy under shear, which reaches its maximum at yielding, whereas Boromand *et al.* [Boromand 2017] focus on bond distribution as an efficient way to characterize $\dot{\gamma}$ -dependent structural evolution during shear. In the same vein, Colombo and Del Gado [Colombo 2014] follow the bond breaking and reformation, emphasizing the relevance of bond orientation relative to shear. In agreement with Masschaele *et al.*, they show that bond breaking only starts occurring beyond 30% deformation, and that the onset of bond breaking is connected to the overstretching of the weakest chains, where the stress gets localized. Interestingly, the authors also discuss the microscopic reversibility of the deformation, by inverting the shear direction after reaching a given strain γ_{inv} and bringing back the system to the initial $\gamma = 0$ state. A comparison between the system at the beginning and at the end of this strain cycle shows that irreversible nonaffine displacements start to occur around $\gamma_{inv} \approx 10\%$, significantly before the onset of bond breaking.

In conclusion, we learn from steady-shear rate experiments that the yielding of network forming systems such as physical gels can occur in a brittle-like fashion under specific conditions. Brittle rupture is associated with a sudden drop of the measured stress, which is caused by a cascade of break-up events weakening the stress-bearing backbone of the network and triggering mechanical instability. This occurs at a characteristic lengthscale equal to the network mesh size, which for a colloidal gel corresponds to the size of the fractal cluster. During the deformation precluding rupture, such materials exhibit minor structural rearrangement, and the network connectivity is mostly preserved. At the same time, strain hardening is observed in the mechanical response, and it is associated to the orientation of the gel network in the shear direction.

A question that remains to a large extent open concerns the amount of bond breaking

events occurring during the deformation, and their eventual space and time correlations. If no bond breaking at all is expected in the linear regime, it is likely that, as it is observed by Masschaele *et al.* and in computer simulations, some bonds will break during nonlinear deformation. The amount of those breaking events, their nature and their relevance for the observed mechanical properties are usefully disclosed by simulations, but experiments are still blind to such information, which is presumably sample- and experimental-protocol dependent. A first indication can be obtained thanks to the models accounting for the macroscopic rheology. For instance, the applicability of durability criteria to model the onset of mechanical instability discussed by Keshavarz *et al.* seems to suggest that in some cases plasticity should occur throughout the deformation, at a well defined and stress-dependent rate (thus precluding avalanche-like dynamics as observed for some other systems [Antonaglia 2014, Kurokawa 2015]). The impressive agreement between the nonlinear model and the experimental data encourages deeper investigation on its microscopic implications: in this perspective, it was shown with the above examples that novel experiments accessing at the same time the mechanical response and the microscopic structure and dynamics tremendously increase our insight in the material behavior.

1.3.2 Creep experiments

Because of the rather robust rheological features observed and the well-defined experiment duration, steady-rate experiments are particularly convenient to study yielding. This explains their widespread application since Leonardo's ancient times [Timoshenko 1953]. The main disadvantage of this technique is perhaps that the shear history imposed to the sample is usually quite distant from the one typically experienced by materials in real life applications. For example, as mentioned above, snow avalanches, rockslides and sandslides occur under the constant force exerted by gravity, which may also cause the delayed collapse of civil structures like buildings and bridges as well as soft materials, whereas earthquakes and volcano eruptions are triggered by a nearly-constant stress due to the underground activity of earth's inner layers. On a smaller scale, failure of cables, fibers or adhesives usually occurs as well under a controlled stress. The latter case is particularly frequent, as it is well known to those who have tried to fix a post-it, a poster or a picture to a vertical surface with the help of an adhesive tape. Those people might have noticed with great disappointment that, despite its apparent initial stability, their creation had a limited lifetime, and it would eventually collapse after a while. The above examples push to address material failure with a second experimental protocol, where the sample is subject to a constant load and its deformation is monitored over time until delayed failure it eventually observed. Because the material is often observed in these experiments to progressively weaken, the term *fatigue* is sometimes used. In particular, when the external load is constant, one speaks about static fatigue (or creep), as opposed to dynamic fatigue, which is typically probed under cyclic stress or strain

[Poncelet 1839].

There is also a second, more fundamental reason for considering static fatigue of materials. Namely, in most of the models introduced in the literature, failure is regarded at the microscopic scale as a stress-controlled phenomenon. Remarkable examples include the Eyring model [Eyring 1936], the original fiber bundle model [Daniels 1945] and many of its derivations [Pradhan 2005, Kun 2003, Jagla 2011]. For this reason, a straightforward comparison between the various models' predictions and experimental results obtained in steady-rate is sometimes difficult to obtain, whereas static fatigue represents a much more natural framework.

1.3.2a Linear and nonlinear creep

The main disadvantage of static fatigue experiments is that sample deformation is not controlled. As a consequence, the duration of the experiments is often long and difficult to predict, sometimes because of experimental reasons like sample to sample variations and uncertainties on the applied stress, and sometimes for more fundamental reasons, like the intrinsically stochastic nature of fracture nucleation and growth [Griffith 1921, Weibull 1939, Bonn 1998]. During the potentially very long induction times, which on structural materials can extend to several years [Maekawa 2016], the effect of fatigue is observed at the macroscopic scale as a slow deformation called creep, which is usually well described either by a logarithm of time [Phillips 1905, Nabarro 2001, Nechad 2005b, Siebenbürger 2012], by a power law [Andrade 1910, Plazek 1960, Caton 2008, Rosti 2010, Grenard 2014, Leocmach 2014, Koivisto 2016, Ballesta 2016], or by combinations of the two [Wyatt 1951, Cherièrè 1997, Siebenbürger 2012].

A major fundamental issue related to creep is to understand the underlying microscopic processes responsible for the observed sublinear deformation. If this is rather understood in crystalline materials [Poirier 1985] like metals [Andrade 1910, Miguel 2002, Cottrell 1952] or ice [Ashby 1985] in terms of defect motion, for amorphous materials the problem is complicated by the fact that structural defects are not as well defined [Widmer-Cooper 2009, Schoenholz 2014]. In particular, amorphous materials are often viscoelastic, thus a time-dependent response may arise as well as a simple consequence of linear viscoelasticity, in absence of damage or plastic events. Decoupling the two contributions is generally far from trivial, all the more since several models, based on radically different assumptions, from pure linear viscoelasticity [Mainardi 2010, Hilfer 2000, Friedrich 1991, Heymans 1994], to pure plasticity [Pradhan 2005, Eyring 1936, Zapperi 2000, Bocquet 2009], to a combination of both [Kun 2003, Jagla 2011], can equally account for the observed macroscopic deformation.

In general, in the limit of small applied stresses, and consequently small deformations, creep is linear viscoelastic: the measured deformation can be described in terms of a linear creep compliance, which can be compared with independent measurements in the linear regime, say in the frequency domain [Evans 2009]. This can be exploited in order to

probe linear viscoelastic processes occurring on timescales too long to be characterized by oscillatory rheology (cf. chapter 5). Upon increasing the applied stress, however, an additional contribution to structural relaxation is introduced by emerging nonlinear processes, which lead to faster (shear thinning) flow in the steady state observed in the long time limit [Erwin 2010].

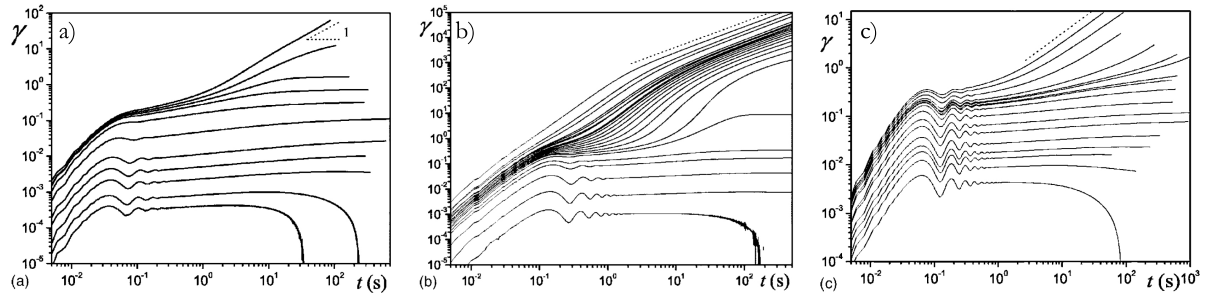


Figure 1.8: Typical aspect of deformation vs time curves for different stress levels σ (increasing from bottom to top) applied to the following soft-jammed systems: (a) Mustard, (b) Bentonite suspension, (c) Hair gel. The inclined dotted line is the curve of slope 1. Adapted from [Coussot 2006].

This is discussed in detail by Coussot *et al.* [Coussot 2006], who introduce the concept of viscosity bifurcation to explain the experimental observation that for a small increase in the applied stress σ from below to above a given threshold σ_y (the so-called yield stress) the steady-state shear rate increases from zero in the solid regime ($\sigma < \sigma_y$) to a finite value, apparently larger than a critical strain rate $\dot{\gamma}_c$ (Fig. 1.8). This phenomenon appears to apply quite generally to a class of yield stress fluids which are called thixotropic. However, from Fig. 1.8 it is clear that the steady state is not reached instantaneously and that transient regimes, e.g. separating solidlike behavior at rest from liquidlike behavior beyond yielding, convey tremendous physical information on the yielding process. In particular, Coussot *et al.* remark that in some cases, close to the yield stress, the induction time can exceed the experiment duration, and that in those cases it is difficult to say whether the material will ultimately stop or reach a steady flow over very long times.

The transient creep deformation before fluidization is addressed for example in the work of Siebenbürger *et al.* on colloidal glasses [Siebenbürger 2012]. Their data (Fig. 1.9) show distinct regimes: (i) an initial transient, dominated by the coupling between sample viscoelasticity and inertia of the measurement tool (called creep ringing [Ewoldt 2015]), is followed by (ii) a first linear viscoelastic response, which corresponds to a quasi-plateau in the measured deformation. Later on, plastic deformation is observed, and takes different forms according to the applied stress σ . At large σ , a steady state characterized by viscoplastic flow (iii) is reached after a superlinear deformation regime (iv), whereas at low σ sublinear creep continues indefinitely (v): creep appears to be logarithmic in the long time limit, but before that a power-law transient is also found, whose duration may extend to nearly one week depending on sample age. Whereas no real explanation is given

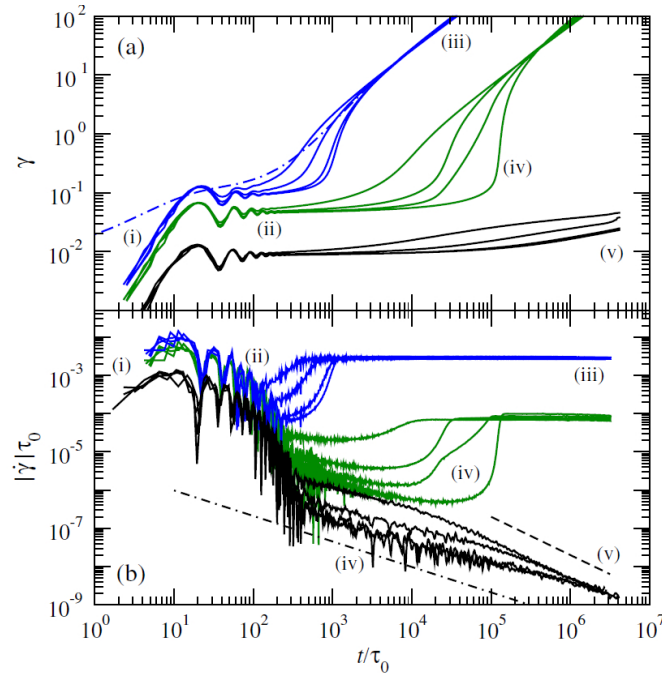


Figure 1.9: Colloidal glass. (a) Deformation $\gamma(t)$ for increasing applied stress (different colors from bottom to top), and increasing waiting times after shear-induced rejuvenation (for each color, increasing from left to right). Time is rescaled using the diffusion time $\tau_0 = R^2/D_0 = 4\text{ms}$ (R being the particle radius and D_0 being the free diffusion coefficient). The different regimes described in text are marked with roman labels (i)-(v). (b) Associated normalized shear rate $\dot{\gamma}(t)\tau_0$. Dash-dotted line: Andrade creep law, $\dot{\gamma}(t) \sim t^{-2/3}$; dashed: logarithmic creep, $\dot{\gamma}(t) \sim 1/t$. Extracted from [Siebenbürger 2012].

for the transient power law creep, the authors propose a nonlinear model accounting for the logarithmic creep, based on the assumption that the nonlinear relaxation modulus is described by a nonlinear generalized Maxwell model [Voigtmann 2011], whose essential ingredient is that in the high shear rate limit the material displays shear thinning as a simple yield stress fluid ($\eta \propto \dot{\gamma}^{-1}$). Other models can be found in literature, relating the logarithmic creep to more microscopic quantities like the activation energy for plastic rearrangements. Nabarro reviews two of them, the work-hardening model and the exhaustion model [Nabarro 2001]. These models were developed to describe the deformation of granular materials, and are essentially elasto-plastic, with no account for linear viscoelastic deformation. Without entering into details, we observe that the amount of different models existent in literature and producing identical predictions for the rheology should be regarded as an indication that it may be hard to get a true microscopic insight from macroscopic measurements alone.

In this regard, an instructive example is discussed by Chérière *et al.*, for the torsional creep of PMMA, a polymer glass [Cheriere 1997]: at low temperatures a simple logarithmic creep is observed, but as temperature is increased the first logarithmic creep regime

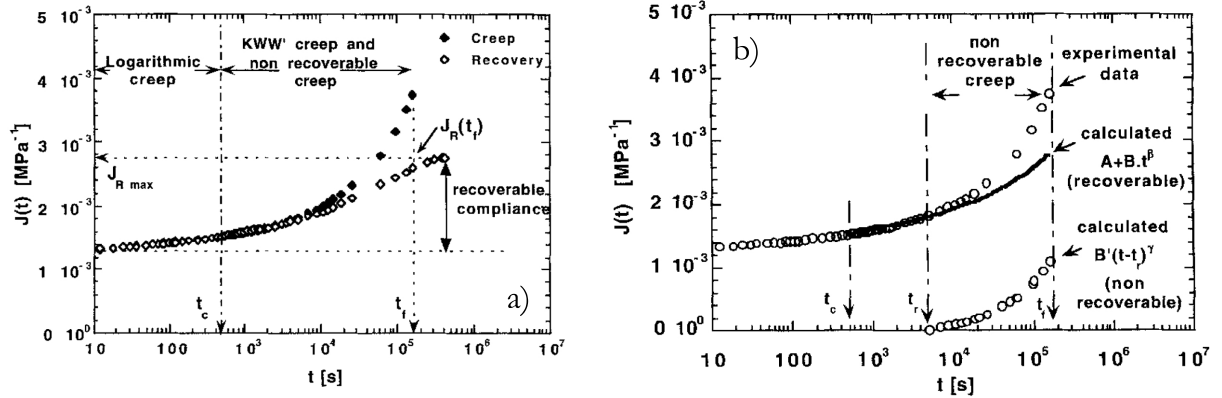


Figure 1.10: Polymer glass. (a) Experimental creep and recovery at 90°C . Creep is partly recoverable. The magnitude of the recoverable creep is $J_{R,max}$; this allows determination of the maximal compliance $J_R(t_f)$ reached by the recoverable creep at $t = t_f$. (b) Beyond of the end of the logarithmic creep, $t_c = 500$ s, analysis of the experimental creep curve obtained by addition of two creep contributions: a recoverable creep deduced creep recovery and a nonrecoverable creep obtained by difference from the total creep. Extracted from [Cheriere 1997].

is eventually followed by a power-law regime. At still higher temperatures, approaching the glass transition from below, a third regime follows, described by a different power law. This is analogous to the behavior of many metals [Wyatt 1951]. The originality of the work of Chérière *et al.* consists in a thorough discussion of the recoverability of creep deformation, which is probed by releasing the applied stress after a given time and by following the relaxation of the strain. If the stress is released during the logarithmic creep, the authors observe a logarithmic strain recovery, which completely recovers the initial zero-deformation state after a time equal to the time spent under stress. Complete recovery is also found when the stress is released during the first power-law creep, but in this case the recovery process takes longer than the creep time. Finally, the second power law creep is only partially recovered. The complete picture is represented in Fig. 1.10. Such observation about macroscopic reversibility is very interesting, because it is contrary to the intuitive notion of creep as presented by the previous works. In those works, creep was regarded as the result of a series of irreversible structural rearrangements, which should leave behind them no or minor driving force for recovering the unstrained state once the macroscopic stress is released. Here, by contrast, the authors correctly point out that plasticity might be reversible, as long as the main stress bearing structure is not damaged: in that case, upon stress release, the system will maintain the tendency of recovering its initial rest state. Moreover, this also explains why recovery is also a gradual processes, since it can attain completion only after a number of plastic rearrangements comparable with the ones that occurred during creep, which explains the symmetry between the two processes as observed by rheology. Following this line of thought, the authors speculate

that entanglements start to be lost only during the third regime, which is only partially recovered.

The potential recoverability of creep is conceptually intriguing and hides a subtle distinction between recoverability of macroscopic strain and reversibility of the single microscopic processes occurring under creep. For example, one may wonder whether the final state after complete strain recovery corresponds to the same microscopic configuration as the one before stress application. In this regard, such a distinction is strongly related with the key questions mentioned above, and deserves deeper investigation. In particular, Fig. 1.10b reveals a rather well defined transition between fully recoverable and only partially recoverable creep. From that same figure, it is clear that a clear distinction between the two regimes can hardly come from an observation of the shape of the creep curve, and that complementary observations may be usefully coupled to the macroscopic rheology.

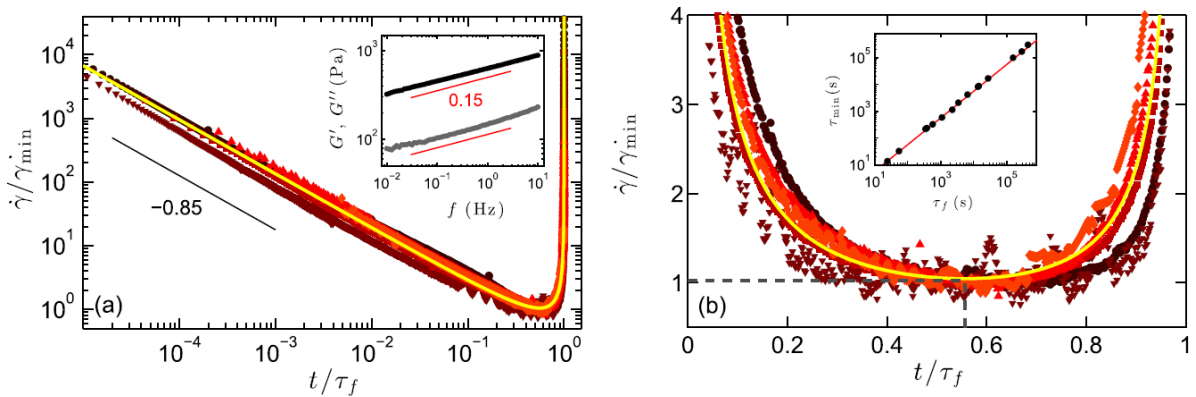


Figure 1.11: Protein gel. (a) Normalized shear-rate responses $\dot{\gamma}(t)/\dot{\gamma}_{min}$ for different values of the applied stress and plotted as a function of the rescaled time t/τ_f , where τ_f is the failure time and $\dot{\gamma}_{min}$ is the minimum shear rate reached at τ_{min} . Inset: Linear viscoelastic moduli G' (top) and G'' (bottom) as a function of frequency f for a strain amplitude of 0.1%. Red lines are power laws $G' \propto G'' \propto f^{0.15}$. (b) Same data as in (a), but with the time axis in linear scale to emphasize the secondary creep. Inset: τ_{min} vs τ_f . The red line is $\tau_{min} = 0.556\tau_f$. Extracted from [Leocmach 2014].

Fully recoverable creep was also found by Leocmach *et al.* on a completely different system, namely a protein gel [Leocmach 2014]. In this case, the creep deformation is characterized by three regimes (Fig. 1.11), with a first power-law creep (called primary creep), which, under large enough stresses, is followed by a secondary creep characterized by an upward deviation from the power law, with a minimum in the deformation rate, and finally a tertiary creep, where the deformation accelerates, exhibiting an ideal power-law divergence at a finite time t_f where macroscopic failure is observed. The authors find that the power law characterizing primary creep corresponds to the linear creep compliance as it can be inferred by independent measurements (Fig. 1.11a, inset). This rules out

most of the mechanisms invoked by the above works, where significant creep was only observed under large enough stresses (cf. Fig. 1.8), and calls for a linear deformation mechanism, perhaps inspired by the rheology of critical polymer gels, which also display extended power laws as a consequence of their fractal structure [Adolf 1990]. As a further confirmation for linearity, the authors perform a series of creep and recovery tests, each time finding a complete recovery, which suggests that no or minor damage is cumulated by the material during primary creep. Thus, very interestingly, the authors point out that the onset of secondary creep in the rheological signal corresponds at a more fundamental level to the onset of irreversible processes, which introduce an additional contribution to the macroscopic deformation, eventually becoming predominant during the tertiary creep. Thus, a clear detection of such transition holds the promise of providing a means of predicting the failure time t_f before the material is excessively damaged, which is a problem of fundamental practical interest. The authors point out that an analysis of the shape of the $\dot{\gamma}(t)$ curves might allow such prediction. Indeed, as it is shown in Fig. 1.11b, in every experiment $\dot{\gamma}$ exhibits a minimum at a time t_m simply related to t_f by a linear relation (Fig. 1.11b, inset): a measurement of t_m would yield a straightforward prediction of the failure time t_f .

An analogous linear relation (first determined by Monkman and Grant in 1956 [Monkman 1956]) is also found on composite materials under tensile creep [Nechad 2005b, Rosti 2010, Koivisto 2016]. In particular, Koivisto *et al.* explicitly discuss the possibility of achieving a robust failure prediction based on the detection of t_m [Koivisto 2016]. They show that despite both t_m and t_f individually suffer huge sample to sample variations, the ratio t_f/t_m is very well defined (and equal to 0.83 in their case, whereas it is 0.556 for Leocmach *et al.*), and it thus represents a very robust and reliable indicator. However, the authors also remark that the experimental measurement of t_m is in practice very delicate, because of both experimental noise and intrinsic fluctuations, and they conclude that such a method for predicting t_f would not be practical. In conclusion, the authors identify two main challenges associated to creep failure time prediction: the first one is to find some physical quantity measurable during the first stages of the creep and displaying strong correlations with the failure time, and the second is to properly measure it, recognizing precursory features as such. These are the same challenges faced by the attempts to predict earthquakes: although foreshocks clearly do exist, the main problem is detecting them on time and recognizing them in their precursory nature [McGuire 2005].

Therefore, it appears that also the effort of predicting delayed failure could largely benefit from a more microscopic insight, where the smooth transition from sublinear primary creep to accelerated tertiary creep observed in rheology might be sharper and easier to detect.

1.3.2b Microscopic dynamics during creep

An insight on microscopic plasticity can be obtained in some cases by recording the crackling noise emitted by the sample under creep. Indeed, many systems under creep

emit a characteristic intermittent noise called crackling, which has been linked to sudden, collective plastic events occurring at the microscopic scale [Myers 2001]. Known since long time in the framework of earthquakes [Ben-Zion 2008] and snow avalanches [Sommerfeld 1983, Van Herwijnen 2011b, Van Herwijnen 2011a], it first entered the framework of material science through an investigation on crumpling paper [Houle 1996], and was thereafter detected on a variety of other systems, from metals [Antonaglia 2014, Abobaker 2015] and ice [Duval 2010, Gudipati 2012] to rocks [Agioutantis 2016], wood [Guarino 2002] and composite materials [Nechad 2005a, Nechad 2005b], including examples relevant to soft matter such as granular materials [Johnson 2013, Amon 2013] or foams [Tewari 1999, Kabla 2007]. The statistical properties of crackling were shown to follow characteristic power-law size distributions, and even the detailed shape of the temporal evolution of one single event was shown to be universal [Antonaglia 2014], and common to a wide class of completely different phenomena, from solar flares [Lu 1993] to fluctuations in the stock market [Bak 1997], with many other examples reviewed by Myers *et al.* [Myers 2001]. This result has been read as an indication that creep and yielding could be described in a sample-independent fashion, and studied in the larger framework of nonequilibrium phase transitions [Hinrichsen 2000], and as such it has whipped up enthusiasm in the scientific community. For this reason, the shape and the statistical properties of crackling noise have been addressed in several analytical [Papanikolaou 2011, Dahmen 2011] and numerical works [Durian 1997, Carmen Miguel 2001, Pradhan 2005, Tsamados 2010, Jaiswal 2016, Bouzid 2017], and concepts borrowed from this field were used to interpret macroscopic stress fluctuations observed in experiments [Antonaglia 2014, Kurokawa 2015].

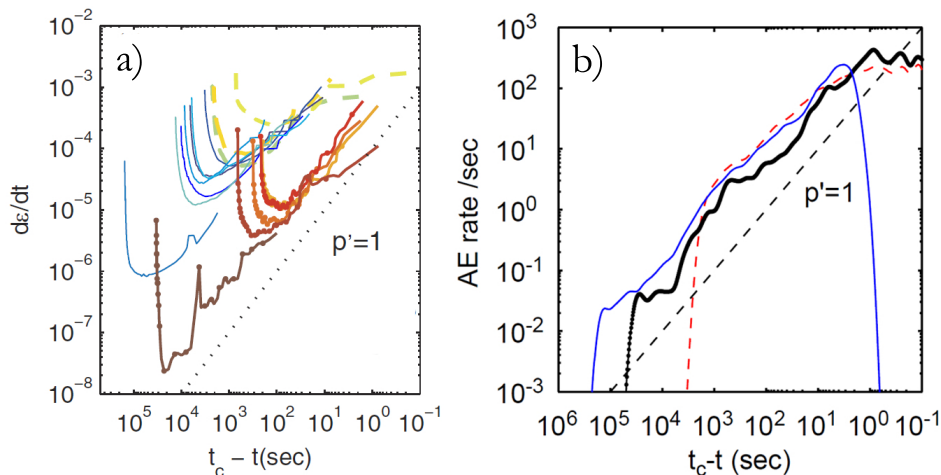


Figure 1.12: Ply glass / polyester composites. (a) Creep strain rate measured for 15 samples, plotted as a function of $t_c - t$ to emphasize the power-law divergence during tertiary creep (adapted from [Nechad 2005b]). (b) Rate of AE events for three representative samples plotted against $t_c - t$ (adapted from [Nechad 2005a]). In both plots, dashed lines correspond to the law $1/(t_c - t)$.

For instance, a remarkable experimental observation has been obtained for the delayed creep failure of composite materials [Nechad 2005a, Nechad 2005b]. Nechad *et al.* show that power laws govern the rate of acoustic emissions (AE) during both primary and tertiary creep, in nice qualitative agreement with the evolution of the macroscopic strain rate (Fig. 1.12). The authors use this observation to attribute the observed deformation entirely to microscopic plastic events (associated to crackling), since the very beginning of the experiment. This idea is supported by a theoretical model based on a modification of the fiber bundle model (FBM) [Pradhan 2010], complemented with ad-hoc viscoplasticity attributed to each fiber in order to reproduce correctly the complete creep curves. Despite the qualitative agreement between the measured $\dot{\gamma}$ and the numerical predictions, the model proposed by Nechad *et al.* suffers a few limitations, as pointed out by Jagla [Jagla 2011], the major defect being the fact that fiber ruptures in their modified FBM happen independently from each other, without any mechanism able to produce collective phenomena such as the microscopic avalanches associated to AE signal. Moreover, the nonlinear rheology attributed to each fiber (or representative element, in the language of Nechad *et al.*) is somehow artificial: both aspects leave the impression that the model proposed is too much coarse grained, and it does not grasp the fundamental dynamics actually occurring at the microscopic scale. Interestingly, it is shown by Jagla that other modifications of the original FBM, based on radically different assumptions, are also able to reproduce the $\dot{\gamma}(t)$ measured by Nechad *et al.*, and that some of these alternative solutions exhibit linear viscoelasticity and collective phenomena, both aspects missing in the original version. Once again, it appears that various models, profoundly different in essence, can nearly equally account for the same rheological features. Thus, if on the one hand AE data are very instructive, indicating the presence of plastic events with well defined statistical features, on the other hand their interpretation in terms of microscopic dynamics is not straightforward. Among the several questions that may arise, it is unclear for example if and how it might be possible to quantify the entity of the microscopic rearrangements producing one AE event, whereas the nature of the microscopic rearrangement is most probably not accessible with this technique.

Studying the tensile creep of paper, another composite displaying the same three creep regimes as the samples just discussed, Alava and coworkers resort to a more straightforward mesoscopic investigation, studying the evolution of spatial fluctuations in the local tensile strain as a way of addressing local plasticity and stress concentration [Rosti 2010, Koivisto 2016]. By coupling tensile creep and digital image correlation (DIC), the authors find that spatial fluctuations of local strain exhibit power-law scaling in time, indicating that power-law creep (also called Andrade creep regime) can be understood in terms of a nonequilibrium phase transition between "jammed" immobile states and "flowing", active states [Rosti 2010]. Moreover, the authors find a correlation between the amplitude of spatial fluctuations and the failure time, which is intriguing in itself, although again they conclude that this approach has only a limited benefit for the prediction of the failure time t_f [Koivisto 2016].

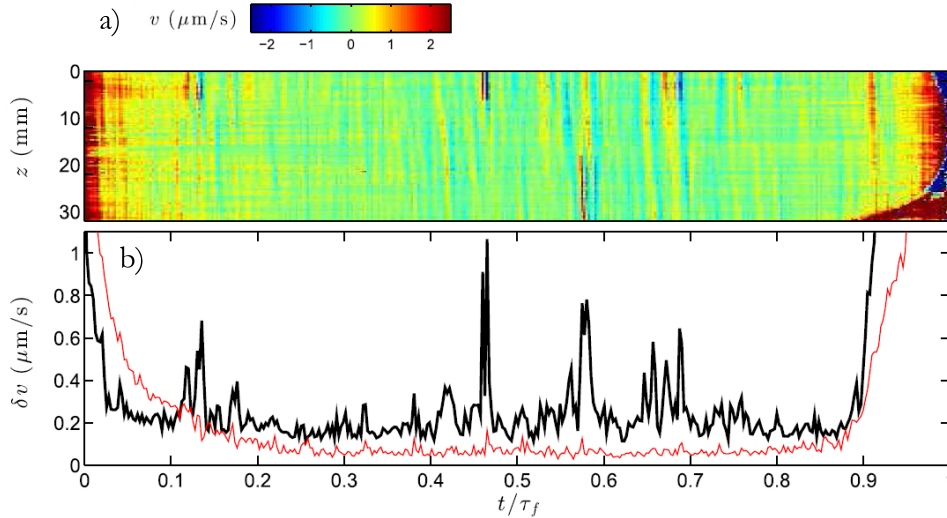


Figure 1.13: Protein gel. (a) Spatiotemporal diagram of the local velocity $\langle v(r, z, t) \rangle_r$ in the shear direction, averaged over the radial direction r and plotted in linear color levels as a function of z (coordinate in the vorticity direction) and t/τ_f (τ_f being the time to failure). (b) Standard deviation $\delta_z v(t)$ of $\langle v(r, z, t) \rangle_r$ taken over the vertical direction z (thick black line) together with corresponding standard deviation $\delta_r v(t)$ computed over the radial direction r on the z averaged $\langle v(r, z, t) \rangle_z$ (thin red line). Adapted from [Leocmach 2014].

Hence, the analysis of spatial heterogeneities in the local strain field appears to be a promising tool to achieve a better understanding of delayed creep failure. A very sensitive and practical probe for such heterogeneities has been developed by Manneville and coworkers, who in a long series of papers starting in 2004 [Salmon 2004, Manneville 2004] and continuing nowadays [Saint-Michel 2017] study the local velocity profiles with a novel ultrasound velocimetry technique. In an already mentioned example, Leocmach *et al.* apply this technique to the study of the creep and fracture of a model protein gel [Leocmach 2014], in order to elucidate in deeper detail the microscopic origin of the deviation from the linear viscoelastic primary creep. This is particularly intriguing since the authors show that the macroscopic $\dot{\gamma}(t)$ curve can be nicely described by the simple sum of a power law decrease $\sim t^{-\alpha}$, accounting for the primary creep, and a power law acceleration $\sim (t_f - t)^{-1}$, accounting for the tertiary creep (Fig. 1.11). Mathematically, this corresponds to a very smooth and gradual transition, implying that in fact plastic damage should occur throughout the experiment, even though it becomes macroscopically relevant only starting from the secondary creep. As a consequence of its gradual nature, this transition appears to be very elusive to macroscopic rheology. For this reason, the authors complement their study with a direct space investigation of strain heterogeneities, finding two interesting features: first, they observe the early nucleation, during secondary creep, of mesoscopic crack patterns, which grow in a subcritical way during tertiary creep,

a feature routinely observed in mechanical fatigue tests [Tomkins 1981]. They also show that the crack growth rate is proportional to the macroscopic shear rate, which sets the basis for a microscopic interpretation of the plastic deformation close to failure. Second, in stark contrast with the smooth rheology, the authors find that cracks nucleate in a discontinuous, intermittent way, which can be well characterized by space resolved ultrasound velocimetry (Fig. 1.13). In particular, the authors observe that the spatial fluctuations of the local velocities, quantified by their standard deviation δv (Fig. 1.13b), exhibit sharp peaks during the secondary creep, which are attributed to sudden plastic events like crack nucleation or intermittent growth. This suggests that the smooth evolution of the deformation observed in rheology is actually the result of an intriguing intermittent plastic dynamics occurring at the micro/mesoscopic scale, potentially showing common features with the crackling paradigm discussed above. This again demonstrates that a microscopic insight into the microscopic details of the dynamics under shear could provide a handy means of detecting the growing damage, which is a crucial parameter to get a better understanding and control on fatigue and delayed failure.

In this perspective, other scattering methods (different from ultrasound) can be coupled to shear rheology, namely light scattering, either in the single [Mohraz 2005] or in the multiple scattering regime [Ballesta 2016], X-ray scattering, either static [Denisov 2015] or dynamic [Leheny 2015], and neutron scattering [Kim 2014]. However, the already mentioned challenge of extracting the signal due to plasticity from the background given by affine deformation makes this technique more easily employed in oscillatory shear, as we will see in a while, whereas in transient experiments the use of scattering techniques is infrequent and limited to static scattering, which focuses on simple features like structural orientation [Mohraz 2005].

The most commonly employed technique to characterize the microscopic structure and dynamics under shear is microscopy. In particular, confocal microscopy has been widely used thanks to the possibility of accessing a full 3D information, essential to detect localized deformations, shear bands and complex microscopic rearrangements involving out-of-plane particle motion. The challenge faced by microscopy is again related to the already mentioned problem of averaging measurements on a statistically relevant ensemble, which typically limits the application of these techniques to the study of steady states, mostly in steady-rate experiments, where statistics can be improved by averaging over time. Nevertheless, there are a few fairly recent exceptions trying to investigate transient creep. For instance, Chan and Mohraz [Chan 2014] compare the microscopic dynamics under creep of a colloidal glass and a colloidal gel, and they observe that, despite their similar rheological behavior, the two systems exhibit rather different microscopic dynamics upon yielding. In particular, the dynamics observed in the gel accelerate abruptly when yielding occurs, whereas in the colloidal glass this transition is more gradual. The strong limitation of this work is that again, presumably because of poor statistics, the authors perform long time averages, which a priori is not justified in a transient experiment such as creep.

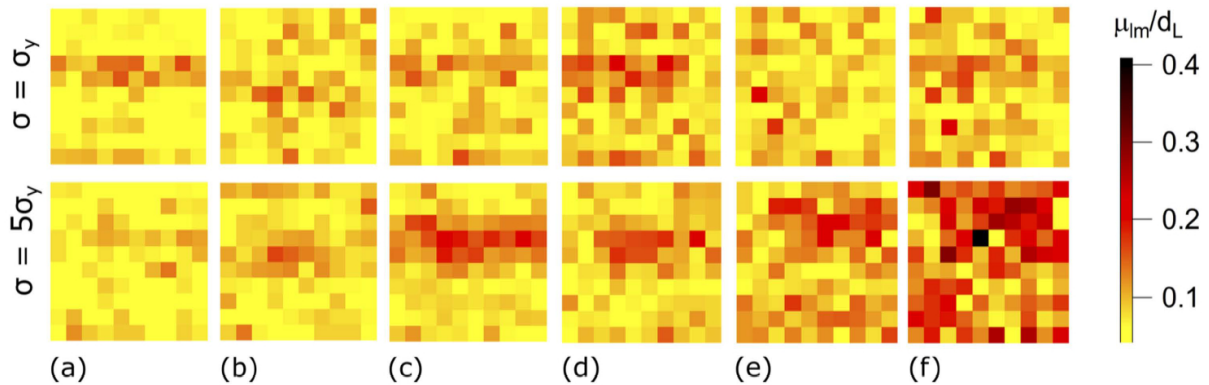


Figure 1.14: Binary colloidal glass. Maps of average particle mobilities $\mu_{lm}(t)$ normalized by the diameter d_L of large particles in the binary glass. Two different stresses are shown, one close to the yield stress ($\sigma \approx \sigma_y$, top) and a larger one ($\sigma \approx 5\sigma_y$, bottom). Different images are taken at different times during creep deformation, increasing from (a) to (f). Extracted from [Sentjabrskaja 2015].

On the other hand, the full space and time dependence of the observed microscopic dynamics is addressed with confocal microscopy under creep on a colloidal glass by Sentjabrskaja *et al.* [Sentjabrskaja 2015], in the attempt of characterizing the dynamics occurring prior to the delayed onset of flow. The authors measure the particles' mean square displacement Δy^2 along the vorticity direction (thus removing all contributions coming from the affine deformation), and observe a quantitative relation between Δy^2 and the macroscopic strain, indicating once again that creep deformation is a simple consequence of the plasticity that develops after the initial linear regime, as also suggested by a comparison with numerical simulations. An intriguing feature emerging from this work is that the onset of flow is associated to an increase of spatial heterogeneity in the plastic activity, with the appearance of regions of high local mobility and super-diffusive dynamics, whereas below the yield stress such heterogeneities remain almost constant in time (Fig. 1.14).

These examples show that the investigation of the slow dynamics occurring during sublinear creep is very challenging, but it is also crucial in order to achieve a better understanding, and possibly a prediction, of delayed creep failure. This is specially interesting since it could provide a means to monitor the health of a structure prior to its collapse. Some works pointed out that macroscopic indicators might exist [Nechad 2005b, Leocmach 2014], although their detectability is arguable [Rosti 2010, Koivisto 2016], whereas interesting dynamics are observed at a more local scale [Nechad 2005b, Leocmach 2014, Rosti 2010, Koivisto 2016, Sentjabrskaja 2015], potentially exploitable for predictions.

Clean experiments accessing at the same time the macroscopic creep deformation and the microscopic dynamics are very scarce, thus the microscopic origin of creep is far from being understood. Nevertheless, a few experimental works suggest the existence of a general framework, potentially able to describe creep and yielding without relying on the

specific details of the sample investigated.

One crucial step forward in this direction is therefore to identify the nature of the microscopic activity observed in the experiments, with particular focus on distinguishing reversible from irreversible processes. This is particularly challenging in transient experiments such as the ones discussed so far, and for this reason creep and steady-rate experiments are usefully complemented with measurements under a periodic stress or strain, where irreversible processes emerge as the only contributions to microscopic rearrangements observed across one or several periods.

1.3.3 Dynamic fatigue test

1.3.3a Reversibility and yielding in oscillatory shear

Thanks to the particularly simple mechanical response in the linear regime, oscillatory shear has been widely used to characterize the viscoelastic response of soft materials. By contrast, the mechanical response becomes generally very complex in the nonlinear regime, and sophisticated analysis is required to obtain a consistent picture [Rogers 2011]. Despite its complexity, it turns out that large amplitude oscillatory shear (LAOS) provides access to amazingly detailed information on the microscopic processes occurring during deformation, and much can be learned by such experiments [Hyun 2011].

As an example, we consider here the work of Carrier and Petekidis on the nonlinear rheology of a model soft colloidal glass [Carrier 2009]. The two main results of this work are summarized in Fig. 1.15: the first-harmonic viscoelastic moduli plotted as a function of the strain amplitude γ exhibit a trend similar to the one of Fig. 1.2, with a linear regime at small γ , a concentration-dependent yielding transition with a characteristic peak of G'' and a terminal regime in the limit of large amplitudes. A Fourier analysis of the detailed shape of the stress response of the sample reveals the appearance of higher order harmonics at finite amplitudes, marking a linear to nonlinear transition which appears to be sharper and shifted at higher strains for denser samples (Fig. 1.15b).

To account for the observed phenomenology, the authors propose a model based on a modification of the fluidity model by Derec *et al.* [Derec 2003]. The main assumption of this model is that the structural relaxation rate τ^{-1} can be decomposed in the independent (additive) contribution of a spontaneous relaxation rate τ_0^{-1} and a nonlinear, shear-induced contribution, which is called fluidity and denoted with the letter D . The structural relaxation time τ is then employed in a Maxwell-type constitutive equation: $\dot{\sigma} = -(D + \tau_0^{-1})\sigma + G(D)\dot{\gamma}$, where the elastic modulus $G(D)$ of the Maxwell fluid is also dependent on shear. Thus, the mechanical response to an arbitrary shear history can be computed once the time evolution of the fluidity is described by a kinetic equation. The expression postulated by Derec and borrowed by Carrier and Petekidis is very general, and reads:

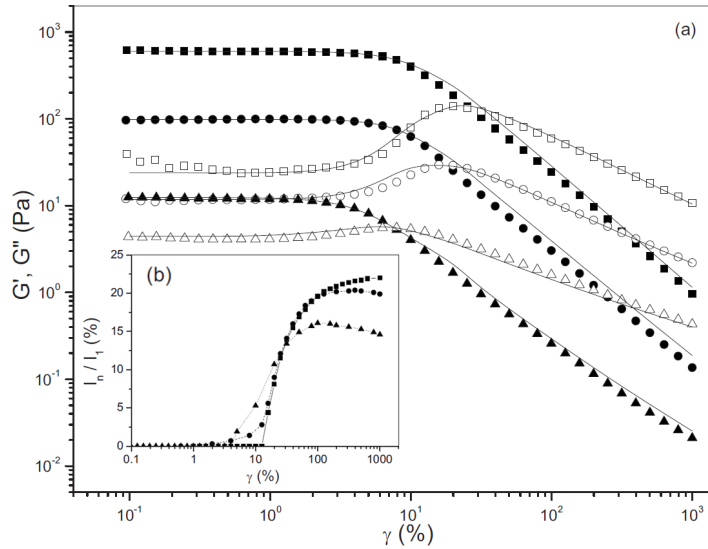


Figure 1.15: Soft colloidal glass. (a) Dynamic strain sweeps for three different volume fractions, decreasing from top ($\phi = 1.29$, squares) to bottom ($\phi = 0.77$, triangles). Experimental storage (closed symbol) and loss (open symbols) moduli. The model predictions are depicted with solid lines. (b) Fourier transform rheology: fraction of third harmonic versus strain amplitude for the same three volume fractions. Adapted from [Carrier 2009].

$$\dot{D} = \left[r + u \left(\frac{\sigma D}{\dot{\gamma}} \right)^\lambda \frac{\dot{\gamma}^{\nu-\varepsilon}}{D^\nu} \right] D^\alpha - v D^{\alpha+\beta} \quad (1.1)$$

where a set of 5 exponents ($\alpha, \beta, \lambda, \nu, \varepsilon$) and 3 coefficients (r, u, v) make the expression rather involved, so that even though experimental data are nicely described, it remains difficult to extract physical meaning from the model parameters. The relevant aspect of this work is that it links the measured nonlinear viscoelasticity to a conceptually simple microscopic quantity, which might be directly probed with techniques such as dynamic light scattering. Not only such measurements would represent a much stronger test of the fluidity model, but they could also provide a deeper insight on the nature of the microscopic processes responsible for the postulated strain dependence of the structural relaxation rate. More generally, a direct measurement of shear-induced structural relaxation would shed light on the microscopic origins of nonlinear rheology, which is one of the major fundamental open questions currently debated in the soft matter community [Schall 2007, Chan 2014], despite decades of attempts to find a general framework for these phenomena [Liu 1998, Trappe 2001].

To this aim, oscillatory rheology can be usefully coupled to more direct probes of the microscopic structure and dynamics. This is specially true since, although the linear and the large amplitude regimes are shared with similar features by all soft solids [Miyazaki 2006], the details of the yielding transition can be complex and reminiscent of the microscopic details of the sample, in particular for samples with a multiscale

structure such as star polymer glasses [Helgeson 2007] or colloidal gels [Koumakis 2011, Brunel 2016, Moghimi 2017]. Such a complex yielding calls for more direct methods to probe how the structure evolves under LAOS, and vice versa how yielding depends on the sample structure.

A first attempt at addressing these questions can be found in the work of Kim *et al.* [Kim 2014], who employ neutron scattering in order to study the structural modification of colloidal gels under large amplitude oscillatory shear. Focusing on the very large amplitude limit (γ_0 as large as 50 strain units), the authors observe that the large scale structure of the gel is periodically modified, which reflects in a periodic, anisotropic modulation of the scattered intensity at low scattering angles. This anisotropy is thoroughly characterized by the authors in both the velocity-gradient and the velocity-vorticity planes, and it is quantified by a structural parameter A_f employed in complicated 3D (σ, γ, A_f) diagrams inspired to the Lissajous plots (Kim *et al.* refer to those diagrams as structural Lissajous plots). We will see similar diagrams in chapter 7, where we argue that the concept of structural Lissajous plots has the potential to inspire and guide the delicate analysis of rheological Lissajous plots.

One limitation of neutron scattering, however, is the typically poor contrast, which limits the analysis to the highest strain amplitudes, preventing the authors from discussing the evolution of the structural signature across yielding. This problem is overcome by Schall and coworkers [Denisov 2015, Dang 2016] by employing synchrotron x-ray radiation on colloidal glasses. In this work, an anisotropy in the structure factor following strain amplitudes from the linear regime up to the large amplitude terminal regime is detected. In particular, the authors focus on tiny variations detected at a scattering vector corresponding to the position of the peak of the structure factor, where scattering techniques probe a lengthscale comparable to the distance between two particles in close contact. The authors argue that at such lengthscale the structural anisotropy stems from elastic shear distortion of the "cage" environment felt by each particle, which is also responsible for the elastic mechanical response observed in the linear regime (cage elasticity). Beyond the yield point, the observed response becomes prevalently liquid-like, a transition that is interpreted as shear-induced out-of-cage particle motion. Coherently, the authors find that the observed anisotropy vanishes beyond yielding. By introducing an ad-hoc order parameter, they measure the quadrupolar symmetry of the scattered intensity, and observe that it drops very sharply from 1 to 0 exactly in correspondence to the crossover between G' and G'' . They interpret this fact as the sign that cage elasticity is instantaneously and abruptly lost in a sharp transition reminiscent of thermodynamic first-order phase transitions. However, the authors admit that their interpretation is rather surprising, given the smooth crossover observed in rheology, and a true explanation of this apparent discrepancy is not proposed.

With the isolated (to the best of our knowledge) exception of this work, there is large consensus in the scientific community on the fact that the microscopic origin of yielding as it is observed in LAOS has to be attributed to a transition in the microscopic dynamics, rather than in the structure [Kawasaki 2015]. A convenient way of addressing irreversible

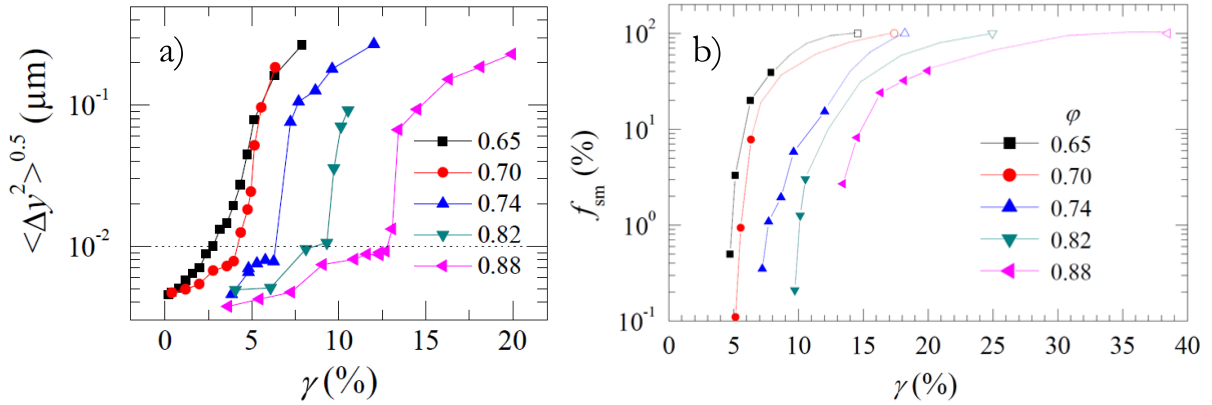


Figure 1.16: Concentrated emulsion. (a) Shear dependence of the rms displacement per shear cycle in the y direction (perpendicular to the applied shear). Data are labeled by the emulsion volume fraction. The dotted line is the threshold used to define the microscopic yield strain, γ_y . (b) Solid symbols: fraction f_{sm} of the "supermobile" drops. The abscissa of the open points correspond to the rheological crossover strain γ_c , where the sample is fluidized. The dotted lines are guides to the eye, consistent with the hypothesis that full fluidization may occur when all drops are supermobile, i.e. for $f_{sm} = 100\%$. Adapted from [Knowlton 2014].

microscopic dynamics under oscillatory shear is to monitor the evolution of the system across one full shear cycle, as it is done for example by Knowlton *et al.* on concentrated emulsions [Knowlton 2014]. The macroscopic rheology of the emulsions again resembles qualitatively Figs. 1.2 and 1.15, with a rather smooth and broad yielding transition that can be characterized by different "yield strains" (cf. Fig. 1.2). In order to shed light on the microscopic origin of yielding, the authors consider as relevant parameter the root mean square displacement $\langle \Delta y^2 \rangle^{0.5}$ of droplets observed stroboscopically, i.e. at two times separated by one full period, in the direction perpendicular to shear.

As expected, no significant irreversible motion is detected at the smallest strain amplitudes, where the emulsion deforms in an elastic, reversible way and all drops appear to be stroboscopically immobile within the measurement noise. With increasing deformation amplitude, however, $\langle \Delta y^2 \rangle^{0.5}$ exhibits a sharp increase (Fig. 1.16a) beyond a microscopic yield strain $\gamma_{y,micro}$, which proves to be much smaller than the crossover strain where $G' = G''$ (γ_f in Fig. 1.2), and closer to the yield strain (γ_y in Fig. 1.2) defined as the onset of the shear thinning regime. More in detail, the authors show that the sudden increase in $\langle \Delta y^2 \rangle^{0.5}$ is linked to the appearance of a population of mobile drops undergoing large deformations. Mobile drops initially represent a minority of the total drops, and they are spatially organized in mobile regions of the sample. Moreover, a careful analysis of the probability density function for irreversible displacements shows that the mobile drops can be further divided in two classes, with different mobilities. When the strain amplitude is increased beyond $\gamma_{y,micro}$, the drops belonging to the population with high-

est mobility, called "supermobile", grow in number while maintain their mobility fixed, until their fraction f_{sm} approaches 100% at a finite strain amplitude (Fig. 1.16b), close to the crossover between G' and G'' . This is consistent with the idea that full fluidization occurs when all (or at least the majority of) the particles are supermobile.

Besides demonstrating the power of real space analysis made possible by microscopy, the global picture presented by Knowlton *et al.* appears to be very instructive in light of the ongoing debate on the nature of the reversible to irreversible transition. In particular, the abrupt jump of the mean square displacement, associated with the appearance of a mobile population that counts an increasing fraction of the total drops, approaching unity at complete fluidization, is strongly suggestive of a first-order transition. In the work of Knowlton *et al.* a clear consistent picture could not be obtained, thus this remains a fascinating hypothesis, which stimulates future work in the field.

If Knowlton *et al.* only focus on stroboscopic experiments, much can be learned as well by following the full shear cycle, as it is done for example by Keim and Arratia on a crowded amorphous 2D assembly of colloidal particles segregated at the oil-water interface [Keim 2014]. An interfacial stress rheometer, based on a magnetic needle actuated by an electromagnetic field, is used to impose a controlled oscillatory stress to the suspension, and the macroscopic deformation, together with the local particle rearrangements, are probed by direct imaging of the interface. Although the general concept of the experiment is similar to the previous one, here the discussion is pushed beyond the stroboscopic analysis, and considers the detailed trajectory followed by each particle during the cyclic deformation. A purely stroboscopic analysis portrays a picture consistent with the one suggested by Knowlton *et al.*, with a first linear regime, where the mechanical response is elastic and reversible, with no microscopic rearrangements, and a well defined onset of microscopically irreversibility, marking a clear microscopic yielding transition beyond a critical amplitude γ_y . However, by analyzing the detailed particle trajectories, the authors argue that a more complex phenomenology hides behind this simple picture. Indeed, even in the linear elastic regime, particle motion is not perfectly affine, a phenomenon that can be interpreted as a consequence of the disordered structure. Even more interestingly, between the true linear regime and γ_y , an interesting intermediate regime is found, characterized by the presence of reversible plastic events. In this regime, the material is still stroboscopically static, but time-reversibility is broken by reversible plastic events that introduce hysteresis in the structural response. As a consequence, this dynamics, while being reversible upon one full cycle, dissipates energy, and contributes to the increase of the loss modulus, which indeed is found to deviate smoothly from its linear value slightly before γ_y . According to the authors, this observation might explain the apparent contrast between the sharp onset of microscopic irreversibility and the smoother transition observed in the viscoelastic properties.

An analogous result is obtained by Höhler *et al.* on aqueous foams, by using multiple light scattering in the DWS regime as a microscopic probe [Höhler 1997]. This technique allows one to probe extremely small rearrangements of the foam bubbles, which are

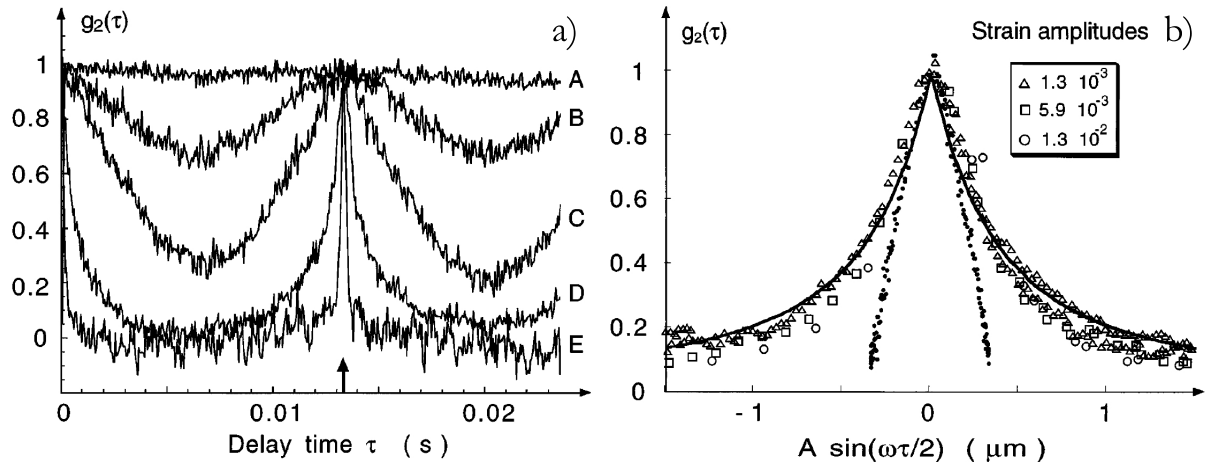


Figure 1.17: Aqueous foam. (a) Intensity autocorrelation data $g_2(\tau)$ plotted as a function of delay time τ . The curve labeled A has been obtained for a quiescent foam, whereas the other data sets have been measured at increasing strain amplitudes from B to E. The arrow indicates the period of the externally applied oscillating strain (correlation echo). (b) $g_2(\tau)$ represented as a function of the reduced variable $A \sin(\omega\tau/2)$ chosen to make plastic rearrangements apparent. The full line corresponds to the reversible plasticity model. To facilitate the comparison with the correlation produced by purely elastic deformation, one amplitude from the true linear regime has also been included, using small filled circles. Adapted from [Höhler 1997].

quantified in terms of an intensity correlation function $g_2(\tau)$, represented in Fig. 1.17a as a function of the time delay τ . The oscillatory deformation of the foam reflects in the observed oscillations of $g_2(\tau)$, which displays peaks for time delays equal to integer multiple of the oscillation period T , and it drops for intermediate τ values of an amount depending on the strain amplitude γ_0 . The peak at $\tau = T$ is the so-called correlation echo, and it contains information on microscopic reversibility: the peak value around 1 proves that at all strain amplitudes investigated the deformation is entirely reversible. On the other hand, detailed information on particle trajectories is encoded in the full shape of $g_2(\tau)$, which reveals that, within each shear cycle, reversible plastic rearrangements start occurring beyond $\gamma_y \sim 0.05\%$, remarkably below the yield point probed by rheology. The observation of reversible plasticity with DWS is much less straightforward than it would be in direct space analysis, and in order to make plastic rearrangements apparent, the authors replot their correlation data as a function of a rescaled variable (Fig. 1.17b). In this representation, $g_2(\tau)$ functions at different values of γ_0 are expected to collapse if the deformation is purely elastic. The fact that large amplitudes (open symbols in Fig. 1.17b) exhibit an upwards deviation from the trend observed in the linear regime (small filled symbols) is the sign that during each cycle the foam is periodically rearranged, such that each particle on average is displaced less than expected. This result, together with the previous ones, shows that the interplay between microscopic dynamics and nonlinear

rheological properties is complex, and it might exceed the intuitive notion of microscopic reversibility.

A slightly different insight into this interplay comes from a series of papers from Petekidis *et al.* [Petekidis 2002a, Petekidis 2002b, Petekidis 2003], who study the shear-induced microscopic rearrangements in colloidal glasses of hard spheres at different concentrations. The microscopic dynamics are probed again by DWS, giving access to intensity correlation functions qualitatively similar to the ones of Fig. 1.17. With respect to Höhler *et al.*, here the deformations are much larger, so that the authors have to restrict their analysis to time delays very close to the correlation echoes, since elsewhere $g_2(\tau) - 1 \approx 0$. Another relevant difference with respect to the previous work is that here the spontaneous Brownian motion of the particles contributes to a substantial decorrelation of higher order echoes even in the linear regime. Thus, in order to emphasize the role of shear-induced rearrangements, the authors normalize the echo peak height by its low strain amplitude limit. The result is shown in Fig. 1.18 as a function of γ_0 for samples at different volume fractions ϕ . The complexity of the figure is rationalized by identifying, for each strain amplitude, two characteristic strains: a smaller one, γ_{c1} (top arrows), indicating the first departure from unity, and a larger one, γ_{c2} , indicating complete disappearance of the echo. A parallel with the work of Knowlton *et al.* can be drawn by interpreting γ_{c1} as the onset of microscopic irreversibility, and γ_{c2} as the strain at which complete fluidization occurs. In particular, the authors discuss the unexpected large values of γ_{c1} , which can be as large as 15% at $\phi = 0.623$ and comes together with the surprisingly large recoverable elastic strains (again around $\sim 10 - 15\%$) that those materials can tolerate before yielding. The authors explain this behavior with the concept of cage elasticity, which they define as the ability of a particle and its cage of neighbors to undergo significant distortion while still retaining its identity. A comparison with rheology shows that for the concentrated samples deviations from linearity can be observed already at strains significantly smaller than γ_{c1} : thus, reversible plastic rearrangements must take place in colloidal glasses as well.

The result is even more apparent at the lowest concentrations (still beyond the glass transition), where γ_{c1} is small, implying that complete reversibility is lost rather early, but the correlation remains significant up to very large deformations, beyond 50%, a value several times larger than the yield strain of the material. This implies that several rearrangements have to occur in sequence within one oscillation: therefore the trajectory of particles must be tortuous, but it must also be largely reversible, which is rather unexpected. In an attempt to explain this phenomenon, the authors refer to an argument that would be more completely disclosed by Pine *et al.* in more recent years, with reference to microscopic reversibility in diluted suspensions [Pine 2005]. They argue that since the equations describing hydrodynamic flow at low Reynolds numbers are symmetric upon time reversal ($t \rightarrow -t$), particles' trajectories should always be reversible in absence of Brownian motion. Thus, they attribute the onset of irreversibility to Brownian motion, whose effectiveness at introducing irreversibility into the particle trajectories increases steeply on approaching random close packing, which explains the monotonic decrease of

γ_{c2} with increasing ϕ .

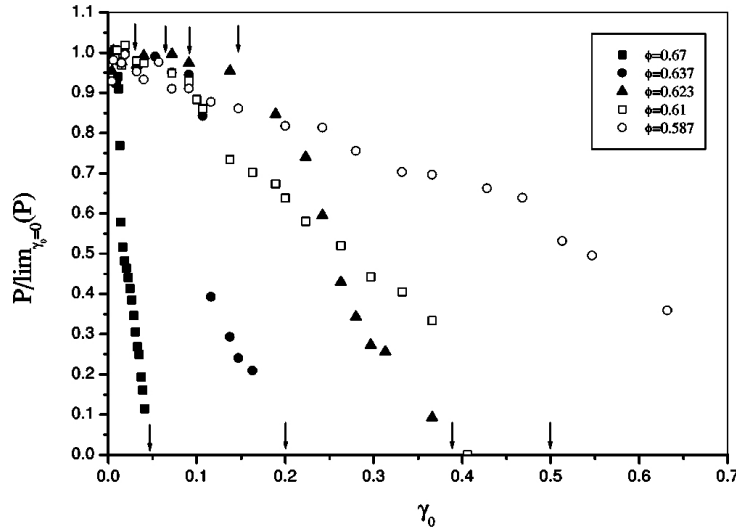


Figure 1.18: Hard sphere colloidal glass. Strain dependence of the relative first echo height ($P/\lim_{\gamma_0 \rightarrow 0} P$) at several volume fractions as indicated. Presenting the data in this form removes the effect of Brownian motion. Thus, when $P/\lim_{\gamma_0 \rightarrow 0} P = 1$ the sample strains elastically, and any reduction below 1 implies irreversible shear-induced rearrangements. Adapted from [Petekidis 2002a].

These examples show that, by comparing the system before and after a cyclic shear of amplitude γ_0 , a rich and complex phenomenology is found, which is further complicated by the observation of reversible plastic deformations, contributing to nonlinear rheology but not to stroboscopic dynamics. In an attempt to rationalize the results, we can identify several regimes: (1) a true linear regime at small γ_0 , where microscopic dynamics are thermally-activated, and eventual nonaffine deformations only stem from the heterogeneity of the structure; (2) a regime where nonlinear rheology might coexist with microscopic (full-cycle) reversibility, as a consequence of reversible plasticity; (3) the onset of microscopic irreversibility beyond a microscopic yield strain; (4) a gradual and generally complex transition where microscopic reversibility is progressively lost and the mechanical response evolves towards full fluidization; (5) a terminal regime, characterized by liquid-like, microscopically irreversible response.

This picture is intriguing, and calls for a deeper investigation of the microscopic processes observed under shear. One natural way to complete the above observations is to extend the analysis from one to several shear cycles, which can help elucidating the nature of irreversible rearrangements (e.g. diffusive, ballistic or something still different) observed in the various regimes. This will be discussed in the next paragraph.

1.3.3b Dynamic fatigue and damage accumulation

Oscillatory shear has the very appealing property of allowing one to investigate the sample in a stationary state: provided that such state exists and can be experimentally reached, it represents a convenient way to investigate the sample mechanical properties, since successive repetitions of the same measurement yield the same result, regardless the complex history of the material. However, when working with disordered, out-of-equilibrium materials, stationarity becomes a delicate concept because of the intrinsic aging dynamics characterizing most of them. As a consequence of aging, the viscoelastic moduli measured in the linear regime display a typically slow evolution in time, which may be safely neglected if the experimental time is short enough. However, one rarely discussed yet important aspect is that nonlinear rheology calls stationarity into play once again. Indeed, the slow time evolution of the mechanical properties measured in the linear regime can be accelerated by additional shear-induced processes, as it is captured for example by the above mentioned fluidity model [Derec 2003] or in a more complex way by theories like mode coupling theory [Yamada 1975, Reichman 2005] or soft glassy rheology [Sollich 1998]. Therefore, under nonlinear solicitations, stationarity may be more difficult to guarantee, so that care has to be taken in the interpretation of the experimental results. This remark might include as well the works mentioned above, since in the presence of strong shear-induced aging the yielding transition can look different when probed with different protocols [Perge 2014]. This effect is very well known since XIX century, when engineers discovered that a bridge designed to withstand the weight of several trains could collapse under the repeated transit of just one train. In a more controlled experiment, one would observe that oscillatory shear with amplitude slightly beyond the linear regime progressively weakens the material, until delayed failure may be observed. This weakening is sometimes called dynamic fatigue, as opposed to the static fatigue observed during creep. Despite the important similarities shared by the two phenomena, which have sometimes inspired intriguing, yet arguable direct analogies [Gibaud 2010], the two delayed failure mechanisms are distinct, and a comparison between the two may be very instructive. We will see an example in chapters 6 and 7. Moreover, the possibility of controlling and predicting delayed dynamic fatigue failure would have an enormous impact in real life applications, which further motivate to address this second mechanism in detail.

The delicate interplay between aging and yielding is discussed in detail using a soft colloidal glass as a model system by Rogers *et al.* [Rogers 2011], who investigate the complex memory of the sample by subjecting it to different oscillatory shear histories, both in a strain-controlled and in a stress-controlled fashion. As expected, the authors observe that aging is only slightly affected by small amplitude oscillations, whereas under large shear amplitudes the sample is fully rejuvenated during each cycle, so that stress and strain imposed protocols yield similar results in the two opposite regimes. However, as intermediate shear amplitudes are imposed, the behavior becomes more complex and dependent on whether the aging protocol was stress- or strain-imposed. A first conclusion

drawn by the authors from this observation is that under moderately nonlinear shear the material exhibits a faster evolution towards stiffer, more homogeneous configurations, since the imposed deformation helps the system to explore the free energy landscape, sooner locating deeper minima. Moreover, by further increasing the shear amplitude closer to the yield point, the authors argue that yielding is a gradual process: when the applied stress or strain in an amplitude sweep causes an event that would ultimately lead to yielding under those conditions, sufficient time must be allowed to elapse in order for that event to fully propagate and for yielding to occur.

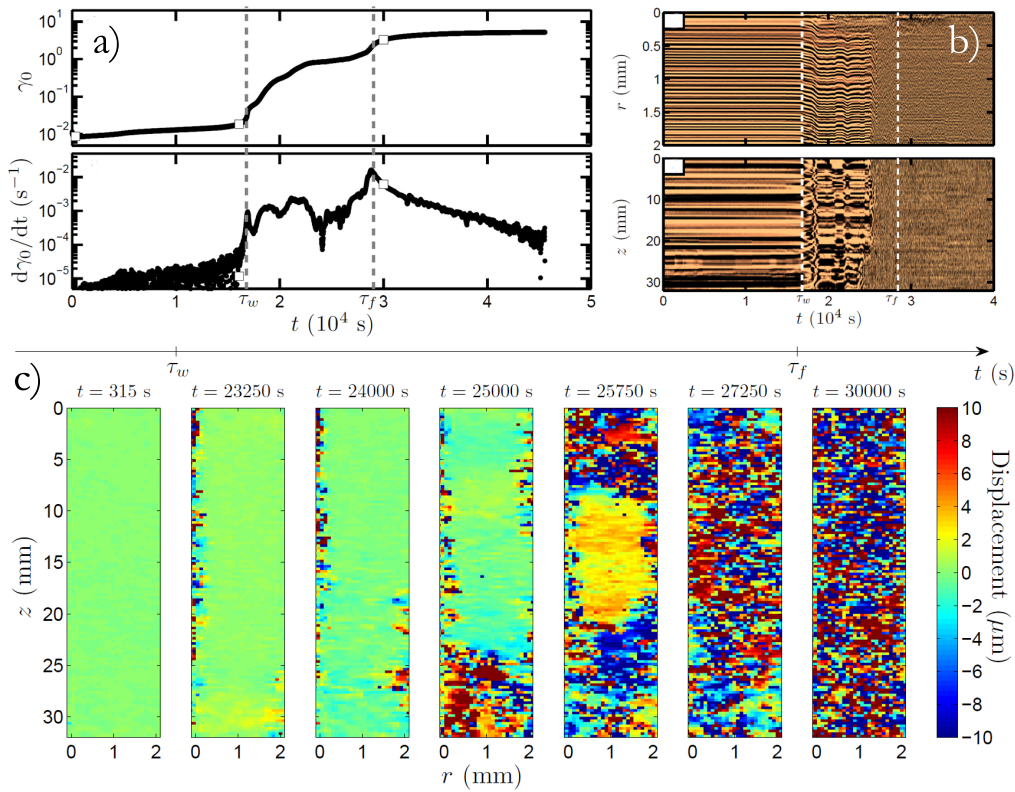


Figure 1.19: Carbon black gel. (a) Time-resolved LAOStress experiment illustrating the yielding and fluidization under an oscillatory stress of constant amplitude σ . Gray dashed lines indicate two characteristic times: the time τ_w such that $G'(\tau_w) = G''(\tau_w)$, which defines apparent yielding, and the time τ_f at which $d\gamma_0/dt$ reaches a global maximum, which corresponds to full fluidization as inferred from ultrasonic imaging. (b) Spatiotemporal diagrams of the ultrasonic speckle images recorded simultaneously to the rheological data shown in panel (a). White dashed lines indicate τ_w and τ_f . (c) Images of the displacement field $\Delta(r, z, t)$ between two successive ultrasonic pulses at various times during the yielding process. Adapted from [Perge 2014].

If this result is true for a colloidal glass like the one investigated by Rogers *et al.*, it is all the more true for network forming systems like colloidal or polymer gels, where a small damage in the stress bearing network reflects in a significant change in the mechanical

properties, which may also imply catastrophic delayed failure beyond a given level of damage. This effect is extensively addressed by Manneville and coworkers with stress imposed LAOS on different gels, namely carbon black gels [Gibaud 2010, Perge 2014] and protein gels [Saint-Michel 2017]. Their experiments consist in applying an oscillating stress with amplitude σ_0 below the yield stress and to follow the amplitude $\gamma_0(t)$ of the resulting deformation as a function of time spent under oscillatory stress. The authors observe that even for stress levels much below the yield stress, $\gamma_0(t)$ is not constant, but slowly increases over time, in a sublinear growth which is read as a manifestation of fatigue. This interpretation is confirmed by the direct observation of delayed fatigue failure, occurring after a waiting time τ_w (Fig. 1.19a). At τ_w , the amplitude $\gamma_0(t)$ displays a strong, sudden acceleration, and enters in an unstable regime characterized by strong temporal fluctuations of its time derivative $d\gamma_0/dt$. This unstable regime lasts until a second characteristic time τ_f , after which the strong fluctuations disappear and $\gamma_0(t)$ approaches a plateau value. While Saint-Michel *et al.* try to predict such delayed failure by looking at an intriguing, yet obscure, power-law scaling of higher order harmonics as a function of the instantaneous amplitude [Saint-Michel 2017], here we are rather interested in understanding the microscopic processes occurring in the sample during the three regimes identified by rheology, with particular focus on the change in dynamics detected close to the two characteristic times τ_w and τ_f . To this aim, Perge *et al.* complement their rheological measurements with a more local insight obtained by the already introduced ultrasound scattering technique. In particular, here the authors fully exploit the coherence of their scattering signal $S(z, r, t)$: following its stroboscopic evolution (Fig. 1.19b), they find that the speckles are mostly static until τ_w , which means that the scatterers are essentially stroboscopically immobile during the first induction time. This is reminiscent of a solid-like behavior, corroborated by the fact that here $G' > G''$. In the opposite regime, after τ_f , the opposite situation holds, and the scatterers are completely rearranged after each shear cycle: this is instead suggestive of a liquid-like behavior, consistent with the dominating loss modulus G'' . The intermediate situation is also intriguing, and it is better addressed in Fig. 1.19c, where a cross-correlation of the speckle images was used to extract the displacement maps. The authors argue that for waiting times between τ_w and τ_f , the results can be interpreted as the gradual fluidization of the gel, starting at time τ_w with slip at the inner moving wall and attaining completion at time τ_f .

The gradual fluidization process observed by Perge *et al.* consolidates the result obtained by Rogers *et al.*, and suggests that the gradual nature corresponds to a progressive erosion of solid-like domains starting from the boundaries (Fig. 1.19c).

The slow process of damage accumulation can also be usefully investigated by coupling the macroscopic deformation to a more direct probe of the microscopic dynamics. With respect to the previous experiments discussed, dynamic fatigue experiments are particularly challenging for direct space approaches based on particle tracking, which proved to be very effective in detecting displacements across one cycle, because of the important and potentially out-of-plane rearrangements. For this reason, scattering techniques prove to be more convenient, because they measure collective dynamics, with no need

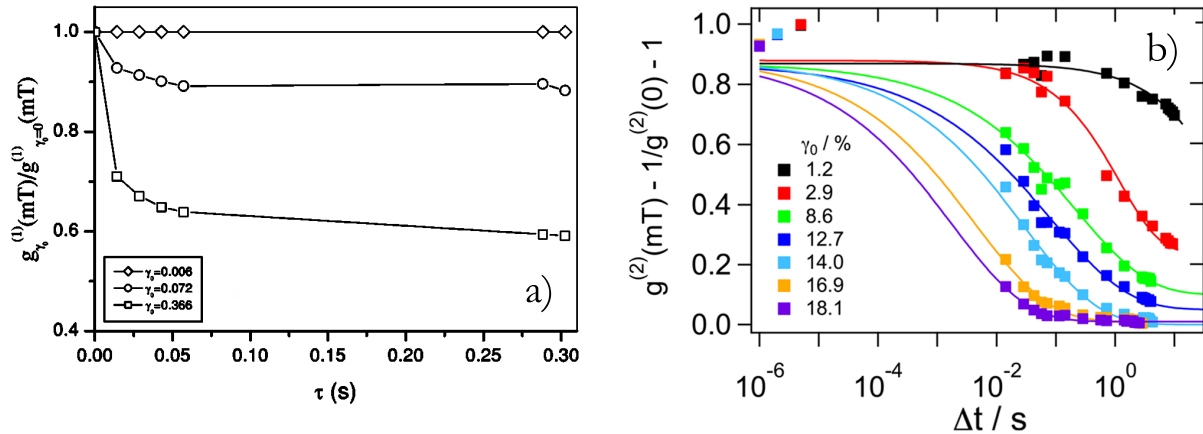


Figure 1.20: (a) Hard spheres colloidal glass. Decay of high order echoes at various strain amplitudes is represented by the ratio of the amplitude of the m th echo at a strain γ_0 to the corresponding amplitude at the lowest strain. This ratio takes into account the decay of the high order echoes due to Brownian motion (adapted from [Petekidis 2002a]). (b) Colloidal gel. Decay of high order echoes at various strain amplitudes, fitted by stretched-exponential functions Adapted from [Laurati 2014].

of identifying single particles. For example, Hébraud *et al.* [Hébraud 1997] study shear-induced rearrangements in concentrated emulsions with DWS, by following the decay of higher order correlation echoes. They find that, after the first correlation drop from $g_2(0) - 1 = 1$ to the value of the first correlation echo, a quasi-plateau is reached, with the level higher order echoes remaining essentially the same of the first one. The authors conclude that most of the rearrangements occur within one shear cycle, and they only discuss the decay of the first correlation echo. On the other hand, Petekidis *et al.* perform a similar experiment on colloidal glasses [Petekidis 2002a], and find that actually higher order correlation echoes slowly decay towards an apparent plateau value, which they call nonergodicity parameter (Fig. 1.20a). Again different is the result obtained by Laurati *et al.* [Laurati 2014] on colloidal gels, where full decorrelation is observed in the long time limit, which suggests that the apparent plateau value observed by Petekidis *et al.* might correspond to a slower relaxation mode. Interestingly, here the authors find that the decay of higher order correlation echoes is well described by a stretched exponential relaxation with a characteristic time rapidly decreasing with increasing strain amplitude beyond yielding (Fig. 1.20b).

Such an acceleration of microscopic dynamics observed at large amplitudes is very interesting if compared with the above mentioned models like the fluidity model, where a $\dot{\gamma}$ -dependent structural relaxation time was postulated: although to the best of our knowledge a comparison has never been attempted, perhaps the correlation echo experiments might represent an interesting way to check the microscopic implications of those models, which prove to describe rheology very accurately. In order to achieve such a quantitative comparison, however, one needs to obtain information about the nature of

the dynamics and their spatial heterogeneities. DWS can easily be performed in a space-resolved fashion [Nagazi 2016], but it is much more difficult to distinguish e.g. ballistic from diffusive motion with such technique. For this reason, single scattering techniques are also appealing, because such distinction can be done by comparing the relaxation times at different scattering vectors q (cf. chapter 2).

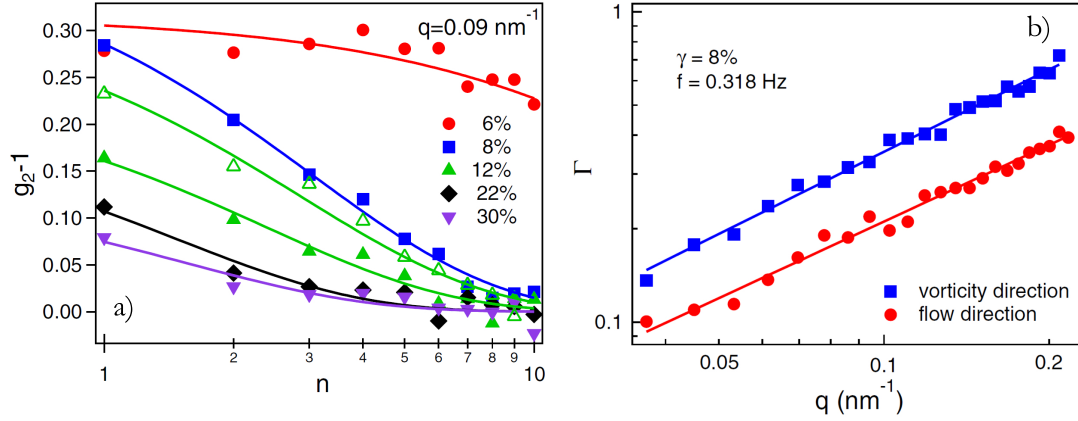


Figure 1.21: Colloidal gel. (a) Echo-peak amplitudes at one representative scattering vector $q = 0.09\text{nm}^{-1}$ along the vorticity direction as a function of delay cycle for different strain amplitudes. Also shown are echo peaks obtained at $\gamma = 12\%$ along the flow direction (open green triangles). Solid lines are exponential fits. (b) Echo-decay rate Γ (in 1/cycle) at one representative amplitude $\gamma = 8\%$ as a function of scattering vector q oriented in the flow direction (red circles) and in the vorticity direction (blue squares). Solid lines represent power-law fits. Extracted from [Rogers 2014].

One of the first examples is represented by the work of Rogers *et al.*, who probe the internal dynamics of a colloidal gel under cyclic shear using X-ray photon correlation spectroscopy (XPCS) [Rogers 2014]. The authors discuss different scattering vectors oriented both along the flow direction and perpendicular to it (in the vorticity direction). An overview of their results is represented in Fig. 1.21a. For the representative scattering vector shown, the decay of correlation echoes coincides with the spontaneous dynamics for strain amplitudes lower than 6%, whereas it becomes much faster starting from 8% deformation. This allows to locate the transition to irreversible deformation to a threshold $\gamma_c \sim 7\%$, higher than the strain at which the deviation from linear viscoelasticity is observed ($\gamma_{nl} \sim 2\%$), which suggests the presence of reversible plasticity. In the probed range of scattering vectors and strain amplitudes, the authors find that the decay of the correlation echoes is well fitted by single exponential decays, from which a relaxation rate $\Gamma(q, \gamma_0)$ can be extracted, shown in Fig. 1.21b. Interestingly, there is evidence that dynamics is non-isotropic, but it is faster in the vorticity direction, which is unexpected. Even more interestingly, $\Gamma(q, \gamma_0)$ exhibits a clear power-law dependence on the scattering vector, which is exploited by the authors to infer the spatial-size distribution of the single plastic events occurring under shear. By means of a simple scaling argument, the authors

conclude that the characteristic length scales rearranged by plastic events during LAOS at one given strain amplitude follow a power-law distribution, which is read as the sign that yielding can be described as a non-equilibrium critical transition. Without entering into the details of this discussion, we observe that an analysis of this kind has the potential to truly shed new light on the interdependence of microscopic dynamics and macroscopic nonlinear rheology, which is a key aspect determining the dynamic fatigue of materials.

1.3.4 Conclusion

To conclude, this (far from exhaustive) overview has shown that a huge effort has been put in recent years to characterize the failure mechanisms of soft materials. Although the phenomenology is generally very rich and complex, showing features that are often sample- and protocol-related, some knowledge has been acquired on the conditions under which a sample may flow viscoelastically or exhibit failure, either in a ductile-like manner or in a brittle-like manner. Failure process is most easily investigated in steady-rate experiments, where failure is expected to occur at large Weissenberg number $Wi = \dot{\gamma}\tau > 1$, where $\dot{\gamma}$ is the imposed shear rate and τ the longest relaxation time in the system. In those experiments, it was shown that deeper insight on the microscopic origin of failure can be obtained by coupling rheology with a microscopic characterization of the microscopic structure and dynamics, coming either from microscopy or from static scattering. These works have shown that brittle fracture occurs as a consequence of a cascade of break-up events weakening the stress-bearing backbone of the structure and triggering mechanical instability. However, the amount of bond breaking needed to produce such failure is still unclear, and likewise it is somehow controversial the nature and the amount of plastic events occurring during sample deformation before failure.

The investigation of delayed failure under a constant load is slightly more complex, not only because of the long and often unpredictable failure times, but also because of the complex time-dependence of the deformation rate during the induction time, which represents an additional challenge for techniques oriented at a microscopic characterization of the dynamics during creep. However, it turns out that the nature of those plastic dynamics and their temporal and spatial distribution might represent an important indicator, potentially opening the way towards a better control of delayed failure. To this end, a crucial aspect emerging from experiments is to be able to distinguish reversible from irreversible dynamics. At the macroscopic level, such distinction is addressed with creep recovery, which shows that, depending on the specific sample and experimental conditions, creep may be completely or partially reversible. Since failure is typically an irreversible phenomenon, the detection of a transition from reversible to irreversible deformation can represent a fundamental first step towards failure prediction. It turns out that such detection, although possible in principle, is in practice extremely delicate, since the yielding transition observed by rheology is typically very smooth and gradual. However, it has also been shown that such smooth rheological behavior might correspond,

at the microscale, to a nontrivial, intermittent behavior, and it has been proposed that indeed the precursors of failure might be identified by an investigation of the microscopic dynamics. Therefore, such observation during creep appears to be very promising, but it is also very challenging, and despite some attempts to the best of our knowledge this has not yet been clearly demonstrated.

On the other hand, similar investigations have been performed under oscillatory shear, where a comparison between the system before and after a cyclic shear with a given amplitude makes irreversible displacements apparent. As a result of these investigations, a rich phenomenology has been revealed. Deformations are elastic and reversible in the linear regime and completely irreversible in the large amplitude limit, but the transition between the two regimes is far from well understood. Interestingly, recent experiments have shown that the shear-induced acceleration of structural relaxation can be characterized following the evolution of the system after many shear oscillations. This is experimentally challenging, but also very promising, since addressing the amplitude-dependent relaxation time might provide a quantitative link between microscopic rearrangements and macroscopic mechanical properties, which is a rather old but still very debated topic.

1.4 Outline of the thesis

In our work we address some of the above challenges by means of a novel experimental setup coupling a stress controlled shear cell, which will be described in chapter 3, with a small angle static and dynamic light scattering apparatus. We cope with the challenges described above, related to performing dynamic light scattering experiments under transient shear, by means of an advanced data analysis technique, which is introduced in chapter 4. As a first model system we choose to investigate a colloidal gel, which exhibits a peculiar power-law rheology discussed in chapter 5. The well-controlled fractal structure and dynamics, as well as the simple phenomenological model accounting for its linear rheology, make this sample the ideal system to study how structure and dynamics are affected by shear. Creep and delayed failure are addressed in chapter 6. We show that affine and nonaffine dynamics can be effectively observed. Although the shear rate appears to be smooth and featureless, at the microscale we can clearly detect a sharp transition to irreversible microscopic dynamics, which we can consider a microscopic dynamic precursor of the failure that would only happen hours later. Moreover, a detailed analysis of the precursor shows an intriguing interplay with the microscopic architecture of the sample, which represents an additional step in the investigation of the microscopic origin of the rheological behavior. On the other hand, in chapter 7 we investigate the linear to nonlinear transition as it is observed in oscillatory shear, and we show that such transition, which is again smooth when probed by rheology, corresponds to a very sharp acceleration of the structural relaxation, which eventually leads to delayed failure under oscillatory stress with moderate amplitudes. In chapter 8 we check the generality of our previous findings by investigating another sample, with completely different microscopic

structure, namely a dense packing of soft microgel particles. Finally, a conclusive chapter closes the thesis with a general discussion on the results obtained and on the perspectives that our work opens to future investigations.

Experimental Methods

Contents

2.1	Light Scattering	49
2.1.1	Basic principle	50
2.1.2	Small angle light scattering	52
2.1.3	Static light scattering (SLS)	53
2.1.4	Dynamic light scattering (DLS)	56
2.2	Rheology	59
2.2.1	Shear deformation: stress and strain	59
2.2.2	Linear viscoelasticity	61
2.2.3	Nonlinear viscoelasticity	65

As anticipated in chapter 1, the ability to couple the macroscopic characterization of the mechanical properties with an insight on the microscopic structure and dynamics is fundamental to tackle the challenging and fascinating issue of material failure and failure precursors. In this chapter, we briefly review the light scattering (section 2.1) and rheology (section 2.2) methods, which will be used throughout this thesis.

2.1 Light Scattering

A scattering experiment can be understood by drawing an analogy of how vision works. When we observe an object, what our eye detects is the response of the object to light illuminating it, and which we interpret as a property of the object itself (color, shape, ...). The general idea underlying a light scattering experiment is similar: an incident light beam interacts with the sample, and as a result a part of it is scattered in a different direction and collected by an optical system, which plays the role of our eye. The main difference with respect to sight is that instead of focusing on the image of the object, therefore distinguishing light coming from different parts of it, a scattering experiment typically studies the intensity scattered by the entire sample in the far field, for example by placing the detector in the focal plane of a lens, thus losing space-resolved information. This is a good method to access average (statistical) properties of the sample, related to its internal microscopic structure.

Different types of radiation other than visible light (for example X rays or neutrons) can also be employed in a scattering experiment, providing valuable complementary information to light scattering thanks to the specific interactions with the sample and the different length scales probed. However, once those differences are taken into account, all scattering experiments can be described to a large extent in a unified way: for this reason, the present section will only focus on light scattering.

2.1.1 Basic principle

A schematic of the basic scattering geometry is shown in figure 2.1. Coherent light from a laser is directed towards the sample, and the intensity scattered at a well defined *scattering angle* θ is collected by a photosensitive element, e.g. a photodiode. In what will follow, we will take the so-called first Born approximation, in which only a small fraction of the incoming beam is scattered: this corresponds to the single scattering regime, where light is scattered no more than once before reaching the detector.

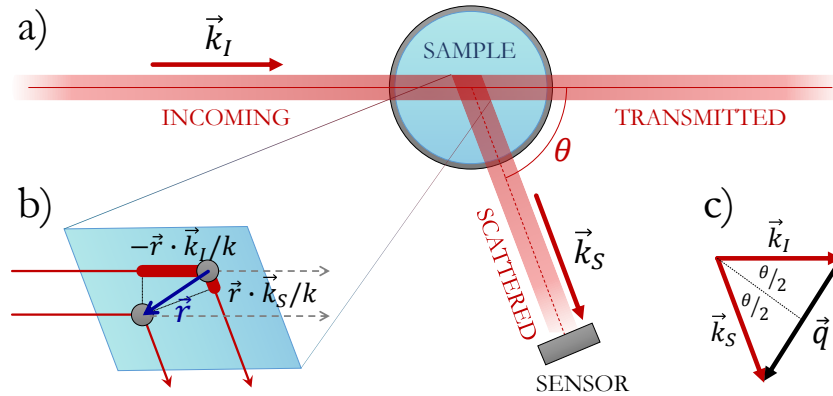


Figure 2.1: (a) General scheme of a light scattering experiment (top view): laser radiation (characterized by an incoming wavevector \vec{k}_I) illuminates the sample, and light scattered at a given scattering angle θ (with wavevector \vec{k}_S) is detected in the far field. In the first Born approximation, the transmitted beam is always much more intense than the scattered beam. (b) Closer look at the scattering volume, highlighting the contribution of two scatterers, at relative distance \vec{r} . The difference in optical path between the two scattered waves is represented by the thick lines, whose total length Δs is given by Eq. 2.2. (c) Geometric construction of the scattering vector \vec{q} , whose modulus is calculated using Eq. 2.3

In order to understand the intensity pattern of scattered light and extract from it some information on the sample, a theoretical model is needed. Two complementary approaches are possible:

- A *continuous*, statistical approach: one can define a response function $\varepsilon(\vec{q}, \omega)$ (well defined in the Fourier space, thus nonlocal), which relates the external perturba-

tion to the system response, i.e. the variation of an observable quantity coupled to the perturbing field. For light scattering, the probe is the electric field, and the response function is the polarizability, a quantity simply related to the refractive index $n(\vec{x}, t)$. The scattered light can thus be linked to the presence of local fluctuations in $n(\vec{x}, t)$, from which one can learn important details about the structure of the sample. Moreover, the time dependence of $n(\vec{x}, t)$, revealed by temporal fluctuations in the scattered light, can be analyzed to get an insight on the sample dynamics.

- A *discrete* approach, starting from one point-like constituent. Its interaction with the incoming beam results in a scattered spherical wave, with a characteristic intensity distribution. Waves scattered by each particle inside the sample superpose in the far field, creating a complex interference pattern (a *speckle* pattern), encoding detailed information about particle shape, size, position and dynamics. This section will follow this second approach, showing how to extract valuable information from the static properties of the speckle pattern and from its temporal fluctuations.

From classical electrodynamics [Jackson 2007], it is known that, when a single charge is accelerated by an electromagnetic wave, it emits a spherical wave, whose intensity profile follows the so-called dipole distribution:

$$\frac{dP_{ed}}{d\Omega} = \frac{ck^2}{8\pi} p^2 \sin^2 \varphi \quad (2.1)$$

where c is light's speed, $k = 2\pi n/\lambda$ is the wavevector of the incoming beam, with λ its wavelength in vacuum and n the refractive index of the medium, p is the induced dipole and φ is the angle between the scattered beam and the polarization axis of the incoming beam, assumed to be linearly polarized. A speckle pattern can be understood as the interference of all spherical waves scattered by the sample: their number is huge, but the basic underlying principle can be grasped by considering the contribution of just two scattering elements (Fig. 2.1b). What makes the interference nontrivial is the relative phase factor coming from the different distance Δs traveled by the waves, which can be expressed as a function of the relative position \vec{r} of the two scatterers:

$$\Delta\phi = k\Delta s = (\vec{k}_S - \vec{k}_I) \cdot \vec{r} = \vec{q} \cdot \vec{r} \quad (2.2)$$

Here \vec{k}_S and \vec{k}_I are the scattered and the incident wavevectors respectively, which have the same modulus $k = \frac{2\pi n}{\lambda}$ since dipoles scatter light with the same wavelength as the incident light. Their difference $\vec{q} = \vec{k}_S - \vec{k}_I$ is called the scattering vector, which is the relevant parameter defining the lengthscale being probed by a scattering experiment. Indeed, one can easily see that the interference changes from constructive ($\Delta\phi = 0$) to destructive ($\Delta\phi = \pi$) for particle relative displacements $\delta r = \pi/q$ along the \vec{q} direction.

The scattering vector is related to the scattering angle θ by the simple relation (Fig. 2.1c):

$$q = 2k \sin \frac{\theta}{2} \quad (2.3)$$

Thus, the larger the scattering angle, the smaller the lengthscale probed, with a lower bound set by $\pi/q_{max} = \lambda/4n$ in the backscattering direction.

2.1.2 Small angle light scattering

Equation 2.3 shows that light scattering typically probes matter on lengthscales comparable to the visible wavelength, but that larger lengthscales (up to more than 100λ) can be probed by analyzing light scattered at small scattering angles, which can be very interesting in some cases, like the ones we will show in the next chapters.

A great advantage of small angle light scattering is that, as it is represented in Fig. 2.2, a multichannel detector (e.g. a CMOS camera) can be used to acquire the intensity scattered at several scattering vectors at the same time. Such detectors are typically much slower than photodiodes, and they also have a smaller dynamic range, but smart acquisition schemes like the one we have developed (see appendix A) and multiple exposure times can be used to improve the detection performance.

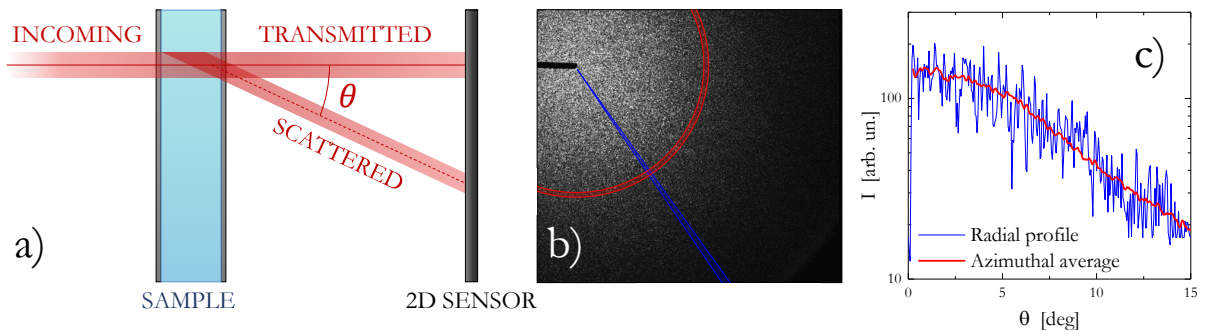


Figure 2.2: (a) General scheme of a small angle light scattering experiment: a flat scattering cell is chosen to improve the quality of the optical interfaces, and a multichannel sensor is used to detect several scattering vectors at the same time. In general, an optical system (not shown) is employed in order to collect the scattered light and send it to the sensor. More details can be found in [Tamborini 2012]. (b) Example of the speckle pattern detected in the far field. The transmitted beam is hidden by the beam stop in the top left corner, the scattering angle θ increases radially. (c) Radial intensity distribution (blue) observed along the blue sector highlighted in panel b, plotted together with the azimuthal average (red), obtained by averaging each scattering angle θ on the azimuthal angle (red circle in panel b).

The detection of light scattered at small angles poses a few technical challenges that have to be addressed with a specific experimental geometry, which may change significantly according to the desired range of scattering angles, the required sensitivity or other

technical constraints. The main challenge associated to small angle scattering comes from imperfections in the optic elements, which typically produce a spurious scattering signal greatly increasing at the smallest angles. The presence of the intense transmitted beam in the field of view of the detector also requires special care in the design of the setup. As a last challenge associated with small angle light scattering, aberrations in the optical system that collects the scattered light usually set a strong upper limitation in the accessible scattering angles.

In our work, we face these challenges with a custom made setup [Tamborini 2012], which uses a flat scattering cell and a complex optical system allowing one to remove the transmitted beam and reducing the effect of aberrations. The range of scattering angles that are typically accessed using this instrument lays in the intermediate range ($0.5^\circ < \theta < 25^\circ$) between the angles typically probed in wide angle ($\theta \gtrsim 20^\circ$) and small angle ($\theta \lesssim 5^\circ$) light scattering.

Figure 2.2b shows an example of speckle image acquired with our setup. Each pixel is associated to a scattering vector. The position of the $q = 0$ transmitted beam is on the top left corner, where the shadow of a beam stop is clearly visible. Superimposed to a radial smooth intensity decay, a speckle pattern of characteristic size slightly higher than one pixel is clearly visible. Different configurations of the same system would have the same overall q dependence of the scattered intensity, but the speckle pattern would be totally different, as a consequence of scatterers' microscopic rearrangement. This suggests that two distinct pieces of information can be extracted: the first deals with the slow smooth intensity decay, which is related to the internal structure of the sample, whereas analyzing the speckle pattern time fluctuations can provide information related to the scatterers' dynamics. These two different kinds of information are provided by static and dynamic light scattering, respectively.

2.1.3 Static light scattering (SLS)

2.1.3a Form factor and structure factor

Static light scattering provides averaged information on the internal structure of the sample, in terms of correlations between the scatterers' positions. For this purpose, the speckle pattern of Fig. 2.2b must be smoothed, by time or ensemble averages, for example by averaging over rings of pixels corresponding to nearly the same scattering angle θ in the case of isotropic samples. Starting from such an averaged profile (red line in Fig. 2.2c), we briefly sketch how static light scattering works by extending the previous discussion, from the interference between the electric field scattered by two scattering elements to a sum over all elements belonging to each of the N particles in the scattering volume. Each particle is indexed by $j = 1, \dots, N$, and contains a number M_j of scattering elements. The total scattered field is:

$$\vec{E}(\vec{q}) = \sum_{j=1}^N \sum_{l=1}^{M_j} \vec{E}_{jl}(\vec{q}) e^{i\vec{q} \cdot (\vec{r}_j + \vec{r}_l^{(j)})} = \sum_{j=1}^N \vec{E}_j(\vec{q}) e^{i\vec{q} \cdot \vec{r}_j} \quad (2.4)$$

where $\vec{E}_{jl}(\vec{q})$ is the electric field scattered by a single element (indexed by l) belonging to particle j . The position of the element in the sample is $\vec{r}_j + \vec{r}_l^{(j)}$, \vec{r}_j being the j -th particle center of mass position, whereas $\vec{r}_l^{(j)}$ denotes the position of the charge in the particle reference frame. In the second equality the sum over all the M_j scattering elements composing the j -th particle was factorized and called $\vec{E}_j(\vec{q}) = \sum_{l=1}^{M_j} \vec{E}_{jl}(\vec{q}) e^{i\vec{q} \cdot \vec{r}_l^{(j)}}$. This represents the electric field scattered by particle j (to within the phase factor $e^{i\vec{q} \cdot \vec{r}_j}$).

If all particles are identical and are illuminated by a uniform field, the scattered field $\vec{E}_j(\vec{q}) = \vec{E}_P(\vec{q})$ is the same for all particles and can be taken outside the sum. The scattered intensity can then be calculated as:

$$I(\vec{q}) = \vec{E}(\vec{q}) \cdot \vec{E}^*(\vec{q}) = \left| \vec{E}_P(\vec{q}) \right|^2 \sum_{j,l=1}^N e^{i\vec{q} \cdot (\vec{r}_j - \vec{r}_l)} = AP(\vec{q})S(\vec{q}) \quad (2.5)$$

where $P(\vec{q}) = |\vec{E}_P(\vec{q})|^2 / |\vec{E}_P(0)|^2$ is the so-called particle *form factor*, accounting for the single particle shape and size, $S(\vec{q}) = N^{-1} \sum_{j,l=1}^N e^{i\vec{q} \cdot (\vec{r}_j - \vec{r}_l)}$ is the sample *structure factor*, only dependent on the relative positions between the particles, and A is a proportionality constant, which will depend on instrumental parameters such as the laser beam size and intensity, as well on physical parameters such as the particle size, number density and refractive index contrast.

2.1.3b $P(q)$ and $S(q)$ for colloidal gels

The power of the factorization of the scattered intensity in the product of a form factor times a structure factor can be sketched in the case of the colloidal gels that will be presented in part II. Figure 2.3 shows three scattering curves, obtained by matching the results of several scattering techniques (small and wide angle light scattering, as well as small angle X ray and neutron scattering), for three different samples: (1) a diluted (particle volume fraction $\phi = 0.037\%$) suspension of colloidal particles, (2) a more concentrated ($\phi = 5\%$) suspension of the same particles interacting via a repulsive electrostatic potential, (3) a $\phi = 5\%$ suspension of the same particles with short range attractive interaction.

1. In the dilute suspension, the average interparticle distance is large and there is no correlation between the particle positions: as a consequence, the structure factor reduces to $S_{dil}(\vec{q}) = \langle e^{i\vec{q} \cdot \vec{r}} \rangle = 1$, and the measured scattered intensity is simply proportional to the particle form factor. The form factor of a sphere can be calculated by casting the sum over individual scattering elements into an integral over the particle volume V_j :

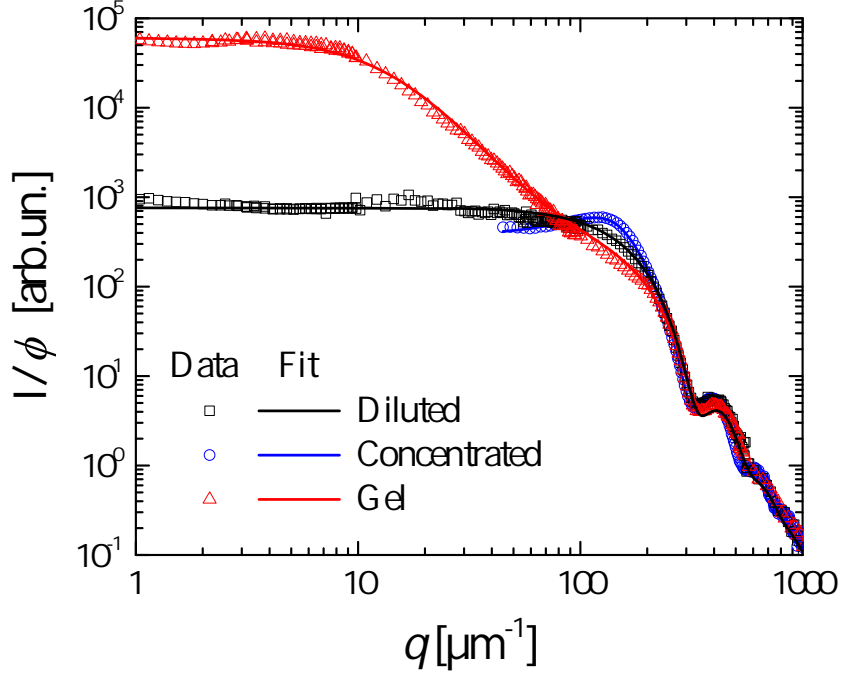


Figure 2.3: Static scattering signal plotted for three different colloidal systems, containing the same colloidal particles 1) diluted suspension ($\phi = 0.037\%$, black), from which the form factor can be extracted, carrying information about the average radius $\bar{R} = 12.5$ nm and size polydispersity $\sigma_R = 10\%$, 2) slightly concentrated suspension ($\phi = 5\%$, blue), with a structure factor peak at $qR \sim 2$ and a suppressed $I(q)$ at small scattering vectors, 3) an attractive colloidal gel ($\phi = 5\%$, red), displaying a fractal structure with fractal dimension $d_f = 2$ up to a characteristic lengthscale of about $0.5\mu\text{m}$.

$$P(\vec{q}) \propto \int_{V_j} \Delta\rho(\vec{r}) e^{i\vec{q}\cdot\vec{r}} d^3r \quad (2.6)$$

where $\Delta\rho$ is the contrast function, essentially proportional to the local density of scatterers. By assuming a uniform density inside a spherical volume, one obtains the form factor of a homogeneous spherical particle of radius R :

$$P_R(\vec{q}) = \left\{ \frac{3}{(qR)^3} [\sin(qR) - qR \cos(qR)] \right\}^2 \quad (2.7)$$

In Fig. 2.3, the form factor $P_R(\vec{q})$ was convoluted with a Gaussian size distribution peaked around an average particle size \bar{R} , to take into account sample polydispersity. A fit to the experimental data yields $\bar{R} = 12.5$ nm with a polydispersity $\sigma_R = 10\%$.

2. As the number density of the particles is increased, the particle positions start to become correlated as a consequence of the interparticle interactions, and the structure function starts to play a nontrivial role in the observed intensity profile. A direct link between the pair correlation function $g(\vec{r})$ (i.e. the probability of finding a pair of particles whose relative position is \vec{r}) and the structure factor $S(\vec{q})$

comes from a decomposition of the double sum defining $S(\vec{q})$ in a "self" ($j = l$) term, which is exactly 1, and a "cross" ($j \neq l$) term, which can be cast into an integral corresponding to the Fourier transform of $g(\vec{r})$:

$$S(\vec{q}) = 1 + \int g(\vec{r}) e^{i\vec{q}\cdot\vec{r}} d^3r \quad (2.8)$$

For example, in a diluted suspension, a virial expansion of the equation of state provides an expression for the pair correlation function: $g(\vec{r}) = \exp[-v(\vec{r})/k_B T]$, where $v(\vec{r})$ is the interaction potential [Landau 2013]. A similar starting point leads with more sophisticated calculations to the Percus Yevick structure factor, which is used in Fig. 2.3 to fit the experimental intensity, using the factorization of equation 2.5 and the form factor obtained from the diluted sample [Vrij 1979]. Note that for the $\phi = 5\%$ suspension, the measured intensity clearly exceeds the value for the form factor at $qR \approx 2$: this is the sign of an emerging peak in $S(q)$, reflecting the fact that as particles get closer to each other the density fluctuates strongly on the length scale of the particle diameter, whereas a suppression of $S(q)$ for small q values reflects the fact that at large lengthscales the density is still rather uniform.

3. Finally, as the interparticle potential is turned into attractive, particles aggregate and form a complex structure spanning a large range of lengthscales. As a result, the structure function develops several interesting features, like a power-law regime, which is a consequence of the fractal structure of the particle clusters, terminating with a shoulder corresponding to the typical cluster size (see part II for more details about the sample structure). Here $P(q)S(q)$ was fitted by an analytic model assuming a distribution of fractal aggregates with fractal dimension $d_f = 2$ and an exponential size distribution with a typical size around 100 nm [Sorensen 1999].

2.1.4 Dynamic light scattering (DLS)

2.1.4a Conventional dynamic light scattering

While static light scattering deals with the smooth variation of the intensity with q , neglecting the detailed appearance of the instantaneous speckle field, dynamic light scattering focuses precisely on the latter, relating intensity fluctuations to the sample dynamics. Indeed, as already pointed out with Eq. 2.2, the bright (dark) spots that one calls speckles are regions of constructive (destructive) interference of light emitted by all scatterers, where the constructive or destructive nature changes if particles are displaced over a distance of the order of q^{-1} .

Thus, the basic principle of dynamic light scattering is to record the intensity fluctuations measured at one specific q vector, and to measure the characteristic time τ needed for a bright speckle to become dark or vice versa. In the schematic representation of Eq. 2.2, where only two scatterers contribute to the observed signal, this implies that the relative phase between the two interfering waves has changed of the or-

der of unity over that characteristic time, which in turn reveals a particle displacement $\langle \Delta \vec{r}(\tau) \rangle_t = \langle \vec{r}(t + \tau) - \vec{r}(t) \rangle_t \sim \lambda / \sin(\theta/2) \hat{u}_q$. Here \hat{u}_q is a unit vector pointing in the \vec{q} direction, which emphasizes that the relative displacement that one observes in dynamic light scattering is projected along the scattering vector. This observation is very relevant in the case of anisotropic dynamics, like the one induced by shear flow, and it will be developed in chapter 4.

An analogous result holds for the more realistic picture of N particles contributing to the scattered intensity. In this case, time dependence can be easily incorporated into Eq. 2.5, by assuming a time-independent form factor and a time-dependent structure factor:

$$I(\vec{q}, t) = AP(\vec{q})S(\vec{q}, t) \propto \sum_{j,l=1}^N e^{i\vec{q} \cdot [\vec{r}_j(t) - \vec{r}_l(t)]} \quad (2.9)$$

Thus, fluctuations of $I(\vec{q}, t)$ provide information on the *average* particle displacements along the scattering vector. Again, a decomposition of the double sum allows to distinguish between "self" dynamics and "collective" dynamics (typically dominant when $S(\vec{q}) \gg 1$), which are linked to collective relaxation of particle density fluctuations [Pusey 1978]. A quantitative measurement of the temporal fluctuations of $I(\vec{q}, t)$ can be obtained by computing the time autocorrelation function of the scattered intensity:

$$g_2(\vec{q}, t, \tau) = \frac{\langle I(\vec{q}, t + \tau) I(\vec{q}, t) \rangle}{\langle I(\vec{q}, t + \tau) \rangle \langle I(\vec{q}, t) \rangle} \quad (2.10)$$

where $\langle \dots \rangle$ denotes an ensemble average, which for ergodic samples can be measured experimentally by performing a time average lasting much longer than the characteristic relaxation time τ_R of g_2 (typically an average over $10^3 - 10^4 \tau_R$ is needed). The intensity autocorrelation function can be related to quantities that can be modeled theoretically, like the intermediate scattering function $f(\vec{q}, \tau)$, which essentially coincides with the ensemble averaged field correlation function:

$$f(\vec{q}, \tau) = \langle g_1(\vec{q}, t, \tau) \rangle_t = \frac{\langle \vec{E}(\vec{q}, t + \tau) \cdot \vec{E}^*(\vec{q}, t) \rangle_t}{\left| \langle \vec{E}(\vec{q}, t) \rangle_t \right|^2} \propto \left\langle \sum_{j,l=1}^N e^{i\vec{q} \cdot [\vec{r}_j(t+\tau) - \vec{r}_l(t)]} \right\rangle_t \quad (2.11)$$

The Siegert relation, which holds as long as the scattered field has Gaussian statistics, relates the intensity and field correlation functions [Berne 2013]:

$$g_2(\vec{q}, t, \tau) = 1 + |g_1(\vec{q}, t, \tau)|^2 \quad (2.12)$$

The intermediate scattering function, in turn, can be directly related to the internal dynamics of the sample: indeed, it represents the (spatial) Fourier transform of the van Hove distribution function $G(\vec{r}, t)$, which is the dynamic counterpart of the pair correlation function $g(\vec{r})$ [Hopkins 2010]:

$$\begin{aligned}
G(\vec{r}, \tau) &= \left\langle \frac{1}{N} \int \rho(\vec{r}' + \vec{r}, t + \tau) \rho(\vec{r}', t) d^3 r' \right\rangle_t \\
&= \left\langle \frac{1}{N} \int \sum_{j,l=1}^N \delta[r' + \vec{r} - \vec{r}_j(t + \tau)] \delta[r' - \vec{r}_l(t)] d^3 r' \right\rangle_t
\end{aligned} \tag{2.13}$$

where $\rho(\vec{r}, t) = \sum_{j=1}^N \delta[\vec{r} - \vec{r}_j(t)]$ is the density of a system comprising N particles and $\delta(\vec{r})$ represents Dirac's delta function. $G(\vec{r}, \tau)$ is the probability of finding at time τ a particle at position \vec{r} , given that a particle (not necessarily the same) was in the origin ($\vec{r} = 0$) at time 0. A substitution of Eq. 2.13 into Eq. 2.11 directly yields

$$f(\vec{q}, \tau) = \int G(\vec{r}, \tau) e^{i\vec{q}\cdot\vec{r}} d^3 r \tag{2.14}$$

Thus, the intermediate scattering function can be considered as the dynamic counterpart of the structure factor (Eq. 2.8).

As an example, we consider Brownian diffusion. In this case, the van Hove function is a Gaussian with variance $\langle \Delta r^2(\tau) \rangle = 6D\tau$, D being the diffusion coefficient. By Fourier transforming such distribution one obtains $f(\vec{q}, \tau) = \exp(-Dq^2\tau)$. One thus predicts an exponential decay of the field correlation, with a characteristic time $\tau_R = 1/Dq^2$. Thus, from the intensity correlation function measured on a Brownian suspension one extracts the diffusion coefficient D . In turn, D can be used to determine the hydrodynamic radius R_h of the particles if the solvent viscosity is known, using the Stokes-Einstein relation $D = k_B T / (6\pi\eta R_h)$, as it is routinely done in DLS-based particle sizing [Berne 2013]. Conversely, one can use known particles as probes, and extract from the DLS signal physical information about the solvent, like the viscosity: this is the essence of DLS-based microrheology.

2.1.4b Multispeckle and time-resolved correlations

Operationally, conventional DLS is based on the assumption that the ensemble average in Eq. 2.10 can be replaced by a time average. Ensemble and time averages are equivalent if, over the averaged time interval, the sample has been able to explore a statistically relevant subset of the phase space, i.e. for the so-called *ergodic* systems. Ordinary diluted suspensions usually fall in this class of systems, since their relaxation time is usually much smaller than 1 s, so that many independent configurations can easily be sampled within the duration of an experiment. However, there are several instances where the relaxation time exceeds 1 s by many orders of magnitude, as is the case for very viscous suspensions studied at small angles or even more importantly for out of equilibrium systems, like colloidal gels or glasses: these systems are said to be *nonergodic*, and require special care for the ensemble average in a DLS experiment to be properly evaluated.

One method is to sample $g_I(\vec{q}, t, \tau)$ for several independent speckles. This can be done by translating or rotating the sample during the measurement, or more conveniently

by detecting the fluctuations of several speckles at the same time using a multichannel detector, like a CMOS camera, and by averaging the contribution of all speckles. The resulting correlation function is:

$$g_2(\vec{q}, t, \tau) = \frac{\langle I_p(t + \tau) I_p(t) \rangle_{p \in ROI(\vec{q})}}{\langle I_p(t + \tau) \rangle_{p \in ROI(\vec{q})} \langle I_p(t) \rangle_{p \in ROI(\vec{q})}} \quad (2.15)$$

where $I_p(t)$ is the intensity detected by pixel p at time t , and $\langle \dots \rangle_{p \in ROI(\vec{q})}$ corresponds to an average over all pixels belonging to a region of interest (ROI) associated to a small region in q space centered around \vec{q} .

Such a technique, called multispeckle, allows one to achieve a good sampling of the gray levels of the speckle pattern, which corresponds to a good sampling of the microscopic configurations of the sample, provided that the scattering volume is larger than any structural and dynamical correlation length. Of course, the speckles averaged with this technique should provide equivalent information, thus they should correspond to nearly the same scattering vector, which sometimes sets a strong limitation, for example in the case of large speckles or of a strong q dependence of the dynamics, as it is the case under shear, as discussed in chapter 4.

More generally, this method provides properly averaged results without time averages, and thus allows one to characterize time-dependent dynamics, like ageing or transient processes. For this reason, such a method, called Time Resolved Correlation (TRC) [Duri 2005], is particularly adapted for probing a sample under shear.

2.2 Rheology

Rheology, as the Greek origin of the name suggests, is the study of the flow of matter. One commonly thinks of gases and liquids as mobile substances subject to flow and of solids as rigid materials that do not flow, but before the critical eyes of the rheologist, nature shows a much more rich and complex variety of behaviors, which one classifies as *viscoelastic*. Indeed, rephrasing the well known statement of Heraclitus from which the name "rheology" was coined ($\tau\alpha \Pi\acute{\alpha}\nu\tau\alpha \rho\acute{\epsilon}\tilde{\iota}$), everything flows, depending on the timescale and the external conditions [Traxler 1939].

2.2.1 Shear deformation: stress and strain

The above distinction between liquids, solids and viscoelastic materials concerns the mechanical properties of an object, i.e. the relationship between any force applied to it and the subsequent change in its shape and size. Both quantities can be generally quantified by tensorial variables: the stress $\underline{\underline{\sigma}}$, representing the force per unit surface acting on different faces of a small cubic element from different directions, and the deformation $\underline{\underline{\gamma}}$ (or its time derivative $\underline{\underline{\dot{\gamma}}}$), describing the relative changes in dimensions and angles of

that cubic element. In a generic deformation geometry, both stress and strain depend on the position \vec{x} , so that the relation between $\underline{\underline{\sigma}}$ and $\underline{\underline{\dot{\gamma}}}$ (the so-called rheological constitutive equation) is a very complex tensorial equation. However, there are a few specific types of uniform (homogeneous) deformations where stress and strain are independent of \vec{x} and assume a relatively simple form. One of them is simple shear, where two opposite faces of the cubic element are displaced by sliding. In this geometry (Fig. 2.4a), one can measure the shear couple $M = eF$, e being the gap separating the two surfaces and F being the force applied to them, and the relative linear displacement δ of the two surfaces. In terms of these quantities, the above tensorial relations reduce to scalar ones, connecting the (scalar) stress $\sigma(t) = F(t)/S$, S being the area of the two opposite faces, to the strain $\gamma(t) = \delta(t)/e$. In this thesis, with the only exception of appendix B, we will only focus on the shear geometry.

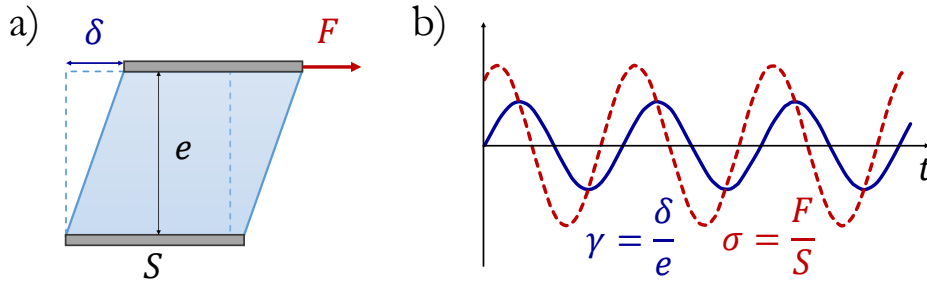


Figure 2.4: (a) Schematic view of shear rheology: the initial shape of the sample (dashed line) is a prism with base surface S and height e equal to the gap between the two confining surfaces (top and bottom plates). A sliding force F is applied to one of the two surfaces, while the other one is kept fixed. This corresponds to a shear couple $M = eF$, and a scalar shear stress $\sigma = F/S$ homogeneously distributed inside the sample volume. The scalar deformation $\gamma = \delta/e$ is also uniform, and corresponds to the relative displacement of the two surfaces δ normalized by the gap. (b) Representative experimental protocol for strain-controlled small amplitude oscillatory shear rheology: as described in text, a sinusoidal deformation $\gamma_\omega(t)$ (blue, solid line) is imposed, and the stress response $\sigma_\omega(t)$ (red, dashed line) is measured. The relative amplitude and phase of the two harmonic signals define the modulus and the phase of the complex modulus $G^*(\omega)$. The result would be the same in stress-controlled rheology, where $\sigma_\omega(t)$ is imposed and $\gamma_\omega(t)$ is measured.

Experimentally, it is possible to access both $\sigma(t)$ and $\gamma(t)$ using sophisticated instruments called rheometers, which can be controlled either in stress or strain. In both cases the geometry can be chosen according to the properties of the sample: liquid-like samples are typically tested in a Couette cell, where the sample fills the gap between two coaxial cylinders, one of which rotates with respect to the other. Solid-like samples, on the other hand, are generally confined between a flat, fixed surface and a cone that is rotated to apply a given deformation (cone-plate geometry). In both cases, strain-controlled

rheometers measure the torque needed to achieve a given rotation, and conversely stress-controlled rheometers apply a controlled torque and measure the rotation. The geometric parameters are then used to convert the torque into a shear stress and the rotation angle into a shear strain. Different shear geometries, like parallel sliding plates are also employed in custom-made shear cells, typically designed to meet special mechanical requirements (e.g. very small sample thickness or very high frequencies) or to be embedded into more complex experimental systems, like the one that will be presented in chapter 3.

When an external shear stress $\sigma(t)$ is applied to a sample, the sample reacts with a shear deformation $\gamma(t)$ following Newton's second law. If inertial effects can be ignored, as is often the case (cf. chapter 3), the internal stresses developed as a consequence of the shear deformation are such that the applied stress is exactly balanced, so that a measure of $\gamma(t)$ for a known stress history $\sigma(t)$ allows one to extract the constitutive equation. Conversely, a strain history $\gamma(t)$ can be imposed, and a measure of $\sigma(t)$ allows the same constitutive equation to be obtained.

As an example of a simple constitutive equation, Hooke's law describes the behavior of elastic solids, for which stress is always directly proportional to strain but independent on the shear rate $\dot{\gamma} = d\gamma/dt$. On the other hand, the classical theory of hydrodynamics deals with viscous liquids, for which stress is always directly proportional to the shear rate, but independent of the strain itself. Both categories are idealizations, and although many solids approach Hooke's law for small strains and many liquids approach Newton's law for small shear rates, under other conditions deviations from these simple, linear laws are observed. Moreover, even if the strain or the shear rate are infinitesimal, a system may exhibit behavior which combines liquid-like and solid-like characteristics: to describe such a *viscoelastic* system, a more general model must be introduced.

2.2.2 Linear viscoelasticity

2.2.2a Viscoelastic moduli

As a starting point for a theoretical description of linear viscoelasticity, a response function $G^*(\omega)$ (called complex modulus) can be defined, in the spirit of Sec. 2.1. In the small perturbation limit, the so-called linear regime, $G^*(\omega)$ is a well defined complex function of frequency: a harmonic strain perturbation $\gamma_\omega(t) = \gamma_0 e^{i\omega t}$ is associated to a stress $\sigma_\omega(t)$ oscillating at the same frequency ω , with amplitude and phase set by the complex modulus: $\sigma_\omega(t) = G^*(\omega)\gamma_\omega(t)$ (Fig. 2.4b) [Macosko 1994].

The ideal cases of purely elastic or viscous materials can be described in terms of real or imaginary complex moduli, respectively: $G^*(\omega) = G_0$ defines the elastic modulus in Hooke's law ($\sigma = G_0\gamma$), whereas $G^*(\omega) = i\omega\eta$ characterizes the viscosity of a Newtonian liquid ($\sigma = \eta\dot{\gamma}$). A complex modulus having both a real and an imaginary part describes a viscoelastic material, whose solid-like and liquid-like behaviors are ascribed to a storage modulus $G' = \text{Re}(G^*)$ and a loss modulus $G'' = \text{Im}(G^*)$, respectively. In practice,

oscillatory rheology consists in imposing a small amplitude harmonic perturbation (either in stress or in strain), and recording the amplitude and phase of the response, from which G' and G'' can be extracted for a given frequency: a complete spectrum of $G'(\omega)$ and $G''(\omega)$ provides a full description of the linear viscoelasticity of a material.

The form of the frequency dependence of the viscoelastic moduli G' and G'' can in general be reproduced by the behavior of a mechanical model with a sufficient number of elastic elements (springs) and viscous elements (dashpots imagined as pistons moving in oil). The force applied to the ends of this mechanical model is analogous to σ , and their relative displacement is analogous to γ . The simplest fully viscoelastic models contain one spring and one dashpot, connected either in series (Maxwell model) or in parallel (Kelvin-Voigt model) [Ferry 1980]. Their complex moduli can be calculated by assigning an elastic modulus G_0 to the spring and a viscosity η to the dashpot, and by developing the mechanical models, obtaining $G_{KV}^*(\omega) = G_0 + i\omega\eta$ for Kelvin-Voigt and $G_M^*(\omega) = G_0(s^2 + is)/(1 + s^2)$, with $s = \omega\eta/G_0$, for Maxwell. Both results are represented in Fig. 2.5a, from which a characteristic angular frequency $\bar{\omega} = G_0/\eta$ emerges as the point where G' and G'' cross each other: for $\omega > \bar{\omega}$ the Maxwell model will be predominantly elastic, with $G' > G''$, whereas for Kelvin-Voigt $G'' > G'$ indicates a rather liquid-like response. The opposite holds for $\omega < \bar{\omega}$.

The characteristic frequency $\bar{\omega}$ can also be read, in the time domain, as a characteristic time $\tau \sim \bar{\omega}^{-1}$ separating the elasticity-dominated from the viscosity-dominated regime, as can be clearly observed in transient experiments.

2.2.2b Transient experiments in the linear regime

Oscillatory shear is of widespread use, and is an extremely practical tool to characterize the linear viscoelasticity of a material, since it probes a stationary state, where the mechanical response of the system depends on frequency but not (or negligibly) on time. However, precious physical information is often contained as well in the time evolution of the system approaching the stationary state, specially when finite, "nonlinear" deformations are attained. To access this information, transient experiments, intrinsically time-resolved, can be performed. Creep, shear start-up and stress relaxation are the most common examples of transient rheological experiments.

The result of transient experiments in the linear regime can be rationalized in terms of two time-dependent quantities related to the viscoelastic moduli: the stress relaxation modulus $G(t)$ and the creep compliance $J(t)$, which are used to calculate the stress $\sigma(t)$ starting from a generic strain history $\gamma(t)$ or vice versa [Macosko 1994]. Their definition is based on Boltzmann's superposition principle, stating that in the linear regime the effects of sequential changes in strain (or stress) are additive:

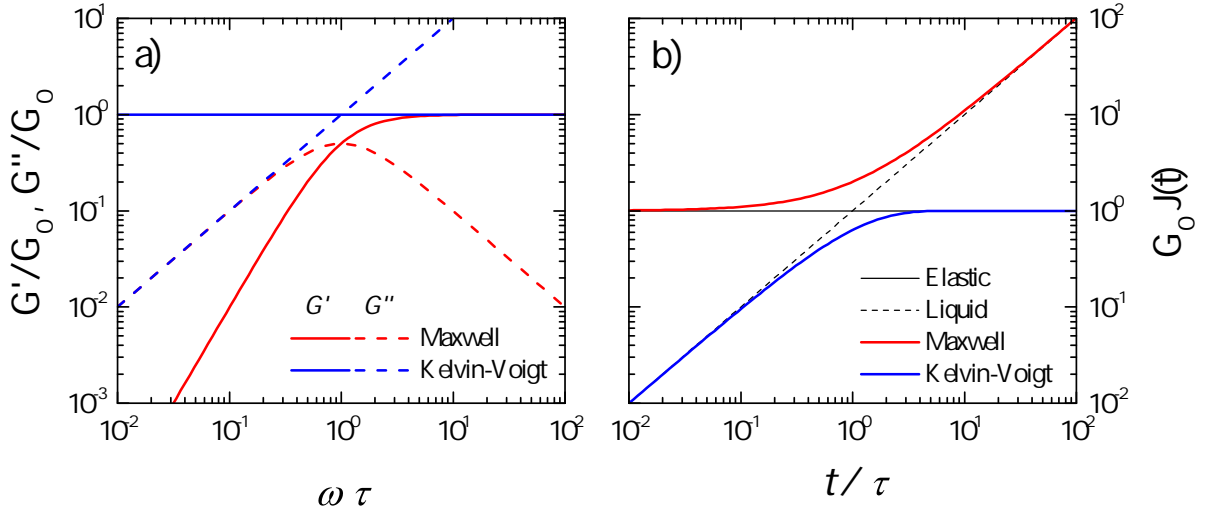


Figure 2.5: (a) Viscoelastic moduli G' (solid lines) and G'' (dashed lines) for Maxwell (red) and Kelvin-Voigt model (blue), normalized by the spring modulus G_0 and as a function of frequency normalized by the relaxation time $\tau = \eta/G_0$. A solid sample would have the same G' as the Kelvin-Voigt ($G' = G_0$), whereas a Newtonian fluid would have the same G'' as the Kelvin-Voigt ($G'' = \eta\omega$). (b) Normalized creep compliance $G_0 J(t)$ as a function of normalized time t/τ for the two viscoelastic models. As a reference, the creep compliance of ideal elastic solids (black, solid line) and Newtonian liquids (dashed line) is also shown.

$$\sigma(t) = \int_{-\infty}^t G(t-t')\dot{\gamma}(t')dt' \quad (2.16)$$

$$\gamma(t) = \int_{-\infty}^t J(t-t')\dot{\sigma}(t')dt'$$

From the knowledge of either $G(t)$ or $J(t)$, the stress-strain relation for any kind of experiment with a prescribed time dependence of stress or strain can be predicted: for example, the particular choice of an oscillating strain allows one to identify the complex modulus $G^*(\omega)$ as the Fourier transform of $G(t)$. In practice, however, direct calculation of the Fourier transform is not possible, since any transient experiment accesses a limited window of timescales, ranging from a generally small enough t_{min} to a maximum time t_{max} limited by the duration of the experiment (typically a few days at most), and numerical methods are needed to convert linear transient data into viscoelastic moduli covering a frequency range from $\omega_{min} \sim t_{max}^{-1}$ to $\omega_{max} \sim t_{min}^{-1}$ [Evans 2009]. This reveals another side advantage of transient experiments, which can typically probe a much larger window of timescales, beyond the small frequency regime that can be typically be accessed in

oscillatory tests. For this reason, creep or stress relaxation experiments in the linear regime are sometimes used to extend the spectrum of viscoelastic moduli at the smallest frequencies [Bird 1987].

Among the typical transient experiments, this chapter discusses the case of creep, where a step stress $\sigma(t) = \sigma_0\theta(t)$ is imposed, $\theta(t)$ being the Heaviside's Theta function, and the strain $\gamma(t) = \sigma_0J(t)$ is measured as a function of time. Apart from inertial effects, discussed in detail in chapter 3, the deformation is constant ($\gamma(t) = \gamma_e = \sigma_0/G_0$) for an ideal elastic solid subject to Hooke's law, whereas it grows linearly in time for a viscous liquid ($\gamma(t) = \dot{\gamma}t$, where $\dot{\gamma} = \sigma_0/\eta$). The deformation of a Maxwell model is approximately constant over times shorter than the characteristic time τ , and starts growing at a constant rate for longer times: $\gamma_M(t) = \gamma_e(1 + t/\tau)$. On the other hand, a Kelvin-Voigt model flows at short times and reaches a constant deformation for $t \gg \tau$: $\gamma_{KV}(t) = \gamma_e[1 - \exp(-t/\tau)]$. Both creep curves are represented in Fig. 2.5b.

The reversibility of creep deformation can be directly addressed by creep recovery, i.e. by releasing the external stress after an arbitrary creep time T : for $t > T$ the deformation $\gamma(t)$ decreases again, reaching a plateau value γ_∞ in the long time limit. $\gamma_\infty = 0$ would then imply that the deformation obtained during creep is completely reversible: this is the case of Kelvin-Voigt model. On the other hand, a partially irreversible deformation would reflect into a strictly positive γ_∞ (for example, $\gamma_\infty = \gamma_e T/\tau$ for a Maxwell model).

The two fully viscoelastic models (Maxwell and Kelvin-Voigt) introduced so far are described by a single characteristic time τ , corresponding to the clear transition between solid-like and liquid-like behavior, which one can observe in Fig. 2.5b. However, as the term "creep" itself suggests, the deformations observed in creep experiments are often characterized by a sublinear growth of $\gamma(t)$ spanning several decades in time. This is for example the case of Rouse motion in polymeric materials, where $\gamma(t)$ increases as a power law with an exponent $\alpha = 0.5$ [Schiessel 2000]. To mimic this behavior more complex mechanical models are required, generally displaying a distribution of relaxation times. For example, a generalized Maxwell (or Kelvin-Voigt) model is composed of N elementary modes, each one with its characteristic time, connected in series (or in parallel). Other models can be imagined as well, like for example branched or nested structures, particularly suited to describe self-similar dynamics. More recently, the concept of fractional element (also called a springpot) has also been introduced [Blair 1947], to provide a compact mathematical description of power law distributions of relaxation times [Bagley 1983, Bagley 1989, Jaishankar 2013]. A fractional element is defined by two parameters: a so-called *quasi-property* \mathbb{V} and a fractional exponent α , and it bridges the mechanical behavior of a spring and a dashpot, where (\mathbb{V}, α) reduces to $(G_0, 0)$ and $(\eta, 1)$ respectively. Its constitutive equation involves the concept of a fractional derivative of order α :

$$\sigma(t) = \mathbb{V} \frac{d^\alpha \gamma}{dt^\alpha} = \mathbb{V} \int_{-\infty}^t (t - t')^{-\alpha} \dot{\gamma}(t') dt' \quad (2.17)$$

This definition of fractional derivative compared with Eq. 2.16 allows to identify the relaxation modulus $G(t) \propto t^{-\alpha}$, which emphasizes the interpretation of a springpot in terms of a power law distribution of relaxation times. A physical example of such a fractional element is represented by the so-called fractional Maxwell model, which will be introduced in chapter 5.

2.2.3 Nonlinear viscoelasticity

All the results obtained so far are bound to the underlying assumption that the deformations are infinitesimal. This assumption characterizes the so-called linear viscoelastic regime, where stress and strain should be regarded as a probing field: since the (linear) response functions do not depend on the magnitude of the probing field, linear rheology teaches us about the mechanical properties of the *unperturbed* sample. However, from a practical point of view, it may remain unclear how to identify the range of deformations where this assumption holds. Moreover, mechanical stimuli beyond the linear regime can be used on purpose to change the sample structure, and the mechanical properties of the modified structure can be probed by nonlinear rheology, which can provide valuable information both from a fundamental point of view and for applications. For this reason, in this section a few relevant aspects of nonlinear viscoelasticity will be briefly discussed.

Nonlinear rheology represents an appealing technique thanks to its straightforward implementation in modern rheometers. However, from a theoretical point of view it is extremely delicate, for several reasons. First of all, when strains are not infinitesimal, the strain tensor itself has to be handled with care, since various alternative ways of defining finite strains are possible [Macosko 1994]. Moreover, the deformation measured macroscopically may deviate significantly from the local deformation actually experienced by the sample, which may become unstable and heterogeneous in a way that may exhibit a delicate dependence on the experimental geometry and boundary conditions. Finally, as a consequence of a nontrivial coupling between spatial dimensions, nonlinear deformations along one direction may produce measurable stresses along orthogonal directions, as is the case for normal stresses in shear rheology, for example. A thorough discussion of those aspects would go far beyond the purpose of this chapter: in the following we will take a phenomenological approach, assuming that a macroscopic shear strain γ is imposed and a macroscopic shear stress σ is measured under specific experimental conditions. Under the working hypothesis (to be verified experimentally) that γ and σ are still representative of the local mechanical perturbation and response of the sample, this section will discuss how the stress-strain relation changes as the strain is increased beyond the linear regime.

2.2.3a Large Amplitude Oscillatory Shear

We start considering the nonlinear transition as it is observed in oscillatory shear at one fixed frequency ω as the strain amplitude γ_0 is increased. For one given γ_0 , a convenient way of showing the stress-strain relation is to plot the two variables against

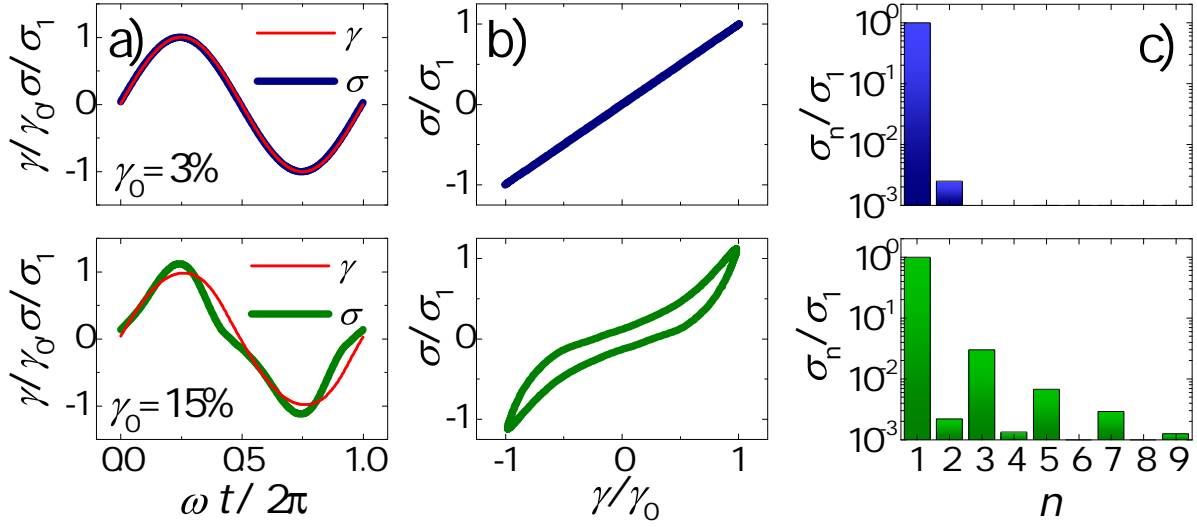


Figure 2.6: Strain imposed large amplitude oscillatory shear measurements at frequency $\omega = 1$ Hz on the colloidal gel presented in part II. (a) Sinusoidal strain γ_ω (red, thin line) normalized by the amplitude γ_0 , compared to the stress response $\sigma(t)$ (colored, thick line), normalized by its fundamental harmonic σ_1 . Two different strain amplitudes are compared: $\gamma_0 = 3\%$ (blue, top) and $\gamma_0 = 15\%$ (green, bottom). (b) Lissajous-Bowditch plots corresponding to the two strain amplitudes. (c) Relative amplitude of harmonic content in the stress signal.

each other: in the stationary state the result is a closed curve parametrized by ωt running from 0 to 2π . In the linear regime, where $\gamma = \gamma_0 \cos(\omega t)$ and $\sigma = \sigma_0 \cos(\omega t + \delta)$, the curve belongs to the family investigated by Nathaniel Bowditch and Jules Antoine Lissajous in the XIX century [Cundy 1954] (which explains why such a plot is often called Lissajous-Bowditch, or simply Lissajous plot), and it is implicitly defined by the equation: $\tilde{\sigma}^2 + \tilde{\gamma}^2 - 2\tilde{\sigma}\tilde{\gamma} \cos \delta = \sin^2 \delta$, where $\tilde{\sigma} = \sigma/\sigma_0$ and $\tilde{\gamma} = \gamma/\gamma_0$. The result corresponds to an ellipse with axes of length $\sin \delta / \sqrt{1 \pm \cos \delta}$ along the $\tilde{\sigma} = \pm \tilde{\gamma}$ directions and an eccentricity $e^2 = 2 \cos \delta / (1 + \cos \delta)$, decreasing from 1 to 0 as the phase difference δ goes from 0 to $\pi/2$. The two extreme cases are again represented by the elastic solid ($\delta = 0$) and the Newtonian liquid ($\delta = \pi/2$), whose Lissajous plots correspond to a straight line across the origin and a unitary circle respectively.

Eccentricity is in turn connected to energy dissipation: since the incremental quantity $dw = \sigma \cdot d\gamma$ represents a mechanical work per unit volume, an elliptical loop including a given area S implies that a finite amount of energy, proportional to S is dissipated by the material each cycle. A purely viscous sample, with a circular LB plot, has an adimensional area $S = \pi$, indicating that the mechanical work is entirely dissipated. Conversely, elastic force is conservative and no energy is dissipated for a purely elastic sample. In general, in the linear regime, $S/\pi = \sin^2 \delta$ will represent the fraction of mechanical energy per cycle that is dissipated by viscous effects.

When the strain amplitude γ_0 is increased, the shape of the Lissajous-Bowditch plot eventually deviates from the elliptical shape characterizing the linear regime (Fig. 2.6b): indeed, at finite strains, the linear response theory may no longer hold, and a harmonic strain perturbation at frequency ω may induce a nonlinear stress response containing a spectrum of frequencies other than ω . Assuming that a stationary state can be reached, the response is still periodic with period $T = 2\pi/\omega$, and the spectrum is discrete in units of ω :

$$\sigma(t) = \sum_{n=1}^{\infty} \sigma_n(\omega, \gamma_0) e^{in\omega t} \quad (2.18)$$

In the linear regime one would have $\sigma_n(\omega, \gamma_0) = \sigma_0(\omega)\delta_{n1}$, where δ_{ij} represents the Kronecker delta, whereas higher harmonics characterize the nonlinear regime. Interestingly, one can show that whenever the stress inside the sample is homogeneous and equal to the one measured experimentally, the spectrum of this last one should only contain odd harmonics. Indeed, for symmetry reasons, the local stress tensor can be expanded in odd power series of the local deformation and deformation rate tensors, whereas even terms are unphysical: a change in the reference frame transforming γ into $-\gamma$ must also transform σ into $-\sigma$. Such expansion can be developed in an harmonic series only containing odd n terms [Hyun 2011]. For this reason, the presence of even harmonics in the macroscopic strain signal indicates that the strain measured macroscopically is different from the local stress experienced by the sample, and this can occur for example because of wall slip [Graham 1995] or shear banding [Tapadia 2006].

In practice, a Fourier transform of the $\sigma(t)$ signal measured at one frequency ω and increasing strain amplitude should reveal the appearance of higher order harmonics ($n = 3, 5, 7, \dots$) in correspondence to the onset of nonlinear viscoelastic response (Fig. 2.6c). In an analogous way, it is also possible to impose a harmonic stress perturbation and to measure the nonlinear strain response: although in the nonlinear regime the two experiments are no longer equivalent, in this case as well higher order harmonics $\gamma_n(\omega, \sigma_0)$ can be observed beyond the linear regime.

In presence of a non-harmonic response to an harmonic perturbation the argument that brought (section 2.2.2) to the definition of the complex modulus does not hold anymore. Thus, in principle $G^*(\omega)$ becomes ill-defined. However, it is sometime of practical use to define the nonlinear viscoelastic moduli, $G'(\omega, \gamma_0)$ and $G''(\omega, \gamma_0)$, by an analysis of the fundamental harmonic $\sigma_1(\omega, \gamma_0)$ (Eq. 2.18). In the $\gamma_0 \rightarrow 0$ limit, these definitions reduce to the linear viscoelastic moduli, but the dependence on γ_0 allows one to explore the regime of finite strain, where G' and G'' start deviating from their linear value. The strain γ_c at which the first deviation is observed is another measure of the limit of the linear regime. For soft viscoelastic solids, the behavior of G' and G'' beyond γ_c carries information on the yielding transition (cf. Fig. 1.2). Indeed, this class of materials is characterized by a storage modulus G' typically larger than G'' in the linear regime, but an increase of γ_0 eventually causes the two moduli to cross each other in correspondence

to a critical strain γ_f , generally weakly dependent on frequency [Miyazaki 2006], and in the largest strain regime one typically has $G'' > G'$, indicating that large strains are able to "fluidize" the sample, which would be solid-like at rest.

2.2.3b Transient experiments and delayed yielding

The high sensitivity of oscillatory shear experiments to nonlinearity is a consequence of the very well defined functional form of the mechanical response to a harmonic probe in the linear regime. The same does not hold, in general, for transient measurements, where the convolution integrals of Eq. 2.16 describe a nonlocal response in the time domain. This is once again due to the fact that the linear response function is originally defined in the frequency domain. Nevertheless, the detection of nonlinearity in transient experiment is of great interest both from a fundamental point of view and for applications. Chapter 6 contains a discussion on the particular case of the nonlinear creep of a colloidal gel: we refer to that chapter for a specific example, whereas this paragraph will be limited to a few general considerations.

From a mechanical point of view, nonlinear contributions to a transient mechanical signal manifest themselves as deviations from the expected (linear) response. For example, in shear start-up experiments a fixed shear rate $\dot{\gamma}$ is imposed, and the stress growth $\sigma(t)$ is measured as a function of time or strain. For solid-like samples, after a first linear increase of $\sigma_{lve}(t) = G_0\gamma(t)$, a deviation is eventually observed, either upwards (strain hardening) or downwards (strain softening). If $\dot{\gamma}$ is sufficiently large (larger than the inverse of the maximum relaxation time τ of the system), this deviation depends on $\dot{\gamma}$, and is generally identified as the beginning of the nonlinear regime. An example of this experimental protocol will be given in appendix B.

Detecting the onset of nonlinearity in creep experiments is even less trivial, mainly because of the typically slow and time-dependent deformation rates involved, but the main idea is similar: independent measurements in the linear regime can be used to model the linear creep compliance $J_{lve}(t)$, and a comparison between the measured $J(t)$ and the expected one shows a deviation from linear viscoelasticity starting from a critical time t_{nl} . Once again the definition of t_{nl} is delicate, and the question of whether a precise time t_{nl} separating linear from nonlinear creep deformation can even be defined remains debated and somehow system-dependent.

Part I

Light scattering under shear

A stress controlled shear cell for small-angle light scattering and microscopy

Contents

- I Introduction
 - II Setup
 - III Setup characterization
 - IV Tests with model samples
 - V Dynamic light scattering under shear
 - VI Conclusion
-

The detection of microscopic dynamics in samples under shear is experimentally very challenging, because it requires to combine the highest mechanical sensitivity to strict requirements on the geometry of the whole setup and on the quality of the optical interfaces. In this work we achieve this aim by using a custom-made, stress-controlled shear cell that works in the linear parallel plates geometry and can be coupled to an optical microscope or a small angle light scattering setup, for simultaneous investigation of the rheological response and the microscopic structure of soft materials under an imposed shear stress. We present our shear cell using a paper recently published on Review of Scientific Instruments [Aime 2016].

A stress-controlled shear cell for small-angle light scattering and microscopy

S. Aime,^{a)} L. Ramos, J. M. Fromental, G. Prévot, R. Jelinek, and L. Cipelletti^{b)}
Laboratoire Charles Coulomb (L2C), UMR 5221 CNRS-Université de Montpellier, Montpellier, France

(Received 15 July 2016; accepted 1 December 2016; published online 20 December 2016)

We develop and test a stress-controlled, parallel plates shear cell that can be coupled to an optical microscope or a small angle light scattering setup, for simultaneous investigation of the rheological response and the microscopic structure of soft materials under an imposed shear stress. In order to minimize friction, the cell is based on an air bearing linear stage, the stress is applied through a contactless magnetic actuator, and the strain is measured through optical sensors. We discuss the contributions of inertia and of the small residual friction to the measured signal and demonstrate the performance of our device in both oscillating and step stress experiments on a variety of viscoelastic materials. *Published by AIP Publishing.* [<http://dx.doi.org/10.1063/1.4972253>]

I. INTRODUCTION

Complex fluids such as polymer solutions, surfactant phases, foams, emulsions, and colloidal suspensions are ubiquitous in everyday life and industrial applications. Their rheological properties are often of paramount importance both during the production process and for the final user.¹ They are also a topic of intense fundamental research in fields as diverse as the physics of polymers,² the glass transition,^{3,4} foams dynamics,⁵ and biological fluids and tissues.^{3,6} Conventional rheology is widely used as a powerful characterization tool,¹ providing valuable information on the macroscopic mechanical properties of a system. As early as in the 1934 study of shear-induced emulsification by Taylor,⁷ however, it was recognized that coupling rheology to measurements of the sample structure and dynamics at the microscopic scale tremendously increases our insight into the material behavior. Most experiments rely on optical and scattering probes of the microstructure, although other methods have also been introduced, e.g., acoustic velocimetry⁸ and nuclear magnetic resonance.⁹ Indeed, in the last 40 years, a large number of apparatuses have been developed, which use microscopy, static and dynamic light scattering, and neutron and X-ray scattering to investigate the microstructure of driven samples. The wide spectrum of topics that have benefited from such simultaneous measurements demonstrates the importance and success of this approach: a non-exhaustive list includes the investigation of the orientation dynamics and deformation of individual objects such as emulsion drops, polymers, liquid crystals, and protein clusters,^{7,10–14} the influence of shear on demixing and critical phenomena,^{15,16} shear-induced structure distortion and non-equilibrium phase transitions,^{17–36} the dynamics of foams^{37,38} and that of defects in colloidal crystals,^{39–43} shear banding^{44–50} and non-affine deformation in polymer gels and glasses,^{51,52} and creep and yielding in amorphous, dense emulsions and colloids, and surfactant phases.^{3,53–65}

Previous works may be classified according to the probe method, the deformation geometry, and the rheological quantities that are measured. In a first group of experiments, mostly performed in the last 30 years of the past century, small angle static light scattering (SALS) was used to monitor the change of the sample structure.^{10–12,15–17,20–22,25} Small angle X-ray scattering (SAXS)^{13,14,24,27,29,31,33,39,42,56} and neutron scattering (SANS,^{23,32,34,35,41,44,46,47,49,66} and references therein) have also been used,^{62,67} although they require large scale facilities and are therefore less accessible than microscopy and light scattering. Quite generally, these experiments were performed under strain-imposed conditions, often using custom-designed shear cells. Stress measurements (or stress-imposed tests) were available in just a few cases,^{11,16,21,68} where a commercial rheometer was coupled to a scattering apparatus.

With the development of advanced microscopy methods, in particularly laser scanning confocal microscopy, many groups have developed apparatuses that couple rheology and microscopy.^{20,28,30,43,45,48,51,57,58,60,61,64,65,69–75} Apparatuses based on a commercial rheometer usually give access to both the shear stress and the strain.^{65,70} With confocal microscopy, both a plate-plate and a cone and plate geometry are possible, since in confocal microscopy the sample is illuminated and the image is collected from the same side. This allows one to avoid any complications in the optical layout due to the wedge-shaped sample volume of the cone and plate geometry. Note that in a torsional rheometer, the cone and plate geometry is preferable to the plate-plate one when a uniform stress is required, e.g., for yield stress fluids or in the non-linear regime. Custom shear cells have also been used in conjunction to microscopy. As for scattering-based setups, custom cells are in general strain-controlled, with no measurement of the stress (see however Refs. 74 and 75 for notable exceptions). In spite of this limitation, custom cells may be an interesting option in terms of cost and because they allow valuable features to be implemented: a fine control and a great flexibility on the choice of the surfaces in contact with the sample, the creation of a stagnation plane through counter-moving surfaces,^{28,45,73} which greatly simplifies the observation under a large applied shear, and the implementation of non-conventional shear

^{a)}Electronic mail: stefano.aime@umontpellier.fr

^{b)}Electronic mail: luca.cipelletti@umontpellier.fr

geometries, e.g., small channels for investigating confinement effects^{48,69,70} or large-amplitude shear with linearly translating parallel plates.³⁰

Real-space microscopy data are unsurpassed in that they provide full knowledge of both the structure and the dynamics of the sample at the particle level. However, microscopy suffers from several limitations: it is quite sensitive to multiple scattering, making turbid samples difficult to study; it requires specifically designed, fluorescently labelled particles if confocal microscopy is to be used; only quite small sample volumes can be imaged; a high resolution, a large field of view, and a fast acquisition rate are mutually exclusive, so that a compromise has to be found between these conflicting requirements. Scattering methods, while not accessing the single particle level, do not suffer from these limitations. Furthermore, advanced scattering techniques such as the Time Resolved Correlation⁷⁶ (TRC) and the Photon Correlation Imaging^{77,78} (PCI) methods can fully capture temporally and spatially varying dynamics, yielding instantaneous coarse-grained maps of the dynamical activity. Thus, scattering techniques are a valuable alternative to real-space methods not only for measuring the sample structure, as in the early works mentioned above, but also to probe its dynamics.

Dynamic light scattering in the highly multiple scattering limit (diffusing wave spectroscopy, DWS⁷⁹) has been used since the 1990s of the past century to measure the microscopic dynamics associated with the affine deformation in the shear flow of a simple fluid⁸⁰ and the impact of shear on foam dynamics.³⁷ In a subsequent series of works, the so-called ‘echo-DWS’ method has been introduced: here, DWS is used to measure the irreversible rearrangements occurring in amorphous viscoelastic solids such as emulsions,⁵³ foams,³⁸ or colloidal gels and glasses^{54,55,59} subject to an oscillating shear deformation. More recently, space-resolved DWS has been applied to the investigation of the microscopic rearrangements in polymeric solids under compression or elongation.^{52,81} By contrast, Dynamic light scattering (DLS) in the single scattering regime⁸² and X-ray Photon Correlation Spectroscopy (XPCS⁸³), its analogous using coherent X rays, have been much less used as a probe of the microscopic dynamics of a driven system,^{43,84,85} perhaps because single scattering conditions require greater care than multiple scattering ones in designing a scattering apparatus, due to the sensitivity of DLS to the scattering angle at which light is collected and its vulnerability to stray light scattered by any imperfections in the optics.⁸⁶ In spite of its greater complexity, DLS has several appealing features, such as its ability to probe the dynamics on a large range of length scales (by varying the scattering angle), the excellent overlap between the probed length scales (from a few tens of nm up to several tens of μm) and the characteristic structural length scales of most complex fluids, and the possibility to extend it to the X-ray domain by XPCS.

In this paper, we introduce a novel, custom-made shear cell that can be coupled both to a microscope and to a static and dynamic small angle light scattering apparatus, such as that described in Ref. 86. The shear cell consists of two parallel plates, one of which can undergo translational motion. In contrast to other custom shear cells previously reported in the literature, for which a shear

deformation is imposed and no stress measurement is available,^{7,10,12,17,22–28,34,37–44,46,47,49,51,53–55,57,58,60,61,64,71–73} our cell is stress-controlled and the strain is accurately measured. Unlike the stress-controlled custom cell of Ref. 74 that is optimized for confocal microscopy in an inverted microscope, our cell can be used in both an inverted or upright conventional or confocal microscope and in light scattering experiments in the transmission or backscattering geometry; furthermore, it can be placed either in a vertical or horizontal position. This versatile design opens the way to the full characterization of the rheological behavior of a sample, simultaneously to its structural and dynamical evolution at the microscopic level. In particular, its compact design allows it to be coupled to state-of-the-art static *and* dynamic light scattering setups, a significant improvement over commercially available light scattering add-ons for rheometers, which are limited to static light scattering.

The rest of the paper is organized as follows: in Sec. II we briefly present the shear cell, before discussing in Sec. III its main features independently of the investigated sample (stress calibration, strain measurement, plate parallelism, effects of inertia, and residual friction). [For the sake of simplicity, here and in the following we shall denote the shear stress and the shear strain simply by “stress” and “strain,” respectively.] Section IV demonstrates the cell performances through a series of tests on model systems, representative of a Newtonian fluid, a perfectly elastic solid, and a viscoelastic Maxwell fluid. In Sec. V, we illustrate how the cell can be coupled to a dynamic light scattering apparatus, by measuring the microscopic dynamics of a Brownian suspension at rest and under shear. Finally, an overview of the characteristics of the shear cell with an emphasis on its strengths and limits concludes the paper, in Sec. VI.

II. SETUP

A scheme of the setup is shown in Fig. 1. The sample is confined between two crossed microscope slides, whose surfaces are separated by a gap e , typically of the order of a few hundreds of μm . The gap can be adjusted using spacers and a set of precision screws to ensure the parallelism of the plates, as described in more detail in Sec. III C. One of the two slides is fixed to an optical table, while the second one is mounted on a mobile frame that slides on a linear air bearing. The air bearing avoids any mechanical contact between the sliding frame and the optical table, therefore minimizing friction. In order to avoid spurious contributions due to gravity, the horizontal alignment of the air bearing rail can be adjusted to within a few 10^{-5} rad using a finely threaded differential screw. To impose the desired shear stress, a controlled force is applied to the mobile frame using a magnetic actuator (see Fig. 1), powered by a custom-designed, computer-controlled current generator. A contactless optical sensor measures the displacement of the moving frame and thus the sample strain. The implementation of the strain sensor is discussed in Sec. III B.

The linear air bearing (model RAB1, from Nelson Air Corp.) is guided by air films of thickness ~ 10 μm , which confine its motion in the longitudinal x direction. The viscous

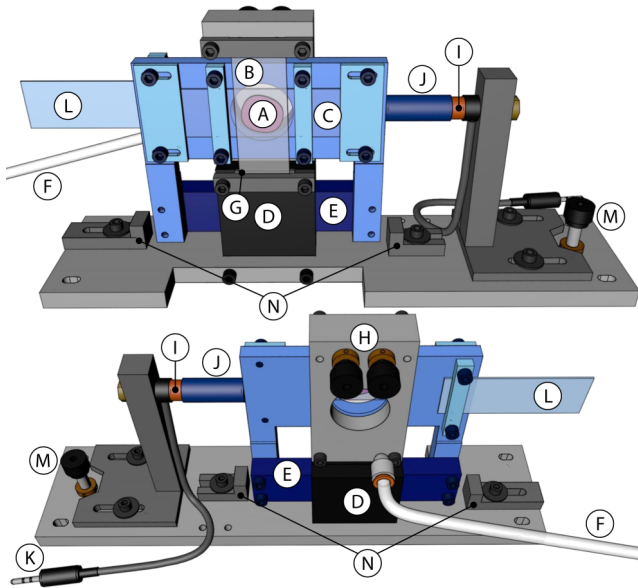


FIG. 1. Scheme of the experimental setup. The moving parts are shown in blue. (A) Sample; (B) fixed glass plate; (C) mobile glass plate; (D) air bearing—fixed body; (E) air bearing—sliding rail; (F) air supply; (G) gap setting spacer; (H) plate alignment screws; (I) coil (fixed); (J) magnet (mobile); (K) cable to PC; (L) frosted glass; (M) tilt adjustment; (N) mechanical stops.

drag of the air films can typically be neglected, whereas a small residual friction, most likely due to dust particles, is seen when a force smaller than 1 mN is applied, as it will be shown in Sec. III D. The maximum linear travel of the system, set by the length of the moving plate, is 75 mm. However, we typically restrain the travel distance to 5–10 mm, over which the imposed force is virtually independent of position (see Sec. III A). This typically corresponds to a strain $\gamma \leq 10$. The nominal straightness of the sliding bar (provided by the manufacturer) is better than $1 \mu\text{m}$ over the whole travel length, whereas the nominal thickness of the plates is constant to within $10 \mu\text{m}$ throughout their entire surface. Therefore, the gap e can be considered to be uniform over the typical working distance. More details on the plates parallelism will be given in Sec. III C. The sliding part of the setup has a relatively small mass, $M \approx 335 \text{ g}$, including the mass of the sliding bar itself, 288.0 g. This allows inertial effects to be kept small, as shown in Sec. IV.

III. SETUP CHARACTERIZATION

In this section, we describe the characterization of the empty shear cell, discussing in particular the force-current calibration of the stress actuator, the optical measurement of the strain, the control and measurement of the plate parallelism, and the effects of inertia and residual friction.

A. Calibration of the applied force

The shear stress imposed to the sample is controlled using a magnetic actuator (Linear Voice Coil DC Motor LVCM-013-032-02, by Moticont), consisting of a permanent magnet and a coil wound on an empty cylinder. The magnet is fixed to the sliding part of the apparatus; it moves with no contact

within the empty cylinder, which is mounted on the fixed part of the apparatus. The device can be easily controlled via a PC, which allows one to synchronously apply a given stress and acquire strain and optical data. Due to the small coil resistance (5.9Ω) and inductance (1 mH), the magnetic actuator response is very fast and its characteristic time (less than 1 ms) will be neglected in the following. The force exerted by the voice coil is proportional to the current fed to the device. We use a custom-designed current generator, which outputs a controlled current I that can be adjusted over a very large range by selecting the appropriate full scale value, between 10^{-5} A and 1 A, in steps of one decade. The current generator noise is smaller than 10^{-4} of the full scale. The current generator is in turn controlled through a voltage input: by feeding different voltage waveforms to the current generator, it is therefore possible to impose a stress with an arbitrary time dependence. In our implementation, the voltage signal is generated by a D/A card (USB-6002 by National Instruments) controlled by a PC. We calibrate the voice coil by measuring the force, F , resulting from the imposed current. The force is measured using a balance, with a precision of 1 mg. The F vs. I curve is shown in Fig. 2. F is remarkably proportional to I over 4.5 decades, with a proportionality constant $k = (0.916 \pm 0.003) \text{ NA}^{-1}$.

An important issue in designing the shear cell apparatus is the requirement that the applied stress be constant regardless of the resulting strain. To check this point, we have measured several calibration curves similar to that shown in Fig. 2, each time slightly changing d , the relative axial position between the magnet and the coil, with $d = 0$ the position of the magnet when it is fully inserted in the coil. The d dependence of the proportionality constant k is shown in the inset of Fig. 2. In the range $7 \text{ mm} < d < 15 \text{ mm}$, we find that k changes by less than 0.5%. In our experiments we typically work in this range, thus ensuring that the applied force is essentially independent

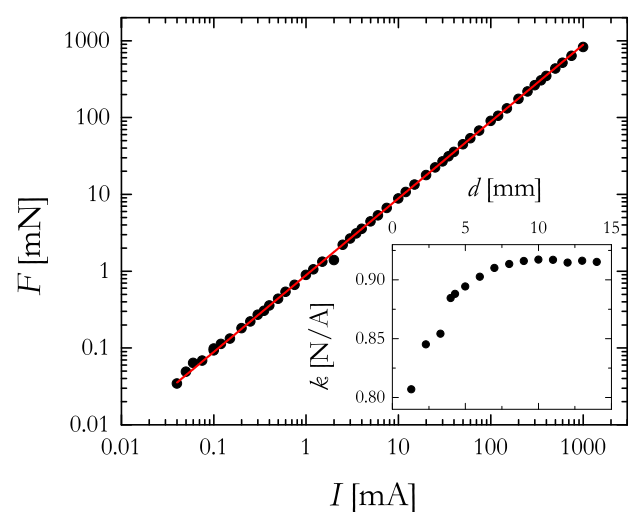


FIG. 2. Calibration of the magnetic actuator: force (measured by a precision balance) as a function of the applied current. The symbols are the experimental data and the line is the best fit of a straight line through the origin, yielding a proportionality constant $k = (0.916 \pm 0.003) \text{ NA}^{-1}$. The upper limit of the imposed current is set by the coil specifications, whereas the smallest current chosen here is limited by the balance precision. Inset: variation of k with the relative axial position between the magnet and the coil, d . The main plot has been measured for $d = 7 \text{ mm}$.

of sample deformation. In order to convert the applied force to a stress value, we measure the surface A of the sample by taking a picture of the shear cell after loading it. The surface is calculated from the image using standard image processing tools. Typical values of A and its uncertainty are 250 mm^2 and a few mm^2 , respectively. When taking into account both the uncertainty of the $F - I$ calibration (0.3%) and that on A , the stress $\sigma = F/A$ is known to within about 1%.

B. Strain measurement

In order to measure the displacement of the mobile frame and hence the sample strain, we use two different optical methods, based on a commercial sensor and on a scattering technique, respectively. The former is a commercial laser position sensor (model IL-S025, by Keyence) that can acquire and send it to a PC up to 1000 points per second with a nominal precision of $1 \mu\text{m}$. This sensor is very convenient to follow large, fast deformations. However, its precision sets a lower bound on the error on the strain measurements of at least 0.5% for a typical gap $e = 200 \mu\text{m}$; moreover, we find that the sensor output tends to artificially drift over time. When more precise, more stable strain measurements are required, we use a custom optical setup, inspired by the work in Ref. 78 and schematized in Fig. 3(a). A frosted glass is fixed to the mobile frame of the shear cell. A laser beam illuminates the frosted glass, which is imaged on a CMOS camera (BU406M by Toshiba Teli Corp). The camera has a $2048 \times 2048 \text{ pixel}^2$ detector, with a pixel size of $5.5 \mu\text{m}$; its maximum acquisition rate at full frame is 90 Hz. The image is formed by a plano-convex lens with a focal length $f = 19 \text{ mm}$, placed in order to achieve a high magnification, $m = 20.5$, such that the pixel size corresponds to 268 nm on the frosted glass. Due to the coherence of the laser light, the image consists of a highly contrasted speckle

pattern (see Fig. 3(a)), which translates as the mobile part of the cell, and hence the frosted glass, is displaced. Using image cross-correlation techniques,⁸⁷ the speckle drift and thus the sample shear can be measured. In practice, a speckle image acquired at time t is spatially cross-correlated with an image taken at a later time t' . The position of the peak of cross-correlation as a function of the spatial shift yields the desired displacement between times t and t' . An example is shown in Fig. 3(b), which shows a cut of the cross-correlation function along the x -direction. The line is a Gaussian fit to the peak: when taking into account the magnification, the fit yields a speckle size $\sigma_{sp} = 16.5 \mu\text{m}$ in the plane of the sensor. The speckle size is controlled by the diameter D of the lens and the system magnification; it has been optimized in order to correspond to a few pixels, which minimizes the noise on the cross-correlation.^{85,88}

To estimate the typical noise on the measurement of the displacement, we take a series of full-frame images of the speckle pattern over a period of 60 s, while keeping the frosted glass immobile. The displacement with respect to the first image ($t = 0$), as measured from the position of the cross-correlation peak, is shown in Fig. 3(c). The displacement fluctuates around a zero average value; the standard deviation of the signal over the full acquisition time, σ_n , may be taken as an estimate of the typical noise on the measured position. We find $\sigma_n = 23 \text{ nm}$, more than 40 times smaller than the nominal precision of the commercial laser sensor. For a typical gap $e = 200 \mu\text{m}$, it is therefore possible to reliably measure strains as small as 10^{-4} . The main limitations of this technique are its time resolution and the largest displacement speed that can be directly measured. The former is limited by the camera acquisition rate and the image processing time: in practice, the position can be sampled at a maximum rate of about 50 Hz. The latter is limited by the acquisition rate

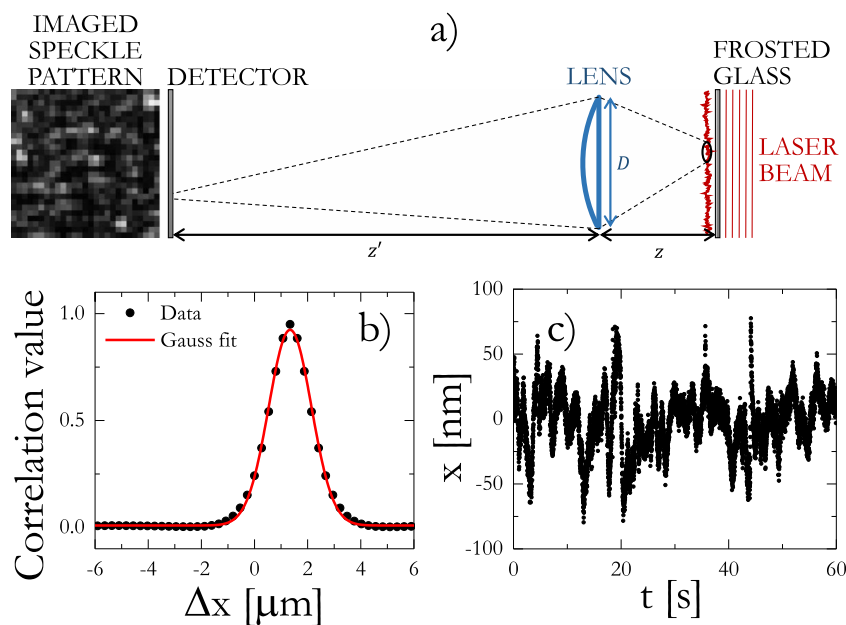


FIG. 3. (a) Optical scheme of the speckle imaging system for measuring the strain: $D = 12.7 \text{ mm}$, $z = 20 \text{ mm}$, and $z' = 410 \text{ mm}$. (b) Cut along the x -direction of the cross-correlation between two speckle images taken at time t and t' . The peak position, $\Delta x = 1.34 \mu\text{m}$, corresponds to the translation of the mobile part of the cell between t and t' . The line is a Gaussian fit to the peak, yielding a speckle size (in the sensor plane) $\sigma_{sp} = 16.5 \mu\text{m}$. (c) Time dependence of the measured displacement while the cell is at rest. The standard deviation $\sigma_n = 23 \text{ nm}$ of the measured position yields an estimate of the measurement error.

and size of the field of view, $l_v \approx 0.5$ mm: if the frosted glass translates by more than l_v between two consecutive images, the speckle pattern is completely changed and no cross-correlation peak is observed. In practice, displacement speeds as high as 1 mm s^{-1} can be measured, corresponding to strain rates up to $\dot{\gamma} = 2 \text{ s}^{-1}$ or $\dot{\gamma} = 5 \text{ s}^{-1}$ for gaps of $500 \text{ }\mu\text{m}$ and $200 \text{ }\mu\text{m}$, respectively. Since the commercial sensor and our custom device have complementary strengths and limitations, we typically use both of them simultaneously. A final point concerns the conversion of the displacement to strain units, for which the gap thickness is required. We determine it after adjusting the plates parallelism (see Sec. III C), by placing the empty shear cell under an optical microscope and by measuring the vertical displacement required to focus the inner surface of the fixed and moving plates, respectively.

C. Adjusting the parallelism between the moving and fixed plates

The parallelism between the two plates is tuned using two differential screws (model DAS110, by ThorLabs), which control the position of the upper side of the fixed plate (see the pictures in Fig. 1). The quality of the alignment is checked by visualizing the interference fringes formed by an auxiliary laser beam reflected by the two inner surfaces of the plates. A change in the local separation between the two plates modifies the relative phase of the two reflected beams, thus changing the fringe pattern. When the plates are parallel, no fringes should be visible. The fringes are imaged on a CMOS camera (DMM 22BUC03-ML, by The Imaging Source, GmbH) with a 744×480 pixel² detector, the pixel size being $6 \text{ }\mu\text{m}$, corresponding to $31 \text{ }\mu\text{m}$ in the sample plane (magnification factor $m = 0.19$). Figure 4(b) shows the fringe pattern observed when a tilt angle of 8×10^{-4} rad between the two plates is imposed on purpose, using the two differential screws. In addition to the finely spaced fringes, due to the tilt, some larger-scale, irregular fringes are also observed, due to slight deviations of the plates from perfectly flat surfaces. When optimizing the alignment (Fig. 4(a)), only the irregular, large-scale fringes are visible. To gauge the precision with which the plates can be aligned, we impose a series of increasingly large tilt angles $\alpha_{imposed}$, acting on the two differential screws. $\alpha_{imposed}$ is estimated from the length of the plate, the nominal thread of the screws, and the imposed screw rotation. For each $\alpha_{imposed}$, we measure the tilt angle $\alpha_{measured} = N\lambda/2L$, where N is the number of fine fringes observed over a distance L and $\lambda = 633 \text{ nm}$ is the laser wavelength. Figure 4(c) shows the measured tilt angle as a function of the imposed one: the data are very well fitted by a straight line with unit slope and a small offset, $\sigma_\alpha \sim 0.3 \text{ mrad}$, most likely due to the difficulty of finding the optimum alignment since the plate surfaces are not perfectly flat. We conclude that the plates can be tuned to be parallel to within a tilt angle of about 0.3 mrad , a value comparable to or even better than for commercial rheometers.⁸⁹ Once the plates have been aligned, they can be removed and placed again in the setup (e.g., for cleaning them) with no need to realign the setup. In this case, we checked that the parallelism is preserved to within 1 mrad .

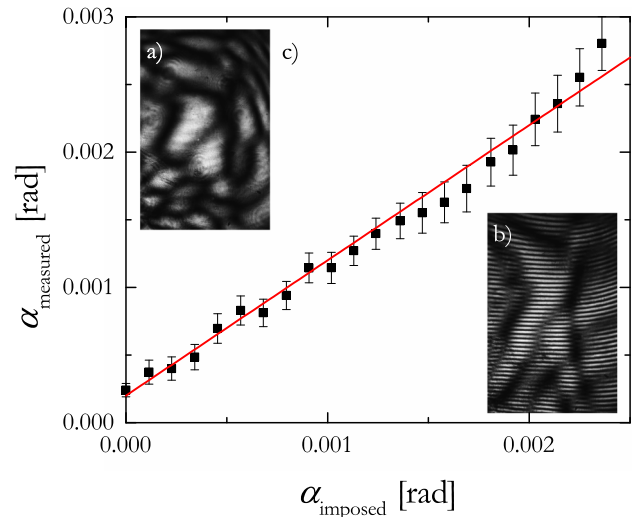


FIG. 4. (a) and (b) Images of the interference fringes observed when the plates are parallel or tilted by an angle $\alpha_{imposed} = 8 \times 10^{-4}$ rad, respectively. The size of the field of view is $15 \times 22 \text{ mm}^2$. (c) Measured tilt angle as a function of the manually imposed tilt angle. The symbols are the data and the line is a linear fit with slope 1.

D. Effects of inertia and friction

Inertia and friction effects may lead to spurious results if they are neglected in the modelling of the setup response. Both effects are best characterized by measuring the cell motion under an applied force in the absence of any sample. Under these conditions, the equation of motion for the moving part of the cell reads

$$M\ddot{x}(t) = F^{(ext)}(t) + F_{fr}[x(t), \dot{x}(t)], \quad (1)$$

where M is the mass of the moving part, x its position (with $x(0) = 0$ the position before applying any force), $F^{(ext)}$ the (time-dependent) force applied by the electromagnetic actuator, and F_{fr} a friction term that may depend on both the position (in the case of solid friction) and the velocity (for viscous-like friction). To characterize the friction term, we measure $x(t)$ after imposing a step force, $F^{(ext)} = F_0\Theta(t)$, with $\Theta(t)$ the Heaviside function. Figure 5(a) shows that $x(t)$ follows remarkably well a quadratic law, suggesting that the friction contribution is negligible for the step force $F_0 = 0.9 \text{ mN}$ used in this test. We perform the same experiment for a variety of applied forces and extract, for each F_0 , the acceleration a from a quadratic fit to $x(t)$. The results are shown in Fig. 5(b): while at large F_0 one finds $a \propto F_0$, as expected if friction is negligible, for $F_0 < 1 \text{ mN}$ the data clearly depart from a proportionality relationship, suggesting that friction reduces the effective force acting on the moving part of the cell. The line in Fig. 5(b) is a fit to the data of the affine law $a = (F_0 - F_{fr})/M$, with M fixed to 335 g , yielding $F_{fr} = 0.12 \text{ mN}$. The fit captures very well the behavior of a over 4 decades, showing that a static friction term accounts satisfactorily for the experimental data. Slight deviations are observed for large forces, suggesting that an additional, viscous-like friction term may set in when the rail slides at high speed. Some small deviations are also observed at low forces, possibly because the friction term may slightly deviate from the simple position- and velocity-independent expression

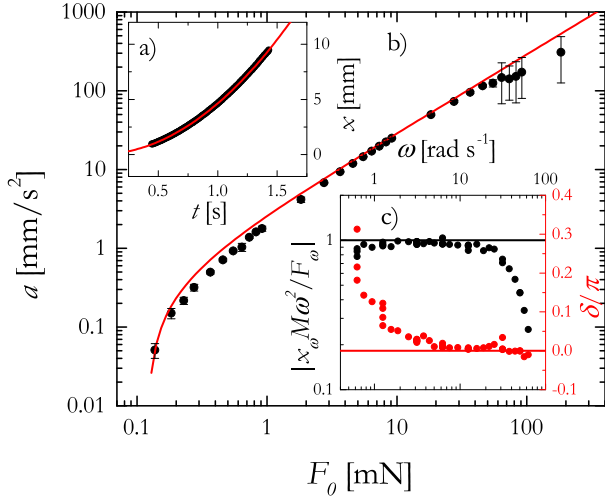


FIG. 5. (a) Time-dependent translation $x(t)$ following the application of a step force $F_0 = 0.9$ mN to the empty cell. The line is a quadratic fit. (b) Acceleration of the empty cell vs. the amplitude of the step force applied. Symbols are the data point and the line is the best fit of an affine law, $a = \frac{F_0 - F_{fr}}{M}$, with $M = 335$ g the mass of the sliding frame, yielding a residual friction force $F_{fr} = 0.12$ mN as the only fitting parameter. (c) Normalized amplitude (black, left axis) and phase (red, right axis) of the oscillating part of the response to a cosinusoidal external force. The symbols are the data points and the lines are the theoretical behavior.

that we have assumed. Since the sample surface is typically $A \sim 2$ cm², the friction term sets a lower bound of the order of 1 Pa on the stress that may be applied in our apparatus.

To probe the frequency dependence of the setup response, we apply an oscillatory force to the empty cell, $F(t) = \text{Re}(\tilde{F}_\omega e^{i\omega t})$, where the tilded variables are complex quantities. Assuming $x(0) = \dot{x}(0) = 0$ and neglecting friction, the expected response is

$$\tilde{x}(t) = \tilde{x}_\omega (e^{i\omega t} - 1 - i\omega t), \quad (2)$$

with $\tilde{x}_\omega = -\tilde{F}_\omega / (M\omega^2)$. Note that, because the physical equation of motion is given by the real part of Eq. (2), inertial effects yield either a nonzero offset $\tilde{F}_\omega / (M\omega^2)$ (for a cosine-like applied force), or a nonzero drift velocity $i\tilde{F}_\omega / (M\omega)$ (for a sinusoidal force), or both of them if the real and imaginary parts of \tilde{F}_ω are nonzero. Thus, in oscillatory shear experiments inertia effects add a constant or linearly growing strain to the sample, whose contribution may or may not be negligible depending on the sample rheological properties and the excitation frequency. To test Eq. (2), we apply a cosinusoidal force to the empty cell, varying the driving frequency from 0.75 rad s⁻¹ to 62.8 rad s⁻¹. For each ω , we adjust F_ω so as to keep the amplitude of the oscillations roughly constant and measure both the modulus and the phase of \tilde{x}_ω from the time dependence of the displacement in the stationary regime. Figure 5(c) shows that the magnitude of the oscillations has the expected value up to 4 rad s⁻¹, beyond which it drops, due to the frequency dependence of the response of the current generator and magnetic actuator and, possibly, to the viscous-like damping mentioned above. The phase of \tilde{x}_ω is close to zero, as expected, except for the lowest frequencies, for which the applied force is too small for friction effects to be neglected.

IV. TESTS WITH MODEL SAMPLES

Having characterized the response of the empty cell, we test its performances on standard rheological samples in oscillatory and step stress experiments. We use a purely viscous fluid, a purely elastic solid, and a viscoelastic material well described by a Maxwell model. For each sample, we briefly discuss the expected behavior in the presence of inertia and compare it to the outcome of experiments, in order to assess the sensitivity and limits of our setup. For the sake of simplicity, we will not introduce the friction term in the equations, but its effects will be highlighted in discussing the experiments.

When a sample is loaded in the shear cell, Eq. (1) has to be modified in order to take into account the force exerted by the sample on the cell, $F^{(s)}(x, \dot{x})$,

$$M\ddot{x}(t) = F^{(ext)}(t) + F_{fr}[x(t), \dot{x}(t)] + F^{(s)}[x(t), \dot{x}(t)]. \quad (3)$$

In principle, $F^{(s)}(x, \dot{x})$ can be divided into an elastic (x -dependent) and a viscous (\dot{x} -dependent) part. To recast Eq. (3) in a form suitable to describe the sample rheological properties, we divide both sides by the sample surface A and express position and velocity as strain $\gamma = x/e$ and strain rate $\dot{\gamma}$, respectively,

$$I\ddot{\gamma}(t) + \sigma[\gamma(t), \dot{\gamma}(t)] = \sigma^{(ext)}(t). \quad (4)$$

Here, $I = eM/A$ is the inertia term, $\sigma^{(ext)}$ the applied stress, and $\sigma = -F^{(s)}/A$ the sample stress, which has opposite sign with respect to $F^{(s)}$ since we adopt the usual notation where σ is the stress exerted by the setup on the sample. This is the general equation that has to be solved given a constitutive equation for $\sigma[\gamma(t), \dot{\gamma}(t)]$, an experimental protocol (i.e., the temporal profile of $\sigma^{(ext)}$), and the initial conditions. In the following, we will systematically assume $\gamma(0) = \dot{\gamma}(0) = 0$ and will only consider either creep tests, $\sigma^{(ext)}(t) = \sigma_0 \Theta(t)$, or oscillatory stresses, $\sigma^{(ext)}(t) = \tilde{\sigma}_\omega e^{i\omega t}$.

A. Newtonian fluid

1. Theoretical background

For a Newtonian fluid of viscosity η , $\sigma = \eta\dot{\gamma}$. Equation (4) therefore reads

$$I\ddot{\gamma} + \eta\dot{\gamma} = \sigma^{(ext)}, \quad (5)$$

which, for a step stress test with stress amplitude σ_0 , has a solution

$$\gamma(t) = \dot{\gamma}_\infty \left[t + \tau_v \left(e^{-\frac{t}{\tau_v}} - 1 \right) \right], \quad (6)$$

where $\tau_v = I/\eta$ is a characteristic time arising from the interplay between inertial and viscous effects and $\dot{\gamma}_\infty = \sigma_0/\eta$. For $t \ll \tau_v$, inertia dominates and $\gamma \approx \sigma_0 t^2 / (2I)$. In the opposite limit $t \gg \tau_v$, the usual simple viscous flow $\gamma = \dot{\gamma}_\infty t$ is recovered. Typical values of the crossover time may be estimated from $\tau_v [s] \approx (2\eta[\text{Pa s}])^{-1}$, where we have assumed $M = 0.3$ kg, $e = 300$ μm , and $A = 2$ cm². Thus, the inertial regime lasts less than 1 s if the viscosity exceeds 0.5 Pa s⁻¹.

For an oscillatory stress, the solution to Eq. (5) is

$$\gamma(t) = \tilde{\gamma}_\omega \left[e^{i\omega t} - 1 + i\omega\tau_v \left(e^{-\frac{t}{\tau_v}} - 1 \right) \right], \quad (7)$$

with

$$\tilde{\gamma}_\omega = -\frac{\tilde{\sigma}_\omega}{\eta\omega} \frac{i + \omega\tau_v}{1 + \omega^2\tau_v^2}. \quad (8)$$

The frequency-dependent complex modulus extracted from the oscillating part of $\gamma(t)$, $G^* = \tilde{\sigma}_\omega/\tilde{\gamma}_\omega$ has magnitude and phase given by

$$\begin{aligned} |G^*| &= \eta\omega\sqrt{1 + \omega^2\tau_v^2}, \\ \arg G^* = \delta &= \arctan \frac{1}{\omega\tau_v}. \end{aligned} \quad (9)$$

At short times $t \ll \tau_v$, viscous dissipation is always negligible and $\gamma(t) \approx \tilde{\gamma}_\omega (e^{i\omega t} - 1 - i\omega t)$, as in Eq. (2), which was derived for an empty cell. At larger times, Eq. (7) simplifies to $\gamma(t) \approx i\tilde{\sigma}_\omega/(\eta\omega) [1 - e^{i\omega t}/(1 + i\omega t)]$: in the high frequency regime $\omega\tau_v \gg 1$ inertial effects are still relevant, but in the opposite regime $\omega\tau_v \ll 1$ the usual behavior for a viscous fluid is recovered: the cell oscillates around a negligible equilibrium position $\tilde{\gamma}_\omega\omega\tau_v$, with an amplitude $\tilde{\gamma}_\omega \approx -i\tilde{\sigma}_\omega/(\eta\omega)$, and the strain lags the stress by an angle $\delta = \pi/2$.

2. Experimental tests

Measurements for step-stresses have been performed with 3 different silicon oils, with viscosities 1.02, 11.98, and 91.68 Pa s, respectively (nominal values at 25 °C). As an example, we show in Fig. 6 results for the less viscous oil, for which the applied stress is varied between 0.3 and 100 Pa. The inset shows the time evolution of the strain following the application of a step stress with $\sigma_0 = 4.5$ Pa. At large times, a pure viscous flow is found, $\gamma(t) = \dot{\gamma}_\infty t$. Deviations at short times from this linear behavior are due to inertia. The data are in excellent agreement with the theoretical expression, Eq. (6) (line), where $\tau_v = eM/(\eta A)$ and $\dot{\gamma}_\infty$ are fitting parameters. We plot in the main figure the steady-state shear rate $\dot{\gamma}_\infty$ vs σ_0 , obtained by fitting $\gamma(t)$ for all applied stresses. At large stresses, data are in excellent agreement with $\dot{\gamma} = \sigma_0/\eta$ using the nominal value of the viscosity, whereas friction causes deviations from this linear dependence for the smallest stresses. Note that friction becomes relevant for $\sigma_0 \lesssim 1$ Pa, in agreement with the lower bound on the stress estimated in Sec. III D. Data over the whole range of applied stresses are very well accounted for by Eq. (6) (line in Fig. 6), with τ_v as the only fitting parameter and using the nominal viscosity. The fit yields $\tau_v = 0.7$ s, in good agreement with the expected value $eM/(\eta A) = 0.8$ s.

Measurements for oscillating stresses have been performed with the same 3 samples and two different values of the gap: $e = 300 \mu\text{m}$ and $e = 600 \mu\text{m}$ (solid and open symbols of Fig. 7, respectively). The stress amplitude was chosen in order to keep the strain amplitude $|\tilde{\gamma}_\omega|$ fixed at 20% for all ω . In Fig. 7 the magnitude of the complex modulus $|G^*|$ (main plot) and its phase δ (inset) are plotted as a function of angular frequency, together with the theoretical expectations given by Eq. (9). The data are in very good agreement with the theory for applied stresses with $|\tilde{\sigma}_\omega| > 1$ Pa. By contrast, when lower stresses are applied to obtain the same strain

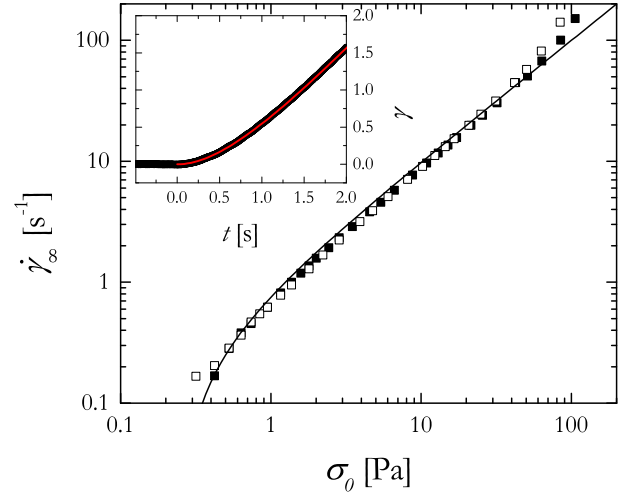


FIG. 6. Main plot: steady shear rate $\dot{\gamma}_\infty$ as a function of the applied stress in a step stress test, for a silicon oil with nominal viscosity $\eta = 1.02$ Pa s. Empty and filled symbols refer to two independent measurements. The line is a fit of $\dot{\gamma}_\infty = (\sigma - \sigma_{fr})/\eta$, where the offset $\sigma_{fr} \sim 0.25$ Pa is due to friction. Inset: time evolution of the strain following a step stress of amplitude $\sigma_0 = 1.58$ Pa. The symbols are the data and the line is a fit of Eq. (6), with $\tau_v = 0.7$ s and $\dot{\gamma}_\infty = 1.18$ s $^{-1}$, in good agreement with $(\sigma_0 - \sigma_{fr})/\eta = 1.27$ s $^{-1}$ as obtained from the nominal viscosity.

amplitude (20% γ)—i.e., for the less viscous samples and the lowest frequencies—deviations are observed due to the residual friction discussed above. Some deviations are also observed at the highest ω , due to the response of the current generator and voice coil, and the viscous-like dissipation, as mentioned in Sec. III D. For the more viscous sample ($\eta = 100$ Pa s), no inertial regime is observed: $|G^*|$ scales as ω , as expected for a Newtonian fluid. This is consistent with the fact that for this sample inertial effects should become significant only for $\omega \gtrsim 1/\tau_v = 100$ rad s $^{-1}$, which

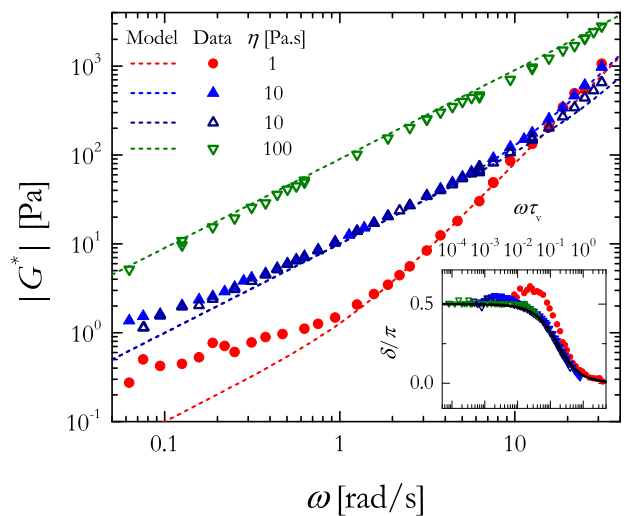


FIG. 7. Main graph: magnitude of the complex modulus of Newtonian viscous fluids measured by oscillatory rheology, as a function of angular frequency. Solid (open) symbols are experiments performed with a gap $e = 300 \mu\text{m}$ ($e = 600 \mu\text{m}$). The data are labelled by the nominal viscosity. The dashed lines are the theoretical predictions, Eq. (9), using the nominal viscosity and the inertia term issued from measurements on the empty cell. Inset: phase δ , as a function of angular frequency normalized by the visco-inertial time τ_v . The line is the theoretical prediction, Eq. (9).

is beyond the range of probed frequencies. For the sample with intermediate viscosity ($\eta = 10$ Pa s), a crossover between $|G^*| \sim \omega$ (viscous regime) and $|G^*| \sim \omega^2$ (inertia-dominated regime) is observed at $\omega \approx 10\text{--}15$ rad s⁻¹, consistent with $1/\tau_v = 10\text{--}20$ s⁻¹ (depending on e). Finally, for the less viscous sample we estimate $1/\tau_v = 2$ s⁻¹: for this sample, all data for which friction is negligible lay in the high frequency regime $\omega\tau_v > 1$ where inertia dominates, leading to the observed $|G^*| \sim \omega^2$ scaling. The inset of Fig. 7 shows the argument of the complex modulus as a function of the normalized frequency $\omega\tau_v$. The data nicely exhibit the transition between the low and high frequency regimes predicted by Eq. (9), characterized by $\delta = \pi/2$ (viscous regime) and $\delta = 0$ (inertial regime), respectively. The discrepancy seen for the fluid with $\eta = 1$ Pa s is again due to residual friction.

B. Purely elastic solid

1. Theoretical background

The constitutive law for a purely elastic sample is $\sigma = G\gamma$, with G the elastic shear modulus. Equation (4) then becomes

$$I\ddot{\gamma} + G\gamma = \sigma^{(ext)}, \quad (10)$$

whose solution involves the characteristic frequency $\Omega = \sqrt{G/I}$, related to an inertial time scale. Inertia is expected to dominate on time scales smaller than Ω^{-1} , whose typical value for our setup, using $M = 0.3$ kg, $e = 300$ μm , and $A = 2$ cm², is given by Ω^{-1} [s] $\approx 0.7/\sqrt{G}$ [Pa].

In a step stress experiment with $\sigma^{(ext)} = \sigma_0\Theta(t)$, the solution to Eq. (10) is

$$\gamma(t) = \gamma_\infty [1 - \cos(\Omega t)], \quad (11)$$

with $\gamma_\infty = \sigma_0/G$. In the inertial regime $\Omega t \ll 1$, one finds the characteristic quadratic time dependence of the strain, $\gamma(t) \approx \frac{1}{2} \frac{\sigma_0}{I} t^2$, while at later times the $\cos(\Omega t)$ term leads to a distinctive “ringing” behavior. Note however that when friction is included, the strain oscillations eventually are damped.

For an oscillatory imposed stress, the solution to Eq. (10) reads

$$\gamma(t) = \tilde{\gamma}_\omega \left[e^{i\omega t} - \cos(\Omega t) - i \frac{\omega}{\Omega} \sin(\Omega t) \right], \quad (12)$$

with $\tilde{\gamma}_\omega = \frac{\tilde{\sigma}_\omega}{G} \left[1 - \left(\frac{\omega}{\Omega} \right)^2 \right]^{-1}$. This corresponds to a complex modulus whose magnitude and phase are

$$|G^*| = G \left[1 - \left(\frac{\omega}{\Omega} \right)^2 \right], \quad (13)$$

$$\delta = 0.$$

At small times $t \ll \Omega^{-1}$ we have again $\gamma(t) \approx \tilde{\gamma}_\omega (e^{i\omega t} - 1 - i\omega t)$, whereas at large t the strain exhibits oscillations at the frequency Ω associated to inertia, superimposed to the elastic response at the forcing frequency ω : their amplitude is $|\tilde{\sigma}_\omega|/G$ and they are in phase with the driving force, a distinctive feature of elasticity.

2. Experimental tests

We use polydimethylsiloxane (PDMS; Sylgard 184 by Dow Corning), a popular elastomer whose elastic modulus can be conveniently tuned by varying the crosslink density,⁹⁰ as a model elastic solid. Using a commercial rheometer, we check that the linear regime extends up to at least $\gamma = 40\%$, larger than the largest strain probed in our tests. A sample with a crosslinker/base volume ratio of 1:60 is used for the step stress measurements. In order to maximize the adhesion to the glass plates, the sample is prepared *in situ*: after adding the crosslinker, the fluid solution is placed between the two plates and cured in an oven at 90 °C for 90 min. The two plates with the cured sample are then mounted on the shear cell. During this operation, care is taken not to stress nor damage the sample. Control measurements are run in a commercial rheometer, with the sample cured *in situ* under similar conditions. We perform a series of step stress experiments, with a gap $e = 570$ μm (as measured before the experiment) and a sample surface $A = 3.3$ cm². Stresses of various amplitude σ_0 are applied, the resulting strain being recorded over time. Figure 8(a) shows a typical time series of strain data acquired simultaneously with the commercial laser sensor (symbols) and with our custom made optical setup (line), for $\sigma_0 = 275$ Pa: note the excellent agreement between the two devices. After an initial transient, lasting a few seconds, γ reaches a constant value γ_∞ dictated by the elastic modulus. Note that the oscillations due to inertia predicted by Eq. (11) are not seen here, indicating that the (small) dissipation of PDMS is sufficient to overdamp them. In Fig. 8(b), γ_∞ estimated by averaging $\gamma(t)$ over 5 min is plotted as a function of the imposed stress. Each data point is

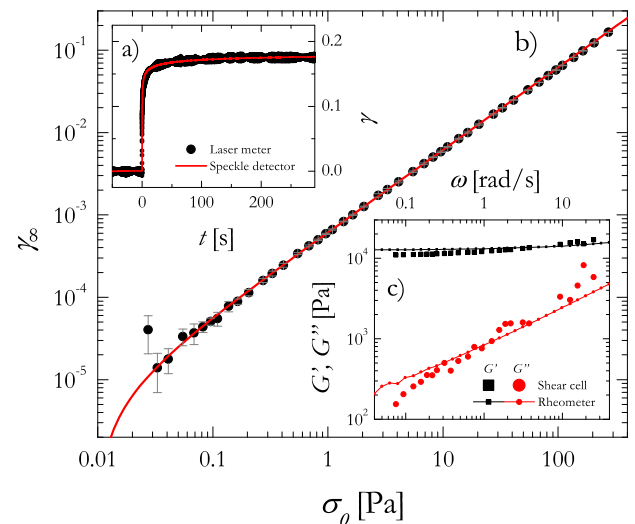


FIG. 8. (a) Time evolution of the strain following a step stress applied at $t = 0$ to a crosslinked PDMS sample, measured with both the commercial laser meter (black dots) and the home-made optical setup (red line). (b) Response to a step stress. The asymptotic strain γ_∞ is plotted against the amplitude of the applied step stress. Data are averaged over 8 experiments, the error bars are the standard deviation over the experiment repetitions. The solid line is an affine fit, yielding an elastic modulus $G = 1620$ Pa. (c) Frequency dependence of the elastic and loss moduli in an oscillatory test, as measured in the custom shear cell ($|\tilde{\sigma}_\omega| = 180$ Pa, large symbols) and in a commercial rheometer ($\gamma_0 = 1\%$, line and small symbols).

an average over 8 experiments, the error bars representing data dispersion. The experimental data are very well fitted by an affine law (red line): $\gamma_\infty = (\sigma_0 - \sigma_{off})/G$, with $G = 1620$ Pa the elastic modulus of the sample and $\sigma_{off} = 13$ mPa an offset stress due to friction. We note that σ_{off} is smaller than the typical friction stress estimated from the experiments with an empty cell, which is of the order of 1 Pa. This discrepancy suggests that the exact value of the friction term depends sensitively on several factors (cleanness of the air bearing, alignment with respect to the vertical direction, etc.) and that 1 Pa should be regarded as a higher bound on its magnitude.

A second series of experiments is performed by imposing oscillating stresses. The sample is prepared at a higher crosslinker density (1:40 v/v), with $e = 590$ μm and $A = 2.5$ cm^2 . After curing the PDMS as described above, an oscillating stress is applied and the amplitude of the strain oscillations is extracted from a sinusoidal fit to $\gamma(t)$. Figure 8(c) shows the frequency dependent elastic and loss moduli. The elastic modulus measured in the custom shear cell is in excellent agreement with data taken in a commercial rheometer (to within 15% or better). By contrast, some discrepancies are seen between G'' as measured in the shear cell and by conventional rheometry. At low frequency ($\omega \leq 0.3$ rad s^{-1}), such a difference is likely to stem from the very small value of G'' as compared to G' , which makes the determination of the loss modulus particularly challenging, as well as to the small friction term discussed in Sec. III D. At high frequency ($\omega \geq 7$ rad s^{-1}), the loss modulus is somehow overestimated by the shear cell. This is probably due to the additional viscous dissipation term not accounted for in our modeling of the shear cell.

C. Maxwell fluid

1. Theoretical background

As an example of a viscoelastic fluid, we consider a Maxwell fluid, for which $\dot{\gamma} = \dot{\sigma}/G + \sigma/\eta$. Here G is the plateau modulus and $\eta = G\tau_M$ the viscosity, with τ_M the Maxwell relaxation time. Using this constitutive law, the equation of motion, Eq. (4), yields

$$I \frac{d^2 \dot{\gamma}}{dt^2} + \frac{I}{\tau_M} \frac{d\dot{\gamma}}{dt} + G\dot{\gamma} = \dot{\sigma}^{(ext)} + \frac{\sigma^{(ext)}}{\tau_M}, \quad (14)$$

whose solutions again involve the characteristic frequency $\Omega = \sqrt{G/I}$.

The general solution for a step stress is

$$\gamma(t) = \frac{\sigma_0}{G} \left(c_0 + \frac{t}{\tau_M} + c_+ e^{-\lambda_+ t} + c_- e^{-\lambda_- t} \right), \quad (15)$$

where $c_0 = 1 - \frac{1}{\tau_M^2 \Omega^2}$, $c_\pm = -\frac{1}{2} \left(c_0 \mp \frac{c_0 + 2}{\sqrt{1 - 4\tau_M^2 \Omega^2}} \right)$, and $\lambda_\pm = \frac{1}{2\tau_M} \left(1 \pm \sqrt{1 - 4\Omega^2 \tau_M^2} \right)$. The regime of slowly relaxing Maxwell fluids (as compared to the inertial time) corresponds to $\Omega\tau_M \ll 1$. In this limit, one recovers $\gamma \approx \sigma t^2/(2I)$, as for a purely viscous fluid (see Eq. (6)). In the opposite limit

$\Omega\tau_M \gg 1$, the solution is

$$\gamma(t) = \frac{\sigma_0}{G} \left[1 + \frac{t}{\tau_M} - \exp\left(-\frac{t}{2\tau_M}\right) \cos(\Omega t) \right], \quad (16)$$

for which three regimes may be distinguished. For $t \ll \Omega^{-1}$, inertia dominates and $\gamma = \sigma_0 t^2/(2I)$. For, $\Omega^{-1} \ll t \ll \tau_M$, the typical oscillations due to the elastic part of the sample response are observed: $\gamma(t) \approx \frac{\sigma}{G} [1 - \cos(\Omega t)]$. Finally, at long times $t \gg \tau_M$ the sample flows as a purely viscous fluid: $\gamma(t) \approx \sigma_0 t/\eta$.

For an applied oscillating stress, focussing on the complex modulus calculated from the oscillating part of the cell response, one finds

$$|G^*| = G \frac{\left(1 - \frac{\omega^2}{\Omega^2}\right)^2 + \frac{\omega^2}{\Omega^4 \tau_M^2}}{\sqrt{\left(1 - \frac{\omega^2}{\Omega^2} - \frac{1}{\tau_M^2 \Omega^2}\right)^2 + \frac{1}{\omega^2 \tau_M^2}}}, \quad (17)$$

$$\tan \delta = \frac{1}{\omega \tau_M} \frac{\Omega^2}{\Omega^2 - \omega^2 - \frac{1}{\tau_M^2}}.$$

In the $\Omega \gg \tau_M^{-1}$ and $\Omega \gg \omega$ limit where inertia is negligible, Eq. (17) simplifies to yield the usual expressions for a Maxwell fluid,

$$|G^*| = G \left(1 + \frac{1}{\omega^2 \tau_M^2} \right)^{-\frac{1}{2}}, \quad (18)$$

$$\tan \delta = \frac{1}{\omega \tau_M}.$$

2. Experimental tests

We test our apparatus on a model Maxwell fluid by performing both oscillatory rheology in the linear regime and creep tests for a wide range of applied stresses, from 1.5 to 150 Pa. The Maxwell fluid is a self-assembled transient network, comprising surfactant-stabilized microemulsions reversibly linked by triblock copolymers, described in detail in Ref. 91. After loading the sample in the shear cell, we wait 5 min before applying a step stress, in order to let the sample fully relax. Similarly, after each creep experiment a waiting time of 2 min is applied before starting the next one. Figure 9(a) shows the comparison between the shear cell data (full symbols) and those collected by conventional rheometry (crosses). An excellent agreement is seen for G' , except at the highest frequencies ($\omega \geq 7$ rad s^{-1}), where inertia becomes important. In this regime, the shear cell data are reasonably well captured by the theoretical expression, Eq. (17) (dashed line). For G'' , we find a very good agreement between the two sets of data up to $\omega \approx 2$ rad s^{-1} . At higher frequency, the shear cell data overestimate G'' , a trend similar to that seen in Fig. 8(b) for the crosslinked PDMS. This lends further support to the hypothesis that an additional viscous dissipation term becomes important at relatively high shear rates.

The time evolution of the strain amplitude in creep tests is shown in Fig. 9(b) for several applied stresses σ_0 . The data are very well fitted by the theoretical expression (Eq. (16)) using the viscoelastic parameters of the Maxwell fluid, τ_M and G ,

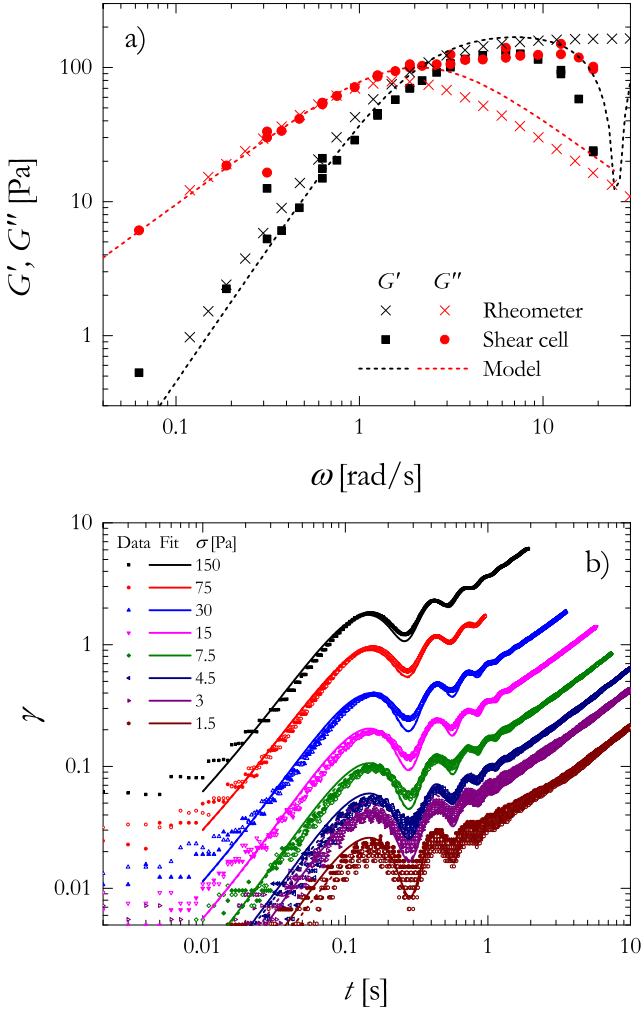


FIG. 9. (a) Frequency dependence of the elastic and loss moduli, for a Maxwell sample. Solid symbols: shear cell, with imposed stress such that $\gamma_0 \approx 10\%$ for all ω ; crosses: commercial rheometer, $\gamma_0 = 10\%$; lines: fit of G' and G'' as calculated from Eq. (17), with the characteristic relaxation time, τ_M , and the plateau modulus, G as fitting parameters. (b) Strain vs. time following a step stress with amplitude σ_0 as given by the labels. Open and filled symbols represent two consecutive measurements on the same sample; lines are best fits to the data using Eq. (16), where the fitting parameters are τ_M and G .

as fitting parameters. For applied stresses within the linear regime, we find a very good agreement between G and τ_m as measured with the shear cell and by conventional rheometry (to within 11% and 3% for G and τ_m , respectively). Note that Eq. (16) captures very well also the ringing effect due to the inertia of the shear cell.

V. DYNAMIC LIGHT SCATTERING UNDER SHEAR

We couple the shear cell to a custom-made small angle light scattering setup⁸⁶ and measure the microscopic dynamics of a colloidal suspension of Brownian particles, both at rest and under shear. The setup uses a CMOS camera as a detector; the microscopic dynamics is quantified by the intensity correlation function $g_2 - 1$,^{82,92}

$$g_2(\mathbf{q}, \tau) - 1 = \left\langle \frac{\langle I_p(t + \tau) I_p(t) \rangle_{\mathbf{q}}}{\langle I_p(t) \rangle_{\mathbf{q}} \langle I_p(t + \tau) \rangle_{\mathbf{q}}} \right\rangle_t - 1. \quad (19)$$

Here, I_p is the time-dependent intensity measured by the p -th pixel, $\langle \cdot \cdot \cdot \rangle_t$ denotes an average over the experiment duration, and $\langle \cdot \cdot \cdot \rangle_{\mathbf{q}}$ is an average over a set of pixels corresponding to a small solid angle centered around the direction associated to a scattering vector \mathbf{q} , whose magnitude is $q = 4\pi n \lambda^{-1} \sin(\theta/2)$, with n the solvent refractive index, $\lambda = 532$ nm the laser wavelength and θ the scattering angle.

The intensity correlation function is directly related to the microscopic dynamics: for particles undergoing Brownian motion, $g_2(\mathbf{q}, \tau) - 1 = \exp(-2Dq^2\tau)$, where D is the particle diffusion coefficient.⁸² Under shear, the relative motion due to the affine displacement also contributes to the decay of $g_2 - 1$. Neglecting hydrodynamic interactions and assuming an homogeneous shear flow in the xz plane (\hat{u}_x and \hat{u}_z being the velocity and the velocity gradient direction, respectively), the particle dynamics are described by the displacement field $\Delta \mathbf{r}(\mathbf{r}, \dot{\gamma}, \tau) = \Delta \mathbf{r}^{(\text{diff})}(\tau) + \Delta \mathbf{r}^{(\text{aff})}(\mathbf{r}, \dot{\gamma}, \tau)$, where $\Delta \mathbf{r}^{(\text{aff})}(\mathbf{r}, \dot{\gamma}, \tau) = \dot{\gamma} \tau (\mathbf{r} \cdot \hat{u}_z) \hat{u}_x$ is the affine shear field, whereas $\Delta \mathbf{r}^{(\text{diff})}(\tau)$ describes Brownian diffusion. Assuming that the two contributions are uncorrelated, the intensity correlation function can be expressed as⁹³

$$g_2(\mathbf{q}, \dot{\gamma}, \tau) - 1 = \text{sinc}^2\left(\frac{e}{2} q_x \dot{\gamma} \tau\right) \exp(-2Dq^2\tau), \quad (20)$$

where $q_x = \mathbf{q} \cdot \hat{u}_x$ is the projection of the scattering vector along the velocity direction. Note that no contribution of the applied shear on the dynamics is expected when selecting a scattering vector $\mathbf{q} = q_y \hat{u}_y$ parallel to the vorticity direction.

We measure the dynamics of a suspension of polystyrene particles with diameter $2a = 1.2 \mu\text{m}$ (Invitrogen Molecular Probes), suspended at a weight fraction of 0.01% in a 1:1 v/v mixture of H_2O and D_2O that matches the density of polystyrene, to avoid sedimentation. A time series of images of the scattered light is acquired using the scheme described in Ref. 94, both at rest and while imposing a constant shear rate $\dot{\gamma} = 0.03 \text{ s}^{-1}$. The intensity correlation function is calculated using Eq. (19), for several \mathbf{q} vectors both along the velocity and the vorticity direction (q_x and q_y , respectively). Figure 10 shows representative correlation functions; for a given magnitude of the scattering vector, the decay time is shorter when \mathbf{q} is oriented parallel to the shear velocity (open symbols), reflecting faster dynamics due to the contribution of the affine shear field. The lines are fits to the data using Eq. (20): for both \mathbf{q} orientations, excellent agreement is seen between the data and the model. We extract from the fits the characteristic relaxation time τ^* , defined by $g_2(\mathbf{q}, \tau^*) - 1 = \exp(-2)$, and plot τ^* vs q in the inset of Fig. 10. For $\mathbf{q} = q_y \hat{u}_x$, τ^* is in excellent agreement with the theoretical prediction, dashed line; its q dependence is very close to a q^{-1} scaling, indicative of ballistic motion and suggesting that over the range of probed q vectors and time scales the displacement due to the affine deformation is significantly larger than that due to Brownian motion. This is confirmed by inspecting $\tau^*(q)$ for a quiescent suspension (solid squares and solid line): for all q , the relaxation time due to Brownian motion is larger than that under shear. The solid circles are the relaxation time of the dynamics in the vorticity direction while shearing the sample. Overall, $\tau^*(q_y)$ closely follows the data for the quiescent suspension, demonstrating that the affine and

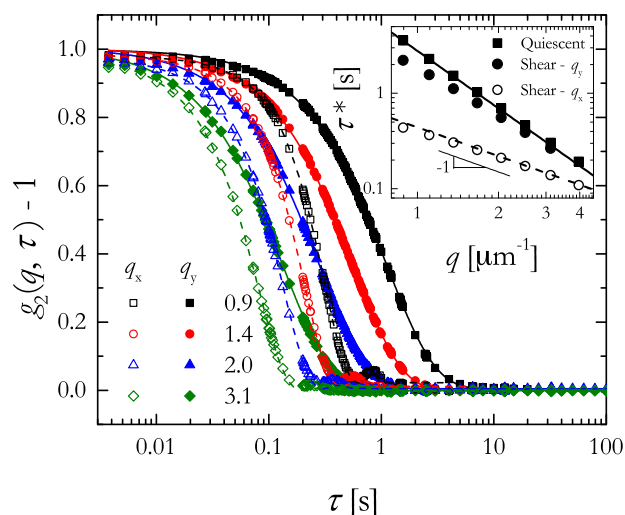


FIG. 10. Main plot: representative intensity correlation functions for a sheared suspension of Brownian particles, for scattering vectors parallel (q_x , open symbols) and perpendicular (q_y , solid symbols) to the shear direction. Data are fitted with Eq. (20) (dashed and solid lines for q_x and q_y , respectively) with D and $\dot{\gamma}$ as fitting parameters. Inset: characteristic time τ^* as defined in the text for the two orientations of \mathbf{q} and for a quiescent sample, as a function of the scattering vector. The lines are the predictions of Eq. (20), using the nominal values of the diffusion coefficient, $D = 0.36 \mu\text{m}^2\text{s}^{-1}$, and the shear rate, $\dot{\gamma} = 0.03 \text{ s}^{-1}$.

non-affine components of the particle dynamics can be resolved by dynamic light scattering. Only at the smallest q vector do the data exhibit some deviations with respect to purely Brownian dynamics: most likely, this discrepancy stems from slight deviations of the velocity field from the ideal one, due to the finite size of the sample.

VI. CONCLUSION

We have presented a custom-made stress-controlled shear cell in the linear translation plate-plate geometry, which can be coupled to both a microscope and a static and dynamic light scattering apparatus. The setup has been successfully tested on a variety of samples representative of simple fluids, ideal solids, and viscoelastic fluids; its coupling to dynamic light scattering measurements has been illustrated by measuring the dynamics of Brownian particles in a suspension at rest or under shear. The main features of the cell include a gap that can be adjusted down to $100 \mu\text{m}$ keeping the parallelism to within 0.3 mrad , the acquisition of strain data at up to 1000 Hz with very good precision (typically better than 0.01%) and for strains as large as $10^4\%$, and the possibility of imposing a user-defined, time-varying stress, ranging from 0.1 Pa (limited by residual friction) to 10 kPa , with a frequency bandpass $0 \leq \omega \leq 4 \text{ rad s}^{-1}$. Most of these specifications meet or even exceed those of a commercial rheometer. Among the limitations intrinsic to the setup, the most stringent is probably inertia, due to the non-negligible mass of the sliding frame $M = 335 \text{ g}$, which restricts viscosity measurements to $\eta \gtrsim 1 \text{ Pa s}$. Other limitations in the current implementation could be improved: for example, the upper stress limit could be pushed to 100 kPa by changing the magnetic actuator. Finally, we remind that care must be taken in aligning both the plate

parallelism and the horizontality of the setup, which makes its use less straightforward than that of a commercial rheometer. These drawbacks are more than offset by the advantages afforded by our shear cell: The possibility of easily changing the plates, e.g., to optimize them against slippage or to replace them when the surface quality does not meet anymore the stringent requirements for microscopy or light scattering; the open design that leaves full access on both sides, thus making it suitable for both inverted and upright microscopes and for small angle light scattering; the linear translation geometry that insures uniform stress in the (optically optimal) parallel plate configuration; the flexibility provided by the choice of the orientation in the vertical or horizontal plane; and, last but not least, a much reduced cost as compared to a commercial rheometer.

ACKNOWLEDGMENTS

We thank J. Barbat and E. Alibert for help in instrumentation and S. Arora for providing us with the bridged microemulsion sample. Funding from the French ANR (Project FAPRES, No. ANR-14-CE32-0005-01) and the E.U. (Marie Skłodowska-Curie ITN Supolen, No. 607937) is gratefully acknowledged.

- ¹R. G. Larson, *The Structure and Rheology of Complex Fluids*, 1st ed. (Oxford University Press, New York, 1998).
- ²M. Rubinstein and R. H. Colby, *Polymer Physics*, 1st ed. (Oxford University Press, Oxford, New York, 2003).
- ³D. T. N. Chen, Q. Wen, P. A. Janmey, J. C. Crocker, and A. G. Yodh, "Rheology of soft materials," *Annu. Rev. Condens. Matter Phys.* **1**, 301–322 (2010).
- ⁴K. Binder and W. Kob, *Glassy Materials and Disordered Solids: An Introduction to Their Statistical Mechanics* (World Scientific, 2011).
- ⁵I. Cantat, S. Cohen-Addad, F. Elias, F. Graner, R. Höhler, R. Flatman, O. Pitois, F. Rouyer, and A. Saint-Jalmes, *Foams: Structure and Dynamics* (OUP Oxford, 2013).
- ⁶P. A. Janmey, P. C. Georges, and S. Hvidt, *Basic Rheology for Biologists* (Academic Press, 2007), pp. 1–27.
- ⁷G. I. Taylor, "The formation of emulsions in definable fields of flow," *Proc. R. Soc. A* **146**, 501–523 (1934).
- ⁸T. Gallot, C. Perge, V. Grenard, M.-A. Fardin, N. Taberlet, and S. Manneville, "Ultrafast ultrasonic imaging coupled to rheometry: Principle and illustration," *Rev. Sci. Instrum.* **84**, 045107 (2013).
- ⁹P. T. Callaghan, "Rheo-NMR: Nuclear magnetic resonance and the rheology of complex fluids," *Rep. Prog. Phys.* **62**, 599 (1999).
- ¹⁰V. B. Tolstoguzov, A. I. Mzhel'sky, and V. Y. Gulov, "Deformation of emulsion droplets in flow," *Colloid Polym. Sci.* **252**, 124–132 (1974).
- ¹¹T. Hashimoto, T. Takebe, and S. Suehiro, "Apparatus to measure small-angle light scattering profiles of polymers under shear flow," *Polym. J.* **18**, 123–130 (1986).
- ¹²J. W. van Egmond, D. E. Werner, and G. G. Fuller, "Time-dependent small-angle light scattering of shear-induced concentration fluctuations in polymer solutions," *J. Chem. Phys.* **96**, 7742 (1992).
- ¹³E. Di Cola, C. Fleury, P. Panine, and M. Cloitre, "Steady shear flow alignment and rheology of lamellae-forming abc triblock copolymer solutions: Orientation, defects, and disorder," *Macromolecules* **41**, 3627–3635 (2008).
- ¹⁴D. C. F. Wieland, V. M. Garamus, T. Zander, C. Krywka, M. Wang, A. Dedinaite, P. M. Claesson, and R. Willumeit-Römer, "Studying solutions at high shear rates: A dedicated microfluidics setup," *J. Synchrotron Radiat.* **23**, 480–486 (2016).
- ¹⁵D. Beysens, M. Gbadamassi, and L. Boyer, "Light-scattering study of a critical mixture with shear flow," *Phys. Rev. Lett.* **43**, 1253 (1979).
- ¹⁶J. Läger and W. Gronski, "A melt rheometer with integrated small angle light scattering," *Rheol. Acta* **34**, 70–79 (1995).
- ¹⁷B. J. Ackerson, J. van der Werff, and C. G. de Kruif, "Hard-sphere dispersions: Small-wave-vector structure-factor measurements in a linear shear flow," *Phys. Rev. A* **37**, 4819 (1988).

- ¹⁸Y. D. Yan and J. K. G. Dhont, "Shear-induced structure distortion in nonaqueous dispersions of charged colloidal spheres via light scattering," *Phys. A* **198**, 78–107 (1993).
- ¹⁹R. Linemann, J. Lauger, G. Schmidt, K. Kratzat, and W. Richtering, "Linear and nonlinear rheology of micellar solutions in the isotropic, cubic and hexagonal phase probed by rheo-small-angle light scattering," *Rheol. Acta* **34**, 440–449 (1995).
- ²⁰T. Kume, K. Asakawa, E. Moses, K. Matsuzaka, and T. Hashimoto, "A new apparatus for simultaneous observation of optical microscopy and small-angle light scattering measurements of polymers under shear flow," *Acta polym.* **46**, 79–85 (1995).
- ²¹J. Vermant, L. Raynaud, J. Mewis, B. Ernst, and G. G. Fuller, "Large-scale bundle ordering in sterically stabilized latices," *J. Colloid Interface Sci.* **211**, 221–229 (1999).
- ²²P. Varadan and M. J. Solomon, "Shear-induced microstructural evolution of a thermoreversible colloidal gel," *Langmuir* **17**, 2918–2929 (2001).
- ²³L. Porcar, W. A. Hamilton, P. D. Butler, and G. G. Warr, "Scaling of shear-induced transformations in membrane phases," *Phys. Rev. Lett.* **89**, 168301 (2002).
- ²⁴L. Ramos and F. Molino, "Shear melting of a hexagonal columnar crystal by proliferation of dislocations," *Phys. Rev. Lett.* **92**, 018301 (2004).
- ²⁵R. Scirocco, J. Vermant, and J. Mewis, "Effect of the viscoelasticity of the suspending fluid on structure formation in suspensions," *J. Non-Newtonian Fluid Mech.* **117**, 183–192 (2004).
- ²⁶I. Cohen, T. G. Mason, and D. A. Weitz, "Shear-induced configurations of confined colloidal suspensions," *Phys. Rev. Lett.* **93**, 046001 (2004).
- ²⁷L. Yang, R. H. Somani, I. Sics, B. S. Hsiao, R. Kolb, H. Fruitwala, and C. Ong, "Shear-induced crystallization precursor studies in model polyethylene blends by *in-situ* Rheo-SAXS and Rheo-WAXD," *Macromolecules* **37**, 4845–4859 (2004).
- ²⁸Y. L. Wu, J. H. J. Brand, J. L. A. van Gemert, J. Verkerk, H. Wisman, A. van Blaaderen, and A. Imhof, "A new parallel plate shear cell for *in situ* real-space measurements of complex fluids under shear flow," *Rev. Sci. Instrum.* **78**, 103902 (2007).
- ²⁹Y. Kosaka, M. Ito, Y. Kawabata, and T. Kato, "Lamellar-to-onion transition with increasing temperature under shear flow in a nonionic surfactant/water system," *Langmuir* **26**, 3835–3842 (2010).
- ³⁰V. Grenard, N. Taberlet, and S. Manneville, "Shear-induced structuration of confined carbon black gels: Steady-state features of vorticity-aligned flocs," *Soft Matter* **7**, 3920 (2011).
- ³¹L. Ramos, A. Laperroussaz, P. Dieudonne, and C. Ligoure, "Structural signature of a brittle-to-ductile transition in self-assembled networks," *Phys. Rev. Lett.* **107**, 148302 (2011).
- ³²C. R. Lopez-Barron, L. Porcar, A. P. R. Eberle, and N. J. Wagner, "Dynamics of melting and recrystallization in a polymeric micellar crystal subjected to large amplitude oscillatory shear flow," *Phys. Rev. Lett.* **108**, 258301 (2012).
- ³³R. Akkal, N. Cohaut, M. Khodja, T. Ahmed-Zaid, and F. Bergaya, "Rheo-SAXS investigation of organoclay water in oil emulsions," *Colloids Surf., A* **436**, 751–762 (2013).
- ³⁴L. Gentile, M. A. Behrens, L. Porcar, P. Butler, N. J. Wagner, and U. Olsson, "Multilamellar vesicle formation from a planar lamellar phase under shear flow," *Langmuir* **30**, 8316–8325 (2014).
- ³⁵J. M. Kim, A. P. Eberle, A. K. Gurnon, L. Porcar, and N. J. Wagner, "The microstructure and rheology of a model, thixotropic nanoparticle gel under steady shear and large amplitude oscillatory shear (LAOS)," *J. Rheol.* **58**, 1301–1328 (2014).
- ³⁶N. Y. C. Lin, X. Cheng, and I. Cohen, "Biaxial shear of confined colloidal hard spheres: The structure and rheology of the vorticity-aligned string phase," *Soft Matter* **10**, 1969 (2014).
- ³⁷A. D. Gopal and D. J. Durian, "Nonlinear bubble dynamics in a slowly driven foam," *Phys. Rev. Lett.* **75**, 2610 (1995).
- ³⁸R. Hohler, S. Cohen-Addad, and H. Hoballah, "Periodic nonlinear bubble motion in aqueous foam under oscillating shear strain," *Phys. Rev. Lett.* **79**, 1154 (1997).
- ³⁹F. R. Molino, J.-F. Berret, G. Porte, O. Diat, and P. Lindner, "Identification of flow mechanisms for a soft crystal," *Eur. Phys. J. B* **3**, 59–72 (1998).
- ⁴⁰P. Schall, I. Cohen, D. A. Weitz, and F. Spaepen, "Visualization of dislocation dynamics in colloidal crystals," *Science* **305**, 1944–1948 (2004).
- ⁴¹S. Reinicke, M. Karg, A. Lapp, L. Heymann, T. Hellweg, and H. Schmalz, "Flow-induced ordering in cubic gels formed by p2vp-*b*-peo-*b*-p(gme-co-ge) triblock terpolymer micelles: A Rheo-SANS study," *Macromolecules* **43**, 10045–10054 (2010).
- ⁴²M. A. Torija, S.-H. Choi, T. P. Lodge, and F. S. Bates, "Large amplitude oscillatory shear of block copolymer spheres on a body-centered cubic lattice: Are micelles like metals?," *J. Phys. Chem. B* **115**, 5840–5848 (2011).
- ⁴³E. Tamborini, L. Cipelletti, and L. Ramos, "Plasticity of a colloidal polycrystal under cyclic shear," *Phys. Rev. Lett.* **113**, 078301 (2014).
- ⁴⁴M. E. Helgeson, P. A. Vasquez, E. W. Kaler, and N. J. Wagner, "Rheology and spatially resolved structure of cetyltrimethylammonium bromide wormlike micelles through the shear banding transition," *J. Rheol.* **53**, 727 (2009).
- ⁴⁵D. Derks, H. Wisman, A. van Blaaderen, and A. Imhof, "Confocal microscopy of colloidal dispersions in shear flow using a counter-rotating cone-plate shear cell," *J. Phys.: Condens. Matter* **16**, S3917–S3927 (2004).
- ⁴⁶R. Angelico, C. O. Rossi, L. Ambrosone, G. Palazzo, K. Mortensen, and U. Olsson, "Ordering fluctuations in a shear-banding wormlike micellar system," *Phys. Chem. Chem. Phys.* **12**, 8856 (2010).
- ⁴⁷M. E. Helgeson, L. Porcar, C. Lopez-Barron, and N. J. Wagner, "Direct observation of flow-concentration coupling in a shear-banding fluid," *Phys. Rev. Lett.* **105**, 084501 (2010).
- ⁴⁸T. J. Ober, J. Soulages, and G. H. McKinley, "Spatially resolved quantitative rheo-optics of complex fluids in a microfluidic device," *J. Rheol.* **55**, 1127–1159 (2011).
- ⁴⁹A. K. Gurnon, C. R. Lopez-Barron, A. P. R. Eberle, L. Porcar, and N. J. Wagner, "Spatiotemporal stress and structure evolution in dynamically sheared polymer-like micellar solutions," *Soft Matter* **10**, 2889–2898 (2014).
- ⁵⁰V. Chikkadi, D. Miedema, M. Dang, B. Nienhuis, and P. Schall, "Shear banding of colloidal glasses: Observation of a dynamic first-order transition," *Phys. Rev. Lett.* **113**, 208301 (2014).
- ⁵¹A. Basu, Q. Wen, X. Mao, T. C. Lubensky, P. A. Janmey, and A. G. Yodh, "Nonaffine displacements in flexible polymer networks," *Macromolecules* **44**, 1671–1679 (2011).
- ⁵²M.-Y. Nagazi, G. Brambilla, G. Meunier, P. Margueres, J.-N. Perere, and L. Cipelletti, "Space-resolved diffusing wave spectroscopy measurements of the macroscopic deformation and the microscopic dynamics in tensile strain tests," *Opt. Lasers Eng.* **88**, 5–12 (2017).
- ⁵³P. Hebraud, F. Lequeux, J. P. Munch, and D. J. Pine, "Yielding and rearrangements in disordered emulsions," *Phys. Rev. Lett.* **78**, 4657–4660 (1997).
- ⁵⁴G. Petekidis, A. Moussaed, and P. N. Pusey, "Rearrangements in hard-sphere glasses under oscillatory shear strain," *Phys. Rev. E* **66**, 051402 (2002).
- ⁵⁵G. Petekidis, P. N. Pusey, A. Moussaed, S. Egelhaaf, and W. C. K. Poon, "Shear-induced yielding and ordering in concentrated particle suspensions," *Phys. A* **306**, 334–342 (2002).
- ⁵⁶T. Bauer, J. Oberdisse, and L. Ramos, "Collective rearrangement at the onset of flow of a polycrystalline hexagonal columnar phase," *Phys. Rev. Lett.* **97**, 258303 (2006).
- ⁵⁷R. Besseling, E. Weeks, A. B. Schofield, and W. C. K. Poon, "Three-dimensional imaging of colloidal glasses under steady shear," *Phys. Rev. Lett.* **99**, 028301 (2007).
- ⁵⁸P. Schall, D. A. Weitz, and F. Spaepen, "Structural rearrangements that govern flow in colloidal glasses," *Science* **318**, 1895–1899 (2007).
- ⁵⁹P. A. Smith, G. Petekidis, S. U. Egelhaaf, and W. C. K. Poon, "Yielding and crystallization of colloidal gels under oscillatory shear," *Phys. Rev. E* **76**, 041402 (2007).
- ⁶⁰J. Zausch, J. Horbach, M. Laurati, S. U. Egelhaaf, J. M. Brader, T. Voigtmann, and M. Fuchs, "From equilibrium to steady state: The transient dynamics of colloidal liquids under shear," *J. Phys.: Condens. Matter* **20**, 404210 (2008).
- ⁶¹N. Koumakis, M. Laurati, S. U. Egelhaaf, J. F. Brady, and G. Petekidis, "Yielding of hard-sphere glasses during start-up shear," *Phys. Rev. Lett.* **108**, 098303 (2012).
- ⁶²D. Denisov, M. T. Dang, B. Struth, G. Wegdam, and P. Schall, "Resolving structural modifications of colloidal glasses by combining x-ray scattering and rheology," *Sci. Rep.* **3**, 1631 (2013).
- ⁶³N. Y. C. Lin, S. Goyal, X. Cheng, R. N. Zia, F. A. Escobedo, and I. Cohen, "Far-from-equilibrium sheared colloidal liquids: Disentangling relaxation, advection, and shear-induced diffusion," *Phys. Rev. E* **88**, 062309 (2013).
- ⁶⁴E. D. Knowlton, D. J. Pine, and L. Cipelletti, "A microscopic view of the yielding transition in concentrated emulsions," *Soft Matter* **10**, 6931–6940 (2014).
- ⁶⁵T. Sentjabrskaja, P. Chaudhuri, M. Hermes, W. C. K. Poon, J. Horbach, S. U. Egelhaaf, and M. Laurati, "Creep and flow of glasses: Strain response linked to the spatial distribution of dynamical heterogeneities," *Sci. Rep.* **5**, 11884 (2015).
- ⁶⁶A. P. Eberle and L. Porcar, "Flow-SANS and Rheo-SANS applied to soft matter," *Curr. Opin. Colloid Interface Sci.* **17**, 33–43 (2012).

- ⁶⁷A. Dhinojwala and S. Granick, "Micron-gap rheo-optics with parallel plates," *J. Chem. Phys.* **107**, 8664–8667 (1997).
- ⁶⁸N. Koumakis, A. B. Schofield, and G. Petekidis, "Effects of shear induced crystallization on the rheology and ageing of hard sphere glasses," *Soft Matter* **4**, 2008 (2008).
- ⁶⁹J. Goyon, A. Colin, G. Ovarlez, A. Ajdari, and L. Bocquet, "Spatial cooperativity in soft glassy flows," *Nature* **454**, 84–87 (2008).
- ⁷⁰R. Besseling, L. Isa, E. R. Weeks, and W. C. Poon, "Quantitative imaging of colloidal flows," *Adv. Colloid Interface Sci.* **146**, 1–17 (2009).
- ⁷¹R. Besseling, L. Isa, P. Ballesta, G. Petekidis, M. E. Cates, and W. C. K. Poon, "Shear banding and flow-concentration coupling in colloidal glasses," *Phys. Rev. Lett.* **105**, 268301 (2010).
- ⁷²D. Chen, D. Semwogerere, J. Sato, V. Breedveld, and E. R. Weeks, "Microscopic structural relaxation in a sheared supercooled colloidal liquid," *Phys. Rev. E* **81**, 011403 (2010).
- ⁷³J.-B. Boitte, C. Vizcaíno, L. Benyahia, J.-M. Herry, C. Michon, and M. Hayert, "A novel rheo-optical device for studying complex fluids in a double shear plate geometry," *Rev. Sci. Instrum.* **84**, 013709 (2013).
- ⁷⁴H. K. Chan and A. Mohraz, "A simple shear cell for the direct visualization of step-stress deformation in soft materials," *Rheol. Acta* **52**, 383–394 (2013).
- ⁷⁵N. Y. C. Lin, J. H. McCoy, X. Cheng, B. Leahy, J. N. Israelachvili, and I. Cohen, "A multi-axis confocal rheoscope for studying shear flow of structured fluids," *Rev. Sci. Instrum.* **85**, 033905 (2014).
- ⁷⁶L. Cipelletti, H. Bissig, V. Trappe, P. Ballesta, and S. Mazoyer, "Time-resolved correlation: A new tool for studying temporally heterogeneous dynamics," *J. Phys.: Condens. Matter* **15**, S257–S262 (2003).
- ⁷⁷A. Duri, D. A. Sessoms, V. Trappe, and L. Cipelletti, "Resolving long-range spatial correlations in Jammed colloidal systems using photon correlation imaging," *Phys. Rev. Lett.* **102**, 085702-1–085702-4 (2009).
- ⁷⁸L. Cipelletti, G. Brambilla, S. Maccarrone, and S. Caroff, "Simultaneous measurement of the microscopic dynamics and the mesoscopic displacement field in soft systems by speckle imaging," *Opt. Express* **21**, 22353–22366 (2013).
- ⁷⁹D. A. Weitz and D. J. Pine, "Diffusing-wave spectroscopy," in *Dynamic Light Scattering*, edited by W. Brown (Oxford, 1993), pp. 652–720.
- ⁸⁰X.-L. Wu, D. J. Pine, P. M. Chaikin, J. S. Huang, and D. A. Weitz, "Diffusing-wave spectroscopy in a shear flow," *J. Opt. Soc. Am. B* **7**, 15 (1990).
- ⁸¹M. Erpelding, A. Amon, and J. Crassous, "Diffusive wave spectroscopy applied to the spatially resolved deformation of a solid," *Phys. Rev. E* **78**, 046104 (2008).
- ⁸²B. J. Berne and R. Pecora, *Dynamic Light Scattering* (Wiley, New York, 1976).
- ⁸³A. Madsen, R. L. Leheny, H. Guo, M. Sprung, and O. Czakkel, "Beyond simple exponential correlation functions and equilibrium dynamics in x-ray photon correlation spectroscopy," *New J. Phys.* **12**, 055001 (2010).
- ⁸⁴M. C. Rogers, K. Chen, L. Andrzejewski, S. Narayanan, S. Ramakrishnan, R. L. Leheny, and J. L. Harden, "Echoes in x-ray speckles track nanometer-scale plastic events in colloidal gels under shear," *Phys. Rev. E* **90**, 062310 (2014).
- ⁸⁵N. Ali, D. C. D. Roux, L. Cipelletti, and F. Caton, "RheoSpectle: A new tool to investigate local flow and microscopic dynamics of soft matter under shear," *Meas. Sci. Technol.* **27**, 125902 (2016).
- ⁸⁶E. Tamborini and L. Cipelletti, "Multiangle static and dynamic light scattering in the intermediate scattering angle range," *Rev. Sci. Instrum.* **83**, 093106 (2012).
- ⁸⁷P. T. Tokumaru and P. E. Dimotakis, "Image correlation velocimetry," *Exp. Fluids* **19**, 1–15 (1995).
- ⁸⁸V. Viasnoff, F. Lequeux, and D. J. Pine, "Multispeckle diffusing-wave spectroscopy: A tool to study slow relaxation and time-dependent dynamics," *Rev. Sci. Instrum.* **73**, 2336–2344 (2002).
- ⁸⁹J. Rodríguez-López, L. Elvira, F. Montero de Espinosa Freijo, and J. de Vicente, "Using ultrasounds for the estimation of the misalignment in plate-plate torsional rheometry," *J. Phys. D: Appl. Phys.* **46**, 205301 (2013).
- ⁹⁰E. Gutierrez and A. Groisman, "Measurements of elastic moduli of silicone gel substrates with a microfluidic device," *PLoS One* **6**, e25534 (2011).
- ⁹¹E. Michel, M. Filali, R. Aznar, G. Porte, and J. Appell, "Percolation in a model transient network: Rheology and dynamic light scattering," *Langmuir* **16**, 8702–8711 (2000).
- ⁹²A. Duri, H. Bissig, V. Trappe, and L. Cipelletti, "Time-resolved-correlation measurements of temporally heterogeneous dynamics," *Phys. Rev. E* **72**, 051401-1–051401-17 (2005).
- ⁹³S. Aime and L. Cipelletti "Probing shear-induced rearrangements in Fourier Space. I. Dynamic Light Scattering" (unpublished).
- ⁹⁴A. Philippe, S. Aime, V. Roger, R. Jelinek, G. Prvot, L. Berthier, and L. Cipelletti, "An efficient scheme for sampling fast dynamics at a low average data acquisition rate," *J. Phys.: Condens. Matter* **28**, 075201 (2016).

Scattering signal from shear-induced nonaffine deformations

Contents

- 1 Introduction
 - 2 Materials and methods
 - 3 DLS for a sheared sample
 - 4 Conclusions
-

Dynamic light scattering (DLS) is a very powerful technique, but its application to materials under shear is not trivial. In a first step we show a theoretical, numerical and experimental investigation of how DLS may be used as a tool to measure the microscopic dynamics in soft systems under shear. This study, presented in this chapter in the form of a paper that will be submitted shortly, allows to identify the crucial parameters that have to be tuned in order to enhance the sensitivity to nonaffine deformations. As a first example, the data analysis protocol developed in this study was applied to the deformation of a weakly crosslinked elastomer, and revealed the presence of reversible nonaffine deformations in the linear regime, stemming from the spatial heterogeneity of the elastic network.

Probing shear-induced rearrangements in Fourier Space. I. Dynamic Light Scattering

S. Aime,^{*a} and L. Cipelletti^a

Understanding the microscopic origin of the rheological behavior of soft matter is a long-lasting endeavour. While early efforts concentrated mainly on the relationship between rheology and structure, current research focuses on the role of microscopic dynamics. We present in two companion papers a thorough discussion of how Fourier space-based methods may be coupled to rheology to shed light on the relationship between the microscopic dynamics and the mechanical response of soft systems. In this first companion paper, we report a theoretical, numerical and experimental investigation of dynamic light scattering coupled to rheology. While in ideal solids and simple viscous fluids the displacement field under a shear deformation is purely affine, additional non-affine displacements arise in many situations of great interest, for example in elastically heterogeneous materials or due to plastic rearrangements. We show how affine and non-affine displacements can be separately resolved by dynamic light scattering, and discuss in detail the effect of several non-idealities in typical experiments.

1 Introduction

Soft matter systems are significantly deformed or even flown by applying modest forces, corresponding to stresses comparable to those due to thermal fluctuations. Consequently, the rheological behavior of soft systems is of great fundamental interest and of paramount importance in technological applications. This makes soft matter rheology the object of a sustained research effort, both in academia and in industry¹. One of the key questions actively investigated concerns the interplay between the rheological properties of soft systems and their microscopic structure and dynamics. Indeed, structure and dynamics determine the microscopic relaxation processes responsible for the macroscopic mechanical properties of a system and are in turn profoundly modified by externally imposed stresses, e.g. in shear alignment or in shear thinning and thickening.

The interplay between rheology and the microscopic structure and dynamics is currently studied intensively by numerical simulations, as well as experimentally. Separate experiments probing rheological properties on one hand and the microscopic structure and dynamics on the other hand are certainly informative and do provide valuable insight, especially in the linear regime and for stationary, non-thixotropic samples. However, simultaneous mechanical and microscopic measurements are highly desirable, in particular when probing the non-linear regime, where both the rheological response and the microscopic behavior are typically non-stationary and often exhibit sample-to-sample or even run-to-run strong fluctuations, e.g. in the onset of shear bands² or in plastic rearrangements with complex spatio-temporal patterns^{3,4}. Opti-

cal and confocal microscopy are now used by several groups to investigate the sample evolution at the single particle scale, in conjunction with rheology, either by coupling a (confocal) microscope to a commercial rheometer^{5,6} or by using a dedicated shear cell⁷⁻¹⁰. Microscopy methods allow the tracking of individual particles, thus providing one with the most complete microscopic information. However, microscopy comes with some limitations: typically, particle-based samples are required, and the particle size has to be larger than about $0.5 \mu\text{m}$; particles must be fluorescently labelled for confocal microscopy and tracking their position to better than about $0.1 \mu\text{m}$ requires special care and intensive image processing¹¹. Even more importantly, a high spatial resolution, a large field of view, and a high acquisition rate are conflicting requirements, so that one cannot resolve minute displacements with good time resolution while imaging a large portion of the sample. Fourier space techniques, and in particular scattering methods, are an attractive alternative to real-space measurements: although no information can be obtained on individual particles, scattering techniques allow a large sample volume to be probed, with no particular constraint on the temporal resolution. Moreover, particles in a wide range of sizes, from a few nm up to several microns, can be easily studied, as well as polymer- or surfactant-based systems. In this paper, we shall focus on scattering methods. In a companion paper¹² we will discuss Differential Dynamic Microscopy^{13,14} (DDM) coupled to rheology. While DDM is based on microscopy, the data analysis is performed in Fourier space, using a formalism close to that of scattering techniques.

Historically, scattering methods coupled to rheology have been first used to investigate the sample structure¹⁵⁻¹⁷, but since the Nineties of the last century, dynamic scattering methods have become increasingly popular as a powerful tool to

^a L2C, University of Montpellier, CNRS, Montpellier, France. E-mail: stefano.aime@umontpellier.fr

probe the microscopic dynamics of mechanically driven soft systems^{18–20}. Most experiments have been performed in the highly multiple scattering limit for visible light (Diffusing Wave Spectroscopy, DWS²¹), thanks to the simplicity of the required optical layout and the high sensitivity of the method, which can detect motion on length scales as small as a fraction of a nm. A few experiments have been performed in the single scattering limit, typically (but not exclusively²²) in a small-angle configuration where several scattering angles can be probed at the same time, using both visible light²³ (Dynamic Light Scattering, DLS²⁴) and coherent X-ray radiation²⁵ (X-photon correlation spectroscopy, XPCS²⁶).

Most scattering experiments have been performed simultaneously to oscillatory rheology, using the so-called echo method^{20,25,27,28}, where the evolution of the sample microscopic configuration is measured stroboscopically, by comparing the pattern of the scattered intensity at each cycle, e.g. when the deformation is zero. This protocol allows the irreversible rearrangements to be highlighted and avoids the complications arising when affine and non-affine displacements are to be separately quantified. To address this key point, let us consider the geometry that we shall discuss in this paper, e.g. a plane-plane cell imposing a linear shear deformation, with the unit vectors $(\hat{u}_x, \hat{u}_y, \hat{u}_z)$ pointing in the shear velocity, shear vorticity and shear gradient directions, respectively. For both an ideal solid and a purely viscous fluid, the displacement field is affine:

$$\Delta \mathbf{r}(\mathbf{r}, \gamma) = \Delta \mathbf{r}^{(\text{aff})}(\mathbf{r}, \gamma) = (\mathbf{r} \cdot \hat{u}_z) \gamma \hat{u}_x, \quad (1)$$

where e is the cell gap and $\gamma = \delta/e$ the shear deformation imposed by displacing the $z = e$ plane by an amount δ in the \hat{u}_x direction. Non-affine displacements may arise as a consequence of heterogeneous elastic response^{29,30}, or as a result of non-linearities³¹, or due to plastic rearrangements²⁷. They represent additional motion, typically not restricted to the direction of the imposed deformation, on top of the affine deformation field. Clearly, being able to discriminate between affine and non-affine dynamics is mandatory in order to fully characterize the complex interplay between rheology and microscopic dynamics, beyond the idealized case of Eq. 1.

In DWS, the microscopic dynamics is quantified by measuring the change of phase of photons undergoing many scattering events in the sample. Since photons propagate following an isotropic, random walk-like path²¹, they probe microscopic displacements along all directions. Hence, DWS is sensitive both to affine and non-affine displacements. For a given macroscopic deformation, it is possible to calculate theoretically the contribution of affine motion to the DWS signal^{32,33}. Any deviations from this behavior can then be ascribed to non-affine displacements. In practice, however, this approach is difficult to implement, because the approximations required to perform the calculation are not fully met in experiments^{33,34},

and because non-affine motion is typically small in comparison to the affine component. Diffusing Wave Spectroscopy is thus generally restricted to the case where the affine displacements vanish, as in the echo protocol or in stress relaxation tests³⁵, where a sample under load is kept at a fixed deformation.

Single scattering, by contrast, probes the dynamics along a well-defined direction, controlled by the experimental geometry. It is therefore possible to selectively probe motion along any of the $(\hat{u}_x, \hat{u}_y, \hat{u}_z)$ directions, thereby allowing affine and non-affine dynamics to be discriminated. This paves the way to measurements of the microscopic dynamics in a wide variety of rheological tests, including steady shear rate or creep tests, currently extensively used to understand the yield transition of amorphous soft solids^{36,37}, or oscillatory tests beyond the echo protocol, where surprising effects such as ‘reversible plasticity’ may be unveiled by inspecting the dynamics throughout the whole oscillation cycle^{38,39}. As we shall show it in the following, the ability of single scattering to resolve motion along one single direction (e.g. along the vorticity direction \hat{u}_y) relies on several assumptions: the sample must be illuminated by an infinitely extended plane wave, the collection optics must be aberration-free, and the size of the detector along the direction orthogonal to the one selected (e.g. along the shear direction \hat{u}_x) must be vanishingly small. Clearly, these conditions cannot be strictly met in experiments.

In this paper, we derive analytical expressions that quantify the decay of correlation functions measured in DLS as a result of both affine and non-affine displacements, taking into account the effect of non-ideal experimental conditions. We provide guidelines for mitigating or correcting for the contributions to the correlation functions arising from non-ideal conditions and successfully test our predictions against experiments and numerical simulations. Although we will focus on simple shear coupled to a small-angle DLS setup, the results presented here are general and can be easily adapted to different experimental layouts, e.g. to a backscattering geometry. The rest of the paper is organized as follows: in Sec. 2 we briefly introduce the samples used for the tests, the DLS apparatus, the shear cell, and the simulation methods. In Sec. 3 we develop a theoretical model of DLS under shear, starting from a discussion of the effect of a simple translation of the sample, and then presenting results for a purely affine deformation and the general case with both affine and non-affine microscopic dynamics. At each step, we show experimental and numerical data that validate our theoretical approach. We recapitulate our main findings and make some concluding remarks in Sec. 4. For the reader’s convenience, Appendix 1 lists all the symbols used in the paper, whereas Appendix 2 contains a more detailed derivation of the analytical results presented in the text.

2 Materials and methods

2.1 Samples

For studying the effect of a pure sample translation, quasi-2D random scatterers were prepared by sandblasting microscope glass slides (sandblaster Otelo OTMT with aluminium oxide particles of diameter $30 \mu\text{m}$). A commercial linear stage (Linear Stage UMR8.25A, by Newport) coupled to a stepper motor (Newport Precision Motorized Actuator LTA-HS) with a nominal precision of $1 \mu\text{m}$ was used to impose a controlled displacement in the \hat{u}_x direction. The actual displacement was measured to within an accuracy of about 60 nm using the speckle imaging technique described in^{40,41}.

As a model sample for investigating 3D shear, we prepared polyacrylamide (PA) gels by polymerizing acrylamide monomers and (bis)acrylamide cross-linkers, using a free-radical polymerization reaction as described in⁴². TiO_2 nanoparticles were added to the monomer solution at a concentration of around 0.01% . The particle diameter is $0.3 \mu\text{m}$ (resp., $0.5 \mu\text{m}$) for the scattering experiments (resp., for microscopy observations, see below). In order to thoroughly disperse the TiO_2 particles, the solution was sonicated for roughly 2h and then filtered before adding the initiators.

2.2 Shear cell

For measurements under shear, the home-made plane-plane shear cell described in²³ was used. The cell consists of two glass plates confining the sample in a gap ranging from $e = 300 \mu\text{m}$ to $e = 1500 \mu\text{m}$. To reduce slip, the inner surfaces of the glass plates are frosted, leaving a small transparent window (of surface a few mm^2) in order to optically probe the sample during deformation. The deformation was imposed and measured as for the 2D samples. The typical accuracy on the strain measurement is of the order of 0.01% .

2.3 Small-angle DLS apparatus

Dynamic light scattering experiments are performed using the custom-made apparatus described in⁴³, allowing simultaneous measurements at scattering angles in the range $0.4 \text{ deg} \leq \theta \leq 25 \text{ deg}$, corresponding to scattering vectors $q = 2k \sin \theta / 2$ in the range $0.1 \mu\text{m}^{-1} \leq q \leq 5 \mu\text{m}^{-1}$, where $k = 2\pi n \lambda^{-1}$ is the wave vector of the incoming beam, with n the refractive index of the solvent and $\lambda = 0.633 \mu\text{m}$ the in-vacuo wave length of the laser source. A simplified scheme of the DLS apparatus is shown in Fig. 1a). The setup uses the typical far-field configuration, where the detector (the 2D sensor of a CMOS camera) is placed in the focal plane of a lens collecting the light scattered by the sample, often termed the Fourier lens. In this configuration, light scattered at the same θ and the same azimuthal angle (with respect to the direction \hat{u}_z of the incoming

beam) is conveyed to a single point on the detector, irrespective of the location of the scatterers in the sample. The incident beam has a Gaussian shape, with a $1/e^2$ radius $w = 0.45 \text{ mm}$ at the sample position, and radius $w_0 = 0.444 \text{ mm}$ in the beam waist, where the radius is minimal⁴⁴. The focal length of the Fourier lens is $f = 17.3 \text{ mm}$.

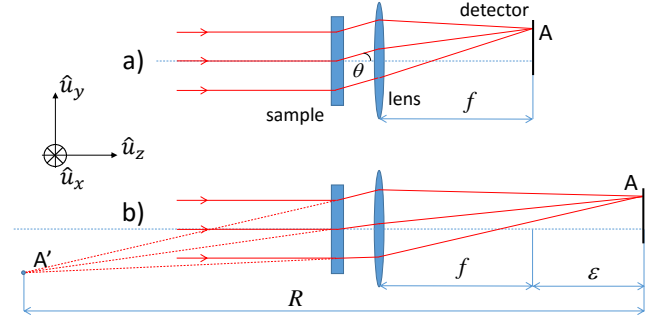


Fig. 1 a): simplified scheme of the light scattering setup. The detector is placed in the focal plane of the Fourier lens. b): scheme used in the discussion of the effect of aberrations. A and A' are conjugated points, separated by a distance R along the direction of the optical axis. The distance ϵ has been exaggerated for the sake of clarity, usually $\epsilon \ll f$.

The images collected by the detector have a distinctive grainy appearance, with dark and bright spots termed speckles, arising from the interference of the photons scattered by the sample⁴⁵. In order to extract information on the dynamics, we quantify the temporal fluctuations of the speckles by calculating the degree of correlation between a pair of images taken at time t and $t + \tau$ ^{24,46}:

$$g_2(\mathbf{q}, t, \tau) - 1 = \frac{\langle I_p(t) I_p(t + \tau) \rangle_{p \in \text{ROI}(\mathbf{q})}}{\langle I_p(t) \rangle_{p \in \text{ROI}(\mathbf{q})} \langle I_p(t + \tau) \rangle_{p \in \text{ROI}(\mathbf{q})}} - 1. \quad (2)$$

Here, $I_p(t)$ is the intensity at time t of the p -th pixel and the average is over a set of pixels or region of interest (ROI) corresponding to a well-defined \mathbf{q} vector. For the optical layout sketched in Fig. 1 and $\mathbf{q} = q_x \hat{u}_x$ (respectively, $\mathbf{q} = q_y \hat{u}_y$), the ROI is centered around the position $(f \tan \theta \hat{u}_x, 0)$ (respectively, around the position $(0, f \tan \theta \hat{u}_y)$, see Ref.⁴³ for more details.

Throughout this paper, the loss of correlation will be due exclusively to the imposed shear deformation or sample translation: the temporal variable τ in Eq. 2 will be then replaced by γ or δ , respectively. The intensity correlation function is related to the field correlation function by the Siegert relation²⁴, which for the case, e.g., of a sheared 3D sample reads:

$$g_2(\mathbf{q}, \gamma) - 1 = |g_1(\mathbf{q}, \gamma)|^2 \propto |\langle \mathbf{E}_S(\mathbf{q}, 0) \cdot \mathbf{E}_S^*(\mathbf{q}, \gamma) \rangle|^2, \quad (3)$$

where the (complex) scattered electric field is given by

$$\mathbf{E}_S(\mathbf{q}, \gamma) \propto \sum_{j=1}^N \mathbf{E}_{in}(\mathbf{r}_j(\gamma)) e^{-i\mathbf{q} \cdot \mathbf{r}_j(\gamma)}, \quad (4)$$

with \mathbf{r}_j the (γ - or δ -dependent) coordinates of the j -th particle and where the sum runs over N scatterers. In writing Eq. 4, we have assumed with no loss of generality that all particles are identical and we have neglected any q dependence of the scattering from an individual particle, i.e. we have set to unity the form factor²⁴. Note that in contrast to the usual expression of \mathbf{E}_S we have included the possibility that the incoming electric field \mathbf{E}_{in} varies spatially (both in phase and amplitude), to account for deviations with respect to illumination by a perfect, infinitely extended plane wave.

2.4 Numerical simulations

Numerical simulations of the scattering signal associated to a given sample deformation were performed by generating a 3D random set of scatterers with the same size as the experimental sample and by propagating the scattered field from the sample to the detector plane, where \mathbf{E}_S is obtained from Eq. 4. For each pixel location, the scattered intensity is then calculated as $|\mathbf{E}_S|^2$; the simulated speckle patterns are then analyzed as the experimental ones, i.e. using Eq. 2. For the experimental data to be easily compared to theory and simulations, all correlation functions were normalized such that $g_2(\mathbf{q}, 0) - 1 = 1$.

2.5 Measurements of non-affine displacements by optical microscopy

For checking purposes, non-affine displacements of the TiO₂ tracer particles in the PA gels were also measured in real space by coupling the shear cell to a bright field microscope, whose condenser diaphragm was fully open in order to reduce the depth of focus. The in-plane non-affine displacements were measured for different depths z and averaged over all particles. We use a custom python code built from the Trackpy Python package⁴⁷ to track the colloidal particles. The non-affine displacements measured by microscopy are compared to those obtained by DLS. Additionally, they are used to obtain a reference value for numerical simulations, where non-affinity is introduced by adding to the affine displacement field a random, isotropic and Gaussian-distributed extra-contribution, in such a way that the resulting rms displacement matches the one measured by microscopy.

3 Dynamic Light Scattering for a sheared sample

Equation 4 shows that all scatterers contribute to the signal detected in a DLS experiment via phase terms: this is what

makes DLS such a powerful and sensitive technique to probe the sample dynamics. Indeed, every change in the \mathbf{r}_j coordinates has an impact on the scattered field, and thus on the correlation function, Eq. 2. Under a shear deformation, the affine displacement field produces a loss of correlation that can be calculated from Eq. 3 and the Siegert relation. In the presence of non-affine displacements, the particles' displacement contains an additional term: $\Delta \mathbf{r}_j = \Delta \mathbf{r}_j^{(aff)} + \mathbf{R}'_j$. The non-affine contribution \mathbf{R}' results in a different, generally faster decay of $g_2 - 1$, as compared to the case of a purely affine deformation. In this section we will show how to decouple the two contributions, by quantifying the average non-affine displacement and 'filtering out' the decorrelation due to the affine deformation.

To this end, it is useful to proceed by steps. Equation 1 indicates that a 3D sample deformed affinely may be modeled by a set of Σ_z planes perpendicular to the optical axis, rigidly translating by a z -dependent amount $\delta_z = \gamma z \hat{u}_x$. The decay of $g_2 - 1$ will then contain a first contribution due to the rigid translation of each plane, plus a second contribution arising from the relative motion of different Σ_z slices. We will thus start by considering the simple case of a 2D sample that rigidly translates along the x axis, discussing all the factors that contribute to the loss of correlation (Sec.3.1). We will then address the more complicated situation of a 3D sample composed of a stack of Σ_z slices (Sec. 3.2). Finally, in Sec. 3.3 we will discuss the general case of both affine and non-affine displacements.

3.1 Rigid translation of a 2D sample

We model a 2D sample by a set of scatterers with positions \mathbf{r}_j such that $\mathbf{r}_j \cdot \hat{u}_z = z = const$ and refer to it as to a Σ_z plane. We consider the case of a rigid translation $\delta = \gamma z \hat{u}_x$ of such plane. If the incident beam was an ideal plane wave, infinitely extended in the \hat{u}_x, \hat{u}_y directions perpendicular to the propagation direction, the term \mathbf{E}_{in} in Eq. 4 would be space-independent and could be factored out of the sum. It is then easy to show that the intensity correlation function $g_2 - 1$ would be invariant under a sample translation, since the total electric field would change only by a phase factor $\exp(-i\mathbf{q} \cdot \delta)$ as the sample drifts. This is why DLS is commonly regarded as a technique sensitive to the relative motion of the scatterers, not to their global drift. However, ideal plane wave conditions cannot be fully met in experiments: the incoming beam has a finite cross section, often with a radial intensity modulation, e.g. a Gaussian profile. In this section we thus discuss the decorrelation expected for rigid translations under a non-uniform incident electric field.

Intuitively, it is clear that translations larger than the beam size lead to the full decay of g_2 , since they completely change the set of illuminated scatterers. Even when the sample is translated by an amount smaller than the scattering volume diameter, some loss of correlation is expected if the sample

illumination is not uniform: as the sample is translated, each scatterer receives a varying illuminating field, which will modify the relative weight of the terms in the sum of Eq. 4 and thus the scattered intensity. To quantify this effect, we consider the realistic case of a Gaussian laser beam propagating along the z axis in the paraxial approximation⁴⁸:

$$\mathbf{E}_{in}(r, z) = \mathbf{E}_0 \frac{w_0}{w(z)} e^{ikz} e^{-\frac{r^2}{w^2(z)}} e^{ik \frac{r^2}{2\rho(z)}} \quad (5)$$

where (r, z) are radial and axial cylindrical coordinates along the optical axis, $w(z) = w_0 \sqrt{1 + (z/a)^2}$ is the beam $1/e^2$ radius and $\rho(z) = z[1 + (a/z)^2]$ is the radius of curvature of the wavefront, as a function of the position z along the optical axis. Here $a = \frac{1}{2}kw_0^2$ is the depth of the Rayleigh region, i.e. the region centered around $z = 0$ where the laser beam can be considered approximatively plane and collimated.

Using this expression in Eqs. 4 and 3, the intensity correlation function is found to be:

$$g_2(\mathbf{q}, \boldsymbol{\delta}) - 1 = e^{-\frac{|\boldsymbol{\delta}|^2}{w^2} \left[1 + \left(\frac{k w^2}{2\rho} \right)^2 \right]} = e^{-\frac{|\boldsymbol{\delta}|^2}{w_0^2}} \quad (6)$$

with $\boldsymbol{\delta}$ the translation vector, along the x axis. As anticipated, the intensity pattern decorrelates significantly when the 2D object translation is comparable to the beam size. Interestingly, Eq. 6 shows that the relevant length scale is w_0 , the beam size at the beam waist ($z = 0$), regardless of the actual z position of the sample. This is because the increase of the beam size $w(z)$ and the decrease of the radius of curvature $\rho(z)$ as the sample departs from the beam waist exactly compensate each other, leading to the simple expression in the far r.h.s. of Eq. 6.

According to Eq. 6, the decay of $g_2 - 1$ should not depend on the scattering vector. However, Fig. 2 shows that the experimental correlation functions decay increasingly rapidly at large q . We now show that this q -dependence is due to the optical aberrations and deviations from the paraxial approximation, which become increasingly important at large q . As far as speckle decorrelation is concerned, the most relevant effect is the fact that the focal surface is curved and not planar, as in the paraxial, aberrations-free approximation. Thus, it is impossible that all points of a flat detector lay in the focal surface. The situation is schematized in Fig. 1b), where ε is the offset along the \hat{u}_z direction of the detector point A, with respect to the focal surface. Figure 1b) shows that under these conditions the point A collects light issued by the whole illuminated sample, but with a scattering angle that slightly depends on the scatterer position. The scattered light collected in A appears to originate from a point A' located before the sample and conjugated to A by the Fourier lens. The z component of the distance AA', denoted by R , plays a key role in the following. Asakura and Takai⁴⁹ have studied mixed spatio-temporal intensity correlation functions describing the

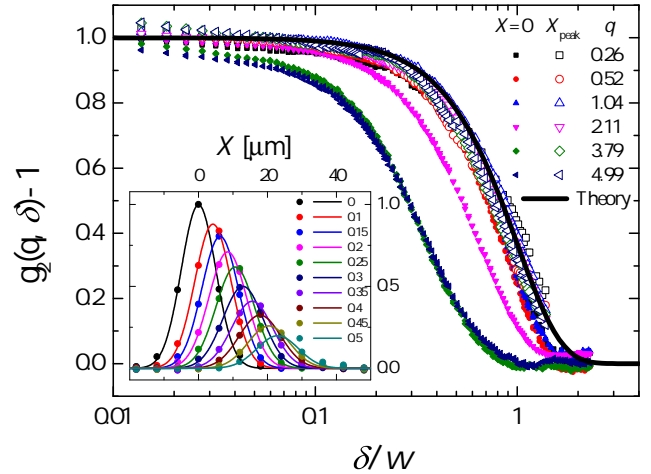


Fig. 2 Main plot: decay of the intensity correlation function due to the rigid translation of a quasi-2D object, measured at different scattering vectors q , as indicated by the label (units: μm^{-1}). Filled symbols: usual $g_2 - 1$, calculated pixel-by-pixel following Eq. 2. Open symbols: correlation function as obtained from the height of the peak in the spatio-temporal crosscorrelation, see text for details. Black line: Eq. 7 evaluated for $\mathbf{X} = \mathbf{X}_{peak} = \sigma\boldsymbol{\delta}$. Inset: cut of the intensity spatio-temporal crosscorrelation, Eq. 7, along the translation direction \hat{u}_x , plotted for different values of δ , as indicated by the legend (in mm), and for $q = 3.79 \mu\text{m}^{-1}$. Symbols: experimental data; lines: fits via Eq. 7.

evolution of the speckle pattern generated by a translating object placed at an arbitrary distance from the detector. Their key result was that a sample translation results in general in a combination of a translation of the speckle pattern and random fluctuations of the speckle intensity ('boiling'). We thus expect both contributes to exist in our experiment, unlike the ideal case of a detector placed exactly in the focal surface and a sample in the beam waist, for which the speckle pattern is reconfigured with no overall drift.

We adapt the results of Ref.⁴⁹ to the geometry described here, and define a spatio-temporal intensity crosscorrelation $g_2(\mathbf{X}, \boldsymbol{\delta}) - 1 \propto |\langle \mathbf{E}_S(\mathbf{r}, 0) \cdot \mathbf{E}_S^*(\mathbf{r} + \mathbf{X}, \boldsymbol{\delta}) \rangle|^2$, where \mathbf{r} and \mathbf{X} are vectors in the sensor plane. For a translating sample illuminated by a Gaussian beam (Eq. 5), one finds:

$$g_2(\mathbf{X}, \boldsymbol{\delta}) - 1 = e^{-\frac{|\boldsymbol{\delta}|^2}{w^2}} e^{-\frac{|\mathbf{X} - \sigma\boldsymbol{\delta}|^2}{\Delta^2}} \quad (7)$$

where $\Delta = R/(kw)$ is the speckle size, $\sigma = 1 + R/\rho$, and \mathbf{X} the relative position of two points on the sensor whose intensity is crosscorrelated. For $\mathbf{X} = 0$, Eq. 7 reduces to the standard pixel-by-pixel intensity correlation function, Eq. 3. In this case, one retrieves $g_2 - 1 = \exp(-\delta^2/l^2)$, similarly to Eq. 6, but with a faster decay, since w_0 is replaced by a shorter

characteristic length l given by

$$\frac{1}{l^2} = \frac{1}{w^2} + \frac{\sigma^2}{\Delta^2} = \frac{1}{w_0^2} \left\{ 1 + \left(\frac{a}{R}\right)^2 \left[1 + \left(\frac{z}{a}\right)^2 \right] \left(1 + \frac{2R}{\rho} \right) \right\} \quad (8)$$

The ideal case of far field scattering (achieved when the detector images the focal surface of the Fourier lens) corresponds to the $R \rightarrow \infty$ limit, where we retrieve as a characteristic length $l = w_0$, as in Eq. 6. On the other hand, a non-vanishing deviation ε of the detector position with respect to the focal surface can be described in terms of a finite value $R(\varepsilon) \approx f^2/\varepsilon$, which results in a faster decorrelation. Both optical aberrations (embedded in σ , via R) and wavefront curvature (embedded again in σ , via ρ) tend to enhance the system sensitivity to rigid translations, which is not desired if one aims to detect non-affine rearrangements. Moreover, equation 7 suggests that both effects have the same physical nature: as a consequence of either one, a collective drift motion superimposes to the normal, ‘boiling’ decorrelation of the speckle pattern. Indeed, when ρ or R assume finite values, it is easy to see from Eq. 7 that the maximum correlation is achieved for a non-null \mathbf{X} value, which reflects the presence of a global drift that adds up to the ‘boiling’ decorrelation (see inset of Fig. 2). To correct the data for this effect, one can follow the collective speckle translation by tracking the position $\mathbf{X}_{peak} = \sigma \delta$ of the crosscorrelation peak. The drift-corrected value of $g_2 - 1$ is then taken as the height of the peak, i.e. the value of the spatio-temporal crosscorrelation for $\mathbf{X} = \mathbf{X}_{peak}$. Following this strategy, one finds that the corrected $g_2 - 1$ decays with the sample drift as

$$g_2(\mathbf{X}_{peak}, \delta) - 1 = \exp(-\delta^2/w^2). \quad (9)$$

The open symbols in the main graph of Fig. 2 show the drift-corrected intensity correlation function: in contrast to the usual pixel-by-pixel correlation function (solid symbols), the decay of $g_2 - 1$ with sample displacement δ is q -independent and very well accounted for by Eq. 7 (line).

To summarize, in this section we have shown that the finite size of the beam, the curvature of the wavefront impinging on the sample, and optical aberrations all contribute to the decay of the intensity correlation function upon translating a 2D sample. When correcting for the speckle drift, there is no q dependence in these effects. Finally, the decay of the correlation function is negligible for $\delta \ll w$, i.e. when the sample translation is (much) smaller than the beam size.

3.2 Affine deformation of a 3D sample

The case of a 3D object undergoing an affine deformation can be treated by decomposing the sample in slices, each of which translates by a z -dependent amount. The decay of $g_2 - 1$ contains a first contribution due to the rigid translation of each

slice, as well as a second contribution arising from the relative motion of scatterers belonging to distinct slices. In the ideal case where an infinite plane wave illuminates the sample and the detector is in the focal plane, the first contribution does not lead to a loss of correlation, while the second one is readily computed (see Appendix 2 for details). One finds

$$g_2(\mathbf{q}, \gamma) - 1 = \text{sinc}^2\left(q_x \gamma \frac{e}{2}\right) \quad (10)$$

where $q_x = \mathbf{q} \cdot \hat{u}_x$ is the component of the scattering vector parallel to the shear direction and $\text{sinc}(x) = x^{-1} \sin(x)$. Equation 10 illustrates the ability of DLS to selectively measure affine or non-affine displacements, as mentioned in Sec. 1. Indeed, if the azimuthal orientation of the scattering vector is chosen such that $q_x = 0$, $g_2 - 1$ is insensitive to affine displacements. Any decay of the correlation function that may be observed is then to be ascribed to non-affine dynamics. The scheme of Fig. 1a) illustrates a geometry where the scattering vector is orthogonal to the shear direction: the scattered rays belong to the (y, z) plane and hence $q_x = 0$ (we remind that $\mathbf{q} = \mathbf{k}_{sc} - \mathbf{k}_{in}$, with \mathbf{k}_{in} and \mathbf{k}_{sc} the wave vector of the incident and scattered light, respectively). Note that the loss of correlation depends on the variable γe , i.e. the relative displacement of the two plates confining the sample. Thus, for a given γ , thinner samples exhibit a smaller loss of correlation.

When the finite beam size and wavefront curvature are taken into account, the expression for $g_2 - 1$ or, equivalently, for $g_1 = \sqrt{g_2 - 1}$, become more complicated, but remains independent of q_y . In Appendix 2 we provide an expression for g_1 for a sample in the waist of a Gaussian beam (see Eq. 15 in Appendix 2). The thin sample ($e \ll w$) and high- q_x ($q_x \gg \frac{e}{\gamma w^2}$) limits of this expression reduce to the simpler Eq. 10. We test these expressions for a scattering vector parallel to the shear direction in Fig. 3. The inset shows $g_2 - 1$ as a function of the imposed shear deformation γ , for simulations (large symbols) and for one experimental run on a PA gel (small black dots). The lines are the result of the numerical integration of Eq. 15 in Appendix 2: an excellent agreement is observed between theory and simulations. The main plot shows the same data, plotted vs the scaled variable $q_x \gamma e / 2$. The experimental data and the simulations for $e \leq 200 \mu\text{m}$ fall onto a single master curve, well reproduced by the simple form of Eq. 10 (line). Additional experimental data for several scattering vectors in the range $0.1 \mu\text{m}^{-1} < q_x < 4 \mu\text{m}^{-1}$ also fall onto the same master curve (data not shown to avoid overcrowding the plot). Since here $w = 450 \mu\text{m}$, this indicates that the thin sample expression mathematically derived for $e \ll w$ actually remains valid up to the somehow more relaxed regime $e \lesssim w$. For $e > w$, by contrast, $g_2 - 1$ significantly departs from Eq. 10 and the numerical integration of the full expression, Eq. 15, is required to account for the simulations.

A key point that has to be taken into account in realistic

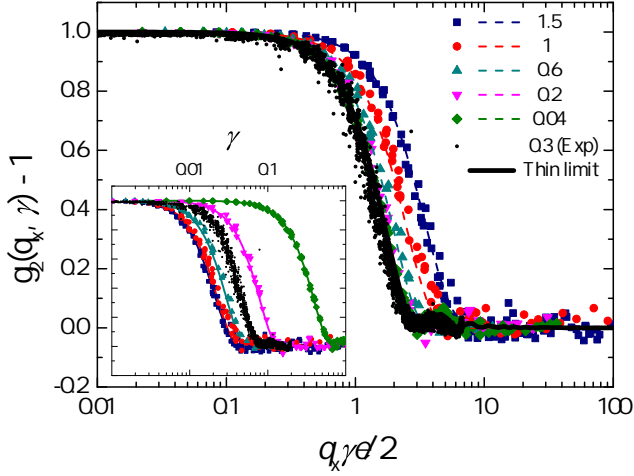


Fig. 3 Inset: $g_2 - 1$ for a 3D sample, as a function of the imposed shear deformation, in the $q_x \gg \frac{e}{\gamma w^2}$ limit, for $q_x = 1.04 \mu\text{m}^{-1}$. Large colored symbols: numerical simulations for sample thickness from 0.04 mm to 1.5 mm, as shown by the label of the main plot. Lines: numerical integration of Eq. 15. Black dots: experimental data for $e = 0.3$ mm. Main plot: same data plotted as a function of the scaled variable $q_x \gamma^2$. Black line: theoretical curve in the $e \ll w$ limit, Eq. 10. The beam size used in simulations is $w = 450 \mu\text{m}$, the same as in experiments. For $e < w$ both experimental data and simulations follow Eq. 10, whereas deviations are observed for thicker samples, in good agreement with theoretical expectations.

simulations and in experiments is the finite size of the ROIs over which the intensity correlation function is averaged (see Eq. 2). Since the ROIs must contain a sizeable number of speckles in order to achieve a good statistics, it is impossible to measure $g_2 - 1$ for a q vector exclusively oriented in the \hat{u}_y direction: any viable ROI will correspond to a range of q vectors with a finite x component. This potentially limits the feasibility of the strategy outlined above for measuring non-affine displacements, which in principle requires to acquire $g_2 - 1$ for a q vector with no component along the shear direction \hat{u}_x .

To explore this issue, we show in Fig. 4 correlation functions obtained from simulations, where the data have been analyzed using a ROI corresponding to q_y in the range $0.1 - 10 \mu\text{m}^{-1}$ and various q_x , expressed here in terms of the ROI size along \hat{u}_x , in pixels (1 pixel corresponds indicatively to $5 \times 10^{-3} \mu\text{m}^{-1}$). The results are independent of q_y : we thus show data averaged over all q_y . The curve for the thinnest ROI (5 pixel along \hat{u}_x) is almost flat up to $\gamma \approx 1$. This demonstrates that under realistic conditions one can indeed measure a correlation function that is sensitive essentially only to non-affine displacements, up to a shear deformation of order one. This comes however at the expenses of statistics: since the ROI is relatively small, large fluctuations are seen in the data,

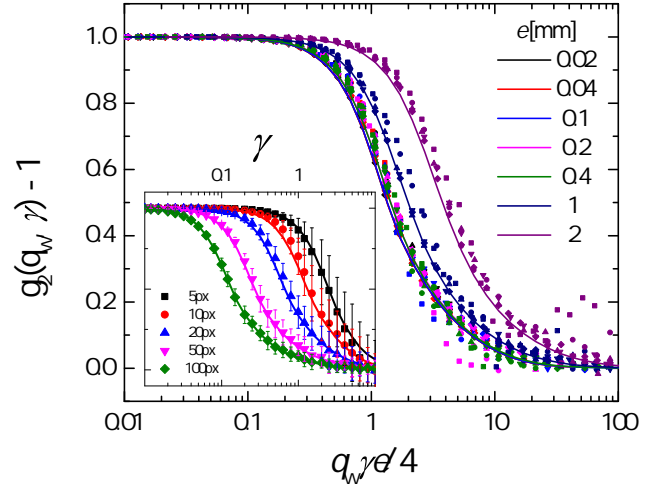


Fig. 4 Inset: effect of the finite q_x component of the scattering vectors associated to the ROI chosen for calculating $g_2 - 1$. Symbols: simulations for a purely affine deformation of a 3D sample. Lines: numerical integration of Eq. 15 over the relevant q_x range, indicated in the legend, in units of pixels. In all cases, the gap is $e = 200 \mu\text{m}$. Main plot: Effect of the finite size of the ROI, for several sample thicknesses, as specified in the legend. Different symbols refer to various ROI sizes: 5 px (squares), 10 px (circles), 20 px (triangles), 50 px (down triangles), 100 px (diamonds). See the text for the definition of q_w , the ROI half width in Fourier space.

as shown by the error bars, which quantify the standard deviation of $g_2 - 1$ over 20 independent runs. As the size of the ROI along \hat{u}_x is increased, the statistics improves significantly, but $g_2 - 1$ start decaying at smaller strains. The lines are theoretical expectations obtained by numerically averaging Eq. 15 over the range of q_x associated to the ROI. They are in excellent agreement with the simulations, indicating that the simple theory developed here can be used to quantitatively predict the impact of the ROI width, thereby providing valuable guidance for the optimization of the analysis parameters.

Based on Eq. 15, one expects that the impact of the ROI width on $g_2 - 1$ varies also with the sample thickness e . The main plot of Fig. 4 rationalizes the dependence on e , showing that data for different widths and a given cell gap fall onto the same master curve, provided that $g_2 - 1$ is plotted against a scaled shear deformation, $q_w \gamma e / 4$. Here, q_w quantifies the width of the ROIs, which extend from $-q_w$ to q_w in the \hat{u}_x direction. The shape of these master curves depend on e ; remarkably, they collapse on top of each other in the thin sample limit. Again, a very good agreement is found between the correlation functions obtained by simulations and their theoretical expression (lines in the main plot of Fig. 4).

To recapitulate the main findings for DLS under a purely affine displacement field, we have shown that the intensity

correlation function decays faster (i.e. at smaller strains) for thicker samples. In the limit $e \gtrsim w$ the effects of the finite beam size are negligible. Under these conditions, correlation functions for \mathbf{q} parallel to the shear direction depend only on the scaled variable $e\gamma$. In experiments and realistic simulations, the finite x component of the scattering vectors associated to a ROI has to be taken into account, even when the ROI corresponds essentially to the direction orthogonal to the applied shear. This (albeit small) x component is responsible for the decay of $g_2 - 1$, which can be rationalized using the scaled variable $q_y e\gamma$. Finally, we emphasize that for the purely affine deformation discussed so far, the dynamics are always independent of q_y .

3.3 Probing non-affine displacements

In Fig. 3 we have shown that experimental correlation functions for a PA gel, measured at q vectors oriented parallel to the shear direction, agree well with numerical and theoretical predictions for a purely affine deformation. We now inspect data from the same experiment, but analyzed for a scattering vector oriented in the perpendicular direction \hat{u}_y . The results are shown in Fig. 5 (small solid points), together with the corresponding correlation functions obtained by theory and simulations using ROIs of the same size as in the experiment (width along $\hat{u}_x = 10$ pixels) and assuming a purely affine deformation (thick black line and small symbols connected by lines for theory and simulations, respectively). The experimental data deviate strongly from theory and simulations, both quantitatively and qualitatively: the decay of the experimental $g_2 - 1$ occurs at much smaller strains γ and depends strongly on q_y .

We attribute this discrepancy to non-affine displacements in the PA gel that were not taken into account in the simulations nor in the theory. In Sec. 1 we mentioned several mechanisms that may lead to a non-affine component of the displacement field. In the experiments, the applied strain is relatively modest, $\gamma \leq 0.3$. Rheology measurements indicate that in this regime the sample response is essentially γ -independent (see Fig. 6a)), suggesting negligible non-linear effects and plasticity. We thus propose that non-affinity stems from spatial fluctuations of the elastic shear modulus G , as reported in Ref. ³⁰ for similar PA gels. Indeed, in real samples inhomogeneities are always present at a microscopic scale; from a mechanical point of view they can be described by local fluctuations of the shear modulus: $G(\mathbf{x}) = \bar{G} + \delta G(\mathbf{x})$, with $\bar{G} = \overline{G(\mathbf{x})}$ the spatially-averaged shear modulus and $\overline{\delta G(\mathbf{x})} = 0$. Due to these fluctuations, the sample deformation locally deviates from affinity, originating a non-affine displacement field $\mathbf{R}'(\mathbf{x})$ that adds up to the affine one. Note that we expect the non-affine component to be small in comparison to the affine one, since correlation functions measured in the shear direction are well reproduced by the affine component alone (see

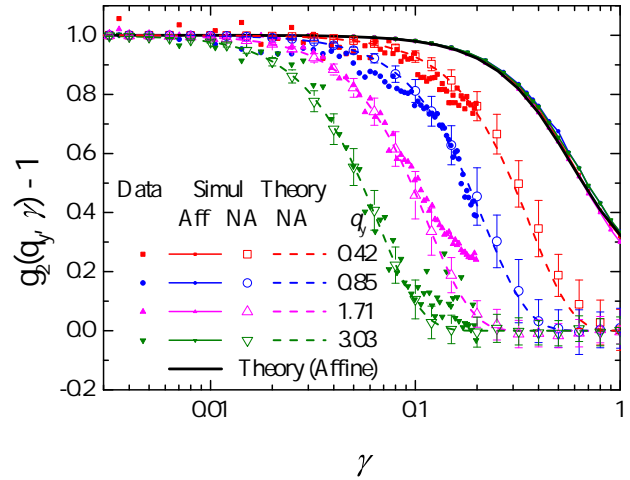


Fig. 5 Strain dependence of the intensity correlation function for a sheared PA gel. Small filled symbols: experimental data for several q_y values, as indicated by the labels (units: μm^{-1}). Thick black line: theoretical prediction for a purely affine deformation, obtained by the numerical integration of Eq. 15. Small solid symbols connected by lines: $g_2 - 1$ obtained from simulations, for a purely affine deformation. Theory and simulations deviate strongly from the experimental data, indicating that non-affine displacements must be included in the modelling. Dashed lines and large open symbols: correlation functions obtained from theory (Eq. 11) and simulations, respectively, assuming Gaussian-distributed non-affine particle displacements, with a rms value given by Eq. 11. In simulations, data are averaged over $N = 50$ independent runs and error bars represent the run-to-run standard deviation. In both theory and simulations, a generalized diffusion coefficient $c = 30 \mu\text{m}^2$ was used.

the small black dots in Fig. 3).

The non-affine displacement field may be quantified by its γ -dependent mean squared value, referred to as the non-affine parameter \mathcal{A} in Ref. ³⁰, and related to the local shear modulus fluctuations. Under reasonable assumptions^{29,30}, the non-affine parameter grows quadratically with the macroscopic deformation:

$$\mathcal{A} = \frac{1}{N} \sum_{j=1}^N |\mathbf{R}'_j|^2 = c\gamma^2, \quad (11)$$

where the rms displacement per unit squared shear deformation, c , is a generalized diffusion coefficient, by analogy to Brownian diffusion originating from thermal fluctuations, with γ^2 playing the role of time in ordinary diffusion.

In order to test whether the decay of $g_2 - 1$ observed in the experiments for q in the \hat{u}_y direction can indeed be ascribed to non-affine displacements, we measure \mathcal{A} in independent microscopy experiments, where the motion of the tracer particles is tracked while applying a shear deformation to the sample. Figure 6b) shows that up to $\gamma = 0.18$ the deformation profile

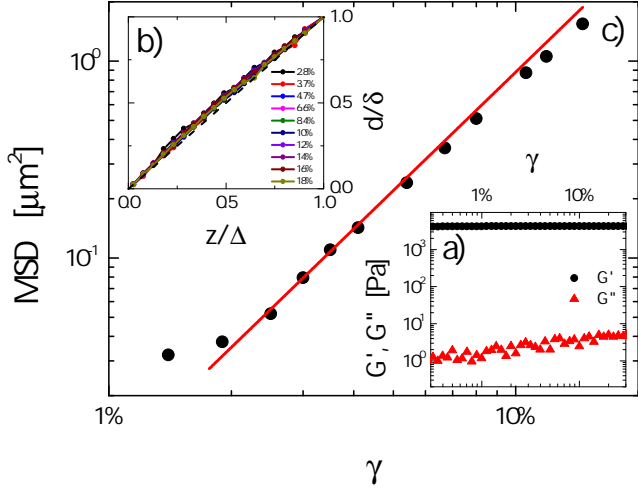


Fig. 6 Microscopy and rheology experiments measuring non-affinity in a PA hydrogel. a): rheological response of the gel in a strain sweep oscillatory test, at a frequency of 1 Hz. b): deformation profile $d(z)$, normalized by the displacement δ imposed to the upper plate of the shear cell. The distance z to the stationary plate is normalized by the gap e . c): Non-affine parameter \mathcal{A} as a function of the imposed strain, as obtained by tracking the displacement of tracer particles. A quadratic fit of $\mathcal{A}(\gamma)$ (line) yields a generalized diffusion coefficient $c = 75 \pm 15 \mu\text{m}^2$.

obtained by averaging the displacements of all particles at a distance z from the immobile plate follows is linear, thus ruling out slip and shear banding. For larger strains, slip starts occurring close to the immobile plate (data not shown). Data with slip are disregarded in the calculation of \mathcal{A} ; moreover, we assume that the non-affine displacements are isotropic and multiply the non-affine parameter obtained by 2D microscopy by a factor of $3/2$, in order to obtain the 3D \mathcal{A} . Figure 6c) shows \mathcal{A} vs the imposed shear deformation in a double logarithmic plot. The quadratic law, Eq. 11, fits very well the data (line), yielding $c = 75 \pm 15 \mu\text{m}^2$.

To model the effect of non-affine displacements on the intensity correlation function, we assume that $\mathbf{R}'(\mathbf{r}, \gamma)$ is isotropically distributed and spatially uncorrelated on the length scales of interest, as indicated by the microscopy experiments. Under these conditions, Eq. 10 can be modified to take into account non-affinity by introducing a new Gaussian term:

$$g_2(\mathbf{q}, \gamma) - 1 = \text{sinc}^2\left(q_x \gamma \frac{e}{2}\right) \exp\left(-\frac{1}{3} q^2 c \gamma^2\right). \quad (12)$$

The argument of the exponential is motivated by the analogy between $c\gamma^2$, the non-affine msd under shear and $6Dt$, the msd in Brownian diffusion, for which $g_2 - 1 = e^{-2q^2Dt}$. The dashed lines in Fig. 5 show the correlation functions obtained

for various q via Eq. 12, with $c = 30 \mu\text{m}^2$. An excellent agreement is seen with both simulations (performed using the same c value) and experiments, thus validating the modelling. The generalized diffusion coefficient c found in DLS experiments is about one half of that measured by optical microscopy: since the two experiments are performed on distinct samples, this discrepancy most likely stems from sample-to-sample variations in the spatial fluctuations of the elastic modulus.

Equation 12 shows that the dominating contribution to the decay of $g_2 - 1$ depends on how fast each term on the r.h.s. decreases with increasing γ . Non-affinities are best measured when the Gaussian term decays faster than the sinc^2 term, i.e. for $q_x < q\sqrt{c}/e$. In other words, DLS can detect non-affine rearrangements provided that the ROI used for the data analysis is ‘thin’ enough, i.e. has a small enough size along the shear direction \hat{u}_x . Correlation functions obtained from ‘thick’ ROIs, by contrast, will be dominated by the affine contribution.

In practice, determining whether or not the thin ROI condition is met may not be trivial, since the upper bound for q_x depends on c , which is not known *a priori*. One way to address this issue is to quantify the characteristic shear deformation γ_R at which $g_2 - 1$ decays and investigate how this quantity depends on the thickness of the ROI: the thin ROI limit will correspond to the regime where γ_R is independent of the ROI thickness and the decay of $g_2 - 1$ is fully dominated by the second factor in the r.h.s. of Eq. 12. We demonstrate this approach in Fig. 7, where we analyze the experimental and numerical correlation functions of Fig. 5. We quantify the thickness of the ROI by q_w , the maximum of the q_x component associated to a ROI, as in the discussion of Fig. 4. We obtain γ_R from a compressed exponential fit of the correlation function: $g_2(q, q_w, \gamma) - 1 = \exp[-(\gamma/\gamma_R(q, q_w))^p]$, where we have explicitly indicated that γ_R and thus $g_2 - 1$ depend on both the modulus of the scattering vector and the ROI thickness q_w . Figure 7 shows γ_R normalized by its $q_w \rightarrow 0$ limit, as a function of the ROI width q_w normalized by q . Two regimes are clearly seen for both simulations and experiments: at low q_w/q (thin ROI regime), γ_R is independent of q_w , while for thicker ROIs γ_R decreases as q_w^{-1} , as expected when the sinc^2 term in Eq. 12 controls the decay of $g_2 - 1$.

By comparing the open and crossed small symbols obtained by simulating samples with two different gaps, one can see that the crossover between the two regimes depends on the sample thickness e , as expected from Eq. 12. We find that an empirical expression that describes well the full behavior of γ_R across the two regimes is given by

$$\gamma_R^{-1}(q, q_w) = \gamma_0^{-1}(q) \sqrt{1 + \left(\frac{q_w e}{5q\sqrt{c}}\right)^2}, \quad (13)$$

where $\gamma_0^{-1} = q\sqrt{c}/3$ is the characteristic strain expected for

an infinitely thin ROI when finite beam size effects can be neglected (see Eq. 12), and the factor of 5 is introduced to obtain the best collapse with simulation data. As shown by the solid and dashed lines in Fig. 7, this expression reproduces numerical and experimental data very well.

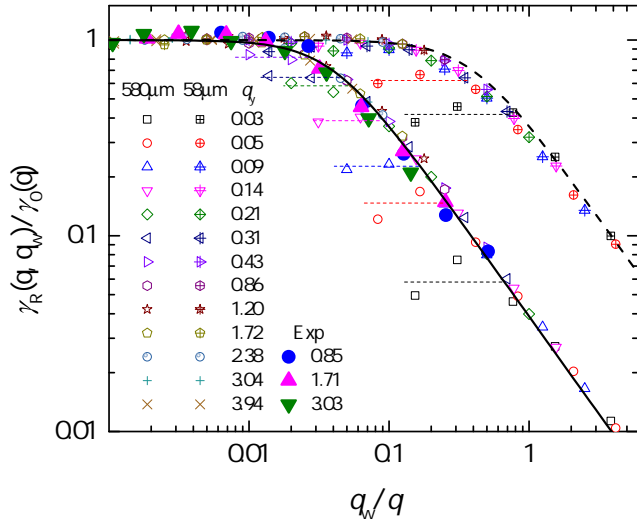


Fig. 7 Characteristic strain for the decay of $g_2 - 1$ vs ROI width along the shear direction, for various q_y , as shown by the label (in μm^{-1}). For a given gap e , data collected at various q collapse on a single curve when using scaled variables, as detailed in the text. The plateau region at low q_w corresponds to the desired thin ROI regime where the relaxation of $g_2 - 1$ is controlled by non-affine displacements. Small symbols: numerical simulations, with $c = 30 \mu\text{m}^2$, $w = 450 \mu\text{m}$, and $e = 580 \mu\text{m}$ (open symbols) or $e = 58 \mu\text{m}$ (open symbols with cross). Large symbols: experimental data obtained by analyzing the correlation functions shown in Fig. 5 ($e = 580 \mu\text{m}$, $c \approx 20 \mu\text{m}^2$). Lines: theoretical curve, Eq. 13, with $c = 30 \mu\text{m}^2$ and $e = 580 \mu\text{m}$ (solid line) or $e = 58 \mu\text{m}$ (dashed line).

So far, we have neglected the contribution due to the finite beam size, which was not included in Eq. 12. Indeed, even in the absence of non-affine rearrangements, a q_w -independent plateau would eventually be reached at low q_w (thin ROI limit) when the translation δ of the moving plate becomes comparable to the beam size w , as discussed in Sec. 3.1. This corresponds to a critical strain $\gamma_{th} \approx \frac{w}{e}$: for $\gamma \geq \gamma_{th}$, finite beam effects dominate and detecting any extra contribution due to non-affine displacements becomes increasingly difficult. Non-affine dynamics are therefore best seen when the characteristic strain γ_0 introduced in Eq. 13 is smaller than γ_{th} . Recalling that $\gamma_0 = q^{-1} \sqrt{c/3}$ and that $q \approx q_y$ in experiments designed to detect non-affine displacements, the condition $\gamma_0 \leq \gamma_{th}$ is re-casted in the form $q_y \gtrsim e/(w\sqrt{c})$ (where we have dropped a factor of $\sqrt{3}$ for simplicity), which may be fulfilled by decreasing the gap and increasing the beam size.

The effect of the finite beam size can be seen in the simulation data of Fig. 7 for the smallest q vectors (see e.g. data for $q_y \leq 0.43 \mu\text{m}^{-1}$ for the gap $e = 580 \mu\text{m}$). As shown by the horizontal dashed lines of Fig. 7, for these scattering vectors, γ_R deviates from the master curve described by Eq. 13 and saturates at values much lower than $\gamma_0(q)$, the expected $q_w \rightarrow 0$ limit. Note that for the thinner cell with $e = 58 \mu\text{m}$, the effect of the finite beam size becomes relevant only at much lower q vectors (see the crossed data points for $q_y \leq 0.05 \mu\text{m}^{-1}$), in agreement with the scaling with the gap of the $q_y \gtrsim e/(w\sqrt{c})$ condition.

To recapitulate the main findings of this section, we have shown that non-affine displacements may be resolved by measuring correlation functions for q vectors oriented perpendicular to the shear direction. Non-affine dynamics can be unambiguously quantified by DLS provided that i) the width of the ROI in the shear direction is small enough ($q_w < q\sqrt{c}/e$); ii) the y component of the probed scattering vector is large enough or the sample thin enough ($q_y \gtrsim e/(w\sqrt{c})$). These bounds depend on the generalized diffusion coefficient c , which is not known a priori. However, the scaling plot of Fig. 7 and Eq. 13 provide consistency checks allowing one to verify a posteriori whether or not the measured dynamics is due only to non-affine displacements.

4 Conclusions

In this work we have shown how DLS may be coupled to a shear cell in order to probe affine displacements and non-affine rearrangements. Correlation functions measured for a q vector oriented parallel to the direction of the applied shear are in principle sensitive to both affine and non-affine displacements. In practice, however, affine displacements typically dominate over non-affine ones (at least in the interesting regime corresponding to the onset of non-linear behavior), such that data for $q \approx q_x$ essentially probe affine displacements. Measuring the affine component is a powerful tool to check for the occurrence of wall slip or shear banding: any deviation from an ideal affine deformation profile would result in correlation functions that depart from the expected theoretical form discussed in the previous sections.

Non-affine dynamics are accessible by measuring correlation functions for a q vector oriented perpendicularly to the shear direction. Under realistic conditions, these correlation functions may contain additional contributions not due to non-affine displacements. These unwanted contributions can be neglected under appropriate experimental conditions. The most important role is played by the finite q_x component of the ROIs over which $g_2 - 1$ is averaged. This component has to be minimized in order to suppress the spurious decay due to the affine deformation. In practice, choosing ROIs with a width along \hat{u}_x smaller than about 5 pixels is sufficient. We

emphasize that the relevant parameter is the absolute value of the ROI width, not the ratio q_x/q_y . Thus, the same (small) width should be used for all ROIs, irrespective of the magnitude of the scattering vector.

Another source of spurious decorrelation stems from the rigid translation of scatterers. A cell with counter-moving plates and a stagnation plane in $z = e/2$ would reduce this effect. Furthermore, this contribution may be reduced by increasing the lateral size of the beam and by decreasing the sample thickness. Thinner samples also help in mitigating the effect of the finite ROI width; additionally, in the $e \ll w$ regime the decay of $g_2 - 1$ is easier to describe with analytical models. Finally, optical aberrations and the curvature of the wavefront impinging on the sample spuriously accelerate the decay of the correlation function. This artifact can be reduced by placing the sample in the beam waist, where the wavefront is plane, and can be fully corrected for using the spatio-temporal crosscorrelation method described in Sec. 3.1. Similarly to the term arising from the sample translation, this contribution becomes negligible in the thin sample limit, $e \ll w$.

As a final remark, we note that although some care must be taken in order to optimize the experimental parameters, none of the required conditions discussed above is impractical to meet. Indeed, typical small-angle light scattering apparatuses use a beam with w in the range 0.5 - 10 mm. When coupled to a shear cell with a gap e in the range 0.3-1 mm, which can be easily achieved, such an apparatus will operate in the thin sample limit, where all the above conditions are easily met for the typical range of accessible q vectors. We thus hope that DLS coupled to rheology will become an increasingly popular method to probe the microscopic dynamics of soft systems under shear.

Acknowledgments

We thank T. Phou for help in preparing the PA gels. This work was funded by ANR (grant n. ANR-14-CE32-0005-01), CNES, and the EU (Marie Skłodowska-Curie ITN Supolen, Grant No. 607937).

Appendix 1: list of symbols

$\hat{u}_x, \hat{u}_y, \hat{u}_z$	unit vectors in the shear, vorticity and shear gradient directions, respectively
\mathbf{r}	coordinates in the scattering volume
$\Delta\mathbf{r}(\mathbf{r})$	particle displacement field
$\mathbf{R}'(\mathbf{r})$	non-affine displacement field
γ	macroscopic shear deformation
e	sample thickness
k	laser wave vector
\mathbf{q}	scattering vector
q_x, q_y, q_z	scattering vector components along $\hat{u}_x, \hat{u}_y, \hat{u}_z$
\mathbf{E}_{in}	(complex) incident field
\mathbf{E}_S	(complex) scattered field
a	Rayleigh range
w_0	$1/e^2$ beam radius in the beam waist
$w(z)$	$1/e^2$ beam radius at distance z from the waist
w	beam radius on the sample plane
$\rho(z)$	radius of curvature of the wavefront at position z
δ	translation of a 2D sample along the \hat{u}_x direction
\mathbf{X}	relative position of two points on the sensor for spatio-temporal correlation function (Eq. 7)
\mathbf{X}_{peak}	position of the spatio-temporal crosscorrelation peak
Δ	speckle size
l	modified spatial correlation length (Eq. 8)
ε	distance between the detector and the focal plane, see Fig. 1b)
R	distance between the detector and the sample image, see Fig. 1b)
σ	$= 1 + R/\rho$
\bar{G}	spatially averaged shear modulus
$G(\mathbf{x})$	local shear modulus
$\delta G(\mathbf{x})$	local shear modulus fluctuations
\mathcal{A}	non-affine parameter (non-affine MSD)
c	generalized diffusion coefficient (non-affine MSD per unit squared strain, Eq. 11)
D	Brownian diffusion coefficient
q_w	detector size (in q space) along \hat{u}_x
$\gamma_R(\mathbf{q}, q_w)$	deformation needed to decorrelate the signal in presence of nonaffinities (Eq. 13)
$\gamma_0(\mathbf{q})$	thin ROI limit of γ_R when finite beam size effects can be neglected
γ_h	deformation needed to decorrelate the signal in the thin ROI limit, for a pure affine deformation

Appendix 2: $g_2 - 1$ for an affine deformation

Equation 10 of the main text can be easily computed starting from the field correlation function (Eq. 3) evaluated by using the scattered field of Eq. 4 and the affine particle displacement of Eq. 1. We start by assuming an ideal plane wave as the incident electric field, $\mathbf{E}_{in}(\mathbf{r}) = \mathbf{E}_0$. The crucial step in

the derivation is to realize that the double sum $\sum_{j,l}$ over the scatterers resulting from injecting Eq. 4 into Eq. 3 actually reduces to a single sum over the self terms ($i = l$), whereas the cross terms ($i \neq l$) vanish for uncorrelated scatterer positions. This simple sum can be evaluated by casting it into an integral weighted by the density functional: $n(\mathbf{r}) = \sum_j \delta_3(\mathbf{r} - \mathbf{r}_j)$, where $\delta_3(\mathbf{r})$ is the three-dimensional Dirac's delta. If the scatterers are distributed homogeneously in the scattering volume, the integral reduces to:

$$g_1(\mathbf{q}, \gamma) = \frac{1}{e} \int_{-e/2}^{e/2} e^{iq_x \gamma z'} dz' = \text{sinc}\left(\gamma q_x \frac{e}{2}\right), \quad (14)$$

which is Eq. 10 of the main text.

A correction for the finite beam size may be obtained by replacing the plane wave with a more realistic Gaussian profile (Eq. 5), which unfortunately results in a rather involved expression. Progress can be made by assuming that the sample lays in the beam waist ($z = 0$, $\rho = \infty$). In this case, Eq. 14 becomes

$$g_1(\mathbf{q}, \gamma) \propto \int_{-e/2}^{e/2} dz' e^{iq_x \gamma z'} \exp\left\{-2\left[1 + \left(\frac{\gamma}{2}\right)^2\right]\left(\frac{z'}{w_0}\right)^2\right\}. \quad (15)$$

Here, the proportional sign indicates that the expression has to be properly normalized, such that $g_1(\mathbf{q}, 0) = 1$. Equation 10 corresponds to the limits $q_x \gg \frac{e}{\gamma w_0^2}$ and $e \ll w_0$. The opposite limit, $q_x \rightarrow 0$, is the desired condition for probing non-affine displacements. In this limit one has

$$g_1(\mathbf{q}, \gamma) = \frac{\text{Erf}\left[\frac{e}{w_0 \sqrt{2}} \sqrt{1 + \left(\frac{\gamma}{2}\right)^2}\right]}{\sqrt{1 + \left(\frac{\gamma}{2}\right)^2} \text{Erf}\left(\frac{e}{w_0 \sqrt{2}}\right)} \quad (16)$$

For thin samples ($e \lesssim w_0$) this expression decays when $\gamma \frac{e}{2} \gtrsim w_0$, which corresponds to the requirement that the absolute displacements are comparable to the beam size. However, one should be aware that this limit cannot be fully reached in practice, since q_x is bounded from below by the speckle size, and thus cannot be smaller than $q_{min} \sim w_0^{-1}$. By taking this limiting value, the validity of Eq. 16 is restricted to $\gamma \ll \frac{e}{w_0}$. While these approximated forms are useful to rapidly grasp the general behavior of $g_2 - 1$, the general form, Eq. 15, can be easily be integrated numerically to obtain precise theoretical predictions, as shown in the main text.

References

1 R. G. Larson, *The Structure and Rheology of Complex Fluids*, Oxford University Press, New York, 1st edn., 1998.

- 2 T. Divoux, D. Tamarii, C. Barentin and S. Manneville, *Physical Review Letters*, 2010, **104**, 208301.
- 3 E. D. Knowlton, D. J. Pine and L. Cipelletti, *Soft Matter*, 2014, **10**, 6931–6940.
- 4 A. Ghosh, Z. Budrikis, V. Chikkadi, A. L. Sellerio, S. Zapperi and P. Schall, *Physical Review Letters*, 2017, **118**, 148001.
- 5 N. Koumakis, M. Laurati, S. U. Egelhaaf, J. F. Brady and G. Petekidis, *Physical Review Letters*, 2012, **108**, 098303.
- 6 T. Sentjabrskaja, P. Chaudhuri, M. Hermes, W. C. K. Poon, J. Horbach, S. U. Egelhaaf and M. Laurati, *Scientific Reports*, 2015, **5**, 11884.
- 7 D. Derks, H. Wisman, A. van Blaaderen and A. Imhof, *Journal of Physics: Condensed Matter*, 2004, **16**, S3917–S3927.
- 8 R. Besseling, E. Weeks, A. B. Schofield and W. C. K. Poon, *Phys. Rev. Lett.*, 2007, **99**, 028301–028301.
- 9 P. Schall, D. A. Weitz and F. Spaepen, *Science*, 2007, **318**, 1895–1899.
- 10 N. Y. C. Lin, J. H. McCoy, X. Cheng, B. Leahy, J. N. Israelachvili and I. Cohen, *Review of Scientific Instruments*, 2014, **85**, 033905.
- 11 M. Bierbaum, B. D. Leahy, A. A. Alemi, I. Cohen and J. P. Sethna, *Physical Review X*, 2017, **7**, 041007.
- 12 S. Aime and L. Cipelletti, in preparation.
- 13 R. Cerbino and V. Trappe, *Physical Review Letters*, 2008, **100**, 188102.
- 14 F. Giavazzi and R. Cerbino, *Journal of Optics*, 2014, **16**, 083001.
- 15 V. B. Tolstoguzov, A. I. Mzhel'sky and V. Y. Gulov, *Colloid and Polymer Science*, 1974, **252**, 124–132.
- 16 T. Hashimoto, T. Takebe and S. Suehiro, *Polym J*, 1986, **18**, 123–130.
- 17 J. W. van Egmond, D. E. Werner and G. G. Fuller, *The Journal of Chemical Physics*, 1992, **96**, 7742.
- 18 X.-L. Wu, D. J. Pine, P. M. Chaikin, J. S. Huang and D. A. Weitz, *Journal of the Optical Society of America B*, 1990, **7**, 15.
- 19 A. D. Gopal and D. J. Durian, *Physical Review Letters*, 1995, **75**, 2610.
- 20 P. Hebraud, F. Lequeux, J. P. Munch and D. J. Pine, *Phys. Rev. Lett.*, 1997, **78**, 4657–4660.
- 21 D. A. Weitz and D. J. Pine, in *Dynamic Light Scattering*, ed. W. Brown, Clarendon Press, Oxford, 1993, pp. 652–720.
- 22 N. Ali, D. Roux, L. Cipelletti and F. Caton, *Measurement Science and Technology*, 2016, **27**, 125902.
- 23 E. Tamborini, L. Cipelletti and L. Ramos, *Phys. Rev. Lett.*, 2014, **113**, 078301.
- 24 B. J. Berne and R. Pecora, *Dynamic Light Scattering*, Wiley, New York, 1976.
- 25 R. L. Leheny, M. C. Rogers, K. Chen, S. Narayanan and J. L. Harden, *Current Opinion in Colloid & Interface Science*, 2015, **20**, 261–271.
- 26 A. Madsen, R. L. Leheny, H. Guo, M. Sprung and O. Czakkel, *New Journal of Physics*, 2010, **12**, 055001.
- 27 R. Höhler, S. Cohen-Addad and H. Hoballah, *Physical review letters*, 1997, **79**, 1154.
- 28 G. Petekidis, A. Moussaid and P. N. Pusey, *Phys. Rev. E*, 2002, **66**, 051402.
- 29 B. A. DiDonna and T. C. Lubensky, *Physical Review E*, 2005, **72**, 066619.
- 30 A. Basu, Q. Wen, X. Mao, T. C. Lubensky, P. A. Janmey and A. G. Yodh, *Macromolecules*, 2011, **44**, 1671–1679.
- 31 J. Liu, G. H. Koenderink, K. E. Kasza, F. C. MacKintosh and D. A. Weitz, *Physical Review Letters*, 2007, **98**, 198304.
- 32 D. Bicout and R. Maynard, *Physica A: Statistical Mechanics and its Applications*, 1993, **199**, 387–411.
- 33 M. Erpelding, A. Amon and J. Crassous, *Phys. Rev. E*, 2008, **78**, 046104.
- 34 M.-Y. Nagazi, G. Brambilla, G. Meunier, P. Marguerès, J.-N. Périé and L. Cipelletti, *Optics and Lasers in Engineering*, 2017, **88**, 5–12.
- 35 M.-Y. Nagazi, *Ph.D. thesis*, Université de Montpellier, Montpellier, 2017.
- 36 D. Bonn, M. M. Denn, L. Berthier, T. Divoux and S. Manneville, *Reviews of Modern Physics*, 2017, **89**, 035005.
- 37 M. Buchanan, *Nat Phys*, 2017, **13**, 620–620.

-
- 38 N. C. Keim and P. E. Arratia, *Physical Review Letters*, 2014, **112**, 028302.
- 39 D. Fiocco, G. Foffi and S. Sastry, *Physical Review Letters*, 2014, **112**, 025702.
- 40 L. Cipelletti, G. Brambilla, S. Maccarrone and S. Caroff, *Optics Express*, 2013, **21**, 22353–22366.
- 41 S. Aime, L. Ramos, J. M. Fromental, G. Prévot, R. Jelinek and L. Cipelletti, *Review of Scientific Instruments*, 2016, **87**, 123907.
- 42 Menter, P., *Acrylamide Polymerization—a Practical Approach.*, 2000.
- 43 E. Tamborini and L. Cipelletti, *Review of Scientific Instruments*, 2012, **83**, 093106.
- 44 M. Born and E. Wolf, *Principles of Optics: Electromagnetic Theory of Propagation, Interference and Diffraction of Light*, Elsevier, 2013.
- 45 J. W. Goodman, *Speckle Phenomena in Optics: Theory and Applications*, Roberts and Company, Englewood, 2007.
- 46 A. Duri, H. Bissig, V. Trappe and L. Cipelletti, *Phys. Rev. E*, 2005/11/00/, **72**, 051401.
- 47 D. Allan, T. Caswell, N. Keim and C. van der Wel, *Trackpy: Trackpy v0.3.0*, Zenodo technical report, 2015.
- 48 O. Svelto, *Principles of Lasers (5th ed.)*, Springer, 2010.
- 49 T. Asakura and N. Takai, *Applied Physics*, 1981, **25**, 179–194.

Part II

Colloidal gels

Structure, dynamics and viscoelastic properties

Contents

5.1	Introduction	101
5.2	Theoretical background	104
	5.2.1 Fractional derivatives in rheology	104
	5.2.2 Fractional Maxwell Model	105
5.3	Material and methods	106
	5.3.1 Sample	106
	5.3.2 Scattering techniques and rheology	107
5.4	Results	108
	5.4.1 Sample structure	108
	5.4.2 Dynamics and viscoelasticity during gelation and aging	109
	5.4.3 Creep-recovery experiments	112
	5.4.4 Reversible structural anisotropy	113
5.5	Discussion	115

As a model system, this work mainly focuses on a colloidal gel characterized by a fractal structure and a power-law rheology. In this chapter we thoroughly characterize the linear viscoelasticity of the gel, showing that it is very accurately described by a Fractional Maxwell (FM) model. In search of the physical bases of such phenomenological model, we discuss the possible relationship between the FM model and the microscopic structure of the gel.

5.1 Introduction

Power-law rheology is of widespread occurrence in complex materials that do not exhibit one unique relaxation time, from biomaterials, such as cells [Fabry 2001, Djordjevic 2003, Desprat 2005, Balland 2006, Kollmannsberger 2011, Hecht 2015], tissues

[Kohandel 2005, Davis 2006, Shen 2013], or biopolymer networks [Gobeaux 2010, Curtis 2015] and pastes [Jóźwiak 2015], to food science [Ma 1996, Zhou 1998, Subramanian 2006, Ng 2008, Caggioni 2007, Korus 2009, Moreira 2011, Ronda 2013, Xu 2013, Jaisankar 2014, Leocmach 2014, Jóźwiak 2015, Faber 2017a, Faber 2017b], colloidal gels [Rich 2011], microgels [Lidon 2017], hydrogels [Hung 2015], polymer gels [Chambon 1986, Durand 1987, Martin 1988, Adolf 1990, Tirtaatmadja 1997, Larsen 2008, Leibler 1991], melts [Plazek 1960, Hernández-Jiménez 2002, Friedrich 1999], elastomers [Curro 1983, Winter 1999, Ferry 1980], and composites [Metzler 1995]. Although the generality of power-law rheology is captured by phenomenological models such as Soft Glassy Rheology [Sollich 1998], in general a well established connection with the microscopic origin of this mechanical behavior is still missing. Few exceptions include the parallel drawn between power-law rheology and microscopic structure and dynamics in the framework of polymer physics. This is for example the case of Rouse motion, where the self-similar relaxation dynamics naturally come into play as a consequence of the fractal nature of the polymer coil [Colby 2003]. In this case, the fractal dimension $d_f = 2$ describing the microscopic structure is directly linked to the fractional order of the rheological model, i.e. the exponent $\alpha = 0.5$ describing the power-law rheology. Similarly, in the attempt of modeling polymer gels at the critical point, Adolf and Martin [Adolf 1990] explicitly derive a power-law distribution of relaxation times from a postulated scale-independence, which is assumed to hold at the critical gel point according to percolation theory. Indeed, direct measurement of the microscopic structure with static light scattering shows clear evidence of a fractal mass distribution [Martin 1991], with the fractal dimension predicted by their model. More generally, a quantitative link between power law rheology and the microscopic structures of critical gels with arbitrary fractal dimension is established by Muthukumar [Muthukumar 1989] in two limit cases of screened and unscreened excluded volume and hydrodynamic interactions, which prove to properly describe a wide class of experimental results [Hung 2015]. This model essentially extends Rouse dynamics from a single chain to a branched, fractal object. Although in this case the mathematical formulation is much more involved, again the power-law rheology reveals the self-similarity of microscopic dynamics, stemming from the fractal structure.

Although fractal structures are very well represented in soft materials, from human tissues [Helmberger 2014, Mauroy 2004, Ahmadi 2013] to colloidal gels [Carpinetti 1993, Bremer 1990], the wide spectrum of systems mentioned above suggests that power-law rheology does not necessarily stem from fractal structure, and that other microscopic mechanisms might produce power-law distributions of relaxation times as well. In absence of a full understanding of such mechanisms, however, fractional rheological models remain largely phenomenological, and the amount of relevant physical information that can be extracted from them remains arguable.

In this regard, one crucial aspect is the scarcity of systems for which a thorough discussion of linear rheology is available. Indeed, the majority of the works finding a power-law rheology only focus on oscillatory shear [Ma 1996, Metzler 1995, Tirtaatmadja 1997, Fabry 2001, Djordjevic 2003, Shen 2013, Caggioni 2007, Rich 2011, Hung 2015, Friedrich 1999],

whereas others only focus on transient experiments, either stress relaxation [Hernández-Jiménez 2002, Curro 1983], creep [Desprat 2005, Xu 2013] or both [Davis 2006]. Transient experiments alone are delicate, and have to be carefully performed in order to ensure that only the linear regime is being probed, since sometimes power-law creep clearly emerges as a nonlinear phenomenon [Duval 2010, Paredes 2013]. Indeed, plastic power-law creep is observed on many systems, from crystalline materials like metals [Andrade 1910, Miguel 2002, Poirier 1985, Cottrell 1952], or ice [Ashby 1985] to colloidal [Siebenbürger 2012, Sentjabrskaja 2015, Coussot 2006, Caton 2008] or polymeric [Nechad 2005b, Karobi 2016] systems, which would have a very different rheology in the linear regime. On the other hand, the challenge of oscillatory shear is that it typically gives access to a limited range of frequencies, which sometimes makes it difficult to distinguish the predictions of different models. In some systems a larger spectrum can be accessed exploiting time temperature superposition (TTS), although its applicability is far from being trivial in the above systems. One instructive example is represented by the work of Subramanian *et al.* on cheese [Subramanian 2006]: here TTS is applied to access data on a broad spectrum of frequency, nicely fitted by a Fractional Maxwell model. However, the authors also show creep and recovery data, clearly displaying a substantial non-recoverable creep strain, which is incompatible with the Fractional Maxwell model. Because the authors do not discuss this inconsistency, it is unclear whether it has to be attributed to nonlinear creep or to the failure of TTS. Similarly, it is interesting to remark that in various independent works on different flour doughs [Korus 2009, Moreira 2011, Ronda 2013] oscillatory rheology reveals clear power laws, whereas creep and recovery on the same samples are nicely fitted by the Burger model, which does not contain any power law. In other cases, a power-law creep was also interpreted as the short time limit of a stretched exponential [Cheriere 1997]. Moreover, a power-law rheology may also be found in both oscillatory shear and creep, but described by incompatible power-law exponents [Lidon 2017], which also questions the applicability of a fractional model.

All these examples show that a comparison between different rheological measurements is essential to truly validate a phenomenological model. This is done for example on individual cells [Balland 2006], where the authors had to cope with the huge sample-to-sample variations (typical of biological systems) by increasing the statistics, but also on collagen networks [Gobeaux 2010], biopolymer gels [Ng 2008, Leocmach 2014], natural gums [Jaishankar 2014] and cheese [Faber 2017b]. For these systems, fractional rheological models provide a consistent description of the observed rheology. However, most of these systems are rather complex, and structural analysis is delicate.

In this chapter we focus on a simpler model system, namely a colloidal gel, for which both microscopic structure and spontaneous dynamics are well known and can be easily measured with scattering methods [Carpinetti 1995, Cipelletti 2000]. Thanks to a careful analysis of both oscillatory and transient shear we show that linear rheology is consistently described by a Fractional Maxwell model, whose parameters are discussed in detail, with

reference to the sample structure and to its aging properties.

This chapter is organized as follows: after reviewing the theoretical background (Sec. 5.2), we describe the sample preparation and the experimental setup (Sec. 5.3). In Sec. 5.4 the experimental results are shown and fully described with the linear viscoelastic model. A conclusive section (Sec. 5.5) closes the chapter, with a detailed discussion about the link between the rheological properties and the microscopic structure.

5.2 Theoretical background

5.2.1 Fractional derivatives in rheology

For systems characterized by a power-law rheology, the relaxation modulus measured, e.g., in a step strain experiment, decays as $G(t) \propto t^{-\alpha}$ with $0 < \alpha < 1$. For such systems, fractional expressions come naturally into play as a result of the superposition principle. Indeed, the stress response to an arbitrary shear history $\gamma(t)$ is given by the convolution integral [Hilfer 2000]:

$$\sigma(t) = \frac{K}{\Gamma(1-\alpha)} \tau^\alpha \int_{-\infty}^t (t-t')^{-\alpha} \dot{\gamma}(t') dt' \quad (5.1)$$

In this expression one recognizes the fractional derivative of order α , d^α/dt^α , which is defined by $\Gamma(1-\alpha) d^\alpha \gamma/dt^\alpha = \int_{-\infty}^t (t-t')^{-\alpha} \dot{\gamma}(t') dt'$. Hence,

$$\sigma(t) = K \tau^\alpha \frac{d^\alpha \gamma}{dt^\alpha} \quad (5.2)$$

By inverting the above equation, one easily finds for example that the creep deformation of the material in response to a step stress applied at time $t = 0$, $\sigma(t) = \sigma_0 \Theta(t)$ ($\Theta(t)$ being Heaviside step function), is a power law:

$$\gamma(t) = K^{-1} \tau^{-\alpha} \frac{d^{-\alpha}}{dt^{-\alpha}} \sigma(t) = \frac{\sigma_0}{K} \frac{\Theta(t)}{\Gamma(1+\alpha)} \left(\frac{t}{\tau}\right)^\alpha \quad (5.3)$$

For $\alpha = 1$ one recovers the linear flow of a dashpot element, $\gamma(t) = \sigma_0 t / K \tau$ (for $t \geq 0$). On the other hand, for $\alpha = 0$, one recovers the step strain of an elastic spring, $\gamma(t) = \sigma_0 / K$. In the general case ($0 < \alpha < 1$), Eq. 5.3 corresponds to a fractional rheological element called Scott-Blair element or springpot [Blair 1947, Bagley 1983, Bagley 1986]. We show in Fig. 5.1 (top) the creep profiles expected for springpot elements with different values of the fractional exponent α .

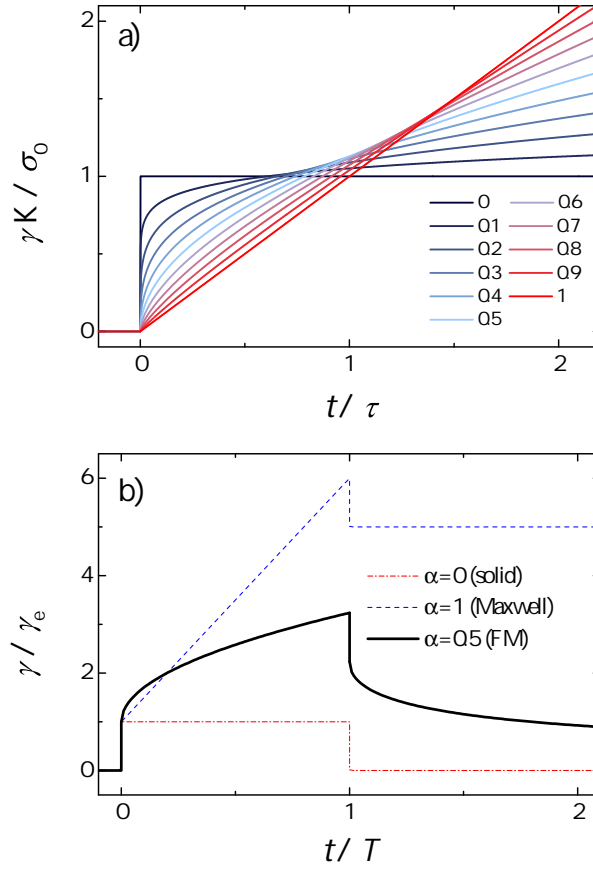


Figure 5.1: (a) Normalized strain as a function of the normalized time upon application of a constant stress of amplitude σ_0 applied at time 0 for a springpot with different exponents α as indicated in the legend. (b) Time evolution of the strain normalized by the initial elastic jump during the creep and recovery of an elastic solid ($\alpha = 0$), a Maxwell fluid ($\alpha = 1$) and a fractional Maxwell fluid with an exponent $\alpha = 0.5$.

5.2.2 Fractional Maxwell Model

The Fractional Maxwell (FM) model is based on two springpots in series, and is thus characterized by four independent parameters, which can be interpreted as an elastic modulus G_0 , a characteristic time τ_{FM} , and two exponents α and β . In this chapter we will consider the special case where one of the two springpots is reduced to an elastic spring ($\beta = 0$). In this case the rheological constitutive equation reads:

$$\frac{d^\alpha \gamma}{dt^\alpha} = \frac{1}{G_0} \left[\frac{\sigma(t)}{\tau_{FM}^\alpha} + \frac{d^\alpha \sigma}{dt^\alpha} \right] \quad (5.4)$$

Note that, for $\alpha = 1$, Eq. 5.3 corresponds to a standard Maxwell fluid.

Solutions of the FM model for standard rheological experiments have been previously computed [Bagley 1989, Jaishankar 2013, Jaishankar 2014, Józwiak 2015]. For a sinusoidal deformation of frequency ω , the storage, G' , and loss, G'' , moduli read:

$$G'(\omega) = G_0 \xi \frac{\cos\left(\frac{\pi}{2}\alpha\right) + \xi}{1 + \xi^2 + 2\xi \cos\left(\frac{\pi}{2}\alpha\right)} \quad (5.5)$$

$$G''(\omega) = G_0 \xi \frac{\sin\left(\frac{\pi}{2}\alpha\right)}{1 + \xi^2 + 2\xi \cos\left(\frac{\pi}{2}\alpha\right)} \quad (5.6)$$

where $\xi = \tau_{\text{FM}}^\alpha \omega^\alpha$.

On the other hand, the creep deformation following the application at time $t = 0$ of a step stress of amplitude σ_0 reads:

$$\gamma(t) = \frac{\sigma_0}{G_0} \left[1 + \frac{1}{\Gamma(\alpha + 1)} \left(\frac{t}{\tau_{\text{FM}}} \right)^\alpha \right] \quad (5.7)$$

This equation can be decomposed as follows:

$$\gamma(t) = \gamma_e^+ + \gamma_{\text{creep}}(t) \quad (5.8)$$

Here $\gamma_e^+ = \sigma_0/G_0$ is the instantaneous elastic part of the mechanical response and $\gamma_{\text{creep}}(t) = \frac{\gamma_e}{\Gamma(\alpha+1)} \left(\frac{t}{\tau_{\text{FM}}} \right)^\alpha$ is analogous to Eq. 5.3 and corresponds to the cumulated creep deformation since the application of the step stress at time $t = 0$.

It is also interesting to investigate the creep recovery, that is the time evolution of the deformation following the release of the stress σ_0 at time T . We here define $t' = t - T$ as the time evolved since the release of the stress, which has been applied from time $t = 0$ to time T . Similarly to the creep, the creep recovery is composed of an instantaneous elastic relaxation of amplitude $\gamma_e^- = \sigma_0/G_0$ and a slow decay function $\gamma_{\text{rec}}(t')$ that reads:

$$\gamma_{\text{rec}}(t') = \gamma_{\text{creep}}(T) \left[\left(1 + \frac{t'}{T} \right)^\alpha - \left(\frac{t'}{T} \right)^\alpha \right] \quad (5.9)$$

We observe that the linear viscoelastic creep of a FM model is completely reversible, since $\gamma_{\text{rec}}(t' \rightarrow \infty) = 0$. Interestingly, Eq. 5.9 predicts that the initial un-deformed configuration is recovered with a characteristic time that uniquely depends on the duration T of the creep, whereas it is independent of the natural timescale τ_{FM} . We show in Fig. 5.1 (bottom) the creep and recovery for a Fractional Maxwell model with $\alpha = 0.5$ together with the asymptotic behaviors, a Maxwell fluid ($\alpha = 1$) and an elastic solid ($\alpha = 0$).

5.3 Material and methods

5.3.1 Sample

The gel is formed by aggregating a water suspension of charged silica particles (Ludox TM50, from Sigma Aldrich) at a volume fraction $\phi = 5\%$. Particle aggregation is triggered by increasing *in situ* the ionic strength of the solvent, by using a chemical reaction (the hydrolysis of urea into carbon dioxide and ammonia: $\text{CO}(\text{NH}_2)_2 + 2\text{H}_2\text{O} \rightarrow \text{NH}_4^+ +$

$NH_3+HCO_3^-$) catalyzed by an enzyme (Urease U1500-20KU, from Sigma Aldrich), which increases the ionic strength of the solvent and thus screens the electrostatic repulsion between particles, eventually triggering particle aggregation [Wyss 2004]. To do so, we add to the suspension urea (concentration 1 Mol/l) and urease (35 U/ml). This induces, at room temperature, a sol-to-gel transition of the suspension roughly 3 hours after addition of urea and urease. Structural information on the gel and on the particles are obtained by neutron and light scattering techniques, comparing the intensity scattered by the gel with the one scattered by a dilute suspension ($\phi = 0.037\%$) of the same particles in pure water. In order to increase the contrast between the particles and the solvent in neutron scattering, water (H_2O) is replaced by heavy water (D_2O). One does not have any indication of any structural and rheological alteration of the sample following the replacement of H_2O by D_2O .

5.3.2 Scattering techniques and rheology

The structure of the sample is probed combining different scattering techniques, allowing one to access a wide range of scattering vectors q , from 0.1 to 2000 μm^{-1} . We use small-angle neutron scattering (SANS) (PA20 beamline at Laboratoire Léon Brillouin, France), and custom made wide-angle (WALS) and small-angle light scattering setups (SALS) [Tamborini 2012]. For SANS, the sample is held in a 2 mm thick rectangular cell, whereas for light scattering experiments the cell thickness was decreased to 1 mm in order to avoid multiple scattering.

Rheological measurements are performed in the Couette cell of a stress-controlled rheometer (Anton Paar MCR502), with a low viscosity silicon oil film on top of the sample to prevent evaporation over very long timescales (several weeks). Frequency sweep, respectively creep, measurements are performed at sufficiently small strain amplitude (typically $\gamma = 0.1\%$), resp. at sufficiently small applied stress, to ensure data are acquired in the linear regime. Strain sweep are also measured at 1 Hz to probe the extension of the linear regime.

In addition, the sample structure and rheological properties are also probed simultaneously using a custom made SALS apparatus [Tamborini 2012], which is coupled to a linear, parallel plate stress-controlled shear cell [Aime 2016]. Such a setup allows one to access scattering vectors q ranging from about 0.4 μm^{-1} to 4 μm^{-1} , essentially oriented in the (vorticity, velocity) plane, and with a minor q -dependent component along the shear gradient direction.

All experiments are performed at room temperature. For both scattering measurements and rheological measurements, the sample is loaded in the scattering or shear cell while still in a liquid state and is then allowed to gel *in-situ*. By monitoring the sample at rest over long time, we observe that the gel is stable, and we can neglect the influence of gravity on the microscopic structure.

5.4 Results

5.4.1 Sample structure

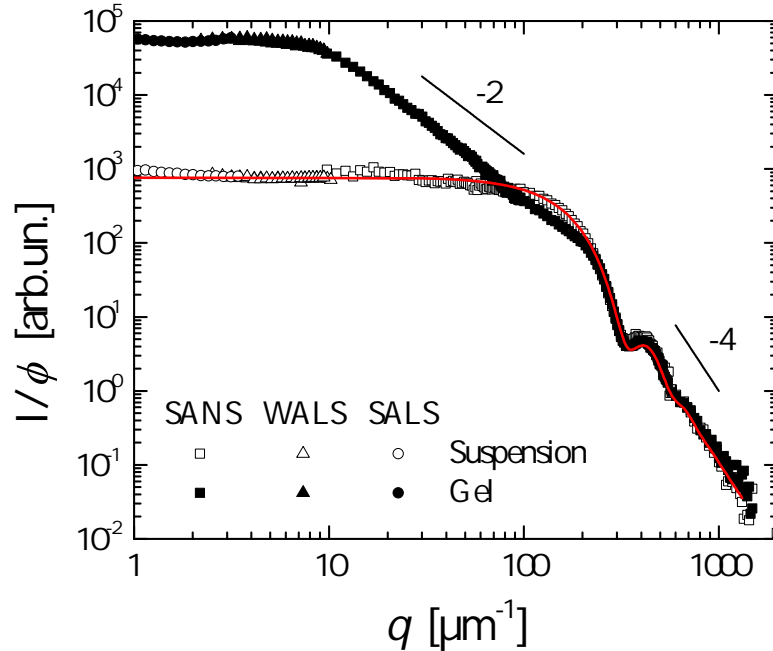


Figure 5.2: Scattered intensity of the colloidal gel at $\phi = 5\%$ volume fraction (filled symbols) and of the stable colloidal suspension, at $\phi = 0.037\%$ (empty symbols), probed with small angle neutron scattering and static light scattering, as indicated in the legend. Red line: theoretical form factor of a polydisperse set of spheres of average diameter 25 nm and polydispersity 10% (consistent with nominal values).

We show in Fig. 5.2 the scattering profiles, i.e. the scattered intensity, I , normalized by particle volume fraction, ϕ , of a dilute stable suspension ($\phi = 0.037\%$) and of a colloidal gel ($\phi = 5\%$) as a function of the scattering vector q , over several orders of magnitude, thanks to the combination of three experimental techniques (SANS, WALS and SALS). Over the whole range of scattering vectors investigated, the scattering profile of the dilute and stable suspension can be quantitatively accounted for by the form factor of polydisperse spherical particles [Bresler 2015]: $I(q) = \int \rho(R)P(q, R)dR$, where $P(q, R) = [3(\sin(qR) - qR\cos(qR))(qR)^{-3}]^2$ is the form factor of a uniform sphere of radius R , and the weighting function $\rho(R)$ is derived from a Gaussian distribution of particle sizes. The best fit of the experimental data yields an average diameter $a = 25$ nm and a 10% polydispersity (defined as the full width at half maximum of the particle size distribution). For the colloidal gel, one observes (Fig. 5.2) that the data at large q , which probe the structure of the individual particles, perfectly superimpose with the measurement for the dilute suspension, as expected. By contrast, data for $q < 200 \mu\text{m}^{-1}$ largely differ.

The scattered intensity is the one expected for crowded fractal clusters of particles [Carpinetti 1993, Manley 2005]. For q in the range $(10 - 200) \mu\text{m}^{-1}$, the scattered intensity decays as q^{-2} , indicating a fractal dimension $d_f = 2$. At very low q ($q < q^*$, with $q^* \approx 10 \mu\text{m}^{-1}$), the scattered intensity becomes almost q -independent, indicating that on length scales larger than $2\pi/q^* \approx 0.6 \mu\text{m}$, the sample structure is rather homogeneous. This value is in good numerical agreement with the theoretical expectation for the cluster size $\xi \sim a\phi^{1/(d_f-3)} \sim 1 \mu\text{m}$ [Carpinetti 1992].

5.4.2 Dynamics and viscoelasticity during gelation and aging

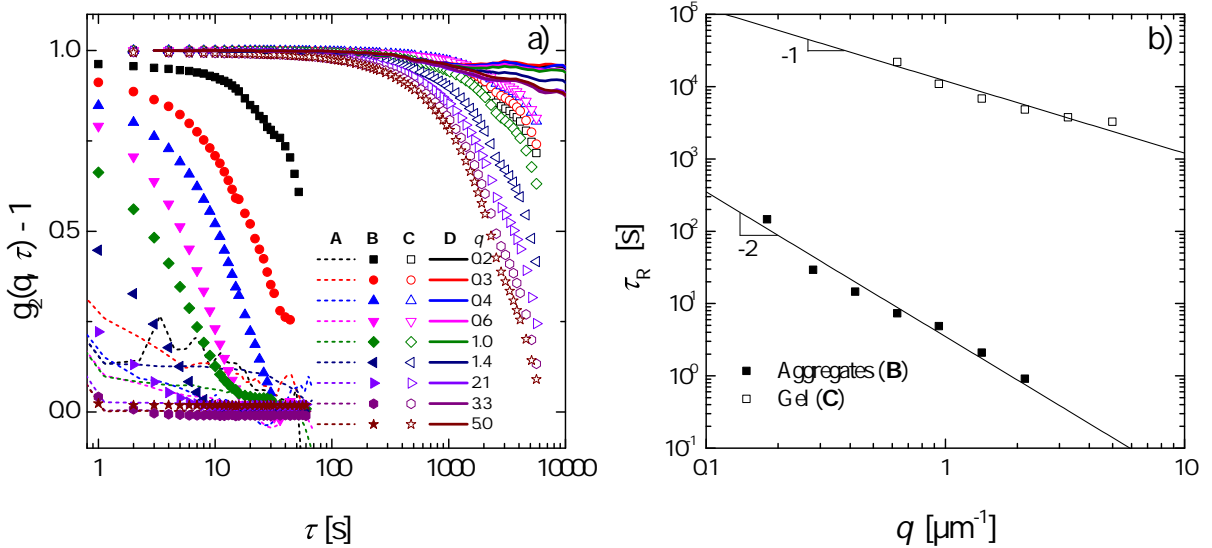


Figure 5.3: (a) Intensity correlation functions plotted as a function of time delay τ for different scattering vectors q (in the legend, units in μm^{-1}) and different stages during gelation: (A) right after sample preparation; (B) some minutes after onset of aggregation; (C) after cluster percolation; (D) after aging for 2 days at rest. (b) Relaxation times τ_R extracted from correlation functions at stages (B) and (C), and plotted as a function of the scattering vector.

At early stages, right after preparation, the sample is a liquid with a viscosity comparable to that of water. As a consequence of enzymatic activity, the ionic strength of the solvent grows in time, and after an induction time t_i , which depends on the amount of enzyme added (typically 8000 s in our experiments), it becomes large enough to trigger particle aggregation. This event can be clearly seen with dynamic light scattering, since the formation of larger particle clusters slows down the microscopic dynamics. A few minutes after the onset of aggregation, the relaxation time τ_R becomes measurable for most accessed scattering vectors. The scaling $\tau_R \sim q^{-2}$ confirms that we probe the diffusive motion the aggregates, and the increasing trend of τ_R in time shows that those aggregates are growing in size. Eventually, clusters become large enough to get in touch

with each other, and at that moment a system-spanning network is formed. When this happens, the dynamics slows down tremendously and changes qualitatively, with correlation functions changing from simple exponentials to compressed exponentials and the τ_R scaling changing from q^{-2} (diffusive-like) to q^{-1} (Fig. 5.3b). Concomitantly, a finite storage modulus G' is measured by rheometry. Starting from that moment, the rheological response of the material rapidly evolves with time towards the elasticity-dominated pattern shown in Fig. 5.4. One defines the sample age t_w as the time elapsed since the gelation time, chosen at the time of crossover between G' and G'' , as measured at an angular frequency $\omega = 0.628$ rad/s.

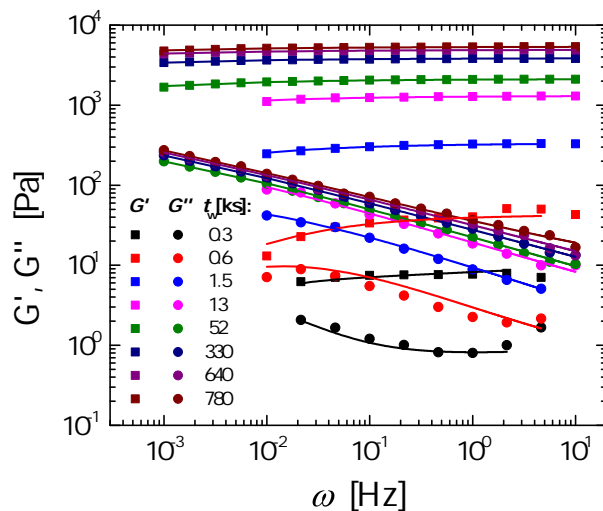


Figure 5.4: Viscoelastic moduli measured during sample aging at a strain amplitude $\gamma_0 = 0.1\%$, and plotted as a function of frequency for different waiting times t_w as indicated in the legend. Solid lines represent fits using Eqs. 5.5 and 5.6. Fit parameters are displayed in Fig. 5.5.

We probe the evolution with sample age of the frequency dependence of the complex modulus. Data are measured for t_w spanning more than 3 orders of magnitude (from 0.3 ks to 800 ks). Over this timescale, the storage modulus increases by almost 3 orders of magnitude, and the loss modulus by more than 2 orders of magnitude. Interestingly, all along the aging process, the sample viscoelasticity is always very well described by the Fractional Maxwell model [Jaishankar 2013], as shown in Fig. 5.4 where the best fits of the experimental data using Eqs. 5.5 and 5.6 are displayed.

The evolution of the fit parameters α , τ_{FM} and G_0 upon sample aging are given in Fig. 5.5. Although the data are somehow noisy, the exponent α is measured to slightly decrease with sample age, from ~ 0.42 to ~ 0.32 , in agreement with what found in literature on biopolymer gels [Curtis 2015]. On the other hand, the elastic modulus, G_0 , and the characteristic time, τ_{FM} , display a smooth and continuous increase with t_w . Both parameters are measured to increase rather rapidly at short time ($t_w \lesssim 10^4$ s), and less steeply at longer times. In the late time regime, we find $G_0 \sim t_w^{1/3}$ and $\tau_{\text{FM}} \sim t_w$, τ_{FM}

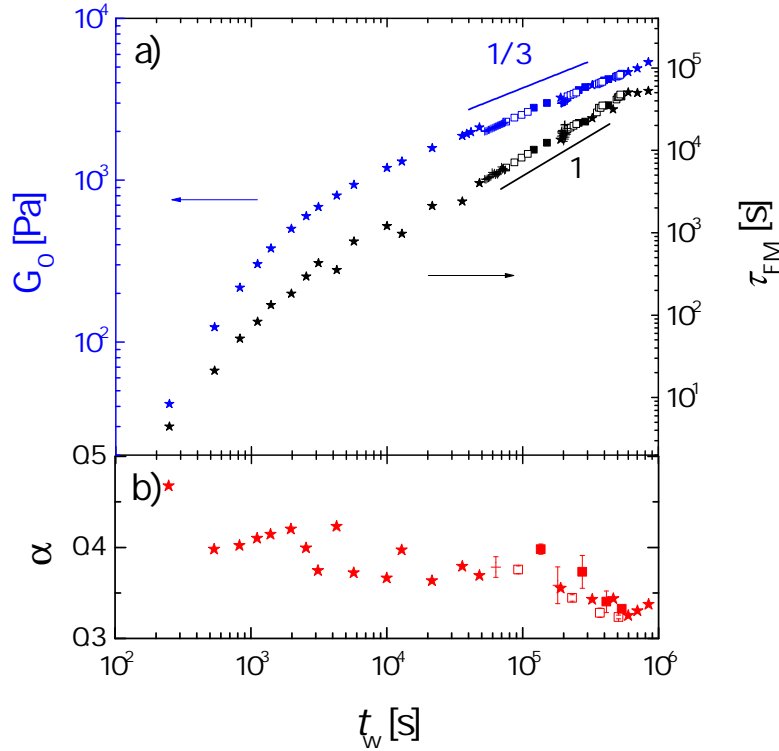


Figure 5.5: Fractional Maxwell parameters extracted from both frequency sweeps (stars) and creep data (squares) fitted by Eqs. 5.5, 5.6 and 5.7 respectively. (a) Elastic modulus G_0 (blue, left axis) and characteristic time τ_{FM} (black, right axis). (b) Exponent α

being more than one order of magnitude smaller than the waiting time.

To check for consistency as well as to probe smaller frequencies, we perform creep experiments in the linear regime. Typical creep profiles are shown in Fig. 5.6 for different waiting times t_w , in the range $(1.2-5.4) \cdot 10^5$ s. Here the sample is rather old, ensuring that during each creep measurement, which lasts 10000 s at most, sample aging is negligible. The shear stress is fixed at $\sigma_0 = 30$ Pa and is sufficiently small (about 2 orders of magnitude smaller than the elastic modulus), ensuring that measurements are performed in the linear regime. Indeed, a strain sweep on an old sample ($t_w = 10^6$ s) shows that linearity extends beyond 1% deformation (Fig. 5.7).

As the sample ages and its shear modulus increases, the initial elastic jump for a fixed applied stress becomes smaller, and the time evolution of the strain becomes smaller as well, as expected. For all sample ages investigated (between 10^5 and 10^6 s), the whole time evolution of the strain is very well fitted by the theoretical prediction of the FM model (Eq. 5.7).

A direct comparison of creep and frequency sweep measurements can be achieved using methods available in literature [Evans 2009]. As an illustration, we show in Fig. 5.8 the direct measurement of the frequency-dependence of the storage and loss moduli, together with the frequency dependence of G' and G'' computed from a creep experiment, and the

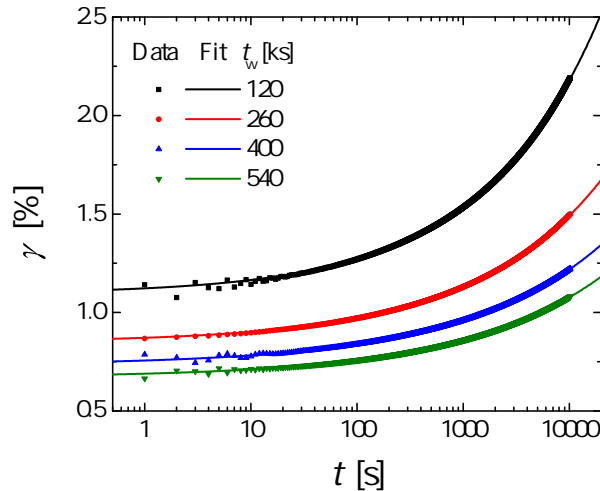


Figure 5.6: Creep deformation under a shear stress $\sigma_0 = 30\text{Pa}$ for 4 different sample ages as indicated in the legend (symbols). Lines are fits of the experimental data using Eq. 5.7. Fit parameters are shown in Fig. 5.5 (filled squares)

fit using the FM model. We find a nice overlap of the two sets of data. Importantly, creep measurements allow the measurements to be extended at lower frequency as compared to oscillatory rheology, about one decade for the data shown in Fig. 5.8). These data allow one to probe the sample behavior almost up to the FM characteristic time τ_{FM} . At low frequencies ($\omega \ll \tau_{FM}^{-1}$), both G' and G'' increase as ω^α , whereas in the high frequency regime ($\omega \gg \tau_{FM}^{-1}$), one has $G' \sim G_0$ and $G'' \propto \omega^{-\alpha}$.

Overall, we find that the evolution of the three parameters of the FM model as extracted from oscillatory shear and creep experiments nicely overlap over the whole range of sample ages, demonstrating the relevance of the Fractional Maxwell model to describe the linear visco-elasticity of our fractal colloidal gel.

5.4.3 Creep-recovery experiments

To further test the FM model, we perform creep-recovery experiments. Here, after a creep of duration T , the stress is released, and the sample is left at rest until the creep strain is fully relaxed, before applying another step stress. T is chosen such that the sample age ($t_w > 10^5$ s) is much larger than the duration of the experiment, in order to have negligible aging during creep.

The strain evolution during a representative creep and recovery experiment is shown in Fig. 5.9, together with the fit with the FM model (Eq. 5.8 for the creep and Eq. 5.9 for the recovery). We find that the FM reproduces extremely well the experimental data. Interestingly, we measure that, for initial elastic jumps γ_e^+ up to 3.5% (obtained by imposing variable stress amplitudes), the instantaneous recovery γ_e^- is exactly equal to γ_e^+ (inset Fig. 5.9). Such equality provides another indication that experimental data

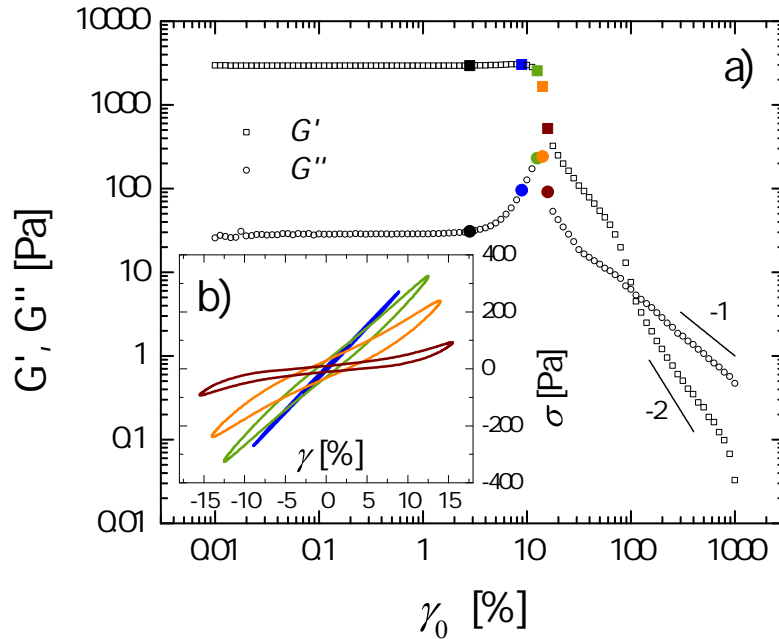


Figure 5.7: Large amplitude oscillatory shear probed at frequency $\omega = 1$ Hz. (a) First-harmonic nonlinear viscoelastic moduli G' and G'' as a function of strain amplitude γ_0 (b) Lissajous-Bowditch (stress vs. strain) plots for different strain amplitudes $\gamma_0 = 2.8\%$ (black), 9% (blue), 12.5% (green), 14% (yellow), 15.8% (red).

correspond to the linear viscoelastic regime, in agreement with what previously shown.

Typical strain relaxations during creep recovery are shown in Fig. 5.10 for an old sample ($t_w \approx 5 \cdot 10^5$ s) that has been submitted to three consecutive creep (with $T = 100, 1000$ and 10000 s) and creep recovery tests. We find that as the duration of the creep is longer, the initial values of γ in the creep recovery are higher, as expected. Equation 5.9 predicts that after the sudden release of the external stress the macroscopic deformation should decay to 0 with a characteristic shape depending on α and scaling as t'/T . Figure 5.10 shows that the t'/T scaling does indeed hold, since data measured for different creep durations collapse on a single curve once the strain is normalized by the strain cumulated at the end of the previous creep step ($\gamma_{\text{creep}}(T)$, cf. Eq. 5.8), and time t' is normalized by the creep duration T .

5.4.4 Reversible structural anisotropy

During creep recovery experiments we find that the cumulated strain γ almost fully relaxes to 0. This suggests that the rearrangements occurring during creep are reversible, despite the sample is not purely elastic. We check for the reversibility at a microscopic level by direct structural measurements during a sinusoidal shear deformation, using the home-made set-up that couples small-angle light scattering to a stress-controlled shear cell described in chapter 3. The microscopic structure of the sample is monitored as a

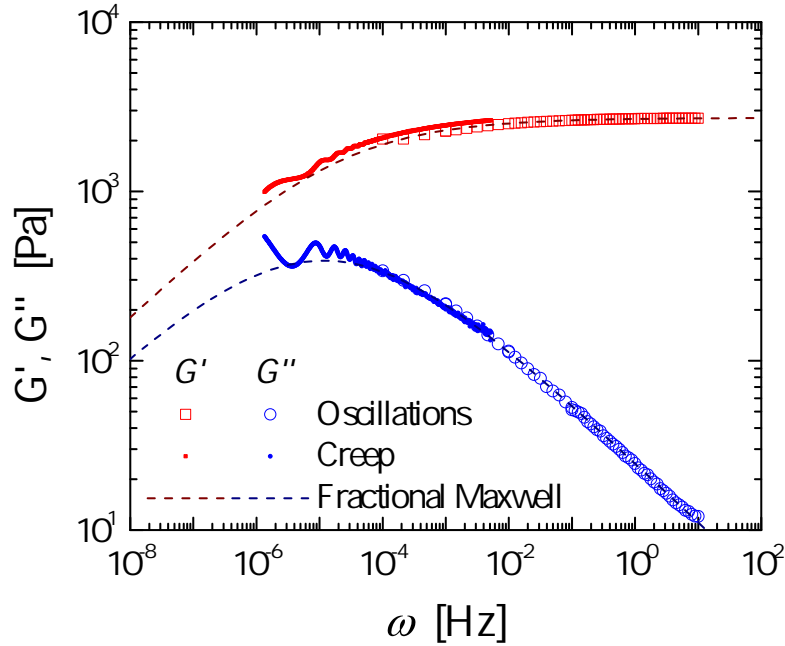


Figure 5.8: Comparison between viscoelastic moduli probed in small amplitude oscillatory strain at $\gamma_0 = 0.1\%$ amplitude (large empty data points) and creep under a constant shear stress $\sigma_0/G_0 = 1.8\%$ (small filled data points) for a sample age $t_w = 5 \cdot 10^5$ s. Dashed lines represent best fits using the Fractional Maxwell model.

function of time during sample deformation for rheological tests similar to those performed in a classical rheometer and presented above. Over the range of wave-vectors q accessible (between 0.4 and 4 μm^{-1}), the scattered intensity does not evolve, suggesting that the structure of the colloidal gel is fundamentally preserved under deformation in the linear regime.

However, as the sample is sheared, a small anisotropy (a few percent) in the static structure factor is detected. We measure that the intensity of the light scattered in the direction perpendicular to the shear direction, $I(\vec{q}_\perp)$, is constant, whereas the one scattered in the parallel direction, $I(\vec{q}_\parallel)$, changes roughly linearly with the macroscopic deformation. To quantify this effect, we define a static anisotropy parameter as $\chi(q) = [I(\vec{q}_\parallel) - I(\vec{q}_\perp)] / [I(\vec{q}_\parallel) + I(\vec{q}_\perp)]$. Figure 5.11a shows that the anisotropy parameter $\chi(q)$ plotted for $q = 2.6 \mu\text{m}^{-1}$ nicely follows the evolution of the strain when the sample is submitted to an oscillatory stress with $\sigma_0/G_0 = 5.5\%$. Similarly, χ follows the time evolution of the measured macroscopic strain during a creep and creep recovery experiment (Fig. 5.11b). More quantitatively, we plot χ as a function of the strain amplitude γ_e in Fig. 5.11b. We can empirically model the observed asymmetry with the linear relation $\chi(q, \gamma) = k(q)\gamma$, with the factor $k(q)$ being a phenomenological proportionality constant. In the range of accessible scattering vector, from 0.3 to 3 μm^{-1} , we find that $k(q)$ decreases, roughly linearly, with decreasing q , from around 0.26 at $q = 3 \mu\text{m}^{-1}$ to a value too small to be measurable below $q = 0.4 \mu\text{m}^{-1}$.

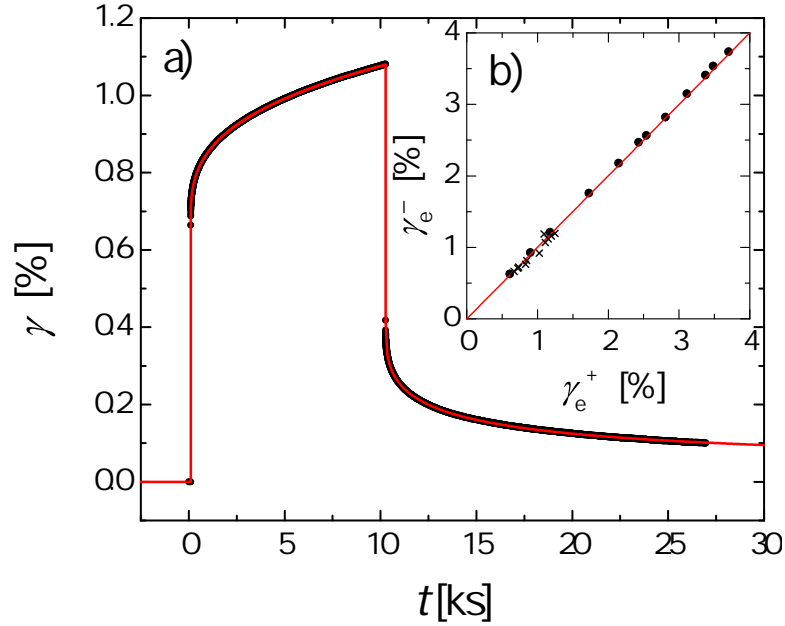


Figure 5.9: (a) Viscoelastic creep under a constant shear stress $\sigma_0 = 30\text{Pa}$, lasting a time $T = 10000\text{s}$ (black) and followed by creep recovery, for a sample with age $t_w \approx 5 \cdot 10^5\text{s}$. Symbols are experimental data and line is a fit with the FM model. (b) Recovery downwards jump γ_e^- plotted as a function of the instantaneous upward elastic jump $\gamma_e^+ = \sigma_0/G_0$. Red line represents the expected $\gamma_e^+ = \gamma_e^-$ behavior.

5.5 Discussion

Overall the rheological data show that the sample viscoelasticity can be perfectly accounted for by the FM model showing that measurements have been taken in the linear regime. As mentioned in the introduction, an expression linking fractal dimension and power-law rheology can be borrowed from the work of Muthukumar [Muthukumar 1989] on critical gels. In the limit of screened hydrodynamic and excluded volume interactions, α is related to the fractal dimension d_f through the expression: $\alpha = [3(5-2d_f)]/[2(5-d_f)]$. Using this expression we find that the slight decrease of the exponent of the FM model, α , with sample age, from 0.45 to 0.35 (Fig. 5.5) would correspond to a fractal dimension slightly increasing from $d_f = 2.05$ to 2.15. Within the experimental error, this prediction is in excellent agreement with the value of d_f extracted from our scattering data (Fig. 5.2). Moreover, while a true argument justifying the screening effect is missing, we remark that a slow increase in d_f is a well known effect of aging in colloidal gels [Cipelletti 2000] and can thus provide a straightforward explanation of the trend observed in rheology.

This result further strengthens the connection between the fractal structure and the power law rheology, extending it beyond the framework of critical gels. This is actually intriguing, since the original derivation [Muthukumar 1989] was based on the assumption that the structure was scale-free, whereas in our case the fractal cluster size ξ clearly

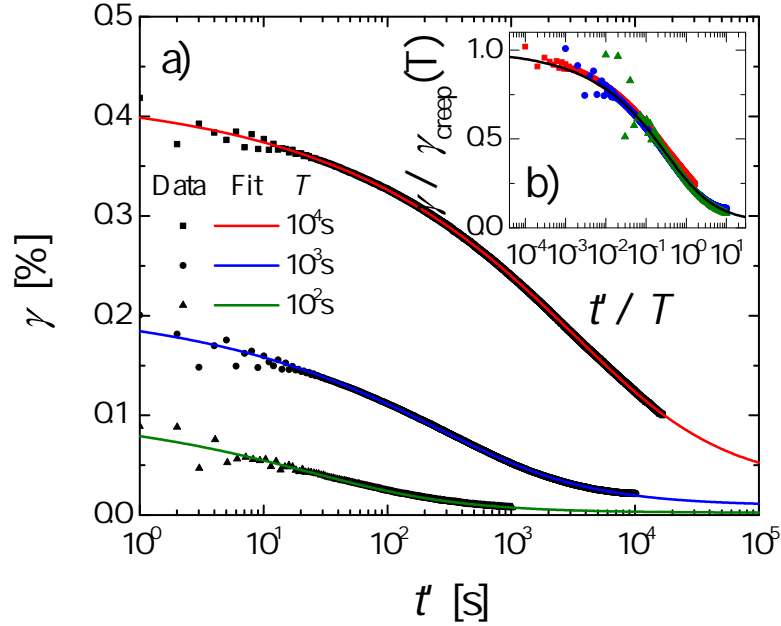


Figure 5.10: (a) Creep recovery curves following creep under a stress $\sigma_0 = 30\text{Pa}$ lasting T seconds, as specified in the legend. (b) Same data plotted in rescaled units, $\gamma_{rec}/\gamma_{creep}$ as a function of the rescaled time t'/T , as in Eq. 5.9. The sample age is $t_w \approx 5 \cdot 10^5\text{s}$.

emerges from Fig. 5.2 as a characteristic lengthscale of the system.

The presence of a cluster network of well defined connectivity challenges the validity of the FM model at the smallest frequencies. The power-law distribution of relaxation times assumed by the model implies for instance that the creep deformation reaches arbitrarily large values at times long enough, whereas one should expect a saturation to a terminal plateau deformation at long times somewhere beyond τ_{FM} . Unfortunately, such timescales are experimentally inaccessible, since the characteristic time grows linearly with sample age: as a consequence, any experiment probing a timescale beyond τ_{FM} would automatically be affected by aging. For this reason, the only way to test the consistency of FM at very small frequencies would be to repeat this analysis on different samples, for example changing the volume fraction. Based on a rough analysis with the time-cure superposition for polymer gels as suggested by Adolf and Martin [Adolf 1990] and discussed in the introduction, one might expect that, with increasing volume fraction, the sample would be increasingly far away from the critical gel point: the range of lengthscales displaying self-similarity would be thus reduced and consequently one might expect an eventual terminal plateau to be shifted at higher frequencies.

On the other hand, we also observe that the impossibility of addressing the putative loss peak around τ_{FM} in any clean experiment whatsoever somehow questions its physical relevance. The usual interpretation of a fractional rheological model is based on the existence of a power-law distribution of relaxation times, of which τ_{FM} should represent some average value. However, one could argue about what physical interpreta-

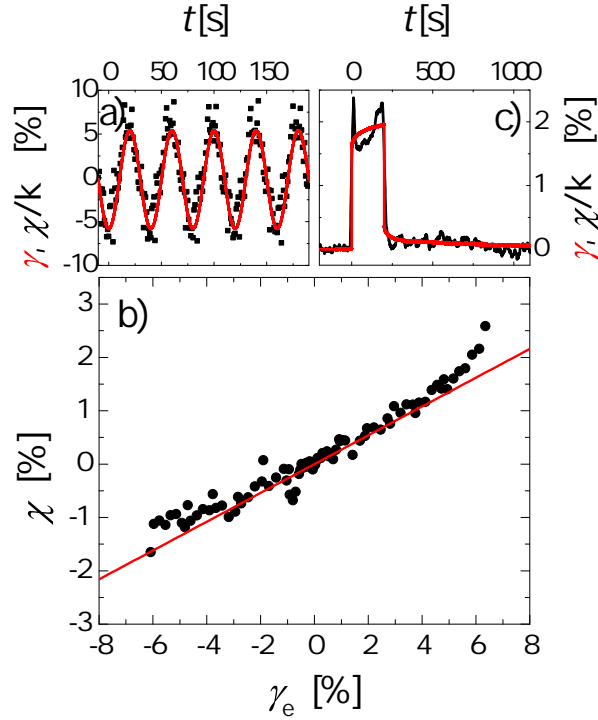


Figure 5.11: (a) Black curve: oscillating strain under an oscillating stress of amplitude $\sigma_0/G_0 = 5.5\%$. Red curve: static asymmetry $\chi(q)$ measured at $q = 2.6\mu\text{m}^{-1}$ divided by the proportionality constant $k(q)$ discussed in the text. (b) Symbols: static asymmetry $\chi(q)$ observed under a step strain deformation of amplitude γ_e . Positive and negative γ_e values represent step strains in opposite directions. Red line: linear fit of the small deformation regime, used to extract the proportionality constant $k(q)$. (c) Black curve: creep deformation and recovery after a creep time $T = 200\text{s}$. Red curve: static asymmetry $\chi(q)$ divided by $k(q)$.

tion should be attributed to relaxation times beyond the characteristic time for physical aging. Indeed, physical aging represents a true challenge for the fractional calculus-based framework presented in this paper, an ingredient that must be manually and somehow artificially introduced in the model in order to account for the experimental data, and which complicates its physical interpretation. Therefore, one might wonder whether a more natural framework could exist to account for both the power law rheology and its time dependence. One potential candidate in this regard is represented by Soft Glassy Rheology (SGR) [Sollich 1997], which considers that the sample mechanics is controlled by disorder, metastability and local structural rearrangements. The advantage of SGR is that aging emerges as a natural consequence of these features, and SGR predicts a virtual structural relaxation time linearly increasing with sample age [Fielding 2000], compatible with our findings. Within this framework, our gel would be represented by an effective "noise temperature" $x = 1 - \alpha \sim 0.6$, well below the glass transition (in SGR occurring at $x = 1$). In this region, the frequency spectrum of the sample would be characterized

by a nearly constant elastic modulus G' and a loss modulus $G'' \sim \omega^{x-1}$ [Sollich 1998], which is in good agreement with the data in the experimentally accessible frequency range (Fig. 5.8). However, one feature that appears to be in stark contrast with the picture offered by SGR is the complete reversibility of the deformation, as it is demonstrated by the creep recovery experiments (see e.g. Fig. 5.10), whereas in SGR creep is never completely recoverable, and the non-recoverable amount depends on the creep duration. Moreover, SGR predicts a logarithmic creep in the glassy regime ($x < 1$) [Fielding 2000], which is clearly incompatible with our experimental data (Fig. 5.6). On the one hand, these considerations explicitly demonstrate that a thorough comparison between different rheological experiments allows one to discriminate between models that would be indistinguishable only looking at one experiment, say oscillatory rheology. On the other hand, they raise the question of whether some concepts of SGR could be borrowed to provide a more natural framework to introduce aging in fractional models. This could represent an intriguing perspective for future theoretical works, towards a deeper understanding of the microscopic origin of power-law rheology.

Microscopic dynamics and failure precursors of a gel under mechanical load

Under a constant shear stress (creep experiment), the colloidal gel exhibits a fast, elastic deformation followed by a slow sublinear power-law creep, which is eventually interrupted after several hours by an upturn in the shear rate, leading to the delayed failure of the material. Our experiments show that the first power-law regime, nicely described by linear viscoelasticity, corresponds at the microscopic scale to partially nonaffine, yet fully reversible dynamics. Upon deviation from the linear viscoelasticity, a sharp acceleration, localized in time of the nonaffine dynamics is observed. These faster rearrangements precede the macroscopic failure of the gel by thousands of seconds: they thus are dynamic precursors of failure that allow one to predict the fate of the gel well before any rheological measurement. We discuss all these features in a paper published in the Proceedings of the National Academy of Sciences of the United States of America (PNAS) journal [Aime 2018].



Microscopic dynamics and failure precursors of a gel under mechanical load

Stefano Aime^{a,1}, Laurence Ramos^{a,1}, and Luca Cipelletti^{a,1,2}

^aUniversity of Montpellier, CNRS, 34095 Montpellier, France

Edited by David A. Weitz, Harvard University, Cambridge, MA, and approved February 27, 2018 (received for review October 4, 2017)

Material failure is ubiquitous, with implications from geology to everyday life and material science. It often involves sudden, unpredictable events, with little or no macroscopically detectable precursors. A deeper understanding of the microscopic mechanisms eventually leading to failure is clearly required, but experiments remain scarce. Here, we show that the microscopic dynamics of a colloidal gel, a model network-forming system, exhibit dramatic changes that precede its macroscopic failure by thousands of seconds. Using an original setup coupling light scattering and rheology, we simultaneously measure the macroscopic deformation and the microscopic dynamics of the gel, while applying a constant shear stress. We show that the network failure is preceded by qualitative and quantitative changes of the dynamics, from reversible particle displacements to a burst of irreversible plastic rearrangements.

failure | colloidal gels | rheology | light scattering | plasticity

Material failure is ubiquitous on length scales ranging from a few nanometers, as in fracture of atomic or molecular systems (1, 2), up to geological scales, as in earthquakes (3, 4). While some attempts have been made to harness failure—for example, to produce new materials with a well-controlled patterning (5)—material failure remains in general an unwanted, uncontrolled, and unpredictable process, widely studied since the pioneering experiments on metallic wires by Leonardo da Vinci in the 15th century (6). Indeed, a better control of the conditions under which material failure may or may not occur and the detection of any precursors that may point to incipient failure are the Holy Grail in many disciplines, from material science (7–10) to biology (11, 12), engineering, and geology (13–16). Failure may occur almost instantaneously, as a consequence of an impulsive load. Often, however, it manifests itself in more elusive ways, as in the sudden, catastrophic breakage of a material submitted to a constant load, where failure may be preceded by a long induction time with little if any precursor signs of weakening. Such delayed failure has been reported in a wide spectrum of phenomena, from earthquakes (17), snow avalanches (18), and failure in biomaterials (11, 12) to the sudden yielding of crystalline (1) solids, composite materials (10, 19), and amorphous systems (20), including viscoelastic soft materials (21, 22), such as adhesives (23) and network-forming materials (24–28).

Delayed failure typically involves creep during the induction time, the sublinear (e.g., power law) increase of sample deformation under a constant load. The microscopic origin of creep is well understood for crystalline solids, where it is attributed to defect motion (29, 30). Power-law creep is also widespread in amorphous materials, but its microscopic origin remains controversial: It has been attributed to the accumulation of irreversible, plastic rearrangements (19, 21, 22, 31, 32), to linear viscoelasticity (12, 28, 33), or to a combination of both (34), with different authors holding contrasting views on similar systems (19, 34). Crucially, a detailed understanding of the creep regime holds the promise of unveiling the origin of the sudden failure of the material, potentially revealing any precursor signs of failure, which are difficult to detect by monitoring macroscopic quantities, such as

the deformation rate (10), or mesoscopic, coarse-grained shear velocity maps (28). Clearly, investigations of the evolution of the microscopic structure and dynamics under creep are required, which are however very scarce to date and essentially restricted to numerical works (35).

Here, we address these questions by studying the microscopic dynamics of a soft solid submitted to a constant shear stress, using a unique custom-made apparatus (36, 37) that couples stress-controlled rheology to small-angle static and dynamic light scattering (see *Supporting Information* for details on the sample and setup geometry). We focus on a gel made of attractive colloidal particles, a model system for network-forming soft solids, which are ubiquitous in soft matter (38) and in biological materials (39). Initially, particles in the gel network undergo both affine (as in ideal elastic solids) and nonaffine displacements, but all displacements are fully reversible. Thus, the initial regime of creep is not due to plasticity but rather to the complex viscoelastic response of the gel network. At larger strains, by contrast, the dynamics are due to irreversible plastic rearrangements that progressively weaken the network, eventually leading to the gel failure. Strikingly, this plastic activity does not increase steadily until failure but rather has a nonmonotonic behavior, peaking thousands of seconds before the macroscopic rupture. Our work thus establishes the notion of dynamic precursor as a powerful tool to understand and predict sudden material failure.

The gel is formed in situ by triggering the aggregation of an initially stable suspension of silica nanoparticles via an enzymatic reaction (see *Materials and Methods*). The nanoparticles have

Significance

The sudden, catastrophic failure of materials under a constant mechanical load is widespread, occurring from geological scales, as in earthquakes, to biological and soft-matter systems, as in protein, polymer, and colloidal gels. Failure is often preceded by a long induction time, with little if any macroscopic signs of weakening, making it unpredictable. Here, we investigate the failure of a model colloidal gel under a constant load, measuring simultaneously its mechanical response and microscopic dynamics. We show that the gel undergoes a burst of microscopic plastic rearrangements that largely precede failure, undetectable by monitoring conventional structural quantities. The notion of a dynamic precursor thus emerges as a powerful tool to understand and predict the sudden failure of solids.

Author contributions: L.R. and L.C. designed research; S.A. performed research; S.A., L.R., and L.C. analyzed data; and L.R. and L.C. wrote the paper.

The authors declare no conflict of interest.

This article is a PNAS Direct Submission.

Published under the PNAS license.

¹S.A., L.R., and L.C. contributed equally to this work.

²To whom correspondence should be addressed. Email: luca.cipelletti@umontpellier.fr.

This article contains supporting information online at www.pnas.org/lookup/suppl/doi:10.1073/pnas.1717403115/-DCSupplemental.

radius $a = 26$ nm and occupy a volume fraction $\varphi = 5\%$. Gelation occurs within 3 h, resulting in a network formed by fractal clusters with typical size $\xi \sim a\varphi^{1/(d_f-3)} \sim 0.5$ μm (40, 41) and fractal dimension $d_f = 2$. All experiments are performed at least 48 h after gelation, when the gel viscoelastic properties do not evolve significantly with sample age. Under a constant load, the gel exhibits delayed failure, a feature reported for many network-forming systems (24–28). Fig. 1 demonstrates delayed failure for our gel, by showing the time evolution of the shear strain γ and of the strain rate $\dot{\gamma}$ upon imposing a constant stress $\sigma_0 = 240$ Pa at time $t = 0$. On time scales shorter than those shown in Fig. 1 ($t < 1$ s), the gel responds elastically: γ jumps to an elastic shear deformation $\gamma_e \sim 4.8\%$, corresponding to a shear modulus $G = \sigma_0/\gamma_e = 5000$ Pa, consistent with the low-frequency elastic modulus G' measured in oscillatory rheology tests (see *Materials and Methods*). Following the elastic jump, γ grows sublinearly: Both the deformation in excess of the elastic response, $\gamma - \gamma_e$, and the shear rate follow power laws, well accounted for by a generalized, or fractional, Maxwell viscoelastic model (42), $\gamma(t) - \gamma_e = \gamma_e \Gamma^{-1}(\alpha)(t/\tau_{FM})^\alpha$, with $\alpha = 0.43 \pm 0.01$, $\tau_{FM} \gtrsim 10^5$ s, and $\Gamma(x)$ the Gamma function. Remarkably, this creep regime extends over more than four decades in time, until the gel abruptly fails at $t \approx 2.8 \times 10^4$ s, as signaled by the sharp upturn of both γ and $\dot{\gamma}$.

To investigate the relationship between the sudden macroscopic failure of the gel and its microscopic evolution, we inspect static and dynamic light-scattering data collected simultaneously to the rheology measurements (see Fig. 1) (36). Light scattering probes density fluctuations as a function of wavevector \mathbf{q} : $I(\mathbf{q}) \propto \sum_{j,k} \exp[-i\mathbf{q} \cdot (\mathbf{r}_j - \mathbf{r}_k)]$, with I the scattered intensity, \mathbf{r}_j the position of the j -th particle, and \mathbf{q} the scattering vector (see *Materials and Methods*). We use a custom-designed small angle setup (37) based on a complementary metal-oxide-semiconductor (CMOS) detector, allowing measurements on length scales $\sim \pi/q$ in the range 0.8 $\mu\text{m} - 10$ μm , compara-

ble to or larger than the cluster size ξ . At rest, the scattering pattern depends only on the magnitude of \mathbf{q} , since the gel is isotropic. During creep, the q dependence of the scattered intensity hardly changes, indicating that the gel structure is fundamentally preserved until sample failure. However, a small anisotropy develops in the static structure factor, similar to that observed for other sheared soft solids (43). We quantify this asymmetry by $\chi(q) = [I(\mathbf{q}_{\parallel}) - I(\mathbf{q}_{\perp})] / [I(\mathbf{q}_{\parallel}) + I(\mathbf{q}_{\perp})]$, with $|\mathbf{q}_{\parallel}| = |\mathbf{q}_{\perp}|$ and where \parallel and \perp refer to orientations of the scattering vector parallel and perpendicular to the shear direction, respectively. The *Inset* of Fig. 1 shows the time dependence of χ . We find that the asymmetry follows the same trend as $\gamma(t)$ —that is, that χ is proportional to γ throughout the whole experiment, up to failure. Moreover, the proportionality coefficient is the same as that measured in independent oscillatory experiments in the linear, reversible regime. Thus, structural quantities simply reflect the macroscopic shear deformation, without providing additional information on the fate of the gel.

We now show that the microscopic dynamics are a much more sensitive probe of the gel evolution, unveiling dramatic plastic events that weaken the network thousands of seconds before its macroscopic failure. We measure the two-time intensity correlation function $g_2(\mathbf{q}, t_1, t_2) - 1 \propto |g_1(\mathbf{q}, t_1, t_2)|^2$, with g_1 the field correlation, or intermediate scattering, function (44) (see *Materials and Methods*). The correlation function is measured simultaneously for several \mathbf{q} vectors; Fig. 2A shows representative $g_2 - 1$ measured at various times t_1 during the creep, for $q = 3.1$ μm^{-1} . As for the static intensity, we analyze data separately for scattering vectors parallel and perpendicular to the shear direction. The curves for \mathbf{q}_{\parallel} (green symbols in Fig. 2A) exhibit a full decay on timescales that grow during creep, eventually reaching $\approx 10^3$ s. The behavior for \mathbf{q}_{\perp} is more complex: Initially, $g_2 - 1$ decays to a quasi-plateau, while a two-step relaxation leading to an almost complete decorrelation is seen at later times. Throughout the experiment, the dynamics along \mathbf{q}_{\parallel} are faster than for \mathbf{q}_{\perp} . This can be understood by decomposing the particle displacement in its affine and nonaffine components: $\mathbf{r}(t_2) - \mathbf{r}(t_1) = \mathbf{u}_0(t_1, t_2) + \mathbf{u}_{na}(t_1, t_2)$. For a particle with coordinate z in the direction of the shear gradient, the affine component is $\mathbf{u}_0 = (\gamma_2 - \gamma_1)z\hat{\mathbf{e}}_{\parallel}$, with $\gamma_i = \gamma(t_i)$ and $\hat{\mathbf{e}}_{\parallel}$ the unit vector parallel to the shear direction. Because $\hat{\mathbf{e}}_{\parallel} \cdot \mathbf{q}_{\perp} = 0$, correlation functions measured for \mathbf{q}_{\perp} are only sensitive to \mathbf{u}_{na} , the nonaffine component of the displacement, while the decay of $g_2(\mathbf{q}_{\parallel}, t_1, t_2) - 1$ reflects both affine and nonaffine motions, resulting in a faster relaxation. In principle, additional contributions to $g_2 - 1$ may also stem from the spontaneous, thermally activated dynamics of the gel (45). However, here this contribution is negligible (see dashed line in Fig. 2A). Thus, the microscopic dynamics is only related to the shear deformation: This suggests analyzing the dynamics as a function of strain increment rather than time delay.

Fig. 2B shows the same data as in Fig. 2A, replotted versus the strain increment $\Delta\gamma = \gamma_2 - \gamma_1$. A remarkable collapse is seen for the \mathbf{q}_{\parallel} data, independent of γ_1 . This indicates that motion in the $\hat{\mathbf{e}}_{\parallel}$ direction is dominated by affine displacements, for which \mathbf{u}_0 is proportional to $\Delta\gamma$, regardless of the cumulated strain. We confirm this interpretation by calculating $g_2(\mathbf{q}_{\parallel}) - 1$ for a purely affine shear deformation (see *Materials and Methods*): The result (line in Fig. 2B) is indeed very close to the data, ruling out sample slip or shear banding, which would result in significant deviations of $g_2 - 1$ with respect to its theoretical form. Note, however, that the data lay slightly below the theoretical curve, showing that a small nonaffine component must also be present. Nonaffine motion is better resolved by inspecting the \mathbf{q}_{\perp} correlation functions, which are insensitive to the affine component.

In the following, we thus focus on the microscopic dynamics in the direction perpendicular to shear, which probes only

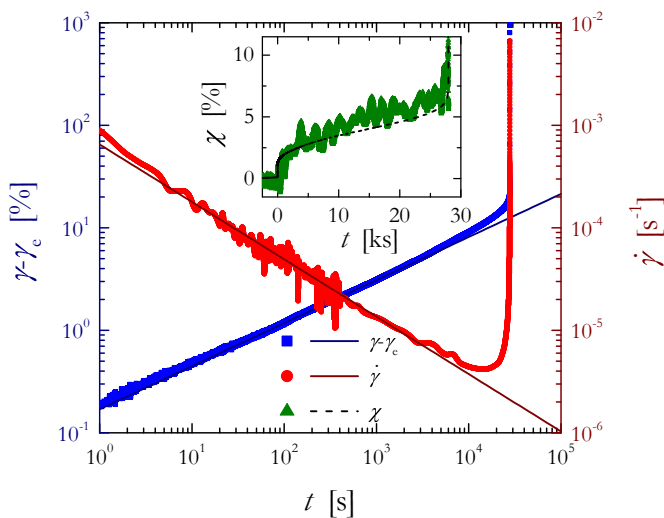


Fig. 1. Mechanical response and structure evolution of a colloidal gel during creep. Main plot: deformation in excess of the elastic jump $\gamma_e = 4.8\%$ (blue squares, left axis) and shear rate (red circles, right axis) following a step shear stress of amplitude $\sigma_0 = 240$ Pa, applied at time $t = 0$. Lines: power law fits to the data in the initial creep regime ($1 \text{ s} \leq t \leq 10^4 \text{ s}$), yielding an exponent $\alpha = 0.43 \pm 0.01$ in the generalized Maxwell viscoelastic model. (*Inset*) Anisotropy χ of the scattered intensity as a function of t , for $q_{\perp} = q_{\parallel} = 2.6$ μm^{-1} . Triangles: data for the creep test. Line: anisotropy as obtained from $\chi = k\gamma(t)$, with the proportionality coefficient $k = 0.26$ determined in independent oscillatory experiments in the linear regime. Solid and dashed lines correspond to the linear regime and to an extrapolation in the nonlinear regime, respectively.

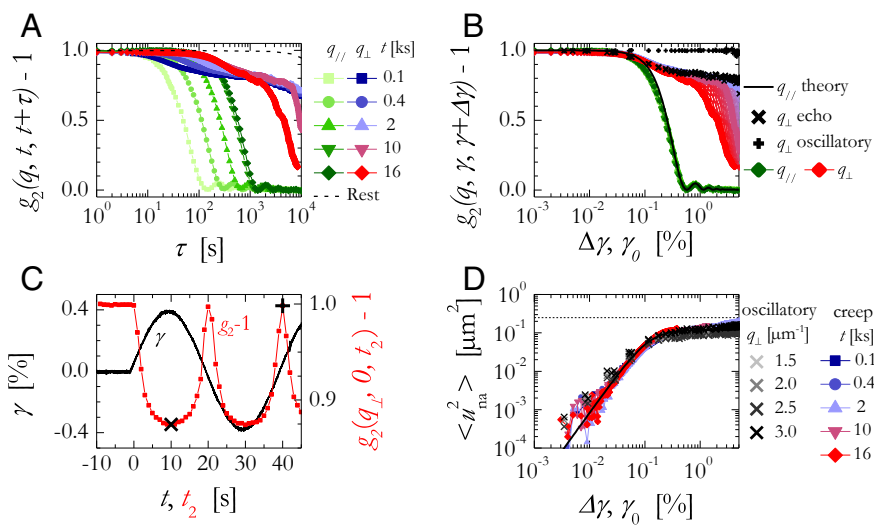


Fig. 2. Microscopic dynamics of the gel during creep. (A) Time correlation functions, $g_2 - 1$, measured in the q_{\parallel} (green) and q_{\perp} (blue to red shades) directions, as a function of time lag τ , for $q = 3.1 \mu\text{m}^{-1}$ and for representative times t after applying a stress step. Black dashed line: spontaneous isotropic dynamics measured on the same sample but at rest. (B) Solid symbols: same data as in A, plotted as a function of the strain increment $\Delta\gamma$. Additional datasets for intermediate t are shown as small symbols. Line: $g_2 - 1$ calculated assuming a purely affine deformation. +, \times : data collected in independent oscillatory experiments following the protocol shown in C. \times : maximum decorrelation during a shear cycle of amplitude γ_0 ; +: correlation echo after a full cycle. (C) Shear deformation and correlation function during a shear cycle of amplitude $\gamma_0 = 0.4\%$. \times and + indicate the correlation values reported in B. (D) Nonaffine mean square displacement vs. strain increment during creep (solid symbols) and vs. γ_0 in oscillatory experiments. The dashed line corresponds to the squared cluster size. The solid line is a fit to the data using $\langle u_{na}^2 \rangle = u_{\infty}^2 \frac{\gamma_0^2}{\gamma_0^2 + \gamma_c^2}$, with $u_{\infty}^2 = 0.12 \mu\text{m}^2$ and $\gamma_c = 0.12\%$.

nonaffine displacements. We shall first discuss the linear viscoelastic regime, where we will show that microscopic displacements are fully reversible, and then the nonlinear regime, where irreversible, plastic rearrangements come into play, ultimately causing the gel failure. In the initial regime, $\gamma - \gamma_e \leq 4\%$ ($t \leq 2000$ s, blue shades in Fig. 2B), all data collapse onto a master curve, exhibiting a decay to a quasi-plateau. This collapse is remarkable and sheds light on the nature of the nonaffine deformation observed in the initial regime of the creep. For an ideal solid, the displacement under a shear deformation is purely affine. Nonaffine displacements indicate a departure from this ideal behavior, which may stem from two different physical mechanisms: elastic, reversible response, but with spatial fluctuations of the elastic modulus (46–49), or plastic, irreversible rearrangements (50). The fact that $g_2(\mathbf{q}_{\perp}, \gamma_1, \gamma_2) - 1$ is independent of the cumulated strain suggests that no plastic events occur in the initial creep regime. We test this hypothesis by measuring reversibility at the microscopic level in separate oscillatory shear experiments, following the “echo” protocol of refs. 51–53. As shown in Fig. 2C, the sample is submitted to a sinusoidal deformation, $\gamma(t) = \gamma_0 \sin(\omega t)$. The overlap between the initial microscopic configuration and a sheared one is quantified by $g_2(\mathbf{q}_{\perp}, t=0, t_2) - 1$. We focus on the maximum of $g_2 - 1$ at the correlation echo, after one full cycle (+ in Fig. 2C), and on its first minimum ($t_2 = 10$ s, \times in Fig. 2C). By repeating the measurements for several γ_0 , we obtain the plus and cross symbols displayed in Fig. 2B, for the maximum and the minimum level of correlation, respectively. Up to $\gamma = 4\%$, we find no loss of correlation upon setting back to zero the macroscopic deformation; furthermore, the crosses follow the same master curve as the creep data. This confirms that for $t \leq 2000$ s, the creep is not due to plastic rearrangements but rather to the slow, fully recoverable deformation of the elastically heterogeneous network, at fixed connectivity. To characterize the strain dependence of nonaffinity, we extract the nonaffine mean-squared displacement $\langle u_{na}^2 \rangle$ via $g_2(\mathbf{q}_{\perp}, \Delta\gamma) - 1 = \exp(-\mathbf{q}_{\perp}^2 \langle u_{na}^2(\Delta\gamma) \rangle / 3)$, the analogous in the strain domain of the usual relationship between correlation functions and mean squared displacement in the low q limit (44). As seen in Fig.

2D, data collected at various q collapse on the same curve, confirming the q^2 scaling. Initially, $\langle u_{na}^2 \rangle$ grows as $\Delta\gamma^2$, eventually saturating to a plateau $\approx 0.1 \mu\text{m}^2$. The quadratic dependence of $\langle u_{na}^2 \rangle$ on strain is the analogous of ballistic dynamics in the time domain; it is the signature of elastic response in an heterogeneous medium (47) and was recently reported for a polymer network (46). The nonaffine displacement saturates at a value close to the cluster size (dotted line in Fig. 2D), consistent with the physical picture that the gel structure cannot be remodeled on length scales larger than the network mesh size without changing its connectivity—that is, without any plastic rearrangements.

We now turn to the $\gamma - \gamma_e > 4\%$ regime ($t > 2000$ s, red shades in Fig. 2B), where $g_2 - 1$ exhibits a two-step relaxation. The initial decay overlaps with that observed at early times, due to reversible nonaffine deformation. The final decay of $g_2(\mathbf{q}_{\perp}) - 1$ indicates additional dynamics, which lead to the relaxation of density fluctuations on length scales comparable to or larger than ξ . In this regime, the macroscopic deformation is not recovered upon releasing the applied stress: We thus attribute the additional dynamics to irreversible plastic rearrangements. To investigate the evolution of plastic dynamics during creep, we show in Fig. 3 the intensity correlation function for several scattering vectors and a fixed strain increment $\Delta\gamma = 5\%$, versus cumulated strain. This quantity is directly related to the amount of plastic rearrangements occurring over $\Delta\gamma$. Strikingly, all curves exhibit a negative peak, indicating that the gel undergoes a burst of plastic activity for $13\% \lesssim \gamma \lesssim 22\%$. Remarkably, the minimum of $g_2 - 1$ occurs at $\gamma \approx 17\%$ ($t = 1.9 \times 10^4$ s), as much as 9,000 s before the gel fails, for $\gamma \approx 30\%$. Fig. 3 reveals that the minimum is more pronounced for the largest \mathbf{q}_{\perp} vectors. Thus, the burst of plastic activity is better seen when probing the dynamics on small length scales, which suggests that macroscopic quantities should be less sensitive to such burst. This is indeed the case for the macroscopic strain: As seen in Fig. 1, only a slight deviation from the sublinear creep is seen around $t = 1.9 \times 10^4$ s, at the burst maximum. The strain rate is a more sensitive quantity: Fig. 3 shows that the onset of plasticity coincides with the departure of $\dot{\gamma}$ from its power law behavior in the linear regime (dotted

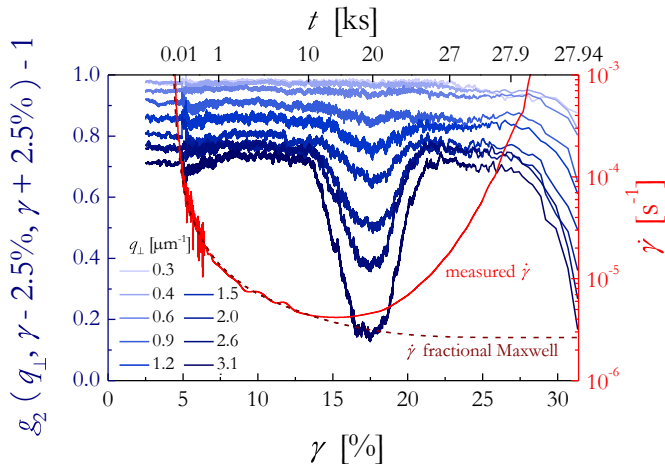


Fig. 3. Microscopic dynamics signals the onset of plasticity. $g_2(\mathbf{q}_\perp, \gamma - \Delta\gamma/2, \gamma + \Delta\gamma/2) - 1$ vs. γ . Right axis, red line: macroscopic deformation rate $\dot{\gamma}$ vs. cumulated shear deformation during creep. Dashed line: generalized, or fractional, Maxwell model. Left axis, blue curves: microscopic non-affine dynamics over a fixed strain increment $\Delta\gamma = 5\%$, for various \mathbf{q}_\perp as indicated by the labels.

line), thus establishing a direct connection between microscopic dynamics and macroscopic creep (see [Supporting Information](#) for a detailed comparison between mechanical and dynamical signatures of plasticity).

To quantify the microscopic plastic activity during creep, we develop a simple model for dynamic light scattering under time-varying conditions. Using strain as the relevant variable and focusing on the dynamics along \mathbf{q}_\perp , we assume that reversible and plastic displacements are uncorrelated processes, leading to the factorization $g_1(\mathbf{q}_\perp, \gamma_1, \gamma_2) = R(\mathbf{q}_\perp, \Delta\gamma)P(\mathbf{q}_\perp, \gamma_1, \gamma_2)$, with R and P the contributions due to reversible and plastic displacements, respectively, and where R only depends on the strain increment, as indicated by the experiments. For a stationary process, a general form that captures well different kinds of dynamics is $g_1 = \exp[-f(q)(A\Delta\gamma)^p]$. The initial decay of the correlation function in the linear, reversible regime discussed in reference to Fig. 2 is an example of this functional form, with $f \sim q^2$, $p = 2$, and A the constant, nonaffine root-mean-square particle displacement per unit strain increment. We generalize this form by expressing $P(\mathbf{q}_\perp, \gamma_1, \gamma_2)$ as a function of a strain-dependent plastic activity per unit strain increment, $A(\gamma)$:

$$g_1(\mathbf{q}_\perp, \gamma_1, \gamma_2) = R(\mathbf{q}_\perp, \Delta\gamma) \exp\left[-f(\mathbf{q}_\perp) \left(\int_{\gamma_1}^{\gamma_2} A(\gamma) d\gamma\right)^p\right]. \quad [1]$$

We extract $f(\mathbf{q}_\perp)^{1/p} A(\gamma)$ from the experimental data using Eq. 1 and assuming that $R(\mathbf{q}_\perp, \Delta\gamma)$ is the same as in the reversible regime of creep (see [Materials and Methods](#) for details). The results are shown in Fig. 4A, for several \mathbf{q}_\perp vectors. Consistent with the findings for the correlation function at a specific strain increment, Fig. 3, the plastic activity per unit strain exhibits a nonmonotonic behavior, with a peak centered around $\gamma = 17.1\%$. The height of the peak strongly increases with q . According to our model, this is due to the q dependence of the prefactor f , since the plastic activity A is a quantity intrinsic to the gel and is thus independent of the probed length scale. We test this assumption by plotting in Fig. 4B the plastic activity scaled by its peak value, A_0 . An excellent collapse is seen for data spanning a factor of 5 in q vectors, thereby confirming the soundness of the model.

To gain insight into the nature of the plastic dynamics, we inspect the q dependence of the prefactor $f(\mathbf{q}_\perp)A_0^p$ and of the exponent p . For $q_\perp \leq 1.5 \mu\text{m}^{-1}$, the prefactor scales as q^2 (see Fig. 4C, where the q^2 dependence has been factored out) and $p \approx 1$. Under these conditions, the contribution of plasticity to the decay of the correlation function over a small strain increment reads $P(\mathbf{q}_\perp, \gamma, \gamma + \Delta\gamma) = \exp[-q_\perp^2 D(\gamma)\Delta\gamma]$, with $D(\gamma) \sim A(\gamma)$ a strain-dependent, but q -independent, diffusion coefficient. Thus, in the low q regime, the plastic dynamics are diffusive, since P is the analogous in the strain domain of the usual diffusive dynamics in the time domain, for which $g_1 = \exp[-q^2 D\tau]$ (44). A change of the plastic dynamics occurs beyond $q_\perp^* \approx 2 \mu\text{m}^{-1}$, corresponding to a length scale $\pi/q_\perp^* \approx 1.6 \mu\text{m}$, slightly larger than the cluster size. For $q_\perp \geq q_\perp^*$, fA_0^p grows sharply, increasingly departing from the q^2 scaling. Concomitantly, the p exponent grows up to $p \approx 1.75$ at the largest probed q vectors (Fig. 4C), approaching $p = 2$, the exponent characterizing ballistic dynamics. The emerging picture is that of plasticity consisting of irreversible rearrangements, most likely due to bond rupture. On small length scales (large q), the dynamics are strongly q dependent and are dominated by local motion associated with such rearrangements. On larger length scales (smaller q), the contribution of many events adds up, leading to a diffusive decay of density fluctuations. These events progressively weaken the network, eventually leading to its catastrophic failure.

The experiments reported here unveil the complex evolution of the microscopic dynamics during the creep of a colloidal gel, from reversible nonaffine motion due to the heterogeneous gel structure to a burst of plastic rearrangements that irreversibly weaken the network, providing a microscopic signature of the onset of plasticity. Remarkably, this dynamic precursor occurs

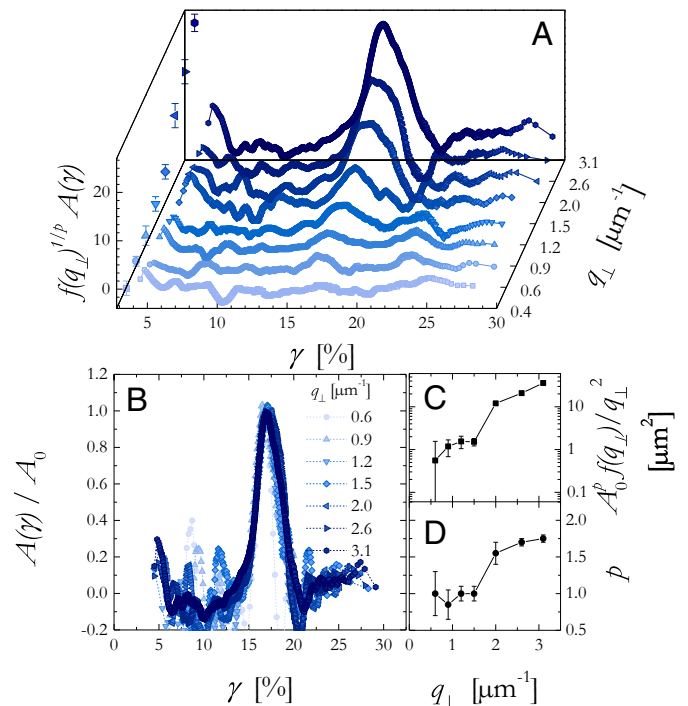


Fig. 4. Plastic activity as revealed by the microscopic dynamics. (A) Plastic activity per unit strain increment vs. cumulated strain, for various \mathbf{q}_\perp . The error bars on the left indicate the uncertainty resulting from averaging data collected at different $\Delta\gamma$. (B) Collapse of the plastic activity measured at various \mathbf{q}_\perp , as indicated by the labels. (C) q dependence of the plastic dynamics. Data are normalized by q^2 , the behavior expected for diffusive dynamics. (D) Exponent p characterizing the plastic dynamics (see Eq. 1), where $p = 1$ corresponds to diffusive dynamics.

midway through the creep. While further theoretical work will be needed to fully understand the origin of the precursor and its temporal location, we emphasize that its occurrence allows one to predict the ultimate fate of the network thousands of seconds before its catastrophic rupture. Ongoing experiments in our group reveal that similar dramatic changes of the microscopic dynamics largely precede failure in a variety of mechanically driven materials, from polymer gels to elastomers and semicrystalline polymers. The notion of dynamic precursor therefore emerges as a powerful concept to understand and predict material failure.

Materials and Methods

Enzyme-Induced Aggregation and Gel Formation. The gel results from the aggregation of a suspension of silica particles (Ludox TM50, from Sigma Aldrich, diameter $a = 26$ nm as determined by small angle neutron scattering, SANS), dispersed at a volume fraction $\varphi = 5\%$ in an aqueous solvent containing urea at 1 M. Particle aggregation is triggered by increasing in situ the ionic strength of the solvent, thanks to the hydrolysis of urea into carbon dioxide and ammonia, a reaction catalyzed by an enzyme (Urease U1500-20KU, from Sigma Aldrich, 35 U/mL) (54), whose activity depends on temperature T . The suspension is prepared at $T \approx 4^\circ\text{C}$ and brought at room temperature after loading the cell, thereby activating the enzyme and initiating aggregation. The sol-gel transition occurs ≈ 3 h after loading the sample in the shear cell. The fractal dimension of the gel network, $d_f = 2$, has been determined from independent SANS measurements on a gel prepared following the same protocol.

Oscillatory Rheology in the Linear Regime. We characterize the mechanical properties of the gel by measuring the frequency-dependent elastic and loss moduli [$G'(\omega)$ and $G''(\omega)$, respectively] in the linear regime ($\gamma_0 = 0.1\%$) using a commercial rheometer (MCR502 by Anton Paar). Over the range $10^{-3} \text{ rad s}^{-1} \leq \omega \leq 10 \text{ rad s}^{-1}$, G' is essentially flat and $G'' \sim \omega^{-0.4}$, a behavior consistent with the fractional Maxwell model that accounts for the gel creep. The gel slowly ages: G' increases as $t^{1/3}$, and the characteristic relaxation time τ_{FM} obtained from the fractional Maxwell model increases linearly with t . We let the gel age for 48 h before running a creep experiment, such that during the duration of one experiment (typically a few hours) the viscoelastic properties of the gel do not evolve significantly, with $G' \sim 5$ kPa and $\tau_{FM} \gtrsim 10^5$ s. The elastic modulus dominates over the loss modulus at all measured frequencies; for $\omega = 1$ Hz, $G'/G'' \approx 125$.

Light Scattering. The small-angle light-scattering apparatus is described in detail in ref. 37. In brief, the scattered light is collected by a lens system and forwarded to the detector of a CMOS camera, such that each pixel corresponds to a well-defined scattering vector \mathbf{q} , with $q = 4\pi n \lambda^{-1} \sin(\theta/2)$, where $n = 1.338$ is the solvent refractive index, $\lambda = 632.8$ nm the laser in vacuo wavelength, and θ the scattering angle. The \mathbf{q} -dependent intensity is obtained as $I(\mathbf{q}) = \langle I_p \rangle_{\mathbf{q}}$, where I_p is the CMOS signal of the p -th pixel, corrected for the dark background as in ref. 55, and $\langle \cdot \cdot \cdot \rangle_{\mathbf{q}}$ is an average over a small region in q space centered around \mathbf{q} . For the silica particles used here, the form factor ≈ 1 in the range of q covered by the setup, such that $I(\mathbf{q})$ is proportional to the static structure factor $S(\mathbf{q})$.

The two-time intensity correlation function is calculated as

$$g_2(\mathbf{q}, t_1, t_2) - 1 = \beta \frac{\langle I_p(t_1) I_p(t_2) \rangle_{\mathbf{q}}}{\langle I_p(t_1) \rangle_{\mathbf{q}} \langle I_p(t_2) \rangle_{\mathbf{q}}} - 1,$$

where $\beta \gtrsim 1$ is a setup-dependent prefactor chosen such that $g_2(\mathbf{q}, t_1, t_2) - 1 = 1$. The intensity correlation function is related to the field correlation function g_1 by $g_2 - 1 = |g_1|^2$ (44), with $g_1 = F(\mathbf{q}, t_1, t_2)/F(\mathbf{q}, t_1, t_1)$ and $F(\mathbf{q}, t_1, t_2) = N^{-1} \sum_{j,k=1}^N e^{i\mathbf{q} \cdot [\mathbf{r}_j(t_1) - \mathbf{r}_k(t_2)]}$, where the sum runs over the N particles in the scattering volume.

Intermediate Scattering Function for a Purely Affine Deformation. Following ref. 44 with strain, rather than time, as the independent variable, the intermediate scattering function is expressed as

$$g_1(\mathbf{q}, \Delta\gamma) = \int Q(\Delta\mathbf{r}) \exp(-i\mathbf{q} \cdot \Delta\mathbf{r}) d\Delta\mathbf{r}, \quad [\text{MM1}]$$

where $Q(\Delta\mathbf{r})$ is the probability distribution function of the particle displacement following a strain increment $\Delta\gamma$. For a purely affine deformation in the direction of $\hat{\mathbf{e}}_{\parallel}$, $Q(\Delta\mathbf{r}) = 1/(\Delta\gamma b)$ and $\Delta\mathbf{r} = z\Delta\gamma\hat{\mathbf{e}}_{\parallel}$, with b and z the cell gap and the coordinate in the direction of the shear gradient, respectively. By inserting these expressions in Eq. MM1, one finds $g_1(\mathbf{q}_{\perp}, \Delta\gamma) = 1$ and $g_1(\mathbf{q}_{\parallel}, \Delta\gamma) = \text{sinc}(q_{\parallel}\Delta\gamma b/2)$. The corresponding $g_2 - 1$ function is shown as a line in Fig. 2B.

Extracting the Plastic Activity $A(\gamma)$ from the Light-Scattering Data. To calculate the plastic activity per unit strain, $A(\gamma)$, we invert Eq. 1:

$$\int_{\gamma_1}^{\gamma_2} A(\gamma) d\gamma = \left[-\frac{1}{f(\mathbf{q}_{\perp})} \ln \frac{g_1(\mathbf{q}_{\perp}, \gamma_1, \gamma_2)}{R(\mathbf{q}_{\perp}, \gamma_2 - \gamma_1)} \right]^{\frac{1}{p}}. \quad [\text{MM2}]$$

Taking the derivative with respect to γ_2 at fixed γ_1 yields

$$A_{\gamma_1}(\gamma) = f(\mathbf{q}_{\perp})^{-\frac{1}{p}} \frac{\partial}{\partial \gamma_2} \left[-\ln \frac{g_1(\mathbf{q}_{\perp}, \gamma_1, \gamma_2)}{R(\mathbf{q}_{\perp}, \gamma_2 - \gamma_1)} \right]^{\frac{1}{p}} \Bigg|_{\gamma_2=\gamma}, \quad [\text{MM3}]$$

where the γ_1 index in the l.h.s. of Eq. MM3 indicates that here A is evaluated using data for a specific value of the initial strain γ_1 . Operationally, we calculate $A_{\gamma_1}(\gamma)$ for several values of γ_1 , using $g_1 = \sqrt{g_2 - 1}$ and $R(\mathbf{q}_{\perp}, \Delta\gamma) = \exp(-q_{\perp}^2 \langle u_{na}^2 \rangle / 3)$, with $\langle u_{na}^2 \rangle = u_{\infty}^2 \frac{\Delta\gamma^2}{\Delta\gamma^2 + \gamma_c^2}$ and $u_{\infty}^2 = 0.12 \mu\text{m}^2$, $\gamma_c = 0.12\%$ (line in Fig. 2D). The derivative in the r.h.s. of Eq. MM3 was performed either numerically on the raw data or analytically on a second order polynomial fit of $\ln(g_1/R)$. We find similar results and use the latter method, which is less sensitive to data noise. Finally, $A(\gamma)$ is obtained by averaging $A_{\gamma_1}(\gamma)$ over different choices of γ_1 , in the range $1\% \leq \gamma \leq 6\%$. The exponent p is chosen by repeating the calculation of $A(\gamma)$ for several test values, finally retaining the p value that minimizes the rms residuals between the experimental $g_2 - 1$ and the correlation functions calculated from $A(\gamma)$ using Eq. 1.

ACKNOWLEDGMENTS. We thank C. Ligoure, K. Martens, T. Divoux, and D. Vlassopoulos for discussions. This work was funded by Agence Nationale de la Recherche (ANR) Grant ANR-14-CE32-0005-01, Centre National d'études Spatiales (CNES), and the EU (Marie Skłodowska-Curie ITN Supolen Grant 607937).

- Weibull W (1939) The phenomenon of rupture in solids. *Ingeniörs Vetenskaps Akademi-Handlingar* (Generalstabens Litografiska Anstalts Förlag, Stockholm), Nr. 153.
- Célerié F, et al. (2003) Glass breaks like metal, but at the nanometer scale. *Phys Rev Lett* 90:075504.
- Sethna JP, Myers CR (2001) Crackling noise. *Nature* 410:242.
- Ben-Zion Y (2008) Collective behavior of earthquakes and faults: Continuum-discrete transitions, progressive evolutionary changes, and different dynamic regimes. *Rev Geophys* 46.
- Nam KH, Park H, Hwan Ko S (2012) Patterning by controlled cracking. *Nature* 485: 221–224.
- Timoshenko SP (1953) *History of Strength of Materials* (McGraw-Hill, New York).
- Pradhan S, Hansen A, Hemmer PC (2005) Crossover behavior in burst avalanches: Signature of imminent failure. *Phys Rev Lett* 95:125501.
- Vinogradov A, Yasnikov IS, Estrin Y (2012) Evolution of fractal structures in dislocation ensembles during plastic deformation. *Phys Rev Lett* 108:205504.
- Amon A, Bertoni R, Crassous J (2013) Experimental investigation of plastic deformations before a granular avalanche. *Phys Rev E* 87 012204.
- Koivisto J, Ovaska M, Miksic A, Laurson L, Alava MJ (2016) Predicting sample lifetimes in creep fracture of heterogeneous materials. *Phys Rev E* 94:023002.
- Bell G (1978) Models for the specific adhesion of cells to cells. *Science* 200:618–627.
- Gobeaux F, Belamie E, Mosser G, Davidson P, Asnacios S (2010) Power law rheology and strain-induced yielding in acidic solutions of type I-collagen. *Soft Matter* 6: 3769.
- Swanson DA, et al. (1983) Predicting eruptions at mount St. Helens June 1980 through December 1982. *Science* 221:1369–1376.
- McGuire JJ, Boettcher MS, Jordan TH (2005) Foreshock sequences and short-term earthquake predictability on East Pacific rise transform faults. *Nature* 434:457–461.
- Wu L, Liu S, Wu Y, Wang C (2006) Precursors for rock fracturing and failure—Part I: IRR image abnormalities. *Int J Rock Mech Mining Sci* 43:473–482.
- Kromer RA, Jean Hutchinson D, Lato MJ, Gauthier D, Edwards T (2015) Identifying rock slope failure precursors using LiDAR for transportation corridor hazard management. *Eng Geology* 195:93–103.
- Onaka M (2013) *The Physics of Rock Failure and Earthquakes* (Cambridge Univ Press, Cambridge).
- Reiweger I, Schweizer J, Ernst R, Dual J (2010) Load-controlled test apparatus for snow. *Cold Regions Sci Technol* 62:119–125.
- Nechad H, Helmstetter A, El Guerjouma R, Sornette D (2005) Creep ruptures in heterogeneous materials. *Phys Rev Lett* 94:045501.

20. Preston FW (1942) The mechanical properties of glass. *J Appl Phys* 13:623–634.
21. Siebenbürger M, Ballauff M, Voigtmann Th (2012) Creep in colloidal glasses. *Phys Rev Lett* 108:255701.
22. Sentjabrskaja T, et al. (2015) Creep and flow of glasses: Strain response linked to the spatial distribution of dynamical heterogeneities. *Sci Rep* 5:11884.
23. Sancaktar E, Schenck SC (1985) Material characterization of structural adhesives in the lap shear mode. 2. Temperature-dependent delayed failure. *Ind Eng Chem Prod Res Dev* 24:257–263.
24. Bonn D (1998) Delayed fracture of an Inhomogeneous soft solid. *Science* 280: 265–267.
25. CK Poon W, et al. (1999) Delayed sedimentation of transient gels in colloid–polymer mixtures: Dark-field observation, rheology and dynamic light scattering studies. *Faraday Discuss* 112:143–154.
26. Skrzyszewska PJ, et al. (2010) Fracture and self-healing in a well-defined self-assembled polymer network. *Macromolecules* 43:3542–3548.
27. Sprakel J, Lindström SB, Kodger TE, Weitz DA (2011) Stress enhancement in the delayed yielding of colloidal gels. *Phys Rev Lett* 106:248303.
28. Leocmach M, Perge C, Divoux T, Manneville S (2014) Creep and fracture of a protein gel under stress. *Phys Rev Lett* 113:038303.
29. Andrade EN (1910) On the viscous flow in metals, and allied phenomena. *Proc R Soc A Math Phys Sci* 84:1–12.
30. Miguel M-C, Vespignani A, Zaiser M, Zapperi S (2002) Dislocation jamming and Andrade creep. *Phys Rev Lett* 89 165501.
31. Coussot P, Tabuteau H, Chateau X, Tocquer L, Ovarlez G (2006) Aging and solid or liquid behavior in pastes. *J Rheol* 50:975–994.
32. Caton F, Baravian C (2008) Plastic behavior of some yield stress fluids: From creep to long-time yield. *Rheologica Acta* 47:601–607.
33. Balland M, et al. (2006) Power laws in microrheology experiments on living cells: Comparative analysis and modeling. *Phys Rev E* 74:021911.
34. Jagla EA (2011) Creep rupture of materials: Insights from a fiber bundle model with relaxation. *Phys Rev E* 83:046119.
35. Landrum BJ, Russel WB, Zia RN (2016) Delayed yield in colloidal gels: Creep, flow, and re-entrant solid regimes. *J Rheol* 60:783–807.
36. Aime S, et al. (2016) A stress-controlled shear cell for small-angle light scattering and microscopy. *Rev Sci Instrum* 87:123907.
37. Tamborini E, Cipelletti L (2012) Multiangle static and dynamic light scattering in the intermediate scattering angle range. *Rev Sci Instrum* 83:093106.
38. Zaccarelli E (2007) Colloidal gels: Equilibrium and non-equilibrium routes. *J Phys Condens Matter* 19:323101.
39. Storm C, Pastore JJ, MacKintosh FC, Lubensky TC, Janmey PA (2005) Nonlinear elasticity in biological gels. *Nature* 435:191–194.
40. Carpineti M, Giglio M (1993) Transition from semioorder to disorder in the aggregation of dense colloidal solutions. *Phys Rev Lett* 70:3828–3831.
41. Manley S, Skotheim JM, Mahadevan L, Weitz DA (June 2005) Gravitational collapse of colloidal gels. *Phys Rev Lett* 94:218302.
42. Jaishankar A, McKinley GH (2013) Power-law rheology in the bulk and at the interface: Quasi-properties and fractional constitutive equations. *Proc R Soc London A Math Phys Eng Sci* 469:20120284.
43. Mohraz A, Solomon MJ (2005) Orientation and rupture of fractal colloidal gels during start-up of steady shear flow. *J Rheol* 49:657–681.
44. Berne BJ, Pecora R (1976) *Dynamic Light Scattering* (Wiley, New York).
45. Cipelletti L, Manley S, Ball RC, Weitz DA (2000) Universal aging features in the restructuring of fractal colloidal gels. *Phys Rev Lett* 84:2275–2278.
46. Basu A, et al. (2011) Nonaffine displacements in flexible polymer networks. *Macromolecules* 44:1671–1679.
47. DiDonna BA, Lubensky TC (2005) Nonaffine correlations in random elastic media. *Phys Rev E* 72:066619.
48. Leonforte F, Tanguy A, Wittmer JP, Barrat J-L (2006) Inhomogeneous elastic response of silica glass. *Phys Rev Lett* 97:055501.
49. Milkus R, Zaccone A (2016) Local inversion-symmetry breaking controls the boson peak in glasses and crystals, 2016 boson peak in glasses and crystals. *Phys Rev B* 93:094204.
50. Falk ML, Langer JS (1998) Dynamics of viscoplastic deformation in amorphous solids. *Phys Rev E* 57:7192–7205.
51. Hebraud P, Lequeux F, Munch JP, Pine DJ (1997) Yielding and rearrangements in disordered emulsions. *Phys Rev Lett* 78:4657–4660.
52. Petekidis G, Moussaid A, Pusey PN (2002) Rearrangements in hard-sphere glasses under oscillatory shear strain. *Phys Rev E* 66:051402.
53. Leheny RL, Rogers MC, Chen K, Narayanan S, Harden JL (2015) Rheo-xpcs. *Curr Opin Colloid Interface Sci* 20:261–271.
54. Wyss HM, Innerlohinger J, Meier LP, Gauckler LJ, Glatter O (2004) Small-angle static light scattering of concentrated silica suspensions during in situ destabilization. *J Colloid Interface Sci* 271:388–399.
55. Duri A, Bissig H, Trappe V, Cipelletti L (2005) Time-resolved-correlation measurements of temporally heterogeneous dynamics. *Phys Rev E* 72:051401.

Supporting Information

Aime et al. 10.1073/pnas.1717403115

Setup and Sample Geometry

The sample is confined between two glass plates, as shown in Figs. S1 and S2. The sample volume is 100 μL , and the gap between the plates is 390 μm . The gel cross-section is approximately circular, with a surface $A = 2.6 \text{ cm}^2$, corresponding to an effective radius $\sqrt{A/\pi} = 0.91 \text{ cm}$. A thin rim of silicon oil is used to seal the lateral surface of the gel, to avoid evaporation.

One glass plate is fixed; the other one can slide along the \hat{e}_{\parallel} direction. The shear stress is applied by means of an electromagnetic actuator; strain is measured by an optical, contactless sensor, as described in ref. 1. A laser beam with a $1/e^2$ diameter of 2 mm and propagating along the \hat{e}_z direction illuminates the sample. The scattered light is collected by a series of lenses (omitted in Fig. S1 for clarity; a full scheme of the scattering apparatus is given in ref. 2), such that a CMOS camera records the speckle pattern formed by the scattered light in the far field. The transmitted beam is removed by a beam block. More details on the scattering apparatus are given in ref. 2.

Fig. S1 shows schematically the setup and the scattering geometry. The intensity correlation functions are obtained from

$$g_2(\mathbf{q}, t_1, t_2) - 1 = \beta \frac{\langle I_p(t_1) I_p(t_2) \rangle_{\mathbf{q}}}{\langle I_p(t_1) \rangle_{\mathbf{q}} \langle I_p(t_2) \rangle_{\mathbf{q}}} - 1,$$

with $\beta \gtrsim 1$ a normalization constant (see *Materials and Methods*), $I_p(t)$ the scattered intensity at time t for the p -th pixel, and $\langle \dots \rangle_{\mathbf{q}}$ the average over a set of pixels corresponding to a small region in \mathbf{q} space, centered around the scattering vector \mathbf{q} . Fig. S1 shows two such sets of pixels, associated with the same scattering angle θ , and thus the same magnitude of the scattering vector, but with different azimuthal orientation. The region highlighted in green corresponds to the scattering vector \mathbf{q}_{\parallel} shown in Fig. S2, parallel to the shear direction. The region highlighted in blue corresponds to the scattering vector \mathbf{q}_{\perp} shown in Fig. S2, parallel to \hat{e}_{\perp} and perpendicular to the shear direction. Intensity correlation functions measured for $\mathbf{q} = \mathbf{q}_{\perp}$ are sensitive only to nonaffine motion, while correlation functions for $\mathbf{q} = \mathbf{q}_{\parallel}$ are dominated by affine deformation.

Reproducibility

We have performed eight creep experiments coupling rheology and light scattering and five complementary rheology tests on samples with the same composition as that described in the main text. The rheological properties are very well reproducible—for example, the elastic modulus of all samples follows the same age dependence to within 25%. All samples exhibited delayed failure

under creep. The failure time varies strongly (from 1 h to 50 h) for a modest variation of the applied stress, $3.5\% \leq \sigma_0/G \leq 5.5\%$. The general trend is for the failure time to decrease with σ_0 , although large run-to-run variations, up to a factor of ≈ 5 , are seen for comparable σ_0/G values. Both the strong run-to-run variation of the failure time and its marked dependence on σ_0 have been reported for other soft solids (see, e.g., refs. 24 and 27 of the main text). In the five experiments (out of eight) where the failure time exceeded 6 h, a dynamic precursor was clearly seen, with the same features as described in the main text: The plastic activity goes through a maximum that corresponds to the minimum of the macroscopic shear rate. One test was performed in a different optical layout, allowing a spatial map of the plastic activity over the full sample to be measured. This test suggests that plasticity is to some extent spatially localized, which may explain why the dynamic precursor was occasionally not seen. (In the layout of Fig. S1, the laser beam illuminates only about 1% of the sample.)

Comparison Between Mechanical and Dynamical Precursors of Failure

Fig. 3 suggests that the onset of plastic activity detected by measuring the microscopic dynamics is approximately concomitant with a deviation of $\dot{\gamma}$ with respect to its initial power law trend. To further investigate the relationship between microscopic and macroscopic quantities, we plot in Fig. S2 the strain dependence of the cumulated plastic activity and the relative deviation of $\dot{\gamma}$ from a power law. The former is defined as

$$\frac{\int_0^{\gamma} A(\gamma') d\gamma'}{\int_0^{\gamma_{max}} A(\gamma') d\gamma'},$$

with $\gamma_{max} = 28.4\%$ the strain at which macroscopic failure starts. The relative deviation of $\dot{\gamma}$ is defined as $\frac{\dot{\gamma} - \dot{\gamma}_{EM}}{\dot{\gamma}}$, with $\dot{\gamma}_{EM}$ the power law fit to the strain rate shown as a dashed line in Fig. 3. Both quantities are defined such that they tend to one at large strain. Fig. S2 shows that both quantities fluctuate around zero (due to noise) at the beginning of the experiment; they start growing significantly when the strain attains about 15%.

Fig. S3 shows the cumulated plastic activity plotted against the relative deviation of $\dot{\gamma}$. At the onset of plasticity, the data follow approximately a power law with exponent 3. This demonstrates that the growth of the plastic activity and the deviation of $\dot{\gamma}$ occur indeed concomitantly. Moreover, it demonstrates that the growth of the microscopic plasticity is sharper than that of the deviation of $\dot{\gamma}$, as suggested by the comparison of the two panels of Fig. S2. This indicates that A is more sensitive than the strain rate as a signal of plasticity.

1. Aime S, et al. (2016) A stress-controlled shear cell for small-angle light scattering and microscopy. *Rev Sci Instrum* 87:123907.

2. Tamborini E, Cipolletti L (2012) Multiangle static and dynamic light scattering in the intermediate scattering angle range. *Rev Sci Instrum* 83:093106.

Irreversible dynamics under large amplitude oscillatory shear

Contents

7.1	Yielding transition in large amplitude oscillatory shear	129
7.2	Delayed yielding in LAOStress	135
7.3	Structural evolution under an oscillatory stress	137
7.4	Correlation echoes track plasticity across cycles	139
7.5	Discussion	143

In chapter 6 we showed the rheological signature of delayed failure in a colloidal gel. We observed that primary creep is characterized by linear viscoelasticity, and that a plastic burst of activity characterizes the linear to nonlinear transition. Another relevant experimental protocol commonly used to investigate the onset of irreversibility is the so-called fatigue test, where a cyclic perturbation is repeated many times, and the evolution of the system is followed as a function of the cumulated deformation. In this chapter we show results obtained in similar experiments, namely large amplitude oscillatory shear experiments. Analogies and differences with respect to chapter 6 are discussed, with special focus on the reversibility of the observed deformation.

7.1 Yielding transition in large amplitude oscillatory shear

Large amplitude oscillatory shear (LAOS) experiments are commonly performed in a strain-controlled fashion: a strain perturbation $\gamma(t) = \gamma_0 e^{i\omega t}$ with a finite amplitude γ_0 is imposed, and the stress response is monitored over time, as sketched in chapter 2. In the nonlinear regime, no guarantee is given a priori that the response is still periodic: for this reason one usually focuses on the stationary state (provided that such state exists and can be reached within experimentally accessible timescales), where nonlinear viscoelastic moduli can still be defined, e.g. through a first-harmonic approximation of the stress signal (cf. chapter 2).

This condition is easily met for a variety of soft samples, the so-called simple yield stress fluids, whose nonlinear mechanical properties are independent on the strain history, whereas it doesn't hold for our colloidal gel, since the macroscopic deformation strongly affects the structure: such a property is usually referred to as thixotropy. As a consequence of thixotropy, the mechanical response of the sample to an oscillatory perturbation with amplitude γ_0 may not be periodic, and a transient regime is often observed, during which any definition of the nonlinear viscoelastic moduli would produce time-dependent G' and G'' . Therefore, when thixotropic materials are studied in the nonlinear regime, special care must be taken in the experimental protocol, in order to obtain reproducible results.

In the specific case of our colloidal gels, we have decided to adopt the following protocol: for each experiment, a new sample is prepared *in situ*, in the Couette cell of the rheometer, as discussed in chapter 5, and it is let age after gelation for 24h. After this waiting time, strain oscillations at frequency $\omega = 1$ Hz are applied, with an increasing amplitude γ_0 starting from the linear regime. We observe that in the nonlinear regime the first oscillations are characterized by a strong evolution of the viscoelastic moduli, which significantly slows down after a few periods. For this reason, we decided to perform 10 strain oscillations for each amplitude γ_0 , and to extract mechanical properties from the last one. Results are shown in Fig. 7.1.

The inset shows a few examples of Lissajous-Bowditch (LB) plots: for small amplitudes (up to $\gamma_{y1} \sim 10\%$) the plots are elliptical, which indicates negligible contributions from higher order harmonics in stress, and eccentricity is large ($e^2 \approx 1$), which means an essentially solid-like response. Beyond γ_{y1} , however, the shape changes abruptly, and the increasing area enclosed by the LB plots (already starting from the blue curve in Fig. 7.1a) tells us that nonlinear energy dissipation mechanisms are occurring during deformation. Such abrupt change is unusual in colloidal gels, where yielding is usually a more gradual process [Koumakis 2011, Laurati 2014, Brunel 2016, Moghimi 2017], and may reflect catastrophic material failure, for example linked to the internal fracture of the attractive gel, in analogy to what it is observed in brittle solids. Close to failure, the LB plots display a tilted shape, commonly found in literature [Colombo 2014], that highlights the presence of strain hardening in the high-strain end of the curve, which means that the structure is not yet totally disrupted.

The main plot of Fig. 7.1 shows the viscoelastic moduli extracted from a first harmonic approximation of the measured stress curves. The linear regime, up to a few percent deformation, is characterized by strain-independent moduli. The higher value of G' (two decades above G'') reflects the solid-like nature of the gel. The value of linear G' corresponds to the one expected from the rubber elasticity [Colby 2003] of a network with mesh size $\xi \sim 1 \mu\text{m}$ equal to the gel cluster size (cf. chapter 5), and it is much higher than what typically found in attractive colloidal gels at similar volume fractions, also taking particle size dependence into account [Koumakis 2011, Laurati 2014, Moghimi 2017]. This reflects the strong cohesion of the sample, probably linked to the experimental protocol: *in-situ* sample preparation leads to a very homogeneous material, where a large number

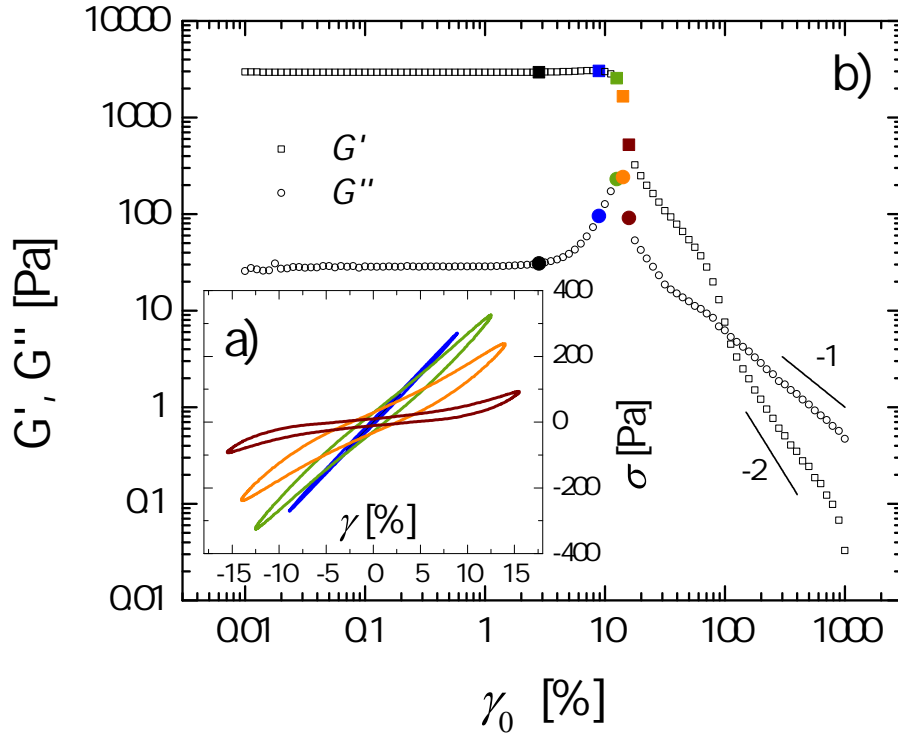


Figure 7.1: (a) Lissajous-Bowditch plots of shear stress vs. strain obtained as described in the text, for $\omega = 1$ Hz and different strain amplitudes: $\gamma_0 = 2.8\%$ (black), 8.9% (blue), 12.5% (green), 14% (yellow), 15.8% (red). (b) Nonlinear viscoelastic moduli G' and G'' extracted from a first harmonic approximation of the measured stress curves. Data corresponding to the Lissajous plots in the inset are highlighted in corresponding colors.

of the interparticle bonds are actively contributing to the stress-bearing structure. This interpretation is in agreement with the work of Moghimi et al [Moghimi 2017], where a colloidal gel is fluidified by large amplitude oscillatory shear, and the strength of the resulting material after flow cessation is related to the homogeneity of its structure.

As γ_0 is increased, a weak strain overshoot [Hyun 2011] is observed, with G' almost constant and G'' increasing by about one decade. This reflects the observation that in LB plots the enclosed area initially increases without significant changes in the major axis orientation. After that, the afore mentioned brittle-like nature of the yielding transition is observed as a sharp drop of G' . Again, as noticed by looking at the tilted shape of the LB plots, the viscoelastic moduli clearly show that even beyond the abrupt yielding the material is not completely fluidified: G' is still larger than G'' , and they both decrease in a nontrivial way with increasing γ_0 until a crossover is observed, around 1 strain unit, which marks a second and last yielding step. Beyond this crossover, $\log G'$ and $\log G''$ vs. $\log \gamma_0$ display slopes of -2 and -1 respectively, which are expected for similar systems in the strongly nonlinear regime, where the structural relaxation time τ is expected to decay with

the imposed shear rate [Miyazaki 2006]. One can qualitatively understand this regime by taking $\tau \propto \dot{\gamma}^{-1}$ [Sollich 1998] and $\omega \ll \tau^{-1}$, where this second inequality derives from the assumption that $\omega \sim \tau^{-1}(\dot{\gamma})$ at the loss peak [Miyazaki 2006]. Since in a first harmonic approximation $\gamma_0 = \dot{\gamma}_0/\omega \propto (\omega\tau)^{-1}$, this allows to relate the large strain regime in the amplitude sweep to the terminal low frequency regime in a typical frequency sweep, where the viscoelastic moduli exhibit the typical slopes of a Maxwell model at low Deborah numbers $De = \omega\tau \ll 1$: $G' \propto \omega^2 \propto \gamma_0^{-2}$ and $G'' \propto \omega \propto \gamma_0^{-1}$. This suggests that flow is finally achieved at the largest amplitudes. Using the analogy with the Maxwell model, one can extract from the terminal regime a viscosity $\eta_L(\gamma_0) \sim G''^2/(\omega G' \gamma_0) \propto 1/\gamma_0$, which corresponds to $\eta_L \sim 0.1$ Pa·s, i.e. ~ 100 times the viscosity of water, at the largest strain amplitude.

In agreement with established works in the literature [Koumakis 2011, Laurati 2014, Brunel 2016], we attribute the observed two-step yielding transition to the disruption of two distinct structures in the gel: the first yielding, around $\gamma_{y1} \sim 10\%$, is expected to be associated to the breakage of the main backbone of the percolating structure, which abruptly weakens the material, whereas the second step around $\gamma_{y2} \sim 100\%$ is expected to correspond to the breakage of particle aggregates into smaller clusters. The large value of η_L , together with clear evidence coming from the visual analysis of the sample after yielding (the material is turbid and macroscopically heterogeneous), shows that in our experiment we do not achieve the complete breakage of the gel down to the particle level: the final state of our sample at the highest amplitudes should rather correspond to a suspension of particle aggregates. One can imagine that, as a consequence of the strong attraction between the particles, a much higher shear stress, not reached in our experiments, would be needed to fully redisperse the sample to its initial state [Tang 2001].

As anticipated in chapter 2, the area S included inside the normalized LB plots $\tilde{\sigma}(\tilde{\gamma})$ (where $\tilde{\sigma} = \sigma/\sigma_0$ and $\tilde{\gamma} = \gamma/\gamma_0$ are instantaneous stress and strain normalized by their first harmonic amplitudes σ_0 and γ_0) represents the fraction of energy dissipated during one cycle. The value of S is shown in Fig. 7.2a as a function of the shear amplitude. In the linear regime, we found in chapter 2 that $S/\pi = \sin^2 \delta$ increases from 0 to 1 as the loss tangent $\tan \delta$ increases (δ being the phase difference between stress and strain signals). Even though in presence of higher harmonics a S/π ratio larger than 1 is in principle allowed, in our case S/π continuously increases with increasing γ_0 , approaching 1 from below in the large deformation limit. The detailed profile of such an increase contains the vestiges of the two-step yielding process, since a plateau is reached at intermediate amplitudes, in between the failure of the network and the complete fluidization. The same trend can be observed in the detailed harmonic content shown in Fig. 7.2b: again, the signature of the two-step yielding is marked by the double peak of the third harmonic σ_3 , where the low value of the even harmonics suggests that no wall slip nor shear banding occur (cf. chapter 2). Moreover, one can observe that, at the highest amplitudes, the low level of higher harmonics suggests again that the structure of the system under large amplitude shear evolves towards that of a simple shear-thinning suspension, as it is observed in the literature for similar samples [Laurati 2014].

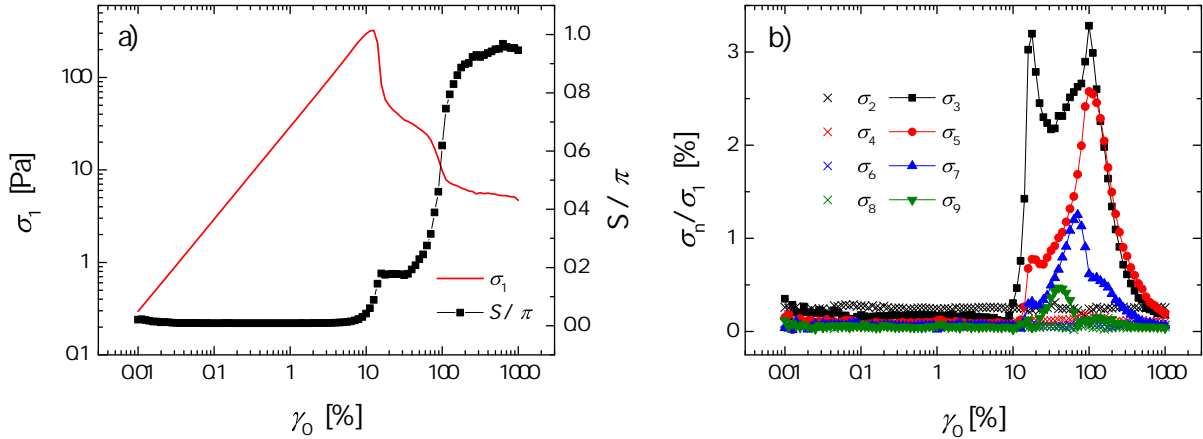


Figure 7.2: (a) First harmonic stress amplitude σ_1 (red, left axis) and area enclosed by LB plots (black, right axis) as a function of strain amplitude γ_0 . (b) Higher harmonics σ_n of the stress signal normalized by the first harmonic σ_1 . Even harmonics (crosses) keep their constant low value throughout the experiment, which suggests that wall slip and shear banding are negligible.

To summarize, our data show that yielding of the colloidal gel in LAOS experiments is a complex phenomenon, spanning widely different strain amplitudes. Macroscopic rheology represents a very practical technique to characterize it, thanks to its straightforward application, and the analysis of the detailed stress signal allows one to distinguish two different processes. Following established works in literature, the first process has been interpreted as the breakage of the main stress-bearing backbone, and the second one as the disruption and densification of individual clusters.

At the same time, our colloidal gel showed a few features, namely the large elastic modulus in the linear regime and its abrupt decay during the first yielding step, which were rather uncommon for that class of soft samples. They are instead reminiscent of hard, brittle solids. Another relevant difference with respect to other colloidal gels is represented by the negligible structure reformation that follows the first yielding. Such structure reformation is usually monitored by performing, after completely breaking the sample, either time-resolved measurements in the linear regime or by a reversed strain amplitude ramp, until reaching again the linear regime [Koumakis 2011, Koumakis 2015, Moghimi 2017]. Although differences with respect to the initial state are not uncommon, and the strong time-dependence has to be taken into account, after yielding the material generally recovers a solid-like response, with an elastic modulus that may be even larger than the one measured before yielding [Moghimi 2017]. To test structure reformation, we use a different protocol: starting from low deformations, we progressively increase the strain amplitude up to a maximum value γ_{max} , after which we start again from the low-deformation regime and we increase again the amplitude up to a larger γ_{max} , until complete yielding is achieved. The results of such a protocol are represented in Fig. 7.3a, which shows that in our case yielding is fully irreversible: once the first yield point is

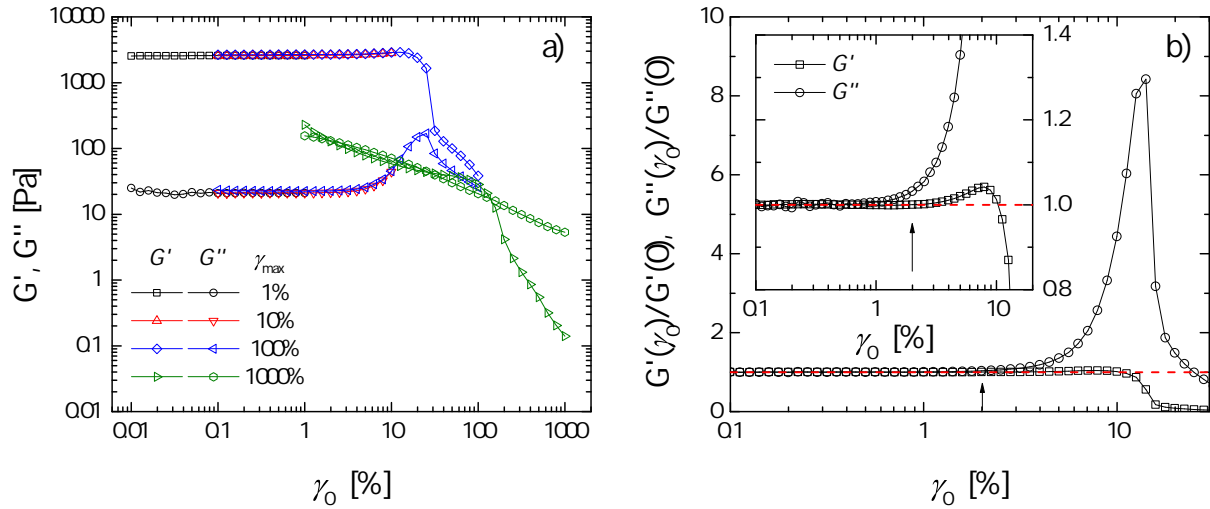


Figure 7.3: ((a) Viscoelastic moduli, G' and G'' , measured by repeating several measurements, each one attaining a maximum strain deformation γ_{max} (specified in the legend). Within each measurement, 1 oscillation was performed for each strain amplitude, and no waiting time was interposed between two consecutive measurements. (b) Storage (squares) and loss (circles) moduli normalized by their value in the linear regime. The arrow marks the departure from unity (red dashed line), defining the critical strain $\gamma_{nl} \sim 2\%$.

reached, the percolating network is irreversibly damaged, and the viscoelastic properties dramatically change. A subsequent measurement would reveal a totally different picture of the system, with minor structure reformation even over long times.

We speculate that the origin of such irreversibility might be attributed once again to the peculiar sample preparation: since our gel slowly forms *in situ*, with no preshear prior to the measurement, one might expect a more homogeneous and stiffer sample as compared to standard procedures. Such material would thus contain a smaller amount of structural defects, which might reflect in the enhanced stiffness and brittleness observed experimentally, as it is well known in crystalline solids [Poirier 1985, Shan 2004]. This hypothesis is consolidated by similar observations found in literature on a casein gel prepared with a similar protocol [Leocmach 2014]. Such an interplay between the microscopic structure of the sample and its mechanical properties is intriguing, and raises interesting questions regarding the microscopic mechanisms underlying the observed rheological response.

In the following we will focus on the onset of the yielding process, where the first plastic events start to occur. Our data allow one to identify a critical strain $\gamma_{nl} \sim 2\%$ beyond which the mechanical response becomes nonlinear. Using the stress-controlled experimental setup described in chapter 3, we address the reversibility of small to medium amplitude deformations, our main goal being to detect and characterize the onset of plasticity at the microscopic level and compare this onset with the nonlinear threshold

γ_{nl} set by rheology.

7.2 Delayed yielding in LAOStress

LAOS experiment can also be performed in a stress controlled fashion, although this choice is less common: despite a few intrinsic limitations that will be discussed in the following, the so-called LAOStress experiments may represent a very instructive way to get insight into the reversible or irreversible nature of the observed deformation. Indeed, as pointed out by the work of Manneville and coworkers [Gibaud 2010, Perge 2014, Saint-Michel 2017], LAOStress puts the emphasis on the transient regime before the steady state is reached, often revealing the transient nature of states that one would be tempted to consider as stationary.

In this spirit, in our experiments we focus on the amplitude $\gamma_0(n)$ that one can detect during different oscillation cycles $n = 1, \dots, N$ at a fixed stress, $N = 100$ being the total number of oscillations imposed in the experiment. In our experiments we probe a range of deformations small enough (below 10%), such that the deformation during each cycle n can be fitted by a sinusoidal signal, with minor presence of higher harmonics except at the very highest amplitudes (cf. Fig. 7.2). Nevertheless, Fig. 7.3b clearly shows that the onset of nonlinear dissipation processes causing the increase of the loss modulus occurs before such a threshold, around $\gamma_{nl} = 2\%$. As a consequence of such nonlinear dissipation, we observe that the strain amplitude $\gamma_0(n)$ is truly constant only at the smallest stress amplitudes, whereas it generally increases with time at finite σ_0 (Fig. 7.4).

As long as σ_0 is kept below a threshold σ_d (which might be considered as a dynamic stress threshold, a concept derived from creep experiments [Brenner 2013]), the observed growth rate $d\gamma_0/dt$ slows down roughly as the inverse of the number of applied cycles, whereas above σ_d it shows three regimes, qualitatively similar to the primary, secondary and tertiary creep discussed in chapter 6: after the first power-law decrease, an acceleration is observed, and at later times the amplitude diverges after a finite number of cycles N_{max} . Experimentally we estimate $\sigma_d/G_0 \approx (4.7 \pm 0.1)\%$, $G_0 \sim 5$ kPa being the plateau elastic modulus defined in chapter 5. Because of this delayed failure, LAOStress experiments are limited to a maximum stress amplitude σ_s (which is a second, static stress threshold), beyond which the sample yields within the first oscillatory cycle. The largest stress amplitude achieved in our experiments is $\sigma_0/G_0 = 6.6\%$, which sets a lower bound for σ_s . For this reason LAOStress experiments on thixotropic materials are best suited to investigate the very beginning of the yielding transition, where the effect of any small plastic contribution to the deformation is cumulated cycle after cycle.

From a comparison between Fig. 7.4 and the creep profiles shown in chapter 6, a straightforward parallel with the results shown in chapter 6 would be tempting. However, a few fundamental differences suggest that such a parallel might be misleading and must

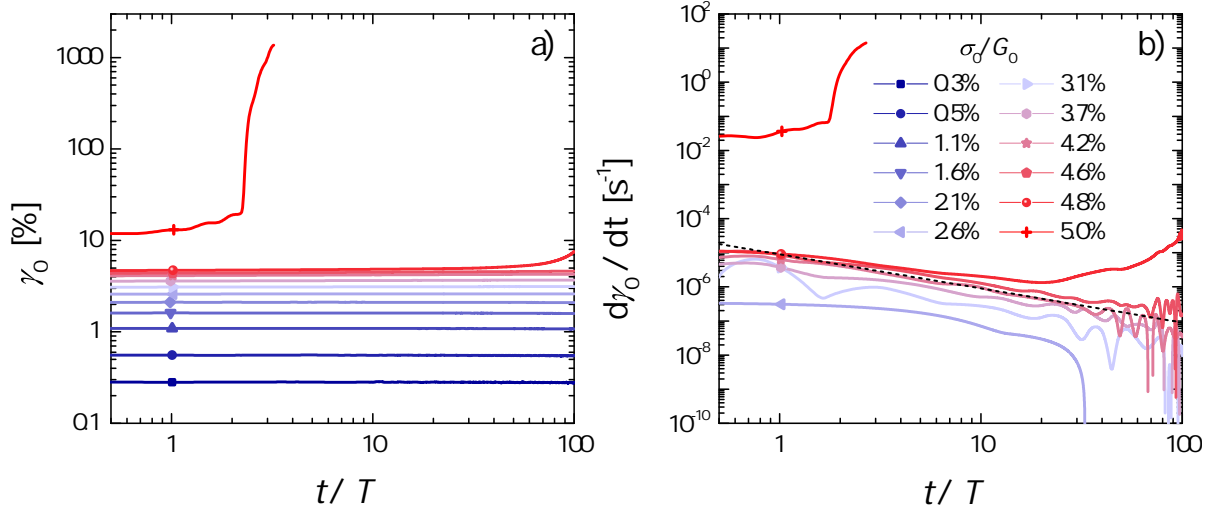


Figure 7.4: (a) Strain amplitude γ_0 measured by a sinusoidal fit of one full strain oscillation, following a stress perturbation $\sigma = \sigma_0 e^{i\omega t}$ with constant frequency $\omega = 1/T = 0.025$ Hz and different amplitudes σ_0 specified in the legend, in units of the plateau elastic modulus G_0 defined in chapter 5. γ_0 is plotted as a function of t/T , where t indicates the waiting time from the onset of oscillations. (b) Rate of change of the strain amplitude, again as a function of t/T . Such quantity is essentially 0 for the smallest amplitudes (below γ_{nl}), which are not represented. Dashed line is drawn as a reference, and represents a power law with slope -1.

be drawn with care. In fact, we have shown in chapters 5 and 6 that in our colloidal gels the power-law creep corresponds to a linear deformation mechanism, well described by a linear viscoelastic model. Accordingly, we observe that it is fully reversible upon stress release. On the other hand, the power law observed in Fig. 7.4b is only observed for large enough σ_0 (namely for $\sigma_0/G_0 \gtrsim 4\%$), and it represents a nonlinear effect. Moreover, we observe that the exponent of the power-law decrease of $d\gamma_0/dn$ in the first regime is higher than the one predicted by linear rheology, and actually close to -1, which would correspond to a logarithmic increase of the strain amplitude. Such difference is actually not surprising, since the stress histories imposed in the two protocols are profoundly different, and involve characteristic timescales separated by several decades: for creep deformation, $\dot{\gamma}^{-1}$ can approach values as large as 10⁶ s, whereas in oscillatory shear one typically has $\omega^{-1} \sim 10$ s.

For these reasons, one might expect that, despite the common features found in both protocols, the fatigue observed in LAOS experiments is governed by different microscopic mechanisms with respect to the ones investigated in the previous chapters. In this regard, the dynamic fatigue represented in Fig. 7.4 might be better suited to an "Andrade-like" description of the power law deformation, involving the concept of damage accumulation. To investigate more in detail this phenomenon, as well as the nature of the delayed yielding observed, we analyze how the sample structure and dynamics are

modified as a function of the stress amplitude σ_0 .

7.3 Structural evolution under an oscillatory stress

In order to obtain a microscopic information related to the processes observed at the macroscopic scale, we couple the shear cell to the small angle light scattering apparatus described in Ref. [Tamborini 2012], with which static and dynamic light scattering experiments can be simultaneously performed. In this section we will start by discussing the results of static light scattering experiments.

Under oscillatory shear, the structure is mostly preserved, so that the scattered intensity profile $I(q)$ hardly changes. However, in agreement with a few works in the literature [Vermant 2005, Mohraz 2005, Kim 2014], we detect the development of a reversible asymmetry in the static scattering signal during each cycle. Numerical simulations [Park 2017] show that under shear the structure factor $S(q)$ of a colloidal gel develops slightly quadrupolar profiles, which are generally referred to as "butterfly" patterns, and are tilted by 45° in the velocity-gradient plane. In our experimental setup the 2D sensor plane maps a nontrivial section of the 3D space, with \vec{q} mainly laying in the velocity-vorticity plane, and with a minor q_z component along the gradient direction, increasing at large scattering angles (cfr. chapter 6). We observe that the scattered intensity under shear is unchanged in the "neutral" direction \vec{q}_\perp (where we use this term to indicate scattering vector having their main component along the vorticity direction and no component along the velocity direction), whereas it changes in a way proportional to the strain in the velocity direction \vec{q}_\parallel . As already described in chapter 5, we characterize such asymmetry by defining an asymmetry factor:

$$\chi(q, \gamma) = \frac{I(\vec{q}_\parallel, \gamma) - I(\vec{q}_\perp, \gamma)}{I(\vec{q}_\parallel, \gamma) + I(\vec{q}_\perp, \gamma)} \quad (7.1)$$

This quantity can be employed in the so-called *structural Lissajous* plot [Kim 2014], that is represented in Fig. 7.5. Instead of a fully 3D plot like the one shown by Kim and coworkers, we prefer for clarity to show only the projections onto the (σ, χ) and the (σ, γ) planes.

Figure 7.5 can be read with the same criteria used to analyze the rheological LB plots of Fig. 7.1: on approaching σ_s from below, the mechanical response becomes slightly nonlinear and, as a result, a small area appears inside the elliptical loop, indicating energy dissipation. At the same time, the $\chi(\sigma)$ plot includes an area, whose precise physical meaning is still unclear, that increases with the applied deformation. Moreover, in this representation, a time evolution of the strain amplitude corresponds to an open loop in the Lissajous curves: this is hardly present at small amplitudes, but it is clearly evident at the highest one, where the curves abruptly end in correspondence to the sample failure. Once again, the same holds for the $\chi(\sigma)$ curve, where the signal amplification between two

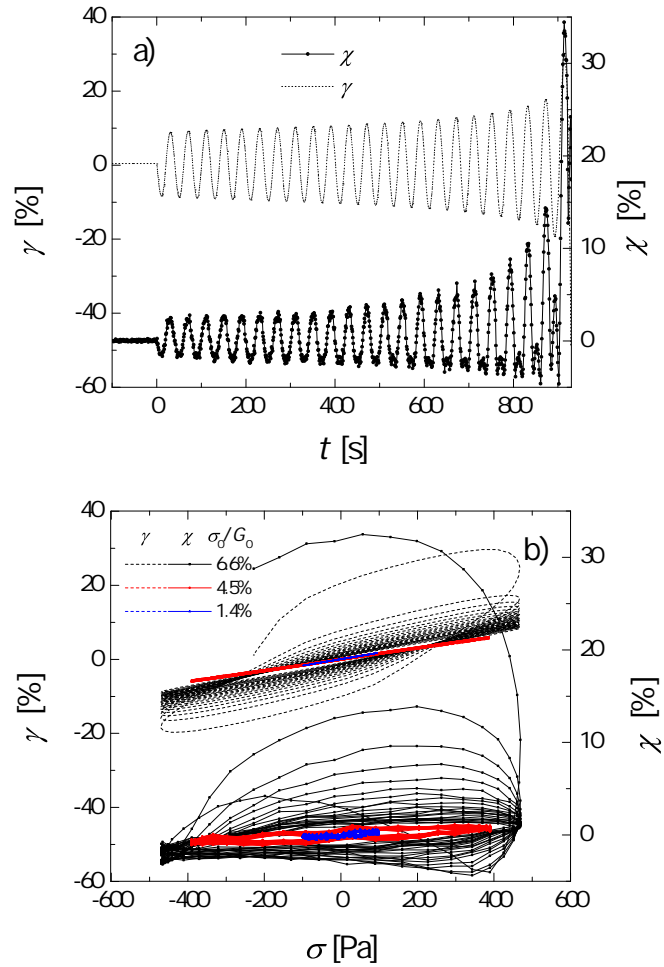


Figure 7.5: (a) Strain (dashed line, left axis) and asymmetry factor (line and symbols, right axis) for the largest stress amplitude $\sigma_0/G_0 = 6.6\%$, leading to delayed yielding. (b) Strain (dashed lines, left axis) and asymmetry factor (lines and symbols, right axis) for different stress amplitudes: $\sigma_0/G_0 = 1.4\%$ (blue), 5.5% (red) and 6.6% (black).

successive periods is now highly enhanced, and even more interestingly a clear asymmetry appears with respect to $\pm\chi$. We attribute such a signature to the creation of irreversible density fluctuations that are amplified until the whole network collapses: in this sense, one could consider it as a structural precursor of the delayed failure, although the practical interest of detecting such a precursor is probably limited, since strong indications of structural damage come as well from the evolution of mechanical properties.

Nevertheless, from a more fundamental point of view such a signal may contain precious information about the stress-induced plasticity that changes the sample structure, modifies the mechanical properties of the sample and in the long run leads to its failure. Such piece of information could not be accessed by the work of Kim and coworkers [Kim 2014], which is limited to the very large deformation limit probably because of the lower sensitivity of neutron scattering, and surely deserves deeper investigation in the

future.

In the following we will try to detect and characterize the very onset of those structural modifications, by using dynamic light scattering.

7.4 Correlation echoes track plasticity across cycles

As sketched in chapter 6, the amount of microscopically irreversible (plastic) deformation can be evaluated with dynamic light scattering, by comparing the system at time t with the system at time $t + nT$, where T is the oscillation period and n is an integer number. Similar experiments have been performed in the past on dense emulsions [Hébraud 1997], foams [Höhler 1997], colloidal suspensions [Petekidis 2002a] and gels [Smith 2007] in the multiple scattering regime, and more recently using x-ray photon correlation spectroscopy [Rogers 2014]. In this kind of test, a given macroscopic deformation would be fully reversible at the microscopic level if the system is static when observed in a stroboscopic way, i.e. after an integer number of full cycles: this corresponds to complete correlation ($g_1(\tau) = 1$) retrieved for time delays $\tau = nT$.

Figure 7.6a shows that the deformation of the macroscopic structure does determine a loss of correlation, mainly in the velocity direction (as expected for an affine deformation) and with a nontrivial component along the neutral direction (which is the signature of the nonaffine deformation discussed in chapter 6). However, the observed correlation decay is reversed when the macroscopic deformation comes back to $\gamma = 0$. Accordingly, one observes regular peaks in the correlation function, named correlation echoes: their value close to 1 shows that when the macroscopic deformation is recovered the microscopic structure of the sample goes back to its initial configuration. Such a deformation is defined as microscopically reversible.

In chapter 6 we have discussed microscopic reversibility by looking at one full cycle ($\tau = T$): the conclusion was that the observed correlation was essentially reversible up to $\sigma_0/G_0 \sim 5\%$. The same analysis can be extended to higher order correlation echoes ($\tau = nT$ with $n > 1$) and to stress amplitudes approaching σ_s from below. In the following we will only show the signal detected in directions perpendicular to the applied shear, for one representative scattering vector $q_{\perp} = 3.1 \mu\text{m}^{-1}$.

Figure 7.6b shows the time dependence of the height of the correlation echoes at two fixed time delays ($\tau = T$ and $\tau = 50T$), for a small stress amplitude, $\sigma_0/G_0 = 0.4\%$. The lack of any appreciable trend indicates that those correlation echoes probe a stationary state, which is expected when σ_0 is very small. However, no guarantee is given *a priori* that a stationary state can be found under larger strain amplitudes as well. To check this, in Fig. 7.7 we plot the correlation functions against the time delay $\tau/T = n$, where only integer values of n were chosen to track the decay of echo peaks. For each stress amplitude, the correlation functions are calculated at different waiting times t_w calculated from the beginning of the oscillation: a collapse of different curves would then indicate that a stationary state is obtained. This is the case of Fig. 7.7a, where two amplitudes

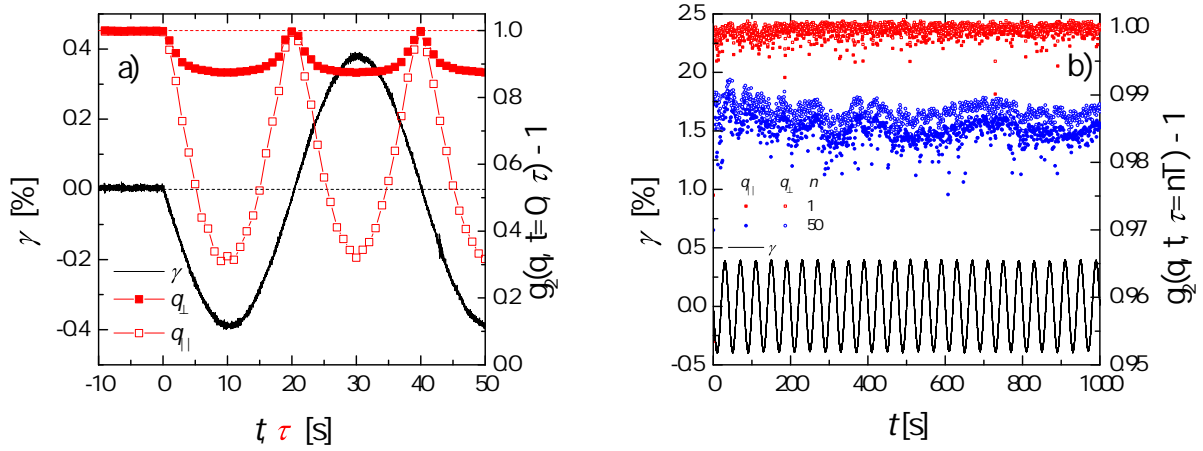


Figure 7.6: (a) Black line, left axis: macroscopic strain response to an oscillating stress $\sigma = \sigma_0 e^{i\omega t}$ applied starting from time $t = 0$. The strain amplitude is $\gamma_0 = 0.4\%$, the oscillation period is $T = 2\pi/\omega = 40$ s. Red data points, right axis: degree of correlation between the system at rest (measured at $t = 0$) and the system after a time delay $t = \tau$, for two scattering vectors with the same magnitude, oriented in the neutral (q_{\perp} , full symbols) and velocity (q_{\parallel} , open symbols) directions. The first correlation echo is represented by the point at $\tau = T = 40$ s. (b) Black line, left axis: macroscopic strain, same data as in panel (a). Data points, right axis: degree of correlation at a fixed time delay $\tau = nT$ for two values of $n = 1$ (red) and $n = 50$ (blue), plotted as a function of waiting time t during the oscillations, for the same two scattering directions as panel (a).

were chosen for the sake of simplicity, all amplitudes below $\sigma_0/G_0 = 3.7\%$ showing a similar result. Above 3.7% , the situation is different, and significant aging is found under oscillatory shear. Figure 7.7b shows that there is a range of amplitudes where the observed decorrelation is faster at the beginning, and slows down as time passes, until a quasi-stationary state might arguably be reached in the long time limit. On the other hand, Fig. 7.7c shows that at still higher amplitudes a sharp acceleration is observed, which accompanies the onset of the accelerated growth of the strain amplitude (cf. Fig. 7.4). The global picture is schematized in Fig. 7.7d, where a sharp dynamic transition accompanies the departure from the logarithmic growth of $\gamma_0(t)$.

By focusing on smaller amplitudes, up to $\sigma_0/G_0 = 4.6\%$, and by comparing the correlation decay obtained at different amplitudes, one obtains the result shown in Fig. 7.8a, which displays a nontrivial decay over a large number of cycles even for stress amplitudes quite far away from σ_s (more than a factor of 3).

This decay is the signature of the nonlinear processes responsible for the enhanced dissipation observed in Fig. 7.2: cycle after cycle the structure is slowly and irreversibly modified, presumably because of stress-induced plastic events. At the largest stress amplitudes, those modifications may eventually significantly affect the mechanical properties of the gel, so that the measured strain amplitude starts to increase (Fig. 7.4). However, the

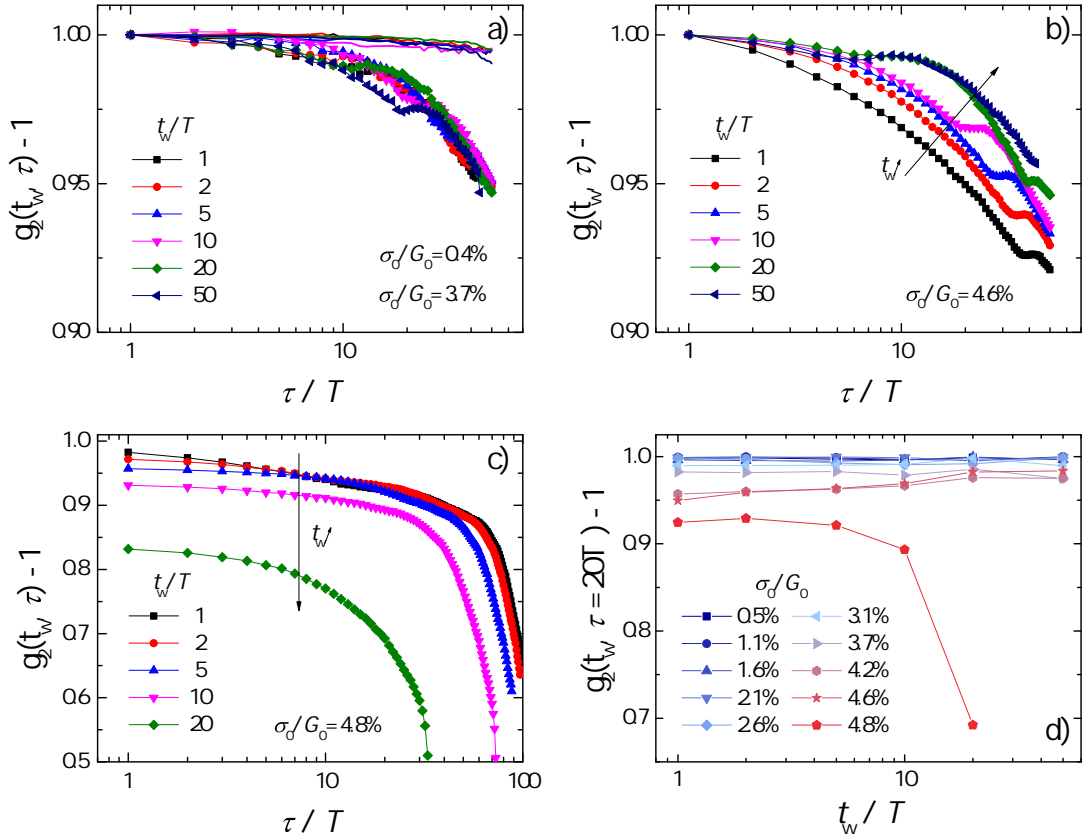


Figure 7.7: (a-c) Decay of higher order correlation echoes for some representative stress amplitudes σ_0 , each one calculated at different waiting times t_w . Different panels show different stress amplitudes, as specified in the labels: $\sigma_0 / G_0 = 0.4\%$ (a, lines), 3.7% (a, symbols), 4.6% (b), 4.8% (c). (d) Evolution of 20th correlation echo as a function of the waiting time t_w for different stress amplitudes (in the legend).

decay of correlation echoes shows that tiny plastic modifications start to occur at smaller stresses, already around 2% deformation, which corresponds to the onset of rheological nonlinear regime (cf. Fig. 7.3b).

To obtain a more explicit link between microscopic plasticity and nonlinear properties we tried to evaluate the relaxation time associated with each stress amplitude. This is of course very delicate because of the very small loss of correlation observed at the smallest amplitudes. To estimate the relaxation time, we assume that all correlation functions, if sampled for a sufficiently long time, would follow the same functional form (e.g. a stretched or compressed exponential with the relaxation time as the only varying parameter). Under this assumption, one can shift horizontally (in logarithmic scale) the correlation curves until they collapse on a mastercurve: the shift factor needed to do so represents the relative decay rate Γ , allowing one to compare the acceleration of microscopic dynamics with increasing stress amplitude. This procedure is more easily performed on $-\ln(g_2 - 1)$ rather than on the correlation functions themselves. Incidentally,

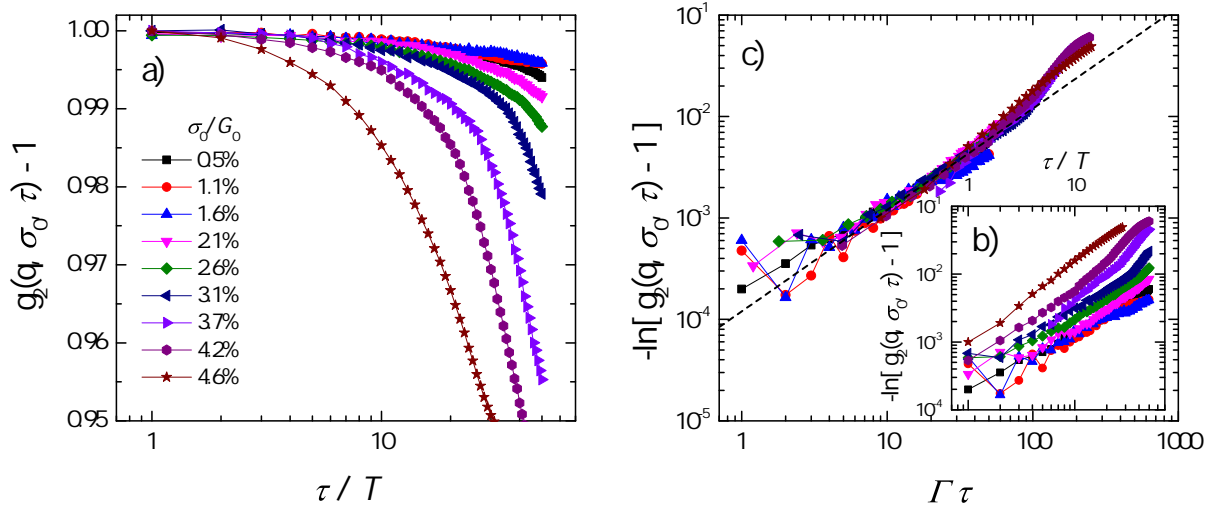


Figure 7.8: (a) Height of higher order correlation echoes for different stress amplitudes σ_0 . (b) Logarithm of the correlation functions shown in panel (a), taken to emphasize departure from unity. (c) Mastercurve obtained for $\sigma_0/G_0 \leq 4.6\%$ by rescaling the time delay by a factor Γ , shown in Fig. 7.9

we remind that $-\ln(g_2 - 1)$ is directly related to particle displacements.

The individual $-\ln(g_2 - 1)$ vs τ/T curves are shown in Fig. 7.8b, whereas the mastercurve resulting from the shift is represented in Fig. 7.8c. The straight line, with slope 1, represents an exponential decay, that would imply a diffusive nature of the observed dynamics. This is not completely the case, however, since some upwards deviation is observed at intermediate rescaled times.

Figure 7.9a shows the relaxation rate measured at different amplitudes. As one can see, in the linear regime, below $\gamma_{nl} \sim 2\%$, Γ is constant ($\Gamma = \Gamma_0$). Γ_0 is related to the spontaneous dynamics that characterize the gel at rest. Beyond γ_{nl} , instead, Γ increases sharply. We can understand this trend by assuming that the observed relaxation rate Γ can be decomposed in a contribution Γ_0 coming from spontaneous dynamics that adds to a plastic contribution Γ' in the nonlinear regime. The additivity of the two contribution comes from the assumption that spontaneous and plastic processes should be statistically independent, as already invoked in chapter 6. Under this assumption, the nonlinear relaxation rate Γ' can be evaluated by subtracting from the overall decay rate the one observed at the smallest stress amplitude: $\Gamma' = \Gamma - \Gamma_0$. The result is shown in Fig. 7.9b, together with the loss tangent extracted from the rheological data. In this representation, a sharp transition is observed around $\sigma_0/G_0 \sim \gamma_{nl}$, where the observed decay rate starts to grow almost exponentially with stress. A comparison with a rheological analogous such as $\tan(\delta)$ shows how sensitive the relaxation time is compared to rheological measurements: the onset of nonlinear regime is revealed by an increase in Γ of more than one decade, while the loss tangent does show an increment, but only of about 50% of its value in the linear regime. A plot of the two quantities against each other (Fig. 7.9c) relates

macroscopic and microscopic observations, clearly linking the departure from rheological nonlinear regime to the onset of microscopic irreversibility.

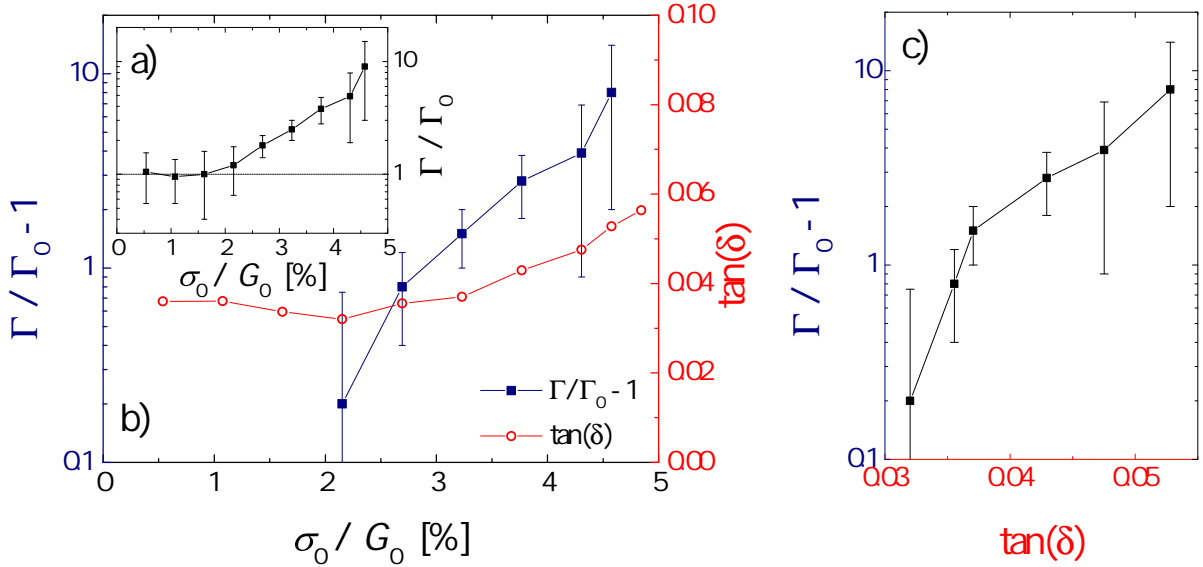


Figure 7.9: (a) Correlation decay rate Γ normalized by the decay rate Γ_0 measured in the linear regime. Error bars are mainly due to low signal to noise ratio at small σ_0 and to slight time dependence at large σ_0 . (b) Blue, left axis: decay rate $\Gamma' = \Gamma - \Gamma_0$ normalized by Γ_0 . Subtraction makes apparent the sharp transition observed at γ_{nl} . Red, right axis: loss tangent as a function of the stress amplitude σ_0 . The linear to nonlinear transition appears to be smoother at the macroscopic scale. (c) Γ' as a function of $\tan(\delta)$.

7.5 Discussion

In conclusion, by coupling oscillatory shear rheology with dynamic light scattering we could follow the decay of higher order correlation echoes, for different values of the stress amplitude σ_0 . When σ_0 is in the linear regime, the microscopic dynamics exhibit a very slow and stress-independent correlation decay. We attribute this decay to the slow spontaneous dynamics observed also on the gel at rest, which we quantify by means of a spontaneous correlation decay Γ_0 .

As the amplitude increases beyond $\sigma_0/G_0 = \gamma_{nl}$, however, a second, strongly stress-dependent contribution adds to the thermal relaxation, and we detect it as a rapidly increasing decay rate $\Gamma(\sigma_0)$. This allows us to rule out (in our case) the concept of "reversible plastic" or "reversible nonlinear" regimes that are sometimes observed in other soft systems such as foams [Höhler 1997], colloidal glasses [Keim 2014] or other colloidal gels [Rogers 2014], where the rheological nonlinear regime seems to anticipate the onset of microscopic irreversibility.

In the nonlinear regime, the existence of a steady state characterized by time-independent microscopic dynamics is not guaranteed. We find that for σ_0/G_0 between 2% and 4% the dynamics are indeed stationary, despite the fact that the strain amplitude is not constant, but increases logarithmically in time. Beyond 4% the picture is more complicated: in a first regime, up to $\sigma_0/G_0 \sim 4.6\%$, the dynamics are initially fast and then they slow down in time, somehow following the macroscopic deformation rate. Such slowing down might be understood by considering that, due to their fragility, many weak bonds presumably break within the first cycles, after which the rate of plastic events decreases together with the decorrelation rate and the rate of increase of the strain amplitude. Until 4.6%, despite the dynamic and rheological signature of microscopic damage, the stress-bearing backbone doesn't appear to be critically corrupted, and the weakening proceed sublinearly both at the macroscopic and the microscopic scale. Remarkably, no structural change is detected in this regime by static light scattering.

At still higher amplitudes, the microscopic dynamics strongly accelerate with time, and eventually the rate of increase of γ_0 also passes through a minimum and starts increasing, which is the sign that finally the structure has been severely damaged. Indeed, delayed failure is eventually observed, in a way that has strong reminiscence of the delayed failure observed under creep, the main difference being that here the first sublinear increase in γ_0 is logarithmic and also governed by plasticity, as opposed to the power law, linear viscoelastic creep observed in chapter 6. A comparison between the two failure mechanisms interestingly shows that under different mechanical solicitations the same system can yield in two ways which may look similar at the macroscopic level, but are actually different at the microscale.

Finally, it is interesting to emphasize that, in agreement with the intuitive notion of yielding, in our case we observe that the onset of rheological nonlinear regime is accompanied by a measurable acceleration in the macroscopic dynamics, which is quantified by a plastic relaxation rate Γ' . We show that, unlike the rheological nonlinear transition, which is very smooth and gradual, Γ' grows of almost 2 decades as σ_0/G_0 increases from 2.1% to 4.6%, after which delayed failure is observed. In the near future we plan to more quantitatively address this transition by measuring the microscopic dynamics close to γ_{nl} . We hope that the behavior of Γ' (e.g. continuously or discontinuously vanishing at γ_{nl}) might disclose fundamental information on the nature of yielding in such soft samples. In the same vein, we are currently extending this analysis to other systems with different structure, dynamics and rheology, with the aim of testing the generality of our results and progressing towards a more comprehensive understanding of the microscopic origin of nonlinear rheology. One example of such systems will be presented hereafter in part III.

Part III

Colloidal glasses

Dense microgel suspension: dynamics under shear

Contents

8.1	Introduction	147
8.2	Sample preparation	148
8.3	Structure and dynamics at rest	150
8.4	Rheology	153
8.5	Reversible and irreversible nonaffine dynamics	154
8.6	Conclusion	161

The study on the colloidal gel in part II revealed intriguing information about the interplay between macroscopic mechanical properties and microscopic dynamics. Namely, reversible nonaffine deformations were detected in the linear regime, with a nontrivial strain dependence well related to the microscopic structure. At larger deformations, an additional nonlinear contribution to the correlation decay was observed, revealing emergent plastic rearrangements and clearly marking the onset of the nonlinear regime. In this chapter we investigate the same features on another type of sample, with completely different microscopic structure, in order to check the generality of our previous observations, and to extend them to a regime of large strain amplitudes that could not be achieved with the colloidal gel.

8.1 Introduction

The sample investigated here is a soft colloidal glass prepared from a dense water suspension of Poly(N-isopropylacrylamide) (PNIPAM) microgels. Microgels are intramolecularly crosslinked soluble macromolecules of colloidal dimensions. Their interparticle interaction potential depends on the crosslink density, and thus microgels exhibit a behavior ranging from that of polymer solution to that of hard spheres. For such systems, volume fraction represents a crucial parameter controlling the phase behavior, which upon concentration can pass from the amorphous liquid state to a solid state, either a crystal or a glass.

Colloidal glasses are out-of-equilibrium materials where particles are kinetically trapped into a metastable, disordered configuration. It is well established that for hard sphere suspensions this happens when their volume fraction exceeds a value of about 0.58 [Sciortino 2005]. While hard-sphere glasses cannot exceed close-packing at an approximate volume fraction of 0.64, soft particles can be arranged at much higher volume fractions due to their softness and deformability, so that the glass transition is shifted by an amount that depends on particle softness. Concentrated suspensions made from soft and deformable particles such as microgels are named soft particle glasses in reference to weaker interaction potentials than observed in hard-sphere glasses.

The rheology of hard sphere glasses, both in the linear and nonlinear regimes, has been widely studied in past years, and it is described to a large extent by theoretical models such as the soft glassy rheology [Sollich 1997] or by various declinations of the mode coupling theory [Miyazaki 2006]. Soft glasses share many of their relevant features with hard-sphere-like glasses, like the divergence of the zero shear viscosity as a critical concentration is approached from below and the emergence of a finite yield stress beyond that concentration, but the additional parameters involved in their response (particle elasticity and softness of interactions), together with their practical importance in widespread applications, makes them a rich and very active field of research [Vlassopoulos 2014].

Important questions that still attract the attention of a large scientific community concern for example the slow time evolution (aging), the coupling between microscopic structure and flow (thixotropy), and the solid-like to liquid-like transition under shear (yielding). As shown in chapter 1, a crucial limitation to reaching a more comprehensive microscopic description of yielding is represented by the scarcity of clean experiments observing at the same time the macroscopic rheology and the dynamics at the microscale. In this chapter we investigate the yielding of a soft glass, using dynamic light scattering coupled to stress-controlled large amplitude oscillatory shear.

To this aim, after a brief description of the sample (section 8.2), we will first characterize the structure and the dynamics of the system at rest (section 8.3). Then, after a qualitative description of yielding as it is observed by pure rheological measurements (section 8.4), we will investigate how the microscopic dynamics change in correspondence of this transition (section 8.5), which will give us indications of the the microscopic processes at play.

8.2 Sample preparation

Microgel samples were synthesized in our lab by Adrian Marie Philippe using free-surfactant emulsion-polymerization as described in [Senff 1999]. The particle radii can be estimated using static light scattering (SLS) and dynamic light scattering (DLS). SLS measures the gyration radius R_g (extracted from the form factor via the Guinier approximation: $I(q) = I_0 \exp[-(qR_g)^2/3]$), whereas DLS measures the diffusion coefficient that can be related to the hydrodynamic radius R_h via the Stokes-Einstein relation.

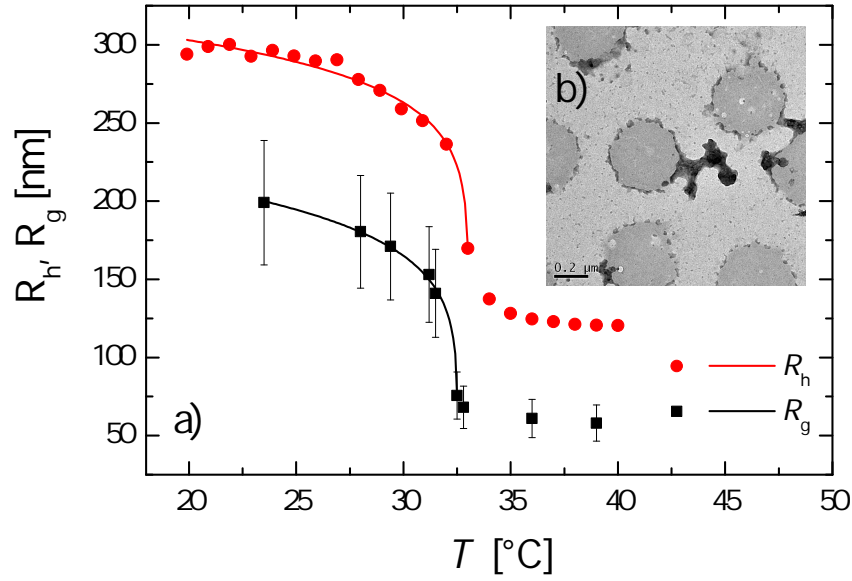


Figure 8.1: (a) Hydrodynamic radius R_h (red dots) and gyration radius R_g (black squares) as a function of temperature. Below $T_c \sim 33^\circ\text{C}$ data were fitted by a critical-like function as described in text. Adapted from D. Truzzolillo *et al.* (in preparation). (b) TEM images of PNIPAM microgels at $T = 20^\circ\text{C}$. Scale bar corresponds to $0.2 \mu\text{m}$. Adapted from Truzzolillo *et al.* (in preparation, courtesy of Dr. S. Sennato - Physics Dept., Sapienza - University of Rome)

The interaction between water and PNIPAM is a highly temperature-sensitive balance of hydrophilic and hydrophobic interactions, which results in a characteristic temperature dependence of the microgel size. As a consequence, both R_h and R_g at low temperatures can be fitted by a critical-like function [Bischofberger 2015] $R_{h,g} = R_{h,g}^{(0)}(1 - T/T_c)^\alpha$ (Fig. 8.1). The fit yields $T_c \sim 33^\circ\text{C}$ and $\alpha \sim 0.1$, with $R_h^{(0)}$ higher than $R_g^{(0)}$ as expected [Senff 1999, Reufer 2009]. In particular, the ratio R_g/R_h is lower than the value (0.77) expected for homogeneous hard spheres, which points out that monomer density is slightly peaked at the center of the microgel [Bischofberger 2015, Arleth 2005].

Concentrated samples are prepared starting from a diluted suspension, whose volume fraction can be inferred by measuring the zero shear viscosity [Truzzolillo 2015]. The suspension is then highly concentrated by centrifugation, and afterwards it is redispersed to the target volume fraction $\Phi = \frac{4}{3}\pi R_h^3 \rho$, where ρ is the number density of colloidal particles. In this chapter we compare samples at two different volume fractions $\Phi_A = 1.5$ and $\Phi_B = 1.0$. One should not be surprised to find a volume fraction greater than 1, since here Φ is calculated by using the number density and the hydrodynamic radius measured in the dilute limit. The softness of the particles allows each microgel to shrink and partially interpenetrate (depending on the crosslink density and radial distribution), so that Φ can easily reach values that would be unphysical for hard spheres. Indeed, at room temperature the sample at $\Phi = \Phi_B$ behaves as a viscoelastic liquid close to the

glass transition: spontaneous dynamics are much faster, and the yield stress, if any, is too small to be measured with our shear cell (i.e. below 0.1 Pa). On the other hand, the sample at $\Phi = \Phi_A$ is a viscoelastic solid, characterized by high elastic moduli, only weakly dependent on frequency, and very slow dynamics. In particular thanks to its ultraslow dynamics, the latter sample is particularly convenient for our experiments, and after a first comparison between the two systems, in the following we will mainly focus on the sample at $\Phi = \Phi_A$.

Throughout the sample preparation, care was taken to keep the temperature well below 40°C, in order to avoid polymer damage and strong attractive interactions that could hinder the homogeneous re-dispersion of the microgels [Bischofberger 2015]. Moreover, since the volume fraction depends on temperature, temperature control is required in order to avoid spurious contribution on sample dynamics coming from temperature fluctuations. For this reason, the temperature of the room is kept constant at $T = 23^\circ\text{C}$, and the temperature is measured in air close to the sample during the experiments, showing fluctuations of less than 0.3°C over 24 hours. Incidentally, we also argue that at such high volume fractions the mechanical properties exhibit only weak dependence on Φ , therefore we don't expect temperature fluctuations to play a major role in structural relaxation.

8.3 Structure and dynamics at rest

Figure 8.2 shows the structure of the two samples as it is probed with small angle light scattering. The less concentrated one displays a scattered intensity $I(q)$ close to the one typical of densely packed materials in the $qR_h \ll 1$ regime, where both $P(q)$ and $S(q)$ are q -independent and close to 1. On the other hand, the intensity scattered by the more concentrated sample reveals a microscopic structure profoundly different from the expected one: in the whole range of scattering vectors probed ($0.11 \mu\text{m}^{-1} \leq q \leq 3.9 \mu\text{m}^{-1}$), $I(q)$ decays as a power law with an exponent -1.5. The power-law decay reminds of the intensity profile typically observed in fractal objects. Two measurements of the same sample separated by 10 days confirm that the structure does not evolve significantly in time, so that the observed power law cannot be easily explained in terms of transient states anticipating phase separation as it is sometimes observed elsewhere [Beyer 2015]. This phenomenon is certainly interesting, and deserves deeper investigation in the future, aimed at verifying for example whether microphase separation is present.

Microscopic dynamics at rest are characterized by dynamic light scattering in the same range of scattering vectors as the static structure, and the intensity correlation functions extracted are shown in Fig. 8.3a. Very slow dynamics characterize the sample at $\Phi = \Phi_A$, whereas for the one at $\Phi = \Phi_B$ the observed correlation decays after a few minutes at most.

For the latter sample and the smallest scattering vectors shown in Fig. 8.3a, the correlation does not decay to zero because of the static contribution of residual light scattered by the imperfections in the optical interfaces (lenses, cell walls, etc.): it is the

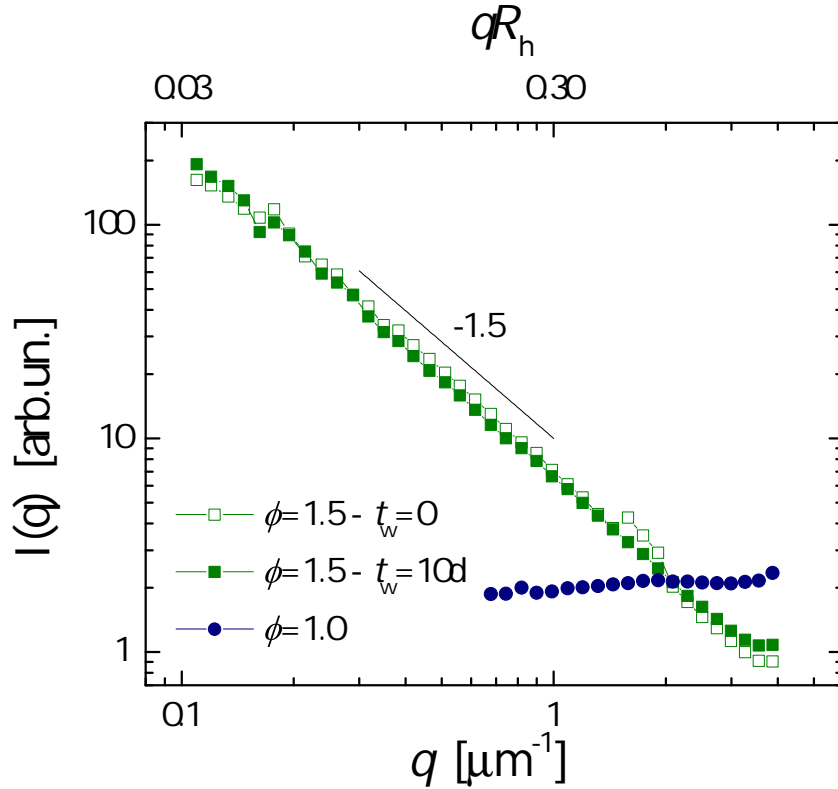


Figure 8.2: Static scattered intensity measured for the low density sample (blue) and for the high density one (green). For the latter, structure measured right after filling the cell (open symbols) and 10 days after (filled symbols) show no indications of time dependence.

so-called *stray light* I_{stray} . The presence of stray light adds a so called *heterodyne* term to the Siegert relation linking the measured intensity correlation function to the field correlation function, whereas the simple expression of Eq. 2.12 was derived under the implicit assumption of purely *homodyne* scattering, where the detected intensity I_{dyn} is entirely dynamic, and varies over time as a consequence of the internal dynamics of the sample. As a consequence of stray light, interpreting dynamic light scattering data taken in a partially heterodyne condition is generally not trivial [Cipelletti 1999]. Usually the ratio $X = I_{stray}/I_{dyn}$ between stray light and dynamically scattered light can be evaluated looking at the terminal plateau of the intensity correlation function: as long as X is reasonably small, such a plateau can quite safely be considered a simple additive term that can be subtracted from the measured intensity correlation functions. However, higher X values typically require a more sophisticated treatment, beyond the purpose of this chapter. In practice, I_{stray} is typically much stronger at the smallest scattering vectors (in our setup we have $I_{stray} \propto q^{-2}$). Therefore, the impact of stray light is negligible in the whole accessible q range for the concentrated sample, where I_{dyn} is also strongly increasing at small q , whereas it becomes very large at small q for the diluted

sample, for which I_{dyn} is almost constant: for this reason, only large scattering vectors ($q > 1 \mu\text{m}^{-1}$) are considered for that sample.

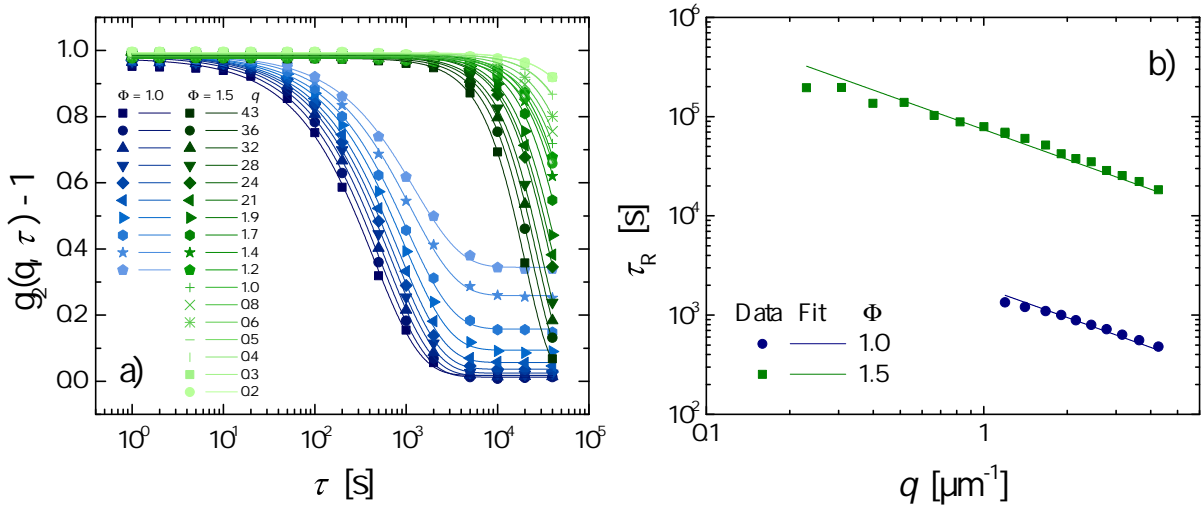


Figure 8.3: (a) Symbols: Intensity time correlation function plotted for different scattering vectors (specified in the legend, values in μm^{-1}) as a function of time delay for the two systems at volume fraction $\Phi_A = 1.5$ (green) and $\Phi_B = 1.0$ (blue). Lines: best fits to experimental data obtained with stretched exponential functions (shared stretching parameter $\beta = 0.85$) for Φ_B and compressed exponentials ($\beta = 1.41$) for Φ_A . (b) Symbols: relaxation times computed as the integral average of the correlation decays for the two systems, as a function of the scattering vector. Lines represent best power law fits with slope q^{-1} .

For both samples all intensity correlation functions can be nicely fitted with stretched exponentials where the stretching exponent β is shared by all q vectors, and it is $\beta = 0.85$ for the less concentrated sample and $\beta = 1.41$ for the more concentrated one. In the former case, $\beta < 1$ again suggests that volume fraction $\Phi_B = 1.0$ is very close to the glass transition, possibly slightly below it: in this case, $\beta < 1$ would be an indication of the heterogeneous local environments that can be found close to dynamic arrest. On the other hand, the compressed exponential observed in the latter case is less common in glassy systems, and might be reminiscent of residual stresses giving rise to ballistic dynamics similar to the ones observed for example in colloidal gels (cf. chapter 5), multilamellar vesicles in a close packed configuration [Ramos 2001], and concentrated emulsions [Cipelletti 2003]. Indeed, the relaxation times τ_R exhibit a q^{-1} dependence for both samples, which is the signature of ballistic dynamics (Fig. 8.3b).

8.4 Rheology

Thanks to its slow dynamics at rest, the more concentrated sample appears to be a good candidate to investigate the microstructural origin of nonlinear rheology, with special focus on the yielding transition. When probed in the linear regime, such system exhibits a solid-like response, with a predominant elastic modulus, only very weakly dependent on frequency, which suggests that all relevant relaxation processes occur outside the probed timescales, as it is also captured by dynamic light scattering (Fig. 8.3). As it is the case of many out of equilibrium systems, this sample slowly ages over time, as can be appreciated by the very slow increase of the elastic modulus.

Solid-like rheology in soft colloidal glasses is typically attributed to the concept of cage elasticity [Erwin 2010], although it is not clear whether this picture could apply to our case, given that the concentration is large enough to squeeze particles to a relevant extent. Within this framework, yielding is imagined as the rupture of cage-like microstructures [Petekidis 2004], but it has also been pointed out that for soft hairy colloids the picture could be more complex [Helgeson 2007], which confirms the interest of a more detailed study.

A practical way of addressing yielding in rheology is once again nonlinear oscillatory shear: an oscillating stress with finite amplitude σ_0 is imposed, and the deformation is measured for different stress amplitudes. As discussed in chapter 2, a careful analysis of the strain signal can reveal many relevant features that help elucidating the underlying processes. In this section we will limit ourselves to a qualitative description of the main rheological features observed, many of which have been thoroughly discussed in the literature [Petekidis 2003, Miyazaki 2006, Carrier 2009, Rogers 2011], whereas in the following section we will address some of the questions that remain open regarding the complex microscopic origin of yielding by coupling the rheological investigation to a direct probe of microscopic structure and dynamics.

In our experiments we apply the following protocol: the sample is loaded into the shear cell taking care to avoid bubble formation, and it is let age for a waiting time $t_w = 12h$, during which we monitor the evolution of structure, dynamics and linear rheology. As shown in Fig. 8.2, no measurable structural evolution is detected, whereas the dynamics and the rheology (not shown) exhibit slow aging. After the aging time t_w , we apply an oscillating stress at frequency $\omega = 0.01$ Hz and amplitude σ_0 , starting from a small amplitude and then increasing it gradually until the large amplitudes limit, where the sample flows, is reached. After that, a reverse stress ramp, starting from large σ_0 and decreasing it until the linear regime, can be subsequently applied to check for eventual hysteresis. For each amplitude, the rheological response is averaged on $N = 10$ full oscillations.

Viscoelastic moduli obtained with this protocol are represented in Fig. 8.4. A single yielding step is observed around a critical strain, which can be measured with different methods: among these, the crossover between G' and G'' (whose position we will call γ_x), the position of the loss peak in G'' (γ_m), and the change in slope of the $\sigma_0(\gamma_0)$ curve (γ_σ).

These methods yield quite different results, with a poorly defined γ_y ranging between $\gamma_\sigma = 6\%$ and $\gamma_x = 25\%$. As an equivalent method to characterize the yielding transition, the full harmonic content of the measured strain signal was analyzed (Fig. 8.6). The results locate the onset of yielding around $\gamma_{nl} = 10\%$. Beyond γ_x , the terminal regime begins, where G' and G'' develop well defined slopes in a log-log plot (-0.6 and -1.2 for G' and G'' , respectively), close to the ones measured in the literature for similar samples, and nicely matching theoretical predictions from mode coupling theory [Miyazaki 2006, Christopoulou 2009, Carrier 2009].

After the sample is fully fluidified, the stress amplitude is decreased again, across the yielding transition, towards the linear regime. This backward amplitude sweep reproduces the qualitative features observed in the forward one, but the value of the viscoelastic moduli in the linear regime is now lower: this is the effect of shear rejuvenation.

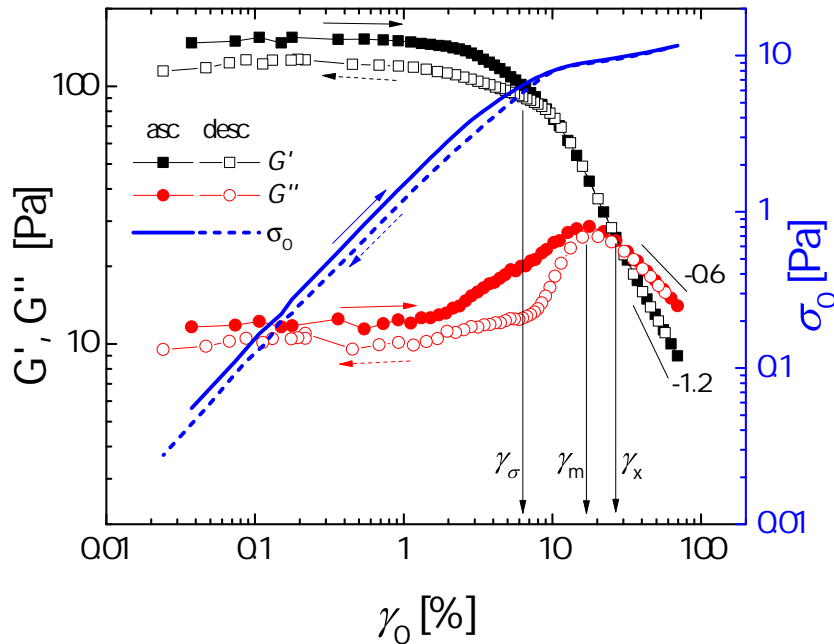


Figure 8.4: Symbols, left axis: viscoelastic moduli plotted as a function of the amplitude γ_0 of the first harmonic component of the strain. Sample is at volume fraction $\Phi_A = 1.5$, and applied frequency is $\omega = 0.01$ Hz. Filled and empty data points represent increasing and decreasing amplitude sweeps, respectively. Lines, right axis: stress amplitude σ_0

8.5 Reversible and irreversible nonaffine dynamics

The picture provided by rheology is that of a rather broad and gradual transition from a solid-like response to small perturbations to liquid-like response at large amplitudes. This is in sharp contrast with the picture provided in part II for the colloidal gel, where yielding was much more abrupt. We now turn to microscopic dynamics in order to better

understand the onset of the solid-like to liquid-like transition, and how this transition develops until complete fluidization.

As shown in part II, reversible and irreversible dynamics can be characterized under oscillatory shear using dynamic light scattering, and by correlating the undeformed system to the system at maximum strain (in which case both reversible and irreversible nonaffine dynamics will contribute to the signal) or with the system at zero macroscopic strain, after one full cycle (in which case only irreversible processes will be observed). Hereafter we will refer to those correlation values as the in-quadrature correlation and the full-cycle correlation, respectively. Note that in this chapter we will only discuss the signal detected in the direction perpendicular to the shear, in order to only detect the nonaffine deformations. This corresponds to the q_{\perp} signal discussed in chapter 6, where the subscript will be hereafter omitted for simplicity.

Both full-cycle and in-quadrature correlations are shown in Fig. 8.5a as a function of strain amplitude, for a frequency $\omega = 0.025$ Hz. One can identify a "linear" range of strain amplitudes, for which the observed correlation goes back to 1 after one full cycle, indicating the microscopic reversibility of the deformation. In this regime, reversible nonaffinities are observed, as one can see from in-quadrature correlation data, and can be studied using the same approach described previously. To this aim, we assume that our experimental data are well described by the phenomenological expression: $g_2 - 1 = \exp\{-[qu_{na}]^{\alpha}\}$, where $u_{na}(\gamma_0)$ represents a nonaffine root mean square (rms) displacement after one cycle or at the maximum strain. To find the value of α we look at the logarithm of the in-quadrature correlations for different scattering vectors q , and we introduce a manual scaling parameter $f(q)$ in order to collapse data for different q values on a mastercurve (Fig. 8.5b). $f(q)$ is then represented in Fig. 8.5c, from which we find a value for $\alpha = 0.6$. Consistently, in the linear regime we find that $-\ln(g_2 - 1) \propto \gamma_0^{0.6}$, implying that $u_{na} \propto \gamma_0$ (Fig. 8.5b). This suggests that, like in colloidal gels, here the observed reversible nonaffinities can be ascribed to the elastic response of the spatially heterogeneous sample. Indeed, by looking at full-cycle correlations, we check that the deformation is microscopically reversible for $\gamma_0 \lesssim 10\%$. Beyond 10% deformation the picture changes: in-quadrature u_{na} deviates from the linear relation, and a residual u_{na} is measured after one full cycle (Fig. 8.5d). The reversible to irreversible transition is better represented in Fig. 8.6, where the u_{na} extracted from full-cycle correlations is compared with the third harmonic content of the strain signal. The comparison between macroscopic rheological properties and the microscopic probe suggests that, as it was the case for the colloidal gels, the nonlinear transition corresponds to the onset of microscopic irreversibility.

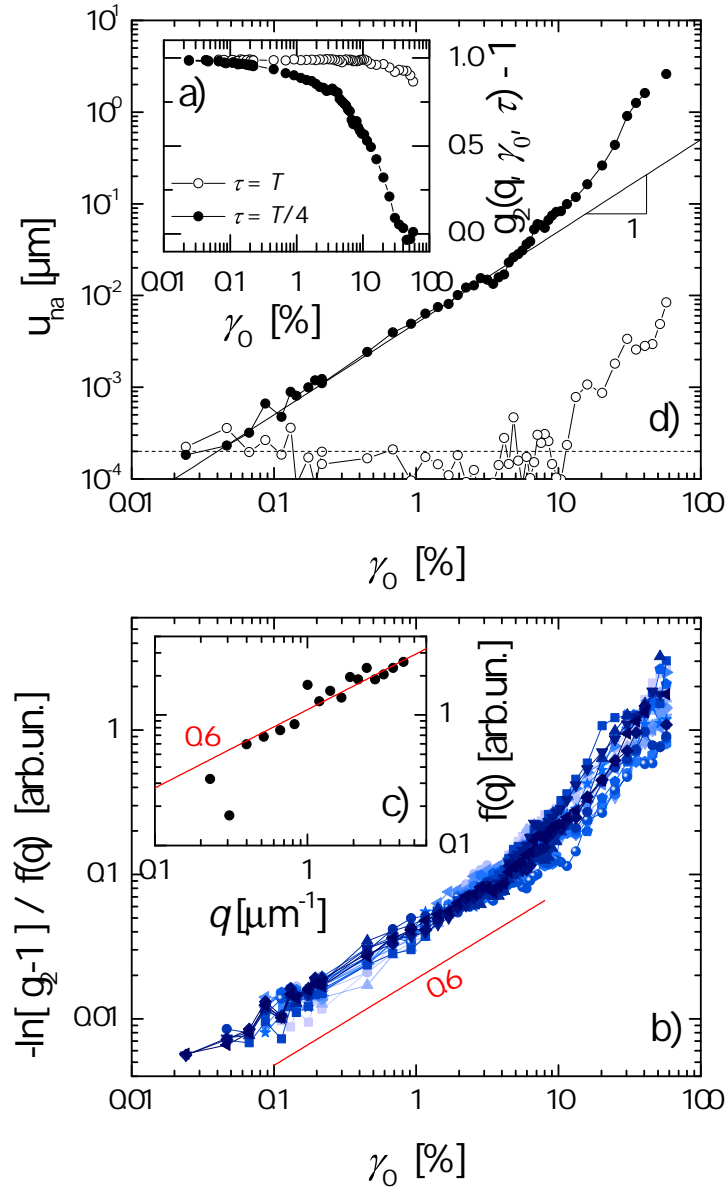


Figure 8.5: (a) Correlation functions obtained by correlating the system at rest with the system after one full cycle (full-cycle correlation, open symbols) and at maximum deformation (in-quadrature correlation, filled symbols), plotted against the deformation amplitude γ_0 for one representative scattering vector $q = 4.3 \mu\text{m}^{-1}$. (b) Logarithm of the in-quadrature correlations plotted against strain amplitude for different scattering vectors, ranging from $0.2 \mu\text{m}^{-1}$ to $4.3 \mu\text{m}^{-1}$. Data were vertically rescaled using an arbitrary function $f(q)$ to collapse them on a mastercurve. (c) Rescaling parameter $f(q)$ as a function of the scattering vector. (d) Nonaffine rms displacement extracted from the data shown in panel (a) as described in text and plotted as a function of γ_0 . Open symbols: residual (irreversible) rms displacement after one full cycle. The dashed line represents the average error of the measurements. Filled symbols: total nonaffine displacements at maximum deformation. The solid line represents a linear fit in the linear regime.

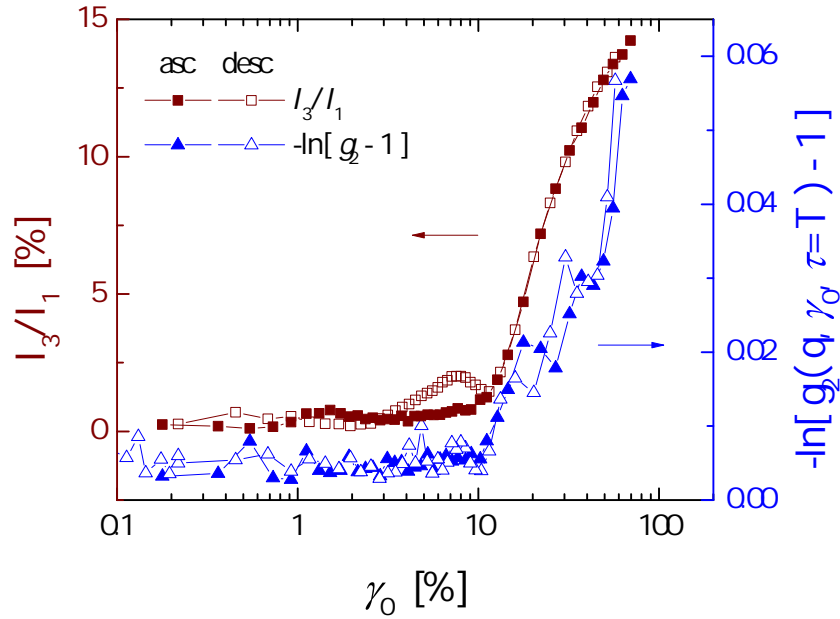


Figure 8.6: Brown, left axis: third harmonic content of strain signal, normalized by the first harmonic. Blue, right axis: logarithm of the intensity correlation function after one full cycle, highlighting irreversible deformations. In both series, filled and open symbols refer to increasing and decreasing stress ramps, respectively.

The transition from linear to nonlinear regimes can be better characterized by looking at higher order correlation echoes, since plastic rearrangements are accumulated upon successive cycles. To this aim we repeat the same experiment by increasing the number of oscillations per stress amplitude to $N = 500$: the decay of higher order echoes is shown in Fig. 8.7. Amplitudes below 6% are not shown for clarity, but substantial collapse with the decay obtained at 6% is found: we attribute the decay observed at $\gamma_0 \leq 6\%$ entirely to spontaneous dynamics. On top of this thermal relaxation, an additional contribution, strongly stress-dependent, is observed for amplitudes beyond 6%, which allows one to locate the onset of microscopic irreversibility somewhere between 6% and 6.6%, remarkably earlier than the threshold previously identified based only on the first correlation echo, but consistent with γ_σ (Fig. 8.4). We will comment on this later on in this section.

Beyond 6% deformation the correlation functions evolve in an intriguing way: in a first stage, from 6.6% to around 10%, they decorrelate increasingly faster while preserving the characteristic shape of thermal dynamics, i.e. a compressed exponential with exponent $\beta_s = 1.55$. By contrast, in the large deformation limit the correlation functions are rather described by stretched exponentials, with a different, and q dependent stretching exponent $\beta_f(q)$. In between the two regimes, a hybrid regime is found, where a sum of the two exponentials seems to provide a reasonable description of the experimental data.

Thus, we find that the whole set of experimental data can be described by the following empirical equation:

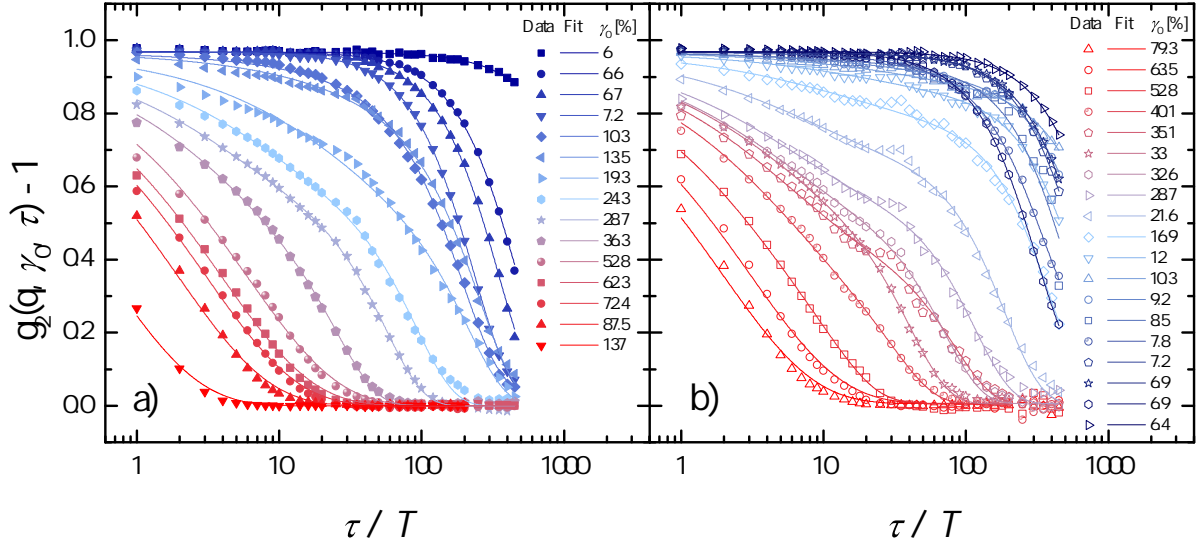


Figure 8.7: Decay of higher order correlation echoes as a function of time delay normalized by the oscillation period T , for one representative scattering vector ($q = 4.3 \mu\text{m}^{-1}$) and different strain amplitudes during the increasing (a) and the decreasing (b) stress ramp. Symbols: experimental data. Lines: best fits obtained using Eq. 8.1.

$$g_2(q, \gamma_0, \tau) - 1 = \left\{ A(q, \gamma_0) \exp \left[- \left(\frac{\tau}{\tau_f(q, \gamma_0)} \right)^{\beta_f(q)} \right] + [1 - A(q, \gamma_0)] \exp \left[- \left(\frac{\tau}{\tau_s(q, \gamma_0)} \right)^{\beta_s} \right] \right\}^2 \quad (8.1)$$

This function represents the superposition of two relaxation modes: a first slower one with characteristic time τ_s and exponent β_s , which is q -independent and equal to the one measured at rest, and a second faster one, with characteristic time $\tau_f < \tau_s$ and a q -dependent (but γ_0 -independent) exponent β_f . The parameter A represents the relative weight of the two modes. Figure 8.7a shows experimental data for a representative scattering vector $q = 4.3 \mu\text{m}^{-1}$ and different amplitudes γ_0 , together with best fits obtained using Eq. 8.1. A global fit of the experimental data yields a stretching exponent $\beta_f = 0.67$ for the second, faster mode. Figure 8.8 shows the fitting parameters extracted at different amplitude.

From Fig. 8.7 and 8.8, several regimes can be identified:

- I) in the linear regime ($\gamma_0 < 6.6\%$) one has $A = 0$, which selects the spontaneous mode alone. In this regime, τ_s is independent of γ_0 , and decreases as q^{-1} (Fig. 8.3), which is typical of many soft systems where relaxation is ballistic and believed to be driven by internal stress relaxation [Ramos 2001].
- II) In a second regime, from 6.6% to around 10%, A is still 0, but τ_s becomes strongly dependent on γ_0 : this suggests that the underlying microscopic processes are the

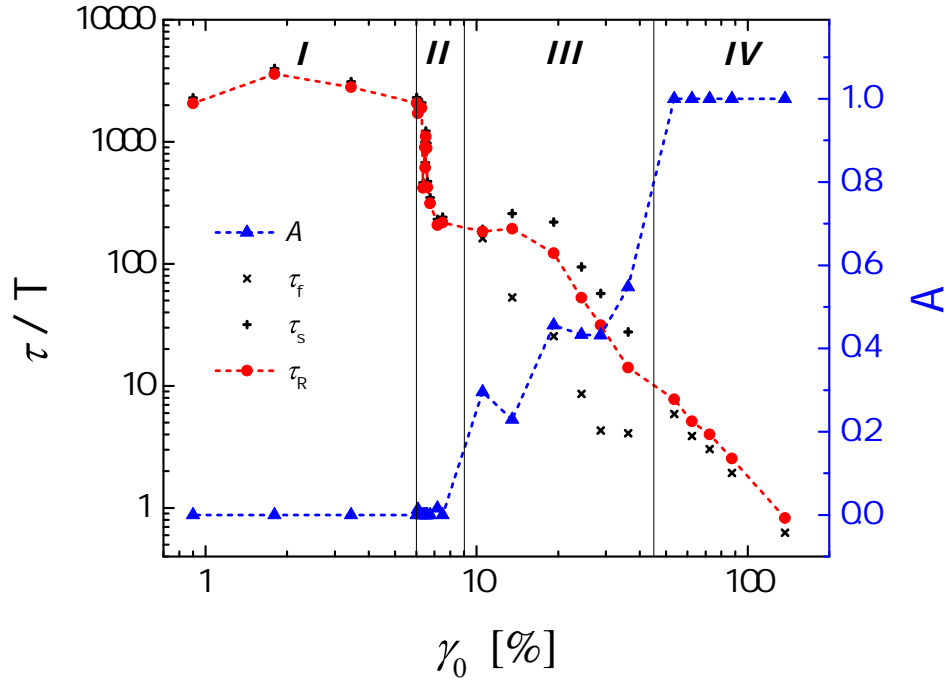


Figure 8.8: Blue, right axis: Relative weight of the two relaxation modes at different strain amplitudes γ_0 . Black, left axis: relaxation times of the two modes (crosses) and total relaxation time defined in Eq. 8.2 (red circles) as a function of strain amplitude, for one representative scattering vector $q = 4.3 \mu\text{m}^{-1}$. Vertical lines are drawn to highlight the four regimes discussed in the text, and identified by the bold labels.

same as the ones observed in the linear regime, but their rate accelerates steeply as soon as the applied stress becomes large enough to help overcoming some activation energy barrier. This marks what we called the onset of microscopic irreversibility. It is worth to mention that this acceleration is only observed at large enough scattering vectors (beyond $1 \mu\text{m}^{-1}$), most probably because of the limited time window accessed in the experiment: indeed, at the smallest scattering vectors the experimental time is too short to observe the thermal relaxation, and only the fast mode is properly observed.

- III) As stress is further increased ($10\% \lesssim \gamma_0 \lesssim 45\%$), the second, faster mode appears. This is the point where irreversibility starts to be observed also by looking only at the first correlation echo (Fig. 8.6). In this range both modes are needed in order to properly describe the correlation functions, but the fast mode becomes increasingly relevant, and A varies continuously from 0 to 1. Unlike the first, slow mode, the fast mode is only observed in the nonlinear regime (note that it appears together with the higher order harmonics in the strain signal): we speculate that it might be associated to the nucleation of "softened" regions inside the sample, which are more prone to plastic deformation. The coexistence of these two modes

in the intermediate deformation range separating the linear regime from the large amplitudes limit might suggest that outside the softened regions the system still relaxes following the same slow mode that characterizes thermal processes at rest. Under this assumption, A would represent the relative abundance of those "softer" zones.

- IV) Beyond 45% deformation, A approaches 1, and only the second, fast mode is visible. In our model this corresponds to complete yielding, and interestingly it occurs in rough correspondence to the development of the terminal slopes in the nonlinear viscoelastic moduli. Beyond this threshold, we find that the characteristic relaxation time scales as q^{-1} , again indicating ballistic dynamics, and decreases as γ_0^{-2} (Fig. 8.9).

As mentioned previously, eventual hysteresis is addressed by increasing the stress amplitude starting from the linear regime until large strains, and then reversing the stress ramp, decreasing the amplitude until the linear regime is again recovered. Results obtained during this second stress ramp are shown in Fig. 8.7b, whereas Fig. 8.10a compares a few representative strain amplitudes chosen during the two ramps. As one can see, good agreement is found at large strains, whereas at lower strains an anomalously slow relaxation time is found, which has to be attributed to the first, slower relaxation mode. A possible explanation of such hysteresis of the slow relaxation time is linked to the interplay between aging and shear rejuvenation, since complete yielding might partially erase the internal stress gradients that represent the driving force for the slow relaxation mode. This hypothesis is corroborated by the observation that eventually the slow relaxation time speeds up as the amplitude is continuously decreased, which causes the correlation curves to cross each other (Fig. 8.7b), an unusual feature that can be interpreted as an effect of aging.

All the regimes discussed so far can be efficiently grasped by looking at the total relaxation time τ_R , which can be extracted from an integral of the correlation functions, and that corresponds to an analytical expression involving all model parameters:

$$\tau_R = A\tau_f\Gamma\left(\frac{1}{\beta_f} - 1\right) + (1 - A)\tau_s\Gamma\left(\frac{1}{\beta_s} - 1\right) \quad (8.2)$$

where $\Gamma(x)$ represents Euler's Gamma function. The τ_R defined in Eq. 8.2 is a robust indicator, less sensitive to the fit quality than τ_s and τ_f separately, and it is represented in Fig. 8.10b for two representative q vectors. By looking at the large q , one can again distinguish the first drop, connected to the stress activation of the slow relaxation mode, a quasi-plateau region, where the coexistence of the two relaxation modes is observed, and the final large strain regime, where τ_R decreases roughly as γ_0^{-2} . Once again, an intriguing qualitative reminiscence can be found with respect to the state diagram of a system undergoing a first order phase transition.

In this representation, hysteresis is observed as an open loop enclosed between the increasing and the decreasing stress ramps, and it is only observed at large scattering

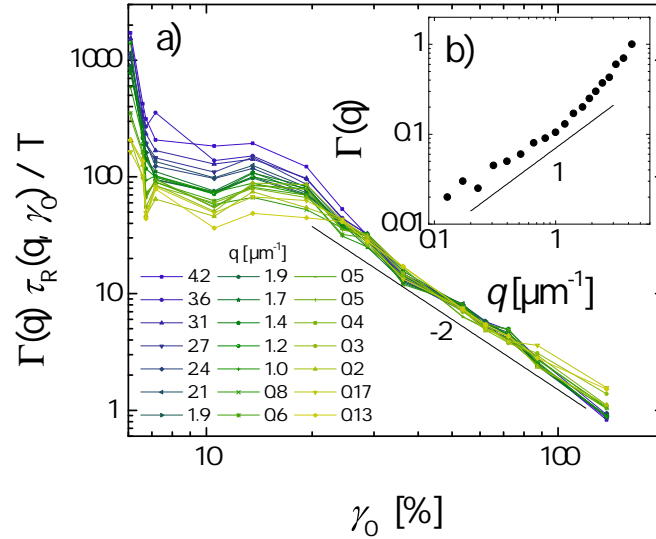


Figure 8.9: (a) Relaxation time τ_R (defined as in Eq. 8.2), rescaled by using a q -dependent scaling parameter $\Gamma(q)$ to obtain best collapse in the large amplitudes regime and plotted as a function of the shear amplitude γ_0 for different values of the scattering vector q (in the legend, increasing from yellow to blue). (b) Scaling parameter $\Gamma(q)$ as a function of q .

vectors, once again possibly because the experimental time is too short to detect variations in the slow relaxation time.

8.6 Conclusion

In this chapter we have studied a soft glass composed of densely packed PNIPAM microgels, at an effective volume fraction $\Phi = 1.5$. The microscopic structure of the sample, probed by static light scattering, showed a power law decrease of the scattering intensity covering the whole range of accessed scattering vectors. This feature was rather unexpected for such a system, and deserves deeper investigation.

On the other hand, the spontaneous dynamics measured at rest are ballistic with compressed exponential relaxations, which is in line with what commonly found on similar systems. The linear and nonlinear rheology was also characterized, mainly in oscillatory shear, and showed a characteristic single step yielding process covering a deformation range around $6\% \lesssim \gamma_0 \lesssim 25\%$, as indicated by different nonlinear features.

To better understand the microscopic origin of yielding, we have coupled dynamic light scattering to shear rheology and have tracked both the reversible nonaffine dynamics and the decay of higher order correlation echoes, up to $N = 500$ cycles. Different regimes are found by increasing the amplitude: unperturbed thermal relaxation is found in the linear regime, and it accelerates sharply as the amplitude is increased in the nonlinear regime. Increasing further γ_0 , a second faster relaxation mode appears, qualitatively

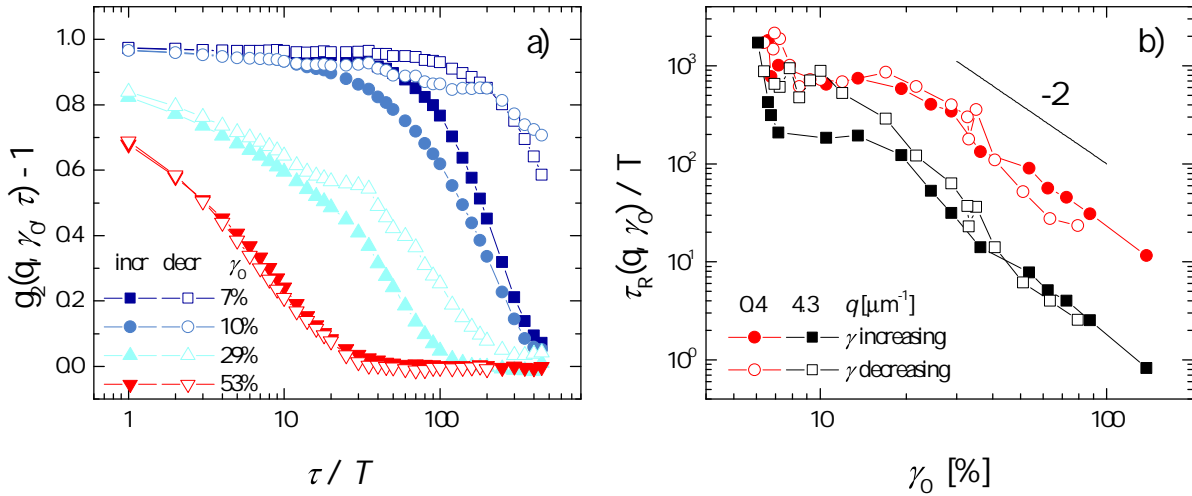


Figure 8.10: (a) Comparison between correlation functions observed during the increasing and the decreasing stress ramp, for some representative strain amplitudes (values in the legend) and $q = 4.3 \mu\text{m}^{-1}$. (b) Relaxation times τ_R for both increasing (filled symbols) and decreasing (open symbols) stress ramp, plotted as a function of the strain amplitude γ_0 for two representative scattering vectors (values in the legend).

different from the first one. Initially both modes can be distinguished, with the second one growing in amplitude, until the first slower mode disappears beyond 25% deformation, which coincides with the development of the terminal regime in the nonlinear viscoelastic moduli G' and G'' .

Upon reversing the stress ramp, a slight hysteresis is observed in the rheological measurements, arising from the interplay between aging and shear rejuvenation. The same hysteresis is retrieved in the microscopic dynamics, in particular in the slow relaxation mode.

The emerging picture has features remarkably similar to the ones observed in first order phase transitions, with the two phases being the solid-like phase found in the linear regime and the fluidized phase in the large strain limit. The two are separated in an intermediate range of deformations by a region of phase coexistence around the loss peak observed in rheology. In order to check the generality of this picture, we investigated in a similar way another soft glassy material, namely a concentrated emulsion. A preliminary comparison between the two is very intriguing and will be sketched in the conclusive discussion.

General Conclusions and Perspectives

Conclusions

In this work I have developed a novel experimental setup coupling a custom-made stress-controlled shear cell in the linear translation parallel plate geometry to a small angle static and dynamic light scattering apparatus. Dynamic light scattering is a very powerful technique, but its application to the investigation of transient shear is far from trivial. For this reason, I have studied how to decouple affine and nonaffine shear deformations, which as a side effect has led to an optimization of the small angle light scattering setup in order to enhance the sensitivity to nonaffine deformations. As a first example, the data analysis protocol developed in this study has been applied to the deformation of a weakly crosslinked elastomer. My experiments have revealed the presence of reversible nonaffine deformations in the linear regime, stemming from the spatial heterogeneity of the elastic network.

As a model system, this work mainly focuses on a colloidal gel characterized by a fractal structure and a power-law rheology. We find that a Fractional Maxwell model provides an accurate phenomenological description of the linear rheology, and we discuss the possible relationship between this model and the structure of the gel. Under a constant shear stress, the colloidal gel exhibits a power-law creep eventually followed by delayed failure when the stress is large enough. The thorough investigation of the microscopic structure and dynamics during the transient creep preceding delayed failure represents the central part of this work. We identify three regimes, which correspond to the primary, secondary and tertiary creep regimes common to a wide spectrum of materials. After the first elastic deformation, the primary creep is characterized by a power-law sublinear deformation, which is very well described by linear viscoelasticity and which is macroscopically recoverable upon release of the applied stress. This suggests that minor damage is cumulated during primary creep, and indeed we find that the microscopic dynamics are partially nonaffine, again as a consequence of spatial heterogeneity, but completely reversible. The secondary creep coincides with an upturn of the deformation rate, which deviates from the power law dictated by linear viscoelasticity and passes through a minimum. We find that such rather smooth deviation from linearity is accompanied at the microscale by a very sharp and clear transition to a regime where particle displacements are no longer reversible, which is the signature of emergent plasticity. In the tertiary regime the network, weakened by plasticity, accelerates its deformation until delayed failure occurs, with a divergence of the shear rate. Interestingly, we find that most of the microscopic plasticity detected during the experiment is confined to two well defined bursts: the first occurs in correspondence to the deviation from linearity, during the secondary creep, and the second occurs at the very end, in correspondence to the failure. The two bursts are

qualitatively different, and separated by several hours, which makes the first of them extremely appealing in order to predict the delayed failure. Remarkably, this change in the microscopic dynamics appears to have no counterpart in the structure, as it is probed by static light scattering: the structure is essentially preserved until failure. For this reason, we like to call the observed plastic burst a microscopic dynamic precursor of the delayed failure.

The onset of microscopic irreversible dynamics is addressed also in a second series of experiments, under oscillatory shear. We use our novel setup to tackle some of the questions that are still open or debated, namely the nature of the yielding transition observed with increasing shear amplitude and the mechanical effect of progressive damage created at intermediate shear amplitudes. We investigate the sample dynamics under shear in a stroboscopic way by looking at the correlation of the microscopic configuration of the sample following an integer number of oscillations (correlation echoes). We find that the onset of the rheological nonlinear regime coincides with the onset of microscopic irreversibility of the colloidal gel. This shows that the initial growth of the loss modulus originates from the energy dissipated by irreversible microscopic plasticity. This can be quantified by a plastic decay rate, which is shown to increase very steeply in the nonlinear regime. The strong correlation between such increase and the much smoother increase of the loss tangent suggests that a link between the macroscopic mechanical properties and the microscopic dynamics, suggested by several theoretical models, can be quantitatively drawn. This is specially interesting since in the nonlinear regime the progressive weakening of the gel network, caused by repeated oscillations at a given stress amplitude, measurably affect the mechanical properties of the sample, causing a sublinear increase in amplitude and even delayed failure in the long run under sufficiently large amplitudes. Our experiments allow one to measure a qualitative change in the microscopic dynamics preceding delayed failure under oscillatory as well, which might be important for many applications.

Finally, the generality of the above conclusions is tested by repeating the oscillatory shear experiments on a different sample, namely a colloidal glass composed of soft microgel particles. This sample does not exhibit catastrophic failure. Hence, a wider range of shear amplitudes can be applied in a controlled way, from the linear regime to the large amplitude regime well beyond the yield stress. The yielding transition which we characterize by following the decay of the correlation echoes appears to be rich of physical information. After a first acceleration of the microscopic dynamics (also measured on colloidal gels), a complex phenomenology is observed, with the correlation decay changing shape in a way that can be described as the coexistence of two relaxation modes. Our results appear to be consistent with the increasingly popular analogy between yielding and first-order phase transitions, where the shear fluidization of a soft solid is described as a gradual process passing through the coexistence of solid-like and liquid-like regions. Reading our results in light of this hypothesis further confirms the potential of our approach, and calls for new, more conclusive experiments, which will be performed in the near future.

Perspectives

As it has been documented in the introduction, the possibility of directly addressing the microscopic plastic rearrangements during shear paves the way for a better understanding of a wide range of phenomena like fatigue, yielding and delayed failure. Not only this is crucial for obtaining a comprehensive view of soft materials [Liu 1998], but it may also represent a key element in many applications, from the development of new materials with enhanced mechanical performance to the monitoring of the health of structures and the prediction of delayed catastrophic events related to geology or engineering. This work shows that this possibility has become a reality, at least for a class of systems for which shear rheology and light scattering are relevant. Moreover, the experiments shown in this work demonstrate that expectations have not been betrayed: microscopic plasticity does display dynamic precursors of delayed failure, which can now be detected and characterized. Given the large amount of potentially relevant applications of our approach, it would be hard and most probably unrealistic to list all the possible perspectives that this work opens to future research on the long run. For this reason, here we limit ourselves to sketch the main axis that we find most promising, and in which direction we are currently progressing.

Power law rheology and fractional models

A first specific point raised by our experiments concern the microscopic origin of power law linear rheology. If this is well established for critical gels, whose structure is fractal up to the largest lengthscales, the role played by the finite cluster size is not trivial. In chapter 5 we have evoked the possibility that a deviation from the pure Fractional Maxwell model might be observed at small frequencies for non-critical gels. However, we have also argued that from an experimental point of view, accessing frequencies lower than the characteristic Fractional Maxwell time is impractical because of physical aging. Therefore, we speculate that such deviation might eventually be probed for gels at higher volume fraction, for which the cluster size would be smaller. At the same time, it would be interesting to better characterize the nonlinear rheology as well, for example by checking the validity of strain-time separability.

The linear and nonlinear rheology can also be studied by numerical simulations: inspired by the work of Jagla [Jagla 2011], we plan to modify the numerical simulations described in appendix B by introducing disorder in the distribution of spring stiffness and a viscous dissipative mechanism in order to mimic the linear viscoelastic spectrum. To us, this model appears to be a good candidate to explore the interplay of plasticity and linear viscoelasticity in the various regimes of deformation.

Delayed failure and plastic activity

Despite the results already obtained on the plastic dynamics during creep and delayed failure, our experimental data are still rich of features that deserve deeper investigation. For instance, we have performed several series of creep and recovery measurements, by varying the applied stress σ_0 and the creep time t_{creep} before stress release. Macroscopic rheology shows that after creep deformation in the linear regime the strain recovery $\gamma(t)$ follows a well defined power-law decay that in the long run brings γ back to the initial $\gamma = 0$ configuration, whereas deviations from the power law are observed when the creep deformation grows beyond the linear regime, resulting in a finite residual strain γ_∞ at the end of the creep recovery. Measuring γ_∞ under different applied stresses and creep times would thus provide a quantitative, macroscopic estimation of the creep reversibility. However, it turns out that γ_∞ is typically very small (which is in line with the already discussed brittleness of our gel): in our preliminary experiments it is always less than 10% of the strain γ_{creep} cumulated during creep, and grows linearly with γ_{creep} , i.e. sub-linearly with t_{creep} . A clean measurement of γ_∞ would thus require very long experiments, which are impractical also because of the spontaneous aging of the gel (cf. chapter 5). On the other hand, the microscopic reversibility probed by dynamic light scattering proves to be once again much easier to access. In such experiments, the sample during recovery is correlated with the sample at rest before creep. We observe that, as the macroscopic strain is recovered, the correlation function grows, indicating that the system is evolving towards a microscopic configuration closer to the one before applying a stress step (Fig. C.1). At the smallest stress amplitudes, the correlation clearly tends towards unity, which would imply complete microscopic reversibility, whereas when the nonlinear regime is approached the correlation growth becomes much slower, and it seems to tend towards a plateau value lower than 1. A measure of such plateau value would provide a quantitative estimation of microscopic irreversibility. We find that such measurement is much easier to obtain than rheological measurements. In the future it could be interesting to investigate the onset of irreversibility using this experimental protocol as well.

Another intriguing feature deserving deeper analysis is certainly the structural asymmetry $\chi(q, \gamma)$. If it is true that no spectacular features are observed at first sight in that signal, it is also worth to remark that under creep large fluctuations are observed, which are not present in the signal at rest (Fig. C.2, also cf. chapter 6), and thus they cannot be simply attributed to experimental noise. Moreover, the anisotropy exhibits a sharp peak at failure, which might contain precious information on the failure mechanism in the very last stages, where dynamics are difficult to probe in a consistent way because of the strong time dependence (Fig. C.2). Moreover, it is not clear whether relevant information can be extracted by the time fluctuations of the correlation signal. One intriguing indication in this sense is that although an overall nice agreement between the local and the macroscopic strain is found, the local strain as it is inferred by the affine component of particle displacements suffer relevant fluctuations at rather high frequency (Fig. C.3), whose statistics might reveal interesting features.

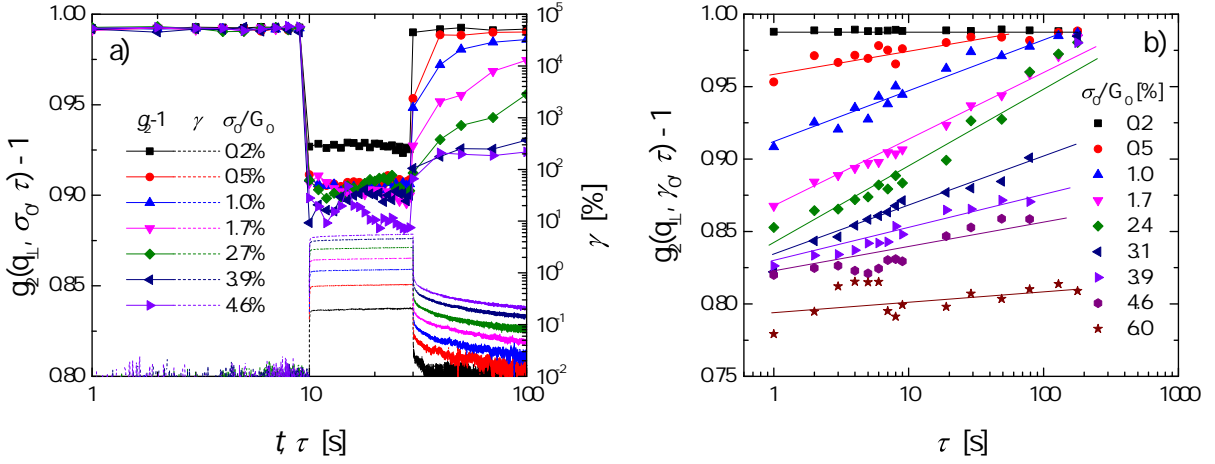


Figure C.1: (a) Dashed lines, right axis: macroscopic strain $\gamma(t)$ during a creep and recovery step under a stress σ_0 specified in the legend (G_0 is the plateau elastic modulus, cf. chapter 5). Stress is applied at $t_{\text{on}} = 10\text{s}$ and released at $t_{\text{off}} = 30\text{s}$. Symbols, left axis: intensity correlation $g_2(q_{\perp}, t = 0, \tau) - 1$ between the system at time $t = 0$ and the system at time $t = \tau$, plotted as a function of time delay τ for one representative scattering vector $q_{\perp} = 1 \mu\text{m}^{-1}$ (oriented perpendicular to shear). (b) Symbols: intensity correlation $g_2(q_{\perp}, \tau) - 1$ between the system at the moment of stress release (time $t = t_{\text{off}}$) and the system at time $t_{\text{off}} + \tau$, plotted as a function of the time delay τ for one representative scattering vector $q_{\perp} = 2.6 \mu\text{m}^{-1}$. Straight lines are a guide to the eye.

Perhaps even more interesting would be to repeat these experiments by changing the sample details. For example, the role of sample structure and in particular of the cluster size as characteristic lengthscale for microscopic plasticity can be demonstrated by changing sample concentration. Taking into account the optical and mechanical requirement, set by turbidity and stiffness respectively, we estimate that concentrations in a range $1\% \leq \phi \leq 30\%$ should be easily accessible, which would allow us to span more than one decade in cluster size, up to a maximum value $\xi_{\text{max}} \sim 2.5 \mu\text{m}$, which would be particularly interesting because that lengthscale would be associated to a scattering vector $q^* \sim \pi/\xi_{\text{max}} \sim 1.2 \mu\text{m}^{-1}$ well into the range probed by our light scattering apparatus. Detecting reversible and irreversible dynamics on samples with different characteristic lengthscales could provide strong indications on the relevance of sample structure for the failure mechanism. Another sample parameter that could be interesting to change in a second instance is the strength and range of the attractive interactions, to check that by weakening the interparticle interaction one can tune the fragility of the system, hence controlling the impact of plastic events on the mechanical properties. In our system, this can be easily tuned by changing the amount of urea in the initial solution, which determines the terminal ionic strength of the solvent, I . From DLVO theory, it turns out that I not only sets the interaction energy, but also the equilibrium interparticle distance: the higher the ionic strength, the stronger the bonds and the smaller the equilibrium distance.

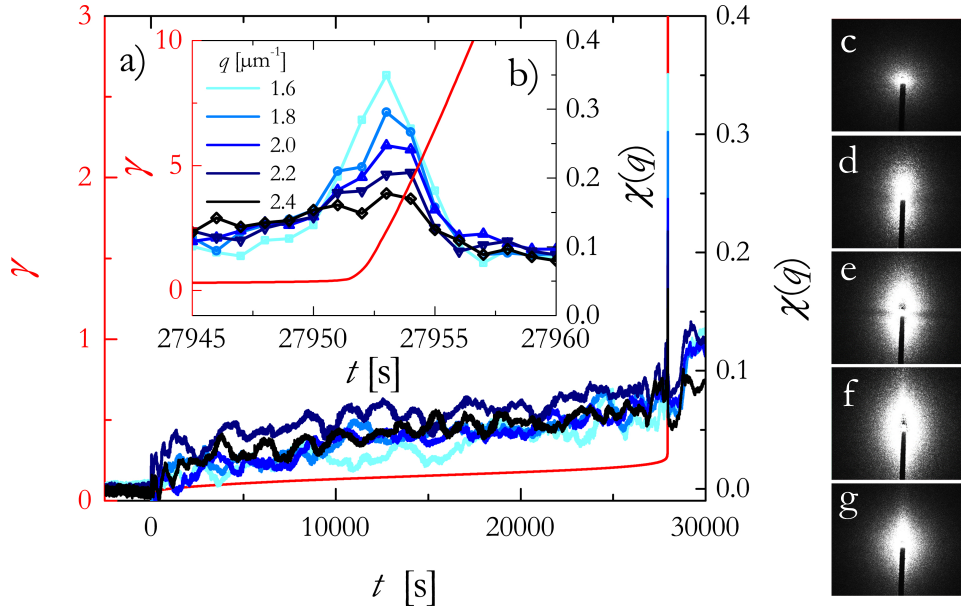


Figure C.2: (a) Creep deformation (red, left axis) and structural anisotropy $\chi(q)$ during creep (blue, right axis). Different shades of blue represent different q vectors (increasing from light to dark, values specified in the legend). (b) Same data as panel (a), zoom on the sharp peak observed at rupture. (c-g) Snapshots of the 2D scattered intensity at rupture. Images are taken at times $t = 27950$ s (c), 27951 s (d), 27952 s (e), 27953 s (f), and 27955 s (g).

This is particularly interesting since during gelation I increases in time as a consequence of enzymatic activity before saturating when the reaction is completed. Therefore, one can expect that at the end of this process the gel will be frustrated, with slightly stretched particle chains, and frustration increases with I . Increasing frustration and strength of attraction should both contribute to producing a more fragile material, whereas in the opposite limit the material should be less stiff but also more ductile. We already have an indication that this guess is correct. Indeed, when the final ionic strength is increased beyond 2 mol/l the material is so much frustrated that we observe that it self-fractures at rest. Therefore, this appears to be a relevant parameter to be changed in the future. Finally, extending the analysis to other network-forming systems might be clearly very interesting.

Furthermore, adding spatial resolution to our analysis can obviously add a fundamental piece of information, allowing to detect eventual dynamic heterogeneities and correlate them with the positions where the crack would be nucleated after yielding, which would be of major interest for applications. Dynamic light scattering experiments can be performed in a spatially-resolved fashion [Duri 2009], although this implies an obvious trade-off between space and wave-vector resolution. Given the overall complexity of our experiments, we chose to perform spatially resolved dynamic light scattering at one fixed scattering vector q . A few preliminary experiments have been performed in

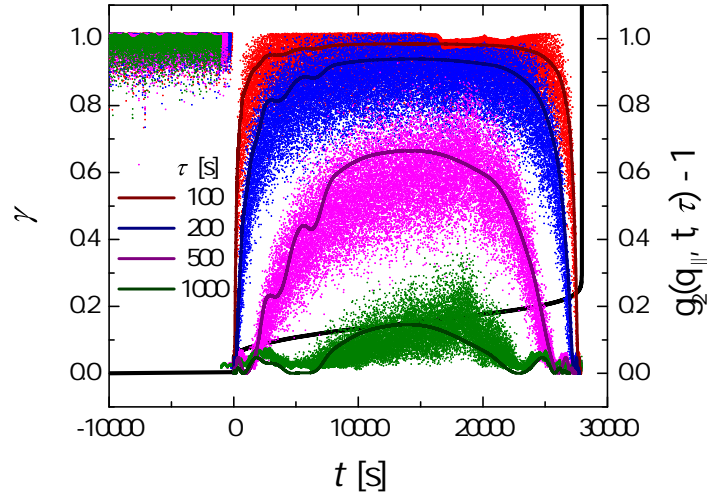


Figure C.3: Black line, left axis: creep deformation $\gamma(t)$. Dots, right axis: correlation functions measured along the shear direction, for $q_{\parallel} = 2.6 \mu\text{m}^{-1}$ and various time delays: $\tau = 100\text{s}$ (red), 200s (blue), 500s (purple), 1000s (green). Colored lines: prediction based on purely affine deformation: $g_2 - 1 = \text{sinc}^2[q_{\parallel}(\gamma(t + \tau) - \gamma(t))e/2]$ (cf. chapters 4 and 6), calculated based on the measured macroscopic strain $\gamma(t)$.

transmission geometry, with $q \sim 1 \mu\text{m}^{-1}$. The results promisingly suggest that plastic activity is spatially heterogeneous, as it is also suggested by other experiments carried on in our group by Angelo Pommella, but they also show that larger scattering vectors are required in these experiments. Hence, we are currently working to finalize a second, spatially resolved light scattering apparatus working in backscattering geometry, which will be able to acquire data simultaneously with the small angle apparatus. This would be crucial in order to correlate the observed plastic dynamics with the distance from places where future cracks would appear after failure.

Given the catastrophic nature of delayed failure, investigating the very last stages before fracture is complicated by the fact that all relevant processes happen in a very short time window and after a very long induction time, which makes their proper detection rather challenging. For this reason, it would be interesting to complement those observations with steady-rate experiments, where failure time can be predicted with much higher precision, and therefore detected with higher accuracy, also thanks to the constant rate. However, this requires a strain-controlled shear cell. We are currently working to equip our shear cell with a piezoelectric actuator and a force sensor, and preliminary experiments are giving promising results. Moreover, a strain-controlled apparatus would allow to couple dynamic light scattering to stress relaxation experiments, which is absolutely straightforward thanks to the absence of macroscopic deformation. Independent experiments performed in our group on semicrystalline polymers under tensile deformation by Yassine Nagazi and Veronica Iadarola suggest that much can be learned from these experiments as well.

Onset of irreversibility and oscillatory yielding

The investigation of the onset of microscopic irreversibility deserves as well further investigation, starting from a refined analysis of experiments already performed. For example, for the colloidal gel it would certainly be interesting to investigate how the microscopic picture presented in chapter 7 depends on the scattering vector. Structural Lissajous curves shown in Fig. 7.5 deserve as well deeper investigation. In particular, it is interesting to remark that, as it might be appreciated from Fig. 7.5b, the structural Lissajous plots seem to develop a more elliptical shape (less eccentric) than the rheological Lissajous plots. In other words, the phase angle between the applied stress and the structural anisotropy χ appears to be larger than expected. Surprisingly, there appears to be a range of amplitudes (like the red curve in Fig. 7.5b) where stress and strain are in phase with each other, but the asymmetry is not. Investigating the origin of this effect might be a way to address complex and partially reversible intra-cycle rearrangements which cannot be detected in a stroboscopic analysis only focused on the decay of correlation echoes. Another effect, even clearer from Fig. 7.5, is that the symmetry of structural Lissajous plots is not necessarily the same as the one of mechanical Lissajous plots. Indeed, at the highest strain amplitudes, $\chi(\sigma)$ is clearly asymmetric with respect to $\pm\sigma$, which indicates the presence of even harmonics in its Fourier spectrum, whereas a Fourier transform analysis of $\gamma(\sigma)$ would still detect minor contribution of even harmonics. The physical origin of this intriguing behavior is still unclear. Since this effect is only observed at the highest amplitudes, where the sample is clearly damaged, it is possible to attribute it to some structural instability, different from wall slip or shear banding (which would produce a strong signal in the rheology as well), but deeper investigation is certainly needed to clarify this interpretation.

Delayed failure of the colloidal gel makes stress-imposed oscillatory shear impossible beyond the yield stress. Nevertheless, strain controlled rheology presented in chapter 7 shows that larger amplitudes might convey valuable information on the complex yielding mechanism. For this reason, it will be interesting to perform light scattering echo experiments in a strain-controlled fashion, and to compare the results obtained in this way with the results shown in chapter 7. For example, it is unclear if and how delayed yielding will manifest under controlled strain. We think that a comparison between the two experimental protocols would be crucial to obtain a comprehensive view of the yielding mechanism. Preliminary experiments are been currently performed, and we plan to address this more carefully in the future. A thorough comparison with transient experiments, including, but possibly not limited to, creep experiments, would also be interesting. Indeed, we have argued in chapter 7 that despite the analogies found in the two protocols (for example, the presence in both experiments of a regime of sublinear deformation grow followed by an acceleration), the two delayed failure mechanisms are profoundly different. Without recalling the previous discussion, it is interesting to mention that whereas primary creep is described by a power law dictated by linear viscoelasticity, the first sublinear increase in the strain amplitude under stress controlled oscillatory shear is logarithmic, and is

entirely attributed to nonlinear effects. It might be interesting to read this observation in view of the old debate on the difference between power-law and logarithmic creep, recalled in the introduction. This suggests that the difference between the two might not be exclusively sample-related, and that a detailed investigation of the conditions under which power-law and logarithmic creep could occur might be of general interest. In particular, in the specific case of a polymer glass [Cheriere 1997] it has been proposed that the difference between the two mechanisms is related to the characteristic size of plastic events: logarithmic creep is produced by local plasticity, whereas in power law creep plastic rearrangements explore a larger sample volume. Without claiming that this picture could be general, we observe that our experimental setup is particularly convenient for similar investigations, and that adding spatial resolution to our analysis would be extremely interesting for this reason as well.

This adds value to the comparison between different systems, like the fractal colloidal gel and soft glass. A key information which would help clarifying the picture sketched in chapter 8 would be once again the spatial distribution of the plastic rearrangements. For example, it would be interesting to check whether the (arguable) double mode decay observed in an intermediate range of amplitudes corresponds to a spatially heterogeneous dynamics, and whether single modes can be isolated by restricting the analysis to smaller regions inside the sample. This is more or less the picture suggested by the work of Knowlton *et al.* on concentrated emulsions [Knowlton 2014] (cf. Fig. 1.16).

In order to verify if the light scattering framework would be applicable to the picture proposed by Knowlton *et al.* I had the opportunity to analyze their original data, in an attempt of extending the analysis from one to several shear cycles. As discussed in the introduction, however, their tracking algorithm, which was very very efficient in following the displacements of drops across one cycle, proved to be very unfit for comparing the system before and after many shear cycles. For this reason, I have processed those data using a technique called differential dynamic microscopy (DDM) [Cerbino 2008], and briefly sketched in appendix A. This technique allows one to extract from microscopy experiments correlation functions analogous to the ones that would be accessed by light scattering. The correlation functions are represented in Fig. C.4a, and are fitted by single stretched exponential functions with variable stretching exponent β . From the fit we extract the value of β together with a relaxation time, calculated with the single-mode analogous of Eq. 8.2. Both parameters are represented in Fig. C.4b. Clear features emerge from this plot: first, the sharp transition from a γ_0 -independent linear regime to a strongly γ_0 -dependent nonlinear regime, which was already observed in the original paper, is observed, and, second, this transition is associated with a sharp, qualitative transition in the nature of the microscopic dynamics, with the correlation function passing from slightly compressed in the linear regime to highly stretched beyond the yield strain γ_y , with β assuming two rather well defined and almost q -independent values. This is consistent with the speculations offered in chapter 8, with the only difference that no coexistence of the two modes is found in this case. Nevertheless, we remind from the introduction (cf. Fig. 1.16) that the authors do observe the coexistence of two populations

of particles in a range of strain amplitudes going from γ_y to complete fluidization. Thanks to a spatially resolved analysis the authors showed that regions with faster dynamics coexist with regions where essentially no dynamics is observed. Therefore, it would be interesting to repeat the DDM analysis, to probe the dynamics of individual mobile or immobile regions. Presumably, even in the case of the soft glass investigated in chapter 8 can benefit from a spatially-resolved investigation, which would add valuable information on the progressive yielding. Moreover, the above analysis also suggests that microscopy techniques, specially combined with a Fourier analysis as it is done in DDM, may in some cases be useful to complete the observations obtained with light scattering. The versatility of our shear cell allows one to easily integrate it onto a microscope stage, which represents a side advantage with respect to standard rheo-optical apparatuses that are typically much less flexible.

More importantly, the preliminary analysis of sheared emulsions suggests that an intriguing common picture might be disclosed by comparing how yielding manifests in different samples. For this reason, it would be interesting to change further the sample details, for example exploring different volume fractions, as a way to change the sharpness of the yielding transition, in order to check whether the microscopic behavior changes accordingly.

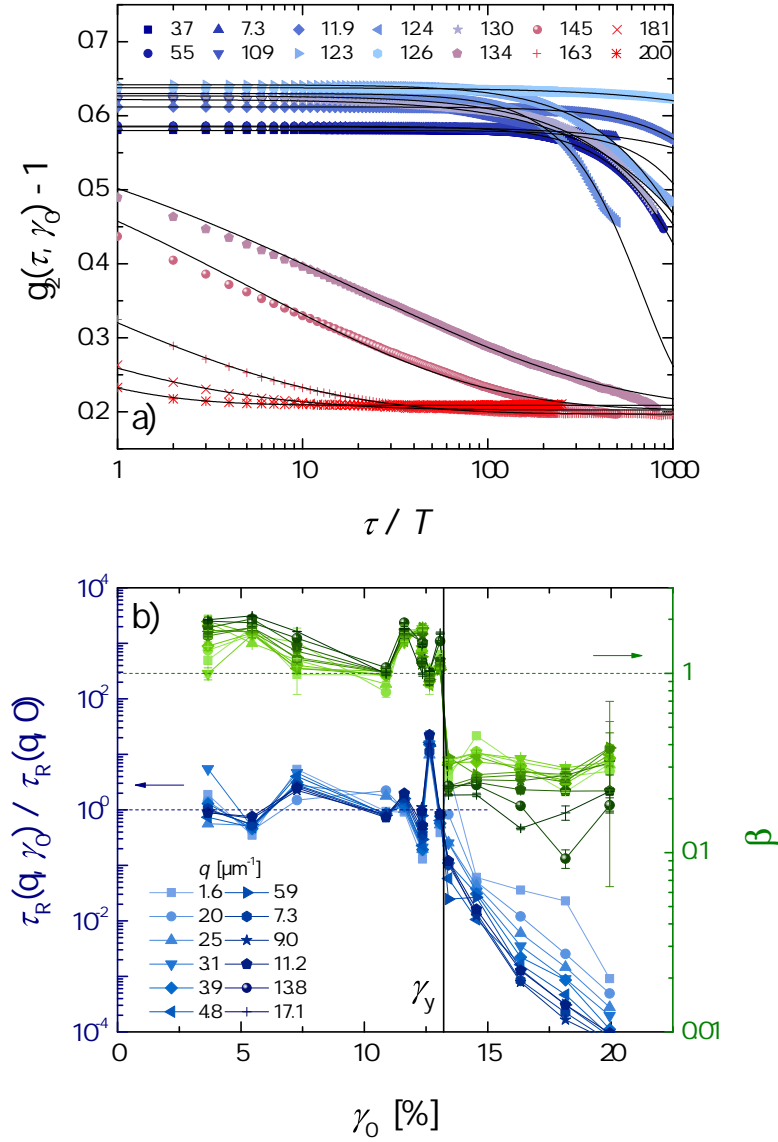


Figure C.4: Concentrated emulsions under oscillatory shear. (a) Symbols: correlation functions provided by DDM analysis as a function of the time delay, in units of the period of the oscillations, for a representative value of the scattering vector $q = 3.9 \mu\text{m}^{-1}$ and different values of the strain amplitude (specified in the legend, increasing from blue to red). Black lines are stretched exponential fits. (b) Relaxation time normalized by the relaxation time in the linear regime (blue, left axis) and stretching exponent (green, right axis) as a function of shear amplitude. Different symbols refer to different wave-vectors q (specified in the legend). Dashed horizontal lines represent $\tau(q, \gamma) = \tau(q, 0)$ and $\beta = 1$. Vertical solid line represents the microscopic yield strain γ_y . Original data from ref. [Knowlton 2014].

An efficient scheme for sampling fast dynamics at a low average data acquisition rate

*One of the major experimental challenges mentioned in chapter 1 concerns the multiscale nature of material failure. In particular, this translates in a very broad spectrum of relaxation timescales, which has to be properly sampled in experiments. Traditionally, this is done by acquiring data at a sufficient, fixed rate. However, this protocol becomes very inefficient when fast and slow dynamics have to be probed simultaneously. The following paper, published on *Journal of Physics: Condensed Matter* [Philippe 2016], introduces an alternative acquisition scheme, designed so as to reduce the average acquisition rate while retaining the information on fast dynamics.*

An efficient scheme for sampling fast dynamics at a low average data acquisition rate

A Philippe, S Aime, V Roger, R Jelinek, G Prévot, L Berthier and L Cipelletti

Laboratoire Charles Coulomb (L2C), UMR 5221 CNRS-Université de Montpellier, Montpellier, France

E-mail: luca.cipelletti@umontpellier.fr

Received 12 October 2015, revised 24 November 2015

Accepted for publication 25 November 2015

Published 25 January 2016



Abstract

We introduce a temporal scheme for data sampling, based on a variable delay between two successive data acquisitions. The scheme is designed so as to reduce the average data flow rate, while still retaining the information on the data evolution on fast time scales. The practical implementation of the scheme is discussed and demonstrated in light scattering and microscopy experiments that probe the dynamics of colloidal suspensions using CMOS or CCD cameras as detectors.

Keywords: data acquisition, image, light scattering, microscopy

(Some figures may appear in colour only in the online journal)

1. Introduction

Since the birth of modern science in the sixteenth century, measuring, quantifying and modelling how a system evolves in time has been one of the key challenges for physicists. For condensed matter systems comprising many particles, the time evolution is quantified by comparing system configurations at different times, or by studying the temporal fluctuations of a physical quantity directly related to the particle configuration. An example of the first approach is the particle mean squared displacement, which quantifies the average change of particle positions, as determined, e.g. in optical or confocal microscopy experiments with colloidal particles [1–3]. The second method is exemplified by dynamic light scattering (DLS) [4], which relates the temporal fluctuations of laser light scattered by the sample to its microscopic dynamics.

Both approaches require to sample repeatedly the system over time, which implies the acquisition of a stream of data. Modern scientific apparatuses often produce large amounts of data: this results in high-rate data flow, making data handling challenging. Two-dimensional (2D) detectors such as CMOS cameras illustrate nicely this challenge. Fast cameras that acquire images of several Mbytes at rates often exceeding 1 kHz are now affordable and increasingly popular in many

setups, raising the issue of dealing with data flows of the order of Gbytes per second. Two-dimensional detectors are widely used in optical or confocal microscopy, e.g. in biology [5], in soft matter [2, 3] or in microfluidics applications [6], but also in experiments based on conventional low-magnification imaging, e.g. for granular systems [7] or in fluid dynamics [8]. Moreover, two-dimensional detectors are increasingly replacing point-like detectors in techniques such as fluorescence imaging [9] or in the multispeckle approach [10] to DLS and X-photon correlation spectroscopy [11]. They are also at the heart of recently introduced techniques that combine features of scattering and imaging, such as photon correlation imaging [12, 13] or differential dynamic microscopy [14] and other digital Fourier microscopy techniques [15].

In this paper, we describe a scheme for acquiring data at a low *average* rate, while still preserving the information on the fast dynamics of the system. For the sake of concreteness, we will assume that the data are 2D images and illustrate the scheme with examples from scattering and microscopy experiments; however, we emphasize that the scheme is quite general and may be applied to the acquisition of any kind of data, possibly as a function of variables different from time (e.g. when sampling some sample property over space). Existing acquisition schemes typically consist in sampling the system

at a constant rate or, in a more refined version, at a rate that slowly changes in time to adapt to a possible evolution of the system dynamics [16]. The drawback of this approach is two-fold: firstly, if the dynamics of interest span several order of magnitudes or the system evolution has to be followed over a long time, a very large amount of data has to be acquired and processed. Secondly, the rate at which a detector can acquire data often exceeds the rate at which data can be processed or stored for later processing. This is typically the case of modern cameras, whose acquisition rate may exceed that at which images can be written to a hard disk (HD), sometimes even if state-of-the-art solid state devices or arrays of independent disks (RAID) are used. Under these conditions, one has to reduce the acquisition rate to match the processing or storage rate, thereby not fully exploiting the capabilities of the detector.

The multitau scheme, first proposed in traditional DLS [17] and later extended to multispeckle DLS [18] and microscopy-based microrheology measurements [19, 20], addresses these issues by coarse-graining the data over time. Several coarse-graining levels are implemented in parallel, allowing one to characterize the system evolution via temporal correlation functions (one per coarse-graining level) that span a large range of time delays with a limited number of channels. This method is particularly well-suited for processing the data on-the-fly, yielding low-noise correlation functions thanks to the massive averaging associated with coarse-graining. However, the rate at which data are acquired and processed decreases with increasing coarse-graining level. This makes it impossible to capture rapid fluctuations of the dynamics at large time delays, as observed, e.g. in the temporally heterogeneous dynamics of many glassy systems [21]. Additionally, the multitau scheme is based on fast, constant-rate data acquisition, which typically makes it impossible to write the data to the HD for later additional processing or for checking purposes. An alternative method could consist in alternating short bursts of fast acquisitions, where the images are transferred to a fast memory storage (e.g. the computer RAM or the on-board memory of the camera or the frame grabber), with long stretches of time where data are acquired at a lower rate and written to the HD. During these long stretches of time, the RAM data acquired in the previous burst should be copied to the HD. The main drawback of such a scheme is the uneven distribution of the fast and slow acquisition phases over time: if the system dynamics are not stationary (e.g. due to aging or dynamical heterogeneity [22]), one misses all changes of the fast dynamics in between two burst phases.

The method introduced in this work addresses these challenges by using a variable-delay acquisition scheme. As it will be shown, the method deliberately under-samples the data with respect to the maximum rate allowed by the detector, so as to limit the data flow rate. However, the scheme is designed so as to interlace the fast and slow acquisition phases, so that the system dynamics is sampled as uniformly as possible in time. The paper is organized as follows: in section 2 we introduce the new acquisition scheme and briefly discuss its

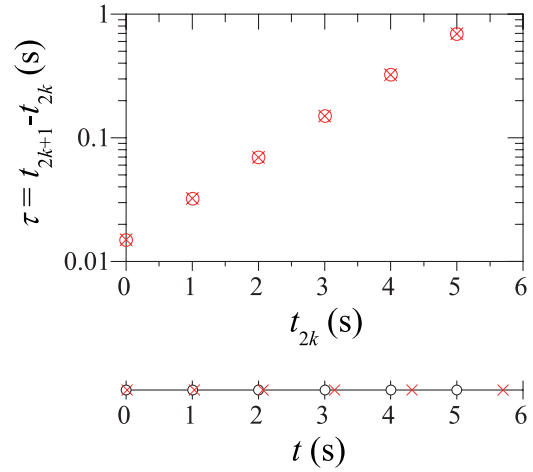


Figure 1. Acquisition scheme for $t_{pp} = 1$ s, $J = 3$, $\tau_{\min} = 0.015$ s. For the sake of clarity, only the first cycle is shown. Bottom: acquisition times. The open circles correspond to the even images, spaced by t_{pp} , the red crosses to the odd images. The cycle contains a total of $2N = 12$ images. Top: time delay between an odd image and the preceding even image, as a function of the acquisition time of the even image.

practical implementation. Section 3 reviews the essential features of the DLS, DDM, and particle tracking methods and provides details on the experimental samples. The results of the light scattering and microscopy experiments are presented and discussed in section 4, which is followed by some brief conclusions (section 5).

2. Acquisition time scheme

The acquisition scheme consists of a sequence of $2N$ images that is repeated cyclically. Each cycle is formed by two interlaced sub-sequences. The even images of the cycle are regularly spaced in time, every t_{pp} seconds (see figure 1 for an example with $t_{pp} = 1$ s). The index pp stands for the time ‘per pairs’ of images. The odd images are taken at a variable time delay τ_k with respect to the preceding even image. The time delay τ_k increases with k as a power law, such that the τ_k ’s are regularly spaced in a logarithmic scale and cover the range between a minimum delay τ_{\min} and t_{pp} :

$$\tau_k = 10^{kJ} \tau_{\min}, \quad (1)$$

with $k = 0, 1, \dots, N - 1$ and J the desired number of time delays per decade. The total number of images per cycle is dictated by the ratio between the time per pair and the minimum delay, and by the number of sub- t_{pp} time delays per decade. From equation (1) and the constraint $\tau_k < t_{pp}$, one finds

$$N = \text{ceil}\left(J \log_{10} \frac{t_{pp}}{\tau_{\min}}\right), \quad (2)$$

where $\text{ceil}(x)$ indicates the smallest integer $\geq x$. Each cycle comprises $2N$ images and lasts $N t_{pp}$; the acquisition times for the images belonging to the $M - th$ cycle are

$$t_m = (M - 1)N t_{pp} + \frac{m}{2} t_{pp} \quad m = 0, 2, 4, \dots, 2N - 2 \quad (3)$$

$$t_m = (M-1)Nt_{pp} + \frac{m-1}{2}t_{pp} + 10^{\frac{m-1}{2J}}\tau_{\min} \quad m = 1, 3, 5, \dots, 2N-1. \quad (4)$$

One may introduce a ‘compression factor’ ξ defined as the number of images that would have been acquired in a cycle with a traditional constant-delay scheme, divided by the number of images acquired over the same period with the variable-delay scheme, assuming the same minimum delay τ_{\min} in both cases. The compression factor is $\xi = (Nt_{pp}\tau_{\min}^{-1})/(2N) = t_{pp}/2\tau_{\min}$, which can be of order 100 or larger.

As an illustration of the scheme, the bottom panel of figure 1 shows the acquisition times for a cycle of $2N = 12$ images. The even images (open circles) are spaced by $t_{pp} = 1$ s; the red crosses indicate the acquisition times for the odd images, each of which is delayed by τ with respect to the preceding image, with $\tau_{\min} = 0.015$ s $\leq \tau < t_{pp}$, and where $J = 3$ logarithmically spaced sub- t_{pp} delays per decade have been used (see top panel).

Usually, τ_{\min} is chosen to be the smallest delay compatible with the camera specifications, i.e. $1/\tau_{\min}$ corresponds to the maximum frame rate. The *average* acquisition rate, however, is $2/t_{pp}$, which can be set to be much lower than the maximum frame rate by choosing $t_{pp} \gg \tau_{\min}$. This allows for enough time for the images to be, e.g. written to a hard disk or processed. In the following, we shall refer to any operation performed on the images after their acquisition as to ‘processing’. In order to decouple the acquisition process (which occurs at a time-varying rate, up to the maximum rate $1/\tau_{\min}$) from the image processing (which needs to be performed at a rate as uniform as possible, in order to cope with the hardware limitations), a buffering scheme must be used. As soon as they are acquired, the images are transferred to a buffer, whose memory space is physically located either in the PC RAM or on the frame grabber board, if available. This transfer is typically very fast and can be easily performed at an instantaneous rate equal to or even faster than the maximum camera frame rate. The buffer is read and emptied progressively by an image processing routine, at an instantaneous rate close to $2/t_{pp}$, the average data acquisition rate. In order to implement this buffering scheme, one should write a software with two separate yet synchronized threads, one for acquiring the images and one for processing them. In the experiments described below, we implement the buffering scheme in two different ways. For the light scattering experiments, the acquisition software is written in Labview FPGA, which has built-in routines for implementing the buffering scheme via a genuine multi-thread mechanism. For the microscopy experiments, we use a simple, single-thread software, where both the image acquisition and the image processing routines are called from the same loop, but the image processing routine is skipped when images have to be acquired rapidly (e.g. when the delay between consecutive images is equal to or slightly larger than τ_{\min}), while it is called repeatedly to empty the buffer when enough time is available before the next image acquisition. A code snippet in Python illustrating this procedure is provided as Supplementary Data.

3. Materials and methods

3.1. Multispeckle dynamic light scattering

Dynamic light scattering [4] experiments are performed using a setup similar to that described in [23]. The sample is placed in a temperature-controlled copper holder and is illuminated by a laser beam with in-vacuo wavelength $\lambda = 532.5$ nm. The scattered light is detected simultaneously by up to four CCD cameras (Pulnix TM-6740GE-w, images cropped to 640×160 pixels), placed at scattering angles in the range $15 \text{ deg} \leq \theta \leq 75 \text{ deg}$. For each CCD, the intensity correlation function $g_2(\tau) - 1$ is calculated from a time series of images of the scattered light using the multispeckle [10] scheme:

$$g_2(\tau) - 1 = \langle c_I(t, \tau) \rangle_t, \quad (5)$$

where the time average is performed on the two-time degree of correlation [24]

$$c_I(t, \tau) = \frac{\langle I_p(t)I_p(t+\tau) \rangle_p}{\langle I_p(t) \rangle_p \langle I_p(t+\tau) \rangle_p} - 1. \quad (6)$$

Here, $I_p(t)$ is the intensity of the p -th pixel at time t and $\langle \dots \rangle_p$ indicates an average over all CCD pixels, which are associated to a small solid angle centered around θ . The purpose of the time average of equation (5) is to reduce the experimental noise; it is performed over the full duration of the experiment for stationary samples, or over a short time window of duration t_{exp} for samples whose dynamics evolve in time. When averaging over time, care has to be taken in order to extract from the variable-delay image sequence the appropriate pairs of images separated by a given time lag. The software provided as Supplemental Data illustrates how this can be accomplished. The images are acquired and saved to hard disks using the scheme of section 2; they are then processed off-line to calculate $g_2 - 1$ according to equations (5) and (6), correcting for the CCD electronic noise and the uneven sample illumination as detailed in [24]. The CCD cameras are triggered by a TTL signal, issued from a PICDEM 2 Plus card (by Microchip Technology Inc.) programmed using in-house C code, or by a National Instrument CompactRIO-9076 card with two TTL output C Ni-9402 modules, controlled via a custom Labview FPGA code.

Dynamic light scattering data are analyzed using the usual DLS formalism for Brownian particles. For a suspension of identical, non-interacting spherical particles, $g_2 - 1$ decays at a rate dictated by the particle diffusion coefficient D and the scattering vector q [4]:

$$g_2(\tau) - 1 = \exp(-2q^2D\tau), \quad (7)$$

with $q = 4\pi n \lambda^{-1} \sin \theta/2$ and n the solvent refractive index. In section 4 we will present data for melamine particles with diameter $2a = 1.14 \mu\text{m}$ (Microparticles GmbH), suspended at a volume fraction $\varphi = 6 \times 10^{-5}$ in a 2/98 w/w water/glycerol mixture, with viscosity $\eta = 290 \text{ mPa s}^{-1}$ at temperature $T = 20 \text{ }^\circ\text{C}$, and for a suspension of PNIPAM microgels, synthesized following [25], for which the volume fraction, as calculated according to the definition of [26], is $\varphi = 0.97$ at

$T = 20$ °C. The microgel radius (and thus φ) changes with temperature [25], a property that we will exploit to illustrate the data acquisition scheme for a system with non-stationary dynamics.

3.2. Microscopy

Two series of images of colloidal suspensions were taken under an optical microscope (Leica DM IRB), using the variable delay scheme of section 2 implemented via the single-thread version of the image acquisition software. The images are taken with a CMOS camera (Basler acA2000-340 km, image format 2048×1088 pixels) using a 10x objective, such that one pixel corresponds to $0.55 \mu\text{m}$ in the sample. In the first series, we study a suspension of small particles (SP in the following), comprising polystyrene spheres of radius $a = 105 \text{ nm}$ (Microparticles GmbH), diluted to 2.5×10^{-3} w/w in a 1 : 1 v/v mixture of H_2O and D_2O that matches the density of polystyrene. The second suspension (large particles, LP) contains polystyrene particles with $2a = 1.2 \mu\text{m}$ (Invitrogen Molecular Probes), suspended at a weight fraction 0.005% in the same solvent as the SP. Data for the SP have been analyzed by DDM, while the dynamics of the LP have been quantified by both DDM and particle tracking.

3.2.1. Differential dynamic microscopy. Differential Dynamic Microscopy is a recently introduced technique that combines features of both microscopy and scattering [14, 15]. The dynamics are quantified by a correlation function similar to $g_2(\tau) - 1$ introduced above for DLS (see equation (5)), rather by tracking the motion of individual particles. The analysis is performed on $\tilde{S}(\mathbf{q}, t)$, the Fourier transform of the 2D signal $S(\mathbf{x}, t)$ recorded by the camera, where \mathbf{x} is the coordinate of an image point, and where the q vector has components $q_{x,y} = 2\pi n_{x,y}/(N_{x,y}l_p)$, with $0 \leq n_{x,y} \leq N_{x,y}$ and l_p and $N_{x,y}$ the pixel size in the sample and the number of pixels of the field of view along the x and y directions, respectively. For the sake of simplicity and efficiency, the images are cropped to a square format $N_x = N_y = 1024$ pixels. The quantity of interest is

$$c_{\text{DDM}}(q, t, \tau) = 1 - \frac{\langle |\tilde{S}(\mathbf{q}, t) - \tilde{S}(\mathbf{q}, t + \tau)|^2 \rangle_{\mathbf{q}}}{\langle |\tilde{S}(\mathbf{q}, t)|^2 \rangle_{\mathbf{q}} + \langle |\tilde{S}(\mathbf{q}, t + \tau)|^2 \rangle_{\mathbf{q}}}, \quad (8)$$

with $\langle \cdot \cdot \rangle$ an azimuthal average over \mathbf{q} vectors with the same magnitude. Equation (8) is the degree of correlation corresponding to the structure function normally used in DDM [15], except for the normalization factor. Note that while the contribution of static optical noise (due e.g. to dust on the microscope optics or the CMOS sensor) cancels out in the numerator of the last term of the rhs of (8), it does not vanish in the denominator. As a consequence, the degree of correlation does not fully decay to 0 at large τ , when the scatterers' configuration is completely renewed, but rather to a finite baseline. The optical noise varies with q ; accordingly, the baseline amplitude is q dependent. It is smallest ($\approx 10^{-2}$) at intermediate q vectors and increases both at larger q (up to

a level of ≈ 0.3) and at small q , reaching 0.9999 at the smallest probed scattering vectors. In the following, when presenting DDM data we subtract off the baseline and renormalize the correlation function such that $c_{\text{DDM}}(\tau \rightarrow 0) = 1$. As for the DLS data, the DDM two-times degree of correlation, equation (8), is averaged over an appropriate time interval to obtain the DDM intensity correlation function

$$g_{2,\text{DDM}}(\tau) - 1 = \langle c_{\text{DDM}}(q, t, \tau) \rangle_t^2, \quad (9)$$

where the rhs is squared since c_{DDM} corresponds to a field correlation function [15], rather than to an intensity correlation function.

3.2.2. Far-field differential dynamic microscopy. The traditional DDM correlation function, equation (8), is sensitive to any global drift of the sample. A collective drift often arises as a consequence of an artifact; for example, for our Brownian samples a spurious drift motion is sometimes observed, most likely due to convection induced by the sample illumination. It is therefore interesting to use a DDM correlation function that is insensitive to drift. A simple choice inspired by light scattering and proposed by Buzzaccaro *et al* [27] is

$$c_{\text{FF-DDM}}(q, t, \tau) = \frac{\langle |\tilde{S}(\mathbf{q}, t)\tilde{S}(\mathbf{q}, t + \tau)|^2 \rangle_{\mathbf{q}}}{\langle |\tilde{S}(\mathbf{q}, t)|^2 \rangle_{\mathbf{q}} \langle |\tilde{S}(\mathbf{q}, t + \tau)|^2 \rangle_{\mathbf{q}}} - 1 \quad (10)$$

and the associated time-averaged function

$$g_{2,\text{FF-DDM}}(\tau) - 1 = \langle c_{\text{FF-DDM}}(q, t, \tau) \rangle_t. \quad (11)$$

The subscript FF-DDM stands for far-field DDM, since in equation (10) the correlation function is calculated on the square of the Fourier transform of S , which corresponds to the far-field intensity distribution that would be observed in a light scattering experiment. The expression above is independent of the phase of \tilde{S} : this makes it insensitive to any global drift, except for the decorrelation arising from the fact that, due to drift, some particles may leave the field of view and be replaced by incoming particles, whose position will in general be totally uncorrelated with respect to that of the scatterers leaving the field of view. This loss of correlation is of course negligible if the drift is much smaller with respect to the field of view, which is the case in our experiments. Finally, we note that optical noise affects the FF-DDM degree of correlation, similarly to the case of the quantity introduced in equation (8). We therefore subtract off the data the large- τ baseline, whose amplitude is comparable to that discussed above for DDM.

3.2.3. Particle tracking. The series of microscope images acquired for the large colloids was also analyzed by tracking the motion of the particles, in order to extract the mean square displacement from real-space measurements. The Python trackpy package [28] was used; by applying filters on the particle shape and size, particles out of focus were rejected. All particle trajectories lasting less than 50 s (because the particles left the field of view or the focal plane) were discarded.

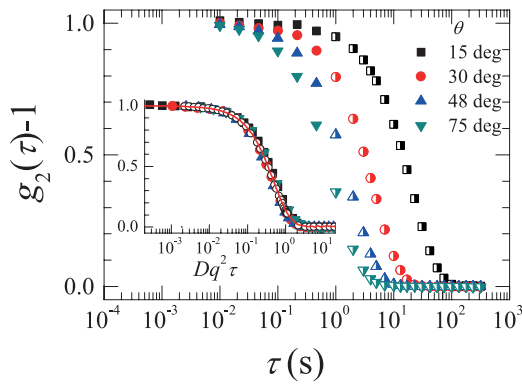


Figure 2. Main plot: intensity correlation functions measured simultaneously at four scattering angles θ by multispeckle DLS, for a diluted suspension of melamine particles with diameter $2a = 1.14 \mu\text{m}$. The solid symbols are the sub- t_{pp} delays, the semi-filled symbols are integer multiples of t_{pp} . For the latter, $g_2 - 1$ is plotted only for selected delays, to avoid overcrowding the plot. Inset: $g_2 - 1$ versus time rescaled by Dq^2 for the same data as in the main figure (same symbols), and for a diluted suspension of melamine particles with $2a = 1.6 \mu\text{m}$ (open circles). The line is $g_2 - 1$ for the $1.6 \mu\text{m}$ particles as measured by conventional DLS, under the same conditions as for the multispeckle experiment. See the text for the details on the acquisition scheme used in the multispeckle measurements.

For each τ , the 2D mean squared displacement is obtained by averaging over at least $N_t \sim 1000$ trajectories:

$$\langle \Delta r^2(\tau) \rangle = \left\langle N_t^{-1} \sum_{i=1}^{N_t} [\Delta x_i^2(t, \tau) + \Delta y_i^2(t, \tau)] \right\rangle, \quad (12)$$

with $\Delta x_i(t, \tau)$, $\Delta y_i(t, \tau)$ the x and y components of the particle displacement between times t and $t + \tau$ for the i -th trajectory. When calculating $\langle \Delta r^2 \rangle$, we reject the contribution of drift motion: for each pairs of frames, the average particle displacement is subtracted off, so that $\sum_{i=1}^{N_t} \Delta x_i = \sum_{i=1}^{N_t} \Delta y_i = 0$.

4. Results and discussion

Figure 2 illustrates an application of the variable-delay acquisition scheme to a DLS experiment. The intensity correlation functions have been obtained from data collected simultaneously at scattering angles $\theta = 15, 30, 48$, and 75 deg, for a diluted suspension of melamine particles. At each angle, 960 images have been acquired using the following parameters: $t_{pp} = 1$ s, $\tau_{\min} = 10^{-2}$ s and $J = 3$ points per decade. The resulting average data acquisition rate is 8×10^5 bytes s^{-1} , a factor $\xi = 50$ less than what it would have been by acquiring the images at a constant rate $\tau_{\min}^{-1} = 100$ Hz. The solid symbols correspond to sub- t_{pp} delays that are obtained from pairs of consecutive even and odd images. The semi-filled symbols correspond to integer multiples of t_{pp} : they are obtained from pairs of even images. (Only some selected time delays multiple of t_{pp} are shown in figure 2). The inset of figure 2 shows the same data as in the main figure, re-plotted versus the scaled time $Dq^2 \tau$. The open circles are additional data for a diluted suspension of melamine particles with $2a = 1.6 \mu\text{m}$, also acquired using the variable-delay scheme. All data collapse

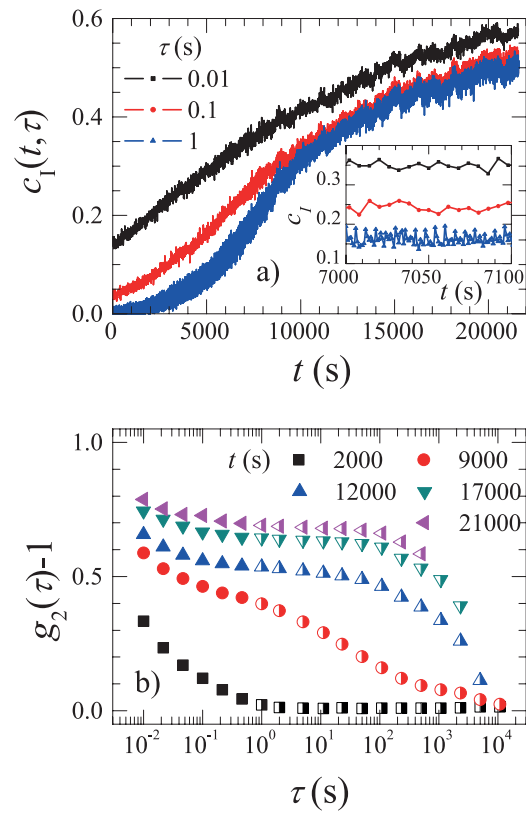


Figure 3. a): time evolution of the degree of correlation c_l , equation (6), for 3 selected delays, as indicated by the label. Data are obtained from multispeckle DLS measurements at $\theta = 46$ deg for a suspension of PNiPAM microgels whose volume fraction slowly increases during the measurements (see text for details). Inset: zoom of the data showing that the dynamics are stationary over a short t interval. b): $g_2 - 1$ obtained by averaging $c_l(t, \tau)$ over a time window of 100 s, for various starting times after the beginning of the experiment, as indicated by the label. Filled and semi-solid symbols correspond to sub- t_{pp} and integer multiples of t_{pp} , respectively. For the latter, $g_2 - 1$ is plotted only for selected delays.

on a master curve that follows the correlation function measured for the $1.6 \mu\text{m}$ melamine beads with a commercial DLS apparatus (Brookhaven AT2000, red line). Since any deviation from the prescribed temporal acquisition scheme would result in an artifactual change of $g_2 - 1$, the collapse shown in the inset of figure 2 demonstrates that the variable-delay acquisition and buffering scheme works correctly.

One advantage of the scheme proposed in this work is to cover a wide range of delay times without alternating between series of images taken at a fast and slow rate, which makes it suitable for system whose dynamics evolve in time. An example is given in figure 3, where we show data obtained by multispeckle DLS for a suspension of thermosensitive PNiPAM microgels. The acquisition parameters used in this experiment are the same as for those in figure 2. Figure 3(a) shows the time evolution of the degree of correlation $c_l(t, \tau)$ for three time delays τ , as shown by the label. As a general trend, c_l increases with time, a behavior typical of systems whose dynamics slow down [24]. Here, the slowing down of the dynamics is due to a change of the volume fraction: throughout the experiment, T decreases at a constant rate $\dot{T} \approx 3.7 \times 10^{-4} \text{ }^\circ\text{C s}^{-1}$,

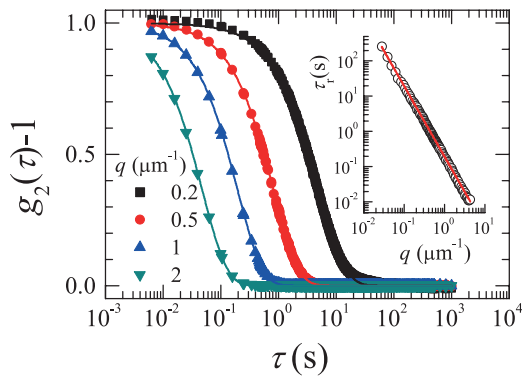


Figure 4. Representative correlation functions obtained by differential dynamic microscopy for the SP sample. The data (symbols) are labelled by the corresponding scattering vector, the lines are exponential fits to the decay of $g_2 - 1$. The amplitude of the baseline that has been subtracted (from the smallest to the largest q) is 0.848, 0.037, 0.015, 0.071. Inset: relaxation time extracted from the fits, as a function of q . The line is a power law fit to the data, yielding an exponent -2.01 ± 0.01 .

which results in a growth of the microgel size and thus of their volume fraction, from $\varphi \approx 0.65$ at $t = 0$ to $\varphi \approx 0.97$ at $t = 21\,000$ s. Thanks to the variable delay scheme, it is possible to follow the evolution of the dynamics with a good temporal resolution: for the two sub- t_{pp} delays shown in figure 3(a), $c_I(t, \tau)$ can be calculated once per cycle (every 6 s), while for $\tau = 1$ s data are available every $t_{pp} = 1$ s. Such detailed information is useful since any local deviation with respect to the general trend may reveal an experimental problem, or simply because the rate of change of the dynamics may not be known beforehand, thus making it impossible to optimize the acquisition parameters *a priori*. Detailed knowledge of the time evolution of c_I provides also guidance for choosing the time window t_{exp} over which the data may be averaged in order to calculate $g_2 - 1$. Figure 3(a) shows that the growth of c_I is steepest around $t = 7000$ s. Accordingly, t_{exp} should be small enough for c_I not to change significantly in the worst-case scenario, i.e. for $\tau = 1$ s and around $t = 7000$ s. The inset of figure 3(a) shows that $t_{exp} = 100$ s satisfies this criterion: we therefore average c_I over such a time window in order to reduce the experimental noise without losing information on the evolution of the dynamics. Figure 3(b) shows $g_2 - 1$ thus obtained for selected values of t . As t grows, the volume fraction of the suspension increases due to the swelling of the microgels and the decay of $g_2 - 1$ shifts to longer times, while the shape of the correlation function changes from a single mode relaxation to a two-step decay, a behavior typical of dense colloidal suspensions [29]. These changes are very well captured by using the variable-delay scheme, which allows to measure efficiently $g_2 - 1$ over 6 orders of magnitude in τ .

As an example of the variable-delay scheme applied to microscopy experiment, figure 4 shows representative correlation functions obtained by conventional DDM for the SP sample. The experimental parameters are $t_{pp} = 0.5$ s, $\tau_{min} = 4 \times 10^{-3}$ s and $J = 5$ points per decade, corresponding to a compression factor $\xi = 62.5$. The data are very well fitted by an exponential decay, $g_2(\tau) - 1 = \exp(-\tau/\tau_r)$ (lines). The inset shows the relaxation time τ_r extracted from the fit as

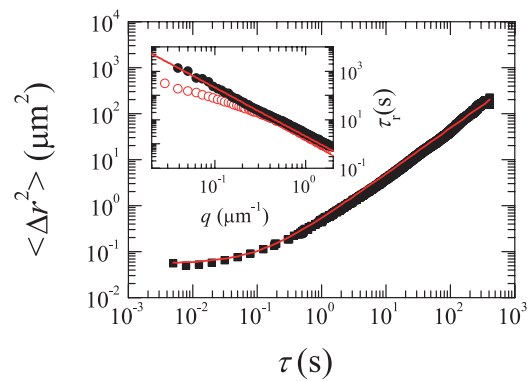


Figure 5. Mean squared displacement for the LP sample, calculated from the particle trajectories obtained by video microscopy. The deviation from a linear behavior at small τ is due to the noise of the tracking algorithm. Inset: Relaxation time versus q issued from a conventional DDM (open symbols) or far field-DDM analysis of the same series of images as in the main panel. The line is the expected behavior for Brownian particles with the same D as in the main panel.

a function of q vector. The line is a power law fit to $\tau_r(q)$, yielding an exponent -2.01 ± 0.01 , fully consistent with the q^{-2} scaling expected for a diffusive process [4]. Both the shape of $g_2 - 1$ and the q dependence of the relaxation time are in excellent agreement with those expected for Brownian particles: this demonstrates that the variable-delay scheme works correctly and that the simple single-thread implementation used here is a viable alternative to a more complex multi-thread acquisition software.

For the SP sample, the particles are too small to be directly visualized by microscopy: accordingly, direct space techniques cannot be applied to them. By contrast, the data for the LP sample can be analyzed both by tracking the particle trajectories and by DDM. The main plot of figure 5 shows $\langle \Delta r^2 \rangle$ obtained by tracking the particles in a series of images taken with the variable-delay method, with parameters $t_{pp} = 0.5$ s, $\tau_{min} = 5 \times 10^{-3}$ s and $J = 5$ points per decade. At large τ , $\langle \Delta r^2 \rangle$ scales with τ , as expected for Brownian motion, whereas at low τ the mean square displacement tends to a constant value. This behavior is due to the uncertainty in the particle position as determined by the tracking algorithm [1]. To account for the tracking errors, we fit the data with the affine law $\langle \Delta r^2 \rangle = 4Dt + 4\varepsilon^2$, where ε is the rms tracking error on each coordinate and the first term on the rhs accounts for 2D diffusive motion. As shown by the red line, the data are very well fitted by this expression, with $D = 0.122 \mu\text{m}^2\text{s}^{-1}$ and an error $\varepsilon = 0.12 \mu\text{m}$ (corresponding to 0.2 pixel) comparable to that typically achievable by low-magnification optical microscopy [2]. The inset of figure 5 shows the results of a DDM analysis of the same series of images. At large q , the relaxation time obtained from an exponential fit of the conventional DDM correlation function, (equations (8) and (9), open red circles), follows the expected q^{-2} scaling. However, at small q τ_r strongly deviates from this behavior, since the relaxation time is increasingly lower than expected as q decreases. A plausible explanation of these observations is that the particles undergo collective drift motion, in addition to Brownian diffusion. A possible source of drift is convective

motion triggered by heating due to sample illumination. Note that collective drift is corrected for by the particle tracking algorithm (see section 3.2.3). This explains why no deviations from diffusive motion are observed in the main plot at large values of $\langle \Delta r^2 \rangle$, which correspond to the small q regime of the inset. We apply the FF-DDM algorithm, equations (10) and (11), to the same series of images: the relaxation time thus obtained (solid black circles in the inset of figure 5 follows the expected diffusive behavior, with no roll-off at small q . Moreover, the data are in good agreement with the red line, which shows the behavior expected for diffusive motion with the same diffusion coefficient as that obtained from the fit of $\langle \Delta r^2 \rangle$. We thus conclude that the variable-delay scheme once again works correctly and that the far-field DDM method is effective in suppressing spurious contributions due to a global drift of the particles.

5. Conclusions

We have introduced a variable-delay temporal scheme that allows data to be acquired at a low average rate, while still sampling the dynamics over a wide range of characteristic times, including times much shorter than the inverse average acquisition rate. This scheme has been demonstrated in light scattering and microscopy experiments on colloidal suspensions, where the setups comprise one or more CCD or CMOS cameras that generate large data flows. In analyzing the microscopy data, we have validated far-field DDM, a variant [27] of the recently introduced DDM method, which allows one to reject the contribution of a global drift to the measured dynamics, e.g. as due to convective motion, slight sample evaporation, or setup vibrations.

Since the acquisition scheme proposed in this paper under-samples the system, it leads in principle to poorer average than that theoretically achievable if data were acquired at the maximum rate. However, this loss of information is more than offset by the ease of coping with a reduced average data flow rate. This is a valuable feature when large amounts of data are generated, as for the 2D detectors in our DLS and microscopy experiments. Another potential application is the processing of relatively small data streams, but with low-cost, low-performance hardware, e.g. based on an Arduino card and a single-board computer such as the Raspberry Pi, or a mobile app run on a smartphone. Setups based on similar hardware are now seen as a valuable alternative to more costly, traditional instruments, e.g. for educational purposes or for developing countries [30].

Acknowledgments

The research leading to these results has received funding from CNES, the French ANR (project FAPRES) and from the European Research Council under the European Union's

Seventh Framework Programme (FP7/2007-2013)/ERC Grant Agreement No. 306845. We thank Y Nagazi and E. Tamborini for help in the experiments, and R Cerbino, M Alaimo and F Giavazzi for enlightening discussions on DDM.

References

- [1] Crocker J C and Grier D G 1996 *J. Colloid Interface Sci.* **179** 298–310
- [2] Elliot M S and Poon W C 2001 *Adv. Colloid Interface Sci.* **92** 133–194
- [3] Prasad V, Semwogerere D and Weeks E R 2007 *J. Phys.: Condens. Matter* **19** 113102
- [4] Berne B J and Pecora R 1976 *Dynamic Light Scattering* (New York: Wiley)
- [5] Kherlopian A R, Song T, Duan Q, Neimark M A, Po M J, Gohagan J K and Laine A F 2008 *BMC Syst. Biol.* **2** 74
- [6] Wereley S T and Meinhart C D 2010 *Annu. Rev. Fluid Mech.* **42** 557–76
- [7] Kudrolli A 2004 *Reports Prog. Phys.* **67** 209–47
- [8] Adrian R J 2005 *Exp. Fluids* **39** 159–69
- [9] Cubeddu R, Comelli R, D'Andrea C, Taroni P and Valentini G 2002 *J. Phys. D: Appl. Phys.* **35** 61–76
- [10] Kirsch S, Frenz V, Schartl W, Bartsch E and Sillescu H 1996 *J. Chem. Phys.* **104** 1758–61
- [11] Leheny R L 2012 *Curr. Opin. Colloid Interface Sci.* **17** 3–12
- [12] Duri A, Sessoms D A, Trappe V and Cipelletti L 2009 *Phys. Rev. Lett.* **102** 85702–4
- [13] Cipelletti L, Brambilla G, Maccarrone S and Caroff S 2013 *Opt. Express* **21** 22353–66
- [14] Cerbino R and Trappe V 2008 *Phys. Rev. Lett.* **100** 188102
- [15] Giavazzi F and Cerbino R 2014 *J. Opt.* **16** 083001
- [16] Brunel L, Brun A, Snabre P and Cipelletti L 2007 *Opt. Express* **15** 15250–9
- [17] Schatzel K 1993 *Dynamic Light Scattering* ed W Brown (Oxford: Clarendon) pp 652–720
- [18] Cipelletti L and Weitz D A 1999 *Rev. Sci. Instrum.* **70** 3214
- [19] Yanagishima T, Frenkel D, Kotar J and Eiser E 2011 *J. Phys.: Condens. Matter* **23** 194118
- [20] Evans R M L, Tassieri M, Auhl D and Waigh T A 2009 *Phys. Rev. E* **80** 012501
- [21] Berthier L, Biroli G, Bouchaud J P, Cipelletti L and van Saarloos W 2011 *Dynamical Heterogeneities in Glasses, Colloids, and Granular Media* (Oxford: Oxford University Press)
- [22] Cipelletti L and Ramos L 2005 *J. Phys.: Condens. Matter* **17** R253–85
- [23] El Masri D, Pierno M, Berthier L and Cipelletti L 2005 *J. Phys.: Condens. Matter* **17** 3543–9
- [24] Duri A, Bissig H, Trappe V and Cipelletti L 2005 *Phys. Rev. E* **72** 051401
- [25] Senff H and Richtering W 1999 *J. Chem. Phys.* **111** 1705–11
- [26] Truzzolillo D, Roger V, Dupas C, Mora S and Cipelletti L 2015 *J. Phys.: Condens. Matter* **27** 194103
- [27] Buzzaccaro S, Alaimo M D, Secchi E and Piazza R 2015 *J. Phys.: Condens. Matter* **27** 194120
- [28] Allan D, Caswell T A, Keim N, Boulogne F, Perry R W and Uieda L 2014 Trackpy vo.2.40 (<http://github.com/soft-matter/trackpy>-doi:10.5281/zenodo.12255)
- [29] Hunter G L and Weeks E R 2011 *Rep. Prog. Phys.* **75** 066501
- [30] Kelley C D, Krolick A, Brunner L, Burklund A, Kahn D, Ball W P and Weber-Shirk M 2014 *Sensors* **14** 7142–55

A model for failure in thermoplastic elastomers based on Eyring kinetics and network connectivity

In the framework of the EU ITN SUPOLEN, which partially financed my PhD thesis, I had the opportunity of spending 2 months in the Netherlands, for an industrial secondment in DSM. The goal of my secondment was the theoretical and experimental investigation of failure mechanisms in thermoplastic elastomers (TPEs). The following paper, published by Journal of Rheology [Aime 2017], presents a selection of the most relevant results obtained during that period.

A model for failure in thermoplastic elastomers based on Eyring kinetics and network connectivity

S. Aime^{a)}

Laboratoire Charles Coulomb (L2C), UMR 5221 CNRS-Universite de Montpellier, Montpellier 34095, France

N. D. Eisenmenger^{b)} and T. A. P. Engels^{c)}

DSM Ahead, Material Science Center Urmonderbaan 22, 6167 RD Geleen, the Netherlands

(Received 31 March 2017; final revision received 14 August 2017; published 1 November 2017)

Abstract

A simple model is introduced to describe the failure mechanisms in soft thermoplastic elastomers. In particular, we address the strong embrittlement with increasing temperature observed in strain rate imposed tensile experiments. This behavior is in sharp contrast to classic thermoplastics and seems to be general for these types of systems, irrespective of their exact chemical nature. We show that a kinetic model describing the supramolecular association of hard blocks in terms of an Eyring rate equation captures the correct stress and temperature dependence of failure strain. We model the material as a transient network, whose failure is associated with the loss of connectivity. The network percolation threshold, a key parameter of the model, is studied with numerical simulations, in order to investigate the interplay between structure, connectivity, and mechanical properties. © 2017 The Society of Rheology. [<http://dx.doi.org/10.1122/1.5000808>]

I. INTRODUCTION

Thermoplastic elastomers (TPEs) are an interesting subset of the engineering plastics family. Their thermoplastic processability in combination with elastomer-like mechanical characteristics [1,2] makes them a valuable addition to the wide range of available polymers. In contrast to the classical thermoset-based elastomers, their thermoplastic nature allows them to be processed just like any other thermoplastic polymer and enables rework and recycle of scrap materials [3,4]. While classical thermoset elastomers can be considered as chemically crosslinked polymers operating above their glass transition temperature (T_g), TPEs should be regarded as physically connected, phase-separated polymers where one phase is in the solid state below its melting temperature (T_m) and the other phase in its rubbery state above T_g [5–13]. They behave mechanically as elastomers with typically low moduli, high elongations before breaking and an overall rubber-like touch-and-feel. It should be noted though that they typically compete at the higher moduli values with classic elastomers. Most TPEs are block or graft copolymers, which makes it possible to tune the desired properties by altering their chemical composition [2]. In this paper, we will focus on polycondensation-based TPEs composed of poly(butylene terephthalate) (PBT) blocks to make up the solid phase [or hard blocks (HBs)] and polyether-based blocks to make up the soft phase [or soft blocks (SBs)].

The deformation of these systems has been quite extensively studied in literature, especially in connection to their morphology [9,13–20]. Most of these studies, however, focused on the behavior at room temperature, and did not describe the effect of temperature on the mechanical properties of the materials, which we address. Quite generally stated, we observe that soft TPEs, characterized by a low content of HBs, below 50%, show an unexpected, and often undesired, drop of extensibility as temperature is increased. This happens in the absence of any thermodynamic or structural transition, and it is in sharp contrast with standard thermoplastic materials, which are rather fragile at low temperatures and increase their ductility when heated as a consequence of the enhanced chain mobility [21,22]. Despite its relevance for applications, to the best of our knowledge this observation has not been studied explicitly in the literature, although some papers do show similar observations [20,23–25]. We find this behavior to be general for this type of systems, irrespective of their exact chemical nature (polyester, polyurethane, and polyamide based systems all show the same phenomenology), and from a fundamental point of view this represents an important challenge for theoretical models describing failure in TPEs.

The rich morphology displayed by these systems is discussed in detail in a paper by Gabriëls *et al.* [26] where a PBT-poly(tetramethylene oxide) (PTMO) system is investigated. The block-copolymer nature suggests the material to consist of two phases, but it is shown that depending on the chemical affinity of the two components the phase behavior can be more complex. In the case discussed in that paper, up to five distinct phases are identified: (1) a pure PBT crystalline phase, (2) a glassy PBT phase, (3) a mixed PBT-PTMO glassy phase, (4) a rubbery PTMO phase, and (5) a crystalline PTMO

^{a)}Author to whom correspondence should be addressed; electronic mail: Stefano.Aime@umontpellier.fr

^{b)}Electronic mail: Nancy.Eisenmenger@dsm.com

^{c)}Present address: Eindhoven University of Technology, Postbus 513, 5600 MB EINDHOVEN, Netherlands; electronic mail: Tom.Engels@dsm.com

phase. Here we will not go into that level of detail and for the sake of simplicity we will treat these systems as simple binary systems, made by crystalline PBT and rubbery SB material.

In this paper we present a kinetic model, qualitatively accounting for the embrittlement of TPEs at high temperatures. The paper is structured as follows: after a first overview of available experimental observations (Sec. III), the kinetic model is presented and qualitatively validated (Sec. IV). For a more detailed comparison with experimental data, in Sec. V, we present an implementation of this kinetic model on a cubic lattice. A conclusive section closes the paper, with a general discussion of the main results.

II. MATERIALS AND METHODS

We use as model systems two different, specifically synthesized poly(ether-ester) block-copolymers based on PBT as HB, and PTMO or poly(ethylene glycol) (PEG) as SBs. The details of the two systems are reported in Table I. The PEG-based system is used to study the effect of molecular weight, and to that aim the synthesis is stopped at a relatively low molecular weight and subsequently grown in discrete steps of molecular weight by solid state postcondensation at high temperature under dry nitrogen conditions [27]. Molecular weights are determined using size-exclusion chromatography in hexafluoroisopropanol (HFIP).

Materials are compression molded into 200 μm thick sheets at a temperature of 225 $^{\circ}\text{C}$. Materials are allowed to equilibrate shortly in the order of minutes at this temperature before being cooled down to room temperature by cooling the press by an internal water circulation system. Tensile bars of ISO 527/1BA standard shape are then punched from those sheets and tested on a standard Zwick Z010 Universal tensile testing machine. In all tests, the samples are equilibrated at target temperature for 10 min. For a tensile test, they are subsequently stretched at a constant engineering strain rate till failure. In the case of a creep experiment, the load is applied within 10 s after which it is held constant until final failure. Strain rates and temperatures are indicated where appropriate in the respective figures and/or captions. Stresses and strains are reported as engineering values unless stated otherwise.

The differential scanning calorimetry (DSC) experiments are performed on a Mettler-Toledo DSC823e equipped with a FRS5 sensor. Calibration was performed by melting peaks of tin and zinc. Scans were performed at heating rates of 20 K/min. Standard 40 μl aluminum crucibles are used and samples weighed approximately 5–10 mg. Nitrogen is used as a purge gas.

TABLE I. Specifications of the two model systems studied in this paper.

	PTMO-based	PEG-based	
	30/70	50/50	HB/SB mass ratio
M_{HB}	880 g/mol	1000 g/mol	HB molecular weight
M_{SB}	2000 g/mol	1000 g/mol	SB molecular weight
M_w	60 kg/mol	Various	Total molecular weight (weight average)
T_g	-80 $^{\circ}\text{C}$	-50 $^{\circ}\text{C}$	Glass transition temperature
T_m	170 $^{\circ}\text{C}$	194 $^{\circ}\text{C}$	Melting temperature

III. EXPERIMENTAL OBSERVATIONS

Figure 1 shows representative engineering stress-strain curves obtained for the PTMO-based system at different temperatures. After a first linear regime, lasting only a few percent deformation (hardly distinguishable in the figure), we observe a broad yield range, around 10% deformation, where plastic deformation causes the slope of stress-strain curves to decrease. This is followed by an ongoing deformation at mildly increasing stress levels until strain hardening is eventually observed at higher deformations, more pronounced at lower temperatures. In this case, strain hardening is enhanced by strain-induced crystallization of SBs [18] (indeed, the melting point for strained PTMO chains is around 30 $^{\circ}\text{C}$). Finally, engineering stress drops as fracture is abruptly encountered. The fracture event occurs earlier at higher temperatures: for example, a sample can withstand a strain higher than 1000% at 50 $^{\circ}\text{C}$, whereas failure is observed at only 300% deformation at 125 $^{\circ}\text{C}$. Remarkably, as one can see from DSC [Fig. 1(b)], the melting temperature of the system is 170 $^{\circ}\text{C}$, and no additional thermodynamic transitions are observed in the temperature range where tensile experiments are performed. The possibility of strain-induced crystallization being connected to the observed reduction in ductility with increasing temperature was ruled out using observations not reported in this paper. Indeed, repeating the same experiments on other TPEs based on soft-blocks that do not exhibit strain-induced crystallization, we could observe a very similar behavior. Therefore, this embrittlement at high temperature, in the absence of any thermodynamic signature, appears to be general for soft TPEs, and it represents the first observation that we want to model.

The influence of strain rate on the stress-strain curves was also tested. Figure 2 shows representative curves obtained by

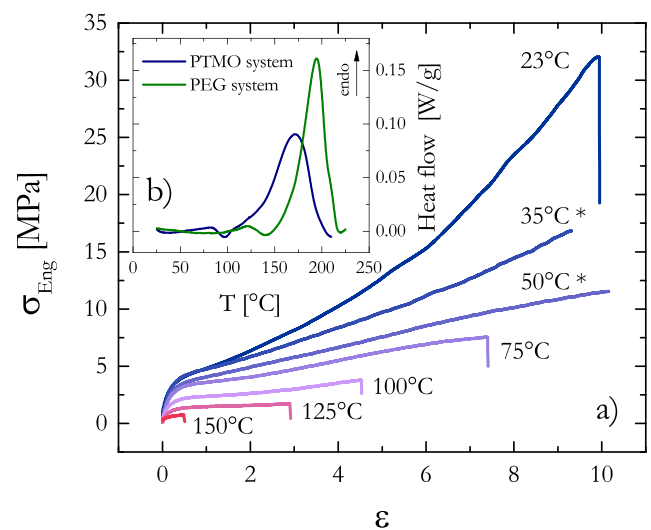


FIG. 1. (a) Engineering stress-strain curves of the PTMO-based system at different temperatures, as indicated in the labels ($T = 23, 35, 50, 75, 100, 125,$ and $150\text{ }^{\circ}\text{C}$ from blue to red), for a fixed strain rate $\dot{\epsilon} = 0.17\text{ s}^{-1}$. Experiments at 35 and 50 $^{\circ}\text{C}$ never reached failure, because of the limited strain range of the tensile machine used. (b) DSC traces measured on heating at 20 K/min. An arbitrary baseline was subtracted from the experimental data.

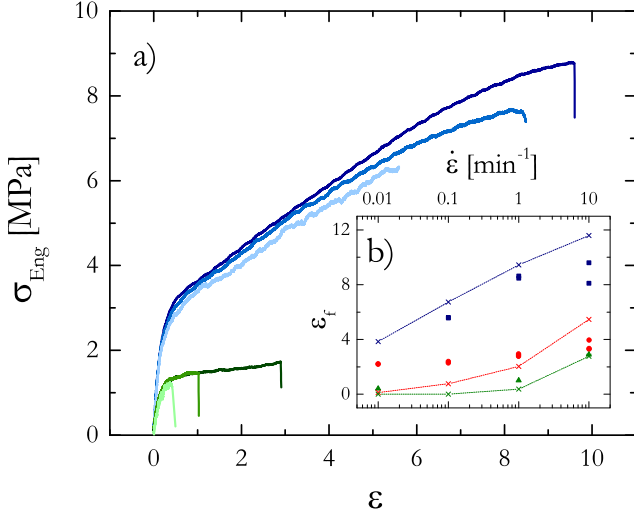


FIG. 2. (a) Representative engineering stress-strain curves obtained experimentally for PTMO-based system at various temperatures (blue: 60 °C, green: 125 °C) and strain rates (decreasing from dark to light). (b) Symbols: maximum elongation at break as a function of the strain rate for the same temperatures (red data: $T = 100$ °C, not shown in the main graph). Crosses and dashed lines: elongation at break obtained by simulations using the experimental stress-strain curves as input. Chain length is $N = 9$ SBs, and kinetic parameters are $\Delta H = 105$ kJ/mol and $v^* = 2.2 \times 10^{-4}$ m³/mol.

repeating the experiment at one temperature for different values of the imposed strain rate. The experimentally applied strain rates ranged from a maximum of 10 min^{-1} to a minimum of about 0.001 min^{-1} (i.e., from 0.17 to $1.7 \times 10^{-5} \text{ s}^{-1}$). Experimental data show that at temperatures above 50 °C, the stress is roughly independent of strain rate, suggesting that the characteristic timescales relevant for stress relaxation should fall outside the range of accessible timescales ($\dot{\epsilon}^{-1}$). Nevertheless, one can see from Fig. 2(b) that the elongation at break shows a weak but clear dependence on $\dot{\epsilon}$, which is the second observation we would like to capture.

Finally, we address the impact of chain length on mechanical properties. For this reason, PEG-based systems of different molar masses are tested, and the tensile curves obtained are shown in Fig. 3. While the linear regime seems to be roughly the same for all samples, strong differences are observed with respect to extensibility and stress levels: as M_w is increased, the failure strain ϵ_f sharply increases until a plateau is reached. At room temperature, samples with higher molar mass also show a strong strain hardening profile, so that toughness is an increasing function of M_w .

To summarize, the experimental observations that we would like to understand and capture with a phenomenological model are the following:

- (1) Elongation at break drops dramatically with increasing temperature (Fig. 1).
- (2) Elongation at break also decreases with decreasing strain rate, and the dependence is weaker at lower temperatures (Fig. 2).
- (3) Elongation at break increases with increasing chain length and then it saturates to a M_w -independent value (Fig. 3).

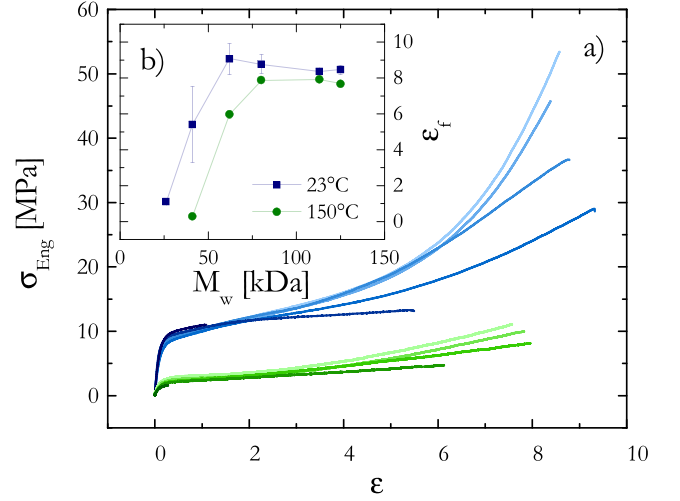


FIG. 3. (a) Engineering stress-strain curves obtained with the PEG-based system, with increasing molar mass (weight average molecular weights $M_w = 26, 41, 62, 80, 113,$ and 125 kDa) from dark to light, at two representative temperatures 23 °C (blue) and 150 °C (green). Strain rate is $\dot{\epsilon} = 0.17 \text{ s}^{-1}$. (b) Elongation at break as a function of M_w . Error bars are included to indicate the variability on the data.

IV. KINETIC MODEL

A. Sample structure

As briefly discussed in the Introduction, at room temperature and in the absence of mechanical constraints, TPEs have a complex morphology: SBs form an amorphous matrix surrounding crystalline domains composed of HBs, which are usually entangled or connected, and form the main stress-bearing structure in the linear regime [11,19]. This picture in both PTMO and PEG systems holds between $T_g \approx -60$ °C and $T_m \approx 170$ – 200 °C (cf. Table I), which is the working temperature range of these materials.

Under stress the morphology changes differently for soft grades (mainly composed of SBs) and hard grades (mainly composed of HBs). Direct experimental observations [9,15,17–20,28–31] show that soft TPE materials break their network of HB crystals and develop a characteristic fibrillar structure when stretched beyond 100%–200% strain. In such a structure, to a lesser extent found in harder TPEs, crystalline domains formed by HBs tend to align in planes perpendicular to the strain direction, whereas SBs, bridging different crystalline domains, are progressively stretched.

The fact that the observed drop of ϵ_f is only observed on soft TPE grades suggests that the failure mechanism might be linked to this fibrillar structure, that we take as a starting point for the description of failure mechanisms.

B. Failure mechanism

In analogy to recent studies on transient networks [32–34], our model describes failure in terms of connectivity loss: the sample will break as soon as two parts get disconnected. Connectivity is thus a key element in our model, and it will be evaluated within the framework of percolation theory. For the sake of simplicity, we assume that the main features of material failure do not rely on the effect of eventual entanglements between SBs, which are neglected here.

Therefore, we attribute the sample's initial connectivity to physical bonds that can be formed between HBs: as long as this network of bonds persists, the structure will be able to withstand the applied load. However, physical bonds are dynamic: they can break and reform as a consequence of temperature and stress. At rest, a dynamic equilibrium is reached, with breaking events balancing the bond formation, but an external stress biases this equilibrium, favoring breaking processes over the reformation: this causes HB crystal fragmentation and weakens the network by reducing the amount of elastically active, stress-bearing chains [32]. In analogy with established work in literature, mainly focusing on yielding [35–42] or creep failure [42–49], we assume that the kinetics for inter-HB bond breaking and reformation can be modeled using Eyring's rate equation [50]:

$$k(\sigma, T) = k_0 \exp\left(-\frac{\Delta G}{k_B T}\right) \sinh\left(\frac{\sigma v^*}{k_B T}\right), \quad (1)$$

where k_0 represents a reference rate, k_B is Boltzmann constant, ΔG is the activation energy of bond breaking, and v^* is the activation volume.

The Eyring rate equation was originally developed to describe chemical reaction rates, but it was soon extended to describe physical processes like viscous flow [51–53]. Since then, it has been widely applied to polymer yielding and plastic flow, and most of the time the rate constants involved in the model were used to describe the rate of flow [42,54–56]. Instead, here we use Eyring rate constants to model the breakdown of those bonds capable of supporting an applied load. In this regard, our application of Eyring theory is less conventional, and closer to the one proposed by Matz *et al.* [49] or Zhurkov [57,58], who present a mathematical framework close to that of Eyring, although it should be noted that in the latter case the author focuses on chain scission as the dominant cause for failure. On the other hand, in the present study the absolute rate $k(\sigma, T)$ describes the evolution of the amount of associated physical bonds (rather than chemical bond breaking). Its value at rest $k_T = k(\sigma = 0, T)$ and below T_m is typically such that almost all HBs are associated at equilibrium [11]. However, the bias introduced by stress shifts the fraction A of associated HBs toward lower values, until the system eventually becomes disconnected: as strain increases, we can describe plasticity in terms of a function $A(\varepsilon)$ decreasing from 1 to a critical value A_{th} , which we will treat as a percolation threshold. Therefore, within this framework, elongation at break can be computed as the strain ε_f at which $A(\varepsilon_f) = A_{th}$.

The evolution of $A(\varepsilon)$ can be computed using Eq. (1), by assuming a first order process for bond breaking and integrating the differential equation

$$\frac{dA[\varepsilon(t)]}{dt} = -k[\sigma(t)]A[\varepsilon(t)]. \quad (2)$$

In order to obtain an analytical solution, an expression for the stress history $\sigma(t)$ is required. This can be easily done in creep [21,43], whereas the calculation is less straightforward when a constant strain rate is imposed. The simplest

assumption, which we will use here, is to require that a simple affine relation between *true* stress σ_{True} and strain holds beyond the yield point of the material: $\sigma_{\text{True}}(t) = \sigma_0 + \sigma_1 \varepsilon(t)$, where $\varepsilon(t) = \dot{\varepsilon} t$, and σ_0 and σ_1 are phenomenological parameters extracted from fits to the individual tensile curves [Fig. 4(a)]. It is clear from this graph that the chosen relation for stress as a function of strain is less than optimal, and, e.g., a fit using a neo-Hookean scaling will result a strongly improved fit [Fig. 4(b)]. However, to allow for an analytical solution to exist we have to compromise on this accuracy and suffice with a simple, less accurate description. Note that toward higher temperatures this assumption is more accurate compared to lower temperatures.

Moreover, we also assume that because of internal stresses two HBs that detach from each other are pulled apart, and will not recombine: under this assumption the hyperbolic sine in Eq. (1) is simplified to a single exponential. This second assumption is not necessary in itself, but makes the calculations easier.

By solving the differential equation with initial condition $A(0) = 1$, we obtain

$$A(\varepsilon, \dot{\varepsilon}) = \exp\left[-\frac{k_0 k_B T}{\dot{\varepsilon} v^* \sigma_1} e^{-(\Delta G - v^* \sigma_0)/(k_B T)} (e^{(v^* \sigma_1/k_B T)\varepsilon} - 1)\right]. \quad (3)$$

Thus, once an assumption on A_{th} is made, the elongation at break ε_f can be easily calculated by inverting this expression

$$\varepsilon_f = \frac{k_B T}{\sigma_1 v^*} \ln\left[1 - \frac{\dot{\varepsilon} v^* \sigma_1}{k_0 k_B T} e^{(\Delta G - v^* \sigma_0)/(k_B T)} \ln A_{th}\right]. \quad (4)$$

C. Model validation

Figure 5 shows a set of ε_f values obtained for one choice of model parameters and plotted as a function of temperature for different strain rates. A qualitative comparison with experimental data shows that

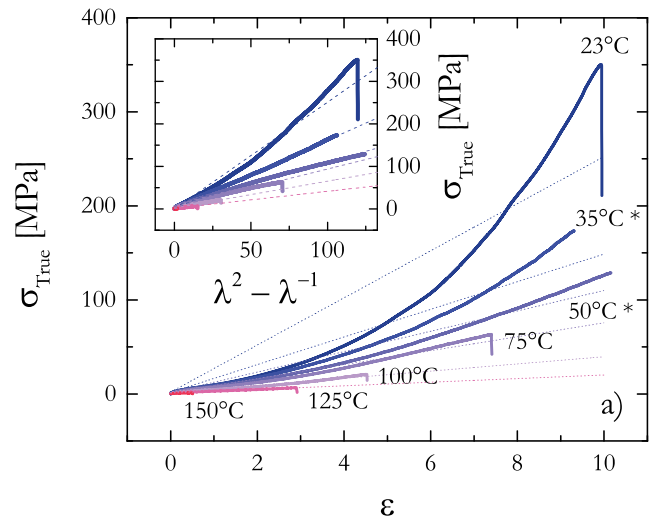


FIG. 4. (a) Experimental data of Fig. 1 (solid lines) along with linear fits (dashed lines) of true stress versus strain. (b) Alternative scaling according to neo-Hookean relation.

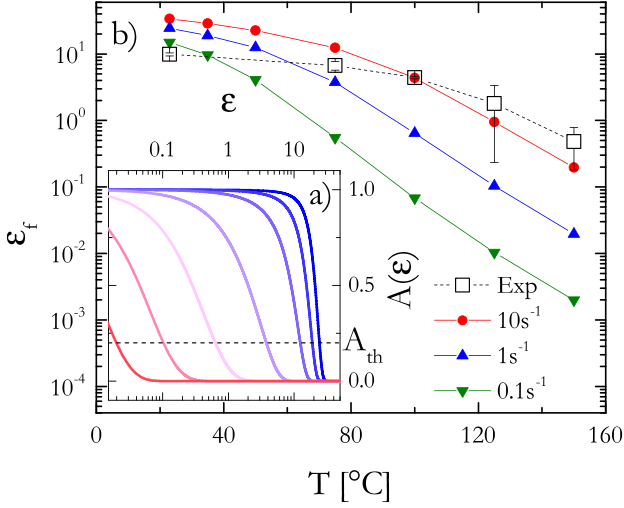


FIG. 5. (a) Predicted evolution of associated fraction $A(\varepsilon)$ as a function of the engineering strain. Model parameters used are $\Delta G = 105$ kJ/mol, $v^* = 2.2 \cdot 10^{-4}$ m³/mol, $\sigma_0 = \sigma_1 = 3$ MPa, $\dot{\varepsilon} = 1$ s⁻¹. T is increasing from blue to red. (b) Predicted strain at break ε_f obtained for a choice of $A_{th} = 0.2$, plotted as a function of temperature and for different strain rates, compared to experimental values extracted from Fig. 1. Error bars represent data dispersion evaluated on 2–6 independent measurements (data not shown).

- (1) By fixing A_{th} and varying T , it is possible to reproduce the drop in ε_f with increasing temperature. For the highest temperatures, we get $\varepsilon_f \propto T^{-1}$, whereas at lower temperatures, the T dependence is weaker.
- (2) The trend with decreasing $\dot{\varepsilon}$ also resembles the one observed experimentally: Eq. (4) predicts $\varepsilon_f \propto \dot{\varepsilon}$ for high temperatures, whereas $\varepsilon_f \propto \ln(\dot{\varepsilon})$ at low temperatures. In any case, the effect of increasing temperature on reduction in elongation at break is stronger than the effect of increasing strain rate.
- (3) Since longer chains (with higher number of HBs per chain) form a better connected structure, the effect of increasing molecular weight may be schematized as a decrease in A_{th} , which in turn increases ε_f (data not shown), as qualitatively observed in Fig. 3.

These observations suggest that our model is able to capture the main features of the observed failure. A next, natural step would be to quantitatively compare our experimental data with predictions based on Eq. (4): this requires an estimation of our model parameters. While σ_0 and σ_1 can be extracted from a linear fit of the tensile curves, the determination of the remaining three parameters (ΔG , v^* and A_{th}) is more delicate. In particular, the physical interpretation of A_{th} may be questionable: in fact, as the deformation is localized around sample defects (in particular during the latest stages before failure), the macroscopic stress measured experimentally deviates from the local stress actually experienced by polymer chains, so that in principle a direct link between the macroscopic stress and the local amount of broken bonds does not exist, and A_{th} appears to be rather ill-defined. For this reason, in a first instance we assume that the sample deformation is homogeneous, and that bond breaking events occur randomly and homogeneously inside the sample.

Numerical simulations shown in Sec. V will help us quantifying to what extent this assumption is acceptable.

Under this approximation, ΔG , v^* and A_{th} can be extracted by using the fits of tensile curves at different strain rates and temperatures as input. In its simplest version, the fitting procedure works as follows: once a set $\{\sigma(\varepsilon, T_i, \dot{\varepsilon}_i)\}$ of tensile curves is provided, we extract from it the mechanical parameters $\sigma_0(T_i, \dot{\varepsilon}_i)$, $\sigma_1(T_i, \dot{\varepsilon}_i)$, $\varepsilon_f^{(obs)}(T_i, \dot{\varepsilon}_i)$. Then, a reasonable set of kinetic parameters ($\Delta G^{(0)}$, $v^{*(0)}$, $A_{th}^{(0)}$) is taken as a starting input, and used to compute, for each $(T_i, \dot{\varepsilon}_i)$, an expected strain at break $\varepsilon_f^{(0)}(T_i, \dot{\varepsilon}_i)$. A Monte Carlo algorithm is then used to find the $(\Delta G, v^*, A_{th})$ set that provide the best set $\{\varepsilon_f^{(fit)}(T_i, \dot{\varepsilon}_i)\}$ of predicted elongations at break, i.e., the choice that minimizes the χ^2 parameter defined as $\chi^2 = \sum_i \{[\varepsilon_f^{(obs)}(T_i, \dot{\varepsilon}_i) - \varepsilon_f^{(fit)}(T_i, \dot{\varepsilon}_i)]^2 / \varepsilon_f^{(fit)}(T_i, \dot{\varepsilon}_i)\}$.

As an example, the fitting parameters extracted for the PTMO-based systems are $\Delta G = 105$ kJ/mol, $v^* = 2.2 \times 10^{-4}$ m³/mol, and $A_{th} = 0.2$. We included the experimental strains-to-failure versus temperature of Fig. 1 in Fig. 5 to enable a direct comparison to experimental data. We show that, as stated before, with the chosen parameters, we can describe the trend of decreasing strain-at-break with temperature well and that the absolute values are captured to a reasonable approximation. Toward the lower temperatures, we see the results to differ more; this might be related to the poorer fit to experimental stress-strain curves as shown in Fig. 4(a).

We find that ΔG is temperature independent, which is an indication that the entropy variation should be negligible with respect to enthalpy. Although it is difficult to quantitatively relate those parameters to some *a priori* knowledge about the system [59] (we will limit ourselves to treat them as fitting parameters), it is worth mentioning that the activation energy ΔG and the activation volume v^* are comparable in magnitude to what is found in literature for other deformation mechanisms [39,43,47,49,56,60], while the percolation threshold A_{th} is close to the one extracted by numerical simulations (see Sec. V).

D. Numerical integration

Once ΔG and v^* are known, we can refine our analysis by dropping the (strong) assumption about the stress-strain affine relationship: starting from the experimental $\sigma(t)$, Eq. (2) can be numerically integrated, and the full $A(\varepsilon)$ profile can be extracted from each tensile curve. Such a result, for the experimental stress-strain curves of Fig. 1, is represented in Fig. 6(a).

Looking at that figure, one can notice that, for temperatures high enough, sample failure occurs as soon as the fraction of broken bonds approaches a threshold value $1 - A_{th}$ close to 100%, and only weakly dependent on strain rate and temperature. We interpret the fact that low temperatures represent an exception, and that failure apparently occurs later than expected, as a direct consequence of strain hardening: in this case, strain-induced crystallization of SBs may represent an additional contribution to connectivity, not considered in our model.

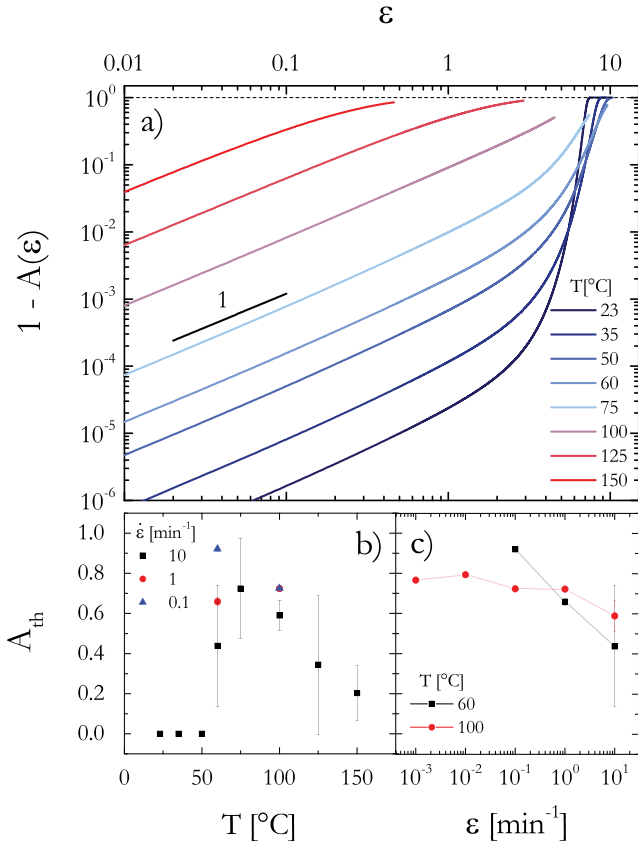


FIG. 6. (a) Fraction of broken bonds as a function of engineering strain, obtained by numerically integrating the differential equation Eq. (2) with $\sigma(t)$ from the tensile curves of Fig. 1. (b) and (c) Percolation threshold A_{th} (extracted by measuring A at break) plotted as a function of temperature and strain rate.

A more detailed analysis of Fig. 6(a) reveals the existence of two different regimes: for high temperatures ($T \geq 100^\circ\text{C}$) the fraction of broken bonds grows linearly with time (or strain) throughout the whole experiment. In this temperature range, σv^* is always smaller than ΔG , and the bond breaking events are essentially thermally activated. This corresponds to the region where $\epsilon_f \propto \dot{\epsilon} T^{-1}$ in Eq. (4). On the other hand, at lower temperatures, this regime is eventually interrupted by a second regime, where bond breaking becomes mainly stress-activated and accelerated with respect to thermal activity. This typically happens at a few strain units deformation, when v^* eventually becomes larger than ΔG : as a consequence, in this regime ϵ_f increases only weakly with decreasing T or increasing $\dot{\epsilon}$. Thus, the numerical approach not only allows to take into account the detailed shape of the stress-strain curve, but it also provides a valuable insight into plastic activity occurring during deformation.

Furthermore, the numerical approach has a third major advantage: it does not require any assumption on the exact A_{th} value. Indeed, A_{th} is no longer a model parameter, but can be extracted by looking at the minimum value reached by $A(\epsilon)$ before failure. Figures 6(b) and 6(c) show A_{th} as a function of temperature and strain rate. As one can see, for temperatures higher than 60°C A_{th} is roughly strain rate independent but displays a clear decreasing trend with increasing temperature. This trend cannot be described by

Eq. (4), that assumes a unique A_{th} value for all temperatures and strain rates. That is why Sec. V will be dedicated to numerical simulations, which will help to attribute such a temperature dependence of A_{th} to the heterogeneity of sample deformation.

V. SIMULATIONS

Until now, homogeneity of sample deformation and plastic activity has been assumed. In this section, we want to discuss the limits of these assumptions, with the help of numerical simulations.

A. General concept

Our numerical simulations are inspired by, and loosely based on, the work of Mora [33], and might show some resemblance to the work of Termonia [61], although the underlying physics are different. The kinetic model is implemented on a 3D cubic lattice, as shown in Fig. 7(a): each site (i, j, k) represents a HB that can be bound either chemically (via a SB) or physically (via weaker supramolecular interactions) to neighbor HBs, with periodic boundary conditions (PBC) along \hat{i} and \hat{j} (strain is applied in the \hat{k} direction). Physical bonding is only allowed within (i, j) planes, that represent HB crystals in the stretched fibrillar structure, whereas chemical bonds can develop both in the strain direction (in this case they will be elastically active, bridging two different crystals) and in the (i, j) plane (in this case they will behave as loops, not contributing to the sample modulus). Thus, within this model, a block copolymer containing N SBs and $N + 1$ HBs is a N -step self-avoiding walk on the lattice. Chemical bonds are permanent, whereas physical bonds can randomly break and reform following the rate given by Eq. (1). Sample connectivity is evaluated in two steps [Figs. 7(b) and 7(c)]: in a first step single crystals are identified in each (i, j) plane. In this model, a crystal is a set of sites connected with each other but disconnected from all the others belonging to the same (i, j) plane. Along the transversal (i, j) directions, PBC are taken. In the second step, the connectivity of crystals belonging to consecutive (i, j) planes is checked: two crystals will be connected if and only if there is at least one chemical bond (i.e., a SB) binding one site of the first crystal with another site of the second. If a percolating set of crystals exists bridging the two opposite surfaces of the sample, then the system will be considered as connected.

The boundary conditions for the model are prescribed by applying a stress that is either constant in the case of creep simulations (Sec. VB), or increasing with time, following the experimental tensile curves (as described in Sec. VD), in the case of tensile tests. In both cases, starting from a fully connected system and breaking supramolecular bonds, connectivity is progressively lost: disconnected or dangling regions are created [Fig. 7(c)] at the expense of the stress-bearing backbone. As a consequence of local mechanical equilibrium, stress is concentrated in the regions with the highest density of disconnected sites, which in turn increases the bond breaking rate in that same region: the fluctuations in

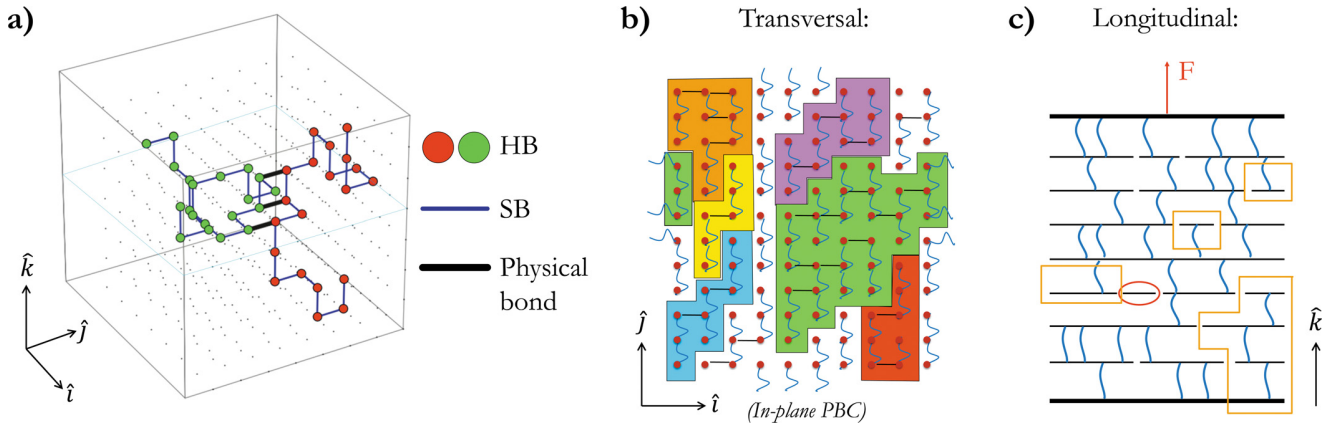


FIG. 7. (a) Sketch of the simulation box filled with two copolymer chains. The stress is applied along the vertical direction. HB segments occupy lattice sites. Segments belonging to different chains are shown in different colors for the sake of clarity. SB segments are represented as blue segments, and can assume all orientations, whereas physical bonds (black segments) only develop in horizontal planes, perpendicular to the stretching direction, in order to mimic the fibrillar structure with oriented HB crystals bridged by SBs. In simulations all lattice sites are occupied by HB segments. (b) Evaluation of transversal connectivity: each horizontal plane is divided in disconnected domains, representing single crystalline fragments. Some of those are highlighted with different colors. PBC are taken in the (i, j) plane. (c) Longitudinal projection of the sample. Horizontal planes are divided in multiple domains that can eventually be connected to adjacent domains along the vertical direction by SB segments. Disconnected domains (highlighted in red) and dangling (orange) ones do not contribute to the stress bearing structure, and are neglected.

the local number of elastically active chains bring information about stress localization and deformation heterogeneity.

B. Tensile creep

Since our kinetic model is governed by Eyring's rate equation [Eq. (1)], which contains stress but no (explicit) strain dependence, creep appears to be the most natural protocol to test the validity of the model. To support that creep failure of TPEs is also governed by an activated process, a limited set of creep experiments were performed on the PTMO system at elevated temperatures, that yield a creep failure time decreasing exponentially with the applied stress, as one would expect from Eq. (1), and decreasing as well with increasing temperature (data not shown), which is also in line with expectations [21,43,44,46,48,49,55,62]. A representative set of creep curves is shown in Fig. 8.

Although numerical simulations cannot grasp the qualitative shape of the full creep curve (they do not contain details about linear viscoelasticity and morphology evolution), they can describe how the failure time varies with stress and temperature (Fig. 9).

For a given applied stress at a fixed temperature, repeated simulations on equivalent samples produce a Weibull distribution of failure times $P(t_f)$ [Fig. 9(a)] [63–66], characterized by an average value τ_f and a shape parameter β ,

$$P(t_f) = 1 - e^{-(t_f/\tau_f)^\beta}. \quad (5)$$

The average failure time τ_f exhibits a sharp dependence on both temperature and applied stress, reflecting the activated nature of failure process [67,68]: both effects can be taken into account by considering an adimensional stress $\tilde{\sigma} = \sigma/\sigma_T$, where $\sigma_T = k_B T = v^*$ is a temperature dependent reference stress for stress-activated dynamics. Indeed, once the Arrhenius temperature dependence is taken into account by rescaling time with the thermal rate $k_T = k_0 \exp(-\Delta G/k_B T)$,

$\tilde{\sigma}$ allows a collapse of all $\tilde{\tau}_f = k_T \tau_f(\sigma, T)$ data onto a master-curve, close to the theoretical expectation $\tilde{\tau}_f = \tilde{\tau}_0 / \text{sinc}(\tilde{\sigma})$ [Fig. 9(d)] [43]. The difference between the master curve obtained by simulations and the theoretical function calculated from Eq. (1) is presumably related to the heterogeneity of the deformation observed in simulations. As a consequence of stress concentration, in fact, bond breaking events tend to be localized around the weakest regions, and this causes sample failure to occur earlier than predicted. This effect, more pronounced for large stresses and low temperatures (since in the opposite regime thermal processes push in the direction of a more homogeneous deformation), can be

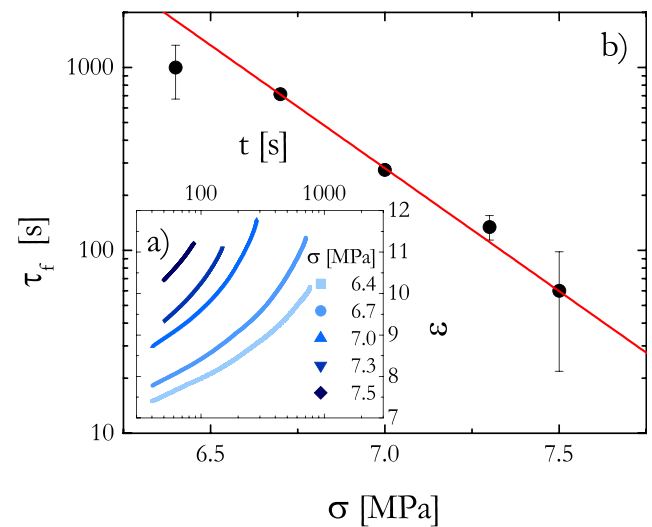


FIG. 8. (a) Representative creep deformations for the PTMO-based system as a function of time since step stress application for different stress values, as indicated in the legend, at a temperature $T = 60^\circ\text{C}$. (b) Symbols: failure times average on three repetitions of the same experiment, as a function of the applied stress. Error bars represent data dispersion. Red line: exponential fit.

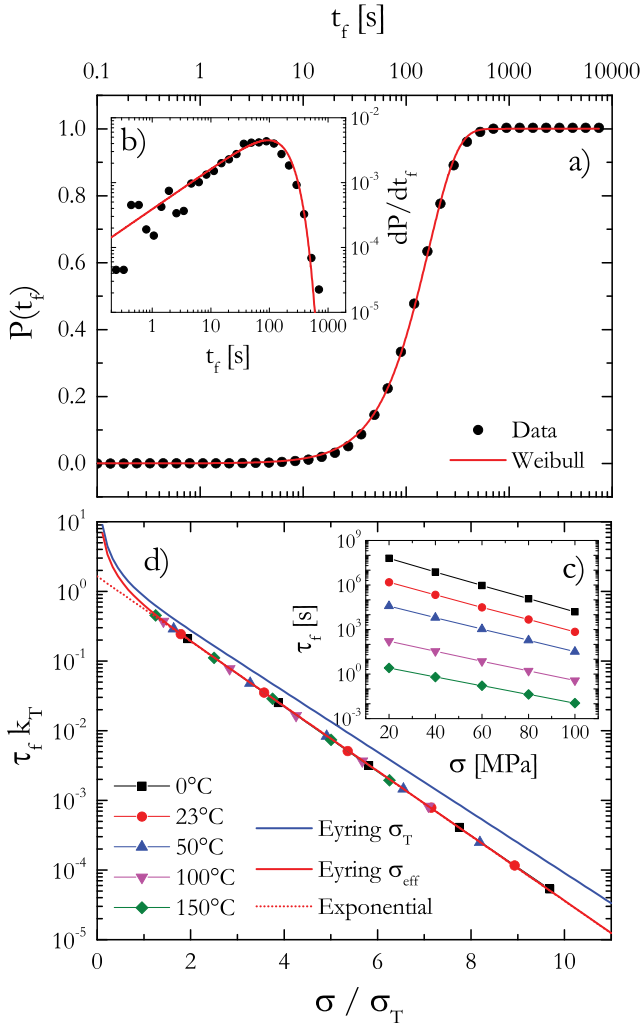


FIG. 9. (a) Symbols: cumulative failure time probability obtained by running 1000 simulations on equivalent samples under equal conditions ($T=100^\circ\text{C}$, $\sigma=20\text{ MPa}$). Solid line: fit with Weibull distribution [Eq. (5)]. (b) Probability distribution of failure times. (c) Average failure time τ_f as a function of the applied stress. Different series represent different temperatures, from top to bottom: 0, 23, 50, 100, and 150°C . (d) Symbols: rescaled average failure time as a function of adimensional stress. Blue line: Eyring σ_T ; Red line: Eyring σ_{eff} ; Red dotted line: Exponential fit.

described in terms of an effective reference stress σ_{eff} , slightly lower than σ_T .

By looking at creep failure time distributions, we can thus identify two main parameters characterizing sample connectivity. The first is a *static* property, just related to structural parameters, which can be evaluated in the homogeneous deformation (i.e., small $\tilde{\sigma}$) limit: in this regime, a sample which is better connected in this sense will withstand a larger number of bond breaking events, thus it will last longer under creep. We can quantify this property by looking at the intercept $\tilde{\tau}_0 = k_T \tau_0$ of an exponential fit of the $\tilde{\tau}_f(\tilde{\sigma})$ plot [39]. However, there is also a second parameter, related to how efficiently the local stress is redistributed, which is a *dynamic* property. Following what was mentioned previously, we quantify this efficiency using the $\sigma_{\text{eff}}/\sigma_T$ ratio: $\tilde{\sigma}_{\text{eff}} = \sigma_{\text{eff}}/\sigma_T = 1$ corresponds to the ideal case of homogeneous deformation, whereas a sample with

$\tilde{\sigma}_{\text{eff}} < 1$ will tend to localize the deformation, specially under large stresses.

Both $\tilde{\tau}_0$ and $\tilde{\sigma}_{\text{eff}}$ depend on sample morphology: as an example, in Fig. 10, we report those parameters for samples where the only varying parameter is the chain length N . In agreement with expectations, longer chains produce better connected samples: $\tilde{\tau}_0$ grows logarithmically with N , whereas $\tilde{\sigma}_{\text{eff}}$ increases only by a few percent in the small N regime and then seems to saturate on a N -independent plateau value, possibly linked to the one observed experimentally (Fig. 3).

C. Percolation threshold

The interplay between morphology and connectivity can also be addressed in numerical simulations by studying the microscopic distribution of plastic events. For example, a direct link with the analytical model can be provided by the local fraction of associated physical bonds: this quantity suffers larger fluctuations for increasingly heterogeneous deformations, whereas its average value at failure represents the percolation threshold A_{th} introduced in Sec. IV.

As already discussed, A_{th} will depend both on sample morphology (samples that are initially better connected will be harder to disconnect) and on the localization of microscopic plasticity (if bond breaking activity is localized in one specific region it will be much more effective [32]): thus, as before, we expect that A_{th} shows both a morphology and a stress/temperature dependence. This is indeed the case, as it is represented in Fig. 11(a): lower values of $\tilde{\sigma}$ are associated to more homogeneous deformations, and thus to a lower threshold, and in an analogous way for a given $\tilde{\sigma}$ better connected samples (larger N) redistribute more efficiently the stress; thus, they also have lower A_{th} values.

Such a rich phenomenology is represented in a simpler way in Fig. 11(b), where a manual rescaling parameter σ_D was introduced to collapse the percolation thresholds on a master-curve. The fact, far from obvious, that such a collapse can be obtained confirms that the important parameter

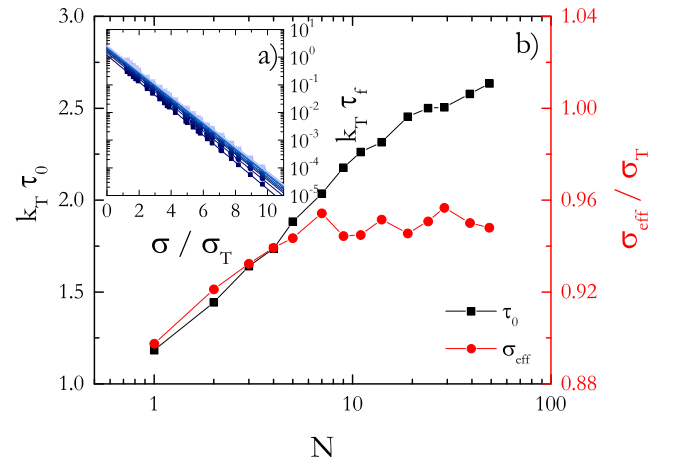


FIG. 10. (a) Symbols: a dimensional average failure time versus adimensional stress for various chain lengths, from dark to light: $N = 1, 2, 3, 4, 5, 7, 9, 12, 15, 20, 25, 30, 40,$ and 50 SB segments. Lines: exponential fits, yielding an intercept ($\tilde{\tau}_0$) and a slope $\tilde{\sigma}_{\text{eff}}$. (b) Fit parameters as a function of chain length. Black, left axis: intercept ($\tilde{\tau}_0$); red, right axis: slope ($\tilde{\sigma}_{\text{eff}}$).

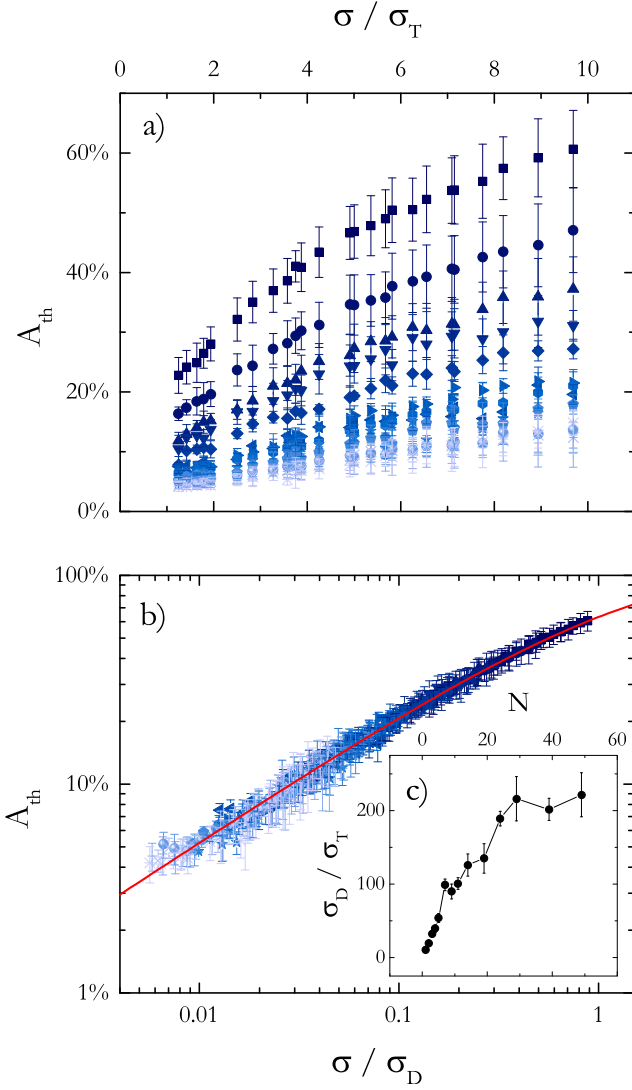


FIG. 11. (a) Fraction of residual physical bonds at failure, as a function of reduced stress for various chain lengths, increasing from dark to light (see Fig. 10 for the values). (b) Same data as panel (a), plotted against a rescaled stress variable. Red line: stretched exponential with stretching exponent $\alpha = 0.63$ (c) Rescaling parameter σ_D plotted as a function of chain length.

controlling the connectivity of a material is indeed how efficiently the local stress is concentrated around defects (here represented, for example, by chain ends that have lower coordination): the effect of macroscopic stress, temperature, and chain morphology can be interpreted in terms of their impact on stress concentration. This is quantified by the stress parameter σ_D , which is represented in Fig. 11(c) as a function of the chain length N . σ_D increasing with N tells us that, at a fixed temperature, a larger external stress is needed to produce the same stress heterogeneities in samples made of longer chains, or that, conversely, such samples deform more homogeneously (thus with a lower A_{th} threshold) under a given applied stress. Furthermore, Fig. 11(c) shows that the impact of chain length on stress concentration becomes negligible for the larger N values, and this offers a practical tool to tackle the M_w dependence of the failure strain observed in Fig. 3. In analogy with simulation results, we can interpret the first growth of $\varepsilon_f(M_w)$ as the sign that longer chains

produce better connected samples, which have higher resistance under tension. In turn, the plateau of ε_f observed in the large M_w limit reminds the fact that connectivity is no longer improved significantly when chain length is increased beyond a given limit.

D. Tensile test simulations

We now turn in this final section to simulating strain rate imposed experiments, which represent a less natural framework for our model, but which can be more directly compared with the experimental data shown in Sec. III. Since our kinetic model does not contain any information about strain, we use stress as a function of time fitted to the experimental tensile curves as an input for numerical simulations.

Starting again from Fig. 2(a), we use the observation that stress seems to be roughly independent on strain rate to extract from experimental data a $\dot{\varepsilon}$ -independent set of stress-strain curves $\sigma(\varepsilon, T)$. These will represent the starting point for our strain rate imposed simulations: for a given strain rate $\dot{\varepsilon}$, a time dependent stress $\sigma(t) = \sigma(\varepsilon = \dot{\varepsilon}t, T)$ is applied to the sample, in order to reproduce the one macroscopically experienced in the experiment. Whenever it was needed, a polynomial fit of the measured $\sigma(\varepsilon, T)$ curves allowed one to extrapolate the mechanical stresses beyond the experimental limit imposed by ε_f . In Fig. 2(b), the maximum elongations measured experimentally are compared to the one extracted by numerical simulations performed on similar conditions. The fair agreement obtained at different temperatures and strain rates can be considered as another indication that despite its intrinsic limitations the model is able to grasp the fundamental features of the sample failure mechanism.

Figure 12 shows, more in detail, the failure strain predicted by numerical simulations using as a starting point the experimental $\sigma(\varepsilon, T)$ curves of Fig. 1 (with the only exception of room temperature, because of strain hardening). In

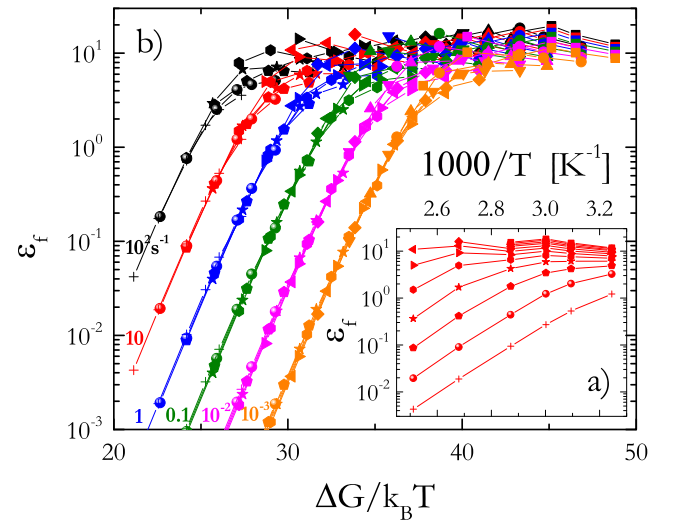


FIG. 12. (a) Elongation at break extracted from numerical simulations for different values of the activation energy ΔG , from 80 to 120 kJ/mol, for a strain rate $\dot{\varepsilon} = 10 \text{ s}^{-1}$, plotted as a function of the inverse temperature. (b) Elongation at break obtained for different values of ΔG and $\dot{\varepsilon}$ (specified in the labels) plotted as a function of the rescaled variable $\Delta G/k_B T$.

agreement with the analytical prediction of Eq. (4), we can again identify two distinct regimes: in the thermal regime, ε_f grows linearly with $\dot{\varepsilon}$ and exponentially with T^{-1} , whereas in the stress-dominated regime, ε_f reaches a plateau value that depends only weakly on T and $\dot{\varepsilon}$.

Strain rate imposed simulations also represent a convenient framework to study the impact of model parameters (ΔG , ν^*) on the observed failure strain. For example, we can take the same experimental tensile curves of Fig. 1 and use them as an input for a series of numerical simulations where only the activation energy ΔG is changed, spanning a narrow interval around the value extracted from the fitting procedure discussed in Sec. IV C. Figure 12(a) shows the resulting failure strain as a function of inverse temperature, for ΔG ranging from 80 to 120 kJ/mol: we observe that ε_f depends strongly on ΔG , and this dependence is stronger at high temperatures. Figure 12(b) quantitatively addresses such dependence: the observed failure strains collapse on $\dot{\varepsilon}$ -dependent mastercurves if plotted against the rescaled variable $\Delta G/k_B T$. This fact, confirmed by preliminary experimental results (not shown), also suggests that the activation energy ΔG is the most relevant parameter controlling the drop in extensibility at high temperatures. Besides its interest from a fundamental point of view, this may indicate the path toward the development of better performing TPEs, with a larger extensibility: indeed, for a fixed strain rate, it may be possible to tune ΔG (for example by modifying the chemistry of the HBs or by improving the HB crystal quality), until the drop in ε_f falls outside the working temperature range.

VI. CONCLUSION

In this paper we have introduced a kinetic model based on Eyring rate equation to describe the breaking apart of physical bonds in a TPE. The sample is regarded as a transient network, whose failure is associated to the loss of connectivity. We apply the model in an analytical and numerically integrated form as well as in numerical simulations, to investigate how it captures the experimental results and to understand its implications for stress localization, with a particular focus on the role of sample morphology. This model captures the experimentally observed (1) drop in elongation at break with increasing temperature, (2) drop in elongation at break with decreasing strain rate (and relatively weaker dependence on strain rate relative to temperature), (3) and the increase in elongation at break with increasing molecular weight.

At the same time, the model neglects some aspects, namely all morphological modifications before fibrillar structure is formed, and the effect of interactions between SBs, either due to entanglements or to crystallization. This restricts the model validity to nonentangled systems in the large strain regime ($\varepsilon > 100\%$) and for temperatures well above the glass transition temperature T_g and below the melting temperature T_m . Another aspect that has been only marginally taken into account in the model is the relevance of the TPE softness. A more detailed investigation on samples

with different HB/SB ratios can offer a more complete perspective on the model validity and on its limitations.

From an experimental point of view, a direct observation of plasticity developed during deformation, for example, with infrared spectroscopy [17], infrared dichroism [5,69–71], light scattering [72], x-ray scattering [15,17,18,39,73–76], NMR [77–80], or other optical techniques [81–84], would provide valuable information about the percolation threshold parameter that our model points out as a practical way to characterize sample connectivity. In particular, space resolved techniques [72,81–83,85] might represent powerful tools to investigate the spatial localization of bond-breaking events, which strongly influences the mechanical properties [86], as it is shown in our simulations. Experimentally accessing this quantity for samples with different microscopic architectures could open new perspectives to the development of more advanced materials.

Finally, our work shows that elongation at break is strongly dependent on the kinetics of physical bonds, which determine the onset of the *thermal* regime, where extensibility is strongly reduced with increasing temperature. Therefore, future development should consider kinetics as the key parameter to tune in order to obtain well-performing TPEs in the whole working temperature range.

ACKNOWLEDGMENTS

The work leading to these results has received funding from the People Programme (Marie Skłodowska-Curie Actions) of the European Union's Seventh Framework Programme (FP7/2007-2013) under REA Grant Agreement No. 607937 SUPOLEN project. The authors also thankfully acknowledge Wilco Appel for the synthesis of the samples studied, Patrick van Soelen for help with instrumentation, Sophia Ganzeboom for mechanical testing, and Carel Fitié for stimulating discussions.

APPENDIX A: BOX SIZE EFFECTS IN NUMERICAL SIMULATIONS

Numerical simulations shown in the text are performed on cubic samples of volume $V = 100^3$ sites. This size is chosen in order to minimize finite size effects while keeping a reasonable simulation time. Finite simulation volume effects were addressed by changing both sample volume and aspect ratio (i.e., by changing, at fixed volume, the sample size along the strain direction).

As a first parameter potentially affected by finite box size we studied the single chain conformation, by looking at the average chain end-to-end distance $\langle R_{ee} \rangle$. Figure 13 shows this quantity for different chain lengths and different (cubic) box sizes. The observed value follows the one expected for a polymer in theta solvent [87], until a deviation is observed as soon as $\langle R_{ee} \rangle$ exceeds half the lateral box size. In our simulations, we chose to work with chains short enough to be well below this regime.

More importantly than chain conformation, we addressed the sample volume dependence of creep failure time. This is a well-known problem, experimentally investigated by

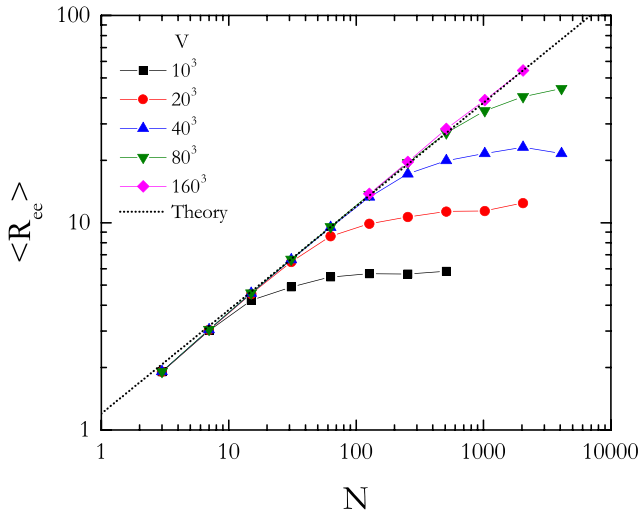


FIG. 13. Chain end to end distance (in units of the lattice size) as a function of the number N of SBs. Different series refer to simulations performed in cubic boxes of different sizes: the number of sites along one edge of the cubic box grows from 10 to 160 as specified in the legend.

looking at the tensile strength of wires since XV century, when Leonardo da Vinci first observed that longer wires were weaker than shorter ones [88,89]. Indeed, in Weibull theory [63], the failure probability is assumed to grow exponentially with the sample volume (the general argument being that larger samples contain a larger amount of critical defects [66]). This is in good agreement with numerical simulations, as it is shown in Fig. 14: under the same experimental conditions, larger samples fail earlier. More precisely, for a fixed transversal section (different colors in Fig. 14), elongated samples are more fragile, and the failure time decreases as $V^{-1/\beta}$ [63]. This happens because thinner samples are more heterogeneous (lower β), thus more prone to

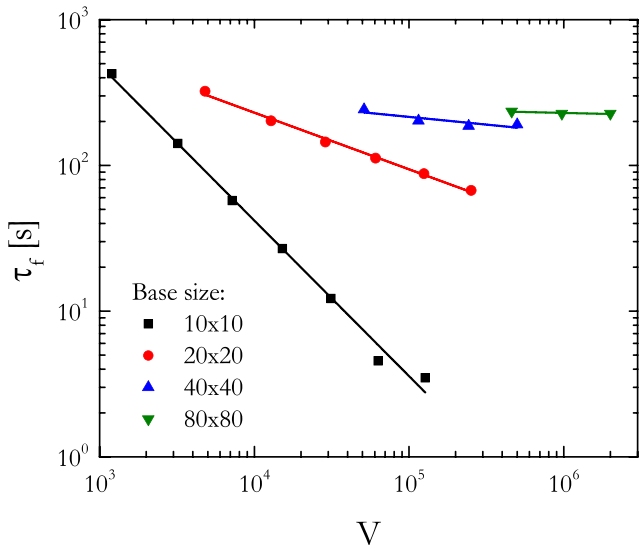


FIG. 14. Symbols: average creep failure time measured as a function of sample size (V represents the volume of the simulation box, in units of the cubic lattice size), under equivalent conditions (temperature $T = 60^\circ\text{C}$, stress $\sigma/\sigma_T = 12$) for a system of chains with $N = 3$ SBs per chain. Lines: power law fits with slope fixed to the expected $-1/\beta$ value, with $\beta = 0.9, 2.6, 9.5,$ and 40 (extracted by a Weibull fit of failure time distributions at different sample sizes).

stress concentration [90], which reflects in a sharper dependence of failure time on sample volume. By contrast, for sample thicknesses large enough, like the one used in this paper, the probability of finding a critical defect just because of random chain disposition is significantly suppressed, and the failure dynamics will be roughly independent on sample size.

APPENDIX B: CREEP COMPLIANCE

Numerical simulations presented in Sec. V do not contain any information on macroscopic strain: the only relevant variables are stress and time. That is why creep compliance cannot be accessed, and we must limit ourselves to analyze the failure time distribution. In order to overcome this limitation, a stress-strain relation is needed, at least for one single SB chain. For example, one can start assuming that each SB acts as an entropic spring, with a given Young modulus E , and use this assumption to link the local stress $\sigma_{loc}(k, t)$ experienced by plane k to a local strain $\varepsilon_{loc}(k, t)$. All SBs being identical, the local stress and strains will be different from the macroscopic ones just because the number $n_{SB}(k, t)$ of SBs bridging any k plane with the nearest ones is not constant. Indeed, $n_{SB}(k, t)$ is initially fluctuating, and it evolves toward even more heterogeneous configurations because of stress concentration.

Because of linearity the total strain will be the arithmetic average of local strains, whereas the macroscopic true stress will be by definition related to local stresses via a harmonic average:

$$\sigma_{\text{True}}(t) = \left[\left\langle \frac{1}{\sigma_{loc}(k, t)} \right\rangle_k \right]^{-1} \leq \langle \sigma_{loc}(k, t) \rangle_k = E \langle \varepsilon_{loc}(k, t) \rangle_k = E \varepsilon. \quad (\text{B1})$$

The inequality is a well-known theorem in mathematics [91]: in particular, since the ratio between arithmetic and harmonic average increases if the local stress profile gets increasingly heterogeneous [92], creep compliance under a constant external stress increases when connectivity is progressively lost, until failure occurs. For the same reason, according to this model we should expect creep compliance at break to show only weak dependence on stress and temperature, which is in good agreement with experimental data [cf. Fig. 8(a) for the stress dependence] [64].

Also in this case, maximum extensibility depends on sample morphology (for example, chain molar mass). However, it is worth to mention that, once plotted against the rescaled stress variable σ/σ_D , again simulation results for ε_f in creep tend to collapse on a master-curve: this is again because creep extension is strictly linked to the heterogeneity of the deformation.

References

- [1] Callister, W. D., and D. G. Rethwisch, *Materials Science and Engineering: An Introduction*, 9th ed. (Wiley, Hoboken, NJ, 2014).
- [2] *Handbook of Condensation Thermoplastic Elastomers*, edited by S. Fakirov (Wiley-VCH Verlag GmbH and Co, Weinheim, 2005).
- [3] Shackelford, J. F., *Introduction to Materials Science for Engineers*, 8th ed. (Pearson, Boston, 2015).

- [4] Spychaj, T., M. Kacperski, and A. Kozłowska, "Condensation and addition thermoplastic elastomers: Recycling aspects," in *Handbook of Condensation Thermoplastic Elastomers* (Wiley-VCH Verlag GmbH and Co, Weinheim, 2005), Chap. 19, pp. 567–592.
- [5] Gaymans, R. J., "Segmented copolymers with monodisperse crystallizable hard segments: Novel semi-crystalline materials," *Prog. Polym. Sci.* **36**, 713–748 (2011).
- [6] Fakirov, S., and T. Gogeva, "Poly(ether/ester)s based on poly(butylene terephthalate) and poly(ethylene glycol), 1. Poly(ether/ester)s with various polyether: Polyester ratios," *Makromol. Chem.* **191**, 603–614 (1990).
- [7] Fakirov, S., and T. Gogeva, "Poly(ether/ester)s based on poly(butylene terephthalate) and poly(ethylene glycol), 2. Effect of polyether segment length," *Makromol. Chem. Phys.* **191**, 615–624 (1990).
- [8] Fakirov, S., A. A. Apostolov, P. Boeske, and H. G. Zachmann, "Structure of segmented poly(ether ester)s as revealed by synchrotron radiation," *J. Macromol. Sci., Part B* **29**, 379–395 (1990).
- [9] Stribeck, N., A. A. Apostolov, H. G. Zachmann, C. Fakirov, M. Stamm, and S. Fakirov, "Small angle x-ray scattering of segmented block copolyetheresters during stretching," *Int. J. Polym. Mater.* **25**, 185–200 (1994).
- [10] Deschamps, A. A., D. W. Grijpma, and J. Feijen, "Poly(ethylene oxide)/poly(butylene terephthalate) segmented block copolymers: The effect of copolymer composition on physical properties and degradation behavior," *Polymer* **42**, 9335–9345 (2001).
- [11] Baeza, G. P., A. Sharma, A. Louhichi, L. Imperiali, W. P. J. Appel, C. F. C. Fitić, M. P. Lettinga, E. Van Ruymbeke, and D. Vlassopoulos, "Multiscale organization of thermoplastic elastomers with varying content of hard segments," *Polymer* **107**, 89–101 (2016).
- [12] Sijbrandi, N. J., A. J. Kimenai, E. P. C. Mes, R. Broos, G. Bar, M. Rosenthal, Y. Odarchenko, D. A. Ivanov, P. J. Dijkstra, and J. Feijen, "Synthesis, morphology, and properties of segmented poly(ether amide)s with uniform oxalamide-based hard segments," *Macromolecules* **45**, 3948–3961 (2012).
- [13] Fakirov, S., "Poly(ether ester) thermoplastic elastomers: Phase and deformation behavior on the nano- and microlevel," in *Handbook of Condensation Thermoplastic Elastomers* (Wiley-VCH Verlag GmbH and Co, Weinheim, 2005), Chap. 5, pp. 167–196.
- [14] Apostolov, A. A., and S. Fakirov, "Effect of the block length on the deformation behavior of polyetheresters as revealed by small-angle x-ray scattering," *J. Macromol. Sci., Part B* **31**, 329–355 (1992).
- [15] Stribeck, N., D. Sapoundjieva, Z. Denchev, A. A. Apostolov, H. G. Zachmann, M. Stamm, and S. Fakirov, "Deformation behavior of poly(ether ester) copolymer as revealed by small- and wide-angle scattering of x-ray radiation from synchrotron," *Macromolecules* **30**, 1329–1339 (1997).
- [16] Wu, L., T. P. Lodge, and F. S. Bates, "Effect of block number on multiblock copolymer lamellae alignment under oscillatory shear," *J. Rheol.* **49**, 1231–1252 (2005).
- [17] Yeh, F., B. S. Hsiao, B. B. Sauer, S. Michel, and H. W. Siesler, "In-situ studies of structure development during deformation of a segmented poly(urethaneurea) elastomer," *Macromolecules* **36**, 1940–1954 (2003).
- [18] Toki, S., B. S. Hsiao, S. Kohjiya, M. Tosaka, A. H. Tsou, and S. Datta, "Synchrotron x-ray studies of vulcanized rubbers and thermoplastic elastomers," *Rubber Chem. Technol.* **79**, 460–488 (2006).
- [19] Niesten, M. C. E. J., and R. J. Gaymans, "Tensile and elastic properties of segmented copolyesteramides with uniform aramid units," *Polymer* **42**, 6199–6207 (2001).
- [20] Biemond, G. J. E., J. Feijen, and R. J. Gaymans, "Tensile properties of segmented block copolymers with monodisperse hard segments," *J. Mater. Sci.* **43**, 3689–3696 (2008).
- [21] Ward, I. M., and J. Sweeney, *An Introduction to the Mechanical Properties of Solid Polymers*, 2nd ed. (Wiley, Chichester, 2004).
- [22] *The Physics of Glassy Polymers* edited by R. N. Haward and R. J. Young (Springer, Netherlands, 1997).
- [23] Smith, T. L., "Tensile strength of polyurethane and other elastomeric block copolymers," *Rubber Chem. Technol.* **49**, 64–84 (1976).
- [24] Smith, T. L., "Strength of elastomers—A perspective," *Polym. Eng. Sci.* **17**, 129–143 (1977).
- [25] Yamakawa, H., and H. Miyata, "High performance thermoplastic aramid elastomers: Synthesis, properties, and applications," in *Handbook of Condensation Thermoplastic Elastomers* (Wiley-VCH Verlag GmbH and Co, Weinheim, 2005), Chap. 5, pp. 141–166.
- [26] Gabriëlse, W., M. Soliman, and K. Dijkstra, "Microstructure and phase behavior of block copoly(ether ester) thermoplastic elastomers," *Macromolecules* **34**, 1685–1693 (2001).
- [27] Marechal, E., "Polycondensation reactions in thermoplastic elastomer chemistry: state of the art, trends, and future developments," in *Handbook of Condensation Thermoplastic Elastomers* (Wiley-VCH Verlag GmbH and Co, Weinheim, 2005), Chap. 2, pp. 33–66.
- [28] Stribeck, N., S. Fakirov, A. A. Apostolov, Z. Denchev, and R. Gehrke, "Deformation behavior of PET, PBT and PBT-based thermoplastic elastomers as revealed by SAXS from synchrotron," *Macromol. Chem. Phys.* **204**, 1000–1013 (2003).
- [29] Niesten, M. C. E. J., S. Harkema, E. Van der Heide, and R. J. Gaymans, "Structural changes of segmented copolyetheresteramides with uniform aramid units induced by melting and deformation," *Polymer* **42**, 1131–1142 (2001).
- [30] Versteegen, R. M., R. Kleppinger, R. P. Sijbesma, and E. W. Meijer, "Properties and morphology of segmented copoly(ether urea)s with uniform hard segments," *Macromolecules* **39**, 772–783 (2006).
- [31] Deplace, F., Z. Wang, N. A. Lynd, A. Hotta, J. M. Rose, P. D. Hustad, J. Tian, H. Ohtaki, G. W. Coates, F. Shimizu, K. Hirokane, F. Yamada, Y.-W. Shin, L. Rong, J. Zhu, S. Toki, B. S. Hsiao, G. H. Fredrickson, and E. J. Kramer, "Processing-structure-mechanical property relationships of semicrystalline polyolefin-based block copolymers," *J. Polym. Sci., Part B* **48**, 1428–1437 (2010).
- [32] Tanaka, F., and S. F. Edwards, "Viscoelastic properties of physically crosslinked networks. 1. Transient network theory," *Macromolecules* **25**, 1516–1523 (1992).
- [33] Mora, S., "The kinetic approach to fracture in transient networks," *Soft Matter* **7**, 4908–4917 (2011).
- [34] Ligoure, C., and S. Mora, "Fractures in complex fluids: The case of transient networks," *Rheol. Acta* **52**, 91–114 (2013).
- [35] Bauwens-Crowet, C., J. C. Bauwens, and G. Homes, "Tensile yield-stress behavior of glassy polymers," *J. Polym. Sci., Part A* **7**, 735–742 (1969).
- [36] Hasan, O. A., M. C. Boyce, X. S. Li, and S. Berko, "An investigation of the yield and postyield behavior and corresponding structure of poly(methyl methacrylate)," *J. Polym. Sci., Part B* **31**, 185–197 (1993).
- [37] Buckley, C. P., and D. C. Jones, "Glass-rubber constitutive model for amorphous polymers near the glass transition," *Polymer* **36**, 3301–3312 (1995).
- [38] Buckley, C., "Deformation of thermosetting resins at impact rates of strain. Part 2: Constitutive model with rejuvenation," *J. Mech. Phys. Solids* **52**, 2355–2377 (2004).
- [39] van Erp, T. B., D. Cavallo, G. W. M. Peters, and L. E. Govaert, "Rate-, temperature-, and structure-dependent yield kinetics of isotactic polypropylene," *J. Polym. Sci., Part B* **50**, 1438–1451 (2012).
- [40] Roetling, J. A., "Yield stress behaviour of isotactic polypropylene," *Polymer* **7**, 303–306 (1966).

- [41] Roetling, J. A., "Yield stress behaviour of polymethylmethacrylate," *Polymer* **6**, 311–317 (1964).
- [42] van Erp, T. B., C. T. Reynolds, T. Peijs, J. A. W. van Dommelen, and L. E. Govaert, "Prediction of yield and long-term failure of oriented polypropylene: Kinetics and anisotropy," *J. Polym. Sci., Part B* **47**, 2026–2035 (2009).
- [43] Coleman, B. D., "Application of the theory of absolute reaction rates to the creep failure of polymeric filaments," *J. Polym. Sci.* **20**, 447–455 (1956).
- [44] Bueche, F., "Tensile strength of plastics below the glass temperature," *J. Appl. Phys.* **28**, 784–787 (1957).
- [45] Bueche, F., "Tensile strength of plastics: Effects of flaws and chain relaxation," *J. Appl. Phys.* **29**, 1231–1234 (1958).
- [46] Janssen, R. P. M., L. E. Govaert, and H. E. H. Meijer, "An analytical method to predict fatigue life of thermoplastics in uniaxial loading: Sensitivity to wave type, frequency, and stress amplitude," *Macromolecules* **41**, 2531–2540 (2008).
- [47] Visser, H. A., T. C. Bor, M. Wolters, T. A. P. Engels, and L. E. Govaert, "Lifetime assessment of load-bearing polymer glasses: An analytical framework for ductile failure," *Macromol. Mater. Eng.* **295**, 637–651 (2010).
- [48] Drozdov, A. D., and J. deC. Christiansen, "Creep failure of polypropylene: Experiments and constitutive modeling," *Int. J. Fract.* **159**, 63–79 (2009).
- [49] Matz, D. J., W. G. Guldmond, and S. L. Cooper, "Delayed yielding in glassy polymers," *J. Polym. Sci., Part B* **10**, 1917–1930 (1972).
- [50] Eyring, H., "Viscosity, plasticity and diffusion as examples of absolute reaction rates," *J. Chem. Phys.* **4**, 283–291 (1936).
- [51] Green, M. S., and A. V. Tobolsky, "A new approach to the theory of relaxing polymeric media," *J. Chem. Phys.* **14**, 80–92 (1946).
- [52] Ree, T., and H. Eyring, "Theory of non-Newtonian flow. I. Solid plastic system," *J. Appl. Phys.* **26**, 793–800 (1955).
- [53] Ree, T., and H. Eyring, "Theory of non-Newtonian flow. II. Solution system of high polymers," *J. Appl. Phys.* **26**, 800–809 (1955).
- [54] Tervoort, T. A., E. T. J. Klompen, and L. E. Govaert, "A multimode approach to finite, threedimensional, nonlinear viscoelastic behavior of polymer glasses," *J. Rheol.* **40**, 779–797 (1996).
- [55] Klompen, E. T. J., T. A. P. Engels, L. C. A. van Breemen, P. J. G. Schreurs, L. E. Govaert, and H. E. H. Meijer, "Quantitative prediction of long-term failure of polycarbonate," *Macromolecules* **38**, 7009–7017 (2005).
- [56] Klompen, E. T. J., T. A. P. Engels, L. E. Govaert, and H. E. H. Meijer, "Modeling of the postyield response of glassy polymers: Influence of thermomechanical history," *Macromolecules* **38**, 6997–7008 (2005).
- [57] Zhurkov, S. N., "Kinetic concept of the strength of solids," *Int. J. Fract. Mech.* **1**, 311–323 (1965).
- [58] Zhurkov, S. N., and S. A. Abasov, "The temperature and the time dependence of the strength of polymer yarns," *Polym. Sci., Ser. A* **41**, 1276–1282 (1999).
- [59] Chen, K., and K. S. Schweizer, "Stress-enhanced mobility and dynamic yielding in polymer glasses," *Europhys. Lett.* **79**, 26006 (2007).
- [60] Wu, J. J., and C. P. Buckley, "Plastic deformation of glassy polystyrene: A unified model of yield and the role of chain length," *J. Polym. Sci., Part B* **42**, 2027–2040 (2004).
- [61] Termonia, Y., "Molecular model for the mechanical properties of elastomers. 1. Network formation and role of entanglements," *Macromolecules* **22**, 3633–3638 (1989).
- [62] Narisawa, I., M. Ishikawa, and H. Ogawa, "Delayed yielding of polycarbonate under constant load," *J. Polym. Sci.* **16**, 1459–1470 (1978).
- [63] Weibull, W., "A statistical theory of the strength of materials," *Ingenjors Vetenskaps Akademiens Handlingar* **151**, 1939.
- [64] Vas, L. M., and P. Bakonyi, "Estimating the creep strain to failure of PP at different load levels based on short term tests and Weibull characterization," *Express Polym. Lett.* **6**, 987–996 (2012).
- [65] Nakada, M., and Y. Miyano, "Statistical creep failure time of unidirectional CFRP," *Exp. Mech.* **56**, 653–658 (2016).
- [66] Coleman, B. D., "Statistics and time dependence of mechanical breakdown in fibers," *J. Appl. Phys.* **29**, 968–983 (1958).
- [67] Liu, A. J., and S. R. Nagel, "Nonlinear dynamics: Jamming is not just cool any more," *Nature* **396**, 21–22 (1998).
- [68] Haxton, T. K., and A. J. Liu, "Activated dynamics and effective temperature in a steady state sheared glass," *Phys. Rev. Lett.* **99**, 195701 (2007).
- [69] Seymour, R. W., G. M. Estes, and S. L. Cooper, "Infrared studies of segmented polyurethane elastomers. I. Hydrogen bonding," *Macromolecules* **3**, 579–583 (1970).
- [70] Seymour, R. W., A. E. Allegrezza, Jr., and S. L. Cooper, "Segmental orientation studies of block polymers. I. Hydrogen-bonded polyurethanes," *Macromolecules* **6**, 896–902 (1973).
- [71] Seymour, R. W., and S. L. Cooper, "Viscoelastic properties of polyurethane block polymers," *Rubber Chem. Technol.* **47**, 19–31 (1974).
- [72] Nagazi, M.-Y., G. Brambilla, G. Meunier, P. Marguers, J.-N. Périé, and L. Cipelletti, "Space-resolved diffusing wave spectroscopy measurements of the macroscopic deformation and the microscopic dynamics in tensile strain tests," *Opt. Lasers Eng.* **88**, 5–12 (2017).
- [73] Bauer, T., J. Oberdisse, and L. Ramos, "Collective rearrangement at the onset of flow of a polycrystalline hexagonal columnar phase," *Phys. Rev. Lett.* **97**, 258303 (2006).
- [74] Addiego, F., S. Patlazhan, K. Wang, S. André, S. Bernstorff, and D. Ruch, "Time-resolved small-angle x-ray scattering study of void fraction evolution in high-density polyethylene during stress unloading and strain recovery: SAXS study of void fraction evolution in HDPE," *Polym. Int.* **64**, 1513–1521 (2015).
- [75] Farge, L., S. André, F. Meneau, J. Dillet, and C. Cunat, "A common multiscale feature of the deformation mechanisms of a semicrystalline polymer," *Macromolecules* **46**, 9659–9668 (2013).
- [76] Farge, L., J. Boisse, J. Dillet, S. André, P.-A. Albouy, and F. Meneau, "Wide-angle x-ray scattering study of the lamellar/fibrillar transition for a semi-crystalline polymer deformed in tension in relation with the evolution of volume strain," *J. Polym. Sci., Part B* **53**, 1470–1480 (2015).
- [77] Loo, L. S., R. E. Cohen, and K. K. Gleason, "Chain mobility in the amorphous region of nylon 6 observed under active uniaxial deformation," *Science* **288**, 116–119 (2000).
- [78] Schaefer, D. J., R. J. Schadt, K. H. Gardner, V. Gabara, S. R. Allen, and A. D. English, "Microscopic dynamics and macroscopic mechanical deformation of poly(p-phenyleneterephthalamide) fibers," *Macromolecules* **28**, 1152–1158 (1995).
- [79] Hansen, M. T., C. Boeffel, and H. W. Spiess, "Phenylene motion in polycarbonate: Influence of tensile stress and chemical modification," *Colloid Polym. Sci.* **271**, 446–453 (1993).
- [80] Loo, L. S., R. E. Cohen, and K. K. Gleason, "Deuterium nuclear magnetic resonance of phenol-d5 in nylon 6 under active uniaxial deformation," *Macromolecules* **32**, 4359–4364 (1999).
- [81] Lee, H.-N., K. Paeng, S. F. Swallen, and M. D. Ediger, "Dye reorientation as a probe of stress-induced mobility in polymer glasses," *J. Chem. Phys.* **128**, 134902 (2008).
- [82] Lee, H.-N., K. Paeng, S. F. Swallen, and M. D. Ediger, "Direct measurement of molecular mobility in actively deformed polymer glasses," *Science* **323**, 231–234 (2009).

- [83] André, S., C. Baravian, N. Renault, and C. Cunat, "In situ mechanical characterization of polymers with the association of three optical techniques," *Appl. Phys. Lett.* **91**, 071919 (2007).
- [84] Baravian, C., S. André, N. Renault, N. Moumini, and C. Cunat, "Optical techniques for in situ dynamical investigation of plastic damage," *Rheol. Acta* **47**, 555–564 (2008).
- [85] André, S., N. Renault, Y. Meshaka, and C. Cunat, "From the thermodynamics of constitutive laws to the thermomechanical experimental characterization of a semicrystalline polymer from IR imaging," *Continuum Mech. Thermodyn.* **24**, 1–20 (2012).
- [86] Ediger, M. D., "Spatially heterogeneous dynamics in supercooled liquids," *Annu. Rev. Phys. Chem.* **51**, 99–128 (2000).
- [87] Colby, R. H., and M. Rubinstein, *Polymer Physics* (Oxford University, Weinheim, 2003).
- [88] Timoshenko, S. P., *History of Strength of Materials* (McGraw-Hill, Weinheim, 1953).
- [89] Lund, J. R., and J. P. Byrne, "Leonardo Da Vinci's tensile strength tests: Implications for the discovery of engineering mechanics," *Civil Eng. Syst.* **18**, 243–250 (2001).
- [90] Amaniampong, G., and C. J. Burgoyne, "Monte-Carlo simulations of the time dependent failure of bundles of parallel fibres," *Eur. J. Mech., A* **2**, 243–266 (1996).
- [91] Xia, D.-F., S.-L. Xu, and F. Qi, "A proof of the arithmetic mean-geometric mean-harmonic mean inequalities," *Res. Rep. Collect.* **2**, 85–87 (1999).
- [92] Limbrunner, J. F., R. M. Vogel, and L. C. Brown, "Estimation of harmonic mean of a lognormal variable," *J. Hydrol. Eng.* **5**, 59–66 (2000).

Bibliography

- [Abobaker 2015] M. Abobaker, O. Bouaziz, M. Lebyodkin, T. Lebedkina and I.V. Shashkov. *Avalanche Dynamics in Crumpled Aluminum Thin Foils*. Scripta Materialia, vol. 99, pages 17–20, April 2015. (Cited on page 27.)
- [Adolf 1990] Douglas Adolf and James E. Martin. *Time-Cure Superposition during Crosslinking*. Macromolecules, vol. 23, no. 15, pages 3700–3704, 1990. (Cited on pages 26, 102 and 116.)
- [Agioutantis 2016] Z. Agioutantis, K. Kaklis, S. Mavrigiannakis, M. Verigakis, F. Valianatos and V. Saltas. *Potential of Acoustic Emissions from Three Point Bending Tests as Rock Failure Precursors*. International Journal of Mining Science and Technology, vol. 26, no. 1, pages 155–160, January 2016. (Cited on pages 4 and 27.)
- [Agrawal 2015] Akanksha Agrawal, Hsiu-Yu Yu, Samanvaya Srivastava, Snehashis Choudhury, Suresh Narayanan and Lynden A. Archer. *Dynamics and Yielding of Binary Self-Suspended Nanoparticle Fluids*. Soft Matter, vol. 11, no. 26, pages 5224–5234, 2015. (Cited on page 9.)
- [Ahmadi 2013] Khodabakhsh Ahmadi, Mehran Ahmadi, Majid Rezazade, Esfandiar Azad-Marzabadi and Firoozeh Sajedi. *Brain Activity of Women Is More Fractal than Men*. Neuroscience Letters, vol. 535, pages 7–11, February 2013. (Cited on page 102.)
- [Aime 2016] S. Aime, L. Ramos, J. M. Fromental, G. Prevot, R. Jelinek and L. Cipelletti. *A Stress-Controlled Shear Cell for Small-Angle Light Scattering and Microscopy*. Review of Scientific Instruments, vol. 87, no. 12, page 123907, December 2016. (Cited on pages 71 and 107.)
- [Aime 2017] S. Aime, N. D. Eisenmenger and T. A. P. Engels. *A Model for Failure in Thermoplastic Elastomers Based on Eyring Kinetics and Network Connectivity*. Journal of Rheology, vol. 61, no. 6, pages 1329–1342, November 2017. (Cited on pages 10 and 183.)
- [Aime 2018] Stefano Aime, Laurence Ramos and Luca Cipelletti. *Microscopic Dynamics and Failure Precursors of a Gel under Mechanical Load*. Proceedings of the National Academy of Sciences, page 201717403, March 2018. (Cited on page 119.)
- [Altmann 2004] N. Altmann, J.J. Cooper-White, D.E. Dunstan and J.R. Stokes. *Strong through to Weak ‘Sheared’ Gels*. Journal of Non-Newtonian Fluid Mechanics, vol. 124, no. 1-3, pages 129–136, December 2004. (Cited on page 9.)

- [Amblard 1996] François Amblard, Anthony C. Maggs, Bernard Yurke, Andrew N. Pargellis and Stanislas Leibler. *Subdiffusion and Anomalous Local Viscoelasticity in Actin Networks*. Physical review letters, vol. 77, no. 21, page 4470, 1996. (Cited on page 7.)
- [Amon 2013] Axelle Amon, Roman Bertoni and Jerome Crassous. *Experimental Investigation of Plastic Deformations before a Granular Avalanche*. Physical Review E, vol. 87, no. 1, January 2013. (Cited on pages 3, 9 and 27.)
- [Ancey 2007] Christophe Ancey. *Plasticity and Geophysical Flows: A Review*. Journal of Non-Newtonian Fluid Mechanics, vol. 142, no. 1-3, pages 4–35, March 2007. (Cited on page 4.)
- [Andrade 1910] E. N. Andrade. *On the Viscous Flow in Metals, and Allied Phenomena*. Proceedings of the Royal Society A: Mathematical and Physical Sciences, vol. 84, pages 1–12, 1910. (Cited on pages 4, 7, 21 and 103.)
- [Antonaglia 2014] James Antonaglia, Wendelin J. Wright, Xiaojun Gu, Rachel R. Byer, Todd C. Hufnagel, Michael LeBlanc, Jonathan T. Uhl and Karin A. Dahmen. *Bulk Metallic Glasses Deform via Slip Avalanches*. Physical Review Letters, vol. 112, no. 15, April 2014. (Cited on pages 15, 20 and 27.)
- [Anwar 2009] Imran Anwar, Gauraang Bhatnagar and Salah Atrah. *Delayed Catastrophic Failure of a Ceramic Head in Hybrid Total Hip Arthroplasty*. The Journal of Arthroplasty, vol. 24, no. 1, pages 158.e5–158.e8, January 2009. (Cited on page 4.)
- [Aoki 1980] S. Aoki and M. Sakata. *Statistical Approach to Delayed Failure of Brittle Materials*. International Journal of Fracture, vol. 16, no. 5, pages 459–469, 1980. (Cited on page 4.)
- [Arleth 2005] Lise Arleth, Xiaohu Xia, Rex P. Hjelm, Jianzhong Wu and Zhibing Hu. *Volume Transition and Internal Structures of Small Poly(N-Isopropylacrylamide) Microgels*. Journal of Polymer Science Part B: Polymer Physics, vol. 43, no. 7, pages 849–860, April 2005. (Cited on page 149.)
- [Ashby 1985] M. F. Ashby and P. Duval. *The Creep of Polycrystalline Ice*. Cold Regions Science and Technology, vol. 11, no. 3, pages 285–300, 1985. (Cited on pages 4, 21 and 103.)
- [Bagley 1983] R. L. Bagley and P. J. Torvik. *A Theoretical Basis for the Application of Fractional Calculus to Viscoelasticity*. Journal of Rheology, vol. 27, no. 3, pages 201–210, June 1983. (Cited on pages 64 and 104.)
- [Bagley 1986] R. L. Bagley and P. J. Torvik. *On the Fractional Calculus Model of Viscoelastic Behavior*. Journal of Rheology, vol. 30, no. 1, pages 133–155, February 1986. (Cited on page 104.)

- [Bagley 1989] R. L. Bagley. *Power Law and Fractional Calculus Model of Viscoelasticity*. AIAA Journal, vol. 27, no. 10, pages 1412–1417, October 1989. (Cited on pages 64 and 105.)
- [Bak 1997] Per Bak, Maya Paczuski and Martin Shubik. *Price Variations in a Stock Market with Many Agents*. Physica A: Statistical Mechanics and its Applications, vol. 246, no. 3-4, pages 430–453, 1997. (Cited on page 27.)
- [Ball 1999] G. J. Ball and R. A. East. *Shock and Blast Attenuation by Aqueous Foam Barriers: Influences of Barrier Geometry*. Shock waves, vol. 9, no. 1, pages 37–47, 1999. (Cited on page 4.)
- [Balland 2006] Martial Balland, Nicolas Desprat, Delphine Icard, Sophie Feriol, Atef Asnacios, Julien Browaeys, Sylvie Hanon and Francois Gallet. *Power Laws in Microrheology Experiments on Living Cells: Comparative Analysis and Modeling*. Physical Review E, vol. 74, no. 2, August 2006. (Cited on pages 7, 101 and 103.)
- [Ballesta 2016] P. Ballesta and G. Petekidis. *Creep and Aging of Hard-Sphere Glasses under Constant Stress*. Physical Review E, vol. 93, no. 4, April 2016. (Cited on pages 21 and 30.)
- [Basquin 1910] O.H. Basquin. *The Exponential Law of Endurance Test*. Proceeding of the American Society for Testing and Materials, vol. 10, pages 625–630, 1910. (Cited on page 4.)
- [Bauer 2006] Teresa Bauer, Julian Oberdisse and Laurence Ramos. *Collective Rearrangement at the Onset of Flow of a Polycrystalline Hexagonal Columnar Phase*. Physical Review Letters, vol. 97, no. 25, December 2006. (Cited on page 4.)
- [Baumberger 2006] Tristan Baumberger, Christiane Caroli and David Martina. *Solvent Control of Crack Dynamics in a Reversible Hydrogel*. Nature Materials, vol. 5, no. 7, pages 552–555, July 2006. (Cited on page 5.)
- [Baxevanis 2007] Theocharis Baxevanis and Theodoros Katsaounis. *Load Capacity and Rupture Displacement in Viscoelastic Fiber Bundles*. Physical Review E, vol. 75, no. 4, April 2007. (Cited on page 10.)
- [Bazant 1991] Z. P. Bazant and Luigi Cedolin. *Stability of Structures: Elastic, Inelastic, Fracture, and Damage Theories*. Courier Corporation, 1991. Google-Books-ID: 0PiHE6rV7ZYC. (Cited on pages 3 and 4.)
- [Bell 1978] G. Bell. *Models for the Specific Adhesion of Cells to Cells*. Science, vol. 200, no. 4342, pages 618–627, May 1978. (Cited on pages 3, 4 and 5.)
- [Bell 2008] J. Bell. *Condition Based Maintenance plus DoD Guidebook*, 2008. (Cited on page 5.)

- [Ben-Zion 2008] Yehuda Ben-Zion. *Collective Behavior of Earthquakes and Faults: Continuum-Discrete Transitions, Progressive Evolutionary Changes, and Different Dynamic Regimes*. Reviews of Geophysics, vol. 46, no. 4, December 2008. (Cited on pages 3, 9 and 27.)
- [Bentil 2014] Sarah A. Bentil and Rebecca B. Dupaix. *Exploring the Mechanical Behavior of Degrading Swine Neural Tissue at Low Strain Rates via the Fractional Zener Constitutive Model*. Journal of the Mechanical Behavior of Biomedical Materials, vol. 30, pages 83–90, February 2014. (Cited on page 7.)
- [Berne 2013] Bruce J. Berne and Robert Pecora. *Dynamic Light Scattering: With Applications to Chemistry, Biology, and Physics*. Courier Corporation, July 2013. Google-Books-ID: xg3CAgAAQBAJ. (Cited on pages 57 and 58.)
- [Besseling 2009] R. Besseling, L. Isa, E. R. Weeks and W. C. K. Poon. *Quantitative Imaging of Colloidal Flows*. Advances in Colloid and Interface Science, vol. 146, no. 1, pages 1–17, February 2009. (Cited on page 10.)
- [Beyer 2015] Richard Beyer, Markus Franke, Hans Joachim Schöpe, Eckhard Bartsch and Thomas Palberg. *From Nuclei to Micro-Structure in Colloidal Crystallization: Investigating Intermediate Length Scales by Small Angle Laser Light Scattering*. The Journal of Chemical Physics, vol. 143, no. 6, page 064903, August 2015. (Cited on page 150.)
- [Bird 1987] R.B. Bird, R.C. Armstrong and O. Hassager. *Dynamics of Polymeric Liquids : Fluid Mechanics*, volume 1. John Wiley and Sons, New York, 2 édition, 1987. (Cited on page 64.)
- [Bischofberger 2015] Irmgard Bischofberger and Veronique Trappe. *New Aspects in the Phase Behaviour of Poly-N-Isopropyl Acrylamide: Systematic Temperature Dependent Shrinking of PNiPAM Assemblies Well beyond the LCST*. Scientific Reports, vol. 5, page 15520, October 2015. (Cited on pages 149 and 150.)
- [Blair 1947] G. W. S. Blair, D. Sc, B. C. Veinoglou, Ph D, J. E. Caffyn and B. Sc. *Limitations of the Newtonian Time Scale in Relation to Non-Equilibrium Rheological States and a Theory of Quasi-Properties*. Proc. R. Soc. Lond. A, vol. 189, no. 1016, pages 69–87, March 1947. (Cited on pages 64 and 104.)
- [Bocquet 2009] Lydéric Bocquet, Annie Colin and Armand Ajdari. *Kinetic Theory of Plastic Flow in Soft Glassy Materials*. Physical Review Letters, vol. 103, no. 3, July 2009. (Cited on pages 10 and 21.)
- [Bonn 1998] Daniel Bonn, Hamid Kellay, Michael Prochnow, Karim Ben-Djemaa and Jacques Meunier. *Delayed Fracture of an Inhomogeneous Soft Solid*. Science, vol. 280, no. 5361, pages 265–267, 1998. (Cited on pages 4, 5 and 21.)

- [Bonn 2017] D. Bonn, M. M. Denn, L. Berthier, T. Divoux and S. Manneville. *Yield Stress Materials in Soft Condensed Matter*. Reviews of Modern Physics, vol. 89, no. 3, August 2017. (Cited on page 9.)
- [Boromand 2017] Arman Boromand, Safa Jamali and João M. Maia. *Structural Fingerprints of Yielding Mechanisms in Attractive Colloidal Gels*. Soft Matter, 2017. (Cited on page 19.)
- [Bouchon 2013] Michel Bouchon, Virginie Durand, David Marsan, Hayrullah Karabulut and Jean Schmittbuhl. *The Long Precursory Phase of Most Large Interplate Earthquakes*. Nature Geoscience, vol. 6, no. 4, pages 299–302, March 2013. (Cited on pages 4 and 5.)
- [Bouzid 2017] M. Bouzid, J. Colombo, L. V. Barbosa and E. Del Gado. *Elastically Driven Intermittent Microscopic Dynamics in Soft Solids*. Nature Communications, vol. 8, page 15846, June 2017. (Cited on page 27.)
- [Bower 1999] C. Bower, C. Gallegos, M. R. Mackley and J. M. Madiedo. *The Rheological and Microstructural Characterisation of the Non-Linear Flow Behaviour of Concentrated Oil-in-Water Emulsions*. Rheologica acta, vol. 38, no. 2, pages 145–159, 1999. (Cited on page 8.)
- [Bremer 1990] L. G. B. Bremer, B. H. Bijsterbosch, R. Schrijvers, T. Van Vliet and P. Walstra. *On the Fractal Nature of the Structure of Acid Casein Gels*. Colloids and Surfaces, vol. 51, pages 159–170, 1990. (Cited on page 102.)
- [Brenner 2013] Tom Brenner, Shingo Matsukawa, Katsuyoshi Nishinari and Ragnar Johannsson. *Failure in a Soft Gel: Delayed Failure and the Dynamic Yield Stress*. Journal of Non-Newtonian Fluid Mechanics, vol. 196, pages 1–7, June 2013. (Cited on pages 5 and 135.)
- [Bresler 2015] Ingo Bresler, Joachim Kohlbrecher and Andreas F. Thunemann. *SASfit: a tool for small-angle scattering data analysis using a library of analytical expressions*. Journal of Applied Crystallography, vol. 48, no. 5, pages 1587–1598, October 2015. (Cited on page 108.)
- [Brunel 2016] Fabrice Brunel, Isabelle Pochard, Sandrine Gauffinet, Martin Turesson and Christophe Labbez. *Structure and Yielding of Colloidal Silica Gels Varying the Range of Interparticle Interactions*. The Journal of Physical Chemistry B, vol. 120, no. 25, pages 5777–5785, June 2016. (Cited on pages 9, 34, 130 and 132.)
- [Buehler 2009] Markus J. Buehler and Yu Ching Yung. *Deformation and Failure of Protein Materials in Physiologically Extreme Conditions and Disease*. Nature Materials, vol. 8, no. 3, pages 175–188, March 2009. (Cited on page 3.)

- [Caggioni 2007] M. Caggioni, P. T. Spicer, D. L. Blair, S. E. Lindberg and D. A. Weitz. *Rheology and Microrheology of a Microstructured Fluid: The Gellan Gum Case*. Journal of Rheology, vol. 51, no. 5, pages 851–865, September 2007. (Cited on pages 7 and 102.)
- [Camacho 1996] Godofredo T. Camacho and M. Ortiz. *Computational Modelling of Impact Damage in Brittle Materials*. International Journal of solids and structures, vol. 33, no. 20-22, pages 2899–2938, 1996. (Cited on page 4.)
- [Carmen Miguel 2001] M. Carmen Miguel, A. Vespignani, S. Zapperi, J. Weiss and J.R. Crasso. *Intermittent Dislocation Flow in Viscoplastic Deformation*. Nature, vol. 410, page 667, 2001. (Cited on page 27.)
- [Carpinetti 1992] Marina Carpinetti and Marzio Giglio. *Spinodal-type dynamics in fractal aggregation of colloidal clusters*. Physical Review Letters, vol. 68, no. 22, pages 3327–3330, June 1992. (Cited on page 109.)
- [Carpinetti 1993] Marina Carpinetti and Marzio Giglio. *Transition from semiorder to disorder in the aggregation of dense colloidal solutions*. Physical review letters, vol. 70, no. 24, page 3828, 1993. (Cited on pages 102 and 109.)
- [Carpinetti 1995] Marina Carpinetti, Marzio Giglio and Vittorio Degiorgio. *Mass Conservation and Anticorrelation Effects in the Colloidal Aggregation of Dense Solutions*. Physical Review E, vol. 51, no. 1, page 590, 1995. (Cited on page 103.)
- [Carrier 2009] Vincent Carrier and George Petekidis. *Nonlinear Rheology of Colloidal Glasses of Soft Thermosensitive Microgel Particles*. Journal of Rheology, vol. 53, no. 2, pages 245–273, March 2009. (Cited on pages 8, 9, 32, 33, 153 and 154.)
- [Caton 2008] Francois Caton and Christophe Baravian. *Plastic Behavior of Some Yield Stress Fluids: From Creep to Long-Time Yield*. Rheologica Acta, vol. 47, no. 5-6, pages 601–607, July 2008. (Cited on pages 7, 21 and 103.)
- [Célarié 2003] F. Célarié, S. Prades, D. Bonamy, L. Ferrero, E. Bouchaud, C. Guillot and C. Marlière. *Glass Breaks like Metal, but at the Nanometer Scale*. Physical Review Letters, vol. 90, no. 7, February 2003. (Cited on page 3.)
- [Cerbino 2008] Roberto Cerbino and Veronique Trappe. *Differential Dynamic Microscopy: Probing Wave Vector Dependent Dynamics with a Microscope*. Physical Review Letters, vol. 100, no. 18, May 2008. (Cited on page 171.)
- [Chambon 1986] Francois Chambon, Zoran S. Petrovic, William J. MacKnight and H. Henning Winter. *Rheology of Model Polyurethanes at the Gel Point*. Macromolecules, vol. 19, no. 8, pages 2146–2149, 1986. (Cited on page 102.)

- [Chan 2014] Hubert K. Chan and Ali Mohraz. *Microdynamics of Dense Colloidal Suspensions and Gels under Constant-Stress Deformation*. Journal of Rheology, vol. 58, no. 5, pages 1419–1439, September 2014. (Cited on pages 30 and 33.)
- [Chen 2010] D. T. N. Chen, Q. Wen, P. A. Janmey, J. C. Crocker and A. G. Yodh. *Rheology of Soft Materials*. Annual Review of Condensed Matter Physics, vol. 1, no. 1, pages 301–322, 2010. (Cited on page 10.)
- [Cheriere 1997] J. M. Cheriere, L. Belec and J. L. Gacougnolle. *The Three Successive Stages of Creep of PMMA between 55 C and 90 C*. Polymer Engineering & Science, vol. 37, no. 10, pages 1664–1671, 1997. (Cited on pages 7, 21, 23, 24, 103 and 171.)
- [Christopoulou 2009] C. Christopoulou, G. Petekidis, B. Erwin, M. Cloitre and D. Vlasopoulos. *Ageing and Yield Behaviour in Model Soft Colloidal Glasses*. Philosophical Transactions of the Royal Society A: Mathematical, Physical and Engineering Sciences, vol. 367, no. 1909, pages 5051–5071, December 2009. (Cited on pages 8 and 154.)
- [Cipelletti 1999] Luca Cipelletti and D. A. Weitz. *Ultralow-Angle Dynamic Light Scattering with a Charge Coupled Device Camera Based Multispeckle, Multitau Correlator*. Review of Scientific Instruments, vol. 70, no. 8, page 3214, 1999. (Cited on page 151.)
- [Cipelletti 2000] Luca Cipelletti, Suliana Manley, R. C. Ball and D. A. Weitz. *Universal Aging Features in the Restructuring of Fractal Colloidal Gels*. Physical review letters, vol. 84, no. 10, page 2275, 2000. (Cited on pages 103 and 115.)
- [Cipelletti 2003] Luca Cipelletti, Laurence Ramos, S. Manley, E. Pitard, D. A. Weitz, Eugene E. Pashkovski and Marie Johansson. *Universal Non-Diffusive Slow Dynamics in Aging Soft Matter*. Faraday Discussions, vol. 123, pages 237–251, January 2003. (Cited on page 152.)
- [Cohen-Addad 2013] Sylvie Cohen-Addad, Reinhard Höhler and Olivier Pitois. *Flow in Foams and Flowing Foams*. Annual Review of Fluid Mechanics, vol. 45, no. 1, pages 241–267, January 2013. (Cited on page 5.)
- [Colby 2003] R. H. Colby and M. Rubinstein. Polymer Physics. Oxford University Press, June 2003. (Cited on pages 102 and 130.)
- [Collacott 1977] R.A. Collacott. Mechanical Fault Diagnosis and condition monitoring. Chapman & Hall/CRC, 1977. OCLC: 940690275. (Cited on page 4.)
- [Colombo 2014] Jader Colombo and Emanuela Del Gado. *Stress Localization, Stiffening, and Yielding in a Model Colloidal Gel*. Journal of Rheology, vol. 58, no. 5, pages 1089–1116, September 2014. (Cited on pages 9, 19 and 130.)

- [Costanzo 2016] Salvatore Costanzo, Qian Huang, Giovanni Ianniruberto, Giuseppe Marucci, Ole Hassager and Dimitris Vlassopoulos. *Shear and Extensional Rheology of Polystyrene Melts and Solutions with the Same Number of Entanglements*. *Macromolecules*, vol. 49, no. 10, pages 3925–3935, May 2016. (Cited on pages 15 and 16.)
- [Cottrell 1952] A. H. Cottrell. *The Time Laws of Creep*. *Journal of the Mechanics and Physics of Solids*, vol. 1, no. 1, pages 53–63, October 1952. (Cited on pages 6, 7, 21 and 103.)
- [Coussot 2006] P. Coussot, H. Tabuteau, X. Chateau, L. Tocquer and G. Ovarlez. *Aging and Solid or Liquid Behavior in Pastes*. *Journal of Rheology*, vol. 50, no. 6, page 975, 2006. (Cited on pages 7, 22 and 103.)
- [Craciun 2003] Lucia Craciun, Pierre J. Carreau, Marie-Claude Heuzey, Theo G. M. van de Ven and Michel Moan. *Rheological Properties of Concentrated Latex Suspensions of Poly(Styrene-Butadiene)*. *Rheologica Acta*, vol. 42, no. 5, pages 410–420, September 2003. (Cited on page 8.)
- [Cundy 1954] Henry Martyn Cundy and A. P. Rollett. *Mathematical Models*. Clarendon Press, 1954. (Cited on page 66.)
- [Curro 1983] John G. Curro and Philip Pincus. *A Theoretical Basis for Viscoelastic Relaxation of Elastomers in the Long-Time Limit*. *Macromolecules*, vol. 16, no. 4, pages 559–562, 1983. (Cited on pages 7, 102 and 103.)
- [Curtis 2015] D.J. Curtis, A. Holder, N. Badiei, J. Claypole, M. Walters, B. Thomas, M. Barrow, D. Deganello, M.R. Brown, P.R. Williams and K. Hawkins. *Validation of Optimal Fourier Rheometry for Rapidly Gelling Materials and Its Application in the Study of Collagen Gelation*. *Journal of Non-Newtonian Fluid Mechanics*, vol. 222, pages 253–259, August 2015. (Cited on pages 102 and 110.)
- [Da Vinci 1972] Leonardo Da Vinci. *I libri di meccanica, reconstructed from the original notes by arturo uccelli*. Kraus Reprint, Nendeln, Liechtenstein, 1972. (Cited on page 12.)
- [Dahmen 2011] Karin A. Dahmen, Yehuda Ben-Zion and Jonathan T. Uhl. *A Simple Analytic Theory for the Statistics of Avalanches in Sheared Granular Materials*. *Nature Physics*, vol. 7, no. 7, pages 554–557, March 2011. (Cited on page 27.)
- [Dang 2016] M. T. Dang, D. Denisov, B. Struth, A. Zaccone and P. Schall. *Reversibility and Hysteresis of the Sharp Yielding Transition of a Colloidal Glass under Oscillatory Shear*. *The European Physical Journal E*, vol. 39, no. 4, April 2016. (Cited on page 34.)
- [Daniels 1945] H. E. Daniels. *The Statistical Theory of the Strength of Bundles of Threads. I*. *Proceedings of the Royal Society of London A: Mathematical, Physical*

- and Engineering Sciences, vol. 183, no. 995, pages 405–435, June 1945. (Cited on pages 10 and 21.)
- [Davis 2006] G.B. Davis, M. Kohandel, S. Sivaloganathan and G. Tenti. *The Constitutive Properties of the Brain Paraenchyma*. Medical Engineering & Physics, vol. 28, no. 5, pages 455–459, June 2006. (Cited on pages 7, 102 and 103.)
- [De Arcangelis 1985] L. De Arcangelis, S. Redner and H. J. Herrmann. *A Random Fuse Model for Breaking Processes*. Journal de Physique Lettres, vol. 46, no. 13, pages 585–590, 1985. (Cited on page 10.)
- [Dealy 2010] J. M. Dealy. *Weissenberg and Deborah numbers - Their definition and use*. Rheol. Bull., vol. 79, no. 2, pages 14–18, 2010. (Cited on page 16.)
- [Denisov 2015] Dmitry V. Denisov, Minh Triet Dang, Bernd Struth, Alessio Zaccone, Gerard H. Wegdam and P. Schall. *Sharp Symmetry-Change Marks the Mechanical Failure Transition of Glasses*. Scientific Reports, vol. 5, no. 1, November 2015. (Cited on pages 30 and 34.)
- [Derec 2003] Caroline Derec, Guylaine Ducouret, Armand Ajdari and Francois Lequeux. *Aging and Nonlinear Rheology in Suspensions of Polyethylene Oxide-Protected Silica Particles*. Physical Review E, vol. 67, no. 6, June 2003. (Cited on pages 8, 9, 32 and 40.)
- [Desprat 2005] Nicolas Desprat, Alain Richert, Jacqueline Simeon and Atef Asnacios. *Creep Function of a Single Living Cell*. Biophysical Journal, vol. 88, no. 3, pages 2224–2233, March 2005. (Cited on pages 5, 7, 101 and 103.)
- [Divoux 2011] T. Divoux, C. Barentin and S. Manneville. *From Stress-Induced Fluidization Processes to Herschel-Bulkley Behaviour in Simple Yield Stress Fluids*. Soft Matter, vol. 7, no. 18, page 8409, 2011. (Cited on page 4.)
- [Djordjevic 2003] Vladan D. Djordjevic, Jovo Jaric, Ben Fabry, Jeffrey J. Fredberg and Dimitrije Stamenovic. *Fractional Derivatives Embody Essential Features of Cell Rheological Behavior*. Annals of Biomedical Engineering, vol. 31, no. 6, pages 692–699, June 2003. (Cited on pages 7, 101 and 102.)
- [Dollet 2014] Benjamin Dollet and Christophe Raufaste. *Rheology of Aqueous Foams*. Comptes Rendus Physique, vol. 15, no. 8-9, pages 731–747, October 2014. (Cited on page 5.)
- [Duputel 2009] Zacharie Duputel, Valerie Ferrazzini, Florent Brenguier, Nikolai Shapiro, Michel Campillo and Alexandre Nercessian. *Real Time Monitoring of Relative Velocity Changes Using Ambient Seismic Noise at the Piton de La Fournaise Volcano (La Reunion) from January 2006 to June 2007*. Journal of Volcanology

- and Geothermal Research, vol. 184, no. 1-2, pages 164–173, July 2009. (Cited on pages 4 and 5.)
- [Durand 1987] D. Durand, M. Delsanti, M. Adam and J. M. Luck. *Frequency Dependence of Viscoelastic Properties of Branched Polymers near Gelation Threshold*. EPL (Europhysics Letters), vol. 3, no. 3, page 297, 1987. (Cited on page 102.)
- [Duri 2005] Agnes Duri, Hugo Bissig, Véronique Trappe and Luca Cipelletti. *Time-Resolved-Correlation Measurements of Temporally Heterogeneous Dynamics*. Physical Review E, vol. 72, no. 5, page 051401, 2005. (Cited on page 59.)
- [Duri 2009] A. Duri, D. A. Sessoms, V. Trappe and L. Cipelletti. *Resolving Long-Range Spatial Correlations in Jammed Colloidal Systems Using Photon Correlation Imaging*. Physical Review Letters, vol. 102, no. 8, page 085702, February 2009. (Cited on page 168.)
- [Durian 1997] D. J. Durian. *Bubble-Scale Model of Foam Mechanics: mMelting, Nonlinear Behavior, and Avalanches*. Physical Review E, vol. 55, no. 2, page 1739, 1997. (Cited on page 27.)
- [Duval 2010] P. Duval, M. Montagnat, F. Grennerat, J. Weiss, J. Meyssonier and A. Philip. *Creep and Plasticity of Glacier Ice: A Material Science Perspective*. Journal of Glaciology, vol. 56, no. 200, pages 1059–1068, 2010. (Cited on pages 27 and 103.)
- [Engineers 1851] Institution of Mechanical Engineers. *Proceedings of the Institution of Mechanical Engineers: 1850 - 1851*. Institution of Mechanical Engineers, 1851. (Cited on page 15.)
- [Erdmann 2004] T. Erdmann and U. S. Schwarz. *Stability of Adhesion Clusters under Constant Force*. Physical Review Letters, vol. 92, no. 10, March 2004. (Cited on pages 3 and 4.)
- [Erwin 2010] Brian M. Erwin, Dimitris Vlassopoulos and Michel Cloitre. *Rheological Fingerprinting of an Aging Soft Colloidal Glass*. Journal of Rheology, vol. 54, no. 4, page 915, 2010. (Cited on pages 22 and 153.)
- [Evans 2009] R. M. L. Evans, Manlio Tassieri, Dietmar Auhl and Thomas A. Waigh. *Direct conversion of rheological compliance measurements into storage and loss moduli*. Physical Review E, vol. 80, no. 1, July 2009. (Cited on pages 21, 63 and 111.)
- [Ewart 1986] L. Ewart and S. Suresh. *Dynamic Fatigue Crack Growth in Polycrystalline Alumina under Cyclic Compression*. Journal of Materials Science Letters, vol. 5, no. 8, pages 774–778, 1986. (Cited on page 4.)

- [Ewoldt 2015] R. H. Ewoldt, M. T. Johnston and L. M. Caretta. *Experimental Challenges of Shear Rheology: How to Avoid Bad Data*. In *Complex Fluids in Biological Systems*, pages 207–241. Springer, 2015. (Cited on page 22.)
- [Eyring 1936] Henry Eyring. *Viscosity, Plasticity and Diffusion as Examples of Absolute Reaction Rates*. *Journal of Chemical Physics*, vol. 4, page 283, 1936. (Cited on page 21.)
- [Faber 2017a] T.J. Faber, A. Jaishankar and G.H. McKinley. *Describing the Firmness, Springiness and Rubberiness of Food Gels Using Fractional Calculus. Part I: Theoretical Framework*. *Food Hydrocolloids*, vol. 62, pages 311–324, January 2017. (Cited on pages 6, 7 and 102.)
- [Faber 2017b] T.J. Faber, A. Jaishankar and G.H. McKinley. *Describing the Firmness, Springiness and Rubberiness of Food Gels Using Fractional Calculus. Part II: Measurements on Semi-Hard Cheese*. *Food Hydrocolloids*, vol. 62, pages 325–339, January 2017. (Cited on pages 5, 7, 102 and 103.)
- [Fabry 2001] Ben Fabry, Geoffrey N. Maksym, James P. Butler, Michael Glogauer, Daniel Navajas and Jeffrey J. Fredberg. *Scaling the Microrheology of Living Cells*. *Physical Review Letters*, vol. 87, no. 14, September 2001. (Cited on pages 7, 101 and 102.)
- [Fairbairn 1864] W. Fairbairn. *Experiments to Determine the Effect of Impact, Vibratory Action, and Long-Continued Changes of Load on Wrought-Iron Girders*. *Philosophical Transactions of the Royal Society of London*, vol. 154, no. 0, pages 311–325, January 1864. (Cited on page 15.)
- [Ferry 1980] J. D. Ferry. *Viscoelastic Properties of Polymers*. John Wiley and Sons, October 1980. (Cited on pages 62 and 102.)
- [Field 2004] J.E. Field, S.M. Walley, W.G. Proud, H.T. Goldrein and C.R. Siviour. *Review of Experimental Techniques for High Rate Deformation and Shock Studies*. *International Journal of Impact Engineering*, vol. 30, no. 7, pages 725–775, August 2004. (Cited on page 4.)
- [Fielding 2000] S. M. Fielding, P. Sollich and M. E. Cates. *Aging and Rheology in Soft Materials*. *Journal of Rheology*, vol. 44, no. 2, pages 323–369, March 2000. (Cited on pages 117 and 118.)
- [Fragiacomo 2004] M. Fragiaco, C. Amadio and L. Macorini. *Finite-Element Model for Collapse and Long-Term Analysis of Steel-concrete Composite Beams*. *Journal of Structural Engineering*, vol. 130, no. 3, pages 489–497, 2004. (Cited on page 10.)

- [Freed 2006] A. D. Freed and K. Diethelm. *Fractional Calculus in Biomechanics: A 3D Viscoelastic Model Using Regularized Fractional Derivative Kernels with Application to the Human Calcaneal Fat Pad*. Biomechanics and Modeling in Mechanobiology, vol. 5, no. 4, pages 203–215, October 2006. (Cited on page 7.)
- [Freeds 2002] A. D. Freeds and A. I. Leonov. *The Bailey Criterion: Statistical Derivation and Applications to Interpretations of Durability Tests and Chemical Kinetics*. Zeitschrift für angewandte Mathematik und Physik ZAMP, vol. 53, no. 1, pages 160–166, January 2002. (Cited on page 17.)
- [Friedrich 1991] C. H. R. Friedrich. *Relaxation and Retardation Functions of the Maxwell Model with Fractional Derivatives*. Rheologica Acta, vol. 30, no. 2, pages 151–158, 1991. (Cited on page 21.)
- [Friedrich 1999] Chr. Friedrich, H. Schiessel and A. Blumen. *Constitutive Behavior Modeling and Fractional Derivatives*. Rheology Series, vol. 8, pages 429–466, January 1999. (Cited on pages 7 and 102.)
- [Galilei 1638] G. Galilei. *Discorsi e dimostrazioni matematiche intorno a due nuove scienze*. Alsevirii, Leida, 1638. (Cited on page 13.)
- [Gardel 2004] M. L. Gardel, J. H. Shin, F. C. MacKintosh, L. Mahadevan, P. Matsudaira and D. A. Weitz. *Elastic Behavior of Cross-Linked and Bundled Actin Networks*. Science, vol. 304, no. 5675, pages 1301–1305, May 2004. (Cited on page 16.)
- [Gibaud 2010] Thomas Gibaud, Damien Frelat and Sébastien Manneville. *Heterogeneous Yielding Dynamics in a Colloidal Gel*. Soft Matter, vol. 6, no. 15, page 3482, 2010. (Cited on pages 4, 5, 8, 9, 40, 42 and 135.)
- [Gobeaux 2010] Frederic Gobeaux, Emmanuel Belamie, Gervaise Mosser, Patrick Davidson and Sophie Asnacios. *Power Law Rheology and Strain-Induced Yielding in Acidic Solutions of Type I-Collagen*. Soft Matter, vol. 6, no. 16, page 3769, 2010. (Cited on pages 3, 4, 5, 7, 102 and 103.)
- [Goh 2003] S. M. Goh, M. N. Charalambides and J. G. Williams. *Mechanical Properties and Sensory Texture Assessment of Cheeses*. Journal of texture studies, vol. 34, no. 2, pages 181–201, 2003. (Cited on page 7.)
- [Golub 2003] V. P. Golub, V. I. Krizhanovskii and A. A. Rusinov. *A Mixed Criterion of Delayed Creep Failure under Plane Stress*. International Applied Mechanics, vol. 39, no. 5, pages 556–565, 2003. (Cited on page 4.)
- [Gopalakrishnan 2007] V. Gopalakrishnan and C. F. Zukoski. *Delayed Flow in Thermo-Reversible Colloidal Gels*. Journal of Rheology, vol. 51, no. 4, pages 623–644, July 2007. (Cited on pages 4 and 5.)

- [Graham 1995] Michael D. Graham. *Wall Slip and the Nonlinear Dynamics of Large Amplitude Oscillatory Shear Flows*. Journal of Rheology, vol. 39, no. 4, pages 697–712, July 1995. (Cited on page 67.)
- [Grenard 2014] Vincent Grenard, Thibaut Divoux, Nicolas Taberlet and Sébastien Manneville. *Timescales in Creep and Yielding of Attractive Gels*. Soft Matter, vol. 10, no. 10, page 1555, 2014. (Cited on pages 4, 5, 7 and 21.)
- [Griffith 1921] A. A. Griffith. *The Phenomena of Rupture and Flow in Solids*. Philosophical Transactions of the Royal Society of London A: Mathematical, Physical and Engineering Sciences, vol. 221, no. 582-593, pages 163–198, January 1921. (Cited on page 21.)
- [Groot 1996] R. D. Groot, A. Bot and W. G. M. Agterof. *Molecular Theory of the Yield Behavior of a Polymer Gel: Application to Gelatin*. The Journal of Chemical Physics, vol. 104, no. 22, pages 9220–9233, June 1996. (Cited on pages 5 and 16.)
- [Guarino 2002] A. Guarino, S. Ciliberto, A. Garcimartin, M. Zei and R. Scorretti. *Failure Time and Critical Behaviour of Fracture Precursors in Heterogeneous Materials*. The European Physical Journal B, vol. 26, no. 2, pages 141–151, March 2002. (Cited on pages 3, 4 and 27.)
- [Gudipati 2012] Murthy S. Gudipati and Julie Castillo-Rogez. *The Science of Solar System Ices*. Springer Science & Business Media, July 2012. Google-Books-ID: L7ISRdYr_3gC. (Cited on page 27.)
- [Gurney 1947] C. Gurney. *Delayed Fracture in Glass*. Proceedings of the Physical Society, vol. 59, no. 2, page 169, 1947. (Cited on page 4.)
- [Hébraud 1997] P. Hébraud, F. Lequeux, J. P. Munch and D. J. Pine. *Yielding and Rearrangements in Disordered Emulsions*. Physical Review Letters, vol. 78, no. 24, page 4657, 1997. (Cited on pages 10, 43 and 139.)
- [Hecht 2015] Fabian M. Hecht, Johannes Rheinlaender, Nicolas Schierbaum, Wolfgang H. Goldmann, Ben Fabry and Tilman E. Schoffer. *Imaging Viscoelastic Properties of Live Cells by AFM: Power-Law Rheology on the Nanoscale*. Soft Matter, vol. 11, no. 23, pages 4584–4591, 2015. (Cited on pages 7 and 101.)
- [Helgeson 2007] Matthew E. Helgeson, Norman J. Wagner and Dimitris Vlassopoulos. *Viscoelasticity and Shear Melting of Colloidal Star Polymer Glasses*. Journal of Rheology, vol. 51, no. 2, pages 297–316, March 2007. (Cited on pages 9, 34 and 153.)
- [Helmberger 2014] Michael Helmberger, Michael Pienn, Martin Urschler, Peter Kullnig, Rudolf Stollberger, Gabor Kovacs, Andrea Olschewski, Horst Olschewski and Zoltán Bálint. *Quantification of Tortuosity and Fractal Dimension of the Lung*

- Vessels in Pulmonary Hypertension Patients*. PLoS ONE, vol. 9, no. 1, page e87515, January 2014. (Cited on page 102.)
- [Hernández-Jiménez 2002] A. Hernández-Jiménez, J. Hernández-Santiago, A. Macias-Garcia and J. Sánchez-González. *Relaxation Modulus in PMMA and PTFE Fitting by Fractional Maxwell Model*. Polymer Testing, vol. 21, no. 3, pages 325–331, 2002. (Cited on pages 7, 102 and 103.)
- [Heymans 1994] Nicole Heymans and J.-C. Bauwens. *Fractal Rheological Models and Fractional Differential Equations for Viscoelastic Behavior*. Rheologica acta, vol. 33, no. 3, pages 210–219, 1994. (Cited on page 21.)
- [Hilfer 2000] R. Hilfer. Applications of fractional calculus in physics. World Scientific, 2000. (Cited on pages 21 and 104.)
- [Hima Nagamanasa 2014] K. Hima Nagamanasa, Shreyas Gokhale, A. K. Sood and Rakesh Ganapathy. *Experimental Signatures of a Nonequilibrium Phase Transition Governing the Yielding of a Soft Glass*. Physical Review E, vol. 89, no. 6, June 2014. (Cited on pages 8 and 9.)
- [Hinrichsen 2000] Haje Hinrichsen. *Non-Equilibrium Critical Phenomena and Phase Transitions into Absorbing States*. Advances in Physics, vol. 49, no. 7, pages 815–958, November 2000. (Cited on page 27.)
- [Höhler 1997] Reinhard Höhler, Sylvie Cohen-Addad and Hussein Hoballah. *Periodic Nonlinear Bubble Motion in Aqueous Foam under Oscillating Shear Strain*. Physical review letters, vol. 79, no. 6, page 1154, 1997. (Cited on pages 36, 37, 139 and 143.)
- [Hooke 1678] R. Hooke. Lectures de Potentia Restitutiva, Or of Spring Explaining the Power of Springing Bodies. John Martyn, 1678. (Cited on page 14.)
- [Hopkins 2010] Paul Hopkins, Andrea Fortini, Andrew J. Archer and Matthias Schmidt. *The van Hove Distribution Function for Brownian Hard Spheres: Dynamical Test Particle Theory and Computer Simulations for Bulk Dynamics*. The Journal of chemical physics, vol. 133, no. 22, page 224505, 2010. (Cited on page 57.)
- [Houle 1996] Paul A. Houle and James P. Sethna. *Acoustic Emission from Crumpling Paper*. Physical Review E, vol. 54, no. 1, page 278, 1996. (Cited on page 27.)
- [Hung 2015] Kun-Che Hung, U-Ser Jeng and Shan-hui Hsu. *Fractal Structure of Hydrogels Modulates Stem Cell Behavior*. ACS Macro Letters, vol. 4, no. 9, pages 1056–1061, September 2015. (Cited on pages 7 and 102.)
- [Hyun 2011] Kyu Hyun, Manfred Wilhelm, Christopher O. Klein, Kwang Soo Cho, Jung Gun Nam, Kyung Hyun Ahn, Seung Jong Lee, Randy H. Ewoldt and

- Gareth H. McKinley. *A Review of Nonlinear Oscillatory Shear Tests: Analysis and Application of Large Amplitude Oscillatory Shear (LAOS)*. Progress in Polymer Science, vol. 36, no. 12, pages 1697–1753, December 2011. (Cited on pages 32, 67 and 131.)
- [Jackson 2007] John David Jackson. Classical Electrodynamics. Wiley, 2007. (Cited on page 51.)
- [Jagla 2011] E. A. Jagla. *Creep Rupture of Materials: Insights from a Fiber Bundle Model with Relaxation*. Physical Review E, vol. 83, no. 4, April 2011. (Cited on pages 7, 10, 21, 28 and 165.)
- [Jaishankar 2013] Aditya Jaishankar and Gareth H. McKinley. *Power-law rheology in the bulk and at the interface: quasi-properties and fractional constitutive equations*. In Proceedings of the Royal Society of London A: Mathematical, Physical and Engineering Sciences, volume 469, page 20120284. The Royal Society, 2013. (Cited on pages 64, 105 and 110.)
- [Jaishankar 2014] Aditya Jaishankar and Gareth H. McKinley. *A fractional K-BKZ constitutive formulation for describing the nonlinear rheology of multiscale complex fluids*. In Journal of Rheology (1978-present), volume 58, pages 1751–1788, 2014. (Cited on pages 5, 7, 102, 103 and 105.)
- [Jaiswal 2016] Prabhat K. Jaiswal, Itamar Procaccia, Corrado Rainone and Murari Singh. *Mechanical Yield in Amorphous Solids: A First-Order Phase Transition*. Physical Review Letters, vol. 116, no. 8, February 2016. (Cited on page 27.)
- [Janmey 2007] Paul A. Janmey, Margaret E. McCormick, Sebastian Rammensee, Jennifer L. Leight, Penelope C. Georges and Fred C. MacKintosh. *Negative Normal Stress in Semiflexible Biopolymer Gels*. Nature Materials, vol. 6, no. 1, pages 48–51, January 2007. (Cited on page 5.)
- [Johnson 2013] P. A. Johnson, B. Ferdowsi, B. M. Kaproth, M. Scuderi, M. Griffa, J. Carmeliet, R. A. Guyer, P-Y. Le Bas, D. T. Trugman and C. Marone. *Acoustic Emission and Microslip Precursors to Stick-Slip Failure in Sheared Granular Material*. Geophysical Research Letters, vol. 40, no. 21, pages 5627–5631, November 2013. (Cited on pages 4 and 27.)
- [Jones 1979] Lucile M. Jones and Peter Molnar. *Some Characteristics of Foreshocks and Their Possible Relationship to Earthquake Prediction and Premonitory Slip on Faults*. Journal of Geophysical Research: Solid Earth, vol. 84, no. B7, pages 3596–3608, 1979. (Cited on pages 4 and 5.)
- [Jóźwiak 2015] B. Jóźwiak, M. Orczykowska and M. Dziubiński. *Fractional Generalizations of Maxwell and Kelvin-Voigt Models for Biopolymer Characterization*. PloS one, vol. 10, no. 11, page e0143090, 2015. (Cited on pages 7, 102 and 105.)

- [Kabla 2007] A. Kabla, J. Scheibert and G. Debregeas. *Quasi-Static Rheology of Foams. Part 2. Continuous Shear Flow*. Journal of Fluid Mechanics, vol. 587, September 2007. (Cited on pages 5, 16 and 27.)
- [Kahn 2004] H Kahn, R Ballarini and A.H Heuer. *Dynamic Fatigue of Silicon*. Current Opinion in Solid State and Materials Science, vol. 8, no. 1, pages 71–76, January 2004. (Cited on page 4.)
- [Karobi 2016] Sadia Nazneen Karobi, Tao Lin Sun, Takayuki Kurokawa, Feng Luo, Tasuku Nakajima, Takayuki Nonoyama and Jian Ping Gong. *Creep Behavior and Delayed Fracture of Tough Polyampholyte Hydrogels by Tensile Test*. Macromolecules, vol. 49, no. 15, pages 5630–5636, August 2016. (Cited on pages 5, 7 and 103.)
- [Kato 2012] A. Kato, K. Obara, T. Igarashi, H. Tsuruoka, S. Nakagawa and N. Hirata. *Propagation of Slow Slip Leading Up to the 2011 Mw 9.0 Tohoku-Oki Earthquake*. Science, vol. 335, no. 6069, pages 705–708, February 2012. (Cited on pages 4 and 5.)
- [Kawasaki 2015] Takeshi Kawasaki and Ludovic Berthier. *Macroscopic Yielding in Jammed Solids Is Accompanied by a Non-Equilibrium First-Order Transition in Particle Trajectories*. arXiv preprint arXiv:1507.04120, 2015. (Cited on pages 9 and 34.)
- [Keim 2013] Nathan C. Keim and Paulo E. Arratia. *Yielding and Microstructure in a 2D Jammed Material under Shear Deformation*. Soft Matter, vol. 9, no. 27, page 6222, 2013. (Cited on page 9.)
- [Keim 2014] Nathan C. Keim and Paulo E. Arratia. *Mechanical and Microscopic Properties of the Reversible Plastic Regime in a 2D Jammed Material*. Physical Review Letters, vol. 112, no. 2, January 2014. (Cited on pages 9, 36 and 143.)
- [Keshavarz 2017] Bavand Keshavarz, Thibaut Divoux, Sebastien Manneville and Gareth H. McKinley. *Nonlinear Viscoelasticity and Generalized Failure Criterion for Polymer Gels*. ACS Macro Letters, pages 663–667, June 2017. (Cited on pages 6, 15, 16, 17 and 18.)
- [Kim 2014] Jung Min Kim, Aaron PR Eberle, A. Kate Gurnon, Lionel Porcar and Norman J. Wagner. *The Microstructure and Rheology of a Model, Thixotropic Nanoparticle Gel under Steady Shear and Large Amplitude Oscillatory Shear (LAOS)*. Journal of Rheology (1978-present), vol. 58, no. 5, pages 1301–1328, 2014. (Cited on pages 8, 30, 34, 137 and 138.)
- [Klatt 2007] Dieter Klatt, Uwe Hamhaber, Patrick Asbach, Jürgen Braun and Ingolf Sack. *Noninvasive Assessment of the Rheological Behavior of Human Organs Using Multifrequency MR Elastography: A Study of Brain and Liver Viscoelasticity*.

- Physics in Medicine and Biology, vol. 52, no. 24, pages 7281–7294, December 2007. (Cited on page 7.)
- [Knowlton 2014] Elizabeth D. Knowlton, David J. Pine and Luca Cipelletti. *A Microscopic View of the Yielding Transition in Concentrated Emulsions*. Soft Matter, vol. 10, no. 36, pages 6931–6940, 2014. (Cited on pages 8, 9, 35, 171 and 173.)
- [Kohandel 2005] M Kohandel, S Sivaloganathan, G Tenti and K Darvish. *Frequency Dependence of Complex Moduli of Brain Tissue Using a Fractional Zener Model*. Physics in Medicine and Biology, vol. 50, no. 12, pages 2799–2805, June 2005. (Cited on pages 7 and 102.)
- [Koivisto 2016] Juha Koivisto, Markus Ovaska, Amandine Miksic, Lasse Laurson and Mikko J. Alava. *Predicting Sample Lifetimes in Creep Fracture of Heterogeneous Materials*. Physical Review E, vol. 94, no. 2, August 2016. (Cited on pages 3, 4, 7, 21, 26, 28 and 31.)
- [Kollmannsberger 2011] Philip Kollmannsberger and Ben Fabry. *Linear and Nonlinear Rheology of Living Cells*. Annual Review of Materials Research, vol. 41, no. 1, pages 75–97, August 2011. (Cited on pages 5, 7 and 101.)
- [Korus 2009] Jaroslaw Korus, Mariusz Witczak, Rafa Ziobro and Leslaw Juszcak. *The Impact of Resistant Starch on Characteristics of Gluten-Free Dough and Bread*. Food Hydrocolloids, vol. 23, no. 3, pages 988–995, May 2009. (Cited on pages 7, 102 and 103.)
- [Koumakis 2011] N. Koumakis and G. Petekidis. *Two Step Yielding in Attractive Colloids: Transition from Gels to Attractive Glasses*. Soft Matter, vol. 7, no. 6, page 2456, 2011. (Cited on pages 9, 16, 34, 130, 132 and 133.)
- [Koumakis 2013] N. Koumakis, J. F. Brady and G. Petekidis. *Complex Oscillatory Yielding of Model Hard-Sphere Glasses*. Physical Review Letters, vol. 110, no. 17, April 2013. (Cited on page 8.)
- [Koumakis 2015] Nick Koumakis, Esmael Moghimi, Rut Besseling, Wilson C. K. Poon, John F. Brady and George Petekidis. *Tuning Colloidal Gels by Shear*. Soft Matter, vol. 11, no. 23, pages 4640–4648, 2015. (Cited on page 133.)
- [Kovacs 2008] K. Kovacs, S. Nagy, R. C. Hidalgo, F. Kun, H. J. Herrmann and I. Pagonabarraga. *Critical Ruptures in a Bundle of Slowly Relaxing Fibers*. Physical Review E, vol. 77, no. 3, March 2008. (Cited on page 10.)
- [Kromer 2015] Ryan A. Kromer, D. Jean Hutchinson, Matt J. Lato, Dave Gauthier and Thomas Edwards. *Identifying Rock Slope Failure Precursors Using LiDAR for Transportation Corridor Hazard Management*. Engineering Geology, vol. 195, pages 93–103, September 2015. (Cited on pages 4 and 5.)

- [Kun 2003] Ferenc Kun, Raul Cruz Hidalgo, Hans J. Herrmann and Karoly F. Pal. *Scaling Laws of Creep Rupture of Fiber Bundles*. Physical Review E, vol. 67, no. 6, June 2003. (Cited on pages 7, 10 and 21.)
- [Kun 2007] F. Kun, M. H. Costa, R. N. Filho, J. S. Andrade, J. B. Soares, S. Zapperi and H. J. Herrmann. *Fatigue Failure of Disordered Materials*. Journal of Statistical Mechanics: Theory and Experiment, vol. 2007, no. 02, pages P02003–P02003, February 2007. (Cited on page 10.)
- [Kun 2008] F. Kun, H. A. Carmona, J. S. Andrade and H. J. Herrmann. *Universality behind Basquin’s Law of Fatigue*. Physical Review Letters, vol. 100, no. 9, March 2008. (Cited on page 10.)
- [Kurokawa 2015] Aika Kurokawa, Valérie Vidal, Kei Kurita, Thibaut Divoux and Sébastien Manneville. *Avalanche-like Fluidization of a Non-Brownian Particle Gel*. Soft Matter, vol. 11, no. 46, pages 9026–9037, 2015. (Cited on pages 20 and 27.)
- [Landau 2013] L. D. Landau and E. M. Lifshitz. Statistical Physics. Elsevier, October 2013. (Cited on page 56.)
- [Landrum 2016] Benjamin J. Landrum, William B. Russel and Roseanna N. Zia. *Delayed Yield in Colloidal Gels: Creep, Flow, and Re-Entrant Solid Regimes*. Journal of Rheology (1978-present), vol. 60, no. 4, pages 783–807, 2016. (Cited on page 9.)
- [Larsen 2008] Travis H. Larsen and Eric M. Furst. *Microrheology of the Liquid-Solid Transition during Gelation*. Physical Review Letters, vol. 100, no. 14, April 2008. (Cited on page 102.)
- [Laurati 2014] M. Laurati, S. U. Egelhaaf and G. Petekidis. *Plastic Rearrangements in Colloidal Gels Investigated by LAOS and LS-Echo*. Journal of Rheology, vol. 58, no. 5, pages 1395–1417, September 2014. (Cited on pages 9, 43, 130 and 132.)
- [Leheny 2015] Robert L. Leheny, Michael C. Rogers, Kui Chen, Suresh Narayanan and James L. Harden. *Rheo-XPCS*. Current Opinion in Colloid & Interface Science, vol. 20, no. 4, pages 261–271, August 2015. (Cited on pages 9 and 30.)
- [Leibler 1991] Ludwik Leibler, Michael Rubinstein and Ralph H. Colby. *Dynamics of Reversible Networks*. Macromolecules, vol. 24, no. 16, pages 4701–4707, August 1991. (Cited on page 102.)
- [Leocmach 2014] Mathieu Leocmach, Christophe Perge, Thibaut Divoux and Sébastien Manneville. *Creep and Fracture of a Protein Gel under Stress*. Physical Review Letters, vol. 113, no. 3, page 038303, July 2014. (Cited on pages 4, 5, 7, 21, 25, 29, 31, 102, 103 and 134.)

- [Lewis 1955] C. S. Lewis. *Surprised by Joy: The shape of my early life*. Geoffrey Bles, 1955. (Cited on page 11.)
- [Lidon 2017] Pierre Lidon, Louis Villa and Sébastien Manneville. *Power-Law Creep and Residual Stresses in a Carbopol Gel*. *Rheologica Acta*, vol. 56, no. 3, pages 307–323, 2017. (Cited on pages 7, 102 and 103.)
- [Lieleg 2010] Oliver Lieleg, Mireille M. A. E. Claessens and Andreas R. Bausch. *Structure and Dynamics of Cross-Linked Actin Networks*. *Soft Matter*, vol. 6, no. 2, pages 218–225, 2010. (Cited on page 5.)
- [Liu 1996] Andrea J. Liu, Sriram Ramaswamy, T. G. Mason, Hu Gang and D. A. Weitz. *Anomalous Viscous Loss in Emulsions*. *Physical Review Letters*, vol. 76, no. 16, pages 3017–3020, April 1996. (Cited on page 5.)
- [Liu 1998] Andrea J. Liu and Sidney R. Nagel. *Nonlinear Dynamics: Jamming Is Not Just Cool Any More*. *Nature*, vol. 396, no. 6706, pages 21–22, 1998. (Cited on pages 33 and 165.)
- [Liu 2007] J. Liu, G. H. Koenderink, K. E. Kasza, F. C. MacKintosh and D. A. Weitz. *Visualizing the Strain Field in Semiflexible Polymer Networks: Strain Fluctuations and Nonlinear Rheology of F-Actin Gels*. *Physical Review Letters*, vol. 98, no. 19, May 2007. (Cited on page 5.)
- [Lockner 2002] David A. Lockner and Nicholas M. Beeler. *Rock Failure and Earthquakes*. *International Geophysics Series*, vol. 81, no. A, pages 505–538, 2002. (Cited on page 4.)
- [Louhichi 2015] Ameer Louhichi, Elisa Tamborini, Julian Oberdisse, Luca Cipelletti and Laurence Ramos. *Viscoelasticity of Colloidal Polycrystals Doped with Impurities*. *Physical Review E*, vol. 92, no. 3, September 2015. (Cited on page 8.)
- [Lu 1993] Edward T. Lu, Russell J. Hamilton, J. M. McTiernan and Kenneth R. Brummund. *Solar Flares and Avalanches in Driven Dissipative Systems*. *The Astrophysical Journal*, vol. 412, pages 841–852, August 1993. (Cited on page 27.)
- [Lund 2001] Jay R. Lund and Joseph P. Byrne. *Leonardo Da Vinci's Tensile Strength Tests: Implications for the Discovery of Engineering Mechanics*. *Civil Engineering Systems*, vol. 18, no. 3, pages 243–250, 2001. (Cited on page 13.)
- [Ma 1996] L. Ma and G.V. Barbosa-Cánovas. *Simulating Viscoelastic Properties of Selected Food Gums and Gum Mixtures Using a Fractional Derivative Model*. *Journal of texture studies*, vol. 27, no. 3, pages 307–325, 1996. (Cited on pages 5, 7 and 102.)

- [Macosko 1994] Christopher W. Macosko. Rheology: Principles, measurements, and applications. Advances in interfacial engineering series. VCH, New York, 1994. (Cited on pages 11, 61, 62 and 65.)
- [Maekawa 2016] K. Maekawa, X. Zhu, N. Chijiwa and S. Tanabe. *Mechanism of Long-Term Excessive Deformation and Delayed Shear Failure of Underground RC Box Culverts*. Journal of Advanced Concrete Technology, vol. 14, pages 183–204, 2016. (Cited on pages 4 and 21.)
- [Mainardi 2010] F. Mainardi. Fractional calculus and waves in linear viscoelasticity: An introduction to mathematical models. Imperial College Press, London ; Hackensack, NJ, 2010. OCLC: ocn619938514. (Cited on page 21.)
- [Manley 2005] S. Manley, J. M. Skotheim, L. Mahadevan and D. A. Weitz. *Gravitational Collapse of Colloidal Gels*. Physical Review Letters, vol. 94, no. 21, June 2005. (Cited on page 109.)
- [Manneville 2004] S. Manneville, L. Becu and A. Colin. *High-Frequency Ultrasonic Speckle Velocimetry in Sheared Complex Fluids*. The European Physical Journal Applied Physics, vol. 28, no. 3, pages 361–373, December 2004. (Cited on page 29.)
- [Martens 2011] Kirsten Martens, Lydéric Bocquet and Jean-Louis Barrat. *Connecting Diffusion and Dynamical Heterogeneities in Actively Deformed Amorphous Systems*. Physical Review Letters, vol. 106, no. 15, April 2011. (Cited on page 10.)
- [Martin 1988] James E. Martin, Douglas Adolf and Jess P. Wilcoxon. *Viscoelasticity of Near-Critical Gels*. Physical review letters, vol. 61, no. 22, page 2620, 1988. (Cited on page 102.)
- [Martin 1991] J. E. Martin and D. Adolf. *The Sol-Gel Transition in Chemical Gels*. Annual review of physical chemistry, vol. 42, pages 311–339, 1991. (Cited on page 102.)
- [Marty 2005] G. Marty and O. Dauchot. *Subdiffusion and Cage Effect in a Sheared Granular Material*. Physical Review Letters, vol. 94, no. 1, January 2005. (Cited on page 9.)
- [Mason 1996] T. G. Mason, J. Bibette and D. A. Weitz. *Yielding and Flow of Monodisperse Emulsions*. Journal of Colloid and Interface Science, vol. 179, no. 2, pages 439–448, 1996. (Cited on pages 5 and 8.)
- [Masschaele 2009] Kasper Masschaele, Jan Fransaer and Jan Vermant. *Direct Visualization of Yielding in Model Two-Dimensional Colloidal Gels Subjected to Shear Flow*. Journal of Rheology, vol. 53, no. 6, page 1437, 2009. (Cited on pages 17 and 19.)

- [Mauroy 2004] B. Mauroy, M. Filoche, E. R. Weibel and B. Sapoval. *An Optimal Bronchial Tree May Be Dangerous*. Nature, vol. 427, no. 6975, pages 633–636, February 2004. (Cited on page 102.)
- [McEvoy 1985] H. McEvoy, S. B. Ross-Murphy and A. H. Clark. *Large Deformation and Ultimate Properties of Biopolymer Gels: 1. Single Biopolymer Component Systems*. Polymer, vol. 26, no. 10, pages 1483–1492, 1985. (Cited on page 5.)
- [McGuire 2005] Jeffrey J. McGuire, Margaret S. Boettcher and Thomas H. Jordan. *Fore-shock Sequences and Short-Term Earthquake Predictability on East Pacific Rise Transform Faults*. Nature, vol. 434, no. 7032, pages 457–461, 2005. (Cited on pages 4, 5, 10 and 26.)
- [Metzler 1995] Ralf Metzler, Winfried Schick, HannsGeorg Kilian and Theo F. Nonnenmacher. *Relaxation in Filled Polymers: A Fractional Calculus Approach*. The Journal of Chemical Physics, vol. 103, no. 16, pages 7180–7186, October 1995. (Cited on pages 7 and 102.)
- [Metzler 2003] Ralf Metzler and Theo F. Nonnenmacher. *Fractional Relaxation Processes and Fractional Rheological Models for the Description of a Class of Viscoelastic Materials*. International Journal of Plasticity, vol. 19, no. 7, pages 941–959, 2003. (Cited on page 7.)
- [Miguel 2002] M.-Carmen Miguel, Alessandro Vespignani, Michael Zaiser and Stefano Zapperi. *Dislocation Jamming and Andrade Creep*. Physical Review Letters, vol. 89, no. 16, September 2002. (Cited on pages 7, 21 and 103.)
- [Miyazaki 2006] K Miyazaki, H. M Wyss, D. A Weitz and D. R Reichman. *Nonlinear Viscoelasticity of Metastable Complex Fluids*. Europhysics Letters (EPL), vol. 75, no. 6, pages 915–921, September 2006. (Cited on pages 9, 33, 68, 132, 148, 153 and 154.)
- [Moghimi 2017] Esmaeel Moghimi, Alan R. Jacob, Nick Koumakis and George Petekidis. *Colloidal Gels Tuned by Oscillatory Shear*. Soft Matter, vol. 13, no. 12, pages 2371–2383, 2017. (Cited on pages 8, 34, 130, 131 and 133.)
- [Mohraz 2005] Ali Mohraz and Michael J. Solomon. *Orientation and Rupture of Fractal Colloidal Gels during Start-up of Steady Shear Flow*. Journal of Rheology, vol. 49, no. 3, page 657, 2005. (Cited on pages 16, 17, 30 and 137.)
- [Monkman 1956] F.C. Monkman and N.J. Grant. *An Empirical Relationship between Rupture Life and Minimum Creep Rate in Creep-Rupture Tests*. Proceedings-American society for testing and materials, vol. 56, pages 593–620, 1956. (Cited on page 26.)

- [Moreira 2011] R. Moreira, F. Chenlo and M.D. Torres. *Rheology of Commercial Chestnut Flour Doughs Incorporated with Gelling Agents*. Food Hydrocolloids, vol. 25, no. 5, pages 1361–1371, July 2011. (Cited on pages 5, 7, 102 and 103.)
- [Morin 1853] A. J. Morin. *Résistance des matériaux*. (Leçons de mécanique pratique). Librairie de L. Hachette et Cie, 1853. (Cited on page 14.)
- [Muthukumar 1989] M. Muthukumar. *Screening Effect on Viscoelasticity near the Gel Point*. Macromolecules, vol. 22, no. 12, pages 4656–4658, 1989. (Cited on pages 102 and 115.)
- [Myers 2001] C. R. Myers and J. P. Sethna. *Crackling Noise*. Nature, vol. 410, page 242, March 2001. (Cited on pages 3 and 27.)
- [Nabarro 2001] F. R. N. Nabarro. *The Time Constant of Logarithmic Creep and Relaxation*. Materials Science and Engineering: A, vol. 309, pages 227–228, 2001. (Cited on pages 21 and 23.)
- [Nagazi 2016] Y. Nagazi, G. Brambilla, G. Meunier, P. Margueres, J.N. Périé and L. Cipelletti. *Space-Resolved Diffusing Wave Spectroscopy Measurements of the Macroscopic Deformation and the Microscopic Dynamics in Tensile Strain Tests*. Optics and Lasers in Engineering, 2016. (Cited on page 44.)
- [Nakasato 1980] F. Nakasato and M. Takahashi. *Delayed-Failure Analysis of High-Strength Structural Bolts*. Metals Technology, vol. 7, no. 1, pages 449–455, January 1980. (Cited on page 4.)
- [Nam 2012] Koo Hyun Nam, Il H. Park and Seung Hwan Ko. *Patterning by Controlled Cracking*. Nature, vol. 485, no. 7397, pages 221–224, May 2012. (Cited on page 3.)
- [Nechad 2005a] H. Nechad, A. Helmstetter, R. El Guerjouma and D. Sornette. *Andrade and Critical Time-to-Failure Laws in Fiber-Matrix Composites: Experiments and Model*. Journal of the Mechanics and Physics of Solids, vol. 53, no. 5, pages 1099–1127, May 2005. (Cited on pages 27 and 28.)
- [Nechad 2005b] H. Nechad, A. Helmstetter, R. El Guerjouma and D. Sornette. *Creep Ruptures in Heterogeneous Materials*. Physical Review Letters, vol. 94, no. 4, January 2005. (Cited on pages 4, 7, 21, 26, 27, 28, 31 and 103.)
- [Ng 2008] Trevor S. K. Ng and Gareth H. McKinley. *Power Law Gels at Finite Strains: The Nonlinear Rheology of Gluten Gels*. Journal of Rheology, vol. 52, no. 2, pages 417–449, March 2008. (Cited on pages 5, 7, 102 and 103.)
- [Ōnaka 2013] Michiyasu Ōnaka. *The physics of rock failure and earthquakes*. Cambridge University Press, Cambridge, 2013. (Cited on page 4.)

- [Papanikolaou 2011] Stefanos Papanikolaou, Felipe Bohn, Rubem Luis Sommer, Gianfranco Durin, Stefano Zapperi and James P. Sethna. *Universality beyond Power Laws and the Average Avalanche Shape*. Nature Physics, vol. 7, no. 4, pages 316–320, April 2011. (Cited on page 27.)
- [Paredes 2013] Jose Paredes, Matthias A. J. Michels and Daniel Bonn. *Rheology across the Zero-Temperature Jamming Transition*. Physical Review Letters, vol. 111, no. 1, July 2013. (Cited on page 103.)
- [Park 2013] J. D. Park and K. H. Ahn. *Structural Evolution of Colloidal Gels at Intermediate Volume Fraction under Start-up of Shear Flow*. Soft Matter, vol. 9, no. 48, page 11650, 2013. (Cited on page 19.)
- [Park 2017] Jun Dong Park, Kyung Hyun Ahn and Norman J. Wagner. *Structure-Rheology Relationship for a Homogeneous Colloidal Gel under Shear Startup*. Journal of Rheology, vol. 61, no. 1, pages 117–137, January 2017. (Cited on pages 19 and 137.)
- [Parsons 1976] W. B. Parsons and R. S. Woodbury. *Engineers and Engineering in the Renaissance*. The MIT Press, London, 2nd edition édition, March 1976. (Cited on page 12.)
- [Patra 2016] Subir Patra and Sourav Banerjee. *Progressive Damage State Evolution and Quantification in Composites*. In Tribikram Kundu, editeur, Health Monitoring of Structural and Biological Systems, page 98050M, April 2016. (Cited on page 4.)
- [Patricio 2015] P. Patricio, C. R. Leal, J. Duarte and C. Januario. *Rheology of the Cytoskeleton as a Fractal Network*. Physical Review E, vol. 92, no. 4, October 2015. (Cited on page 7.)
- [Payne 1963] A. R. Payne. *Dynamic Properties of Heat-Treated Butyl Vulcanizates*. Journal of Applied Polymer Science, vol. 7, no. 3, pages 873–885, 1963. (Cited on page 8.)
- [Perge 2014] C. Perge, N. Taberlet, T. Gibaud and S. Manneville. *Time Dependence in Large Amplitude Oscillatory Shear: A Rheo-Ultrasonic Study of Fatigue Dynamics in a Colloidal Gel*. Journal of Rheology, vol. 58, no. 5, pages 1331–1357, September 2014. (Cited on pages 8, 40, 41, 42 and 135.)
- [Petekidis 2002a] G. Petekidis, A. Moussaïd and P. N. Pusey. *Rearrangements in Hard-Sphere Glasses under Oscillatory Shear Strain*. Physical Review E, vol. 66, no. 5, November 2002. (Cited on pages 9, 38, 39, 43 and 139.)
- [Petekidis 2002b] G. Petekidis, P. N. Pusey, A. Moussaïd, S. Egelhaaf and W. C. K. Poon. *Shear-Induced Yielding and Ordering in Concentrated Particle Suspensions*.

- Physica A: Statistical Mechanics and its Applications, vol. 306, pages 334–342, April 2002. (Cited on page 38.)
- [Petekidis 2003] Georgios Petekidis, Dimitris Vlassopoulos and Peter N. Pusey. *Yielding and Flow of Colloidal Glasses*. Faraday Discussions, vol. 123, pages 287–302, January 2003. (Cited on pages 8, 38 and 153.)
- [Petekidis 2004] G Petekidis, D Vlassopoulos and P N Pusey. *Yielding and Flow of Sheared Colloidal Glasses*. Journal of Physics: Condensed Matter, vol. 16, no. 38, pages S3955–S3963, September 2004. (Cited on page 153.)
- [Pham Trong 2008] Liem Chau Pham Trong, Madeleine Djabourov and Alain Ponton. *Mechanisms of Micellization and Rheology of PEO–PPO–PEO Triblock Copolymers with Various Architectures*. Journal of Colloid and Interface Science, vol. 328, no. 2, pages 278–287, December 2008. (Cited on pages 8 and 9.)
- [Philippe 2016] A. Philippe, S. Aime, V. Roger, R. Jelinek, G. Prévot, L. Berthier and L. Cipelletti. *An Efficient Scheme for Sampling Fast Dynamics at a Low Average Data Acquisition Rate*. Journal of Physics: Condensed Matter, vol. 28, no. 7, page 075201, 2016. (Cited on page 175.)
- [Phillips 1905] Percy Phillips. *XLIX. The Slow Stretch in Indiarubber, Glass, and Metal Wires When Subjected to a Constant Pull*. The London, Edinburgh, and Dublin Philosophical Magazine and Journal of Science, vol. 9, no. 52, pages 513–531, 1905. (Cited on page 21.)
- [Pine 2005] D. J. Pine, J. P. Gollub, J. F. Brady and A. M. Leshansky. *Chaos and Threshold for Irreversibility in Sheared Suspensions*. Nature, vol. 438, no. 7070, pages 997–1000, December 2005. (Cited on page 38.)
- [Plazek 1960] Donald J. Plazek. *Dynamic Mechanical and Creep Properties of a 23% Cellulose Nitrate Solution; Andrade Creep in Polymeric Systems*. Journal of Colloid Science, vol. 15, no. 1, pages 50–75, 1960. (Cited on pages 7, 21 and 102.)
- [Poirier 1985] Jean-Paul Poirier. *Creep of crystals*. Cambridge University Press, 1985. (Cited on pages 4, 7, 21, 103 and 134.)
- [Poncelet 1839] J. V. Poncelet. *Mécanique industrielle*. 1839. (Cited on page 21.)
- [Poon 1999] W. CK Poon, LAURA Starrs, S. P. Meeker, A. Moussaid, R. ML Evans, P. N. Pusey and M. M. Robins. *Delayed Sedimentation of Transient Gels in Colloid–polymer Mixtures: Dark-Field Observation, Rheology and Dynamic Light Scattering Studies*. Faraday Discussions, vol. 112, pages 143–154, 1999. (Cited on pages 4 and 5.)

- [Pouliquen 2003] O. Pouliquen, M. Belzons and M. Nicolas. *Fluctuating Particle Motion during Shear Induced Granular Compaction*. Physical Review Letters, vol. 91, no. 1, July 2003. (Cited on page 9.)
- [Pouzot 2006] M. Pouzot, T. Nicolai, L. Benyahia and D. Durand. *Strain Hardening and Fracture of Heat-Set Fractal Globular Protein Gels*. Journal of Colloid and Interface Science, vol. 293, no. 2, pages 376–383, January 2006. (Cited on page 16.)
- [Pradhan 2002] S. Pradhan, P. Bhattacharyya and B. K. Chakrabarti. *Dynamic Critical Behavior of Failure and Plastic Deformation in the Random Fiber Bundle Model*. Physical Review E, vol. 66, no. 1, July 2002. (Cited on page 10.)
- [Pradhan 2003] Srutarshi Pradhan and Bikas K. Chakrabarti. *Failure Due to Fatigue in Fiber Bundles and Solids*. Physical Review E, vol. 67, no. 4, April 2003. (Cited on page 10.)
- [Pradhan 2005] Srutarshi Pradhan, Alex Hansen and Per C. Hemmer. *Crossover Behavior in Burst Avalanches: Signature of Imminent Failure*. Physical Review Letters, vol. 95, no. 12, September 2005. (Cited on pages 3, 21 and 27.)
- [Pradhan 2010] S. Pradhan, A. Hansen and B. K. Chakrabarti. *Failure Processes in Elastic Fiber Bundles*. Reviews of Modern Physics, vol. 82, no. 1, pages 499–555, March 2010. (Cited on pages 10 and 28.)
- [Preston 1942] F. W. Preston. *The Mechanical Properties of Glass*. Journal of Applied Physics, vol. 13, no. 10, pages 623–634, October 1942. (Cited on page 4.)
- [Priezjev 2016] Nikolai V. Priezjev. *Reversible Plastic Events during Oscillatory Deformation of Amorphous Solids*. Physical Review E, vol. 93, no. 1, January 2016. (Cited on page 9.)
- [Priezjev 2017] Nikolai V. Priezjev. *Collective Nonaffine Displacements in Amorphous Materials during Large-Amplitude Oscillatory Shear*. Physical Review E, vol. 95, no. 2, page 023002, 2017. (Cited on page 9.)
- [Pusey 1978] P. N. Pusey. *Intensity Fluctuation Spectroscopy of Charged Brownian Particles: The Coherent Scattering Function*. Journal of Physics A: Mathematical and General, vol. 11, no. 1, page 119, 1978. (Cited on page 57.)
- [Radhakrishnan 2016] R. Radhakrishnan and S. M. Fielding. *Shear Banding of Soft Glassy Materials in Large Amplitude Oscillatory Shear*. Physical Review Letters, vol. 117, no. 18, October 2016. (Cited on page 9.)
- [Raghavan 1995] Srinivasa R. Raghavan and Saad A. Khan. *Shear-Induced Microstructural Changes in Flocculated Suspensions of Fumed Silica*. Journal of Rheology, vol. 39, no. 6, pages 1311–1325, November 1995. (Cited on page 8.)

- [Raghavan 1997] Srinivasa R. Raghavan and Saad A. Khan. *Shear-Thickening Response of Fumed Silica Suspensions under Steady and Oscillatory Shear*. Journal of colloid and interface science, vol. 185, no. 1, pages 57–67, 1997. (Cited on page 8.)
- [Ramos 2001] Laurence Ramos and Luca Cipelletti. *Ultraslow Dynamics and Stress Relaxation in the Aging of a Soft Glassy System*. Physical Review Letters, vol. 87, no. 24, November 2001. (Cited on pages 152 and 158.)
- [Regev 2015] Ido Regev, John Weber, Charles Reichhardt, Karin A. Dahmen and Turab Lookman. *Reversibility and Criticality in Amorphous Solids*. Nature Communications, vol. 6, page 8805, November 2015. (Cited on page 9.)
- [Reichman 2005] D. R. Reichman and P. Charbonneau. *Mode-Coupling Theory*. Journal of Statistical Mechanics: Theory and Experiment, vol. 2005, no. 05, page P05013, 2005. (Cited on page 40.)
- [Reiweger 2010] Ingrid Reiweger, Jürg Schweizer, Robert Ernst and Jürg Dual. *Load-Controlled Test Apparatus for Snow*. Cold Regions Science and Technology, vol. 62, no. 2-3, pages 119–125, July 2010. (Cited on page 4.)
- [Reufer 2009] M. Reufer, P. Diaz-Leyva, I. Lynch and F. Scheffold. *Temperature-Sensitive Poly(N-Isopropyl-Acrylamide) Microgel Particles: A Light Scattering Study*. The European Physical Journal E, vol. 28, no. 2, pages 165–171, February 2009. (Cited on page 149.)
- [Rich 2011] Jason P. Rich, Gareth H. McKinley and Patrick S. Doyle. *Size Dependence of Microprobe Dynamics during Gelation of a Discotic Colloidal Clay*. Journal of Rheology, vol. 55, no. 2, pages 273–299, March 2011. (Cited on page 102.)
- [Richardson 1996] M. O. W. Richardson and M. J. Wisheart. *Review of Low-Velocity Impact Properties of Composite Materials*. Composites Part A: Applied Science and Manufacturing, vol. 27, no. 12, pages 1123–1131, 1996. (Cited on page 4.)
- [Ritchie 2011] Robert O. Ritchie. *The Conflicts between Strength and Toughness*. Nature Materials, vol. 10, no. 11, pages 817–822, October 2011. (Cited on page 9.)
- [Rogers 2011] Simon A. Rogers, Brian M. Erwin, Dimitris Vlassopoulos and Michel Cloitre. *Oscillatory Yielding of a Colloidal Star Glass*. Journal of Rheology, vol. 55, no. 4, page 733, 2011. (Cited on pages 8, 32, 40 and 153.)
- [Rogers 2014] Michael C. Rogers, Kui Chen, Lukasz Andrzejewski, Suresh Narayanan, Subramanian Ramakrishnan, Robert L. Leheny and James L. Harden. *Echoes in X-Ray Speckles Track Nanometer-Scale Plastic Events in Colloidal Gels under Shear*. Physical Review E, vol. 90, no. 6, December 2014. (Cited on pages 9, 44, 139 and 143.)

- [Ronda 2013] Felicidad Ronda, Sandra Perez-Quirce, Alessandro Angioloni and Concha Collar. *Impact of Viscous Dietary Fibres on the Viscoelastic Behaviour of Gluten-Free Formulated Rice Doughs: A Fundamental and Empirical Rheological Approach*. Food Hydrocolloids, vol. 32, no. 2, pages 252–262, August 2013. (Cited on pages 7, 102 and 103.)
- [Rosti 2010] Jari Rosti, Juha Koivisto, Lasse Laurson and Mikko J. Alava. *Fluctuations and Scaling in Creep Deformation*. Physical Review Letters, vol. 105, no. 10, August 2010. (Cited on pages 21, 26, 28 and 31.)
- [Saint-Michel 2017] Brice Saint-Michel, Thomas Gibaud and Sebastien Manneville. *Predicting and Assessing Rupture in Protein Gels under Oscillatory Shear*. Soft Matter, vol. 13, no. 14, pages 2643–2653, 2017. (Cited on pages 29, 42 and 135.)
- [Salmon 2004] J.-B. Salmon, A. Colin and S. Manneville. *A Spatio-Temporal Study of Rheo-Oscillations in a Sheared Lamellar Phase Using Ultrasound*. The European Physical Journal E - Soft Matter, vol. 13, no. 2, pages 197–212, February 2004. (Cited on page 29.)
- [Sancaktar 1985] Erol Sancaktar and Steven C. Schenck. *Material Characterization of Structural Adhesives in the Lap Shear Mode. 2. Temperature-Dependent Delayed Failure*. Industrial & Engineering Chemistry Product Research and Development, vol. 24, no. 2, pages 257–263, 1985. (Cited on page 4.)
- [Schall 2007] Peter Schall, David A. Weitz and Frans Spaepen. *Structural Rearrangements That Govern Flow in Colloidal Glasses*. Science, vol. 318, no. 5858, pages 1895–1899, December 2007. (Cited on page 33.)
- [Schiessel 2000] H. Schiessel, C. Friedrich and A. Blumen. *Applications to Problems in Polymer Physics and Rheology*. In Applications of Fractional Calculus in Physics. R. Hilfer, 2000. (Cited on page 64.)
- [Schmoller 2013] Kurt M. Schmoller and Andreas R. Bausch. *Similar Nonlinear Mechanical Responses in Hard and Soft Materials*. Nature materials, vol. 12, no. 4, pages 278–281, 2013. (Cited on page 6.)
- [Schoenholz 2014] S.S. Schoenholz, A.J. Liu, R.A. Riggleman and J. Rottler. *Understanding Plastic Deformation in Thermal Glasses from Single-Soft-Spot Dynamics*. Physical Review X, vol. 4, no. 3, July 2014. (Cited on page 21.)
- [Sciortino 2005] F. Sciortino and P. Tartaglia. *Glassy Colloidal Systems*. Advances in Physics, vol. 54, no. 6-7, pages 471–524, September 2005. (Cited on page 148.)
- [Senff 1999] H. Senff and W. Richtering. *Temperature Sensitive Microgel Suspensions: Colloidal Phase Behavior and Rheology of Soft Spheres*. The Journal of Chemical Physics, vol. 111, no. 4, pages 1705–1711, July 1999. (Cited on pages 148 and 149.)

- [Sentjabrskaja 2015] T. Sentjabrskaja, P. Chaudhuri, M. Hermes, W. C. K. Poon, J. Horbach, S. U. Egelhaaf and M. Laurati. *Creep and Flow of Glasses: Strain Response Linked to the Spatial Distribution of Dynamical Heterogeneities*. Scientific Reports, vol. 5, page 11884, July 2015. (Cited on pages 4, 5, 7, 31 and 103.)
- [Shan 2004] Z. Shan. *Grain Boundary-Mediated Plasticity in Nanocrystalline Nickel*. Science, vol. 305, no. 5684, pages 654–657, July 2004. (Cited on page 134.)
- [Shen 2013] Jing Jin Shen, Cheng Gang Li, Hong Tao Wu and Masoud Kalantari. *Fractional Order Viscoelasticity in Characterization for Atrial Tissue*. Korea-Australia Rheology Journal, vol. 25, no. 2, pages 87–93, May 2013. (Cited on pages 7 and 102.)
- [Shih 1990] Wei-Heng Shih, Wan Y. Shih, Seong-Il Kim, Jun Liu and Ilhan A. Aksay. *Scaling Behavior of the Elastic Properties of Colloidal Gels*. Physical review A, vol. 42, no. 8, page 4772, 1990. (Cited on page 19.)
- [Siebenbürger 2012] M. Siebenbürger, M. Ballauff and Th. Voigtmann. *Creep in Colloidal Glasses*. Physical Review Letters, vol. 108, no. 25, June 2012. (Cited on pages 4, 5, 7, 21, 22, 23 and 103.)
- [Sinha 1988] Nirmal K. Sinha. *Crack-Enhanced Creep in Polycrystalline Material: Strain-Rate Sensitive Strength and Deformation of Ice*. Journal of materials science, vol. 23, no. 12, pages 4415–4428, 1988. (Cited on page 4.)
- [Sinkus 2007] Ralph Sinkus, Katja Siegmann, Tanja Xydeas, Mickael Tanter, Claus Claussen and Mathias Fink. *MR Elastography of Breast Lesions: Understanding the Solid/Liquid Duality Can Improve the Specificity of Contrast-Enhanced MR Mammography*. Magnetic Resonance in Medicine, vol. 58, no. 6, pages 1135–1144, December 2007. (Cited on page 7.)
- [Skrzeszewska 2010] Paulina J. Skrzyszewska, Joris Sprakel, Frits A. de Wolf, Remco Fokkink, Martien A. Cohen Stuart and Jasper van der Gucht. *Fracture and Self-Healing in a Well-Defined Self-Assembled Polymer Network*. Macromolecules, vol. 43, no. 7, pages 3542–3548, April 2010. (Cited on pages 4, 5 and 16.)
- [Slotterback 2012] Steven Slotterback, Mitch Mailman, Krisztian Ronaszegi, Martin van Hecke, Michelle Girvan and Wolfgang Losert. *Onset of Irreversibility in Cyclic Shear of Granular Packings*. Physical Review E, vol. 85, no. 2, February 2012. (Cited on page 9.)
- [Smith 2007] P. A. Smith, G. Petekidis, S. U. Egelhaaf and W. C. K. Poon. *Yielding and Crystallization of Colloidal Gels under Oscillatory Shear*. Physical Review E, vol. 76, no. 4, October 2007. (Cited on page 139.)

- [Sollich 1997] Peter Sollich, François Lequeux, Pascal Hébraud and Michael E. Cates. *Rheology of Soft Glassy Materials*. Physical review letters, vol. 78, no. 10, page 2020, 1997. (Cited on pages 117 and 148.)
- [Sollich 1998] Peter Sollich. *Rheological Constitutive Equation for a Model of Soft Glassy Materials*. Physical Review E, vol. 58, no. 1, page 738, 1998. (Cited on pages 9, 40, 102, 118 and 132.)
- [Sommerfeld 1982] R.A. Sommerfeld. *A Review of Snow Acoustics*. Reviews of Geophysics, vol. 20, no. 1, pages 62–66, 1982. (Cited on pages 4 and 5.)
- [Sommerfeld 1983] R. A. Sommerfeld and H. Gubler. *Snow Avalanches and Acoustic Emissions*. Annals of Glaciology, vol. 4, no. 1, pages 271–276, 1983. (Cited on pages 4 and 27.)
- [Sorensen 1999] C. M. Sorensen and G. M. Wang. *Size Distribution Effect on the Power Law Regime of the Structure Factor of Fractal Aggregates*. Physical Review E, vol. 60, no. 6, page 7143, 1999. (Cited on page 56.)
- [Sornette 1992] Didier Sornette and Christian Vanneste. *Dynamics and Memory Effects in Rupture of Thermal Fuse Networks*. Physical review letters, vol. 68, no. 5, page 612, 1992. (Cited on page 10.)
- [Spagnolie 2015] S. E. Spagnolie, editeur. *Complex Fluids in Biological Systems*. Biological and Medical Physics, Biomedical Engineering. Springer New York, New York, NY, 2015. (Cited on page 6.)
- [Sprakel 2011] Joris Sprakel, Stefan B. Lindström, Thomas E. Kodger and David A. Weitz. *Stress Enhancement in the Delayed Yielding of Colloidal Gels*. Physical review letters, vol. 106, no. 24, page 248303, 2011. (Cited on pages 4, 5 and 6.)
- [Stokes 2012] J. R. Stokes. *'Oral' Rheology*. In *Food Oral Processing: Fundamentals of Eating and Sensory Perception*, page 390. Wiley Blackwell, Hoboken, 2012. (Cited on page 6.)
- [Storm 2005] C. Storm, J. J. Pastore, F. C. MacKintosh, T. C. Lubensky and P. A. Janmey. *Nonlinear Elasticity in Biological Gels*. Nature, vol. 435, no. 7039, page nature03521, May 2005. (Cited on page 16.)
- [Subramanian 2006] R. Subramanian, K. Muthukumarappan and S. Gunasekaran. *Linear Viscoelastic Properties of Regular- and Reduced-Fat Pasteurized Process Cheese During Heating and Cooling*. International Journal of Food Properties, vol. 9, no. 3, pages 377–393, September 2006. (Cited on pages 7, 102 and 103.)
- [Swanson 1983] D. A. Swanson, T. J. Casadevall, D. Dzurisin, S. D. Malone, C. G. Newhall and C. S. Weaver. *Predicting Eruptions at Mount St. Helens, June 1980*

- Through December 1982*. Science, vol. 221, no. 4618, pages 1369–1376, September 1983. (Cited on page 4.)
- [Tamborini 2012] E. Tamborini and L. Cipelletti. *Multiangle static and dynamic light scattering in the intermediate scattering angle range*. Review of Scientific Instruments, vol. 83, no. 9, page 093106, 2012. (Cited on pages 52, 53, 107 and 137.)
- [Tang 2001] S. Tang, Y. Ma and C. Shiu. *Modelling the Mechanical Strength of Fractal Aggregates*. Colloids and surfaces A: Physicochemical and Engineering aspects, vol. 180, no. 1, pages 7–16, 2001. (Cited on page 132.)
- [Tapadia 2006] Prashant Tapadia, Sham Ravindranath and Shi-Qing Wang. *Banding in Entangled Polymer Fluids under Oscillatory Shearing*. Physical Review Letters, vol. 96, no. 19, May 2006. (Cited on page 67.)
- [Taylor 1934] G. I. Taylor. *The Formation of Emulsions in Definable Fields of Flow*. Proceedings of the Royal Society of London A: Mathematical, Physical and Engineering Sciences, vol. 146, no. 858, pages 501–523, October 1934. (Cited on pages 14 and 15.)
- [Tewari 1999] Shubha Tewari, Dylan Schiemann, Douglas J. Durian, Charles M. Knobler, Stephen A. Langer and Andrea J. Liu. *Statistics of Shear-Induced Rearrangements in a Two-Dimensional Model Foam*. Physical Review E, vol. 60, no. 4, page 4385, 1999. (Cited on page 27.)
- [Timoshenko 1953] S. P. Timoshenko. History of strength of materials. McGraw-Hill, 1953. (Cited on pages 12, 13, 14 and 20.)
- [Tirtaatmadja 1997] V. Tirtaatmadja, K. C. Tam and R. D. Jenkins. *Superposition of Oscillations on Steady Shear Flow as a Technique for Investigating the Structure of Associative Polymers*. Macromolecules, vol. 30, no. 5, pages 1426–1433, 1997. (Cited on pages 8 and 102.)
- [Tomkins 1981] B. Tomkins, H. K. Grover and T. G. F. Gray. *Subcritical Crack Growth: Fatigue, Creep and Stress Corrosion Cracking*. Philosophical Transactions of the Royal Society of London A: Mathematical, Physical and Engineering Sciences, vol. 299, no. 1446, pages 31–44, January 1981. (Cited on page 30.)
- [Trappe 2001] V. Trappe, V. Prasad, L. Cipelletti, P. N. Segre and D. A. Weitz. *Jamming Phase Diagram for Attractive Particles*. Nature, vol. 411, no. 6839, pages 772–775, June 2001. (Cited on page 33.)
- [Traxler 1939] R. N. Traxler. *Everything Flows*. Scientific American, vol. 160, no. 1, pages 16–18, 1939. (Cited on page 59.)

- [Troiano 1959] Alexander R. Troiano. *Delayed Failure of High Strength Steels*. Corrosion, vol. 15, no. 4, pages 57–62, April 1959. (Cited on page 4.)
- [Troyan 2004] S. D. Troyan. *Medieval Rhetoric: A Casebook*. Routledge, London, 2004. (Cited on page 11.)
- [Truzzolillo 2015] D Truzzolillo, V Roger, C Dupas, S Mora and L Cipelletti. *Bulk and Interfacial Stresses in Suspensions of Soft and Hard Colloids*. Journal of Physics: Condensed Matter, vol. 27, no. 19, page 194103, May 2015. (Cited on page 149.)
- [Tsamados 2010] M. Tsamados. *Plasticity and Dynamical Heterogeneity in Driven Glassy Materials*. The European Physical Journal E, vol. 32, no. 2, pages 165–181, June 2010. (Cited on page 27.)
- [Van de Laar 2016] T. Van de Laar, S. Ten Klooster, K. Schroen and J. Sprakel. *Transition-State Theory Predicts Clogging at the Microscale*. Scientific Reports, vol. 6, no. 1, September 2016. (Cited on page 4.)
- [Van der Linden 2003] E. Van der Linden, L. Sagis and P. Venema. *Rheo-Optics and Food Systems*. Current Opinion in Colloid & Interface Science, vol. 8, no. 4, pages 349–358, November 2003. (Cited on page 10.)
- [Van Herwijnen 2011a] Alec Van Herwijnen and Jorg Schweizer. *Monitoring Avalanche Activity Using a Seismic Sensor*. Cold Regions Science and Technology, vol. 69, no. 2-3, pages 165–176, December 2011. (Cited on pages 4 and 27.)
- [Van Herwijnen 2011b] Alec Van Herwijnen and Jorg Schweizer. *Seismic Sensor Array for Monitoring an Avalanche Start Zone: Design, Deployment and Preliminary Results*. Journal of Glaciology, vol. 57, no. 202, pages 267–276, April 2011. (Cited on pages 4, 5, 10 and 27.)
- [Van Vliet 2013] T. Van Vliet. *Rheology and fracture mechanics of foods*. CRC Press, 2013. (Cited on page 5.)
- [Vermant 2005] J. Vermant and M. J. Solomon. *Flow-Induced Structure in Colloidal Suspensions*. Journal of Physics: Condensed Matter, vol. 17, no. 4, page R187, 2005. (Cited on pages 17 and 137.)
- [Vinogradov 2012] A. Vinogradov, I. S. Yasnikov and Y. Estrin. *Evolution of Fractal Structures in Dislocation Ensembles during Plastic Deformation*. Physical Review Letters, vol. 108, no. 20, May 2012. (Cited on page 3.)
- [Vlassopoulos 2014] Dimitris Vlassopoulos and Michel Cloitre. *Tunable Rheology of Dense Soft Deformable Colloids*. Current Opinion in Colloid & Interface Science, vol. 19, no. 6, pages 561–574, December 2014. (Cited on page 148.)

- [Vliet 1995] T. Vliet. *Large Deformation and Fracture Behaviour of Gels*. Faraday Discussions, vol. 101, pages 359–370, 1995. (Cited on page 5.)
- [Voight 1988] B. Voight. *A Method for Prediction of Volcanic Eruptions*. Nature, vol. 332, no. 6160, page 125, March 1988. (Cited on pages 4 and 5.)
- [Voigtmann 2011] Th. Voigtmann. *Yield Stresses and Flow Curves in Metallic Glass Formers and Granular Systems*. The European Physical Journal E, vol. 34, no. 9, September 2011. (Cited on page 23.)
- [Vrij 1979] A. Vrij. *Mixtures of Hard Spheres in the Percus-Yevick Approximation. Light Scattering at Finite Angles*. The Journal of Chemical Physics, vol. 71, no. 8, pages 3267–3270, October 1979. (Cited on page 56.)
- [Wagner 1998] N. J. Wagner. *Rheo-Optics*. Current Opinion in Colloid & Interface Science, vol. 3, no. 4, pages 391–400, August 1998. (Cited on page 10.)
- [Wagner 2006] B. Wagner, R. Tharmann, I. Haase, M. Fischer and A. R. Bausch. *Cytoskeletal Polymer Networks: The Molecular Structure of Cross-Linkers Determines Macroscopic Properties*. Proceedings of the National Academy of Sciences, vol. 103, no. 38, pages 13974–13978, September 2006. (Cited on page 5.)
- [Weibull 1939] W. Weibull. *A Statistical Theory of the Strength of Materials*. Ingeniors Vetenskaps Akademiens Handlingar, vol. 151, 1939. (Cited on pages 3, 13 and 21.)
- [Widmer-Cooper 2009] Asaph Widmer-Cooper, Heidi Perry, Peter Harrowell and David R. Reichman. *Localized Soft Modes and the Supercooled Liquid Irreversible Passage through Its Configuration Space*. The Journal of Chemical Physics, vol. 131, no. 19, page 194508, 2009. (Cited on page 21.)
- [Winter 1999] H. H. Winter and M. Mours. *Rheology of Polymers near Liquid-Solid Transitions*. In Advances in Polymer Science. B. Ewen, 1999. (Cited on page 102.)
- [Wu 2006] Lixin Wu, Shanjun Liu, Yuhua Wu and Chuanyin Wang. *Precursors for Rock Fracturing and Failure-Part I: IRR Image Abnormalities*. International Journal of Rock Mechanics and Mining Sciences, vol. 43, no. 3, pages 473–482, April 2006. (Cited on page 4.)
- [Wyatt 1951] O. H. Wyatt. *Transient Creep in Pure Metals*. Nature, vol. 167, no. 4256, pages 866–866, May 1951. (Cited on pages 21 and 24.)
- [Wyss 2004] Hans M. Wyss, Josef Innerlohinger, Lorenz P. Meier, Ludwig J. Gauckler and Otto Glatter. *Small-angle static light scattering of concentrated silica suspensions during in situ destabilization*. Journal of Colloid and Interface Science, vol. 271, no. 2, pages 388–399, March 2004. (Cited on page 107.)

- [Xu 2013] Zheng Xu and Wen Chen. *A Fractional-Order Model on New Experiments of Linear Viscoelastic Creep of Hami Melon*. *Computers & Mathematics with Applications*, vol. 66, no. 5, pages 677–681, September 2013. (Cited on pages 7, 102 and 103.)
- [Yamada 1975] T. Yamada and K. Kawasaki. *Application of Mode-Coupling Theory to Nonlinear Stress Tensor in Fluids*. *Progress of Theoretical Physics*, vol. 53, no. 1, pages 111–124, January 1975. (Cited on page 40.)
- [Yziquel 1999] F. Yziquel, P. J. Carreau and P. A. Tanguy. *Non-Linear Viscoelastic Behavior of Fumed Silica Suspensions*. *Rheologica Acta*, vol. 38, no. 1, pages 14–25, 1999. (Cited on page 8.)
- [Zapperi 2000] Stefano Zapperi, Hans J. Herrmann and Stéphane Roux. *Planar Cracks in the Fuse Model*. *The European Physical Journal B-Condensed Matter and Complex Systems*, vol. 17, no. 1, pages 131–136, 2000. (Cited on page 21.)
- [Zhou 1998] N. Zhou and S. J. Mulvaney. *The Effect of Milk Fat, the Ratio of Casein to Water, and Temperature on the Viscoelastic Properties of Rennet Casein Gels*. *Journal of Dairy Science*, vol. 81, no. 10, pages 2561–2571, 1998. (Cited on pages 7 and 102.)
- [Zuriguel 2015] Iker Zuriguel, Daniel Ricardo Parisi, Raul Cruz Hidalgo, Celia Lozano, Alvaro Janda, Paula Alejandra Gago, Juan Pablo Peralta, Luis Miguel Ferrer, Luis Ariel Pugnaroni, Eric Clement, Diego Maza, Ignacio Pagonabarraga and Angel Garcimartin. *Clogging Transition of Many-Particle Systems Flowing through Bottlenecks*. *Scientific Reports*, vol. 4, no. 1, May 2015. (Cited on page 4.)

Résumé: La fracture des matériaux, omniprésente aussi bien en science des matériaux qu'en géologie, implique souvent des événements soudains et imprévisibles, sans précurseurs détectables macroscopiquement. Une compréhension approfondie des mécanismes microscopiques conduisant in fine à la rupture est requise, mais les expériences restent rares. La détection de la dynamique microscopique dans les échantillons cisailés est expérimentalement très difficile, car elle nécessite de combiner sensibilité mécanique, qualité optique et exigences strictes sur l'encombrement. Dans ce travail, nous présentons l'une des premières tentatives réussies de mesure des précurseurs microscopiques de fracture dans des matériaux mous modèles, grâce à des mesures de la plasticité microscopique à l'aide d'un nouvel instrument, couplant une cellule de cisaillement à contrainte contrôlée à un appareil de diffusion de lumière statique et dynamique (DLS) à petits angles.

Dans un premier temps, nous montrons théoriquement, numériquement et expérimentalement comment la DLS, une technique très puissante mais difficile à utiliser pour un échantillon sous cisaillement, peut être utilisée comme outil de mesure de la dynamique microscopique dans les systèmes mous sous cisaillement. Pour un solide parfait et un fluide visqueux simple, le champ de déplacement résultant d'une déformation de cisaillement est purement affine. Nous montrons comment les déplacements affines et non affines, qui sont présents dans de nombreuses situations d'intérêt (matériaux élastiquement hétérogènes ou en raison de réarrangements plastiques) peuvent être évalués séparément par DLS et discutons de l'effet des non-idéalités dans des expériences typiques.

Ce travail est centré sur un gel colloïdal fractal modèle, dont nous caractérisons la rhéologie linéaire en loi de puissance. Nous montrons que celle-ci est décrite par un modèle phénoménologique Fractional Maxwell (FM), et discutons la relation possible entre FM et la structure microscopique du gel.

Sous une contrainte de cisaillement constante (expérience de fluage), le gel colloïdal présente une déformation rapide élastique suivie d'un fluage lent en loi de puissance, puis, après plusieurs heures, par une accélération du taux de cisaillement, entraînant la rupture retardée du gel. Nos expériences montrent que le premier régime en loi de puissance, bien décrit par la viscoélasticité linéaire, correspond à l'échelle microscopique à une dynamique partiellement nonaffine, mais entièrement réversible. Lorsque la viscoélasticité dévie de la linéarité, une accélération nette, localisée dans le temps, de la dynamique non-affine, est observée. Ces réarrangements rapides précèdent la fracture macroscopique du gel de plusieurs heures: ce sont des précurseurs dynamiques de la fracture qui permettent de prédire l'évolution du gel bien avant toute mesure rhéologique.

Pour obtenir une image plus complète de la fracture, nous étudions l'apparition de l'irréversibilité lors d'une perturbation cyclique répétée plusieurs fois (expérience de fatigue). En suivant l'évolution stroboscopique du système en fonction de la déformation cumulée, on constate que, au-delà du régime linéaire, le taux de relaxation augmente brusquement, signature de plasticité. Si la contrainte appliquée est suffisamment grande, le gel à long terme montre une rupture retardée, en analogie avec celle observée en fluage. Les différences et similitudes entre les deux mécanismes de fracture sont discutées.

Enfin, la généralité des résultats obtenus sur les gels colloïdaux est vérifiée en étudiant comme second système modèle un verre colloïdal, dont la mise en écoulement sous contrainte oscillante est un processus progressif, pour lequel deux modes de relaxation contribuent à la dynamique observée. Les analogies qualitatives trouvées avec des systèmes similaires (par ex. des émulsions concentrées) suggèrent qu'une image unifiée pourrait être obtenue, motivant des recherches futures.

Abstract: Material failure is ubiquitous, with implications from geology to everyday life and material science. It often involves sudden, unpredictable events, with little or no macroscopically detectable precursors. A deeper understanding of the microscopic mechanisms eventually leading to failure is clearly required, but experiments remain scarce. The detection of microscopic dynamics in samples under shear is experimentally very challenging, because it requires to combine the highest mechanical sensitivity to strict requirements on the geometry of the whole setup and on the quality of the optical interfaces. In this work we present one of the first successful attempts to measure microscopic failure precursors in model soft solids. Here, microscopic plasticity under shear is observed using a novel setup, coupling a custom-made stress controlled shear cell to small angle static and dynamic light scattering (DLS).

DLS is a very powerful technique, but its application to materials under shear is not trivial. In a first step we show a theoretical, numerical and experimental investigation of how DLS may be used as a tool to measure the microscopic dynamics in soft systems under shear. In ideal solids and simple viscous fluids, the displacement field resulting from an applied shear deformation is purely affine. Additional non-affine displacements arise in many situations of great interest, for example in elastically heterogeneous materials or due to plastic rearrangements. We show how affine and non-affine displacements can be separately resolved by DLS, and discuss the effect of several non-idealities in typical experiments.

As a model system, this work mainly focuses on a fractal colloidal gel. We thoroughly characterize the linear power-law rheology of the gel, we show that it is very accurately described by the phenomenological Fractional Maxwell (FM) model, and we discuss the possible relationship between the FM model and the microscopic structure of the gel.

Under a constant shear stress (creep experiment), the colloidal gel exhibits a fast, elastic deformation followed by a slow sublinear power-law creep, which is eventually interrupted after several hours by an upturn in the shear rate, leading to the delayed failure of the material. Our experiments show that the first power-law regime, nicely described by linear viscoelasticity, corresponds at the microscopic scale to partially nonaffine, yet fully reversible dynamics. Upon deviation from the linear viscoelasticity, a sharp acceleration, localized in time of the nonaffine dynamics is observed. These faster rearrangements precede the macroscopic failure of the gel by thousands of seconds: they thus are dynamic precursors of failure that allow one to predict the fate of the gel well before any rheological measurement.

To obtain a more comprehensive picture of material failure, we next address the onset of irreversibility under a cyclic perturbation repeated many times (fatigue experiment). By following the stroboscopic evolution of the system as a function of the cumulated deformation, we observe that as soon as the shear amplitude is increased beyond the linear regime the relaxation rate increases abruptly, indicating that irreversible plasticity is at play. If a large enough stress amplitude is applied, the system on the long run displays delayed fatigue failure, with reminiscences of the one observed in creep. Differences and similarities between the two failure mechanisms are discussed.

Finally, the generality of the results obtained on colloidal gels is checked by investigating as second model system a soft colloidal glass. In this case, our experiments indicate that oscillatory yielding is a gradual process, where two relaxation modes contribute to the observed dynamics. Qualitative analogies found with similar systems (e.g. concentrated emulsions) suggest that a general picture might be obtained with our study, which motivates ongoing and future investigations.

